UNIVERSIDADE DE LISBOA

FACULDADE DE CIÊNCIAS

DEPARTAMENTO DE GEOLOGIA

Rui Miguel Leal Miranda

PETROGENESIS AND GEOCHRONOLOGY OF THE LATE CRETACEOUS ALKALINE MAGMATISM IN THE WEST IBERIAN MARGIN

DOUTORAMENTO EM GEOLOGIA

(GEODINÂMICA INTERNA)

2010

UNIVERSIDADE DE LISBOA
FACULDADE DE CIÊNCIAS
DEPARTAMENTO DE GEOLOGIA

Rui Miguel Leal Miranda

PETROGENESIS AND GEOCHRONOLOGY OF THE LATE CRETACEOUS ALKALINE MAGMATISM IN THE WEST IBERIAN MARGIN

DOUTORAMENTO EM GEOLOGIA
(GEODINÂMICA INTERNA)

Tese orientada pelos Profs. Drs. João Mata e Pedro Terrinha

2010

Abstract

The Late Cretaceous alkaline magmatism is the most voluminous of the three cycles of magmatic activity that took place on the West Iberian Margin (WIM) during the Mesozoic. It was preceded by a tholeiitic cycle in the Early Jurassic (200-198 Ma) and by a transitional episode during the Late Jurassic-Early Cretaceous transition (147-142 Ma).

The alkaline cycle took place in a post-rift setting, after oceanic break-up, and is contemporaneous of the opening of the Bay of Biscay and consequential 35º counterclockwise rotation of Iberia, as well as with the first phases of tectonic inversion in the Mesozoic Lusitanian and Algarve Basins, as a result of the onset of the convergence and collision between the Iberian, European and African plates.

Onshore, this cycle includes the intrusive Sintra, Sines and Monchique igneous complexes, the extrusive Lisbon Volcanic Complex as well as several other minor intrusions scattered in the Lusitanian and Algarve basins, such as the Foz da Fonte sill, the Paço d'Ilhas sill, the Mafra Radial dyke complex, the Oeiras Cascais dykes and the lamprophyre-basanite suite of the littoral Algarve. It extends offshore where it is represented by the Madeira-Tore Rise and the Ormonde peak in the Gorringe Bank.

In this study, the geochronology of the Late Cretaceous onshore occurrences was updated through the acquisition of new U-Pb, $^{40}Ar/^{39}Ar$, K-Ar and Rb-Sr. The combination of these data with previously published ages allowed to better constrain the duration of this cycle (94-72 Ma), as well as for the identification of two separate magmatic pulses.

The first pulse took place between 94 and 88 Ma and is restricted to the Foz da Fonte and Paço d'Ilhas sills, both of which occur in the Lusitanian basin, between N39º and N38º20'. This pulse is contemporaneous with the opening of the Bay of Biscay and consequent rotation of Iberia (118-80 Ma).

The second pulse has a younger age (75-72 Ma,) wider geographical distribution, between the Lisbon region (≈ 39ºN) and the Algarve (≈ 37ºN), and occurred simultaneously with the initial stages of the Alpine orogeny in the WIM, which culminated in the formation of the Betics and Pyrenees as well as to the inversion of the Mesozoic basins.

The age obtained for the Sintra granite (79.2 Ma ± 0.8), is equivalent within error to the oldest age obtained for the syenite (78.3 ± 1.9 Ma, Storetvedt et al., 1987)

but older than the other K-Ar ages obtained for these rocks (76.4 ± 1.4 and 76.1 ± 1.1 Ma, Storetvedt et al., 1987) and for the gabbros (74.9 ± 1 Ma Storetvedt et al., 1987). The combination of the geochronological data with the observed field cross-cutting relations and geophysical data (gravimetry and AMS), appears to indicate that the Sintra granite corresponds to an older phase that was intruded by a more recent gabbro to syenite suite.

Geochemical analysis of samples from both pulses revealed that these rocks derive from small degrees (1-6%) of partial melting of trace element enriched garnet peridotite sources, with fairly homogenous isotopic compositions reflecting low time-integrated Rb/Sr and high Sm/Nd and U/Pb ratios, which are compatible with a sub-lithospheric origin. However, there are clear differences in the trace element abundance patterns in rocks from the first and second pulses. Samples from the second pulse show negative K, Zr, Hf and sometimes even Ti anomalies, which are absent in the first pulse and that are probably related to a metasomatic event. The metasomatic agent is likely to correspond to a melt of carbonatitic to siliceous volatile (CO_2+H_2O) rich nature that promoted, for example the stability of a hydrated K rich phase such as amphibole. Amphibole is unstable at the temperatures that characterize the asthenosphere or mantle plumes and therefore the negative K anomalies should indicate interaction of the ascending sub-lithospheric magmas the metasomatized lithospheric mantle or melting of the latter. This metasomatic signature is more noticeable in the rocks which derived from smaller fractions of melting, becoming progressively diluted as melting degree increases.

In terms of isotopic composition, no major differences are observed between the rocks of the second pulse, which show a clear metasomatic contribution, and the rocks of the first pulse which do not show such a signature. This indicates that the metasomatic agent probably originated from the same sublithospheric source which had earlier produced the magmas of the first pulse.

The differences in trace element signatures between the two pulses created by this metasomatic episode can be related to their contemporaneous geodynamic context. During the first pulse, the rotation of Iberia created a stress regime favorable to quick magma ascent while from 80 Ma onwards, the onset of continental collision restricted the opening of fractures and magma ascent, favouring the interaction of the ascending magmas with the lithosphere, probably resulting in the metasomatism of the lithospheric mantle and the formation of amphibole during or previous to the second pulse.

Uncontaminated samples show isotopic signatures ($^{87}Sr/^{86}Sr_i$ 0.7030-0.7037; εNd_i 5.7–3.7; $^{206}Pb/^{204}Pb_i$ 19.564-19.20, $^{207}Pb/^{204}Pb_i$ 15.609-15.580, $^{208}Pb/^{204}Pb_i$ 39.245-39.00) that are distinct from the previous tholeiitic and transitional cycles and point towards a sublithospheric source, unlike the previous cycles, which show an important lithospheric contribution. These signatures are also very similar to the ones observed in the rocks derived from the melting of the Canaries mantle plume, which was located near the WIM during the Late Cretaceous, according to paleogeographic reconstitutions and paleomagnetic data, and is therefore considered the most likely source for the melts and metasomatic agents that were identified in this study.

The large volume of magmatism that took place in the onshore and offshore WIM during the Late Cretaceous is also compatible with an origin from a deep seated hot mantle anomaly, such as a mantle plume. However, the differences between the volumes erupted onshore and offshore must be related to different lithospheric thicknesses in these two domains, since larger volumes of decompression melting are possible under the thinner oceanic and transitional lithospheres than under the thicker continental lithosphere. Also, the Iberian plate kinematics and pre-existing structure must have played a major role in controlling the timing and location of this magmatism, thus explaining the absence of a spatial age progression and the scattered location of the intrusive and extrusive features.

Mineral chemistry data (e.g reverse zoning) indicates that magma mixing between liquids of basic/ultrabasic and intermediate natures took place at upper mantle/lower crustal depths but that does not seem to have greatly affected the composition of the resulting magmas.

These magmas seem to have ascended to upper crustal levels by taking advantage of pre-existing fractures related with Mesozoic rifting and/or the Paleozoic Variscan orogeny. Many of these occurrences in the western Mesozoic basins seem to be related to WNW-ESE to E-W transfer faults that were active during rifting but, their exact location seems to be controlled by the intersection of these structures with other also previously existing fault systems with NE-SW and NNW-SSE orientations.

After emplacement at upper crustal levels, the rocks from both pulses seem to have evolved through combined fractional crystallization of olivine, clinopyroxene, Fe-Ti oxides and more or less plagioclase and amphibole, with assimilation of crustal lithologies. Fractionation and accumulation of some of these minerals led to specific

major and trace element characteristics of some of the intrusive rocks, such as the Sines and Sintra gabbros and the Paço d'Ilhas sill.

Assimilation seems to have been an important factor in generating the observed petrological diversity and in creating the observed radiogenic Sr ($^{87}Sr/^{86}Sr_i$ up to 0.7049), unradiogenic Nd (εNd_i as low as 3.1) and variable Pb ($^{206}Pb/^{204}Pb_i$ and $^{208}Pb/^{204}Pb_i$ decrease to 18.827 and 38.603, respectively, while $^{207}Pb/^{204}Pb_i$ increases up to 15.634) signatures seen in the more evolved rocks. Two different contamination trends are observed and thus require the existence of two different contaminants. Increasing Th/La, Zr/Nb, $^{87}Sr/^{86}Sr$, $^{207}Pb/^{204}Pb$ and K/Nb and decreasing Nb/U, $^{206}Pb/^{204}Pb$ and $^{208}Pb/^{204}Pb$ towards values closer to crustal compositions with increasing SiO_2 are related to contamination by a siliceous upper crustal lithology. The other trend is characterized by only increasing $^{87}Sr/^{86}Sr$ without causing significant changes in other isotopic ratios and is probably related to a Sr rich contaminant that is simultaneously depleted in Nd and Pb, which is likely to be of carbonated nature.

Keywords: intraplate alkaline magmatism; geochronology; geochemistry; petrogenesis; West Iberian Margin; Late Cretaceous.

Resumo

O magmatismo alcalino do Cretácico Superior constitui o mais volumoso dos três ciclos de actividade magmática que tiveram lugar na Margem Oeste Ibérica (MOI) durante o Mesozóico. Este ciclo alcalino foi antecedido por um de natureza toleítica durante o Jurássico Inferior (200-198 Ma) e outro de quimismo transicional durante o Jurásico Superior-Cretácico Inferior (147-142 Ma).

O ciclo alcalino teve lugar num contexto pós-rifting, após o início da oceanização, contemporâneo da abertura do golfo da Biscaia e consequente rotação sinistrógira de 35º da Ibéria. Coincide também com as primeiras fases de inversão das bacias Mesozóicas do Algarve e Lusitaniana, que resultam da convergência rápida das placas Ibérica, Europeia e Africana, e que se inicia no final do Cretácico.

Em terra, este ciclo encontra-se representado pelos complexos ígneos intrusivo de Sintra, Sines e Monchique, pelo Complexo Vulcânico de Lisboa, e por uma série de outras ocorrências de menor volume distribuídas pelas bacias Lusitaniana e do Algarve, como as soleiras da Foz da Fonte e de Paço d'Ilhas, o complexo filoniano radial de Mafra, os filões de Oeiras-Cascais e o magmatismo lamprofirico-basanitico do Algarve litoral, entre outras. Na parte imersa da margem este ciclo inclui a Crista Madeira-Tore, várias intrusões menores entre a montanha submarina de Tore e/no Esporão da Estremadura e o magmatismo do pico Ormonde no banco do Gorringe.

A aquisição de novas datações U-Pb, $^{40}Ar/^{39}Ar$, K-Ar e Rb-Sr permitiu a actualização da geocronologia das ocorrências da parte emersa desta província o que, em conjunto com dados previamente publicados, possibilitou um melhor constrangimento da sua duração, entre 94 e 72 Ma, e a detecção de dois pulsos independentes.

O primeiro pulso teve lugar entre os 94 e os 88 Ma e está limitado às soleiras da Foz da Fonte e de Paço d'Ilhas, que se encontram na bacia Lusitaniana entre N39º e N38º20'. Este pulso é contemporâneo da abertura da baía da Biscaia e consequente rotação da Ibéria (124-80 Ma).

O segundo pulso ocorreu entre os 75-72 Ma, tem uma distribuição geográfica mais abrangente entre a região de Lisboa (≈ 39ºN) e o Algarve (≈ 37ºN) e teve lugar durante as primeiras manifestações da orogenia Alpina na MOI, que culminou na inversão das bacias Mesozóicas e na formação das cadeias dos Pirinéus e das Béticas.

A idade obtida para o granito de Sintra (79.2 ± 0.8 Ma), é equivalente dentro do erro analítico à idade mais antiga adquirida para o sienito (78.3 ± 1.9 Ma, Storetvedt et al., 1987), mas no entanto é mais antigo que as restantes idades K-Ar obtidas para estas rochas (76.4 ± 1.4 e 76.1 ± 1.1 Ma, Storetvedt et al., 1987) e para os gabros (74.9 ± 1 Ma Storetvedt et al., 1987). Esta informação, quando combinada com as relações de corte observadas entre os corpos intrusivos de diferentes naturezas e dados geofísicos adquiridos no maciço (gravimetria e ASM), parece indicar que o granito corresponde a um lacólito formado numa fase anterior de actividade que é por sua vez intruído por uma série magmática de natureza gabróica a sienítica.

Análises geoquímicas de amostras de ambos os pulsos demonstram que estas rochas derivam de pequenas quantidades de fusão parcial (1-6%) de um peridotito granatífero ± anfíbola enriquecido em elementos incompatíveis e com uma assinatura isotópica relativamente homogénea, e compatível com fonte(s) mantélica(s) sub-litosférica(s) carcterizada(s) por baixo Rb/Sr, e alto Sm/Nd e U/Pb, integrados no tempo..

No entanto, existem diferenças importantes entre as rochas dos dois pulsos no que respeita aos padrões de elementos incompatíveis. As amostras do segundo pulso mostram anomalias negativas em K, Zr, Hf e por vezes Ti, que estão ausentes nas amostras que representam magmas não fraccionados do primeiro pulso. Estas anomalias estarão relacionadas com um evento metassomático que terá afectado o manto na região da MOI entre os dois pulsos. O agente metassomático é provavelmente de natureza carbonatítica a siliciosa rica em voláteis (CO_2+H_2O) que, entre outros efeitos terá promovido a estabilidade de anfíbola. A anfíbola não é uma fase estável às temperaturas que caracterizam a astenosfera ou as plumas mantélicas e como tal, a presença de anomalias negativas de K será indicativa da interacção dos magmas sub-litosféricos em ascensão com domínio(s) metassomatizado(s) da litosfera ou da fusão desses mesmos domínios. Esta assinatura metassomática é mais notória nas rochas derivadas de menores quantidades de fusão parcial, tornando-se progressivamente mais diluída com o aumento do grau de fusão.

Não se observam variações sistemáticas na composição isotópica entre as rochas com uma contribuição metassomática evidente (2º pulso) e as que não apresentam esse componente (1º pulso), sugerindo que a litosfera metassomatizada terá herdado a assinatura isotópica e elementar do agente metassomático e que este agente provavelmente terá tido a mesma origem dos magmas sublitosféricos do primeiro pulso.

As diferenças nas abundâncias de elementos traço entre os dois pulsos terão sido então criadas por um episódio metassomático cuja ocorrência poderá estar relacionada com os diferentes contextos geodinâmicos vigentes durante cada pulso. Durante o primeiro pulso, a rotação da Ibéria terá eventualmente criado um campo de tensões favorável à abertura de fracturas e à ascensão rápida dos magmas, enquanto que a partir dos 80 Ma, o inicio da colisão entre as placas Ibérica, Africana e Europeia terá restringido a abertura de fracturas dificultando a ascensão magmática e favorecendo assim a interacção dos magmas em ascensão com a litosfera.

Os magmas não contaminados do ciclo alcalino têm assinaturas isotópicas ($^{87}Sr/^{86}Sr_i$ 0.7030-0.7037; εNd_i 5.7–3.7; $^{206}Pb/^{204}Pb_i$ 19.564-19.20, $^{207}Pb/^{204}Pb_i$ 15.609-15.580, $^{208}Pb/^{204}Pb_i$ 39.245-39.00) que apontam para uma fonte sublitosférica, distinta das dos ciclos toleítico e transicional que o precederam, e que apresentam uma clara contribuição litosférica. Estas composições isotópicas são também muito semelhantes às apresentadas pelas rochas derivadas da fusão da pluma das Canárias. Reconstituições paleogeográficas e dados de paleomagnetismo indicam que durante o Cretácico Superior a MOI estaria localizada nas proximidades da pluma das Canárias, que poderá portanto ser considerada a fonte provável para os magmas e agentes metassomáticos aqui identificados e estudados.

O elevado volume de magmatismo produzido nas regiões imersa e emersa da MOI durante o Cretácico Superior é também compatível com uma origem a partir de uma anomalia quente e profunda como uma pluma mantélica. Neste contexto, as diferenças entre o volume de magma gerado em terra e na parte submarina devem estar relacionadas a diferenças na espessura litosférica entre estes dois domínios. A menor espessura litosférica na região imersa permitirá maiores quantidades de fusão parcial por descompressão do que na região emersa onde a litosfera será mais espessa, o que limita o volume de magma gerado. Adicionalmente, a cinemática da placa Ibérica e a estrutura pré existente deverá ter tido um papel fundamental no controlo da distribuição espacial e temporal deste magmatismo, o que explicar+a a localização dispersa das ocorrências magmáticas e a ausência de uma progressão espacial das idades neste episódio.

Os dados de química mineral (e.g. zonamentos inversos) apontam para a ocorrência de mistura entre magmas de natureza básica/ultrabásica e intermédia a profundidades correspondentes ao manto superior ou crosta inferior, embora este evento não pareça ter afectado significativamente a composição dos magmas daí resultantes.

Estes magmas parecem ter ascendido até níveis correspondentes à crosta superior através de fracturas pré existentes herdadas do rifting Mesozóico e/ou da orogenia Varisca. Muitas das ocorrências nas bacias Mesozóicas ocidentais parecem relacionadas com falhas de transferência WNW-ESE a E-W que estiveram activas durante o rifting, ainda que a sua localização exacta pareça ter sido condicionada pela intersecção destas estruturas com outros sistemas de falhas pré existentes de direcção NE-SW a NNW-SSE.

Após a instalação na crosta superior, as rochas de ambos os pulsos parecem ter evoluído através dos processos de cristalização fraccionada de olivina, clinopiroxena, óxidos de Fe-Ti e mais ou menos plagioclase e anfíbola, em conjunto com a assimilação de litologias crustais. A fraccionação e acumulação de alguns destes minerais levou à formação de cumulados com assinaturas elementares específicas, como as rochas gabróicas de Sintra e Sines e as diferentes litologias da soleira de Paço d'Ilhas.

A assimilação crustal parece ter desempenhado um papel importante na geração da diversidade petrológica observada, sendo responsável pelas assinaturas com Sr radiogénico ($^{87}Sr/^{86}Sr_i$ até 0.7049), Nd menos radiogénico (εNd_i até 3.1) e Pb variável ($^{206}Pb/^{204}Pb_i$ e $^{208}Pb/^{204}Pb_i$ descem para 18.827 e 38.603, respectivamente, enquanto que $^{207}Pb/^{204}Pb_i$ sobe até 15.634) nas rochas mais evoluídas. Foram identificadas duas tendências evolutivas nas amostras estudadas que deverão corresponder a assimilação de dois contaminantes distintos. Um de natureza siliciosa supracrustal que explicará o aumento de Th/La, Zr/Nb, $^{87}Sr/^{86}Sr$, $^{207}Pb/^{204}Pb$ e K/Nb e diminuição de Nb/U, $^{206}Pb/^{204}Pb$ e $^{208}Pb/^{204}Pb$ para valores semelhantes aos de composições crustais com o aumento simultâneo de SiO_2. Outro de provável natureza carbonatada, rico em Sr mas com concentrações baixas de Nd e Pb e que terá induzido aumento de $^{87}Sr/^{86}Sr$, sendo que este não é acompanhado por modificações significativas em outras razões isotópicas ou elementares.

Palavras-chave: magmatismo alcalino intraplaca; geocronologia; geoquímica; petrogénese; Margem Oeste Ibérica; Cretácico Superior.

Acknowledgements

Given that this will very likely turn out to be a long and boring list of acknowledgements, I should warn the reader that it might be in its best interest to skip this and proceed directly to the first chapter.

First of all I have to thank my supervisors, Dr. Pedro Terrinha and Prof. João Mata, for their time, patience, advices and for helping me become a far better scientist than I was 4 years ago, while giving me enough freedom to make important decisions during the course of this project. More specifically, I have to thank João for putting up with my infamous stubbornness and for never complaining whenever I showed up with some last minute abstract, chapter or something similar that had to be reviewed until the next day. I am also grateful to Pedro for encouraging this project and for continuous support throughout its duration and for always trusting my decisions and listening to my opinions.

The LATTEX/IDL, CeGUL and EMEPC are thanked for providing me with crucial equipment, workspace and data without which this thesis could not have been completed.

Prof. Maria do Rosário Azevêdo from the University of Aveiro deserves a special thanks for letting me use the Laboratório de Geologia Isotópica and for all the encouragement and thorough reviews of all the scientific texts where we were both authors.

I am also very grateful to Eng. Sara Ribeiro for welcoming me in the clean lab and teaching all there is to know about sample preparation for isotopic analysis and also for being very helpful whenever my samples required a different approach than what the lab was accustomed to do. I also have to thank fellow postgrad students Mafalda, Paulo, César, Marina, Mariana and Marta from Aveiro for taking me in so easily, showing me around and making me feel at home in their department.

Drs. Gareth Davies and Jane Chadwick of the department of Petrology of the Vrije Universiteit, Amsterdam are thanked for letting me use their clean lab and MC-ICP-MS for Pb isotopic analysis. I am especially grateful to Jane for assisting me in the lab and also making sure I had everything I needed, and of course for lending me the fastest bike in Amsterdam. A word of thanks also Jelle, Oliver, Laura, Elodie, Eric and the other students and researchers at the VU for making me feel welcome in the Netherlands.

This work could not have been completed without the excellent thin sections prepared by Alberto Verde, who was also very helpful during the time I spent preparing samples in the basement, and without the microprobe analysis made under the guidance of Dr. Pedro dos Reis Rodrigues, and Octávio Chaveiro to whom I am thankful.

Prof. Línia Martins is acknowledge for making sure the sample preparation labs were managed in the best way possible and for helpful discussions during the course of this work.

I am also indebted to Dr. Mário Moreira of the Centro de Geofísica da Universidade de Lisboa and Dr. Nuno Lourenço of the EMEPC for providing the data that allowed the precise location and sampling of the Fontanelas seamount and to Dr. Michael Ivanov, Prof. Luis Pinheiro and the crew of the RV Prof. Logachev for making sure that the sampling operations during TTR-17 were as successful as they could.

Vasco Valadares is thanked for providing me with the samples and data from the Monchique igneous complex, for the preparation of samples for geochronological studies and also for continuous support and for giving me lot of basic textbooks that have been very useful along the duration of the project.

Prof. Miguel Gaspar is thanked for providing the U-Pb geochronological data on the zircon separates from the Sintra and igneous complexes.

I am grateful to Marta Neres and Eric Font for very helpful discussions about paleomagnetism and the geodynamic evolution of Iberia in the past few months which really helped to put things into perspective.

During these years I have had the luck of being able to count on the help of many friends both in Portugal and abroad. This is my attempt to thank them all:

A special thanks to Paula Marques Figueiredo, Ana Maria Nobre Silva and Rita Matildes who had to share the office with me during the final months of writing and who showed great patience and tolerance towards my mood swings and strict “please do not bother” policy.

From the emigrant gang I can’t thank enough to Davide Gamboa, Inês Nobre Silva, Raúl Fonseca, Ícaro Silva, Vera Fernandes and Duarte Soares for all their friendship, advice, support and very importantly hundreds of pdf files which saved me countless hours of searches in the library and quite some euros on photocopying.

On a more local scale I have to thank João Duarte, André Pinto, Gil Machado, Sofia Martins, Cyntia Mourão, Catarina Guerreiro, Isabel Martins Loureiro, Rita Folha, Filipa Marques, Pedro Almeida, Cristina Ventura, Sandra Silva, among others for

helpful discussions, advice, for listening to my seemingly endless complaints and most of all for the friendship and constant support over the years.

A very special thank you to Drs. (Doctors!) Fiona Meade, Sebastian Wiesmaier, Aoife O'Halloran, Eleanor Donoghue and Audray Delcamp for the being a sort of online technical support line in Igneous Geochemistry and random postgrad fits. Thank you guys for the endless discussions, help, support, tips and good moments in congresses across the world, all this would have been much harder without you.

I also have to thank all my non geologist friends for reminding me there is a world outside the Geology department, for keeping me (relatively) sane, sending me silly youtube videos when the days were not looking that bright and making everyday life a lot more interesting. So André Santos, Pedro Gomes, Gonçalo Pina, Markus Almeida, Diogo Homem Marques, Manuel Poças, Ana Gavina, Fábio Costa, Joana Vieira, Rita Sousa, Miguel Pereira, Pedro Fernandes and Marta Fonseca, you'll never read this but you were a great help.

At last I have to thank my father Francisco, my mother Isabel and my brother Luís for everything they have given me over the years, for always being there for me and making sure I had all the conditions I needed to finish this task.

Table of contents

1. Objectives

This study concerns the post rift Late Cretaceous alkaline intraplate magmatism of the West Iberian Margin. The work that culminated in this dissertation was integrated in the MAGMAFLUX (POCTI/CTA/48450/2002) project.

The main objectives of this work were: i) the re-evaluation of the geochronology of the alkaline intrusions; ii) the understanding of the petrogenesis of the alkaline rocks; iii) to reach a better understanding between the deep lithospheric and/or asthenospheric and shallow crustal control of the origin and emplacement of the alkaline intrusions; iv) to evaluate the extent of the onshore alkaline magmatism in the Lisbon region towards the offshore along the Estremadura Spur.

The re-evaluation of the geochronology of this magmatic event was carried out in order to improve its temporal resolution in the context of the evolution of Iberia during the Late Cretaceous. This was done by the acquisition of new ages using the U-Pb, Ar-Ar, K-Ar and Rb-Sr isotopic dating methods on a series of whole rock and mineral separate samples.

After careful sampling of representative lithologies of the main igneous Late Cretaceous alkaline features of the WIM, Sr-Nd-Pb isotopic data and elemental whole rock geochemistry, along with the chemical characterization of the major mineral phases, allowed for the characterization of the sources and processes that generated these magmas, together with those that controlled their evolution.

The Fontanelas seamount was identified as one of the magnetic anomalies present between the Sintra complex and the Tore seamount based on inspection of multibeam bathymetry and offshore magnetic anomaly maps. The study of this seamount allowed for the understanding of the extension of the intraplate alkaline magmatism as far as 100 km offshore and at depths of 1500 m below sea level.

All these data were integrated, along with previously published information on other Late Cretaceous alkaline occurrences in the region and concerning the geodynamic evolution of Iberia during this period, in a model that characterizes the tectono-magmatic evolution of the passive West Iberian Margin during the Late Cretaceous in a broader Iberian geodynamic context.

2. Introduction and geological setting

The Late Cretaceous alkaline magmatism (fig. 2.1) that took place in the emerged part of the West Iberian Margin (WIM) is materialized by the Sintra, Sines and Monchique subvolcanic complexes, the Lisbon Volcanic Complex (LVC), among other minor intrusions and has attracted the attention of both Portuguese (e.g. Costa and Machado, 1929; Assunção, 1937; Matos Alves, 1964; Palácios, 1985; Martins, 1991) and international (e.g. Kaiser, 1914; Rock, 1982, Bernard-Griffiths et al., 1997) geologists since the 19th century.

However, despite the abundant geochemical and mineralogical studies undertaken in the past decades (e.g. Sintra – Matos Alves, 1964; Leal, 1990, 1991, Palácios *et al.*, 1999; Sines – Canilho, 1972, Martins and Olivença 1998; Monchique – Rock, 1977, 1982; LVC – , Palácios, 1985), the characterization of the source(s) and geodynamic processes responsible for the genesis of this magmatism remains incomplete due to the scarcity of available isotopic data. The exception is the Monchique complex, for which an important isotopic dataset exists, allowing for the existence of reasonably well constrained genetic models (Bernard-Griffiths et al., 1997; Valadares, 2004).

Recent studies in the Sintra complex based on structural geology, gravimetry and anisotropy of the magnetic susceptibility (Kullberg and Kullberg, 2000, Terrinha et al., 2003), detailed geological mapping of the Monchique complex (Clavijo and Valadares, 2003, Valadares, 2004) and anisotropy of the magnetic susceptibility work made on dykes of the Mafra Radial Dyke Complex (Nogueira, 2008) have shed some light on the emplacement mechanisms of these intrusions. However, the level of understanding of these mechanisms regarding the other intrusions and their relationship with the observed chemical compositions is very limited, which combined with the aforementioned insufficiencies in terms of available geochemical data, renders the currently available models for the late Cretaceous geodynamical evolution of the West Iberian Margin rather incomplete.

Meanwhile, in the immersed part of the WIM and neighbouring oceanic crust a series of additional seamounts of igneous, basic to intermediate, alkaline nature have been identified, studied, and likewise dated as Late Cretaceous. Among these are the Ormonde peak in the Gorringe Bank (Auzende et al., 1978, Cornen 1982, Bernard-

Griffiths et al., 1997), as well as several seamounts of the Madeira-Tore Rise (Geldmacher *et al.*, 2006; Merle *et al.*, 2006).

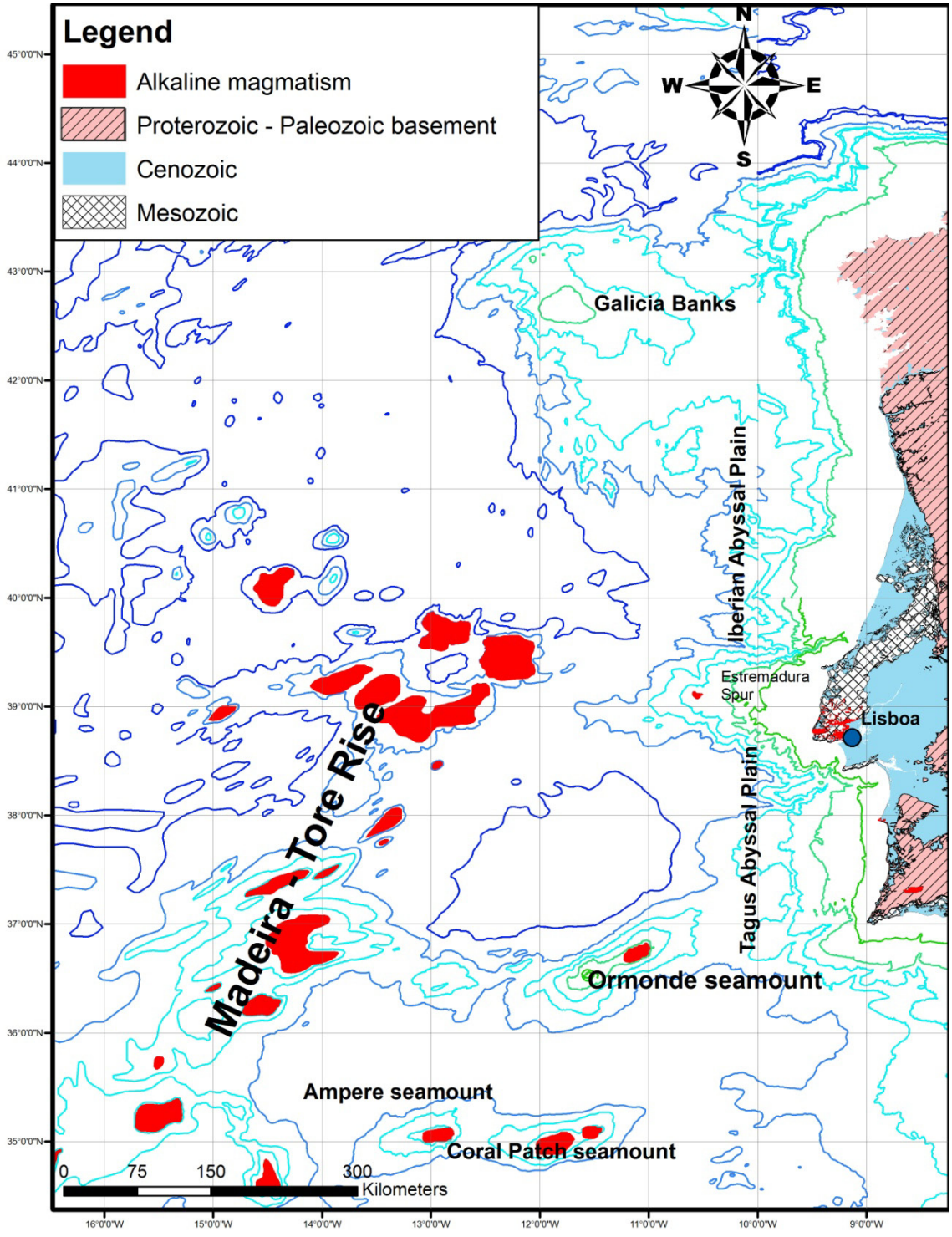

Fig. 2.1: Map of the alkaline igneous occurrences in the West Iberian Margin.

Furthermore, a series of magnetic anomalies forming a WNW-ESE alignment from the Sintra complex to the Tore seamount have been detected (e.g. Silva, 2000, fig.

2.18). These anomalies might correspond to further alkaline igneous activity. A dredging operation in the vicinity of one of these anomalies yielded an ankaramite that was dated with an age of 74 Ma (Mougenot, 1989).

The Ampére and Coral Patch seamounts that bound the southern part of the Horseshoe Abyssal Plain are also of alkaline nature but are of Oligocene age (Matveyenkov et al., 1994 in Geldmacher et al., 2000).

Nevertheless, the joint existence of both onshore and offshore alkaline igneous rocks during the Late Cretaceous that lack a clear spatial age progression has never been properly addressed and the relationship between them remains unknown.

Although this event was included in very large provinces such as the Circum-Mediterranean Cenozoic Anorogenic Igneous Province (Lustrino and Wilson, 2007) and the Peri-Atlantic Alkaline Pulse (Matton and Jébrak, 2009), both of which group rocks with very different locations and ages, the mechanisms for magma genesis provided by these authors are of general nature and do not take into account the geodynamic particularities of the Late Cretaceous in Iberia, which will be addressed in more detail in the section below.

2.1 Iberia during the Cretaceous

The beginning of the Mesozoic era was marked by the onset of tectonic extension in the Early Triassic which marked the end of the Paleozoic Variscan orogeny and the breakup of Pangea, resulting in rifting in the Algarve and Lusitanian basins (e.g. Pinheiro et al., 1996, Terrinha, 1998, Rasmussen et al., 1998, Kullberg, 2000).

By the end of the Early Cretaceous both the Lusitanian and Algarve basins suffered their last rifting event. In the Lusitanian basin this event started in the Late Jurassic (Tithonian-Barremian) and is characterized by angular unconformities between the Jurassic and Cretaceous deposits and by a change from marine carbonate sedimentation to siliciclastic continental sedimentation (Rasmussen et al., 1998). This unconformity was caused by thermal uplift exceeding the isostatic subsidence induced by the lithospheric stretching during this rifting phase (Rasmussen et al., 1998). The last rifting event in the Algarve basin is probably of Albian age (Terrinha, 1998).

Rifting ended and was followed by oceanization and formation of oceanic crust in the WIM, with no evidence of significant syn-rift volcanism (Pinheiro et al., 1996), which classifies this margin as non volcanic (e.g. White and McKenzie, 1989).

The most landward magnetic anomaly detected in the Tagus Abyssal Plain corresponds to M11, placing the onset of seafloor spreading at approximately 133 Ma, in Hauteverian times (Pinheiro et al., 1996). On the Iberian Abyssal Plain the first magnetic anomaly to be detected corresponds to M3, which places the beginning of oceanization at 126 Ma, in the Barremian (Pinheiro et al., 1996), while in the Galicia Banks region the beginning of seafloor spreading is dated by the breakup unconformity as late Aptian, near the Aptian/Albian, boundary around 112 Ma (Pinheiro et al., 1996).

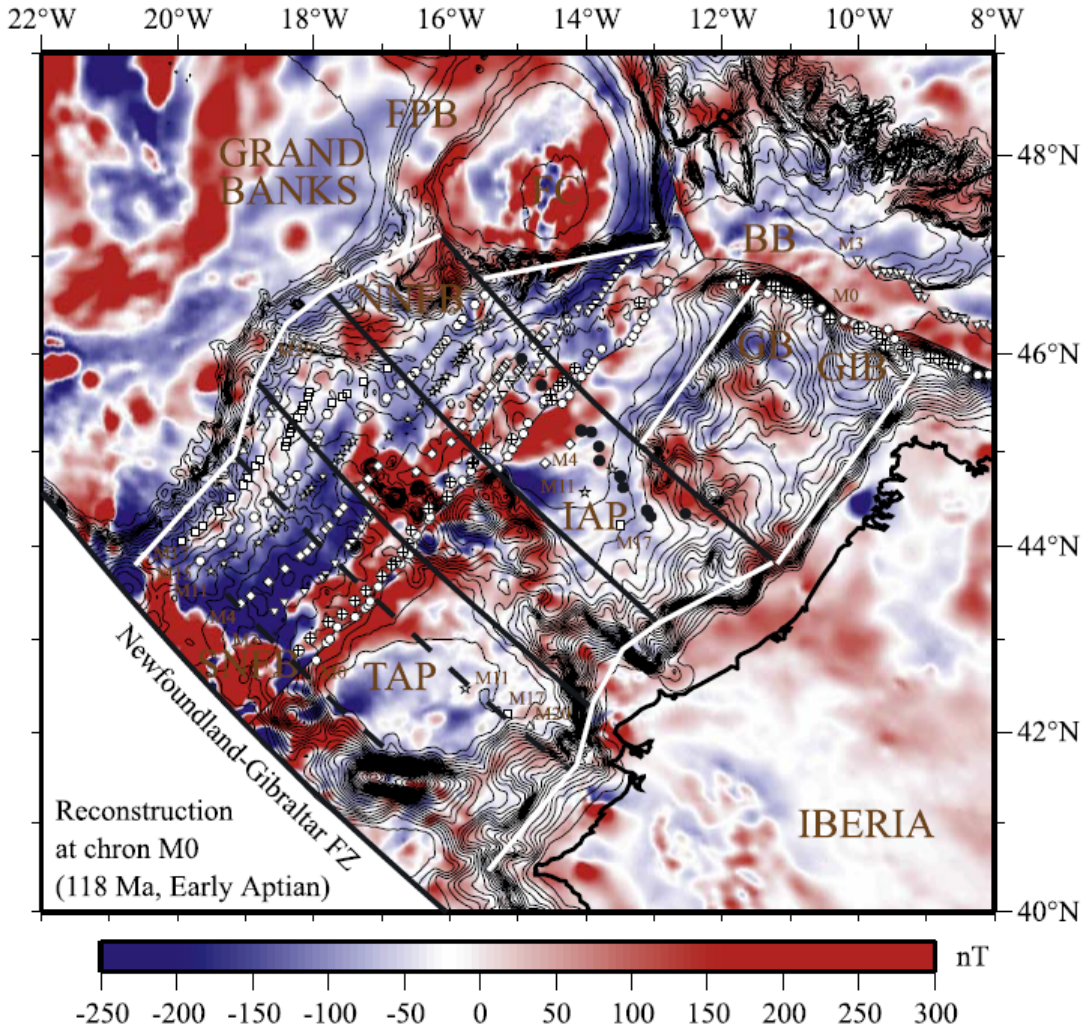

Fig. 2.2: Magnetic anomaly map of the reconstruction of the positions of Iberia and Grand banks at chron M0 (118-124 Ma).TAP – Tagus Abyssal Plain, IAP – Iberian Abyssal Plain, GB – Galicia Banks, FC - Flemish Cap, BB – Bay of Biscay, FPB Flemish Pass Basin. From Sibuet *et al*., 2007.

However, it has been recently proposed that these first magnetic anomalies are not the result of ocean crust formation but of serpentinization of exhumed continental sublithospheric mantle during extension (Sibuet et al., 2007). In this model, the formation of oceanic crust started only in the J (M0-M3) anomaly, around 118-124 Ma and the last rifting phase lasted until the Aptian/Albian boundary (Sibuet et al., 2007).

The Cretaceous in Iberia was also characterized by the opening of the Bay of Biscay, which started between magnetic anomalies M0 and M3 (118 Ma 124 Ma), ending in chron A33o (80 Ma, Campanian) (Sibuet et al., 2004). This subject is still under intense debate and several different models have been proposed.

The formation of the Bay of Biscay resulted on a counter clockwise rotation of the Iberian plate of roughly 35º, first detected in paleomagnetic data collected by van der Voo (1969) who constrained it to having occurred between the Triassic and the Late Cretaceous. Galdeano et al. (1989) studied the paleomagnetic properties of sediments from the Lisbon area and proposed a counter clockwise rotation of 27º between the Hauteverian (136-130 Ma) and the Barremian (130-125 Ma), followed by a second rotation in the same sense of 14º from 110 Ma to today. Moreau et al. (1997) presented data collected in sedimentary rocks from the Algarve basin and identified one quick anticlockwise rotation phase of 22º during the Barremian. Paleomagnetic data from igneous rocks in continental Portugal collected by Márton et al. (2004) indicate a rotation of 26º in the same sense between the Toarcian (ca. 180 Ma) and the extrusion of the Lisbon Volcanic Complex (72 Ma, Ferreira and Macedo, 1979). Other data collected in igneous intrusions in Portugal and France by Storetvedt et al. (1987) show a 40º counter clockwise rotation of Iberia between 90 and 75 Ma based on the K-Ar they obtained for the same intrusions and a second clockwise rotation of the same magnitude between the end of the Cretaceous and the present day, associated with compressive alpine tectonics. In two subsequent publications Storetvedt et al., (1990, 1999) detect a first 40º counter clockwise rotation phase between 90 and 75 Ma, followed by a rotation of 70º in the opposite sense in the Campanian (75Ma), these data are, however, hard to reconcile with geological observations. The most recently published paleomagnetic data limits the duration of the previously identified 35º anti clockwise rotation to the Aptian (125-112 Ma, Gong et al., 2008), with that rotation progressing at a faster rate during the early Aptian relatively to the rest of that age.

Despite some spread, most paleomagnetic data seems to point to an approximately 35º rotation centered around the Barremian and Aptian.

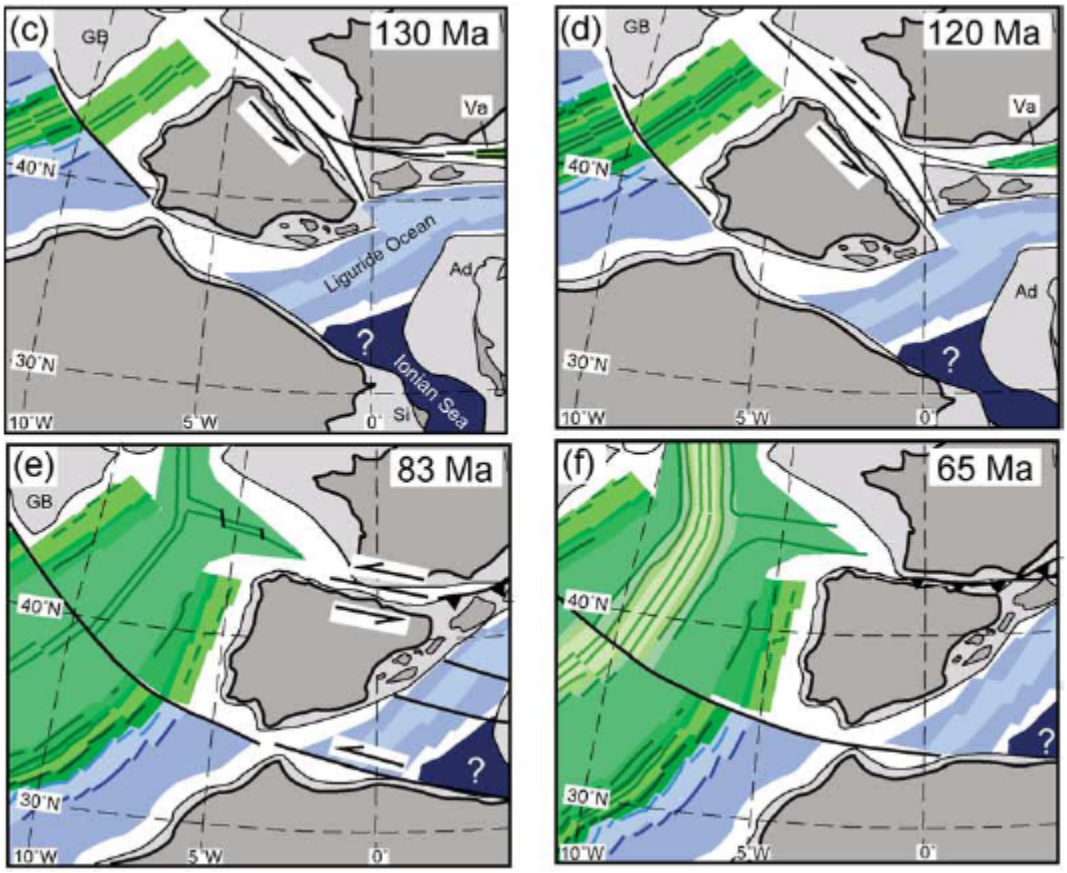

Fig. 2.3: Evolution of the Iberian plate during the Cretaceous. From Rosembaum *et al*., 2002.

During the opening of the Bay of Biscay, extension comes to an end in the existent sedimentary basins in Pyrenean region while new basins are formed in a transtensional regime due to the left strike-slip movement between the Iberian and Eurasian plates along the North Pyrenean fault (Sibuet et al., 2004). Contemporaneously to this movement metamorphic and magmatic events took place in the pull-apart basins resulting in the incorporation of lherzolitic mantle material and intrusion of small igneous bodies in the previously mentioned basins between 105 and 85 Ma (Fabriès et al., 1998; Montigny et al., 1986). Also, in the Catalan ranges the small volume alkaline magmatism occurred between 82 and 69 Ma (Solé et al., 2003), while in Galicia rare dykes of similar age (96-87 Ma, Ancochea et al., 1992) have been identified. In the Basque-Cantabrian basin, alkaline pillow lavas sills and stocks are intercalated with sediments of Late Cretaceous age (Upper Albian-Santonian) and appear to be related with an extensional episode in the same basin (Carracedo et al., 1992).

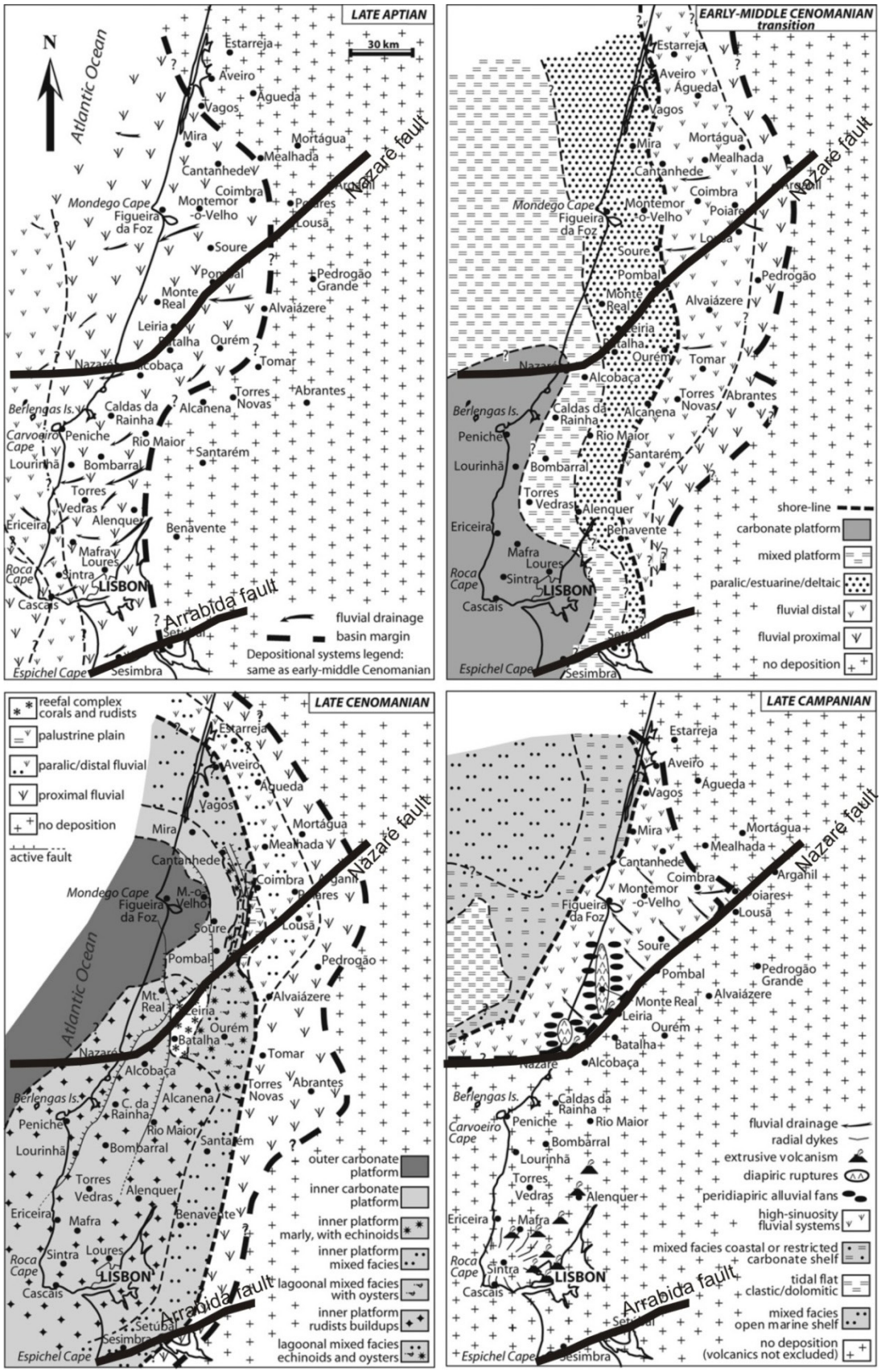

Fig. 2.4: Palaeogeographic maps of depositional environments for selected times of the late Early and Late Cretaceous. Notice the uplift and exposure of the bloc south of the Nazaré fault contemporaneously with alkaline magmatism in the Campanian. Adapted from Dinis et al., 2008.

In the western Bay of Biscay - Cantabrian region, subduction took place between the Campanian and the Miocene (Sibuet et al., 2004), while in the Pyrenees, subduction ensued in two different phases, from the Aptian to the Santonian in the south and from the Campanian to the Miocene, in the north (Sibuet et al., 2004).

After oceanic break up and for the remainder of the Lower Cretaceous, the Lusitanian basin went through a phase of generalised subsidence caused by the thermal relaxation of the lithosphere, resulting in fault controlled fluvial sedimentation. During the Early Cretaceous-Late Cretaceous transition, a generalized marine transgression promoted the deposition of carbonates until the end of the Cenomanian when it was interrupted by the uplift of the crustal block limited by the Nazaré and Arrábida faults (fig. 2.4, Proença da Cunha and Pena dos Reis, 1995; Dinis et al., 2008).

This uplift, which is contemporaneous with the installation of the Sintra igneous complex and the extrusion of the Lisbon Volcanic Complex, is thought to be the cause of the erosion of approximately 300m of Cretaceous sediments inferred from the comparison between the thickness of onshore and offshore deposits (Rasmussen et al., 1998).

The tectonic inversion of the Mesozoic Lusitanian and Algarve basins started as early as the Late Cretaceous, as a consequence of the onset of rapid collision and even subduction between the Iberian, Eurasian and African plates (Mougenot, 1980; Terrinha, 1998, Rosembaum et al., 2002) but reached its climax during the Miocene in the Lusitanian Basin and offshore WIM (Ribeiro et al., 1990, Kullberg et al., 2000, Neves et al., 2009). However, the Algarve Basin experienced the compressive effects of the Africa-Iberia convergence mainly during the latest Cretaceous through Oligocene-Early Miocene times (Terrinha, 1998).

Meanwhile, central Iberia was affected by thermal metamorphism events that resulted in the formation of hydrothermal Hg deposits in the Iberian Ranges (Espadán deposits) dated around 85 Ma (Tritlla and Solé, 1999) and low degree thermal metamorphism in the Cameros basin, which occurred between 105 and 86 Ma (Casquet et al., 1992 *in* Casas-Sainz and Gil-Imaz, 1998).

Moreover, the WIM was the locus of important magmatic activity of transitional and alkaline affinities during the Cretaceous. The transitional magmatism took place within the Lusitanian basin and is commonly associated with diapiric structures (Martins, 1991) and spans from the latest Jurassic to the earliest Cretaceous (147-141

Ma, Grange et al., 2008; Alves, 2010). This event has been attributed to the melting of metasomatized mantle during a phase of high lithospheric thinning associated with the ongoing rifting and is characterized by relatively high $^{87}Sr/^{86}Sr$ and low $^{206}Pb/^{204}Pb$ and $^{207}Pb/^{204}Pb$ ($^{87}Sr/^{86}Sr_i$ 0.704441–0.706462; εNd_i 3.2-0.6; $^{206}Pb/^{204}Pb$ 18.418–18.978; $^{207}Pb/^{204}Pb$ 15.594–15.925, Grange et al., 2008; Alves et al., 2010).

The Late Cretaceous alkaline magmatism, represented by the igneous rocks mentioned earlier (see fig. 2) is the main subject of this dissertation and will be thoroughly described and discussed later in this work.

Although the conjugate West Iberian and Newfoundland margins are commonly used as examples of amagmatic margins that suffered non volcanic rifting (e.g. White and McKenzie, 1989), a series of small intrusions of Cretaceous age have been identified on the stretched and faulted lithosphere present on the offshore WIM, in peridotite ridges in the Galicia banks and the Iberian Abyssal plain, and also in the Gorringe bank (e.g. Auzende et al., 1978; Boilot et al., 1989; Beslier et al., 1990; Malod et al., 1993; Schärer et al., 1995; Cornen et al., 1999; Schärer et al., 2000; Beard et al., 2002; Chazot et al., 2005).

The peridotites outcropping in the ridges are interpreted as being part of exhumed subcontinental lithospheric mantle that has experienced depletion during several previous melt extraction events during the Variscan (e.g. Malod et al., 1993; Cornen et al., 1999; Chazot et al., 2005). They are intruded by late gabbros and dolerites and can be locally covered by tholeiitic lavas that extruded between the end of rifting and the high temperature deformation of the peridotite (e.g. Auzende et al., 1978; Beslier et al., 1990; Boilot et al., 1989; Schärer et al., 1995; Schärer et al., 2000; Beard et al., 2002; Chazot et al., 2005).

This magmatic episode lasted from 138 to 121 Ma (U-Pb ages in zircon separates, Schärer et al., 2000) and should have preceded continental breakup, with the younger rocks being found in the North and the older ones in the South. These rocks derived mostly from the melting of an asthenospheric, MORB like, LILE (Large Ion Lithophile Element) depleted source, according to their Hf and Nd isotopic signature, but with the lower εNd values probably being an indication of the involvement of a less LILE depleted lithospheric component (εHf 20.5 – 14.0, εNd 10.3 – 3.6 Schärer et al., 1995, 2000).

The gabbroic pegmatites found in the peridotite ridges of the Iberian abyssal plain and studied by Beard et al. (2002) systematically show a more enriched trace element and isotopic signature (εNd_i 4.7 – 4.9; $^{87}Sr/^{86}Sr_i$ 0.70362 - 0.70463; $^{206}Pb/^{204}Pb_i$ 18.65, $^{207}Pb/^{204}Pb_i$ 15.48, $^{208}Pb/^{204}Pb_i$ 38.3) and are thought to represent melts generated in the upper lithospheric mantle, probably at shallow depths, in the plagioclase stability field during the rifting and unroofing of these peridotites. These tholeiitic MORB-like melts are also considered to be responsible for the syn-rift metasomatic event that affected the subcontinental lithosphere peridotites and refertilized previously depleted hazburgites by interacting with them and creating different, enriched trace element and isotopic signatures. These signatures are also observed on the previously described intrusives contemporary with rifting, which also show evidence for interaction with the refertilized lithospheric mantle (Chazot et al., 2005).

The clinopyroxene and amphibole separates from lherzolites in the Galicia bank have isotopic signatures characterized by radiogenic Nd and unradiogenic Sr ($^{143}Nd/^{144}Nd$ 0.512804 – 0.513402 $^{87}Sr/^{86}Sr$ 0.702100 - 0. 703887), while pyroxenes from the websterites in the Iberia Abyssal Plain have lower Nd isotopic compositions ($^{143}Nd/^{144}Nd$ 0.512283 – 0.512553) with higher Sr isotopic ratios ($^{87}Sr/^{86}Sr$ 0.704170 – 0.705919) indicating the existence of Cretaceous metasomatic events with different natures in these two regions (Chazot et al., 2005).

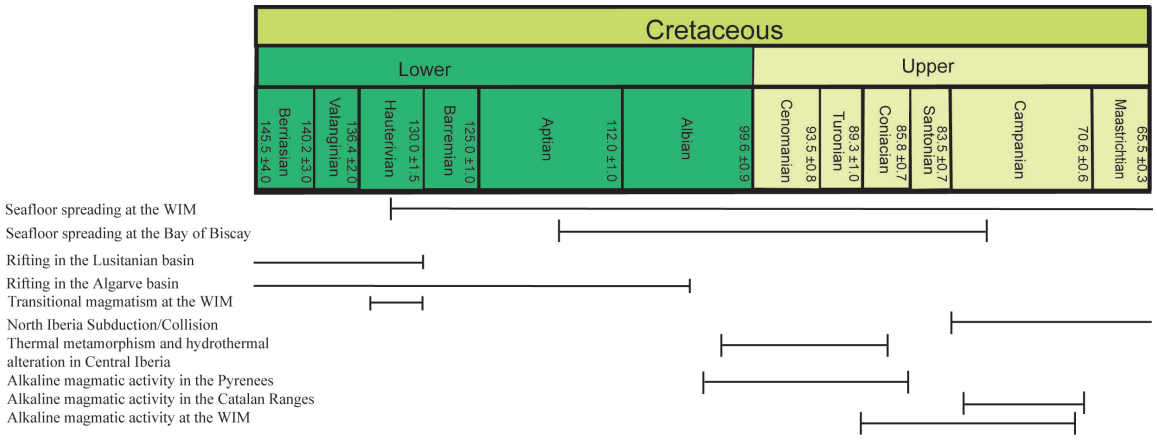

Fig. 2.5: Summary of the most important geodynamic events in Iberia during the Cretaceous (from Miranda et al., 2009). Dates for the limits of the epochs and ages of the Cretaceous period from Gradstein et al. (2004). Ages from geochronological data in full lines.

2.2 Magmatism in the conjugate and Newfoundland margin

The Newfoundland margin constitutes the conjugate margin of the WIM and separated from it during the aforementioned rifting process. It encompasses the Mesozoic Jeanne d'Arc, Carson, and Salar-Bonnition basins, and is also a non volcanic (i.e. free of any significant thickness of volcanic rocks or magmatic underplating, e.g. Tucholke and Sibuet, 2007). As in the WIM, peridotite ridges are present in this margin, with the difference that the Newfoundland peridotites (hazburgites) are more depleted relative to the ones found in the WIM, due to pre-rift melting events that possibly took place in an arc-like environment during a previous orogeny (Müntener and Manastchal, 2006).

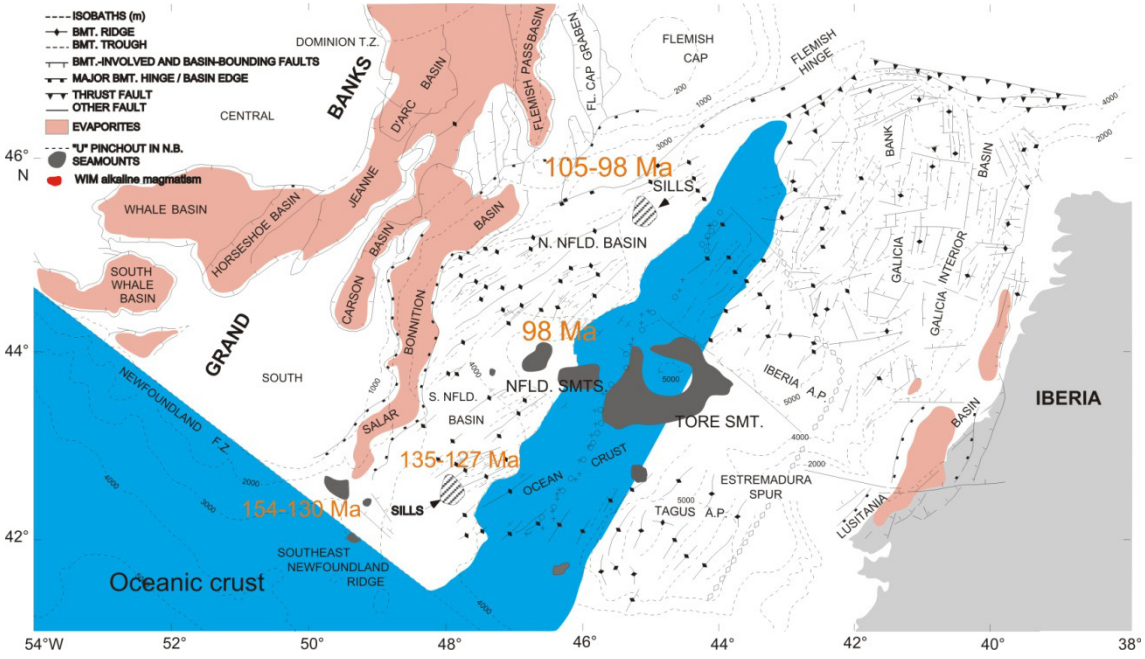

Fig. 2.6: Reconstitution of the positions of Iberia and the Newfoundland/Grand Banks region at the time of anomaly M0 (approximately 118-124 Ma). From Tucholke and Sibuet., 2007. Also shown is the structure and sedimentary basins of the region as well as the position of the Newfoundland (NFLD) and Tore seamounts. Ages of the oceanic basement, seamounts and sills are from Sullivan and Keen (1977), Pe-Piper *et al*., 1994; Hart and Blusztajn (2006).

Small volume, post-rift alkaline magmatism also took place in this margin and is represented by a series of alkaline sills recently drilled in Site 1276 of Leg 210 of the Ocean Drilling Program (Karner and Shillington, 2005; Hart and Blusztajn, 2006). They are constituted by more or less altered alkali basalts and hawaiites that intruded between

105 and 98 Ma (fig. 2.6) and are enriched in incompatible elements. Their isotopic composition ($^{87}Sr/^{86}Sr$ 0.705898 - 0.706259, $^{143}Nd/^{144}Nd$ 0.512740 – 0.512598, $^{206}Pb/^{204}Pb$ 18.4666 - 20.5031, $^{207}Pb/^{204}Pb$ 15.5536 - 15.6686, $^{208}Pb/^{204}Pb$ 37.8681 - 38.4478; Hart and Blusztajn, 2006) suggests the participation of enriched mantle components in the genesis of these rocks, as well as a possible crustal contribution. This enriched mantle component may derive from preferential melting of enriched mantle domains embedded in depleted MORB mantle or reflect the activity of a mantle plume in the region that may as well be responsible for the formation of the Milne seamounts further east of this location (Hart and Blusztajn, 2006).

The Newfoundland seamounts correspond to chain of submarine volcanic peaks that positions itself East of the Newfoundland margin. They were extruded in an area which during magnetic anomaly M0 (118-124 Ma) was separated from the Tore seamount by the Mid-Atlantic Ridge, according to paleogeographic reconstructions (e.g. Tucholke and Sibuet, 2007; Müntener and Manastchal, 2006; Sibuet et al., 2007; fig. 2.6). The data available on these seamounts is scarce but it is known they are constituted by alkaline basalts and trachytes that were dated around 98 Ma (Sullivan and Keen, 1977 in Pe-Piper et al., 2007). Little else is known about these seamounts except for their εNd_i value of 4.1 (Sullivan and Keen, 1977 in Pe-Piper et al., 2007) and that they have low radiogenic Pb values (Pe-Piper et al., 1994).

Also present in oil exploration wells near this area is an Early Cretaceous alkaline bimodal suite (135-127 Ma) that is genetically related to the Grand Banks Jurassic transform margin (Pe-Piper et al., 1994). Trace element and isotopic signatures of the more basic magmas ($^{87}Sr/^{86}Sr_i$ 0.70350 - 0.70388, $^{143}Nd/^{144}Nd$ 0.51263 – 0.51282, $^{206}Pb/^{204}Pb$ 18.538 - 18.752, $^{207}Pb/^{204}Pb$ 15.598 - 15.636, $^{208}Pb/^{204}Pb$ 38.505 - 38.674) suggest that they were generated by melting of the continental lithosphere induced by extensional decompression mechanisms along the reactivated transform margin. A plume component is also detected in their isotopic signature and a thermal anomaly related to this possible plume could have supplied the extra heat that allowed for the initiation of melting (Pe-Piper et al., 1994). Major faults in the region acted as magma conduits, and the rocks further away from the continental margins display stronger signs of crustal contamination (Pe-Piper et al., 1994), perhaps due to stronger interaction with the crust during magma transport.

The southern limit of this margin corresponds to the Newfoundland-Azores-Gibraltar fracture zone, on top of which sit the Fogo seamounts of Late Jurassic to Early

Cretaceous age (154-130 Ma, Pe-Piper et al., 2007, Fig. 2. 6). This seamount chain is constituted by both tholeiitic and alkaline rocks who are thought to have formed from magmas generated by decompression melting from ascending asthenosphere as a result of edge-controlled convection in the upper mantle due to thermal and density gradients at the transform transition between the spreading ocean and the continental block of the Grand Banks (Pe-Piper et al., 2007). Pe-Piper et al. (2007) also suggested that thermal effects of the volcanism promoted mid-crustal partial melting and detachment faulting on the Grand Banks and consequentially the development of the asymmetric Grand Banks–Iberia rift system.

2.3 Late Cretaceous Alkaline magmatic occurrences in the West Iberian Margin: the state of the art

The Late Cretaceous igneous alkaline activity is the most important Mesozoic magmatic event in the WIM in terms of both area and volume. This magmatic activity, initially established as having occurred between 100 Ma and 70 Ma, was included in the 4th cycle of Meso-Cenozoic magmatic activity in Portuguese territory by Ferreira and Macedo (1979). Previous cycles of alkaline with shoshonitic affinities (235-205 Ma), tholeiitic (ca. 200 Ma) and transitional (ca. 135 Ma) magmatism were proposed by the same authors.

As was previously mentioned Rock (1982) grouped the Portuguese Late Cretaceous alkaline magmatism along with other occurrences of similar age and composition located around the Pyrenees in the Iberian Late Cretaceous Alkaline Igneous Province and argued for a close relation between this magmatism and the opening of the North Atlantic. Martins (1991) integrated the same alkaline episode in the third and last cycle of Mesozoic magmatic activity in Portugal, associating it with the ascent and melting of asthenospheric mantle as a consequence of the thinning of lithospheric mantle occurred during the various rifting phases of the WIM. Occurrences related to the first two cycles defined by Martins (1991) display tholeiitic and transitional affinities (Martins, 1991; Martins et al., 2008; Grange et al., 2008) and ages around 200 Ma (e.g. Dunn et al., 1998, Verati et al., 2007) and 130-146 Ma (Ferreira and Macedo, 1979; Grange et al., 2008), respectively.

Onshore, the Late Cretaceous alkaline cycle includes subvolcanic complexes of Sintra, Sines and Monchique, the Lisbon Volcanic Complex and several other minor intrusions, such as the Foz da Fonte and Paço d'Ilhas sills, the Mafra radial dyke complex, the Oeiras-Cascais dykes and the lamprophyre-basanite suite of the Algarve coast (fig. 2.14). These rocks are discontinuously exposed between parallels 39º N and 37º N and cover an area of approximately 325 km^2 (fig. 2.8). The Sintra, Sines and Monchique intrusions are aligned along a NNW-SSE direction, which coincides with the trend shown by some rift faults as well as some Variscan structures.

All the alkaline rocks in the Lisbon area, i.e. north of 38.5ºN, were emplaced within the Mesozoic Lusitanian rift basin. The Sines complex sits just east of the boundary of the Alentejo Basin and in the southern limit of the small Mesozoic Santiago do Cacém basin. The Monchique nepheline syenites were emplaced well into the non-rifted Paleozoic basement, while a complex of the coeval dykes and necks were mapped and dated in the Algarve rift basin (fig. 2.8).

The alignment of the Sintra, Sines and Monchique Late Cretaceous alkaline complexes has been a matter of intense debate in the past. Ribeiro et al. (1979) suggested the complexes were emplaced along a dextral strike-slip fault during the rotation of Iberia. Mougenot (1980) proposed that these intrusions were emplaced along crustal pull-apart strain domains between en echelon faults during tectonic inversion of the WIM. Terrinha (1998) and Kullberg (2000) demonstrated the existence of Early-Middle Jurassic age sin-rift faults along the lineament and proposed that these faults controlled the magma ascent in the Late Cretaceous, while decompression melting in releasing bends on the deep structure allowed for the melt generation (fig. 2.7).

In recent times, offshore alkaline magmatic activity has been identified in thinned continental or oceanic crust between 34.5º N and 39º N between the Tore and Lion seamounts in the Madeira-Tore Rise (MTR) and the Ormonde seamount in the Gorringe Bank, totalling a much larger area and volume than its onshore counterpart (e.g. Cornen, 1982; Féraud et al., 1982; Geldmacher et al., 2006; Merle et al., 2006).

The relationship between the onshore and offshore occurrences is highly debated, with Bernard-Griffiths *et al.* (1997) first proposing a consanguinity relation between the Monchique Massif and the alkaline magmatism of the Gorringe bank, which in turn served as the basis for the proposal that Monchique would represent the oldest known activity of the Madeira hotspot made by Geldmacher and Hoernle (2000).

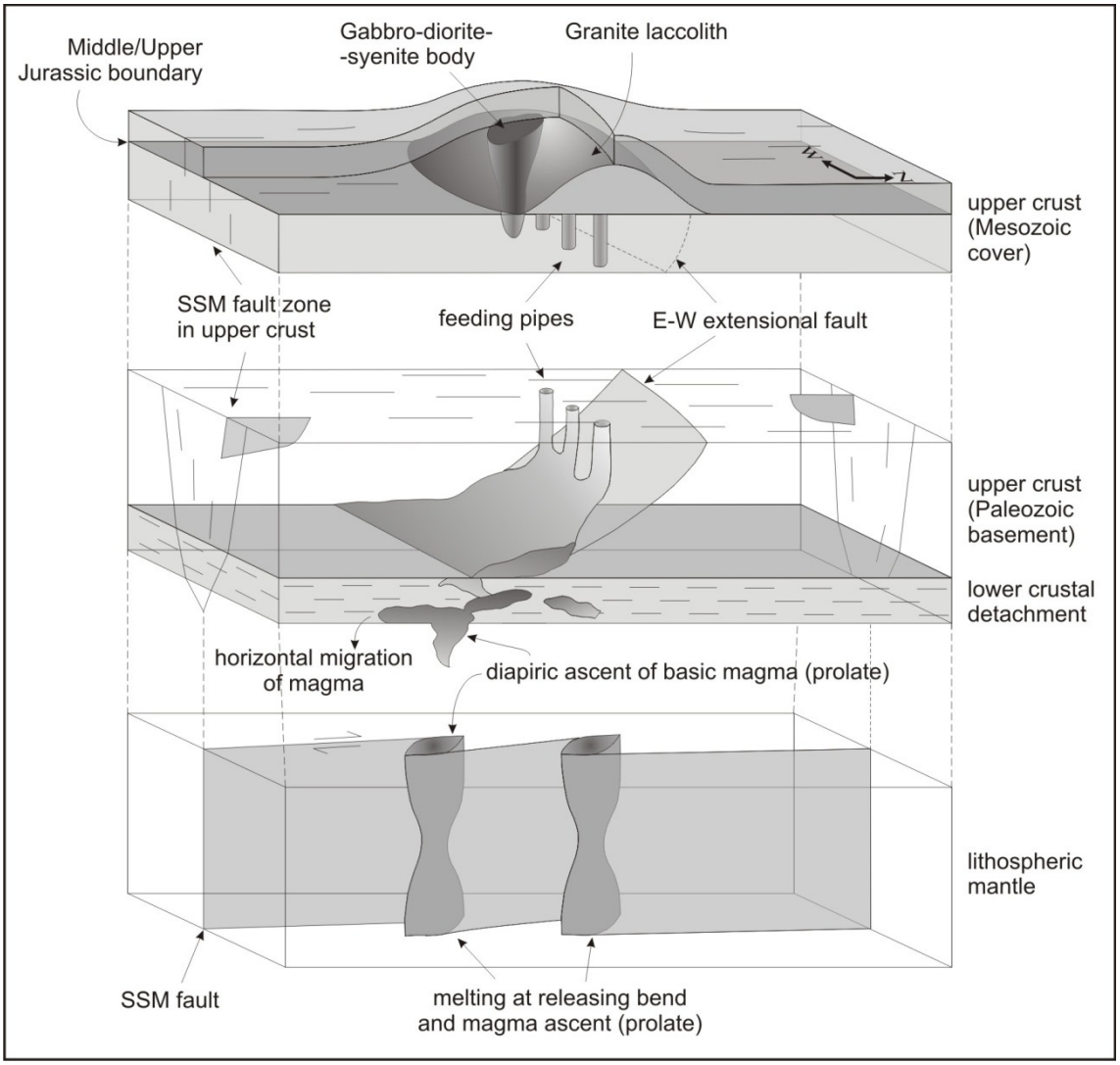

Fig. 2.7: Schematic representation of the mechanisms of generation, ascension and installation of the magmas that constitute the Sintra igneous complex. From Terrinha et al., 2003.

This author later proposed that all the observed magmatism in the offshore WIM could be explained by the activity the Madeira and Canaries hotspots and their interaction with the late Cretaceous mid Atlantic Ridge (Geldmacher et al., 2006, figs. 2.15, 2.16). Merle et al. (2006, 2009) proposed that the Madeira-Tore seamounts would be the result of a long lived and wide mantle thermal anomaly present in the region during the Cretaceous that emitted several magmatic pulses. The space–time distribution of this magmatism results from the interaction between these pulses and the complex kinematics of the Iberian plate (Merle et al., 2009).

In his turn, Ribeiro (2002) proposed that the onshore portion of this magmatic event could be related to a fracture resulting from a meteorite impact occurred in the

Late Cretaceous, whose crater corresponds to the Tore seamount, but further studies of this location do not support this hypothesis (Merle et al., 2006, 2009).

Recently, Solé et al. (2003) proposed that the magmatism assigned to the Late Cretaceous Alkaline Igneous Province of Iberia had been generated by decompression and intruded the margins of the Iberian plate, where thinning and cortical relaxation had taken place during its rotation and contemporaneous opening of the Bay of Biscay.

Despite their older age, Lustrino and Wilson (2007) included these occurrences in the Circum-Mediterranean Cenozoic Anorogenic Igneous Province and suggested that they could be related to the existence of small passive convective diapiric instabilities in the upper mantle where enriched magmas would ascend. These diapiric instabilities would lead to the rise of asthenospheric mantle with a similar composition in the entire region, which is known as the Common Mantle Reservoir (CMR) which represents a sublithospheric mantle domain enriched by the recycling of lithospheric material during subduction or delamination (Lustrino and Wilson, 2007).

However, it has also been suggested that the constant isotopic composition observed in such a large area was the result of a mantle contamination episode during the Cretaceous by the same mantle plume responsible by the magmatism of the Central Atlantic Magmatic Province (Piromallo *et al*., 2008). For these authors, this deeply rooted plume is nowadays responsible for the volcanism in the Canaries and Cape Verde hotspots.

More recently, Matton and Jebrák (2009) included both the onshore and offshore intrusions and volcanics of the WIM in the Peri Atlantic Alkaline Pulse (PAAP) along with other paired onshore and offshore igneous alkaline rocks along the Atlantic margin. They have envisaged a model where edge driven asthenospheric convection and the resulting mantle upwelling acted simultaneously with the reorganization of intraplate stresses and consequential reactivation of deep seated zones of weakness to promote magma generation through decompression melting and the ascension of the resulting alkaline magmas to the surface.

In the following part of this section detailed information about the age, geochemistry and emplacement mechanism for each of the studied onshore and offshore Late Cretaceous alkaline magmatic occurrences will be provided.

2.3.1 The onshore West Iberian Margin

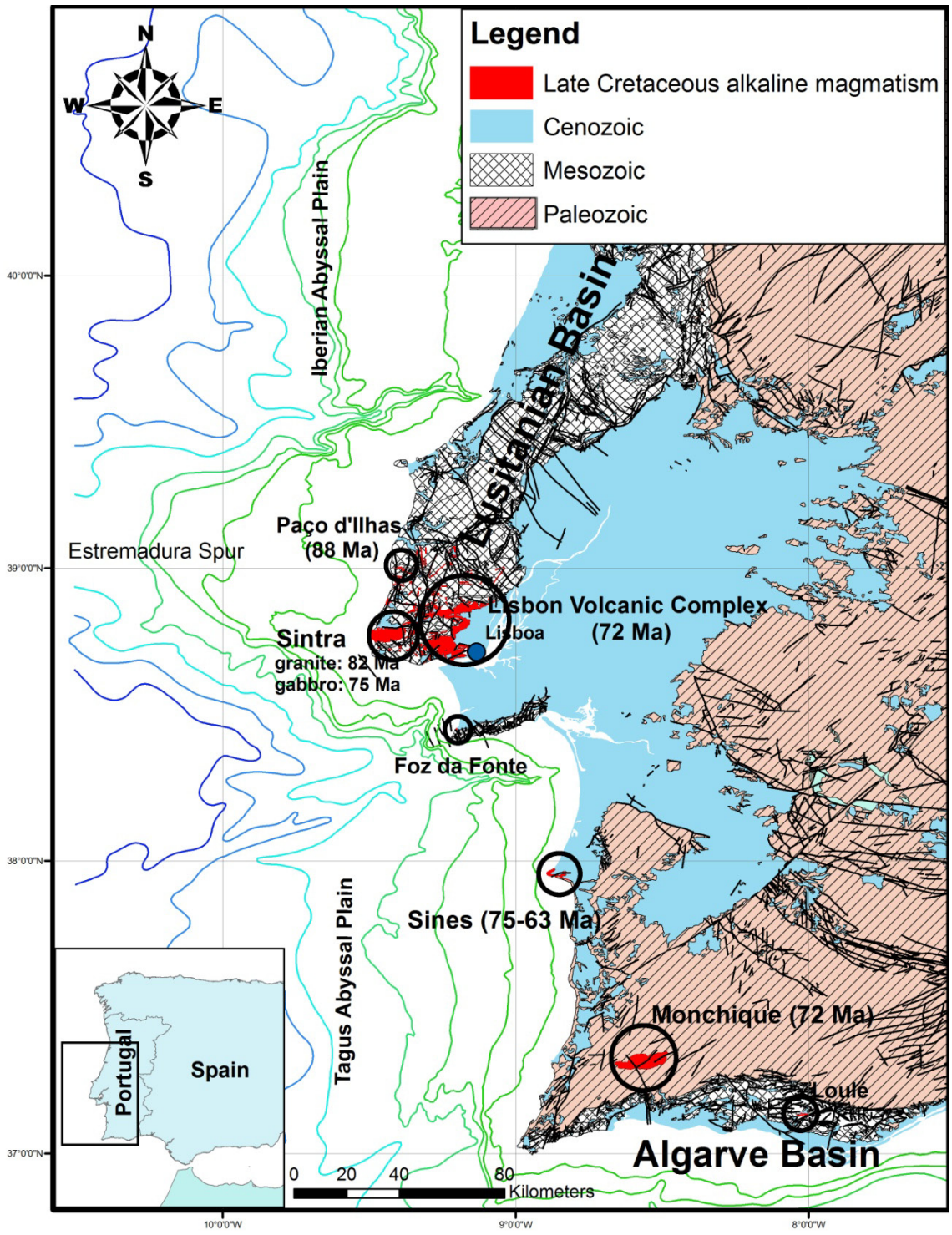

Fig. 2.8: Late Cretaceous alkaline magmatism on the onshore WIM. See text for the exact ages.

2.3.1.1 The Sintra igneous complex

The Sintra igneous complex outcrops approximately 25 km west of Lisbon, having an emerged area of approximately 40 km^2. It was also mapped underwater, towards the west, where it is thought to occupy a similar area to the one observed on land. With a maximum height of over 500 m, it constitutes one of the most prominent geomorphological features in the region.

The complex intrudes Upper Jurassic carbonates and Early Cretaceous sandstones, forming a ring of contact metamorphism that produced mostly calc-silicate hornfels and recrystallized sandstones. These lithologies also make up some stoped blocks observed in the interior of the complex.

The complex can be considered as being constituted by three main units, as follows: i) the Sintra granite that occupies most of the outcropping area and envelops a second unit, ii) the Cabo da Roca complex, a unit located in the western part of the complex and formed by amphibole rich gabros (mafraites), quartz diorites, quartz syenites and igneous breccias (fig. 2.9); note that there is also a small array of altered gabbroic bodies that outcrop in the northern contact, parallel to the Sintra northern thrust (fig. 2.9), and iii) the surrounding complex of dykes.

Wright (1968) recognised four distinct syenite units and two overlapping ring complexes inside the Cabo da Roca complex, which have different ages, geochemistry and degrees of contamination, while Sparks and Wadge (1975) identified five syenite units and also a stratified sequence of eruptive rocks (from trachybasalts to rhyolites). They also classified the some of the breccias as lavas and pyroclastic breccias of the basalt-trachyte suite and recognised net veined complexes formed by magma mixing. Both Wright (1968) and Sparks and Wadge (1975) argued that the granite pre-dates the Cabo da Roca complex with only Matos Alves (1964) arguing that all the rocks present in Sintra are co-genetic.

The intrusion of the complex was accompanied by the intrusion of a series of sills and dykes of different compositions that can be divided in radial dykes, cone sheets and sills (Matos Alves, 1964). The sills are mostly altered, basic to intermediate porphyritic rocks, which include the sampled Malveira da Serra sill and intrude mostly in the sedimentary country rock in the southern and eastern flanks of the complex, as are the mafic radial dykes that occur in the same area. The cone sheets are mainly felsic to

intermediate and are observed mainly in the southern flank of the complex dipping towards it (Matos Alves, 1964).

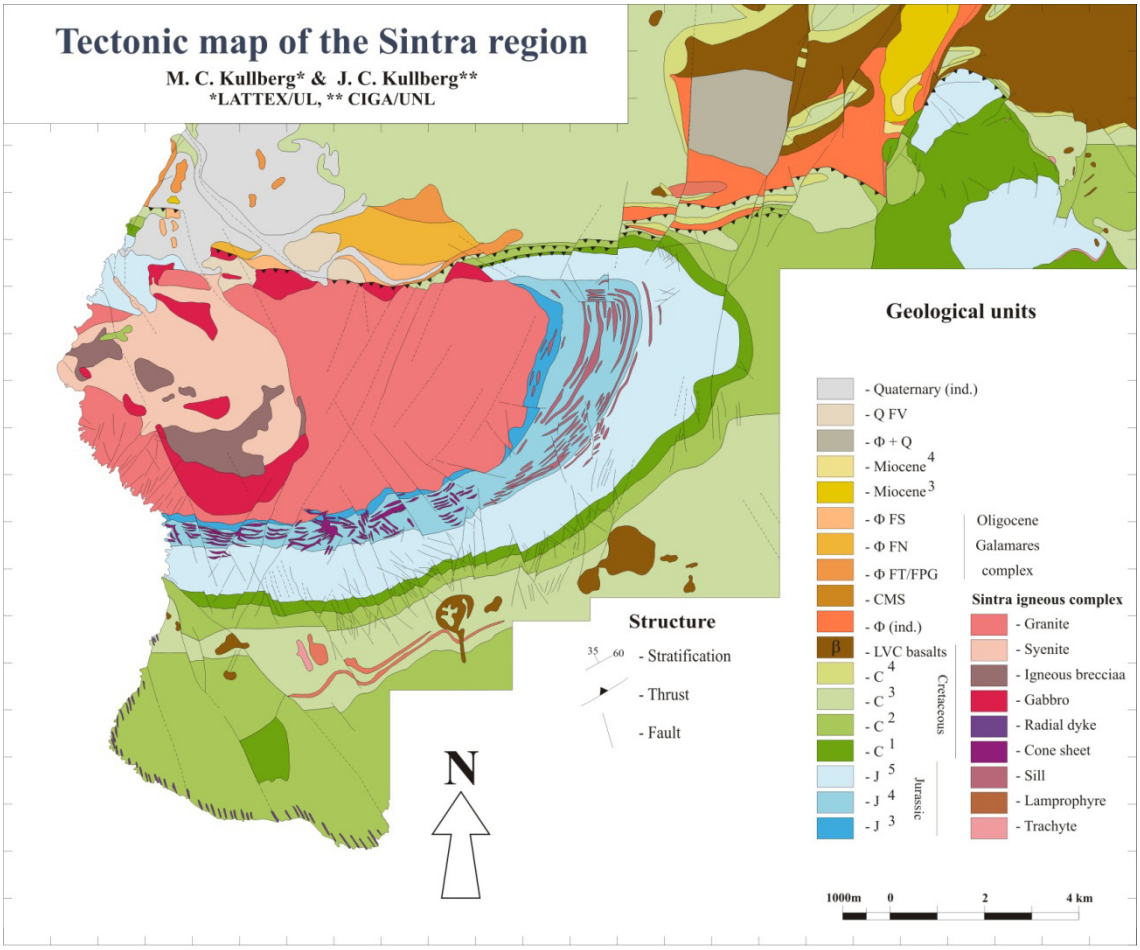

Fig. 2.9: Geological map of the Sintra region. Adapted from Kullberg *et al*., 2006.

Geothermobarometric studies on rocks belonging to the intrusion suggest that the complex was emplaced at a pressure of 1.5 kb (depth around 5-6 km) and had crystallization temperatures between 1100-1000ºC for the gabbros and 700ºC for the granites (Palácios et al., 1995).

Gravimetric data collected in and around the complex points towards distinct geometries for the granite and central gabbro-diorite-syenite complexes. The granite has a laccolithic shape being 12 km long , 8 km wide and 1 km thick (Terrinha et al., 2003; Kullberg et al., 2006, 2010). Based on the analysis of gravimetric and anisotropy of the magnetic susceptibility data, these authors propose that the granitic magma intruded through conduits with E-W, NE-SW and NNW-SSE directions which were afterwards reused during the intrusion of the gabbroic to syenitic magmas that show a subvertical

plug like shape reaching depths of 4 km (fig. 2.9B). The NNW-SSE structures were active during the Middle Jurassic as rift faults. These faults extend as a fault zone intruded by a complex of dykes that extends to the south of the Sintra complex until the Arrábida chain for more than 40km and were re-worked as a dextral strike-slip faults during the Cenozoic tectonic inversion. The E-W faults were also active during the Mesozoic rifting and served as thrusts during tectonic inversion, such as the main Sintra thrust located in the northern part of the complex (fig. 2.10a,b and c). The NW-SE faults served as sinistral strike-slip faults during inversion (fig. 2.2a, 10).

The petrogenesis of this complex has been intensely debated along the years and up to the present (e.g. Matos Alves, 1964; Wright, 1968; Sparks and Wadge, 1975; Leal, 1990, 1991; Palácios et al., 1995, 1999). Matos Alves (1964) proposed the generation of all the observed lithologies through processes of fractional crystallization and assimilation of a granitic contaminant by a parental basic undersaturated magma with a mafraite like composition. Wright (1968) favoured a model where the granite and the gabbro-syenite suite were not comagmatic, with the granite resulting from crustal anatexis and being emplaced before the gabbros and syenites, which in their turn resulted from the differentiation and contamination of a basic mafraitic magma by a more evolved felsic liquid, leading to enrichment in alumina, alkalis and volatiles.

Sparks and Wadge (1975) supported that high pressure garnet and clinopyroxene fractionation from an hypersthene normative picritic basalt, or partial melting of a phlogopite rich source at pressures above 15 kb are the mechanisms that might have generated the undersatured basic magmas seen in Sintra and in the Lisbon Volcanic complex, while the syenites and trachytes of the same region should have evolved directly from the hypersthene normative basalts that did not go through high pressure fractional crystallization.

More recently, Leal (1990, 1991) analysed petrographic and geochemical data and concluded that the granite was generated by melting of a felsic rock, probably from the Variscan basement, while the other rocks in the complex evolved from the gabbroic to the syenitic term by fractional crystallization of clinopyroxene, amphibole, plagioclase and biotite coupled with assimilation of crustal lithologies. The Rare Earth Element (REE) and incompatible trace element geochemistry also confirms the genetic link between gabbros and syenites and implies a more important role for crustal assimilation in the generation of the granites (Palácios *et al*., 1999) when compared to the syenites.

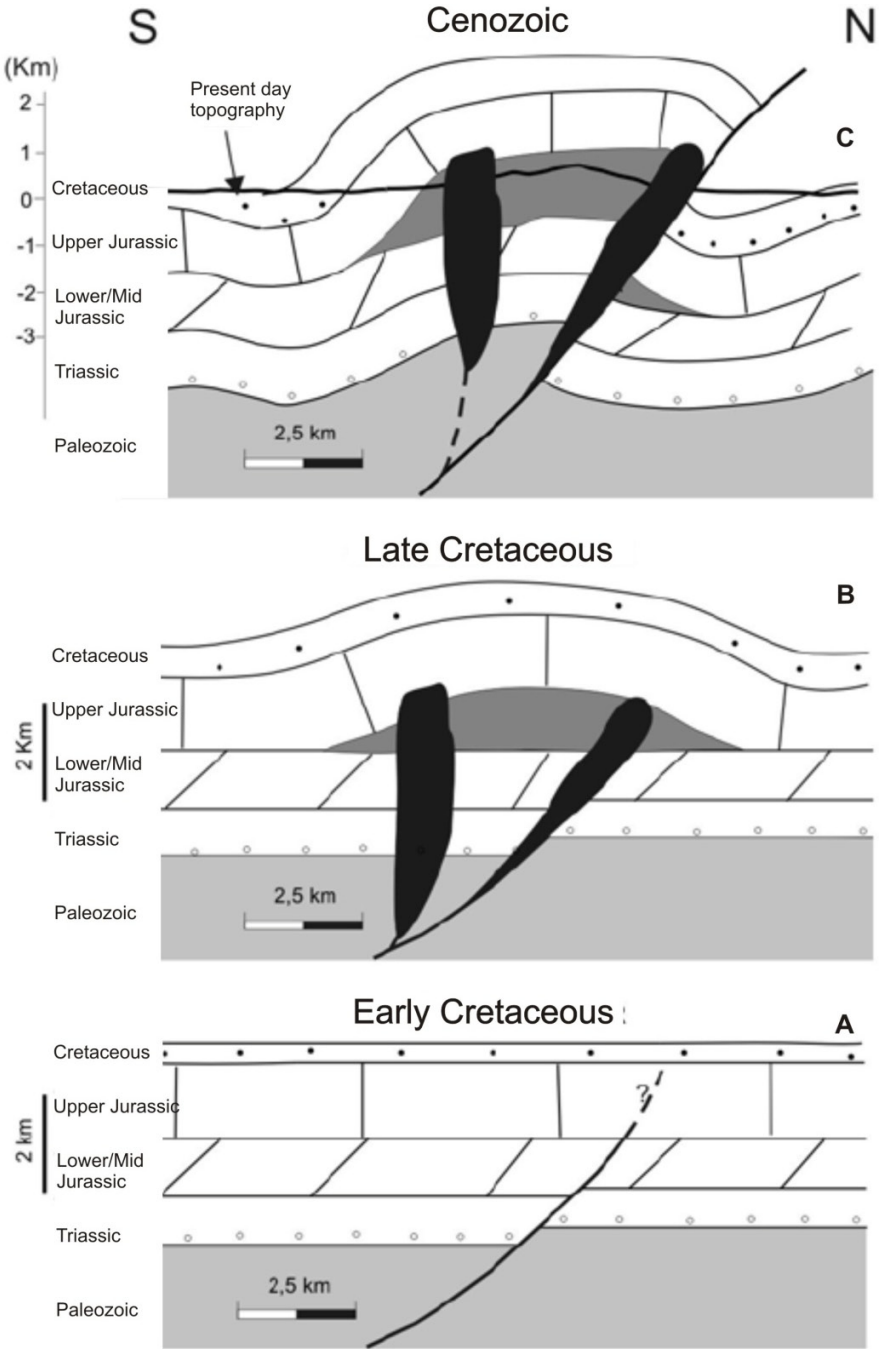

Fig. 2.10: Schematic representation of the evolution of the Sintra intrusion. Adapted from Kullberg et al., 2006.

Concerning geochronology, the granite has systematically yielded older ages than the suite of gabbro-diorite-syenite and associated breccias present in the complex. According to the published data, the emplacement of the granite (85 ± 8 Ma, Rb-Sr, Bonhome et al., 1961; 81.9 ± 0.4 Ma, K-Ar in biotite, MacIntyre and Berger, 1982; 84.0 ± 1.1, K-Ar in K-feldspar, Storetvedt et al., 1987) occurred before the intrusion of the

gabbro and syenite magmas (76.1 ± 1.1 to 78.3 ± 1.9 Ma, K-Ar in whole rock syenite, Storetvedt et al., 1987; 74.9 ± 1.0 Ma whole-rock K-Ar in gabbro, Storetvedt et al., 1987). This is compatible with field relations and the geophysical studies that revealed the complex's structure in depth and show that the gabbroic and syenitic rocks intrude the granite (Terrinha et al., 2003; Kullberg et al., 2006, 2010).

The available Sr isotopic data for the Sintra complex point towards a common origin for the gabbroic and syenitic magmas ($^{87}Sr/^{86}Sr_{74}$ = 0.7039 to 0.7042, Mendes, 1968; Abranches and Canilho, 1981) that could correspond to a basic magma with unradiogenic Sr which was slightly contaminated by a more radiogenic crustal lithology to produce the syenites. The more radiogenic composition of the granites ($^{87}Sr/^{86}Sr_{80}$ = 0.7052 to 0.70601 Mendes, 1968; Abranches and Canilho, 1981) favours its generation by higher amount of crustal contamination of a relatively unradiogenic, probably mantle derived, magma and not by pure crustal anatexis, due to the observed isotopic values being quite lower than what would be expected for felsic continental crust.

Contemporaneously with the tectonic inversion of the Lusitanian basin, the Sintra region suffered substantial deformation, resulting in the development of an E-W thrust, probably reactivating an older extensional fault, in front of the northern limit of the complex which also led to the exhumation of the complex during the Paleogene (Kullberg *et al*., 2006). The field evidence is supported by fission-track data on apatites that point towards exhumation in Eocene times (Stapel *et al*., 1996).

2.3.1.2 The Sines igneous complex

The Sines igneous alkaline complex delineates a well defined promontory in the western Portuguese coast, at approximately 38ºN (fig. 2.8). It has an onshore outcropping area of about 6 km^2, but most of the complex is covered by Pliocene and Quaternary littoral deposits and dunes. Its outcrop area in the continental shelf is approximately the same size of the Sintra submarine part, i.e. roughly 40 km^2 (Monteiro, 1984), increasing the size of the complex while also changing its shape to an ellipse with an WNW-ESE major axis approximately 12 km long and with a minor axis with 3.5 km (Inverno et al., 1993).

The Sines complex is overlain by Upper Jurassic limestones of the Santiago do Cacém Mesozoic basin (part of the Alentejo basin) along its northern boundary, whilst

along the southern one it is bordered by Carboniferous turbiditic meta-sediments of the Mira Formation (Namurian; Oliveira, 1990). The intrusion produced a contact aureole that includes calcic and pelitic hornfels. It is associated with the formation of a dense dyke complex that shows a very wide range of lithologies, from basic to intermediate and acid (lamprophyres, pyroxenites, basalts, microdiorites, trachybasalts, trachytes, microsyenites, microgranites) and occur in all directions although N-S and E-W dominate (Canilho, 1972).

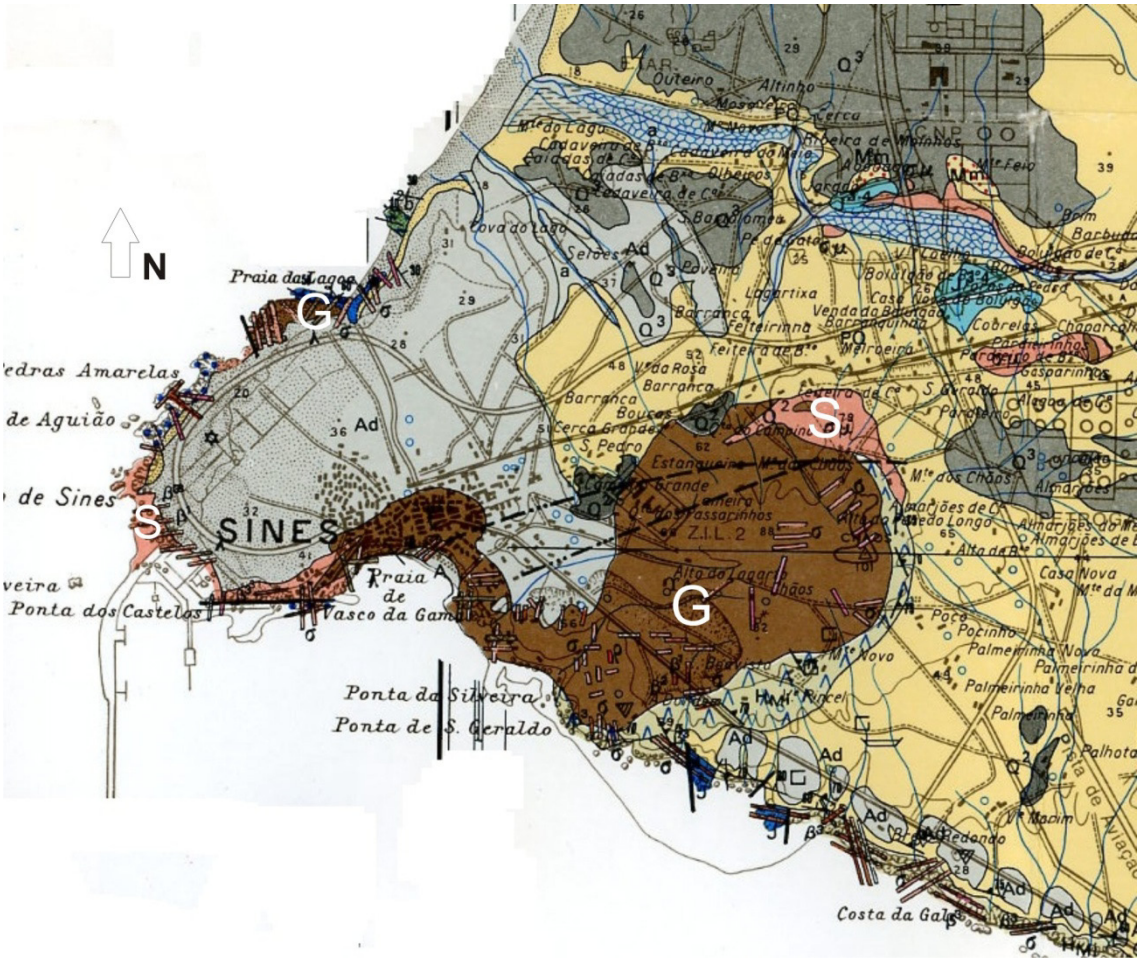

Fig. 2.11: Geological map of the Sines complex. S – syenites; G – gabbros and diorites.

Inside the complex, the main outcropping rocks are quartz syenites, diorites and gabbros both of the amphibole rich variety observed in Sintra (South, at Vasco da Gama beach) or of an another olivine rich and amphibole poorer variety that appears to show some banding (North, in Pedras de Sal). All these rocks are cut by the previously mentioned dyke complex.

The Sines complex was also subject to several dating attempts using the K-Ar and Rb-Sr methods. The wide range of displayed "ages" (78.9 ± 1.5 to 62.0 ± 1.3 Ma K-Ar in whole rock diabase dykes; 75.2 ± 0.8 to 63.8 ± 0.8 Ma K-Ar age in K-feldspar from the syenite; 72.0 ± 1.5 Rb-Sr whole rock isochron, Canilho and Abranches, 1982), particularly the values below 70 Ma are probably the result of a late thermal overprint that may have caused argon loss (Storetvedt et al., 1987) and its central age should be somewhere between 72 and 75 Ma.

The incompatible element enriched nature of the more basic magmas, jointly with the observed negative K anomalies in primitive mantle normalized incompatible element diagrams and light REE enrichment ($(La/Yb)_n$ = 17.25 – 3.29) and low initial $^{87}Sr/^{86}Sr$ ratios (0.70331, Canilho e Abranches, 1982) suggest that the basic magmas were the result of small volume partial melting in the presence of residual garnet and a K-rich phase (possibly phlogopite or amphibole) of a mantle source enriched in incompatible elements but with a time integrated Sr depletion, with a possible affinity with the HIMU mantle component (Martins and Olivença, 1998).

As for the generation of the remaining observed lithologies, it has been proposed that a common basic source represented by the gabbros then generated the diorites and syenites by fractional crystallization of olivine, clinopyroxene, amphibole and plagioclase in a closed system (Canilho, 1972; Martins and Olivença, 1998).

2.3.1.3 The Monchique igneous complex

The Monchique igneous alkaline complex is located in the Western Algarve, has an approximately elliptical shape and occupies an area of about 80 km^2. It is formed by two concentric nepheline syenite bodies, with associated lamprophyre dykes and breccias enclosing small mafic to ultramafic rock outcrops (Rock, 1978; Gonzalez-Clavijo and Valadares, 2003; Valadares, 2004). It intrudes the Paleozoic South Portuguese Zone, namely Carboniferous shales and quartzitic sandstones of the Brejeira Formation (Middle Namurian–Early Westphallian; Oliveira, 1990) that underwent earlier Variscan metamorphism. The intrusion produced a 200 m thick contact metamorphism aureole. This is the most voluminous of the southern alkaline intrusions and has the particular characteristics of being the only one emplaced exclusively in

rocks of Paleozoic age that remained unaffected by Mesozoic rifting, and to show a silica undersaturated character for its entire lithological spectrum.

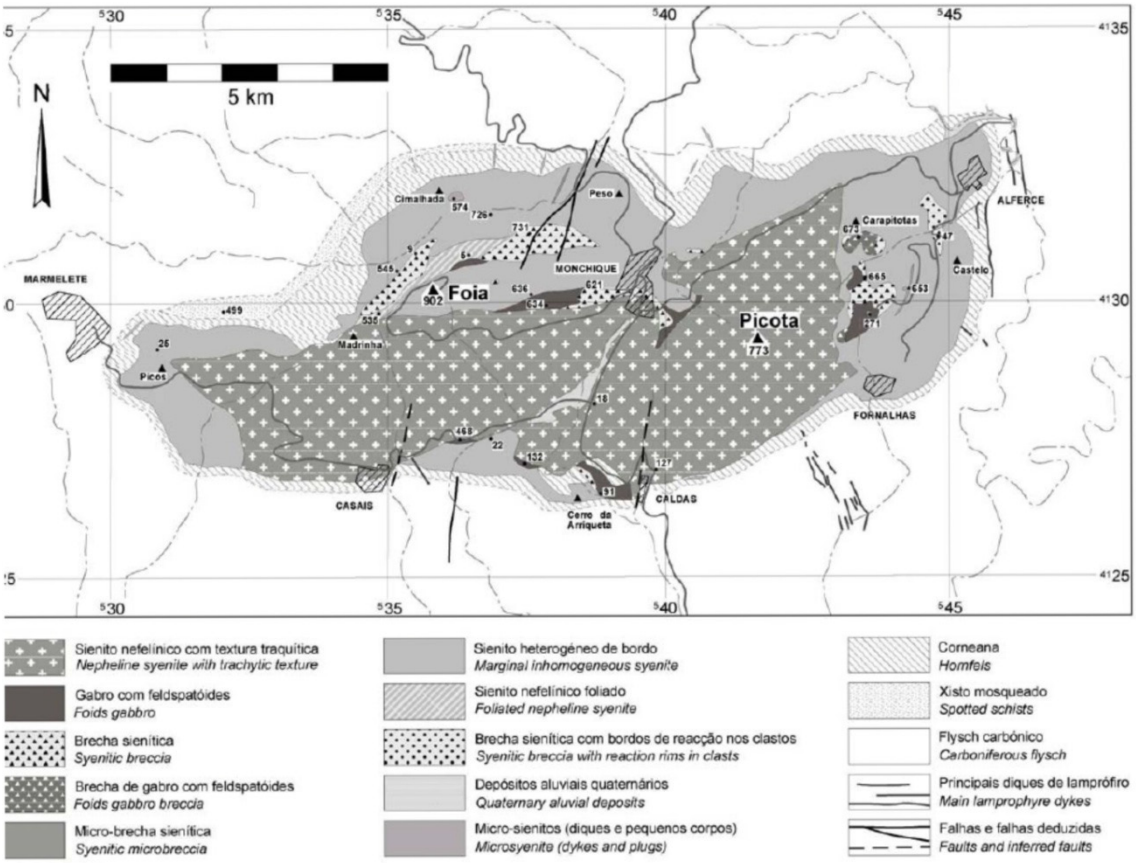

Fig. 2.12: Geological map of the Monchique igneous complex. From Gonzalez-Clavijo and Valadares, 2003.

Recent revision of the geological mapping of this complex allowed the identification of two concentric units of different nepheline syenites, the inner of which encloses various bodies of basic and ultra-basic rocks (fig. 2.12; Gonzalez-Clavijo and Valadares, 2003). These authors also proposed an intrusion mechanism where basic magmas initially ascended through pre-existing ENE-WSW faults that were reactivated during a Cretaceous extensional regime. They were followed by the emplacement of several heterogenous nepheline syenite bodies that ascended through the same conduits, and were afterwards followed by a last pulse characterized by the ascension of the homogenous nepheline syenite body that intrudes all of the previous ones (fig. 2.13; Gonzalez-Clavijo and Valadares, 2003).

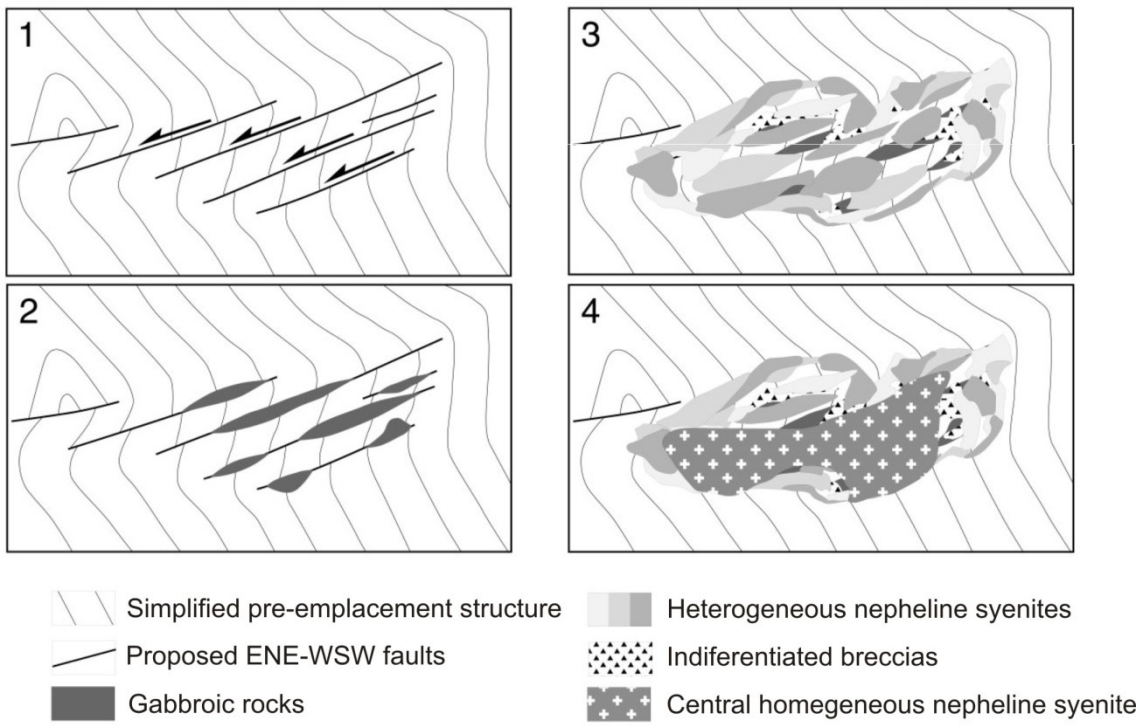

Fig. 2.13: Diagram illustrating the installation mechanism proposed by Clavijo and Valadares (2003) for the Monchique igneous complex.

The Monchique complex has been dated with both the K-Ar and the Rb-Sr method (table 1), with the obtained ages clustering around 72 Ma (72.0 ± 2.0 mean K-Ar ages on mineral separates, MacIntyre and Berger, 1982; 72.0 Ma Rb-Sr whole rock isochron, Rock, 1976, Bernard-Griffiths et al., 1997; Valadares, 2004), although the K-Ar ages obtained for K-feldspar and nepheline separates show some spread, attributed to Ar loss (MacIntyre and Berger, 1982).

The geochemical evolution of the complex appears to have happened through fractional crystallization of clinopyroxene, magnetite, kaersutite, titanite and apatite from an initial basic magma represented by the mafic and ultramafic rocks in the complex (Valadares, 2004). That primary magma must have derived from the low volume partial melting of a mantle source enriched in incompatible elements and in the presence of residual garnet ($(La/Yb)_n$ = 20.9 to 29.1) and a K-rich phase (probably amphibole or phlogopite) similar to the one proposed for the Sines igneous complex. The isotopic signatures for these rocks show unradiogenic initial Sr ($^{87}Sr/^{86}Sr_{72} \approx 0.703$, Bernard Griffiths et al., 1997; Valadares, 2004), high εNd (εNd_{72} 4.3 - 5.6, Bernard Griffiths et al., 1997) values and a Pb isotopic signature ($^{206}Pb/^{204}Pb_{72}$ - 19.13 to 19.42;

$^{207}Pb/^{204}Pb_{72}$ - 15.61 to 15.64; $^{208}Pb/^{204}Pb_{72}$ - 38.8 to 39.2; Bernard-Griffiths et al., 1997) that plots on the Northern Hemisphere Reference Line (NHRL; Hart, 1984).

These isotopic characteristics, together with the silica undersaturation, and the absence of negative Nb and Ta anomalies in the Monchique rocks, exclude the hypothesis of crustal contamination playing a major role on the generation and evolution of this rock suite and allow the deduction that these resulted from the partial melting of an asthenospheric mantle reservoir of the PREMA (the Prevalent Mantle of Zindler and Hart, 1986) type (Bernard Griffiths et al., 1997; Valadares, 2004), although some interaction with the overlying lithospheric mantle is thought to have had a minor role in enriching the Monchique magmas in light REE, consequentially lowering its εNd when compared with the nearby alkaline and possibly cogenetic magmatism in the Ormonde seamount (Bernard Griffiths et al., 1997)

It has been proposed that the Monchique complex is part of a possible Madeira hotspot track before it was ~200 km displaced to the West through right lateral offset along the Azores–Gibraltar Fracture zone (Geldmacher and Hoernle, 2000).

2.3.1.4 The Lisbon Volcanic Complex

The Lisbon Volcanic Complex (LVC) is an intrusive and extrusive event constituted by a series of volcanic necks, lava flows, breccias, plugs, dykes and sills, occupying a total area of approximately 200 km^2 (fig. 2.14). Their composition is mostly basaltic (s.l.), although intermediate and acid terms are also present (trachybasalts, trachytes and rhyolites) but correspond to a much smaller volume (Palácios, 1985). It is the most recent known alkaline occurrence in the Lusitanian Basin (72 ± 3 Ma; K-Ar isochron by Ferreira and Macedo, 1979) and outcrops in the block limited by the Nazaré and Arrábida faults, more specifically in the Lisbon region. The volcanic activity is contemporaneous with the previously mentioned uplift of the Nazaré-Arrábida block of the Lusitanian basin and sits on top of a paleokarst formed by the erosional unconformity carved on Cenomanian limestones. The subaerial volcanism is divided in at least six effusive and explosive events that originated a sequence of flows and pyroclastic ash deposits at least 400 m thick (Serralheiro, 1978; Ramalho et al., 2001).

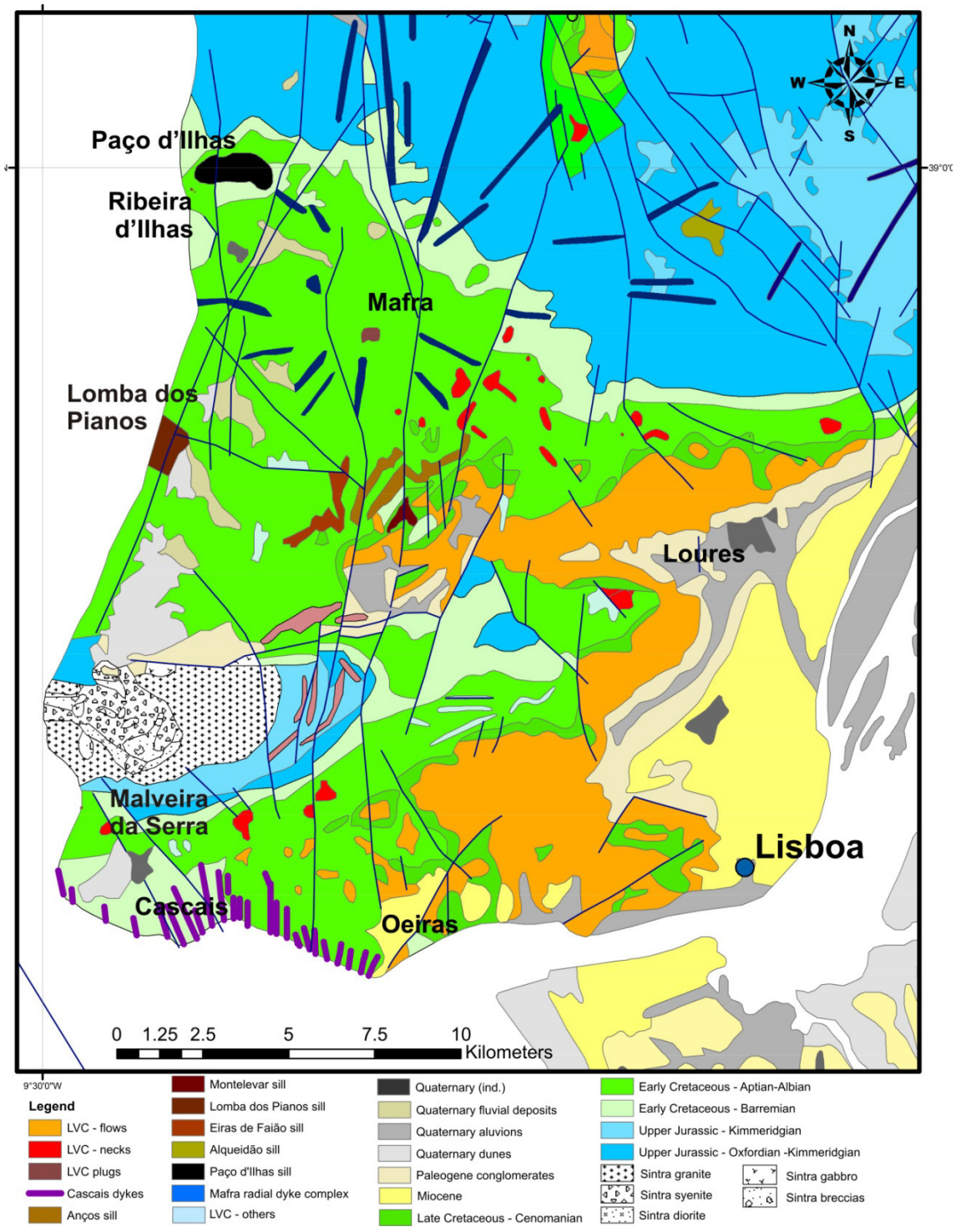

Fig. 2.14: Geological map of the Lisbon region showing all the main magmatic occurrences. Adapted from the 1:500 000 geological map of Portugal (Oliveira et al., 1992).

The enrichment in incompatible elements and low $^{87}Sr/^{86}Sr_{72}$ (approximately 0.70325, Palácios, 1985) of the basic magmas suggest they were generated by a low volume partial melting of an incompatible element enriched mantle source, characterized by a time integrated Sr depletion and the presence of residual garnet and

K-rich mineral, similarly what was described for the intrusive igneous complexes. The isotopic Sr ($^{87}Sr/^{86}Sr_{72}$ = 0.70325-0.70812) and O ($\delta^{18}O$ = 6.22-11.19) signatures of the entire suite point towards the evolution from the more basic to the more acid members taking place by the joint action of low pressure fractional crystallization of a basic alkaline magma along with the assimilation of crustal materials (Palácios, 1985).

2.3.1.5 The Mafra radial dyke complex, Oeiras-Cascais dykes, Paço d'Ilhas and Foz da Fonte sills and other minor occurrences in the Lusitanian basin

Several other smal alkaline intrusions of Late Cretaceous age can be found in the Lusitanian basin. They are not integrated in the LVC because some of them appear to be associated with a different stress field (Mafra radial dyke swarm, Oeiras-Cascais dykes), have older ages (Paço d'Ilhas sill) or are located relatively far from the LVC (the Foz da Fonte sill and the intrusions associated with the Sesimbra salt diapir).

Among them, one of the most discussed is the Mafra radial dyke complex (fig. 2.14). It is constituted by a series of dykes that radiate from a central gabbroic plug located in the vicinities of Mafra. These dykes are substantially altered alkaline basic rocks and are best observed in the coastal area around Ericeira. Their outcropping pattern suggests intrusion with a stress field characterized by radial σ1 (where: σ3 – maximum compression; σ2 intermediate compression; σ1 – minimum compression) controlled by a deep intrusion. They were recently subject of an integrated Anisotropy of Magnetic Susceptibility (AMS) and analysis of preferred mineral and vesicle orientation study that points towards the magmatic flow coming from the direction of the central plug and at an angle that suggests the presence of a larger magma chamber at a depth of approximately 3.2 km (Nogueira et al., 2008).

The Paço d'Ilhas sill (fig. 2.14), also known as the Ribamar gabbro (Zbyszewski et al., 1955), was previously included in the LVC due to its similar chemical and petrographic characteristics (Palácios, 1985), but subsequent age determinations showed that it is actually between 88 and 86 My old (K-Ar ages in biotite and K-feldspar separates, respectively, Mahmoudi, 1991) and therefore significantly older than the LVC. The sill intrudes Lower Cretaceous sediments (Albian and Aptian-Barremian sandstones and limestones), having an outcropping area of around 6 km^2. It is a layered

intrusion made up of monzonitic and syenitic sheets in a monzograbbroic body (Mahmoudi, 1991). These correspond to segregations produced by fractional crystallization processes with the lighter plagioclases accumulating on top of the sill by flotation and the heavier mafic minerals sinking to the bottom (Mahmoudi, 1991).

The 8 m thick Foz da Fonte sill (fig. 2.8) is located in the Setúbal Peninsula, on the cliffs just South of the beach with the same name and corresponds to the southernmost intrusion in the Lusitanian basin. It outcrops for around 150m along the coast, and it terminates against the Aptian sediments it intrudes in the north, while in its southern limit it is cut by an NNW-SSE trending dextral strike-slip fault (Kullberg, 2000). It has recently been the target of an AMS study that proposed that the magmatic conduit for this sill has a NNE-SSW direction and could be possibly related to a reactivated Variscan fault or to a secondary fracture related with the NNW-SSE Sintra-Sines-Monchique deep fault (Miranda et al., 2006).

The Oeiras-Cascais dykes (fig. 2.14) outcrop in the coastal area between the Carcavelos beach and Cabo Raso. They display orientations between NNE-SSW and NNW-SSE and are constituted by alkaline basalts, lamprophyres and hawaiites (Miranda *et al*., 2005). They are thought to have intruded pre-existing fractures formed by a stress field characterized by N-S σ3, vertical σ2 and approximately E-W σ1, with σ2 and σ3 inverting during the installation of the dykes (Costa, 1980). A more recent work on the westernmost dykes concluded that these were emplaced in previously existing cleavage fractures contemporaneously with an important left strike slip movement along these same fractures within a stress field characterized by an E-W to NW-SE σ3 (Maia and Gonçalves, 2006).

2.3.1.6 Minor occurrences in the Algarve basin

The Late Cretaceous alkaline magmatism is also represented in the Algarve basin by a series of dykes, plugs, sills and necks of basanitic to lamprophyric nature (Martins, 1991). They outcrop mostly in the coastal region and are also associated with salt diapirs. Their emplacement is contemporaneous with the above mentioned Monchique igneous complex (72 to 75 Ma, Martins, 1991; 61.5-70.4 Ma, Storetvedt et

al., 1990) with which they also share geochemical affinities, pointing to a similar sublithospheric mantle source (e.g. $^{87}Sr/^{86}Sr_{75}$ = 0.70276-0.70385, enrichment in incompatible elements and light REE, Martins 1991). Their mineralogy, namely the existence of green core clinopyroxenes and amphiboles with partly resorpted cores, points towards an important contribution of magma mixing in the generation of the observed lithotypes, with the basanites representing a complete mix between a more evolved and a more basic magma and the lamprophyres corresponding to only partial mixing of these liquids due to smaller residence times in the magma chamber and faster extraction (Martins, 1999).

2.3.2 The offshore West Iberian Margin

The significant advances made recently in the Marine Geosciences domain have allowed researchers to identify, sample and study a series of previously unknown igneous alkaline seamounts in the WIM. The purpose of this section is to describe these occurrences and, when possible, discuss the mechanisms responsible for their generation.

2.3.2.1 The Madeira-Tore Rise

The Madeira-Tore rise groups a series of mid ocean ridge parallel seamounts between the Tore seamount and its several peaks, and the Madeira archipelago (fig. 2.15). It encompasses the Josephine and Lion seamounts, among many others whose name changes depending on author and publication. It is cut in across by the Azores-Gibraltar fracture zone, dividing it in a northern branch that includes all the seamounts between Tore and Josephine and a southern branch that groups the remaining seamounts from Josephine to Madeira. The rise has a total estimated volume of erupted magma of 10^5 km^3 (Merle et al., 2009)

The rise is located on transitional to oceanic crust and extruded onto seafloor with an age corresponding to the J magnetic anomaly (≈ 124-118 Ma) and is paired with the J Anomaly ridge across the Mid Atlantic Ridge (MAR), on the American plate (Peirce and Barton, 1991).

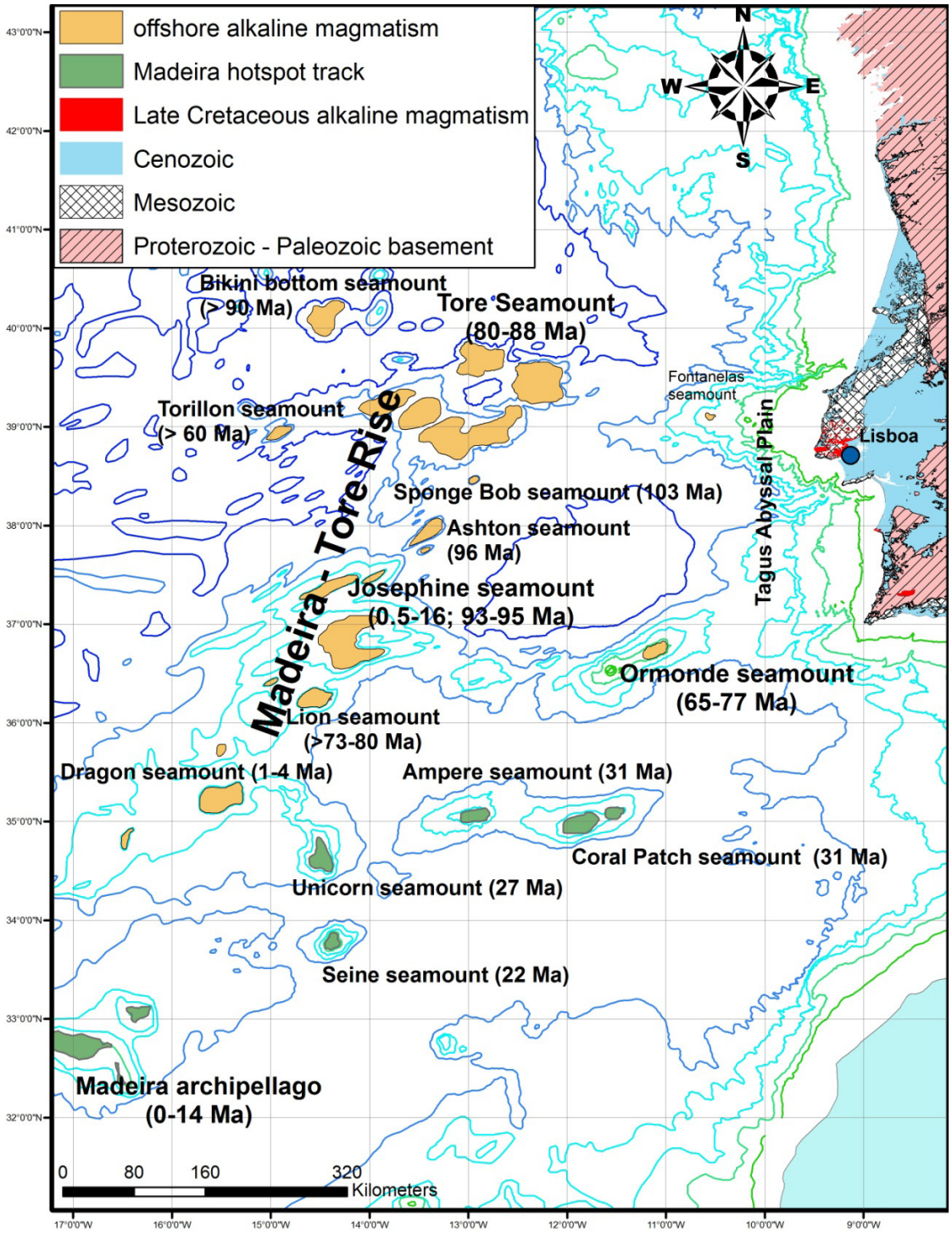

Fig. 2.15: Map of the alkaline igneous occurrences in the West Iberian Margin. Ages from Geldmacher et al., 2006, and Merle et al., 2006, 2009.

Its origin was initially attributed to the Madeira hotspot, with the seamounts representing its hotspot trail (Morgan, 1982; Crough, 1983; Ferreira et al., 1988), but the existence of the conjugate J Anomaly ridge led Peirce and Barton (1991) to propose that they had been generated during a period of intense volcanism in the MAR which

produced a thicker, isostatically balanced oceanic crust. However, the most recent studies revealed that some of the seamounts that constitute the Madeira-Tore rise have ages more recent than the magnetic J anomaly, which argues for a different generation mechanism (Merle et al., 2006, 2009; Geldmacher et al., 2006).

Merle et al. (2006) analyzed several intermediate igneous alkaline rocks from the northern branch of the rise, which they also dated using the U-Pb method in zircon and titanite separates. The ages obtained show a range from 80 to 104 Ma and show no spatial age progression. The isotopic signatures shown by these rocks ($^{206}Pb/^{204}Pb$ 19.139 - 19.620, $^{207}Pb/^{204}Pb$ 15.544 - 15.828, $^{208}Pb/^{204}Pb$ 38.750 - 39.936, $^{87}Sr/^{86}Sr_i$ 0.70231 - 0.70340, and εHf_i 6.9 a 12) are distinct from the ones shown by normal Mid Ocean Ridge Basalts (MORBs) and the rocks associated with the Madeira and Azores hotspots. They were interpreted by the authors as being derived from the interaction between a long lived thermal anomaly with an OIB-like (Ocean Island Basalt) composition associated with some crustal recycling, probably through delamination or interaction with the Iberian lithospheric mantle and crust (Merle *et al*., 2006).

The southern branch of the Madeira-Tore rise was dated through the Ar-Ar and biostratigraphic methods and yielded ages that can be divided into two groups (Geldmacher et al., 2006). The first phase of magmatism took place during the Late Cretaceous, between 80 and 95 Ma, and is detected in the base of the larger seamounts and around to the Azores-Gibraltar fracture zone, while the second phase is of Neogene age (16 – 0.5 Ma) and was identified on the top of some seamounts, especially the ones closer to the Azores-Gibraltar fracture in the elevations just north to the Madeira Archipelago (Geldmacher et al., 2006). The Late Cretaceous rocks are trace element enriched and their isotopic composition is compatible ($^{206}Pb/^{204}Pb_i$ 19.44 – 19.55, $^{207}Pb/^{204}Pb_i$ 15.58–15.59, $^{208}Pb/^{204}Pb_i$ 38.73 – 39.15, $^{87}Sr/^{86}Sr_i$ 0.702797 – 0.702883, $^{143}Nd/^{144}Nd_i$ 0.512878 – 0.512885 $^{176}Hf/^{177}Hf_i$ 0.282976) with a derivation from the Canary mantle plume, while the Neogene show a wider range of isotopic compositions ($^{206}Pb/^{204}Pb_i$ 18.792– 20.245, $^{207}Pb/^{204}Pb_i$ 15.485–15.619, $^{208}Pb/^{204}Pb_i$ 38.334– 39.968, $^{87}Sr/^{86}Sr$ 0.702800 – 0.703238, $^{143}Nd/^{144}Nd_i$ 0.512842– 0.513090 $^{176}Hf/^{177}Hf_i$ 0.283004 - 0.283163) that overlap both the Madeira and Canary domains with the northern occurrences being more isotopically enriched than the southern ones (Geldmacher et al., 2006). The authors explain these differences in composition and age with a model considering that the first phase generated by the interaction of the Canary

hotspot with the MAR whereas the second pulse is a mix of activity derived from the Madeira hotspot in the southernmost part of the ridge and from the melting of lithospheric mantle on extensional basins in the vicinities of the Azores-Gibraltar fracture zone. That lithospheric mantle either contained pyroxentic material or had been previously metasomatized and overprinted by the Canary plume in the Cretaceous (Geldmacher et al., 2006).

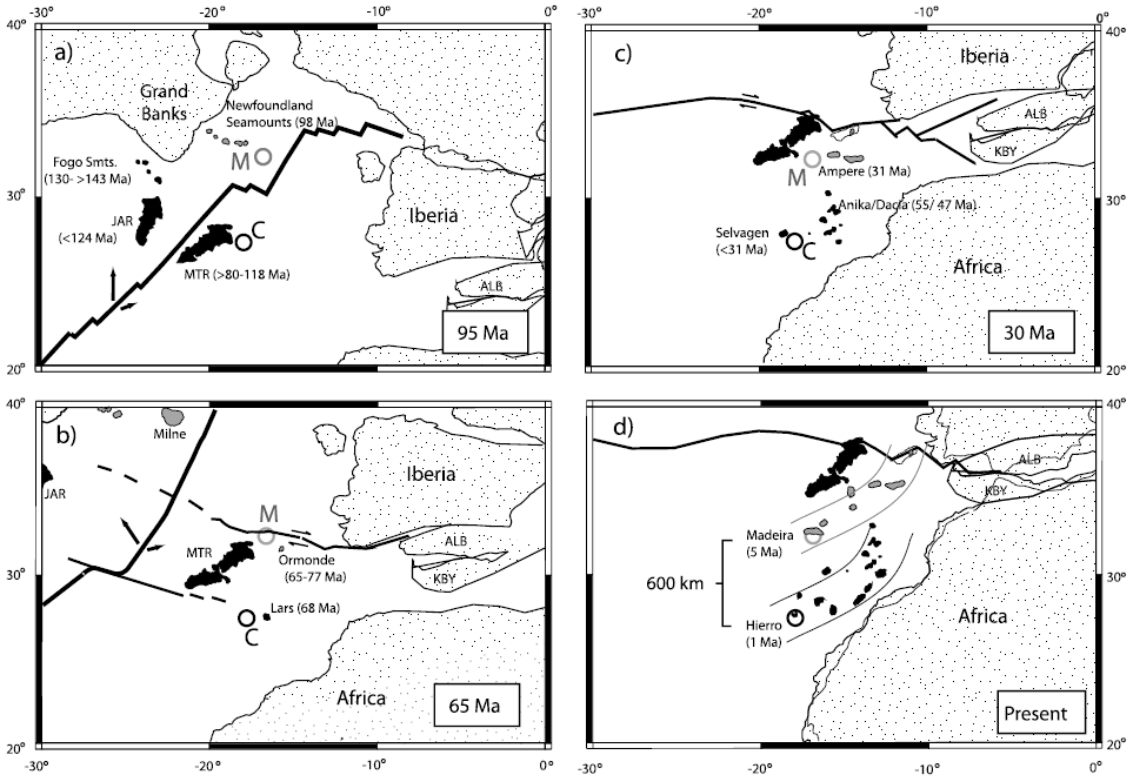

Fig. 2.16: Evolution of the Madeira-Tore rise according to Geldmacher et al., 2006.

Further geochronological work by Merle et al. (2009) led these authors to recognize a total of three pulses between 103 Ma and the present. The first and oldest taking place between 103 and 80.5 Ma in the northern and central part of the Rise, the second c. 68 Ma and finally a third one between 28 Ma and the present day.

However, if one considers the onshore magmatic activity and includes the Ormonde, Ampére and Coral patch seamounts, six distinct stages are identified during these pulses, with some of them defining linear trends (Merle et al., 2009).

According to Merle et al. (2009) the first stage occurred during the first pulse and defined the lineament between the Sponge Bob and Jo Sister seamounts between 108 and 88 Ma (fig. 2.17), while the Iberian plate was moving in a NE direction. The second

stage also occurred during the first pulse, but has a different distribution, occurring randomly in the rise but also in the continent between 88 and 81 Ma (fig. 2.17). From 83 Ma onward the direction of movement of the Iberian plate changes again with the ceasing of seafloor spreading in the Bay of Biscay which caused the rocks of stage 3 to be aligned in an NNW-SSE direction while they intruded between 80 and 69 Ma due to the new NNW movement direction of the plate (fig. 2.17).

The fourth stage took place between 68 and 60 Ma and is again randomly distributed in the oceanic domain. It was followed by stage 5, a period during which no magmatism took place in the region and finally by stage 6, ongoing from 32 Ma to the present with activity occurring from the Azores Gibraltar fault zone area down to the Madeira archipelago (fig. 2.17).

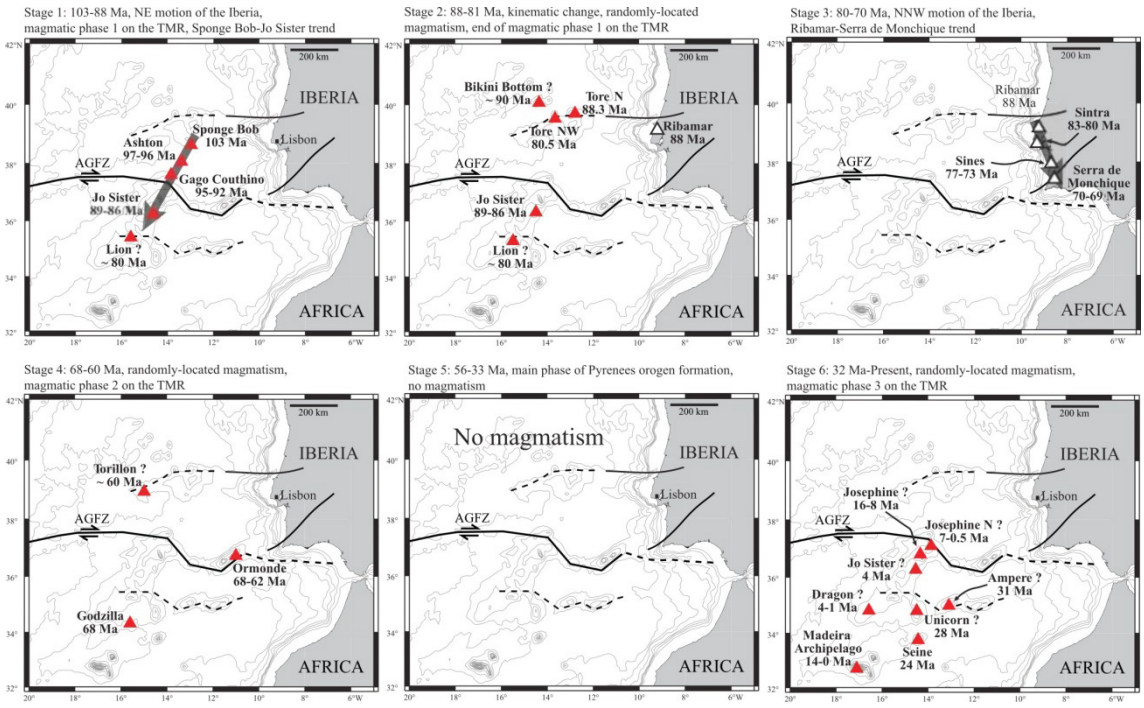

Fig. 2.17: Distribution of the pulses of alkaline igneous activity in the Central North Atlantic according to Merle *et al*., 2009.

Merle et al. (2009) attribute the stages where the magmatic activity seems to have a random distribution (stages 2 and 4) to times of little or no movement in the Iberian plate that led to heat accumulation in the mantle due to the blanketing effect of the lithosphere and inducing magmatism in random locations. They also justified the lack of magmatism during stage 5 with the collision of Iberia and Europe and consequent formation of the Pyrenees creating a compressive stress field in both the

oceanic and continental lithosphere of the Iberian plate that prevented magma ascent. At last, during stage 6 the continuing compression still prevented the emission of magma at the surface, but the continuous thermal blanketing effect of the lithosphere led to magma generation, with its release being only possible on the African plate or in the border between Africa and Iberia, where lithospheric structures might have facilitated magma ascent.

2.3.2.2 The Sintra-Tore lineament

This lineament is defined by a series of magnetic anomalies (e.g. Silva et al., 2000, fig. 2.18) and small seamounts present between the Sintra igneous complex and the Tore seamount.

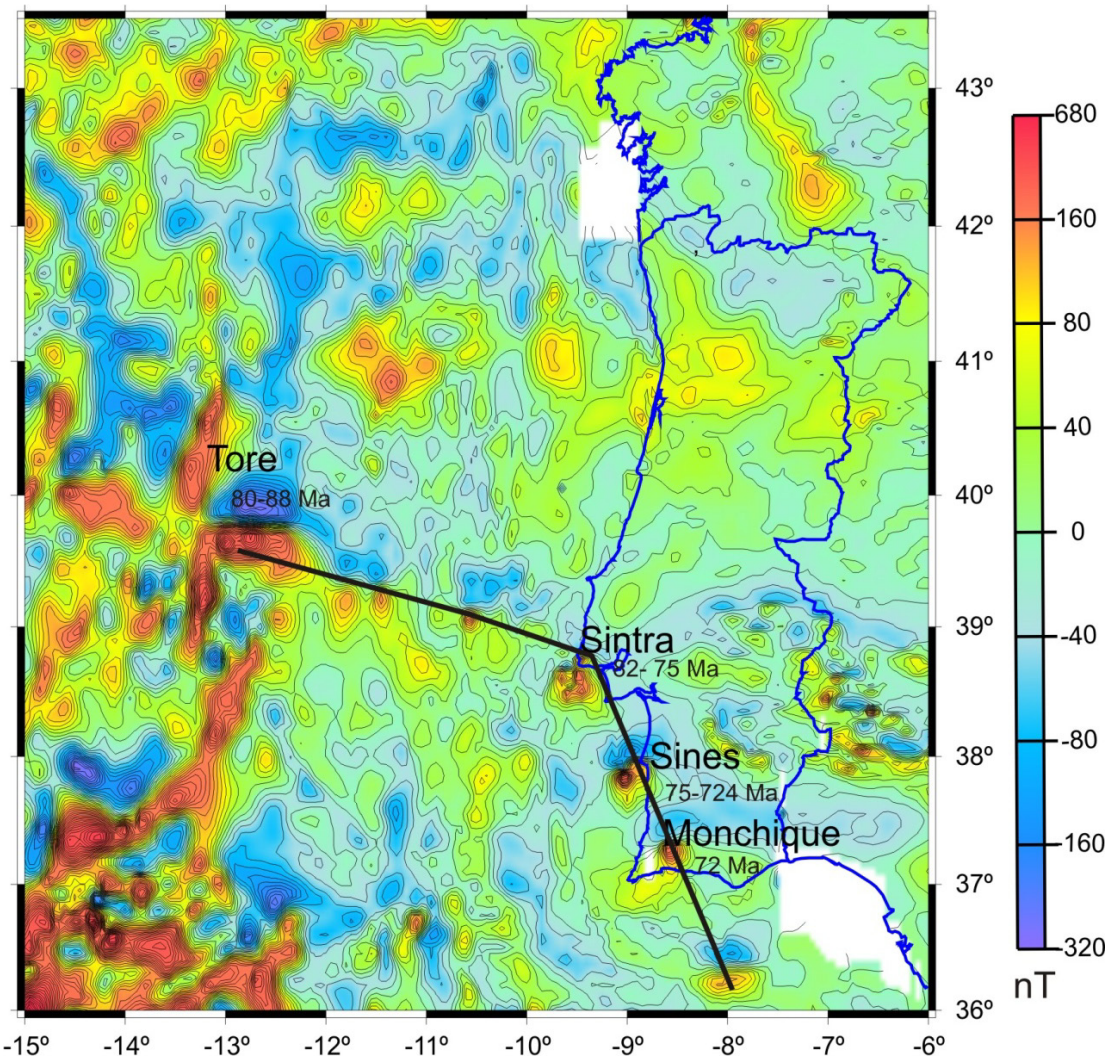

Fig. 2.18: Magnetic anomalies of the West Iberian Margin and the lineaments defined by them. Adapted from Silva et al., 2000.

The nature of the rocks that constitute it is still mostly unknown, except for one ankaramite dredged by Mougenot (1989) near one of the magnetic anomalies and dated at 74 Ma (Ar-Ar; Feraud *in* Mougenot, 1989). Only one of these seamounts has been sampled and will be discussed later in this study.

Moreover, Alves et al. (2006) identify an intrusive body in the continental platform West of Sintra based on seismic reflection data.

This lineament roughly coincides with the boundary between the Paleozoic Ossa Morena Zone and South Portuguese Zone terranes and is the equivalent to Collector anomaly in the North American plate, which might correspond to the Theic ocean suture (Lefort et al., 1996; Capdevila and Mougenot, in Boilot and Winterer (eds.), 1988). Badagola (2008) showed that the morphological expression of this lineament on the Estremadura Spur corresponds to the seafloor trace of a NW-SE to WNW-ESE strike-slip fault.

Roque et al. (2009) identified a series of WNW-ESE to E-W structures in the Estremadura Spur and between that feature and the Tore seamount that correspond to thrusts and backthrusts that deform sediments up to the Pliocene-Pleistocene.

2.3.2.3 The Ormonde seamount, Gorringe bank

The Gorringe bank is a major morphological feature that rises from the seafloor of the Tagus Abyssal Plain at rougly -5000m to -24m at the top of Gettysburgh seamount. The Ormonde seamount corresponds to the northeastern peak of the Gorringe bank, where one can find alkaline basalts, nephelinites, nepheline syenites, phonolites and monchiquites outcropping in the seabottom (Cornen, 1982). These rocks intrude or cover Cretaceous peridotites, and tholeiitic gabbros and basalts that are thought to represent a section of oceanic lithosphere thrusted onto the Tagus Abyssal Plain along the Azores-Gibraltar fracture zone in mid Miocene times (Auzende et al., 1978; Féraud et al., 1986, fig. 2.19). The ages obtained for these rocks vary between 67-65 Ma (Ar-Ar, in whole rock, phlogopite and secondary hornblende Féraud et al., 1982, 1986) and 77 Ma (U-Pb in zircon separate, Schärer et al., 2000). This age variation with method suggests that the more recent ages obtained with the Ar-Ar method might represent later deformation phases that reset the Ar system or indicate very slow cooling (Schärer et al., 2000), although Merle et al. (2009) suggested that the sample dated by Schärer et al. (2000) might be a dropstone that originally came from the Sines igneous complex.

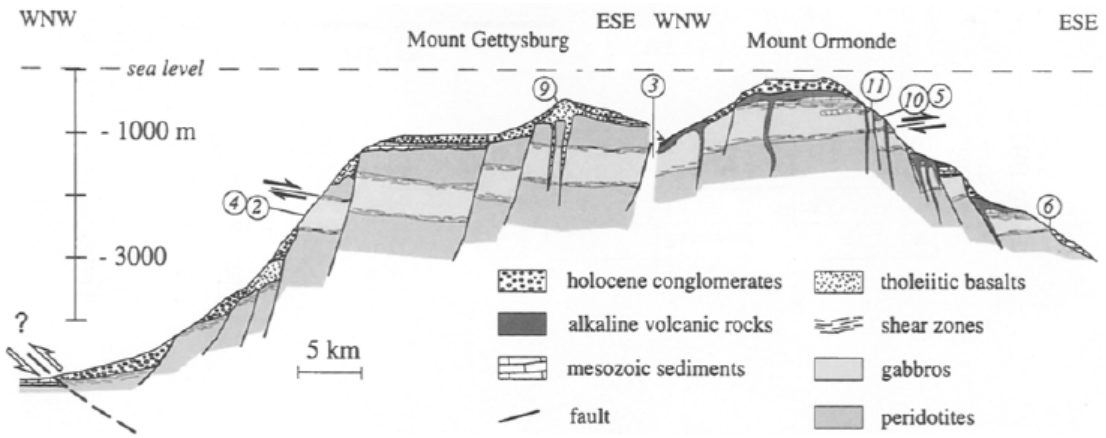

Fig. 2.19: Diagram showing the Gorringe bank, its structure and the position of tholeiitic lithosphere and posterior alkaline magmatism. From Scharër et al., 2000.

Bernard-Griffiths et al. (1997) studied the geochemical and isotopic composition of the alkaline rocks of the Ormonde seamount and concluded that these bear many similarities with the ones found in the Monchique igneous complex ($^{87}Sr/^{86}Sr_i$ 0.70304 – 0.70482, εNd_i 6.0-6.9, $^{206}Pb/^{204}Pb_i$ 19.07– 19.81, $^{207}Pb/^{204}Pb_i$ 15.57–15.77, $^{208}Pb/^{204}Pb_i$ 38.8– 39.5 for whole rock and 87Sr/86Sri 0.70303 – 0.70306, εNd_i 0.3-6.7 for clinopyroxene separates) although the εNdi values for Ormonde are either higher (whole rock) or much lower (clinopyroxene separates) than the ones seen in Monchique. The lower εNdi values were interpreted by these authors as reflecting the presence of a mantle lithosphere component in the Ormonde rocks similar to the one observed in Monchique, while the higher ones are associated with the dominating asthenospheric component.

Along with the Monchique complex, this seamount has been included in the hotspot track for the Madeira plume (fig. 2.16, Geldmacher and Hoernle, 2000; Geldmacher et al., 2000; Geldmacher et al., 2005).

3. Continental intraplate alkaline anorogenic magmatism and its geodynamic implications

Although it is not the most important type of magmatism in terms of total erupted volume, alkaline anorogenic magmatism can act as a marker for important geodynamic processes, such as rifting, the presence of mantle plumes and their interaction with the subcontinental lithospheric mantle, and the influence of major structure on controlling the emplacement and location of these magmatic features, while also providing a good proxy record for the chemical and physical evolution of the deep continental lithosphere and underlying mantle.

Basic magmas can be generated by adiabatic decompression, volatile addition that results in the lowering of the protolite's solidus, and by the supply of extra heat by a thermal perturbation of the geotherm (e.g. Wilson, 1989). In an intraplate setting, decompression is usually associated with extension and rifting, fluid addition to a metasomatic event that may or may not be related to a mantle plume, which can also add the heat necessary to for partial melting to take place.

The mantle plume definition used from here onwards is identical to the one of Morgan (1971, 1983) that defines a plume as a location where anomalously hot material that rises from a major mantle discontinuity (e.g. the D'' discontinuity that separates the mantle from the outer core or the 670 km discontinuity that separates upper from lower mantle) and ascends until it meets the lithosphere where it will start promoting the generation of large amounts of melts due to the addition of heat and decompression melting.

Potential sources for these basic liquids are usually ultramafic rocks (peridotites) in the upper mantle, which are mostly found in the rigid, conductive Continental Lithospheric Mantle (CLM) or in the underlying asthenosphere, a plastic, convective portion of the upper mantle. The CLM, however, is divided in two distinct layers: the Mechanical Boundary Layer (MBL) where heat transfers by conduction and deformation occurs in a fragile regime and the Thermal Boundary Layer (TBL) where heat is transferred both by convection and advection and that may suffer periodical recycling into the asthenosphere (e.g. Wilson, 1993, fig. 2.20).

Besides the initial composition of both the lithosphere and asthenosphere, several other factors control the composition of the generated liquids, such as the extent

of partial melting, the potential temperature of the mantle (the temperature of a mantle rock if brought to the surface adiabatically), the thickness of the lithosphere, the amount of tectonic extension, the initial thickness of the Thermal Boundary Layer (TBL), the nature and efficiency of the magmatic extraction processes and the degree of interaction between the melts, the mantle lithosphere and the crust (Wilson, 1993).

The liquids generated in these conditions in intraplate environments are divided into two major series, the alkalic and the tholeiitic. Alkaline intraplate continental basalts usually have lower silica and higher alkali (sodium and potassium) contents than tholeiitic basalts, which also show a characteristic pattern of initial iron enrichment during differentiation. Alkaline magmas are thought to result either from smaller partial melt fractions of the same source that also generates the tholeiitic liquids (e.g. Hirose and Kushiro, 1993) or from melting of mantle that contains metasomatically introduced, potassium rich, hydrous minerals such as phlogopite and amphibole (e.g. Foley, 1992).

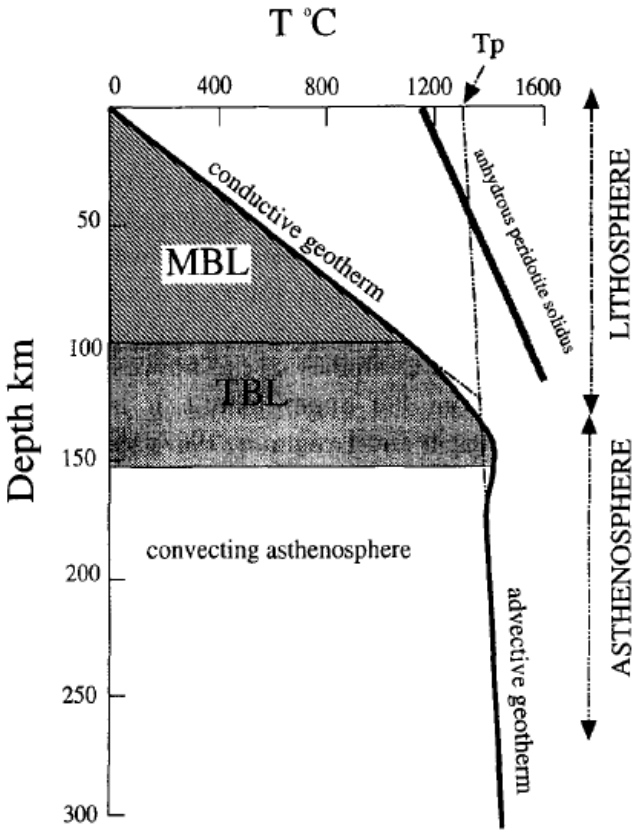

Fig. 2.20: Schematic representation of the location of the Mechanical Boundary Layer and Thermal Boundary Layer in the mantle and their relation with the advective and convective heat transfer regimes .Tp is the mantle's potential temperature. From Wilson, 1993.

In the following sections the mechanisms for the generation and installation for the alkaline magmatism will be presented and discussed.

3.1 Possible sources for alkaline anorogenic magmatism

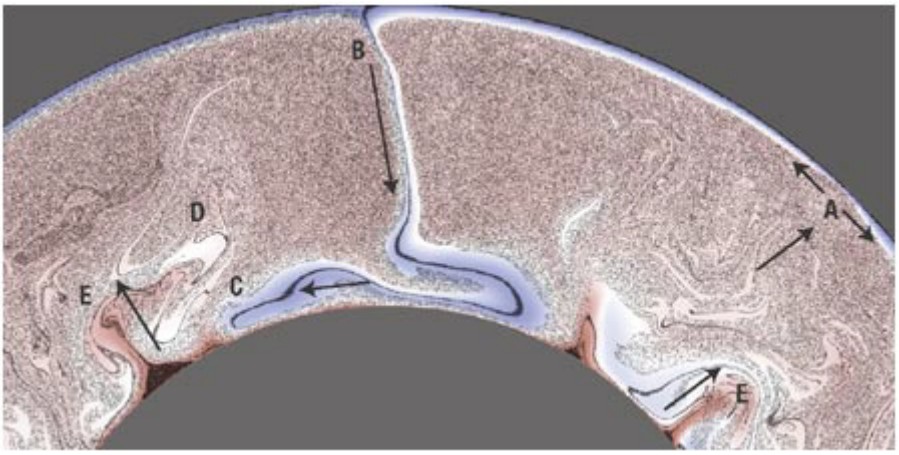

Fig. 2.21: Mathematical model of Brandenburg and van Keken (2007) illustrating mantle dymanics. Upon subduction (B), the lithosphere is recycled to the lower mantle (C) and returned to the mantle (D), and can be brought up at mid-oceanic ridges or through plumes (E) at ocean island hotspots.

Basic magmas can be generated in either the lithospheric or the sublithospheric mantle (asthenosphere). This section aims to discuss these two as possible sources for anorogenic continental alkaline magmatism.

3.1.1 The Continental Lithospheric Mantle

The Continental Lithospheric Mantle has long been proposed as a possible source for the magmas generated during rifting or the eruption of Large Igneous Provinces (LIPs). It represents a geochemical reservoir that can remain isolated from the convective mantle during long periods of time, allowing it to develop considerable chemical and isotopic heterogeneities, and whose later melting would lead to the formation of magmas with enriched trace element and isotopic compositions (McDonough, 1990).

According to Hawkesworth et al., (1990) the CLM's ability to generate basaltic melts depends on its age, which also controls its thickness, composition and density. For instance, an Archaic CLM would be too thick and depleted in FeO due to the extraction of komatiites and therefore have low density and fertility. On the other hand, post Archaic CLM should be produced by the incorporation of asthenospheric material by

conductive cooling after rifting or intraplate magmatism. In comparison, this asthenosphere has not been so strongly depleted, since komatiite formation is mostly limited to the Archean, and is consequently richer in FeO, and as a result more dense and fertile and has also been enriched by the later percolation and crystallization of magmatic liquids rich in incompatible elements (McDonough, 1990).

The liquids responsible for these alterations can be hydrous, carbonated or even siliceous melts enriched in incompatible elements that result from very small partial melt fractions of the asthenosphere (e.g. Yaxley et al., 1998; Niu and O'Hara, 2003; Pilet et al., 2008; Humphreys and Niu, 2009) and/or mantle plumes, generated by adiabatic decompression or simply by the heat addition of the plume.

The circulation of these silicate or carbonated melts and hydrous fluids produces mantle metasomatism, which divides itself in two main types, modal metasomatism, i.e. modifications to the original mineralogy of the mantle rocks, often introducing hydrated phases, and cryptic metasomatism which only affects the chemical composition and isotopic signatures of the same rocks (e.g. Bodinier and Godard, 2003 and references within).

Pilet et al. (2008) put forward a model where metasomatic events would create metasomatic amphibole rich veins, with nephelinite-like compositions. When these nephelinitic veins melt, the resulting liquids interact with the host peridotite and generate the compositional spectrum of silica undersaturated alkaline rocks from the initial nephelinite through basanite and up to alkali basalt, depending on the degree of interaction (low or non existent for nephelinites and higher for alkali basalts). These authors did not provide contrains on the nature of the metasomatic agent. However, Niu (2008) suggested that these might be low degree partial melts from the low velocity zone in the asthenosphere.

Volatile addition through metasomatic processes can, at a given pressure (or depth) significantly lower the solidus of the rocks it affects (e.g. Falloon and Green, 1990 *in* Wilson, 1993). This favors the formation of magmas in regions where the mantle potential temperature is elevated by the proximity of a mantle plume and even in regions with low extension rates (Wilson, 1993)

These metasomatic events can occur in different time scales, creating heterogeneous enrichments in the mantle and producing reservoirs with diversified

isotopic and chemical signatures. For example, metasomatic events have been detected between two different eruptive phases in the Cantal massif in France (Pilet et al., 2002), while the episode that enriched the CLM whose fusion generated the Cretaceous lamprophyres in Moravia is attributed to an event occurred during the Variscan orogeny in the late Paleozoic (Dostal and Owens, 1998).

Such episodes would render the CLM a possible source for the basalts associated with LIPs and other continental basaltic magmatism with low εNd, variable $^{87}Sr/^{86}Sr$ and low $^{206}Pb/^{204}Pb$, with the combination of slightly high $^{87}Sr/^{86}Sr$ with low $^{206}Pb/^{204}Pb$ acting as tracers for a continental lithospheric component (Hawkesworth *et al.*, 1990). McDonough (1990), however, implies that this fertilization could not generate the large volume of magmas seen on LIPs, neither the Nb and Eu anomalies that characterize them and are not detected on mantle lithosphere xenoliths. Nevertheless, this author does not exclude that the CLM might be an important contributor in the generation of incompatible element enriched alkaline basalts.

A "pure" CML component would be sampled by undersaturated basic to ultrabasic magmas such as lamprophyres or lamproites and would have low εNd, moderate $^{87}Sr/^{86}Sr$, mantle δO^{18}, low $^{206}Pb/^{204}Pb$ and both high $^{207}Pb/^{204}Pb$ and $^{208}Pb/^{204}Pb$ as weel as characteristically unradiogenic $^{187}Os/^{188}Os$ (Pearson et al., 2004). This isotopic signature would reflect the CLM's different evolution due to isolation from the convecting mantle, which allowed for a time integrated increase of Rb/Sr, Nd/Sm, Pb/Th and decrease of U/Pb (Saunders et al., 1992; Daley and DePaolo, 1992).

However, the signature of the lithospheric component can change with the age of the lithosphere and nature of the metasomatic event(s) it is affected by. Gibson et al., (1995) distinguished two mafic alkaline potassic suits with different major and trace element abundances and isotopic compositions in the Paraná Basin, Brazil. They interpreted the TiO_2 rich, high CaO/Al_2O_3, $^{143}Nd/^{144}Nd$ and low La/Nb and $^{87}Sr/^{86}Sr$ magmas as originating in older, Archaic enriched cratonic CLM, while the TiO_2 poor, low CaO/Al_2O_3 and $^{143}Nd/^{144}Nd$, and high La/Nb and $^{87}Sr/^{86}Sr$ should have been generated by partial melting of CLM under Proterozoic mobile belts that are more refractory and less enriched.

During lithospheric thinning resulting from continental rifting it is expectable to come across products derived from the partial melting of metasomatized CLM but also from the ascending asthenosphere (e.g. Hawkesworth and Gallagher, 1993; Wilson,

1993). Hawkesworth and Gallagher (1993) state that the metasomatized CLM has a lower solidus and is the first to initiate melting in an extensional setting but with the continuation of rifting, the asthenosphere will also start melting and its contribution to the total melt generated should increase, quickly becoming dominant and masking or overwriting the geochemical imprint of the mantle lithosphere contribution, giving rise first to mixed trace element and isotopic signatures and afterwards to magmas that will show completely asthenospheric values (Wilson and Downes, 1992).

In addition to being a possible source for alkaline magma generation, the CLM can also control magma location and composition.

Watson and MacKenzie (1991) proposed that magma generation from anhydrous peridotites with potential temperatures above 1300ºC (as in a mantle plume) is impossible in lithospheres with an MBL thicker than 125 km. This would limit the localities where continental anorogenic magmatism could take place, as well as the volume of magma produced at a fixed temperature and uphold lithospheric thickness as a major control on the location of any kind of magmatism.

Also, for a given temperature and pressure (and depth), the generated melts will be richer in MgO in situations where the amount of partial melting is higher. For a fixed partial melt fraction, the MgO content increased with depth and pressure. According to that, alkaline mafic and ultramafic magmas are usually the product of small partial melt fractions at high depths, while tholeiitic magmas are produced by higher amounts of partial fusion of a shallower mantle source (Wilson, 1993).

Furthermore, Ellam (1992) suggested that the depth of the base of the lithosphere can be deduced from its chemical composition, since it will influence the REE abundances of the magmas given that it will control the mineralogy of the asthenospheric and lithospheric mantle rocks and consequentially the composition of the magmas generated in either of these layers. Stable phases in peridotite change with depth, with spinel occurring from 20-30 km to 60 km depth, from that depth onwards garnet is stable and completely replaces spinel below 80 km (Ellam, 1992).

This results in different magma compositions of melts due to equilibration of the melts with different mantle parageneses and especially very different abundances in REE for magmas generated in the presence or absence of residual garnet since this mineral has very different partition coefficients (D), which are functions of the physical conditions

during melting and of the melt composition (D = mineral/melt partition coefficient = (concentration of element, i, in mineral)/ (concentration of i in coexisting melt)) for the light and heavy REE, with the first concentrating on the melt phase in case of partial melting and the one remaining on the residual garnets if the melt fraction is small enough not to completely consume them. Consequently, using a proxy for the light REE/ heavy REE ratio (such as Ce/Yb, Ce/Y or La/Yb) we can estimate the thickness of the lithosphere during magma generation and study its variation in prolonged eruption sequences (Ellam, 1992; Kerr, 1994).

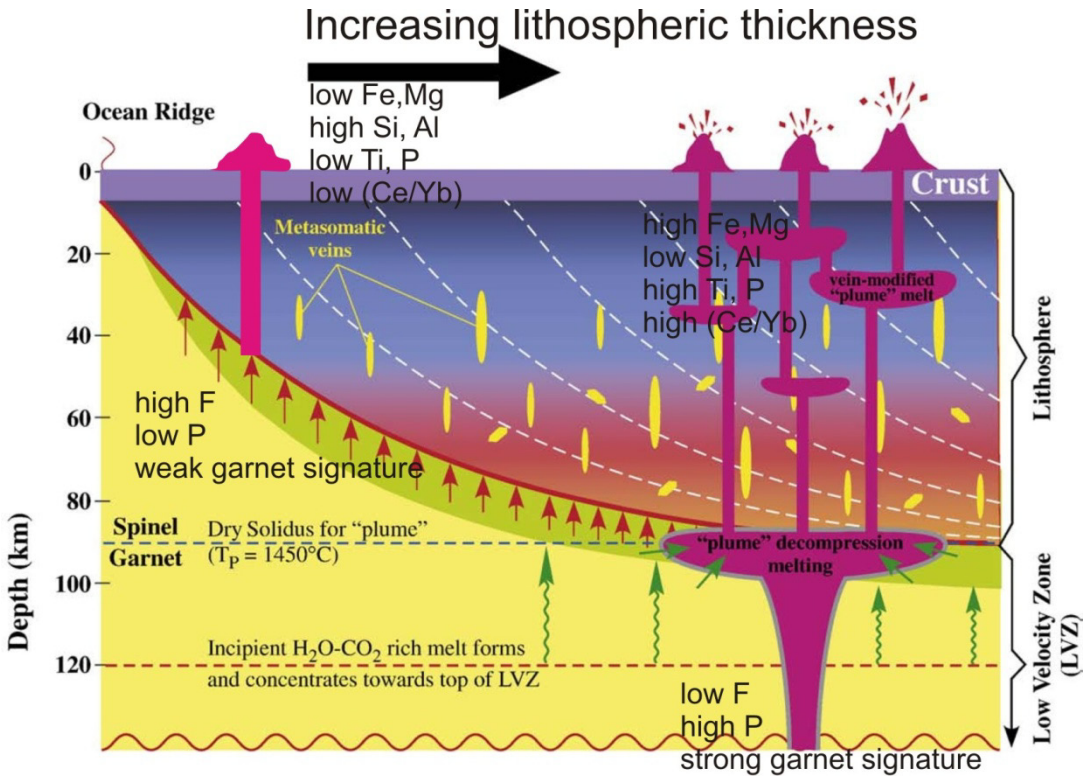

Fig. 2.22: Illustration of the differences in chemistry observed in areas where magma generation took place under lithospheres with different thicknesses. Also depicted are the possible metasomatic veins that might be responsible for the generation of mafic alkali magmas, according to Pilet et al. (2008). Adapted from Humphreys and Niu, 2009.

Consequentially, for a 125 km thick lithosphere it is estimated that extension with a stretching factor β (β = l1/l0) lower than 1.5, would originate magmas by adiabatic decompression of the asthenosphere, representing a small partial melt fraction of deep garnet peridotites. These melts will be enriched in light REE in relation to heavy REE (high Ce/Yb), while magmas generated during and extensive phase with a higher stretching factor (β > 2) would result from higher amounts of fusion of a shallower, garnet free peridotite (originally garnet free or where the small amounts of this mineral

are exhausted during melting) and necessarily have lower Ce/Yb values as spinel peridotites do not fraction REE (Ellam, 1992).

This lithospheric lid effect has recently been found to also influence the major element composition of OIBs (Humphreys and Niu, 2009) with Si and Al decreasing, whereas Ti, Fe, Mg and P increase with increasing lithospheric thickness and consequentially increasing pressures and decreasing extents of melting (fig. 2.22).

3.1.2 The Sub-Lithospheric Mantle

The Sub-Lithospheric Mantle is the source of the majority of the basic magmatism observed in the Earth's crust. It encompasses two main reservoirs, the geochemically depleted asthenosphere and the enriched mantle plumes.

The asthenosphere has been previously depleted by melt extraction (2-3% Workman and Hart, 2005) to form the oceanic crust, and its melts have unradiogenic isotopic compositions and are depleted in incompatible elements. Asthenospheric melts are widely represented in Mid Ocean Ridge Basalts (MORBs). Present day melts generated by this reservoir and that have not significantly interacted with the lithosphere or mantle plume melts during their ascent should have isotopic and trace element signatures similar to the ones known for MORBs that are characterized by the component named **D**epleted **M**ORB **M**antle (**DMM**: $^{87}Sr/^{86}Sr$ 0.70219 - 0.70307; $^{143}Nd/^{144}Nd$ 0.51326 - 0.51300; $^{206}Pb/^{204}Pb$ 17.573 - 18.977; $^{207}Pb/^{204}Pb$ 15.404 - 15.568; $^{176}Hf/^{177}Hf$ 0.28350 - 0.28310; Workman and Hart, 2005).

Oceanic Islands are largely constituted by basalts that have not interacted with continental crust and are supposed to represent uncontaminated mantle melts. Geochemical studies of these Ocean Island Basalts (OIBs) allowed the definition of several isotopically and geochemically distinct mantle end member components (e.g. Zindler and Hart, 1986; Weaver, 1991; Hofmann, 2003) which indicate derivation from mantle sources with diverse differentiation histories.

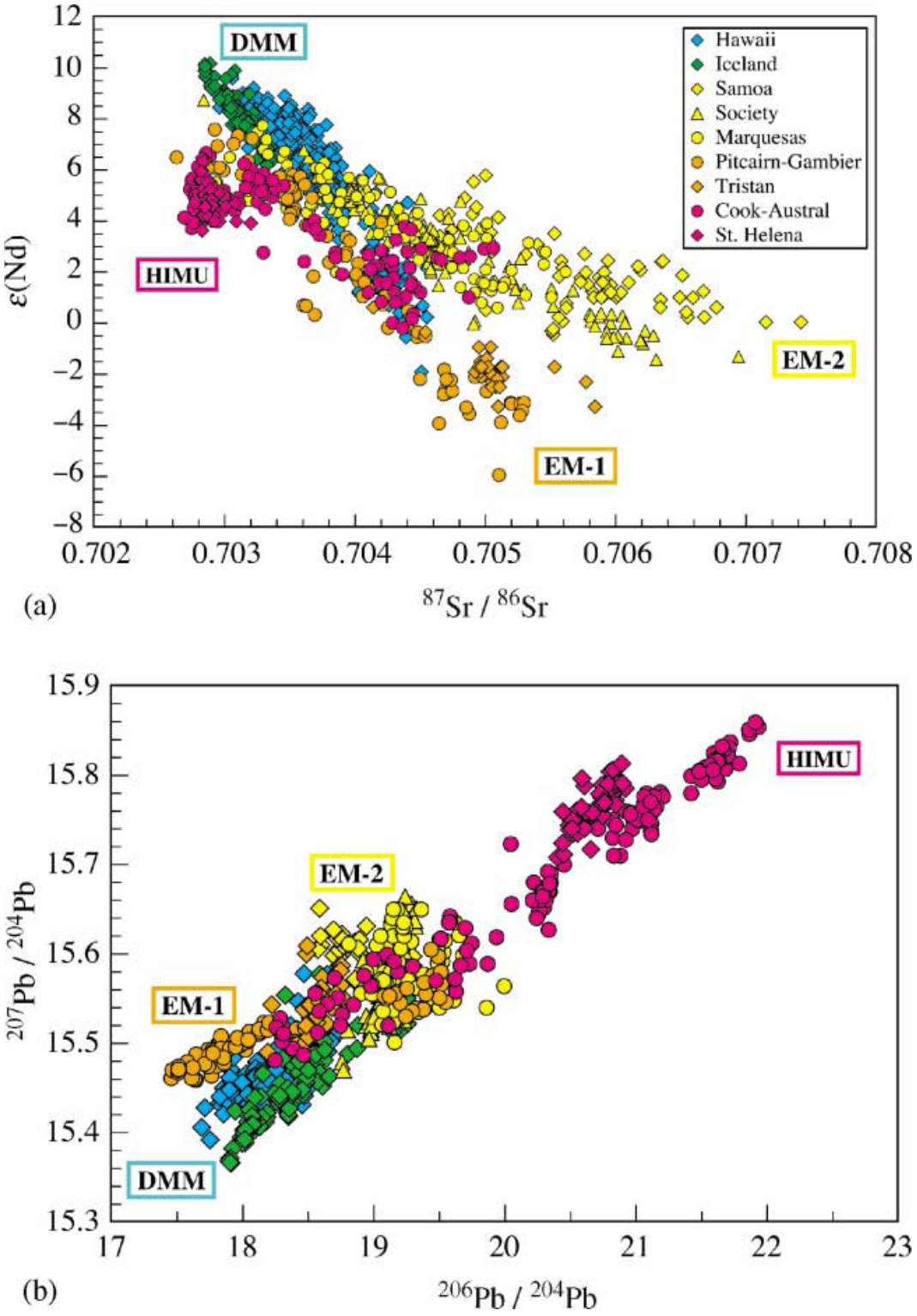

Fig. 2.23: (a) $^{87}Sr/^{86}Sr$ versus ε(Nd) for OIB. The islands or island groups selected are chosen to represent extreme isotopic compositions in isotope diagrams. They are the "type localities" for HIMU (Cook-Austral Islands and St. Helena), EM-1 (Pitcairn-Gambier and Tristan), EM-2 (Society Islands, Samoa, Marquesas), and PREMA (Hawaiian Islands and Iceland). (b) $^{207}Pb/^{204}Pb$ versus $^{206}Pb/^{204}Pb$ for the same OIB as plotted in (a). Note that the 207Pb/204Pb ratios of St. Helena and Cook- Australs are similar but not identical, whereas they overlap completely in the other isotope diagrams. From Hoffman, 2003.

The geophysical (especially tomographical) work developed in these islands allowed their pairing with thermal anomalies in the mantle, corresponding to mantle plumes that rise from deep within the mantle (e.g. Davies, 1990; Sleep, 1990), although this connection is still the subject of vigorous debate (e.g. King and Anderson, 1998, King and Ritsema, 2000, www.mantleplumes.org) .

These end members can be viewed as isolated reservoirs in the mantle whose mixing among themselves and with DMM would produce the entire observed isotopic mantle array or as extremes in a continuum of isotopic compositions existing in mantle rocks (Hofmann, 2003). However one chooses to view them, these end members help to identify specific characters of mantle differentiation found on other OIBs with less extreme isotopic compositions.

Isotopic compositions of rocks from these mantle end members show systematically more enriched in radiogenic strontium and less radiogenic in neodymium and hafnium isotopic ratios than DMM although considerable overlap can exist. In the case of lead, the overlap is complete but they extend to more extreme values in each of the isotopic ratios. The main characteristics, possible origins and the end member values for the Sr, Nd and Pb isotopic compositions of each of the components defined by Zindler and Hart (1986) will be described below:

HIMU (**HI**gh **μ**): this component is characterized by high μ (μ = $^{238}U/^{204}Pb_{t=0}$) and highly radiogenic Pb isotope ratios, requiring a source with very high U/Pb and Th/Pb ratios, and relatively unradiogenic Sr, pointing towards a low Rb/Sr source similar to DMM. Chase (1981) and Hoffman and White (1982) suggested that this end member evolved from ancient subducted oceanic crust depleted Sr and enriched in U by hydrothermal alteration, which also depleted it in alkalis and Pb (Chauvel et al., 1992). Another, less popular explanation is that this end member is generated by enriching oceanic lithosphere during metasomatic episodes caused by the infiltration of low degree partial melts with high U/Pb and Th/Pb.

HIMU: $^{87}Sr/^{86}Sr$ 0.70285; $^{143}Nd/^{144}Nd$ 0.51285; $^{206}Pb/^{204}Pb$ 21.80; $^{207}Pb/^{204}Pb$ 15.86; $^{208}Pb/^{204}Pb$ 40.12; (Hart et al., 1992).

EM-1 (**E**nriched **M**antle **1**) and **EM-2** (**E**nriched **M**antle **2**): the enriched mantle components are characterized by low $^{143}Nd/^{144}Nd$, variable $^{87}Sr/^{86}Sr$, high $^{207}Pb/^{204}Pb$ and $^{208}Pb/^{204}Pb$ (at a given value of $^{206}Pb/^{204}Pb$) and, as such, derive from sources enriched in LILE (Rb) and light REE (Sm). EM-1 has less radiogenic Sr and has lower $^{143}Nd/^{144}Nd$ than EM-2.

They are both thought to represent recycled oceanic crust with the addition of small amounts of subducted sediment. That sediment would be of pelagic nature in the case of EM-1 and from a terrigenous continental source in the case of EM-2 (Weaver, 1991). Other possible origins for these components are the recycling of metasomatized and melt impregnated oceanic lithosphere (Workman et al., 2004) or of upper continental crust (Jackson et al., 2007) for EM-2 and of delaminated subcontinental lithosphere for EM-1 (e.g. Hawkesworth *et al*., 1986)

On the other hand, Willbold and Stracke (2006) found no clear distinction between the EM-1 and EM-2 components in terms of incompatible trace element ratios, despite the different isotopic signatures. However, each EM suite has its unique trace element signature that must reflect differences in source composition. These authors also support the notion that the different isotopic signature of the EM components cannot be generated by the incorporation of sediment alone, but also require the input of some upper or lower continental crust via subduction erosion.

EM-1: $^{87}Sr/^{86}Sr$ 0.70530; $^{143}Nd/^{144}Nd$ 0.51236; $^{206}Pb/^{204}Pb$ 17.40; $^{207}Pb/^{204}Pb$ 15.47; $^{208}Pb/^{204}Pb$ 38.85; Hart *et al*., 1992).

EM-2: $^{87}Sr/^{86}Sr$ 0.70780; $^{143}Nd/^{144}Nd$ 0.51258; $^{206}Pb/^{204}Pb$ 19.00; $^{207}Pb/^{204}Pb$ 15. 61; $^{208}Pb/^{204}Pb$ 38.86; Hart *et al*., 1992).

A possible fourth component than can go by the name of **PREMA** (**PRE**valent **MA**ntle), **FOZO** (**FO**cal **ZO**ne), **C** (**C**ommon) or **PHEM** (**P**rimitive **HE**lium **M**antle) is supposed to represent material from the lower mantle that is present in all mantle plumes as a mixing component (e.g. Zindler and Hart, 1986; Hart et al., 1992; Farley et al., 1992; Hanan and Graham, 1996; Stracke et al., 2005). It has also been suggested that the ubiquitous FOZO is simply the result of continuous subductions and aging of oceanic crust during recycling through the mantle (Stracke et al., 2005). Compositionally, it is very similar to DMM but has moderately more radiogenic Sr, less

radiogenic Nd and Hf and significantly more radiogenic Pb (Hofmann, 2003 and references therein).

The origin of many of these mantle components by recycling of oceanic lithosphere has been recently backed up by seismic tomography data that shows subducting slabs penetrating deep into the Earth down to circa 2900 km, near the core-mantle boundary (e.g. Burke and Torsvik, 2004 and references therein), where many of these plumes are thought to originate.

An alternative for the requirement of different mantle end members formed by recycling of lithospheric slabs of different nature is to assume that the melts result from different degrees of partial melting from peridotite and eclogites derived from heterogeneous, recycled lithosphere with different ages and composition that form a marble cake like mantle (e.g. Armienti and Gasperini, 2007). This would also provide an explanation for the observed small scale variability of isotopic signatures observed, for instance, in only one island.

Hirschmann et al. (2003) suggest that alkali trace element enriched melts with strong recycling signatures can be produced simply from melting of mantle pyroxenites at high pressure, although this conclusion was later challenged by Keshav *et al*. (2004) and is still the object of lively debate with other authors (e.g, see Lustrino, 2005 and references therein) defending the importance of the role of pyroxenites on the genesis of OIB.

3.2 Anorogenic Intraplate Continental Alkaline magmatism and global tectonic processes

Anorogenic Intraplate alkaline magmatism can be related to several types of geodynamic contexts: continental rifting, the action of mantle plumes, lithospheric delamination, edge driven convection and movement across lithospheric strike-slip faults.

In this section the magma generation and ascent mechanisms for each of these geodynamic settings will be discussed.

3.2.1 Continental Rifting

During tectonic extension of a continental lithosphere with normal thickness, magmatism can be inhibited for several reasons, the most relevant probably being the duration of the extensive pulses (Keen et al., 1994, Ziegler et al., 2004). If the separating continental blocks do not have their motion constrained laterally, rifting will be quick and extension more localized and will not result in the eruption of a significant magma volume since the generated melts will concentrate on the rift axis and be rapidly consumed when oceanization and oceanic crust generations begins (Harry and Bowling, 1999; Ziegler et al., 2004, fig. 2.24).

Alternatively, White (1992) argues that low extension rates allow for conductive cooling of the ascending asthenospheric mantle, which stops it from melting by adiabatical decompression.

Also, as discussed above, the thickness of the lithosphere will control the amount of partial fusion for a mantle at a certain potential temperature, with the partial melt fraction increasing as the lithospheric thickness decreases.

Therefore, alkaline magmas should be mostly associated with the first rifting phases, before the amount of partial melting increases tholeiitic melts are generated. As decompression of normal CML should not result in magma generation unless there is addition of fluids and/or heat, the source for these alkaline melts generated during rifting should be associated with upwelling asthenosphere or mantle plumes. Some authors have even suggested (e.g. Asmeron et al., 1994) that changing from higher to lower thinning rates during rifting would firstly induce melting on the metasomatized lithospheric mantle due to the heat addition provided by the ascent of the asthenosphere, originating basic alkaline melts with low εNd.

Consequently, the eruption sequence observed during continental rifting should first show alkaline melts with lithospheric signatures that would become progressively more asthenospheric and less alkaline until finally they show tholeiitic characteristics (e.g. Furman, 1995; MacDonald et al., 2001). However, Reiners (2002) refers that Os isotope data indicates that extraction of melt increased with depth, with the tholeiitic melts coming from deeper $^{187}Os/^{188}Os$ enriched fertile sources such as pyroxenites and the alkalic ones deriving from shallower, $^{187}Os/^{188}Os$ depleted peridotites.

In the Rio Grande rift, the alkaline magmatism of the Potrillo volcanic field is characterized by trace element enrichment, higher $^{87}Sr/^{86}Sr$ and lower $^{143}Nd/^{144}Nd$ than DMM. This event has been attributed to the fusion of lithospheric mantle metasomatized by the infiltration of melts during a previous magmatic event that promoted the formation of metasomatic amphibole, lowered its solidus and enriched it in incompatible elements (Thompson et al., 2005). The trigger for the initiation of the magmatism was the extension and thinning that took place in the area, coupled with the ascent of a convective mantle cell.

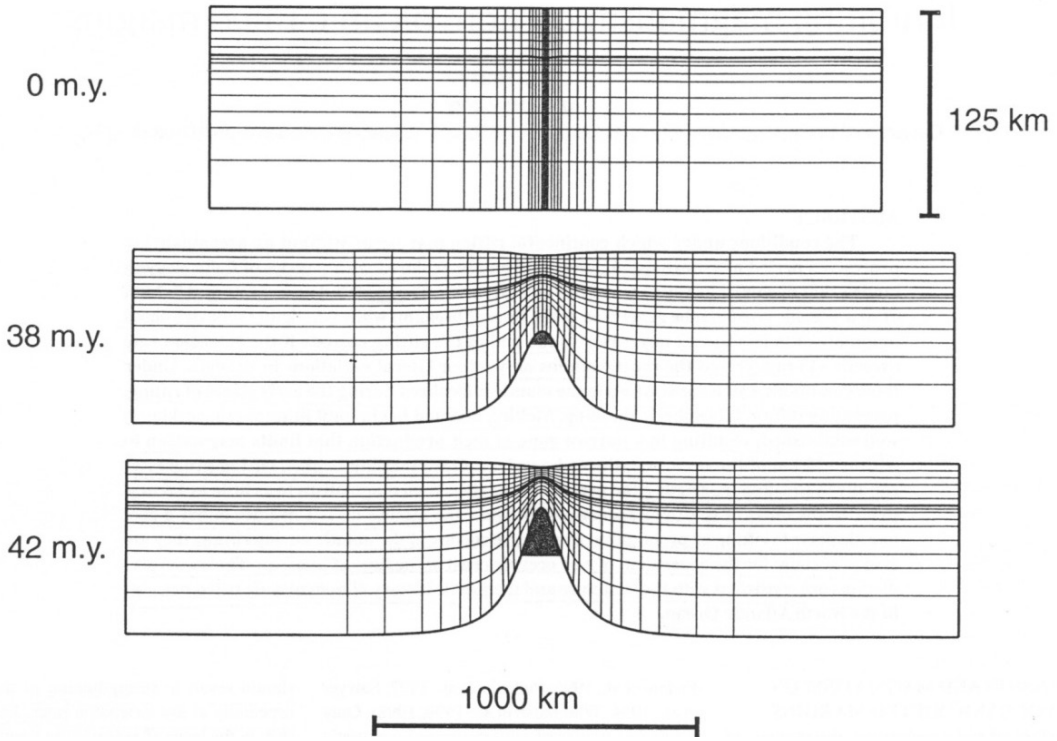

Fig. 2.24: Representation of the model for magma production by Harry and Bowling. From Harry and Bowling, 1999.

3.2.2 Mantle plumes and their interactions with the lithosphere

Along with lithospheric thickness, the temperature of the sublithospheric mantle is also a crucial controlling factor in what concerns the location and composition of the generated magmas.

The hotter the asthenosphere, the greater the depth of initiation of melting and the greater the volume of magma produced in the upwelling mantle, even in the absence of significant lithosphere thinning. Therefore high potential temperature mantle plumes are of great importance in the generation of continental magmatism. Also, even

relatively small temperature anomalies can generate partial melts that can metasomatize the overlying lithosphere or trigger melting in an already metasomatized lithospheric mantle.

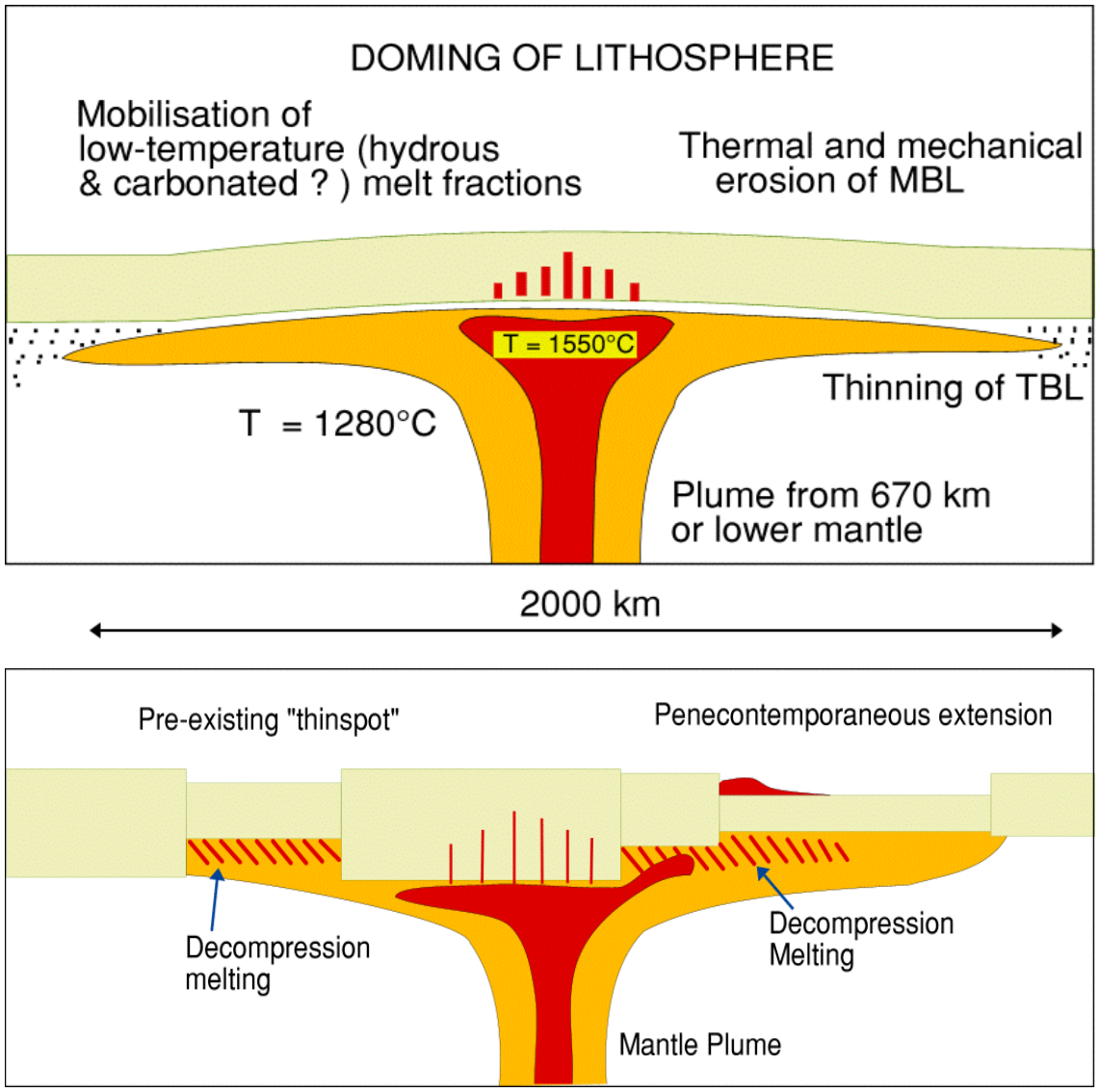

Fig. 2.25: Schematic representation of the effects of the impact of a plume on the base of the lithosphere. Upper and lower diagrams impact on unthinned lithosphere and on a previously thinned lithosphere, respectively.

Another phenomenon commonly associated with mantle plumes is the uplift and thermal erosion usually associated with the impingement of a plume at the base of the lithosphere (fig. 2.25). The thermal erosion of the lithosphere, associated with the higher potential temperatures of the plume, can greatly increase the melt production on the impact site and is usually quoted as one of the causes for the formation of LIPs and may even evolve towards extension and continental rifting (e.g. Morgan, 1983; Wilson,

1989; Saunders et al., 1992; Wilson, 1993, Ziegler and Cloetingh, 2004). In other cases, the impact of a plume head on lithosphere that is already being rifted results in an increase of the deviatoric stresses which would intensify the ongoing rifting (Morgan, 1983; Ziegler and Cloetingh, 2004; fig. 2.25).

Such interactions make it harder to distinguish the lithospheric from the asthenospheric and plume components with mixed signatures being the most likely outcome in many continental intraplate basic magmas.

Magmas enriched in incompatible elements, with moderate $^{87}Sr/^{86}Sr$, low $^{206}Pb/^{204}Pb$ and εNd, and Th/Nb >1 are generally associated to assimilation, mixing and hybridization of asthenospheric DMM-like magmas and CLM melts, while negative anomalies in Nb, Ta, Sr and P, high $^{87}Sr/^{86}Sr$, $^{206}Pb/^{204}Pb$, La/Nb and Th/Nb are usually attributed to crustal contamination processes (Saunders et al., 1992).

The present day magmatism observed in the East and West African rifts is considered to result from the interaction between mantle plumes and the CLM (e.g. Furman, 1995; Furman and Graham, 1999; MacDonald et al., 2001; Spath et al., 2001). These interactions are thought to be responsible for extensive metasomatism observed in the CLM within this region, mostly due to the action of carbonatitic and silicate melts.

For example, these metasomatic events resulted in the formation of residual amphibole, ilmenite, apatite and zircon in the CLM of the Rungwe area, between the East and the West African rifts, that later controlled the trace element compositions of the magmas generated by partial melting of this source (Furman, 1995).

In the Kivu province of the East African rift, the differences in composition of the observed magmas is related to changes on the thickness of the lithosphere in the area which in turn are controlled by lithospheric extension and thermo-mechanical erosion of the TBL (Furman and Graham, 1999). These authors also found that the main contributions to this magmatism come from the melting of metasomatized CML ($^{87}Sr/^{86}Sr \approx 0.7050$, $\varepsilon Nd \approx 0$ and $^{206}Pb/^{204}Pb \approx 19$) and from a plume with an HIMU like composition whose role is more important in regions with thinner lithosphere. MacDonald et al., (2001) studied basalts from the Kenya Rift and came to the similar conclusions, identifying plume and lithospheric mantle components in the rocks of that region, although it has also been suggested that only the metasomatized CLM was involved in the genesis of these basalts, with the observed different isotopic signatures

corresponding to melts coming from areas with different degrees of metasomatic enrichment (Späth et al., 2001).

Fodor et al. (1998) found evidence for a lithospheric component with an EM-1 like composition (relatively high $^{87}Sr/^{86}Sr$, high Ba/Nb and low La/Nb) in the Cenozoic basalts of NE Brazil that mixed with melts resulting from the fusion of the HIMU like Fernando Noronha plume and surrounding asthenosphere (DMM).

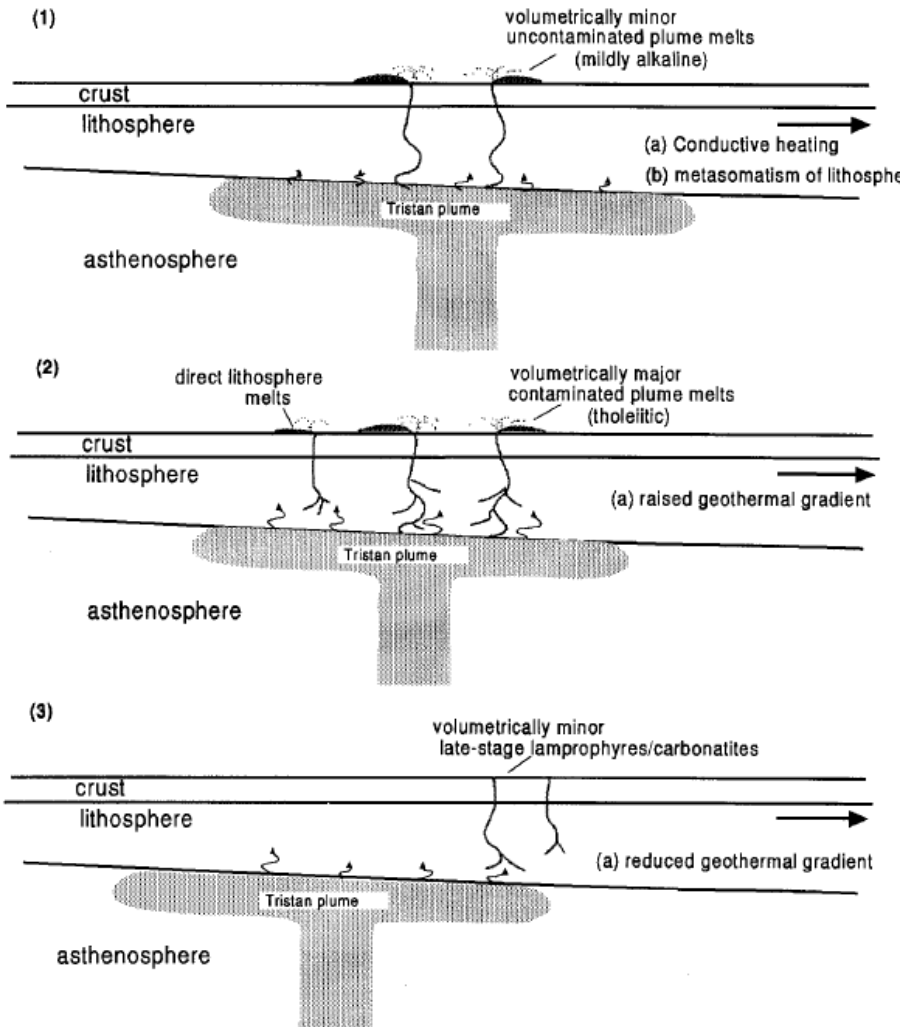

Fig. 2.26: Schematic representation of the effects of the impact of the Tristan plume on the lithosphere of the African plate in Namibia. From Le Roex and Lanyon, 1998.

The passage of a mantle plume under continental lithosphere can, in addition to being associated with contemporaneous magmatism, also be responsible for metasomatism in the CLM that will allow it to melt if there is later extension or heat addition, originating late alkaline magmatic events. That seems to be the case in Namibia, where the late alkaline lamprophyres and carbonatites studied by Le Roex and

Lanyon (1998) were generated by the low degree melting of CLM that had been previously metasomatized by the passage of the Tristan plume. These rocks show isotopic signatures similar to others associated with this plume since they were metasomatized by fluids originating in it (relatively high $^{87}Sr/^{86}Sr$, low $^{143}Nd/^{144}Nd$ and Pb isotopic ratios that project under the Northern Hemisphere Reference Line) but erupted later, when the plume's thermal anomaly was already residual (fig. 2.26).

The same kind of explanation is used to justify the late, post-rift magmatism of the eastern coast of Greenland (Price et al., 1997; Bernstein et al., 1998; Storey et al., 2004), with the Iceland plume being responsible for the metasomatism of the CLM and the diffuse extension that took place in the area due to the contemporaneous northern propagation of rifting (Price et al., 1997) or the decompression resulting from erosion and subsequent isostatic adjustment (Storey et al., 2004).

Other authis even argue that plumes can be channeled under continents, through corridors of thinned lithosphere and be responsible for intraplate continental magmatism as well as further lithosphere delamination on the same corridor (e.g. the Atlas Cenozoic alkaline magmatism, Duggen et al., 2009, fig. 2.27)

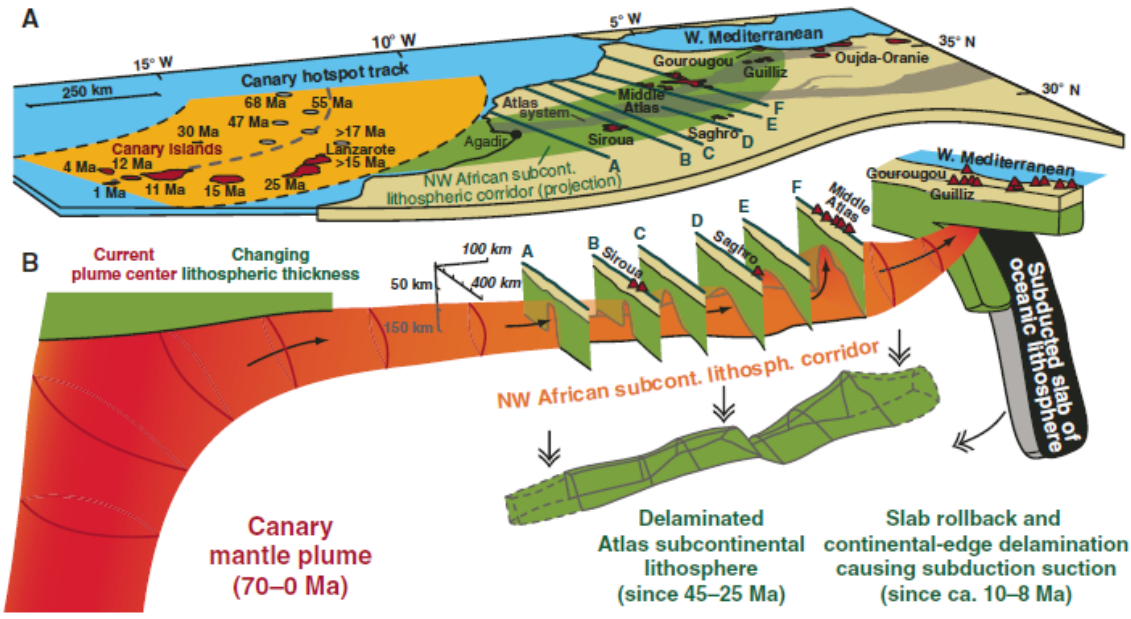

Fig. 2.27: Representation of the model of Duggen *et al.* (2009) for the generation of the Atlas magmatism by channeling of material from the Canaries plume through thinned lithosphere.

In summary, the interactions between CLM and mantle plumes can be used to explain the existence of alkaline magmatism in different geodynamic contexts: sin-

rifting magmatism (e.g. East and West African rifts) and post-rifting magmatism (e.g. East Greenland). The plume contribution can be limited to supplying the thermal anomaly that will trigger melting or to the metasomatism the overlying CLM (e.g. Furman, 1995; Gibson et al., 1995; Furman e Graham, 1999; Späth et al., 2001) or the plume head may as well actively melt and contribute more directly to the volume of the observed magmatism (e.g. Furman and Graham, 1999; MacDonald et al., 2001). Alternatively, a plume can contribute simultaneously with both direct melting and indirect melting from lithosphere that was previously metasomatized by fluids deriving from it (Gibson et al., 1995; Le Roux e Lanyon, 1998; Furman e Graham, 1999; Larsen et al., 2003).

3.2.3 Delamination of the CLM

Metamorphic reactions occurred during continental collision can lead to an increase of the density of the lithospheric roots of the thickened continental area, leading to its gravitational destabilization and consequential delamination causing the lithospheric root to sink into the asthenosphere (Lustrino, 2005, fig. 2.28).

The space released by the delaminated lithospheric keel will then be filled by upwelling asthenosphere which would react with the silica rich continental crust, to form orthopyroxene rich domains with strong crustal signatures, before asthenospheric accretion takes place by conductive cooling, forming a new subcontinental lithosphere. The delaminated keel will also start to dehydrate and melt, releasing liquids that would metasomatize the overlying newly formed lithosphere (Lustrino, 2005, fig. 2.27).

These metasomatized crust and lithospheric mantle can remain static for several million years until they another geological process (e.g. extension) induces partial melting, generating basaltic liquids with trace element and isotopic signatures similar to EM-1, with $^{87}Sr/^{86}Sr \approx 0.706$; $^{143}Nd/^{144}Nd \approx 0.5121$; $^{206}Pb/^{204}Pb \approx 17$ and $^{176}Hf/^{177}Hf \approx 0.2826$ (Lustrino, 2005).

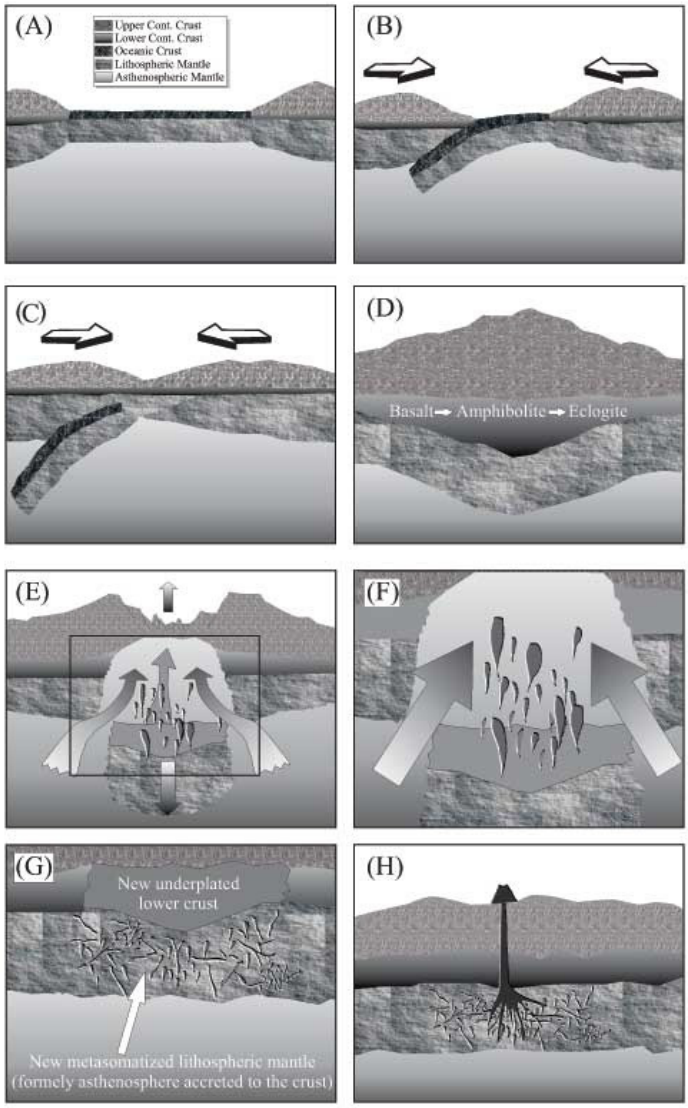

Fig. 2.28: Schematic representation of the model proposed by Lustrino (2005) for the generation of intraplate magmatism due to the delamination of a lithospheric keel. (A) to (D) continental collision and lithospheric thickening; (E) and (F) the high density of the lithospheric keel causes it to become unstable and sink into the asthenosphere, dehydrating and undergoing partial melting; (G) the space left by the keel will be filled by the ascending asthenospheric mantle and metasomatized by the liquids from the sinking keel, it will later cool and become lithospheric mantle; that metasomatized lithosphere can melt and origin to alkaline magmas if there is decompression or head addition in the region (H).

3.2.4 Edge driven convection

Small convective cells can form on the asthenosphere located near the edge of cratons due to horizontal temperature gradients between the cold cratonic lithosphere that provides thermal insulation to the underlying warmer asthenosphere, and the oceanic lithosphere that is warmer than the cratonic lithosphere, but is coupled with an asthenosphere that in its turn is not as warm as the one underneath the craton.

This difference induces downwelling of asthenospheric material close to the craton's edge that is compensated by upwelling between 600 and 1000 km away from the same edge where decompression melting would occur and give rise to magmatism (Vogt, 1991; King and Ritsema, 2000; fig. 2.29). These convective instabilities in the upper mantle can also form following lithospheric delamination (Elkins Tanton and Hager, 2000).

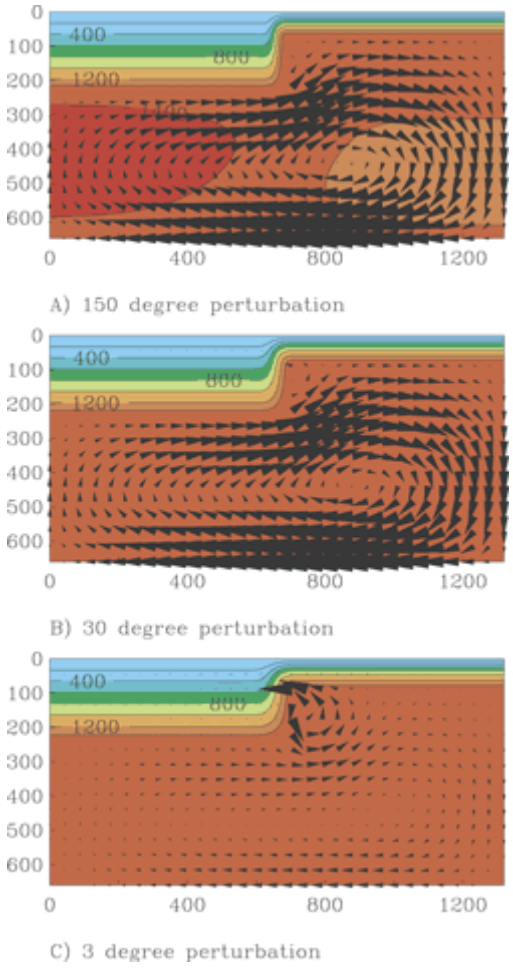

Fig. 2.29: Edge driven convection forming where a mantle temperature perturbation was added to an otherwise isothermal mantle beneath the boundary layer structure illustrated by the isotherms. The size of the mantle temperature perturbation varies from about 3°C to 150°C. From King and Anderson, 1998.

This hypothesis was developed to explain the Bermuda swell as an alternative explanation to generation by the action of a mantle plume (Vogt, 1991), and continued work involving numerical modeling of edge driven convection suggests that this process can responsible by the high magmatic productivity rates observed in LIPs located in the edge of cratons, by continuously supplying more material to the part of the mantle being subject to partial melting (King and Anderson, 1998). This would eliminate the need for

the presence of thermal anomalies and associated mantle plumes and explain the high volume of magmas produced in certain locations (King and Anderson, 1998).

More recently, seismic tomography and numerical modeling study suggested that several island and submarine seamount chains and even their counterparts in continental margins do not correspond to hotspot tracks but to the superficial expression of such small scale convective cells (King and Ritsema, 2000).

Edge driven convection was also the mechanism proposed by Matton and Jébrak (2009) to explain the magmatism associated with the continental Peri-Atlantic Alkaline Pulse (PAAP). The PAAP includes intrusive and extrusive alkaline events in passive margins in the North, Central and South Atlantic which these authors have attributed to magmas generated by decompression of the asthenosphere due to edge driven convection that later ascended through reactivated lithospheric faults (Matton and Jébrak, 2009).

3.2.5 Reactivation of translithospheric faults

Black et al., (1985) argued that many of the alkaline provinces that appear aligned, but do not show any sort of spatial age progression, are actually the result of magma generation and ascent along translithospheric transfer faults, whose age distribution reflects changes in relative plate motions due to plate reorganization or orogenic events in their edge.

In this kind of geodynamic context, the movement along the fault increases temperature and reduces viscosity with depth, due to the increased shear stress at the base of the lithosphere. This would lead to decompression, metasomatism and volatile addition to the lithosphere that could ultimately lead to partial melting and the ascent of these melts through the faults and to the surface (Black et al., 1985).

The inversion of the direction of movement along the same fault system can lead to the propagation of tensil fractures down to the asthenosphere, and repeat the process of magma formation and ascent mentioned above, creating a different phase of magmatism (Black et al., 1985).

The Cenozoic magmatism in Hoggar, NW Africa, is justified as a consequence of the reactivation of mega shear zones, formed during the Proterozoic Pan-African orogeny. This reactivation took place due to intraplate stresses caused by the collision

between the African and Eurasian plates. This process led to linear lithosphere delamination along the shear zones and consequential ascent, decompression and partial melting of the asthenosphere and metasomatized lithosphere (Liégeois et al., 2005). The magmas generated during this process occur along the Pan-African shear zones, have mantle signatures corresponding to mixes between the EM-1 and HIMU components and their ages agree with the major Cenozoic collision phases between Africa and Eurasia (Liégeois et al., 2005).

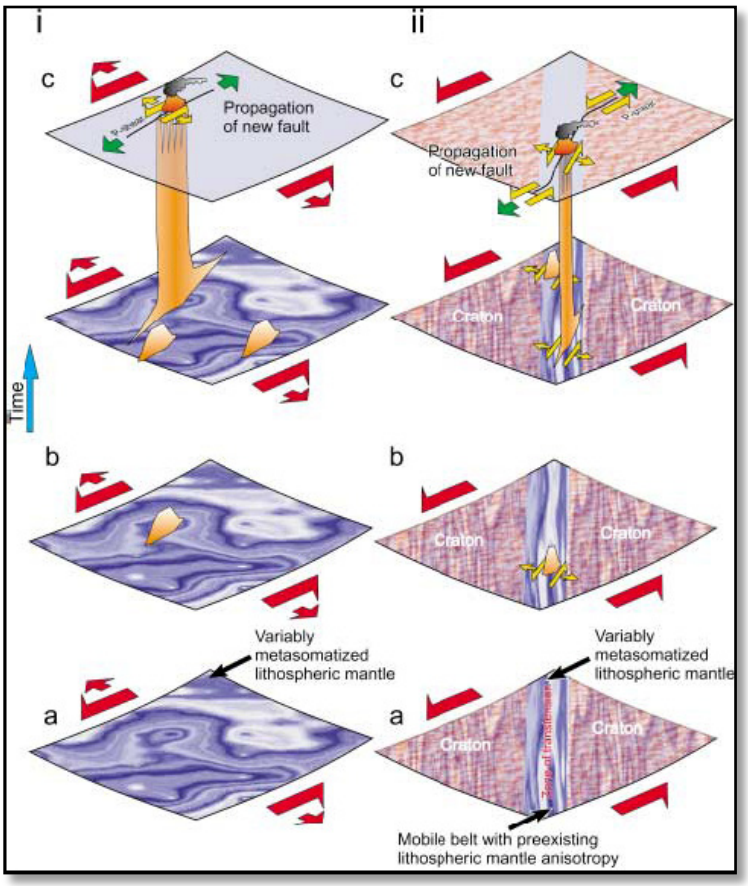

Fig. 2.30: Two representations of the hypothesis advanced by Vaughan and Scarrow to the formation of strike-slip faults in regions subjected to potassic metasomatism. From Vaughan and Scarrow (2003).

A similar mechanism is cited by Harmand and Cantagrel (1984) to justify the alkaline magmatism that accompanies the several deformation phases of the Atlas chain, with the difference that the reactivated faults were generated during Mesozoic continental rifting. Localized decompression and melting of previously metasomatized lithosphere along translithospheric fractures is also used to explain the Cenozoic

alkaline magmatism and its isotopic signature ($^{87}Sr/^{86}Sr$ 0.70299–0.70372, εNd 4.2–6.3) of the Ross Embayment area in Antarctica (Rocchi *et al*., 2002).

Vaughan and Scarrow (2003), however, propose a reverse relation between metasomatism and faulting. They suggest that potassic mantle metasomatism by K-rich melts resulting from small amounts of asthenospheric partial melting control the nucleation of translithospheric structures. For these authors, a local or regional transtensive stress field will tend to use areas that were previously the target of potassic metasomatism as nucleation points for shear zones or strike-slip structures. This will also trigger small amounts of extension, decompression and associated partial melting. These melts will then infiltrate the lithosphere, concentrating deformation and promoting further nucleation and propagation of fractures along the lithosphere, until they reach the surface, accompanied by contemporaneous potassic magmatism (fig. 2.30).

4. Sample collection

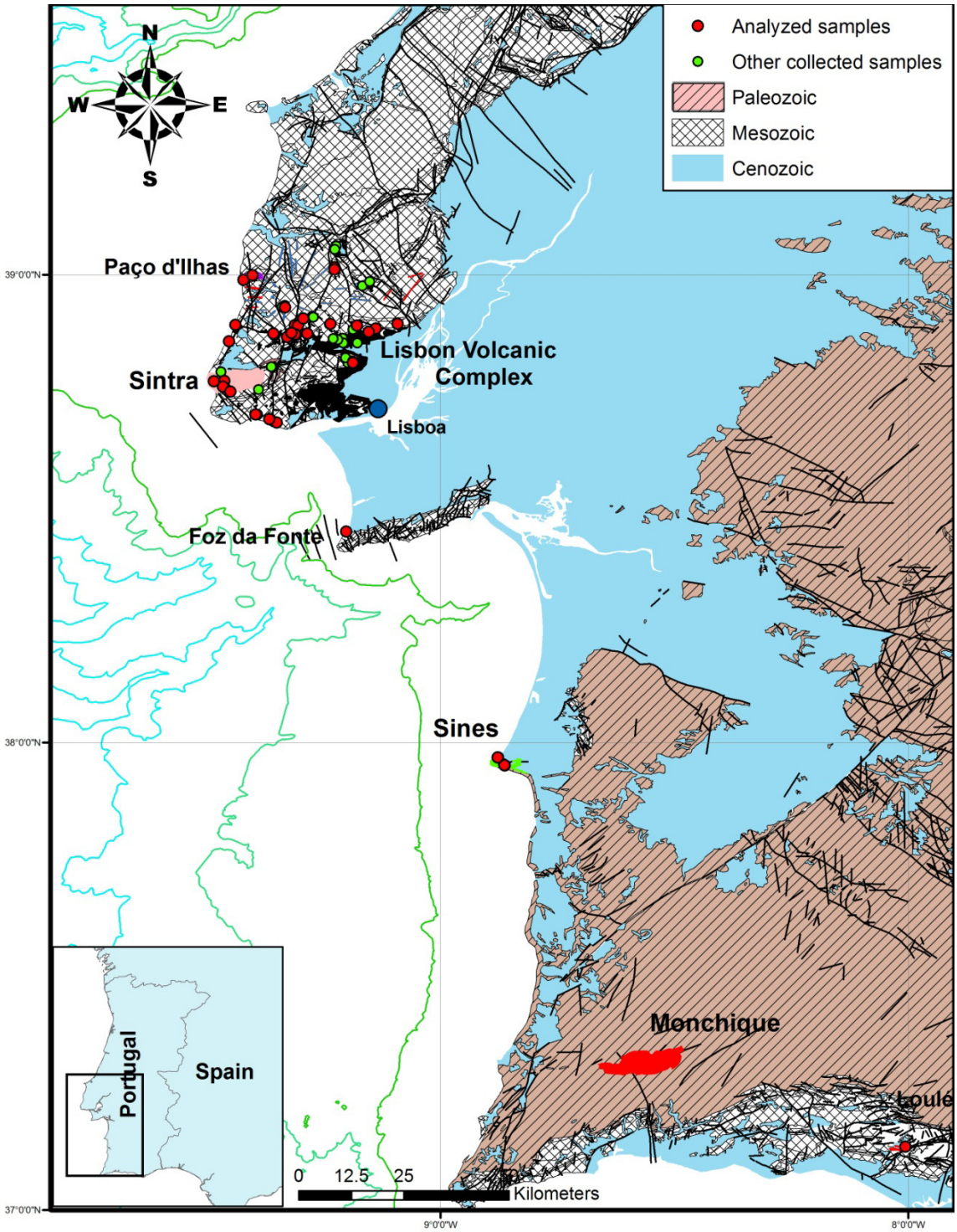

Fig. 4.1: General map showing all the sampled locations.

Several samples representative of the Late Cretaceous alkaline cycle were collected both on the onshore and offshore West Iberian Margin. The aim of this sampling campaign was to characterize the geochemistry of the more primitive rocks,

their source, and to provide additional constrainsts to the geochronology of the Late Cretaceous alkaline cycle. Morever, it this study will allow the detection of possible geochemical variations with age and/or location of the collected samples.

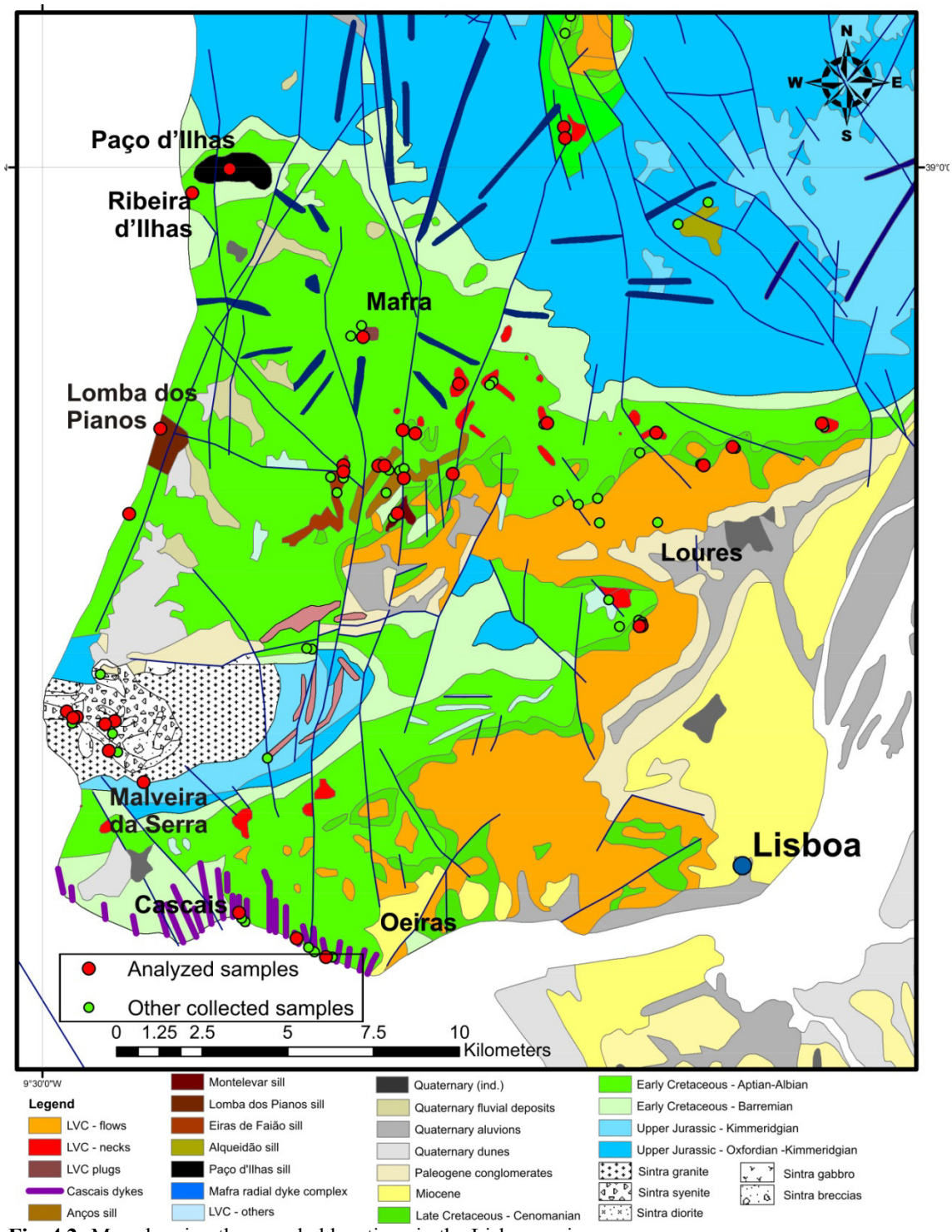

Fig. 4.2: Map showing the sampled locations in the Lisbon region.

The samples were gathered during a time interval from 2006 to 2008 and subsequently processed in the sample preparation laboratories of GeoFCUL to allow for detailed petrographic, geochemical and geochronological studies.

The collected samples belong primarily to the most basic lithologies in each complex, so that the effects of crustal contamination could be minimized and the original source signatures better distinguished.

The sample locations are summarized on figures 4.1 and 4.2 and listed along with the respective geographic coordinates in annex I.

The samples from the Monchique complex collected and described by Clavijo and Valadares (2003) and Valadares (2004) were also integrated in this study resulting in the addition of further mineral chemistry and isotopic geochemistry data.

4.1 Onshore sampling

4.1.1. The Lisbon Volcanic Complex

Several of the occurrences associated with the Lisbon Volcanic Complex (LVC) were sampled (fig. 4.2). Namely the basal and top flows of its basic lava sequence, some of the associated necks, and also several of the basic to intermediate sills and plugs associated to the complex.

- The lava flows:

The basal lava flows are exposed on the contact between the LVC lava pile and the Cenomanian limestones. The basal unit always occurs on top of a pyroclastic sequence with variable thickness, which itself overlays a paleokarst formed on the limestone. The pyroclastic sequence can also show some signs of previous erosion, with the lava flows filling paleochannels on the pyroclastic layer, as can be seen in Negrais (fig. 4.3).

Samples of the basal unit were collected near Lexim, (RM 7), Negrais (RM 42-45), Fanhões (RM 69-74), Ramada (RM 79-80), Bolores (RM 59-61), and Ponte de Lousa (RM 40-41), for coordinates see annex I.

This unit constituted by alkaline basalts which are usually moderately to lightly porphyritic, with olivine and pyroxene phenocrysts in a dark grey matrix with few vesicles filled by secondary calcite or zeolite. Some amphibole phenocrysts are also observed in Negrais. Alteration is more important in Bolores, Ponte de Lousa and some of the Ramada and Fanhões samples.

Due to important erosional events that took place during the Cenozoic and even in recent times, the topmost unit that was sampled is not likely to correspond to the last effusive event of the LVC. The samples from the highest position in the stratigraphic sequence of the lava pile were collected in Ramada (RM 102) and near Murteira (RM 103) (fig. 4.3) and correspond to more or less altered porphyritic basalts with abbundat olivine and scarcer clinopyroxene phenocrysts. The most altered samples show chloritized or serpentinized olivines and thin calcite veins.

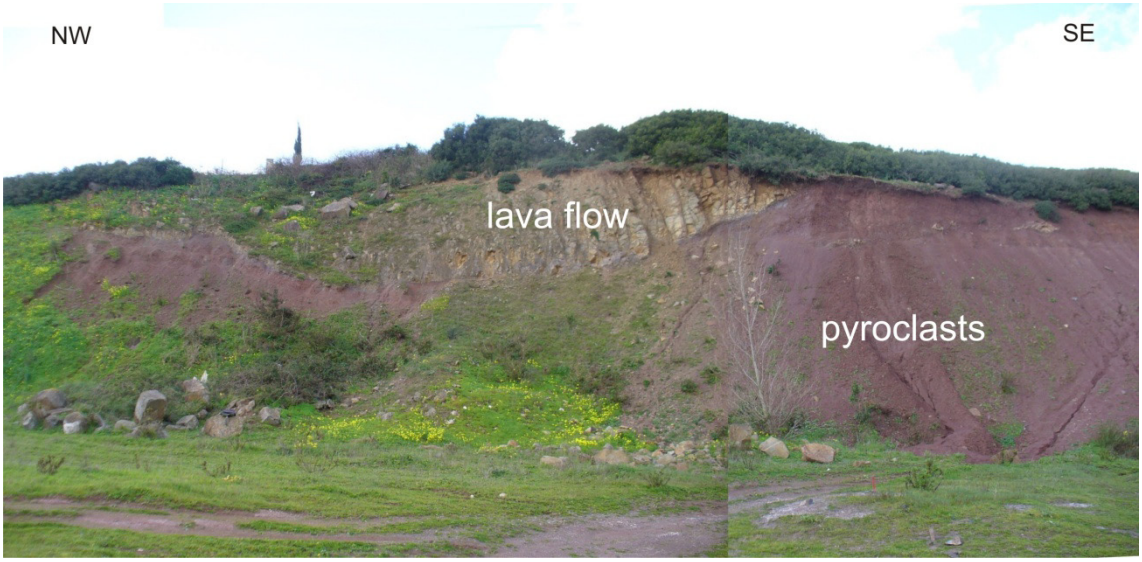

Fig. 4.3: The basal LVC flow filling a paleovalley in the LVC pyroclasts near Negrais, in the area where samples RM 42-45 were collected.

Porphyritic basalts with clinopyroxene and olivine phenocrysts and also some aphanitic basalts were recovered from outcrops in the small Runa basin, near Torres Vedras (RM 34-35). However, these outcrops mostly consist of sparse boulders on cultivated areas, with little or no field relations visible between them or with the remaining lithologies present in the region. Therefore, their stratigraphic position and occurrence mode could not be accurately determined and evaluated. Also, most of the rocks are quite altered, so no further studies were made with these samples.

- The necks:

Several basaltic necks across the LVC were sampled for this study. They intrude marls and limestones of Albian-Cenomanian age or the sandstones, limestones and mudstones of the Barremian-Aptian "Grés de Almargem" unit.

These necks (fig. 4.4) commonly display two different facies, the fine grained, often aphanitic marginal facies and the coarser central facies, both of which were sampled.

The coarser interior facies can be very porphyritic, displaying milimetric clinopyroxene and olivine crystals. Samples taken from these occurrences are mostly fresh, with the only signs of alteration being some reddish altered olivines and the presence of carbonate and zeolites filling vesicles and secondary fractures.

Fig. 4.4: The Lexim (left) and Torre da Besueira (right) necks, showing columnar jointing.

The sampled necks were Monte Serves (RM 65-66), Torre da Besueira (RM 1-3), Montemuro (RM 57-58), Funchal (RM 93-94), Gare de Mafra (RM 92), Penedo do Lexim (RM 4-6) located between Vialonga, Negrais and Malveira, and the Serra do Socorro (RM 26-28) and nearby São Sebastião necks (RM 29-30), further to the north (fig. 4.2).

- The plugs:

Three small, half sphere shaped plugs outcrop in the abrasion platform of the Ribeira d'Ilhas beach (fig. 4.5) intruding the sandstones, limestones and mudstones the Aptian-Albian "Belasiano" unit. They are also related to small sills that occur on the

country rock above them and to irregular shaped dykes made out of similar material (fig. 4.5).

In general, these rocks are very porphyritic and rich in centimetric xenoliths and xenocrysts that are scattered in a black groundmass. Most of the phenocrysts observed are amphibole and pyroxene, with auxiliary olivine. Both the south (RM 36) and central (RM 37) plugs were sampled.

The interior of the central and largest plug is more altered than its chilled margin, displaying a greener color, abundant vesicles and completely altered olivines.

Fig. 4.5: The Ribeira d'Ilhas plugs. On the right you can also observe the irregularly shaped dyke associated with the south plug outcropping in the cliff behind it.

- The Oeiras-Cascais dykes:

These dykes outcrop mostly in the abrasion platform and cliffs of the beaches near the cities of Oeiras and Cascais (fig. 4.6).

Many of them intruded pre-existing fractures that cut the Lower Cretaceous sedimentary units that outcrop in that area. Their maximum thickness rarely exceeds 2m.

These fractures were reactivated after the intrusion of the dykes, during the inversion of the Lusitanian basin. This promoted intense fracturation and fluid circulation in many of them, which caused significant alteration, namely oxidation and carbonatization of the original magmatic rocks and filling of the fractures with secondary carbonate material.

The dykes show two preferential directions: NNE-SSW and NNW-SSE, but no crosscut criteria were observed between them. The NNE-SSW direction seems to be more abundant between the Parede-Estoril sector, while the NNW-SSE appears to dominate from Estoril to Cabo Raso (see fig. 4.2).

They also divide themselves compositionally between very porphyritic olivine and clinopyroxene basalts and plagioclase and amphibole phyritic hawaiites with abundant carbonate filled vesicles.

Both these types occur in the two observed directional trends, although the basalts seem to intrude predominantly NNE-SSW fractures. Sometimes it is also possible to observe a linear basaltic dyke surrounded by what seems to be a more irregular trending, more evolved dyke, but again, the relation between the two is unclear.

Fig. 4.6: Several dykes outcropping in the marine abrasion platform in the Avencas (left) and Parede (right) beaches between Cascais and Oeiras. The larger dyke on Avencas beach is of basaltic nature while the other two are trachybasaltic.

In this region, several dykes were sampled between the Parede and Tamariz beaches (RM 52-54; 62-64; 87-91), but only three of them were fresh enough to study, namely the aphanitic basaltic dyke in the beach in front of the Parede sanatorium (RM 52), the porphyritic basalt that outcrops in Bafureira beach (RM 64) and the porphyritic hawaiite with plagioclase phenocrysts just west of Praia da Poça (RM 90).

- The sills:

Several sills with compositions ranging from basic to acidic and nepheline normative to quartz normative have been included in the LVC by several authors (e.g.

Palácios, 1985). They are mostly found closer to the Sintra igneous complex but also occur in other locations.

For this work, the more basic sills were sampled as well as some of the intermediate ones, in order to understand the processes that characterized the magmatic evolution of the complex.

The Lomba dos Pianos sill (fig. 4.2) was sampled (RM 9-10) in an abandoned quarry north of Magoito beach, that is presently being used as a landfill. The sill shows a thickness of around 10m in that location and intrudes marls and limestones of Albian-Cenomanian age (fig. 4.7).

The rock is melanocratic and porphyritic, with plagioclase and clinopyroxene phenocrysts in a dark matrix. The outcrop shows abundant zeolite filling in fractures and cavities.

Fig. 4.7: The Lomba dos Pianos sill (top) and two aspects of the Anços sill (bottom).

The Montelevar sill (fig. 4.2) intrudes marls and limestones of Albian-Cenomanian age and was sampled in a construction site next to the Montelevar

cemetery (RM 49-50) where the sill was well exposed and relatively fresh. Neither the top nor bottom portions of the sill were exposed in this location making it impossible to estimate its thickness.

The rock is medium grained and, viewed in hand sample, constituted mostly by plagioclase with some clinopyroxene. Alteration was important with some of the minerals looking brown due to oxidation and clay alteration.

The Anços sill intrudes (fig. 4.2) marls and limestones of Albian-Cenomanian age and was sampled in two different locations: in a quarry near Rebanque (RM 67-68, fig. 4.7) and in a road cut along the road that connects Anços and Maceira (RM 55). On the quarry, the top of the sill dipps approximately 12º South and is approximately 20m thick. No layering or other internal structure was distinguished within the sill.

The samples show a porphyroid texture with plagioclase and pyroxene phenocrysts in a finer grained matrix. All of the samples showed some alteration, with the mafic minerals and some plagioclases transforming into phyllossilicates.

The Eiras do Faião sill (fig. 4.2) is located near the previously mentioned sills and intrudes the same stratigraphic unit. It was sampled in outcrops exposed near the locality with the same name (RM 46-47). The sill displays a very fine grained texture and abundant vesicles filled with orange to pink zeolites. Some rare centimetric xenoliths are also observed.

The Alqueidão sill (fig. 4.2) near Sobral de Monte Agraço was also sampled but its samples proved to be too altered to pursuit further studies. This sill intrudes Upper Jurassic (Tithonian) rocks, has a medium grained texture, and is constituted mostly by plagioclase and clinopyroxene.

4.1.2. The Malveira da Serra sill

This sill is located in the southern flank of the Sintra intrusion and has been attributed to a first phase of igneous activity in the region that preceded the installation of the granite laccolith (e.g. Kullberg and Kullberg, 2000).

It outcrops on a roadcut just outside Malveira da Serra, where it intrudes limestones of Oxfordian-Kimmeridgian age. It is a very porphyritic rock with abundant clinopyroxene and amphibole phenocrysts in an aphanitic matrix (RM 25).

4.1.3. The Mafra plug

This gabbroic plug was sampled in a construction site near Almada (RM 83), just outside of Mafra (fig. 4.2). The rock was quite altered but some fresh boulders separated by disaggregated alteration zones were sampled. Near this outcrop another mesocratic, porphyritic igneous rock with plagioclase and an altered mafic mineral phenocrysts occurred, but no age relation between these two was observed.

The Mafra gabbroic rock is similar to the gabbros present in Sintra, with large amphibole and clinopyroxene aggregates giving it a glomoporphyric texture. However, this rock possesses a finer matrix between the more porphyritic phases and is also less altered showing a darker grey colour.

In the vicinities of this gabbroic plug, many other igneous rocks are present in the shapes of dykes and of what may be sills. They are altered and often more evolved, varying from melano to mesocratic and usually porphyritic, showing plagioclase and mafic mineral phenocrysts, but the alteration makes their classification a difficult task.

4.1.4. The Foz da Fonte sill

The 8m thick Foz da Fonte sill (fig. 4.2) outcrops for an extension of approximately 200 m at a N-S coastal section in the Setúbal peninsula (fig. 4.8), south of Lisbon, and intrudes sedimentary sequence of Aptian age (Kullberg, 2000).

Fig. 4.8: The Foz da Fonte sill in a general view (left) and a detail of its upper contact (right).

It is a fine grained melanocratic rock with abundant, carbonate filled vesicles towards its top (fig. 4.8). Its samples correspond to FF 2-4.

4.1.5. The Paço d'Ilhas sill

The Paço d'Ilhas sill was sampled in a quarry near the locality with the same name (PI 1-11). Sections of this sill with approximately 20m thickness are exposed in the quarry walls and the top contact between sill and Lower Cretaceous sediments (Albian and Aptian-Barremian sandstones and limestones) is also observed. The sill is a layered intrusion and both the fine grained melanocratic monzogabbroic layers and the mesocratic monzosyenitic layers were sampled.

4.1.6. The Sintra mafic rocks

The Sintra gabbros, also known as mafraites (Matos Alves, 1964), occur in several distinct outcrops inside the Sintra intrusive complex. Two of these were sampled, the Peninha (RM 11-17) and the Azóia (RM 18-23) outcrops, both of which are part of the Cabo da Roca complex (see section 2.3.1.1).

Fig. 4.9: Details of the Sintra gabbros in the Azoía (left) and Peninha (right) outcrops.

The Peninha gabbros contact with syenite and igneous breccias (e.g. Ramalho et al., 2001). They were collected on a roadcut along a forest road near Peninha and show significant heterogeneity in terms of grain size (fig. 4.9) and preferred mineral orientation.

All samples show plagioclase, amphibole and pyroxene but these may range in grain size from medium to coarse and almost pegmatitic. Amphiboles and pyroxenes

can either display a preferential orientation or form aggregates in a characteristic glomoporphyric texture. Some alteration and secondary veins are visible but overall, alteration is not very important in these rocks.

The Azóia outcrop corresponds to a series of boulders inside a walled terrain near the village of Azóia. These rocks are very coarse grained, and show plagioclase, amphibole and pyroxene as well as abundant green alteration minerals and light colored secondary veins that sometimes showed epidote rich centers. The same glomoporphyric texture that was observed in Peninha is also present here (fig. 4.9).

The diorite was sampled on a roadcut between Malveira da Serra and Biscaia, near the entrance to Quinta da Tomélia (RM 24). It is a medium grained rock showing plagioclase, amphibole and biotite and some greenish alteration products.

4.1.7. The Sines mafic rocks

The Sines gabbros occur in two distinct outcrops within the complex, one in the North, near Pedras Negras and the other in the South, closer to the Sines city center.

Fig. 4.10: Details of the Sines gabbros at Praia Vasco da Gama (top left) and Pedras negras outcrops showing crosscutting dykes (top right) and apparent compositional layering (bottom left and right).

The southern outcrop was sampled at Praia Vasco da Gama (RM 96-98), and contacts with diorites in the south and with syenites in the west. These rocks are coarse grained, with amphibole crystals that can be several centimeters long (fig. 4.10). In hand specimen, amphibole, plagioclase, and some green alteration products can be observed. The amphiboles can in some places show the same glomoporphyric texture observed in Sintra and Mafra.

The northern Pedras Negras outcrop (RM 99-101) contacts with Jurassic limestones to the North and syenite to the South. It appears to show some layering (fig. 4.10) which is not horizontal, probably reflecting accumulation parallel to the walls of the magma chamber. This gabbro is profusely intruded by later mafic and felsic dykes. It is medium to coarse grained with distinguishable olivine, pyroxene and plagioclase.

The diorite contacts with the Paleozoic metassediments to the south and with the gabbros to the north. It was sampled just south of Praia Vasco da Gama and is a medium to coarse grained rock, with a lighter color than the gabbros and constituted by abundant plagioclase and biotite and clinopyroxene.

4.1.8. The Monchique mafic and ultramafic rocks

These samples were provided by Vasco Valadares. For the location and description of these samples, see Clavijo and Valadares (2003) and Valadares (2004) and for more information on the Monchique igneous complex, go to section 2.3.1.3.

4.1.9. The Loulé dykes

Fig. 4.11: Loulé dykes inside the salt mine appearing still with a tabular shape (left) and as a boundin (right).

These dykes outcrop inside the Loulé salt diapir and were sampled with the permission of the CUF group. They are frequently very deformed, being often folded and separated into individual boudins (fig. 4.11). They were sampled inside the Loulé salt mine in galleries C-20 and C-12-1.

Dyke C-20 is around 2m thick and showed abundant igneous and metamorphic xenoliths in its centre but none in the margin. The sampled margin was fresh and porphyritic with pyroxene and biotite phenocrysts.

Dyke C-12-1 is less than 1m thick and shows altered olivine phenocrysts in an aphanitic groundmass.

4.2 Offshore sampling

Given the recent identification of large volumes of Late Cretaceous alkaline magmatism in the offshore WIM (e.g. Geldmacher et al., 2006; Merle et al., 2006, 2009), an attempt was made to complement the sampling of these occurrences.

4.2.1 The Fontanelas seamount

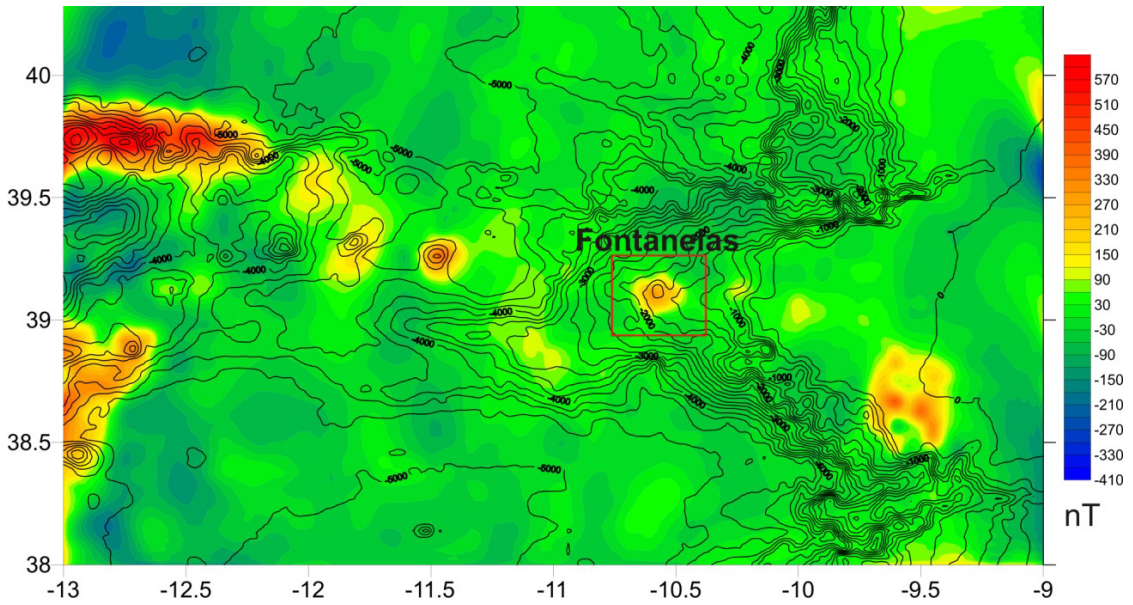

Fig. 4.12: Magnetic anomalies between Sintra and the Tore seamount. Figure by Mário Moreira.

On the summer of 2008, as a part of the MAGMAFLUX research project (POCTI/CTA/48450/2002), one day of dredging took place on board the RV Professor

Logachev, during the TTR-17 cruise, allowing for sampling of the Fontanelas seamount.

This seamount is located 100 km west of Ericeira (fig. 4.12, 4.13) and was selected as a sampling target among a series of magnetic anomalies occurring in the Estremadura Spur, between the Sintra igneous complex and the Tore seamount (see section 2.3.2.2, fig. 4.12). It was chosen due to its shallower depth (top at approximately -1250m and base at around -1600m; fig. 4.13), which facilitated dredging operations on board.

High resolution multibeam bathymetry and magnetic anomaly data provided by the "Estrutura de Missão para a Extensão da Plataforma Continental" (EMEPC) and processed by members of the team in the MAGMAFLUX project were crucial during the identification of the targets and planning of the sampling campaign. Also, a dive with the onboard TV-Grab device that preceded the dredging, allowed for the unequivocal identification of outcropping basic igneous rocks before the sampling with a round dredge.

Table 4.1: Location of the start (S) and finish (F) points for each of the dredging operations.

Station number	Time (GMT)	Latitude	Longitude	Depth (m)
TTR17AT689D S	05:27	39º05,066N	10º33,602W	-1250
TTR17AT689D F	06:32	39º05,022N	10º33,247W	-1194
TTR17AT690D S	07:49	39º04,740N	10º34,329W	-1498
TTR17AT690D F	09:40	39º04,775N	10º34,114W	-1340
TTR17AT691D S	12:35	39º05,317N	10º34,354W	-1460
TTR17AT691D F	13:13	39º05,220N	10º34,060W	-1308
TTR17AT692D S	14:34	39º04,810N	10º32,853W	-1415
TTR17AT692D F	15:50	39º04,991N	10º33,112W	-1230
TTR17AT693D S	16:48	39º04,841N	10º33,229W	-1270
TTR17AT693D F	17:51	39º05,082N	10º33,483W	-1110

A total of five successful dredge hauls were recovered along the top and flanks of the seamount (fig. 4.14, table 4.1). The contents of the dredges varied from having more or less brown pelagic mud, biogenic material (mainly dead coral of different sizes and ages but also some sponges and numerous cirripedia plates), igneous rocks, allochthonous material (probably dropstones and rocks used as weights in fishing nets) as well as occasionally abundant phosphate and Fe-Mn nodules and crusts.

The recovered pieces of igneous rocks were mostly fragments of pillow lavas that sometimes even displayed the characteristic breadcrumb textures (fig. 4.15). They ranged in size from boulders with a diameter of approximately 10 cm to one entire pillow with over 40 cm diameter.

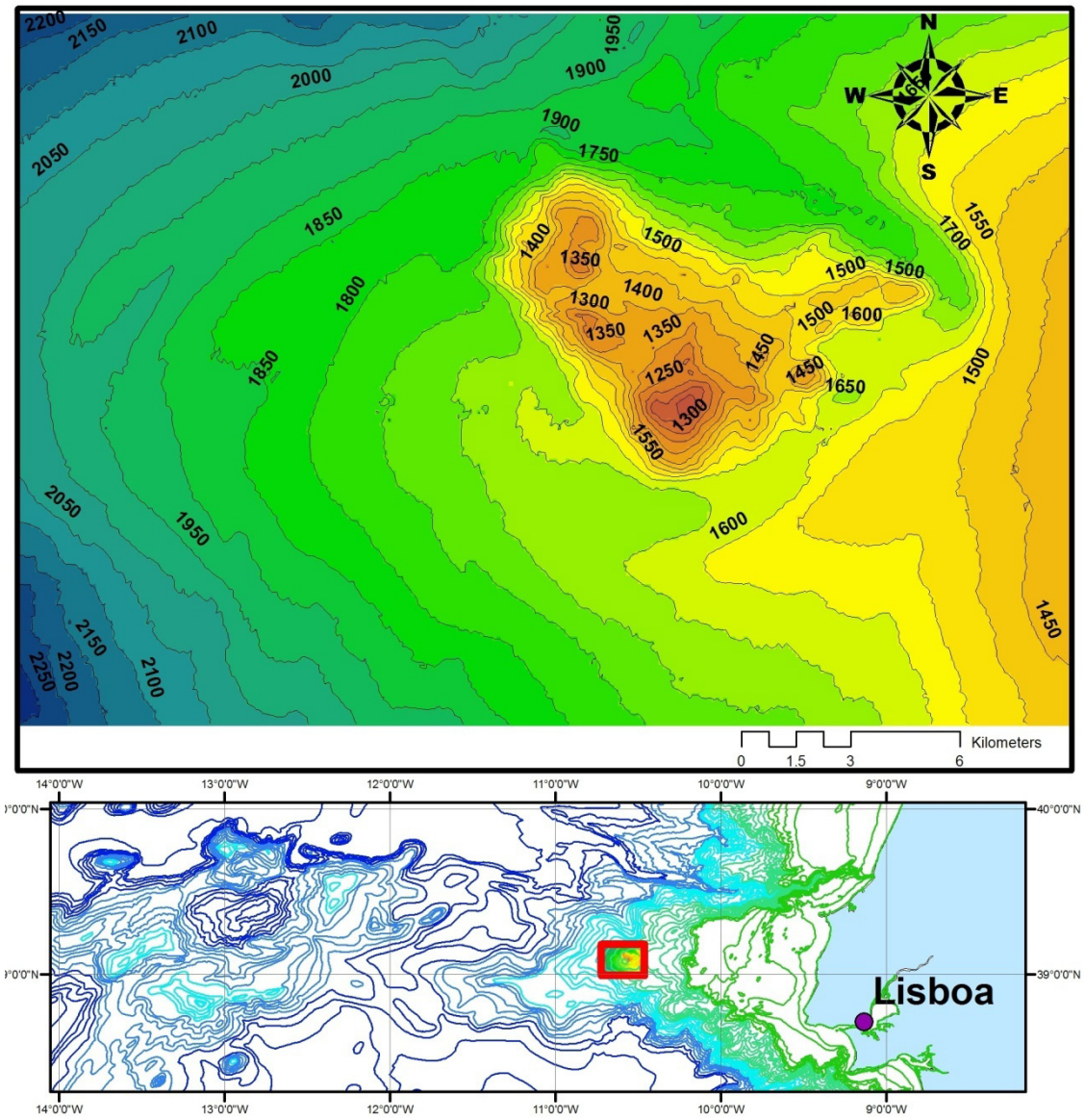

Fig. 4.13: Location and detailed bathymetric map of the Fontanelas seamount. High resolution bathymetric data for the Fontanelas seamount by EMEPC. Lower resolution bathymetric contours from GEBCO (www.nbi.ac.uk).

The pillow lavas consisted of very vesicular and altered basalts with a greenish to brown color. In most cases the vesicles were filled with carbonate and clay minerals. Many of the pillow lavas were also covered with a mantle of Fe-Mn oxides of variable

thickness and could display corals growing on top. The high vesicle abundance is suggestive of extensive degassing of volatile rich lava.

The lavas display a porphyritic texture, with phenocrysts of fresh pyroxene and amphibole accompanying much altered olivine set in an equally altered groundmass.

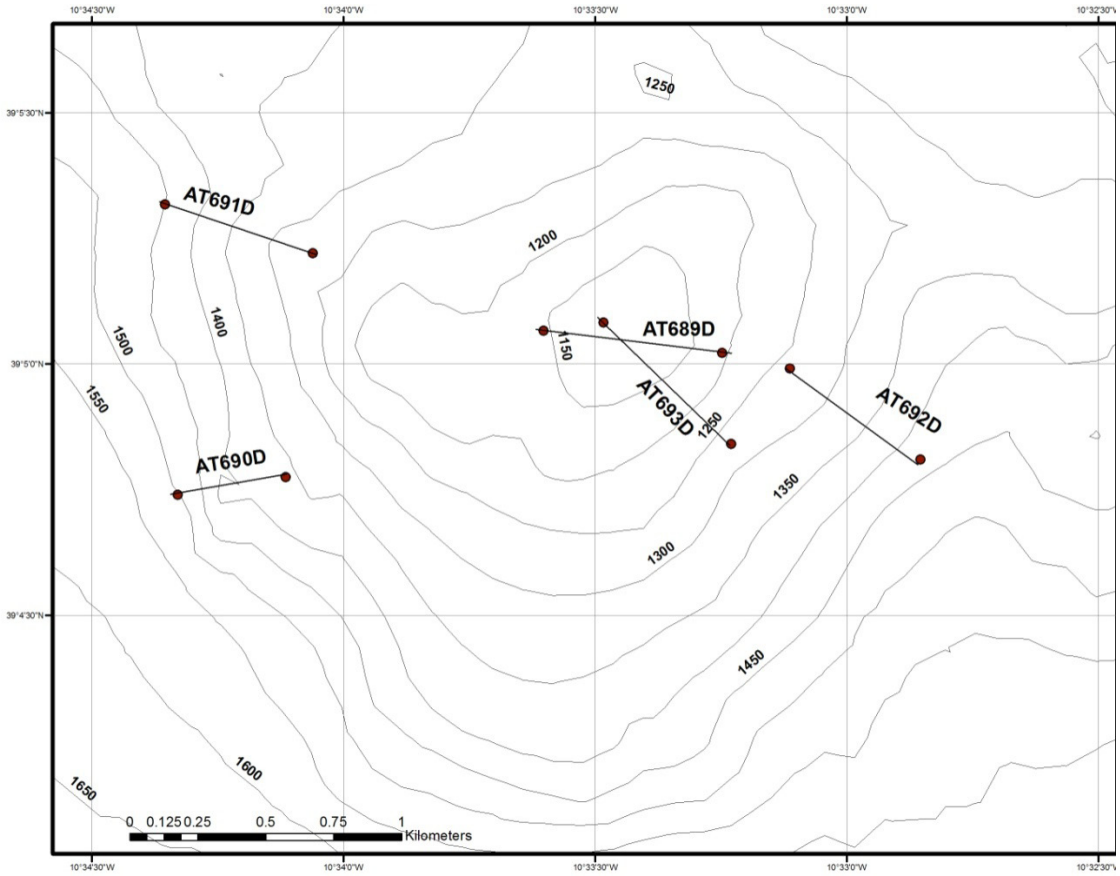

Fig. 4.14: Detail of the Fontanelas seamount showing the location of each of the dredging operations.

Some breccias made of mostly clasts of altered basalt cemented by carbonate were also sampled.

The dredged nodules are rounded and can either exhibit concentric layers of Fe-Mn oxides or be of mainly phosphate nature, with only a thin Fe-Mn oxide cover. The crusts that were sampled along with the nodules show similar compositions and features but do not have a round shape, showing flat, irregular shapes.

The allochthonous material seems to have diverse origins. Some of it corresponded to sedimentary rocks, mostly limestones but there were also high grade metamorphic rocks with gneissic or granulitic textures and even a tholeiitic basalt. It is likely that they may correspond to weights put in fishing nets that were lost by fisherman or correspond to dropstones, carried by icebergs to lower latitudes.

Fig. 4.15: Dredge haul AT693D arriving to deck containg the largest pillow lava sampled (top left) and general aspects of dredge hauls AT692D (top right), AT689D (bottom left) and AT691D (bottom right) after washing and selection.

5. Geochronology

The geochronological data presented in this section was already discussed in the paper "Age constrains on the Late Cretaceous alkaline magmatism on the West Iberian Margin", authored by R. Miranda, V. Valadares, P. Terrinha, J. Mata, M. do Rosário Azevedo, M. Gaspar, J. C. Kullberg, C. Ribeiro and published in 2009 in the journal "Cretaceous Research" (vol. 30, pp. 575-586).

Further sampling took place and during 2009, a total of 13 separates of matrix material and amphibole were obtained in order to acquire further geochronological data on the LVC (flows and necks), the Cascais dykes, the Sintra gabbros and diorites, the Mafra radial dyke swarm, the Malveira da Serra sill and the Fontanelas seamount.

Unfortunately, due to unforeseen difficulties, the data were not available in time to be integrated into this manuscript.

5.1 Previous geochronological work

The Late Cretaceous alkaline igneous activity in the onshore section of the WIM took place in a post rift setting, 30 My after the oceanic break-up in the Tagus Abyssal Plain (Pinheiro et al., 1996; Sibuet et al., 2007) and partially coincides with the Pyreneean continental collision in Northern Iberia (e.g. Sibuet et al., 2004) and the onset of tectonic inversion of the Mesozoic basins (e.g. Mougenot, 1980, Terrinha, 1998, Rosembaum et al., 2002), thus making the Late Cretaceous alkaline magmatism a key episode in the history of this passive margin. These rocks have been object of several previous dating attempts, summarized in table 5.1.

As shown in table 5.1, the chronology of the main magmatic events associated with the Late Cretaceous alkaline cycle has been established on the basis of a large number of K-Ar ages and Rb-Sr whole rock isochrons. These two isotopic systems are extremely sensitive to post-emplacement disturbance which may explain, at least to some extent, the significant scatter of the published geochronological data (sometimes exceding 15 Ma for the same occurrence using one single method, table 5.1). The use of more reliable dating techniques (e.g. incremental release $^{40}Ar/^{39}Ar$ dating and/or U-Pb zircon geochronology) is therefore fundamental to obtain precise age constraints. In order to refine the geochronology of the Late Cretaceous alkaline cycle, several of the

Table 5.1: Age summary for the main Late Cretaceous alkaline occurrences in the West Iberian Margin. 1 – Ferreira and Macedo, 1979; 2 – MacIntyre and Berger, 1982; 3 – Storetvedt et al., 1987; 4 – Canilho and Abranches, 1982; 5 – Bernard-Griffiths et al., 1997; 6 – Rock, 1976; 7 – Mahmoudi, 1991.

Occurrence	Age	Reference	Method	Material
Lisbon volcanic complex	72.6 ± 3.1	[1]	K-Ar	whole rock isochron
Sintra (granite)	81.9 ± 2	[2]	K-Ar	biotite
	84.0 ± 1.1	[3]	K-Ar	K feldspar
	79.2 ± 0.8	this study	U-Pb	zircon
Sintra (gabbro)	74.9 ± 1	[3]	K-Ar	whole rock
(syenite)	76.1 ± 1.1	[3]	K-Ar	whole rock
	76.4 ± 1.4	[3]	K-Ar	whole rock
	78.3 ± 1.8	[3]	K-Ar	whole rock
Sines	72.0 ± 1.5	[4]	Rb-Sr	whole rock isochron
	78.9 ± 1.5	[3]	K-Ar	diabase dyke
	62.0 ± 1.3	[3]	K-Ar	diabase dyke
	75.2 ± 0.8	[3]	K-Ar	K feldspar
	63.8 ± 0.8	[3]	K-Ar	Kfeldspar
	75.4 ± 0.6	this study	U-Pb	zircon
Monchique	72.0 ± 2	[2]	K-Ar	mineral separates
	72.0 ± 1.5	[5]	Rb-Sr	whole rock isochron
	72.0 ± 2	[6]	Rb-Sr	whole rock isochron
	72.7 ± 2.7	this study	Ar-Ar	amphibole
	71.5 ± 3.6	this study	Rb-Sr	whole rock isochron
Paço d'Ilhas	88.0 ± 2.7	[7]	K-Ar	biotite
	86.8 ± 2.5	[7]	K-Ar	K feldspar
Loulé dykes	71.8 ± 1.9	this study	K-Ar	biotite
Foz da Fonte sill	93.8 ± 3.9	this study	Ar-Ar	amphibole

exposed occurrences were selected for further geochronological studies and/or whole-rock geochemistry. These include:

A) the granite from the Sintra laccolith body (Terrinha et al., 2003) that had systematically yielded ages older than the suite of gabbro-diorite-syenite and associated breccias present in the complex (see table 5.1).

B) the Foz da Fonte microgranular tephritic sill, which corresponds to the southernmost intrusion of the Lusitanian basin.

C) the syenites of the Sines sub-volcanic intrusion. Of all the known alkaline intrusions, this is the occurrence that shows a wider range of ages (table 5.1).

D) the Monchique alkaline complex. This is the most voluminous of the southern alkaline intrusions, as well as the only one emplaced in unrifted Paleozoic

basement. The Monchique complex has been dated with both the K-Ar and the Rb-Sr method (table 5.1), with the obtained ages clustering around 72 Ma (72.0 ± 2.0 mean K-Ar ages on mineral separates, MacIntyre & Berger, 1982; 72.0 Ma Rb-Sr whole rock isochron, Rock, 1976, Bernard-Griffiths *et al*., 1997), although the K-Ar ages obtained for K-feldspar and nepheline separates show some spread, attributed to Ar loss (MacIntyre & Berger, 1982).

E) the ultrabasic lamprophyre dykes that occur within the Loulé salt diapir in the Mesozoic Algarve basin. These rocks are representatives of the minor alkaline igneous activity hosted in the Algarve Basin.

5.2 New geochronological data

The samples were prepared for analysis at the Departamento de Geologia da Universidade de Lisboa. They were hydraulically crushed, in order to ensure the removal of all the signs of alteration, and then reduced in size by a jaw crusher and powdered in an agate swing mill.

Sr isotopic analyses were performed on a VG SECTOR 54 multicollector thermal ionization mass spectrometer (TIMS) in the Laboratory of Isotope Geology of the University of Aveiro, Portugal. Rb and Sr contents were determined by ICP-MS at Actlabs Ancaster, Ontario, Canada. The analytical data were corrected for mass fractionation using an exponential law ($^{86}Sr/^{88}Sr = 0.1194$). Average levels of blanks for Sr were in the range 0.25-1.0 ng. The standard NBS-987 gave a repeated value of 0.710254 +/- 34 for (2sd of 49 analyses) during the period of analysis. Regression lines have been calculated using the least-squares method of York (1969) as implemented in the Isoplot program (Ludwig, 2000).

For $^{40}Ar/^{39}Ar$ dating purposes whole rock samples from the Foz da Fonte sill and a Monchique lamprophyre were sent to Actlabs Ancaster, Ontario, Canada, where amphibole separates were obtained by crushing several kg of sample, sieving, washing and separation using magnetic methods and heavy liquids. The separates were wrapped in Al foil and loaded in an evacuated and sealed quartz vial with K and Ca salts and flux monitors (LP-6 biotite, with and assumed age of 128.1 Ma, Ingamells and Engels, 1976; Odin et al., 1982). They were irradiated in the McMaster University, Ontario, Canada, nuclear reactor for 48 hours. After the flux monitors were run, J values were calculated,

using the measured flux gradient. Neutron gradients did not exceed 0.27% on sample size. The Ar isotope composition was measured in a Micromass 5400 static mass spectrometer. 1200º C blank of ^{40}Ar did not exceed $2\text{-}5*10^{-10}$ cc STP. Heating time for each step was 10 minutes. After each analysis, the extraction temperature is elevated to 1800º C for few minutes and the furnace is prepared for next analysis. The reported errors correspond to 1σ.

The K-Ar age determination was also performed by Actlabs Ancaster, Ontario, Canada on a biotite separate from an ultrabasic lamprophyre obtained after crushing, washing and sieving the sample and then using heavy liquids to obtain the mineral separate. The determination of the K concentration was obtained by ICP on Thermo Jarrell Ash Enviro II ICP Spectrometer after an aliquot of the sample was weighted into graphite crucible with lithium metaborate/tetraborate flux and fused using LECO induction furnace. For the Ar analysis an aliquot of the sample was weighted into an Al container, loaded into the sample collector of the extraction system, and degassed at 100º C for two days to remove the surface gases. Argon was extracted from the sample in a double vacuum furnace at 1700º C. The Ar concentration was then determined using isotope dilution with a ^{38}Ar spike, which is introduced to the sample system prior to each extraction. The extracted gases are cleaned up in a two step purification system. Pure Ar was then introduced into a custom built magnetic sector mass spectrometer (Reynolds type) with a Varian CH5 magnet. The ion source has an axial design (Baur-Signer source), that provides more than 90% transmission and extremely small isotopic mass discrimination. Ar isotope ratios measurements were corrected for mass discrimination and atmospheric argon was removed assuming that ^{36}Ar is of atmospheric origin. The concentration of radiogenic ^{40}Ar was calculated using a ^{38}Ar spike. After each analysis the extraction temperature is elevated to 1800º C for few minutes and the furnace is prepared for the next analysis.

Zircon separates for U-Pb analyses were obtained after crushing, washing and sieving the rock and then using a standard gravimetric (Wifley and heavy liquids) and magnetic (Frantz magnetic separator) separation techniques. Zoning patterns and inclusions were investigated by cathodoluminiscence and transmitted light microscopy prior to LA-ICP-MS analyses. Analyses were performed in the Geoanalytical Laboratory at Washington State University using a New Wave UP213 Nd-YAG (213 nm) laser ablation system, and a ThermoFinnigan Element2 single collector double focusing magnetic sector ICP-MS. The analytical parameters included a repetition rate

of 10 Hz, 40 and 30 microns spot sizes, and a total analysis time of 30 sec per spot. See Chang et al. (2006) for complete analytical and data reduction procedures. Two zircon samples with ages of 564 Ma and 55.5 Ma were used as external standards to correct for elemental fractionation, and mass bias. Accuracy, based on age determinations for standards, is generally 2-3% or better.

5.2.1 Foz da Fonte sill

The $^{40}Ar/^{39}Ar$ isotopic analyses for amphibole separates from the Foz da Fonte sill give a plateau age of 93.6 Ma ± 2.3 Ma, corresponding to 98% of released ^{39}Ar (fig. 5.1). The reverse isochron diagram results in an age of 93.8 ± 3.9 Ma, MSWD = 0.47 and $(^{40}Ar/^{36}Ar)_0$ = 293 ± 11 (fig. 5.2). The plateau age appears to correspond to the closing of the amphibole and provides a good estimate for the rock crystallization age, which corresponds to the oldest known age obtained for the entire alkaline magmatism of the onshore WIM.

Table 2: $^{40}Ar/^{39}Ar$ analytical data for the Foz da Fonte amphiboles. J = 0.007063 ± 0.000130.

T^0C	t (min)	^{40}Ar (STP)	$^{40}Ar/^{39}Ar$ ±1σ	$^{38}Ar/^{39}Ar$±1σ	$^{37}Ar/^{39}Ar$±1σ	$^{36}Ar/^{39}Ar$±1σ	Ca/K	$\sum^{39}Ar$ (%)	Age (Ma) ± 1σ
550	10	$5.53*e^{-9}$	22.36 ± 0.08	0.125 ± 0.004	1.06 ± 0.01	0.0516 ± 0.0033	3.8	1.2	88.5 ± 12.0
700	10	$8.61*e^{-9}$	14.13 ± 0.03	0.034 ± 0.001	0.53 ± 0.01	0.0226 ± 0.0018	1.9	4.3	92.6 ± 6.7
850	10	$8.43*e^{-9}$	13.06 ± 0.02	0.049 ± 0.001	0.24 ± 0.01	0.0196 ± 0.0016	0.9	7.5	90.2 ± 6.0
1000	10	$9.12*e^{-9}$	9.09 ± 0.01	0.105 ± 0.001	0.57 ± 0.01	0.0053 ± 0.0012	2.1	12.5	93.5 ± 4.6
1200	10	$143.6*e^{-9}$	8.19 ± 0.01	0.613 ± 0.001	4.46 ± 0.005	0.0019 ± 0.0008	16.0	99.9	94.7 ± 3.2
1250	10	$2.50*e^{-9}$	127.68± 8.51	1.008 ± 0.136	22.82 ± 1.60	0.3966 ± 0.0345	82.2	100.0	128.9 ± 78.4

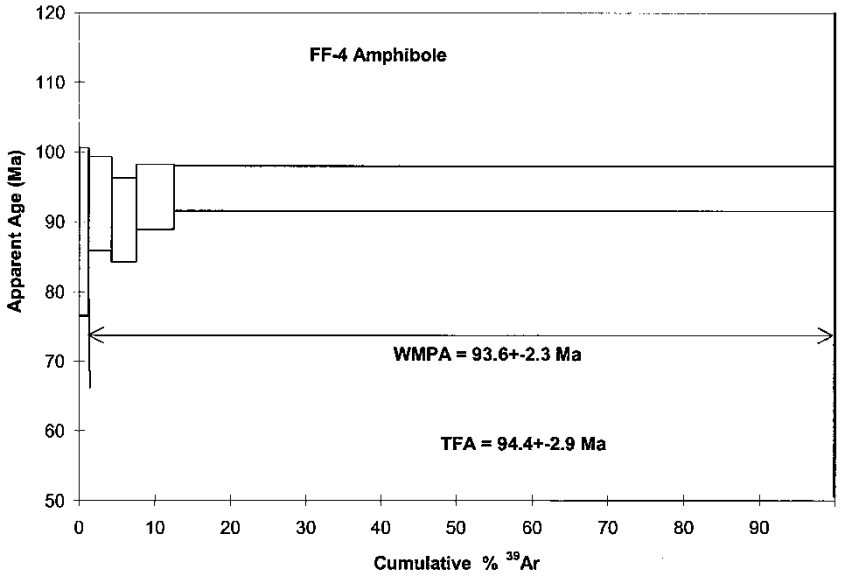

Fig. 5.1: Age temperature spectra diagram for the Foz da Fonte amphibole separate. Weighted Mean Plateau age, WMPA = 93.6 ± 2.3 Ma (including J). Total fusion age, TFA= 94.4 ± 2.9 Ma (including J).

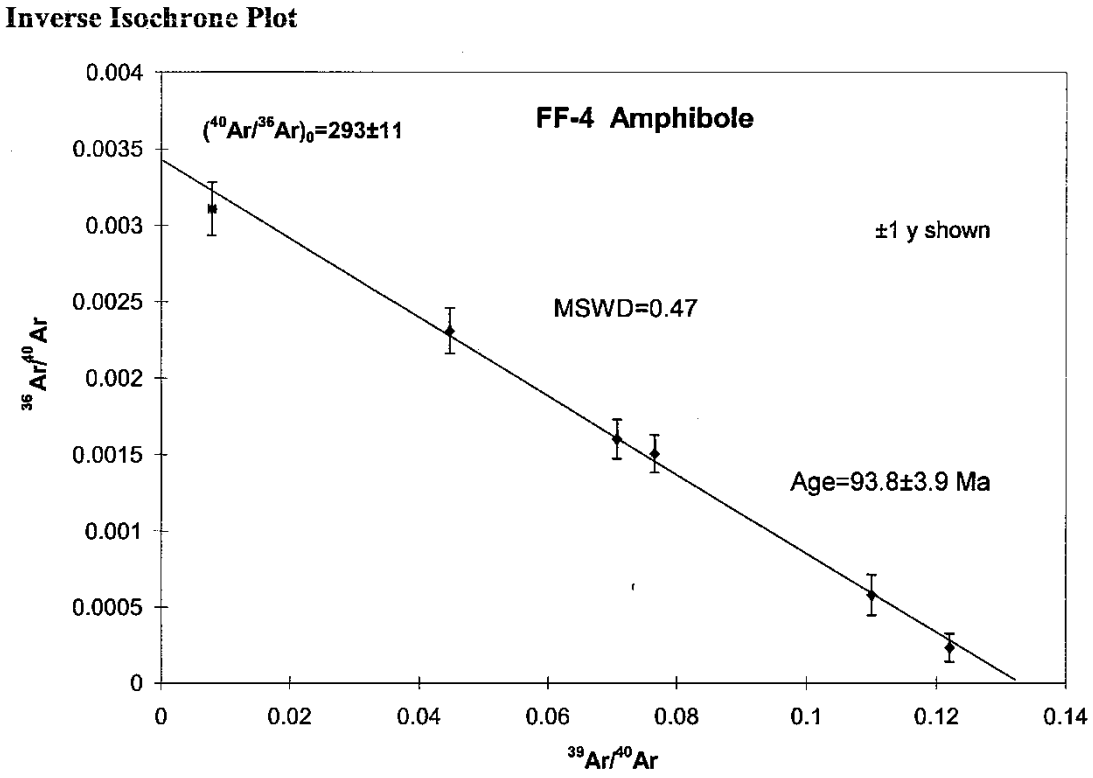

Fig. 5.2: Inverse isochron diagram for the Foz da Fonte amphibole. Inverse isochron age = 93.8 ± 3.9 Ma. (MSWD =0.47; $^{40}Ar/^{36}Ar = 293 \pm 11$).

5.2.2 Sintra granite

The Sintra subvolcanic complex has been the target of several age determinations. According to the published data, the emplacement of the granite (81.9 ± 0.4 Ma, K-Ar in biotite, MacIntyre & Berger, 1982; 84.0 ± 1.1, K-Ar in K-feldspar, Storetvedt *et al*., 1987) occurred before the intrusion of the gabbro and syenite magmas (76.1 ± 1.1 to 78.3 ± 1.9 Ma, K-Ar in whole rock syenite, Storetvedt *et al*., 1987; 74.9 ± 1.0 Ma whole-rock K-Ar in gabbro, Storetvedt *et al*., 1987).

In order to obtain a reliable crystallization age for the Sintra granite laccolith and to assess whether the emplacement of this magma occurred before or after the intrusion of the other units of the complex, a zircon separate from the granite was dated with the U-Pb method, using LA-ICP-MS. The results are shown in fig. 5.3 and table 3.

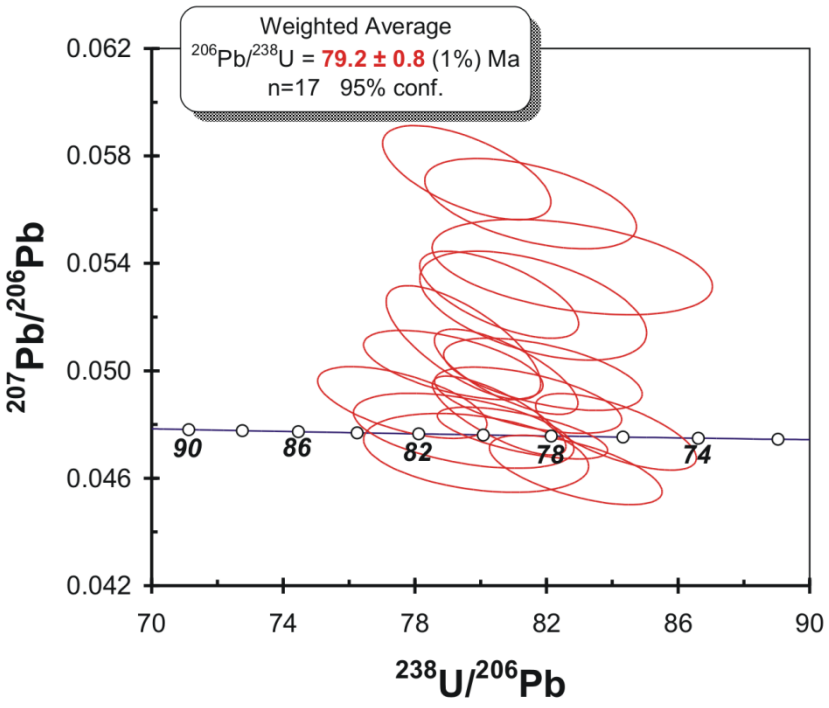

Fig. 5.3: U-Pb Tera-Wasserburg plot for the analysed zircons from the Sintra granite. Error ellipses 2σ error. Ages at 95% confidence level.

The 79.2 ± 0.8 Ma age obtained for the zircons from the Sintra granite (fig. 5.3), although younger than most of the previously published ages (table 5.1), is still older than the central values for the known ages for the gabbro and syenite (although within the error limits o some of these) and close to the K-Ar age determined in biotite separates from that same granite (table 5.1). This is compatible with: (i) field observations that show that the gabbroic and syenitic rocks define intrusive

relationships with the granite and (ii) recently obtained gravity data showing that in this composite massif vertical gabbro plugs intrude an older granite laccolith (Terrinha et al., 2003). Also, the known K-Ar ages for the syenite and gabbro suite can be subject to previously mentioned problems, such as excess Ar, which may exaggerate their age, as it appears to be the case with the 84 ± 1.1 age obtained in a K-feldspar separate (Storetvedt et al., 1987) from the Sintra granite.

5.2.3 Sines syenite

The Sines complex was also previously dated, using the K-Ar and Rb-Sr methods. The wide range of "ages" displayed by these rocks (78.9 ± 1.5 to 62.0 ± 1.3 Ma K-Ar in whole rock diabase dykes; 75.2 ± 0.8 to 63.8 ± 0.8 Ma K-Ar age in K-feldspar from the syenite; 72.0 ± 1.5 Rb-Sr whole rock isochron, Canilho and Abranches, 1982), particularly the values below 70 Ma are probably the result of a late thermal overprint that may have caused argon loss (Storetvedt et al., 1987).

With the aim of constraining the age of installation for this subvolcanic complex, a zircon separate from the syenite facies was dated using U-Pb geochronology by LA-ICP-MS. The obtained results are plotted in Figure 6 and table 3.

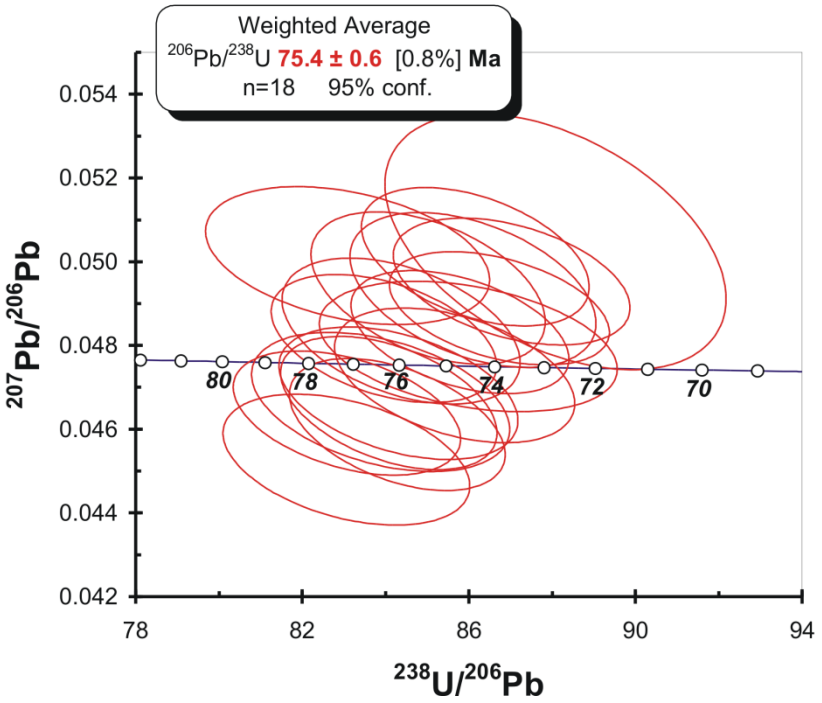

Fig. 5.4: U-Pb Tera-Wasserburg plots for the analysed zircons from the Sines syenite. Error ellipses 2σ error. Ages at 95% confidence level.

Table 3: U-Pb isotopic data obtained by LA-ICP-MS for the analysed zircons.

Locality	Sample name / Zircon grain	$^{207}Pb/^{235}U$ intercept	2σ abs err	$^{206}Pb/^{238}U$ intercept	2σ abs err	RHO	$^{207}Pb/^{206}Pb$ average	2σ abs err	$^{207}Pb/^{235}U$ age	2σ abs err	$^{206}Pb/^{238}U$ age	2σ abs err	$^{207}Pb/^{206}Pb$ age	2σ abs err
Sintra	STR1_18A	0.081046	0.004036	0.012522	0.000438	0.876	0.048043	0.001227	79.1	3.8	80.2	2.8	101.4	59.9
	STR1_17B	0.080892	0.003152	0.012305	0.000320	0.948	0.047683	0.000787	79.0	3.0	78.8	2.0	83.6	38.9
	STR1_17A	0.099415	0.004586	0.012567	0.000330	0.906	0.057378	0.001432	96.2	4.2	80.5	2.1	506.1	54.4
	STR1_16A	0.083967	0.003863	0.012212	0.000368	0.916	0.049872	0.001098	81.9	3.6	78.2	2.3	189.0	50.9
	STR1_15A	0.088568	0.004780	0.012583	0.000304	0.900	0.051053	0.001730	86.2	4.5	80.6	1.9	243.2	77.2
	STR1_14A	0.087453	0.003836	0.012632	0.000356	0.922	0.050215	0.001054	85.1	3.6	80.9	2.3	205.0	48.3
	STR1_13A	0.077031	0.003387	0.012064	0.000312	0.915	0.046311	0.001057	75.3	3.2	77.3	2.0	13.8	54.4
	STR1_12A	0.078235	0.003456	0.011889	0.000282	0.915	0.047728	0.001165	76.5	3.3	76.2	1.8	85.8	57.4
	STR1_11B	0.085289	0.003818	0.012380	0.000273	0.920	0.049967	0.001296	83.1	3.6	79.3	1.7	193.5	59.7
	STR1_11A	0.082720	0.003554	0.012413	0.000256	0.934	0.048334	0.001201	80.7	3.3	79.5	1.6	115.7	58.1
	STR1_10A	0.088589	0.005076	0.012256	0.000423	0.879	0.052428	0.001657	86.2	4.7	78.5	2.7	304.1	71.2
	STR1_9A	0.082863	0.004183	0.012581	0.000433	0.910	0.047770	0.001140	80.8	3.9	80.6	2.8	87.9	56.1
	STR1_8A	0.095096	0.004702	0.012267	0.000396	0.905	0.056225	0.001374	92.2	4.4	78.6	2.5	461.3	53.7
	STR1_7B	0.086724	0.003844	0.012884	0.000349	0.915	0.048822	0.001091	84.4	3.6	82.5	2.2	139.3	52.0
	STR1_5C	0.082794	0.003626	0.012279	0.000350	0.923	0.048907	0.001007	80.8	3.4	78.7	2.2	143.4	48.0
	STR1_5B	0.089706	0.005239	0.012079	0.000508	0.907	0.053863	0.001451	87.2	4.9	77.4	3.2	365.3	60.2
	STR1_5A	0.090422	0.004089	0.012413	0.000304	0.910	0.052834	0.001324	87.9	3.8	79.5	1.9	321.7	56.4
								Wtd avg (95%)	82.7	2.7	79.2	0.8	199.0	72.0
Sines	SNS_14A	0.077714	0.003117	0.011530	0.000287	0.860	0.050030	0.001131	76.0	2.9	73.9	1.8	196.4	52.1
	SNS_13A	0.078990	0.003922	0.011615	0.000325	0.831	0.050480	0.001546	77.2	3.7	74.4	2.1	217.2	70.1
	SNS_12A	0.075151	0.003611	0.012040	0.000351	0.843	0.046330	0.001308	73.6	3.4	77.1	2.2	14.9	67.1
	SNS_11B	0.083217	0.004146	0.012036	0.000404	0.864	0.051321	0.001377	81.2	3.9	77.1	2.6	255.3	61.1
	SNS_11A	0.076927	0.003837	0.011630	0.000395	0.867	0.049098	0.001301	75.3	3.6	74.5	2.5	152.5	61.5
	SNS_10A	0.076682	0.003800	0.011922	0.000360	0.842	0.047743	0.001389	75.0	3.6	76.4	2.3	86.5	68.3
	SNS_8B	0.076987	0.003433	0.012038	0.000323	0.847	0.047470	0.001239	75.3	3.2	77.1	2.1	72.9	61.5
	SNS_8A	0.076631	0.003570	0.011861	0.000330	0.843	0.047955	0.001322	75.0	3.4	76.0	2.1	97.0	64.6
	SNS_7A	0.078468	0.003410	0.011491	0.000307	0.852	0.050687	0.001267	76.7	3.2	73.7	2.0	226.6	57.3
	SNS_6B	0.079020	0.005899	0.011353	0.000431	0.805	0.051661	0.002556	77.2	5.5	72.8	2.7	270.4	111.5
	SNS_5B	0.080210	0.003594	0.011607	0.000301	0.841	0.051292	0.001382	78.3	3.4	74.4	1.9	254.0	61.4
	SNS_5A	0.079097	0.003491	0.011910	0.000314	0.846	0.049293	0.001279	77.3	3.3	76.3	2.0	161.8	60.1
	SNS_4B	0.079000	0.003815	0.011852	0.000328	0.835	0.049475	0.001456	77.2	3.6	76.0	2.1	170.4	68.0
	SNS_4A	0.077659	0.003277	0.011657	0.000290	0.848	0.049449	0.001230	75.9	3.1	74.7	1.9	169.2	57.6
	SNS_3C	0.075436	0.003415	0.011865	0.000298	0.835	0.047190	0.001319	73.8	3.2	76.0	1.9	58.9	65.9
	SNS_3B	0.076110	0.003547	0.011674	0.000321	0.841	0.048392	0.001346	74.5	3.3	74.8	2.0	118.5	64.9
	SNS_3A	0.080066	0.003886	0.011762	0.000318	0.831	0.050527	0.001520	78.2	3.6	75.4	2.0	219.3	68.9
	SNS_1A	0.076458	0.003464	0.011894	0.000300	0.836	0.047715	0.001331	74.8	3.3	76.2	1.9	85.2	65.5
								Wtd avg (95%)	77.2	2.6	75.4	0.5	214.7	94.3

The 75.4 ± 0.6 Ma U-Pb age acquired for the zircons from the Sines syenites (fig. 6) is concordant, within analytical error, with the oldest previously obtained K-Ar age on K-feldspar separates (Storetvedt et al., 1987) but older than the whole rock Rb-Sr isochron (Canilho and Abranches, 1982) and the ages obtained by the K-Ar method on diabase

dykes and other feldspar separates (table 5.1), which may be an indicator of significant Ar loss since cooling.

5.2.4 Monchique

The Monchique plutonic complex has been previously dated using both the K-Ar and the Rb-Sr methods. The obtained ages cluster around 72 Ma (Rock, 1976, MacIntyre and Berger, 1982; Bernard-Griffiths et al., 1997).

Recent revision of the geological mapping of this complex allowed the identification of two concentric units of different nepheline syenites, the inner of which encloses various bodies of basic and ultra-basic rocks (Gonzalez-Clavijo and Valadares, 2003). We dated some of the nepheline syenites and ultrabasics identified by these authors with the aim of clarifying some intriguing ages obtained previously that may be related to the previously identified problem with Ar loss and its effect on some of the K-Ar ages obtained even in feldspar and nepheline separates (MacIntyre and Berger, 1982).

Representative samples from the different magmatic units of the Monchique massif were selected for Rb-Sr whole-rock dating. The Rb-Sr isotope data together with the Rb and Sr concentrations are given in table 5.4.

Table 5.4: Rb and Sr isotopic data for the Monchique rocks. Rb and Sr concentrations obtain by ICP-MS, estimated error for the values of 2%. Sample location can be found in Gonzalez-Clavijo and Valadares, 2003.

Sample	Lithology	Sr	Rb	$^{87}Rb/^{86}Sr$	$^{87}Sr/^{86}Sr$	Error (2σ)
468B	ultrabasic lamprophyre	2240	28	0.036	0.703205	0.000052
629	syeno-diorite	1580	87	0.159	0.703447	0.000052
598	nepheline syenite	1290	214	0.480	0.703783	0.000055
745	nepheline syenite	291	189	1.881	0.705189	0.000056
746	nepheline syenite	593	160	0.781	0.704078	0.000048
747	nepheline syenite	999	223	0.646	0.703898	0.000046
749	nepheline syenite	1310	190	0.420	0.703674	0.000052

As shown in figure 5.5a, the five nepheline syenite samples are roughly co-linear on the $^{87}Sr/^{86}Sr$ vs. $^{87}Rb/^{86}Sr$ diagram yielding a model 1 type Isoplot® Rb-Sr whole-rock isochron of 72.3 ± 4.2 Ma (MSWD = 0.98; $^{87}Sr/^{86}Sr_i$ = 0.703258 ± 0.000049). Due to the low MSWD, the 72.3 ± 4.2 Ma age appears to reflect the real intrusion age of the nepheline syenite magma.

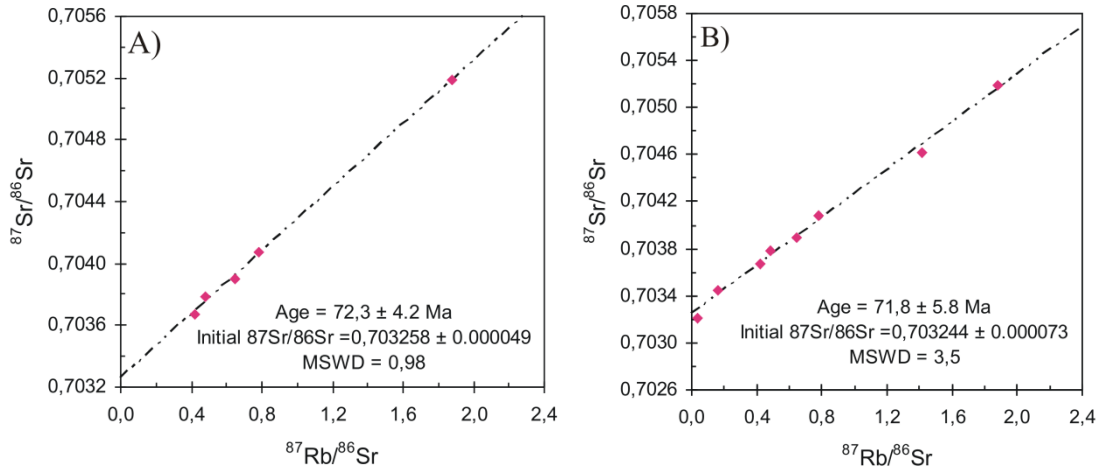

Fig. 5.5: Rb-Sr isochrons for the Monchique samples: (a) 5 nepheline syenites; (b) all samples.

A similar age was obtained by adding two samples from the mafic intrusives (71.8 ± 5.8 Ma, initial $^{87}Sr/^{86}Sr_i$ = 0.703244 ± 0.000073 and MSWD = 3.5, fig. 5.5b) suggesting a coeval emplacement and a genetic link between all units. The reported ages are concordant, within analytical error, with the 72 ± 2 Ma and 72 ± 1.5 Rb-Sr whole-rock isochrons determined by Rock (1976) and Bernard-Griffiths et al. (1997), respectively.

Table 5.5: $^{40}Ar/^{39}Ar$ analythical data for the Monchique amphiboles. J=0.006625 ± 0.000110.

T^{0}C	t (min)	^{40}Ar(STP)	$^{40}Ar/^{39}Ar$ ±1σ	$^{38}Ar/^{39}Ar$±1σ	$^{37}Ar/^{39}Ar$±1σ	$^{36}Ar/^{39}Ar$±1σ	Ca/K	$\sum^{39}$Ar (%)	Age (Ma) ± 1σ
500	10	3.03*e^{-9}	17.04 ± 0.19	0.216 ± 0.013	0.96 ± 0.02	0.0289 ± 0.0110	3.5	0.5	98.9 ± 36.7
600	10	4.58*e^{-9}	12.63 ± 0.06	0.115 ± 0.004	1.59 ± 0.01	0.0159 ± 0.0047	5.7	1.6	92.4 ± 15.9
700	10	8.44*e^{-9}	10.75 ± 0.02	0.067 ± 0.001	0.51 ± 0.01	0.0134 ± 0.0018	1.8	4.0	79.5 ± 6.1
800	10	11.24*e^{-9}	10.22 ± 0.02	0.066 ± 0.001	0.26 ± 0.01	0.0099 ± 0.0015	0.9	7.3	85.1 ± 5.1
900	10	8.10*e^{-9}	10.25 ± 0.02	0.081 ± 0.002	0.39 ± 0.005	0.0107 ± 0.0019	1.4	9.7	82.7 ± 6.4
950	10	4.71*e^{-9}	10.58 ± 0.04	0.103 ± 0.001	0.56 ± 0.01	0.0094 ± 0.0036	2.0	11.1	90.8 ± 12.2
1000	10	5.46*e^{-9}	10.23 ± 0.03	0.143 ± 0.004	1.07 ± 0.01	0.0098 ± 0.0025	3.9	12.7	85.6 ± 8.5
1050	10	10.38*e^{-9}	8.22 ± 0.01	0.275 ± 0.001	2.70 ± 0.01	0.0049 ± 0.0013	9.7	16.5	79.3 ± 4.4
1100	10	94.81*e^{-9}	6.67 ± 0.01	0.238 ± 0.001	3.47 ± 0.01	0.0012 ± 0.0006	12.5	59.6	74.0 ± 2.0
1150	10	85.91*e^{-9}	6.47 ± 0.01	0.245 ± 0.001	4.13 ± 0.01	0.0006 ± 0.0006	14.9	99.8	73.8 ± 2.1
1200	10	2.36*e^{-9}	40.73 ± 1.27	0.512 ± 0.034	21.77 ± 0.680	0.1154 ± 0.0313	78.4	100.0	77.6 ± 105.1

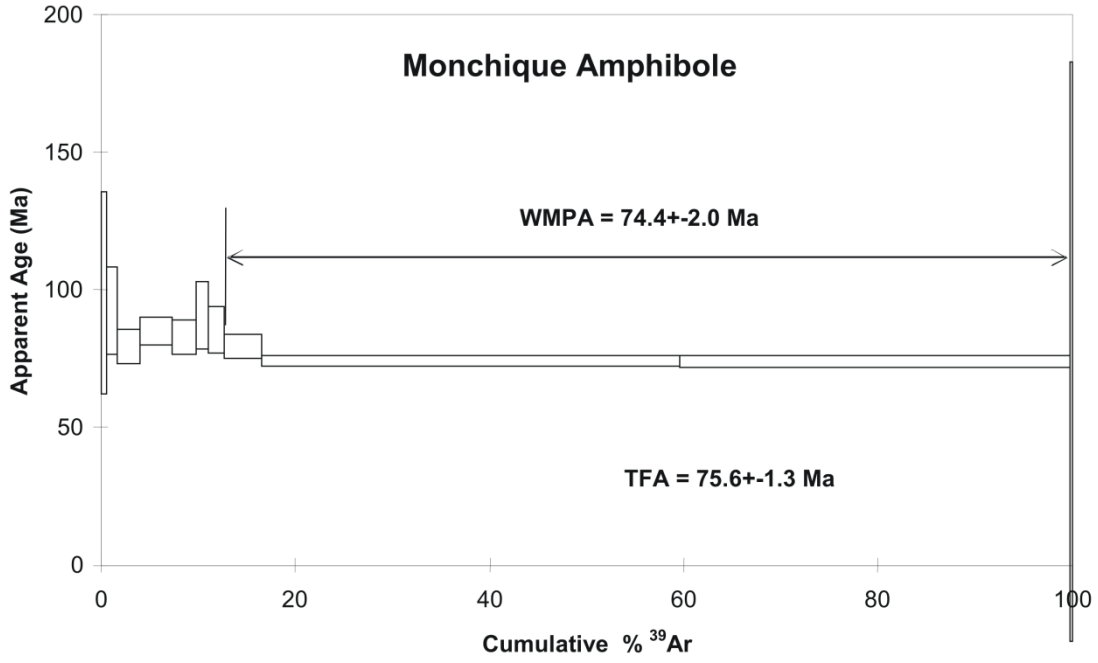

Fig. 5.6: Age temperature spectra diagram for the Monchique amphibole separate. Weighted Mean Plateau age, WMPA = 74.4 ± 2.0 Ma (including J). Total fusion age, TFA= 75.6 ± 1.3 Ma (including J).

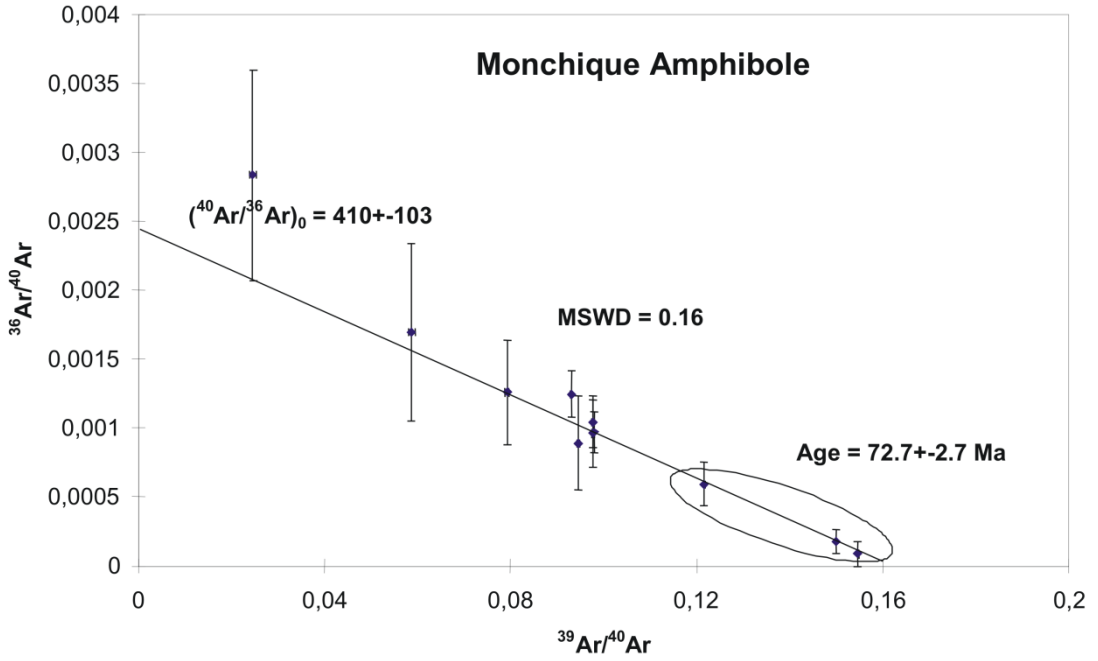

Fig. 5.7: Inverse isochron diagram for the Monchique amphibole. Inverse isochron age = 72.7 ± 2.7 Ma. (MSWD =0.16; $^{40}Ar/^{36}Ar$ = 410 ± 103)

The amphibole separate obtained from an ultrabasic lamprophyre in the Monchique complex defines a weighed mean plateau age of 74.4 ± 2.0 Ma,

corresponding to 87 % of released ^{39}Ar (table 5.5, fig. 5.6). On the reverse isochron plot, the plateau points define a linear trend with an age of 72.7 ± 2.7 Ma, MSWD = 0.16 (fig. 5.7) and an initial $^{40}Ar/^{36}Ar$ of 410 ± 103, which is higher than the atmospheric value and suggests presence of excess Ar. The total fusion age (75.6 ± 1.3 Ma) shows a good agreement with the plateau age (74.4 ± 2.0 Ma) but the presence of excess Ar suggests that the reverse isochron should reflect the crystalization age for these amphiboles.

The general concordance between the results of $^{40}Ar/^{39}Ar$ amphibole dating for the ultrabasic lamprohyres and the Rb-Sr whole-rock age of the nepheline syenites appear to indicate that the different units of the Monchique massif may have been intruded within a short time interval, centered around 72-73 Ma. This is also consistent with the geochronological data obtained in previous studies.

5.2.5 Loulé

The Loulé lamprophyre dykes belong to a small group of alkaline intrusives exposed in the Algarve basin, showing strong petrographical and chemical similarities with their equivalents in the nearby Monchique complex (Martins, 1991).

A biotite separate from the Loulé lamprophyre dyke was selected for K-Ar isotopic analysis. The results are summarized in table 5.6. The biotite K-Ar age (71.8 ± 1.9 Ma) is concordant, within analytical error, with the $^{40}Ar/^{39}Ar$ age obtained for the Monchique lamprophyre (74.4 ± 2.0 Ma). This suggests that the K-Ar system was not disturbed by subsequent thermal episodes and that the age of the biotite separates from this sample still dates the time of crystallization. From the obtained data, it is also possible to conclude that the lamprophyres intruding both the Monchique complex and the Algarve basin are coeval.

Table 5.6: K-Ar analytical data for the biotite from one of the Loulé lamprophyres.

Location	Material	% K	$^{40}Ar_{rad}$, nl/g	% $^{40}Ar_{air}$	Age, Ma
Loulé	biotite	6.75+0.13	18.851+0.310	6.5	71.8+1.9

5.3 Summary and discussion

The new age determinations, combined with previously published data, allow us to constrain the duration of the Late Cretaceous alkaline cycle to circa 22 Ma and to define two distinct pulses of alkaline magmatic activity. The first one (94-88Ma) occurred during the opening of the Bay of Biscay and consequent rotation of Iberia (123-80 Ma; Sibuet et al., 2004) and clusters around the Lisbon area (approximately N38º 20' and N39º) where it occurs mainly as sills (Foz da Fonte and Paço d'Ilhas). The second pulse lasted from 75 Ma to 72 Ma corresponds to a more widespread event with scattered occurrences from the Algarve Basin in southernmost Portugal (37ºN) to the Lisbon area (N39º) and comprises both intrusive and extrusive complexes. This final pulse is synchronous with the first pulses of tectonic inversion of the Mesozoic basins due to the onset of rapid convergence between the African and Iberian plates (e.g. Mougenot, 1980, Terrinha, 1998, Rosembaum et al., 2002). The Sintra granite laccolith has an age of ca. 79 Ma and was emplaced between these two pulses of magmatism.

It should be noted that until the publishing of the new geochronological data by Miranda et al. (2009), only a single alkaline episode was known in the WIM. However, considering the reduced number of known occurrences with ages compatible with the first pulse, it is possible that the acquisition of further geochronological data might result in the recognition of a continuing age spectra between the two proposed pulses.

Radiometric dating of the Sintra granite gives an 79.2 ± 0.8 Ma age, which although equivalent within error to the oldest age obtained for the syenite (78.3 ± 1.9 Ma, whole rock K-Ar, Storetvedt et al., 1987) its still older than the other K-Ar ages obtained for these rocks (76.4 ± 1.4 and 76.1 ± 1.1 Ma, Storetvedt et al., 1987). This, combined with the observed field cross-cutting relations and geophysical data (gravimetry and AMS, Terrinha et al., 2003), allows us to hypothesize that the granite corresponds to an older phase that is intruded by a more recent gabbro to syenite suite.

As shown by geochronological and isotopic data, all the members of the Monchique alkaline suite are co-magmatic and appear to have been emplaced in a short interval of time, within the analytical error of the used geochronological methods.

The similar ages obtained for the lower volume of alkaline magmatism intruding the opposite rifted and thinned margins of the Iberian plate (105-69 Ma in the Pyrenees and Catalan ranges, Fabriès et al., 1998; Montigny et al., 1986, Solé et al., 2003) suggest a relationship between the Late Cretaceous magmatism and the changes in plate

kinematics and seafloor spreading geometry contemporaneous with the opening of the Bay of Biscay.

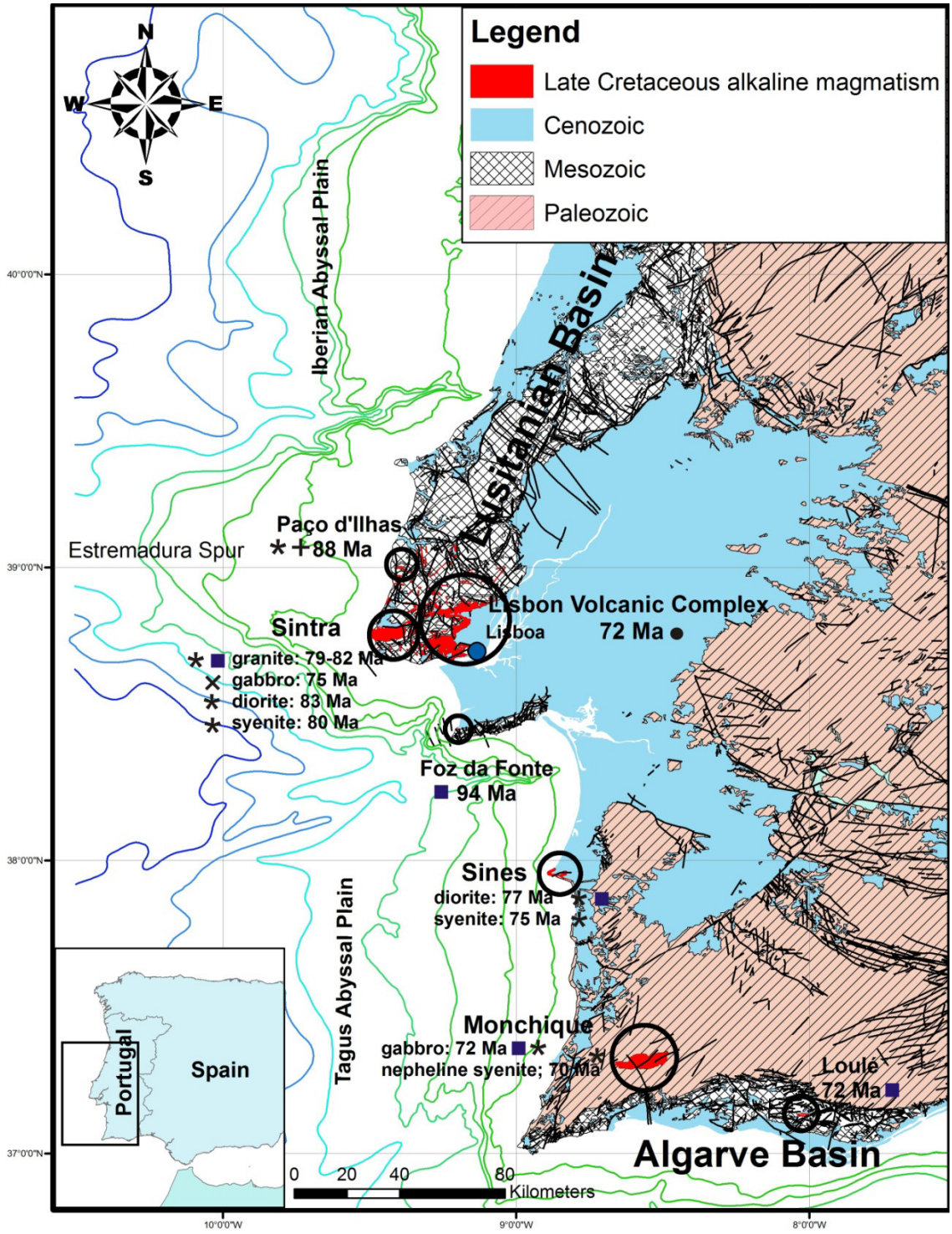

Fig. 5.8: Summary for the obtained ages for the Late Cretaceous alkaline magmatism on the onshore WIM. Symbols correspond to the reference for the age information: + Mahmoudi, 1991; ● Ferreira e Macedo, 1979; **x** Storetvedt et al., 1987; * Grange et al., 2010; ■ Miranda et al., 2009 and this study.

A recent study by Grange et al. (2010) dated the Paço d'Ilhas sill and the Sintra, Sines and Monchique igneous complexes. These authors argue that there is a clear age progression from north to south in the alkaline rocks present in the onshore WIM. They correspond to 88.3 ± 0.5 Ma for Paço d'Ilhas sill, while in Sintra the obtained ages were of 83.4 ± 0.7 for the Sintra diorite, 82.0 ±0.7 and 81.7 ± 0.4 for the Sintra granite, and 80.1 ± 1.0 Ma for the Sintra syenite. The Sines complex yielded ages of 77.2 ± 0.6 and 77.2 ± 0.4 for the diorite and of 76.1 ±1.3 Ma for the syenite. In Monchique the obtained ages were of 70.0 ± 2.9 for the gabbro and 68.8±1.0 Ma for the Monchique nepheline syenite (Grange et al., 2010).

Some of the ages obtained by these authors agree within error with the ones presented in this study (Sines syenite and Monchique gabbro), while the Sintra granite seems to show older ages by 2 Ma. These authors also report the oldest yet ages obtained for basic rocks and syenites in Sintra as well as for the Sines intrusive basic rocks. On the other hand, the age obtained for the Monchique nepheline syenites is equivalent to the youngest ages obtained by the K-Ar method and attributed to Ar loss (e.g. MacIntyre and Berger, 1982; Storetvedt et al., 1990).

The presence of zircon fractions that yield younger ages (74.8 to 81.3 Ma, Grange et al., 2010) in the Sintra diorite and older ages in the Sintra syenite (up to 142 Ma, Grange et al., 2010), Sines diorite (up to 132 Ma, Grange et al., 2010) and of six titanite fractions in the Monchique syenite that yield an average age of 70.0 ± 2.9 Ma complicate the interpretation of the results.

Another factor that can contribute for the slightly different age values obtained by these authors could be related with slight difference between the initial Pb isotope composition of the zircon (and titanite) and the feldspar. As the zircon (and titanite) ages have been corrected with the initial Pb measured in the feldspar, a difference between the initial Pb present in the feldspars and in the zircons could result in minor discordance in the obtained ages (Grange et al., 2010).

6. Petrography and mineral chemistry

6.1. Petrography

This section includes a summarized petrographic characterization of the sampled rocks within each major occurrence and of the xenoliths that are contained in some of them. A detailed petrographic description is beyond the scope of this study, given the complete petrographic works developed by previous authors which are referenced below.

All of the major mineral phases are identified, along with the observed textural features. These textures are interpreted in order to extract the highest possible amount of information on the formation conditions of these rocks and xenoliths as well as the mineral phases that they contain.

6.1.1. The Lisbon Volcanic Complex

The petrography of the LVC has been covered in detail by Palácios (1985) and references cited therein, so only an abridged petrographic description of the main lithotypes will be given below.

- The lava flows:

The lava flows are mostly constituted by porphyritic alkaline basalts (*s.l.*) and basanites, containing abundant olivine, clinopyroxene, sometimes titanomagnetite and more rarely plagioclase phenocrysts in a very fine grained matrix constituted by plagioclase, clinopyroxene and Fe-Ti oxides, more infrequently olivine and in some very rare cases even biotite. Brown amphibole (kaersutite) phenocrysts are also present in some flows (e.g. Negrais) but are seldom observed.

Olivine phenocrysts (Fo_{85-68}) can be euhedral, subhedral and sometimes rounded and have inclusions of opaque oxides. They are often the only altered mineral observed in the rock and show substitution by either chlorite or serpentine. In the basal flows that

outcrop in the Ribeira de Fanhões and Ramada areas olivine is the only phenocrystic phase present.

The clinopyroxene phenocrysts vary in size from 0.5 to over 2 millimeters, are euhedral and often zoned, showing a stronger pink to purple color in the rims and a more pale shade of the same color in the core, which indicates an increase in Ti contents (0.8-5.5 % TiO_2) with progressing crystallization. Sometimes these phenocrysts are subhedral and show embayments filled with matrix material. They can also show patchy zoning or, more rarely, they can show oscillatory zoning as well. Inclusions of Fe-Ti oxides and olivine are common.

The Ti-Fe oxides are euhedral to subhedral and often have a bimodal distribution, with the flows containing two generations of oxides with different sizes (phenocrysts and microphenocrysts).

Plagioclase phenocrysts are very rare and occur in only three slightly more evolved samples (MgO < 8%) such as the Lexim and Besueira vents and the Negrais flow.

The rare kaersutite phenocrysts are surrounded by a reaction rim where amphibole breaks down to clinopyroxene, plagioclase and opaque minerals. In some cases, a pink clinopyroxene rim is observed around this reaction rim. Clinopyroxenes with clear rims, but whose core is dotted with oxide and plagioclase inclusions are relatively common within the basalts and may correspond to completely retrograded amphiboles where the previously mentioned reaction was completed.

The crystals in the matrix usually show an elongated shape, except for the Fe-Ti oxides, and a preferred orientation, most likely due to crystallization during flow. The matrix is mostly fresh, except for olivine that might be completely altered to chlorite or serpentine.

- The necks:

The necks that acted as conduits for the LVC's lavas are also basalts and basanites which are frequently texturally zoned, with the areas near the contact with the country rock being aphanitic to weakly porphyritic, showing only olivine phenocrysts and very fine grained matrixes. The interior of the necks, however, is usually very porphyritic and shows a coarser, sometimes almost granular, matrix.

Vesicles with secondary carbonate or zeolite fillings are rare but amigdulaes with radial inward growth of clinopyroxene and plagioclase were observed.

Otherwise, the necks are quite similar to the flows in terms of mineralogy, with olivine and clinopyroxene being the main phenocrystic phases, along with some minor Fe-Ti oxides. The matrix is generally made of plagioclase, clinopyroxene, Fe-Ti oxides and olivine, with the latter being altered to serpentine at times.

The clinopyroxene phenocrysts present in the center of the necks can have olivine and Fe-Ti oxides inclusions both in the core and rims. The Fe-Ti oxide inclusions can either be numerous and concentrate in the core area, or be located near the rims but absent in the core. The rims of these phenocrysts usually show a darker shade of pink-purple. Concentric zoning is rare but was also observed.

Olivine phenocrysts can be either rounded or subhedral to euhedral, and occasionally more than one of these habits can be observed in the same thin section. Alteration to serpentine is common along the rims and fractures of the olivines present in the more altered samples.

The Ti-Fe oxides are usually euhedral.

The matrix is constituted by plagioclase, clinopyroxene, Fe-Ti oxides and olivine. It varies from very fine grained to fine grained from the contact to the center of the vent, and its crystals are mostly fresh except for olivine in that might be completely altered to chlorite or serpentine.

- The plugs:

From the total of 3 small, semi circular basaltic (*s.l.*) plugs that outcrop in the Ribeira d'Ilhas beach, only the two largest ones (central and southern) were sampled.

The southern plug (RM 36) is made out of a very porphyritic rock, with clinopyroxene, Fe-Ti oxides and pseudomorphs of olivine phenocrysts in a fine grained matrix constituted by plagioclase, clinopyroxene, brown amphibole, Fe-Ti oxides. Brown amphibole megacrysts and xenoliths made out of brown amphibole, Fe-Ti oxides, apatite and clinopyroxene are common. One titanite megacryst with a reaction rim of Fe-Ti oxides and clinopyroxene was also observed.

The clinopyroxene phenocrysts can be divided in two groups. The first one is made out of clinopyroxene crystals similar to the ones identified in the alkaline basalts, with pink phenocrysts showing darker rims and common Fe-Ti oxide inclusions. A

second type of clinopyroxene phenocryst was also identified, being characterized by an irregularly shaped green core, a colorless to light pink mantle and darker pink rim.

The olivine phenocrysts (Fo_{86-77}) are almost completely pseudomorphosed by serpentine and carbonate.

The matrix is fine grained and is constituted mostly by plagioclase, pink clinopyroxene, brown amphibole and Fe-Ti oxides. It shows some vesicles filled by carbonate.

The amphibole xenocrysts invariably show numerous small oxide and sulphide inclusions, as well as reaction rim that is distinguished from the one shown by amphiboles in the lava flows since it is constituted solely by clinopyroxene and opaque Fe-Ti oxides, with plagioclase being absent.

The central and largest plug is quite similar to its southern counterpart, with the difference that a central, vesicular and more altered facies can be observed. Also, brown amphibole is absent in the matrix of the central plug, and the olivine phenocrysts are mostly unaltered in the fresher outer facies (RM 37). Otherwise it is also a very porphyritic rock with phenocrysts of olivine, Fe-Ti oxides and the same two kinds of clinopyroxene in a matrix constituted by plagioclase, clinopyroxene and Fe-Ti oxides.

- The Oeiras-Cascais dykes:

Most of the dykes associated with the LVC are extremely altered, to the point in which their original mineralogy is no longer identifiable, making their classification exceedingly difficult.

The only fresh basic alkaline dykes available for sampling are located in the coastline within the vicinities of Oeiras and Cascais. Although the exact age of these dykes remains unknown, geochemical affinities and the proximity of LVC's flows indicate that these were likely feeders for the subaerial magmatism (Miranda et al., 2005).

The dykes can be separated in two main categories. Some are porphyritic basalts, and the others more evolved and lighter colored hawaiite-like rocks.

The basalts are usually very porphyritic, with abundant olivine and in some cases clinopyroxene phenocrysts in a fine grained matrix constituted by plagioclase, clinopyroxene, serpentinized olivine and Fe-Ti oxides. The olivine is commonly altered to serpentine or carbonate. Carbonates also fill all of the vesicles and fractures and can even substitute clinopyroxene in more altered rocks.

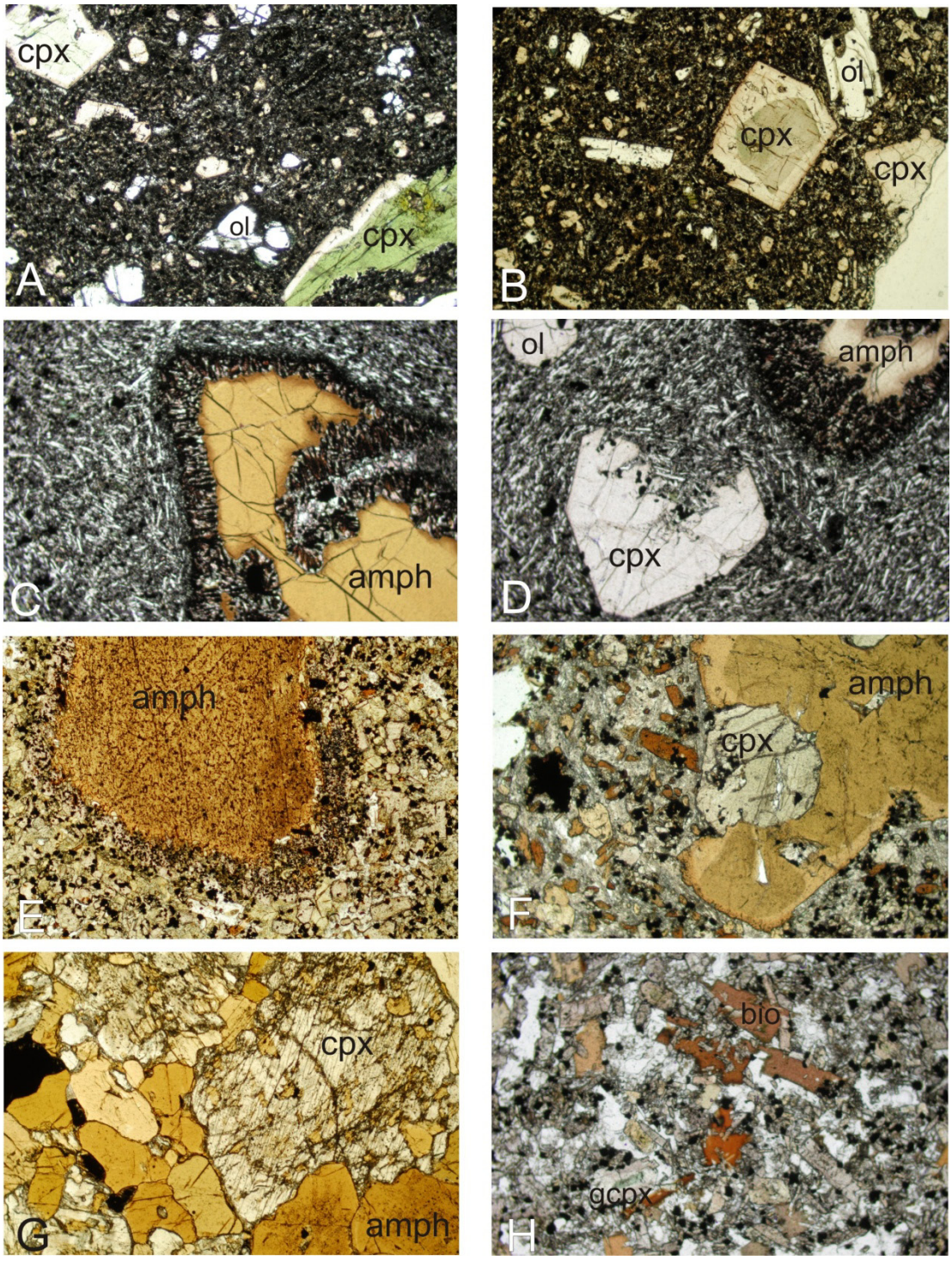

Fig. 6.1: Several textural aspects in the collected samples. Width of field of vision≈ 2.5 mm. A, B) the Ribeira d'Ilhas central plug: olivine, green cored and normal clinopyroxene phenocrysts; C, D) Negrais flow: amphibole with reaction rim of clinopyroxene, plagioclase and opaque minerals, clinopyroxene and olivine phenocrysts; E) Ribeira d'Ilhas plug: amphibole with reaction rim of clinopyroxene, plagioclase and opaque minerals in a matrix of clinopyroxene, plagioclase and Fe-Ti oxides; F) Malveira da Serra sill: amphibole and green cored clinopyroxene aggregate in the a clinopyroxene, amphibole, Fe-Ti oxide and feldspar matrix; G) Eiras do Faião sill: detail of xenolith showing mostly clinopyroxene and amphibole; H) Loulé lamprophyre C-20: general aspect showing biotite and green cored and normal clinopyroxenes.

The hawaiites are usually more vesicular, have coarser but still fine grained textures, and their phenocrystic phases can be brown amphibole, clinopyroxene and plagioclase. The matrix is fine grained and constituted by plagioclase, clinopyroxene, and Fe-Ti oxides, with brown amphibole being present in some cases where olivine is not found.

Amygdulae with larger plagioclase and amphibole crystals are common in these rocks. Vesicules and fractures are commonly filled with secondary carbonate.

- The sills:

Numerous sills are integrated into the LVC. All of them were described by Palácios (1985), with the ones present in the Anços-Montelevar region being the subject of a specific study by Matos Alves et al. (1972).

The Lomba dos Pianos sill has a porphyritic texture with clinopyroxene, plagioclase and rare olivine phenocrysts occurring in a fine grained matrix with plagioclase, clinopyroxene, Fe-Ti oxides and accessory feldspar, biotite, apatite, titanite and analcime. This matrix can show significant chloritic alteration. Amphibole megacrysts with reaction rims of plagioclase, clinopyroxene and oxides are found in this sill, but are rare. This rock has lamprophyric affinities and has been previously classified as a teschenite (Mahmoudi, 1991).

The olivine phenocrysts are in the majority of cases completely altered to pale green mineral that might correspond to chlorite.

As in the Ribeira d'Ilhas plug, there are two types of clinopyroxene phenocrysts present, the clinopyroxene crystals with pink cores with darker rims and a second type of clinopyroxene phenocryst with irregularly shaped green cores, colorless to light pink mantles and darker pink rims.

Plagioclase phenocrysts can be euhedral or have rounded edges. They often show concentric zoning or rims with optical characteristics that are different from their cores. Their cores are frequently subject of some sericitic alteration while the rims can remain unaltered.

Also present are clinopyroxenes dotted with numerous oxide and plagioclase inclusions that may correspond to completely retrograded amphiboles.

In certain parts of the sill it is possible to observe small layers with a coarser adcumulate texture. They are constituted mostly by plagioclase with euhedral cores and large cloudy rims with interstitial clinopyroxene, feldspar, and Fe-Ti oxides and quartz.

The Montelavar sill displays a bimodal texture with porphyrocrystals of feldspar and plagioclase and grey to colorless clinopyroxene that are inserted in a medium grained matrix of plagioclase, clinopyroxene, Fe-Ti oxides and interstitial feldspar, apatite and rare quartz. This sill could be classified as a monzodiorite.

The plagioclase megacrysts (An_{64-14}) are often zoned and can display some sericitic alteration. Chlorite and other philosilicates, along with some rare carbonate, are the main alteration phases seen in the matrix.

The Anços sill has a porphyroid texture with plagioclase, feldspar, and colorless clinopyroxene porphyrocristals in a fine grained matrix composed of plagioclase, clinopyroxene, Fe-Ti oxides and accessory titanite and apatite and sometimes even quartz. The matrix and feldspar phenocrysts show some alteration to phyllossilicates and carbonate. Similarly to the Montelevar sill, this intrusion could be classified as a monzodiorite.

The Eiras do Faião sill shows a bimodal granular texture, with larger green clinopyroxene, titanite, Fe-Ti oxides and rare brown amphibole crystals in a fine grained matrix of mostly plagioclase, colorless clinopyroxene and Fe-Ti oxides with accessory apatite, biotite, titanite, zeolites and analcime. Given its relative abundance in foids, this rock can be classified as a foid monzodiorite.

This sill is formed by a very vesicular rock with most of these being filled by fibrous zeolite.

One of the samples collected in this sill contained a medium grained xenolith made out of mostly brown amphibole and greenish clinopyroxene with accessory Fe-Ti oxides and apatite.

The Alqueidão sill has a medium grained texture, with mostly plagioclase, Fe-Ti oxides, clinopyroxene and interstitial feldspar. It is very altered, with most of the mafics

being replaced by fibrous looking minerals, probably phyllossilicates, while the dominating plagioclase remained relatively fresh. In some of the more altered samples, even plagioclase could show important chloritic and sericitic alteration. Like other sills in the region, this intrusion could be classified as a monzodiorite.

6.1.2. Malveira da Serra sill

This sill is constituted by a mafic, very porphyritic rock with phenocrysts of brown amphibole, clinopyroxene, Fe-Ti oxides and olivine pseudomorphosed by chlorite in a very fine matrix of plagioclase, clinopyroxene, brown amphibole, Fe-Ti oxides, biotite, apatite and olivine pseudomorphosed by chlorite. According to its texture and mineralogy, this sill can be classified as a camptonite (Rock, 1986).

Vesicles are rare but are usually filled with carbonate.

Similarly to the Lomba dos Pianos sill and the Ribeira d'Ilhas plug, we can observe two types of clinopyroxene phenocrysts, namely clinopyroxene crystals with pink phenocrysts with darker rims and also green cored clinopyroxenes with irregularly shaped green cores, surrounded by a colorless to light pink mantle and darker pink rim.

The brown amphibole phenocrysts can also be divided in two groups, one with abundant small oxide inclusions in the darker cores, which are enveloped by a lighter brown mantle and a darker rim. This group also commonly shows clinopyroxene and olivine inclusions, which may themselves contain oxide inclusions. The second type of observed brown amphibole has a lighter brown core and a darker brown rim and less abundant inclusions.

Some of the Fe-Ti oxide phenocrysts have distinctive irregularly shaped rims, resembling small appendixes.

6.1.3. Mafra plug

The Mafra plug is a gabbroic rock with a bimodal granular poikilitic texture, with the larger brown amphibole and clinopyroxenes involving plagioclase (An_{78-33}), olivine, biotite, Fe-Ti oxides and rarer nepheline and apatite. Given the presence of nepheline, this rock classifies as a foid gabbro.

The clinopyroxenes are commonly zoned, with darker purple rims, as a consequence of enrichment in Ti (TiO_2 1.2-3.8%) or can even show oscillatory zoning. Olivine (Fo_{86-85}) is often altered to chlorite. Amphibole seems to be a later phase, as it envelops both these minerals.

All these are inserted in a fine grained matrix of plagioclase, smaller clinopyroxene, Fe-Ti oxides, nepheline, apatite and biotite.

6.1.4. Foz da Fonte sill

This tephritic sill has a fine grained texture with plagioclase, brown amphibole, clinopyroxene, Fe-Ti oxides, and accessory apatite and feldspathoids. Inclusions of oxides are common in amphiboles and plagioclase.

Secondary carbonate can be observed, filling vesicles and fractures.

6.1.5. Paço d'Ilhas sill

The Paço d'Ilhas sill is a layered intrusion, displaying two different lithotypes with different mineralogies and textures. Its petrographic features are discussed in detail by Mahmoudi (1991).

The mafic layers have a monzogabbroic composition and display a medium grained texture with dominating plagioclase (An_{72-20}) and lesser biotite, clinopyroxene, Fe-Ti oxides and intersticial feldspsar. Often the plagioclases show a more irregular, probably Na-rich rim, as a likely result of growth from an intercumulus liquid. The plagioclases might show larger crystals than the remaining minerals that constitute the rock.

The felsic monzosyenite layers have a similar texture, only with more abundant plagioclase (> 75%) and less abundant, smaller, mafic minerals.

Both the varieties are considerably altered, with the clinopyroxenes being almost completely replaced by alteration products and carbonate substituting both plagioclase and mafic minerals as well as occupying interstices. Also, the plagioclases commonly show alteration to phyllossilicates.

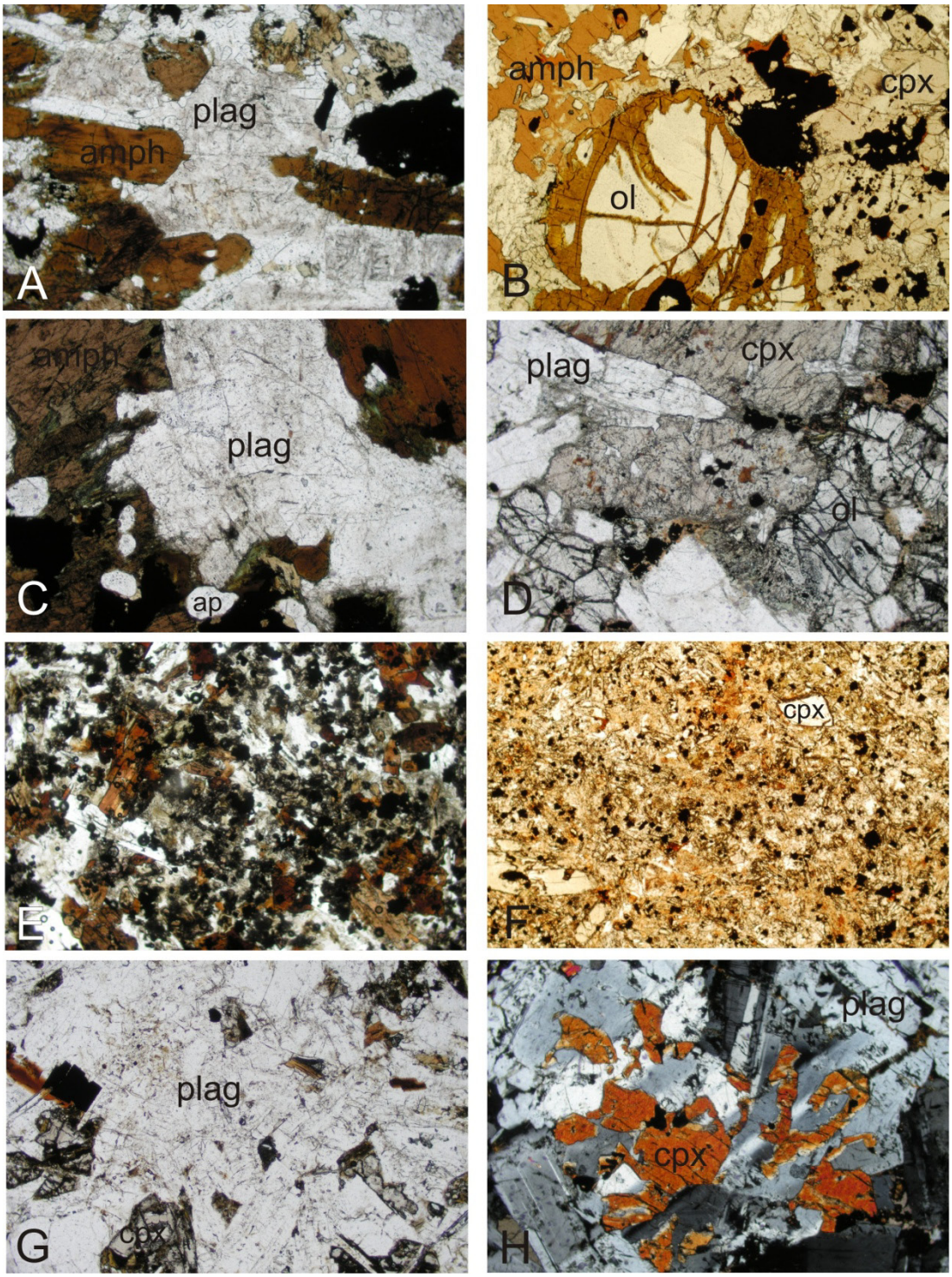

Fig. 6.2: Several textural aspects in intrusive samples. Width of field of vision 2.5 mm. A) gabbroic rock from the Peninha outcrop, Sintra, showing large amphibole, plagioclase and Fe-Ti oxide crystals; B) Mafra gabbro with altered olivine, amphibole, clinopyroxene and Fe-Ti oxides; C) detail of the Praia Vasco da Gama gabbro in Sines; D) Pedras Negras gabbro, Sines, showing olivine, clinopyroxene, plagioclase and Fe-Ti oxides; E) Foz da Fonte sill showing amphibole, plagioclase, clinopyroxene and Fe-Ti oxides; F) Eiras do Faião sill showing the larger clinopyroxene crystals in a fine matrix of plagioclase, oxides, clinopyroxene and biotite; G) Paço d'Ilhas sill showing mostly plagioclase but also some clinopyroxene, Fe-Ti oxides and biotite. H) detail of the Montelevar sill in plane polarized light, showing clinopyroxene and plagioclase intergrowth.

6.1.6. The Sintra mafic rocks

The two gabbros sampled in the Sintra complex show extremely varied textures. These and the other lithologies present in this complex have been extensively described by Matos Alves (1964), Wright (1969), Sparks and Wadge (1976) and Leal (1990).

The Peninha gabbro has medium grained to coarser, poikilitic textures and is constituted mostly by plagioclase (An_{72-20}), clinopyroxene, Fe-Ti oxides, interstitial feldspar and apatite, as well as by brown amphibole that envelops all of the previous phases. The brown amphibole can in addition show biotite growing on its rims or partial replacement by secondary, fibrous, green amphibole.

Besides green amphibole, the other secondary alteration phases present are epidote, feldspar, chlorite, rare carbonate and even more rarely, tourmaline. These minerals can be either concentrated in late veins or dispersed in more plagioclase-rich areas. Plagioclase and feldspar can also display some sericitic alteration.

Locally the amphibole can form aggregates that give the rock a glomoporphyric texture that is characteristic of many of its outcrops (see fig. 4.9).

The gabbros in the Azóia outcrop show a coarse grained poikilitic and even glomorporphyric texture, with brown amphibole envolving clinopyroxene, plagioclase, Fe-Ti oxides and apatite. Accessory minerals include biotite, which can be observed growing in the rims of amphibole crystals, as well as some interstitial feldspar and a mineral completely pseudomorphosed by alteration products, possibly olivine.

These gabbroic rocks are substantially more altered than those at Peninha, often showing a greener color due to a higher degree of transformation of brown amphibole into fibrous green amphibole, chlorite substituting clinopyroxenes and plagioclase, and to the existence of veins of feldspar, epidote and carbonate that substitute the original mineralogy. The alteration seems to affect the plagioclase and feldspars more than it affects the other minerals.

The diorite, sampled in the Malveira da Serra-Azóia outcrop, is similar to these more altered gabbros, except it has more abundant plagioclase and biotite and less clinopyroxene, brown amphibole and Fe-Ti oxides. Otherwise it shows similar textural features, with the amphiboles enveloping clinopyroxene, apatite and opaque minerals and analogous secondary alteration phases, except in this case the green amphibole is

much more common and often completely substitutes the rims of clinopyroxene and amphibole.

6.1.7. The Sines mafic rocks

The Sines igneous complex has two gabbro outcrops with distinct textural and mineralogical features (see 4.1.7). These outcrops, as well as the remaining lithologies present in the complex are described in detail by Canilho (1972).

The gabbros that outcrop at Praia Vasco da Gama are similar to the ones observed in Sintra and show a very coarse, granular poikilitic texture with very large crystals of brown amphibole enveloping plagioclase, apatite, Fe-Ti oxides and rare clinopyroxene. The amphibole can be surrounded by biotite in some areas. Interstitial feldspar and biotite are also observed.Secondary alteration minerals include chlorite and rarer epidote.

The Pedras Negras gabbro shows macroscopic layering, smaller grain size and a different mineralogy. These rocks have an orthocumulate texture where clinopyroxene and olivine (Fo_{70-67}) megacrysts are surrounded by a finer matrix of plagioclase (An_{82-48}), Fe-Ti oxides and some clinopyroxene and olivine, as well as rare apatite and biotite. The megacrysts can sometimes be enveloped by later brown amphibole.

Alteration is present, although it is less important than in the amphibole rich gabbros. It is characterized by the alteration of olivine to serpentine and oxides, and of plagioclase to phyllossilicates and chlorite. In more altered zones, green amphibole and phyllossilicates may be present.

The diorite was sampled near the gabbro outcrop of Praia Vasco da Gama and corresponds to a medium grained rock constituted by abundant plagioclase, colorless to brown clinopyroxene, biotite, brown amphibole, Fe-Ti oxides and accessory amounts of apatite and titanite. The most important alteration mineral is chlorite that affects mostly plagioclase, clinopyroxene and biotite.

The cumulate and more basic nature of the Pedras Negras gabbro in Sines may indicate that this outcrop is representative of a deeper level in the magma chamber when compared to its southern counterpart that outcrops in Praia Vasco da Gama. As the amphibole rich Praia Vasco da Gama gabbro also shows a much

coarser texture, it could represent a higher, more evolved and hydrated part of the same magma chamber that cooled later than the deeper Pedras Negras gabbro.

The different gabbroic outcrops are separated by one E-W trending fault, whose movement might have caused uplift of the northern block causing the deeper level of the magma chamber, represented by the olivine rich Pedras Negras gabbro, to be exposed.

6.1.8. The Monchique mafic and ultramafic rocks

The samples used in this study were previously described and classified by Valadares (2004), and include essexites, sieno-diorites and also ijolites and lamprophyres.

The ijolite has a poikilitic texture where nepheline and plagioclase involve purple to pink clinopyroxene, greenish clinopyroxene, biotite, Fe-Ti oxides, titanite, and apatite. In the lamprophyre, larger brown amphibole, clinopyroxene and olivine crystals are observed in a finer matrix of clinopyroxene, nepheline, feldspar, Fe-Ti oxides, biotite and apatite. The clinopyroxenes and amphiboles seem to have continued growing until the latest crystallization stages since they can involve poikilitically the matrix crystals.

The remaining rocks are mostly theralites (nepheline gabbros) constituted by clinopyroxene, plagioclase, more or less abundant brown amphibole, feldspar, biotite, nepheline, Fe-Ti oxides and apatite, with textures varying from coarsely granular, to poikilitical and to bimodal.

The sieno-diorites show the same mineralogy, but are richer in plagioclase, feldspar and nepheline than the theralites.

These rocks are mostly fresh but some minor alteration is observed, with the main alteration phases present being sericite, carbonate and actinolite.

6.1.9. The Loulé dykes

Although these dykes were both sampled in the same location (the Loulé salt mine) and quite close to each other, they are texturally and mineralogically distinct.

Dyke C-20 is a very porphyritic rock, showing phenocrysts of clinopyroxene and phlogopite in a fine grained matrix of plagioclase, Fe-Ti oxides, clinopyroxene, nepheline and rare carbonate. This carbonate might be primary since this rock is not in contact with carbonated country rocks on the sampling location. Given its texture and mineralogy, this dyke can be classified as a monchiquite lamprophyre (Rock, 1986).

The clinopyroxene phenocrysts show, as in other rocks described in this section, two types of cores. There are clinopyroxene phenocrysts that are light pink to colorless in the cores and with darker rims, as well as green cored clinopyroxenes with irregularly shaped green cores, surrounded by a colorless to light pink mantle and darker pink rim.

The biotite phenocrysts often show inclusions of Fe-Ti oxides and/or apatite and can partially involve clinopyroxene crystals.

In its turn, dyke C-12-1 seems more basaltic as it shows phenocrysts of rounded olivine completely substituted by serpentine, plus some rarer clinopyroxene in a fine grained matrix of clinopyroxene, plagioclase, Fe-Ti oxides, apatite and minor biotite. Although the olivine phenocrysts are completely altered, the remaining rock seems quite fresh.

6.1.10. The Fontanelas seamount

All of the samples from igneous rocks dredged from the Fontanelas seamount corresponded to pillow lavas and hyaloclastites and show important signs of alteration, including calcite filled vesicles and an overall brown to greenish color.

In thin section these rocks are very vesicular (they can have over 40% vesicles), have an aphanitic to porphyritic texture, with a deeply altered groundmass.

The porphyritic rocks show phenocrysts of extremely altered olivine, but unaltered clinopyroxene, Fe-Ti oxides and sometimes even amphibole.

The clinopyroxene phenocrysts present are of the green cored and normal (pink to purple) varieties already observed and described in outcrops of the same basic alkaline nature on land.

Alteration in the groundmass is pervasive, but still, the clinopyroxenes and oxides are always identifiable matrix phases, with plagioclase being present only in the

fresher samples where it has not been substituted by secondary alteration phases, such as clays or carbonate.

The vesicles are commonly partially or completely filled with carbonate, clays and even Fe-Mn oxides.

One sample shows a single xenolith that is constituted by one very large brown amphibole with clinopyroxene, biotite, titanite and apatite inclusions.

6.1.11 Xenoliths and megacrysts

Although xenoliths are quite rare in these rocks, they can be found in reasonable amounts at the Ribeira d'Ilhas plug, in the Eiras do Faião sill and more rarely in the Fontanelas seamount. Most of them are of igneous origin and show shapes that vary between sub-angular and rounded in cross section.

Sedimentary xenoliths of limestone with significant siliciclastic component were also identified in the Ribeira d'Ilhas plug, but are very rare.

In addition to the xenoliths, megacrysts of amphibole and clinopyroxene can also be found in the Ribeira d'Ilhas plug and Lomba dos Pianos sill.

The amphiboles invariably show a rim of pink clinopyroxene and very small oxides. This rim distinguishes these amphibole megacrysts from the ones described in the in the Negrais flow which show a reaction rim of clinopyroxene + plagioclase + oxides.

The igneous xenoliths are consistently olivine free and typically constituted mainly by brown amphibole and clinopyroxene, that may have green or colorless cores, with accessory apatite, Fe-Ti oxides, and in the case of the Eiras do Faião sill and Fontanelas lavas, minor titanite, with the second additionally having biotite. They can be therefore classified as hornblendites or (hornblende bearing) clinopyroxenites, depending if either hornblende or clinopyroxene are modally dominant, respectively.

Grain size among the crystals contained in the xenoliths is is usually constant within single xenoliths, but is heterogenous between different xenoliths, and can varying between 0.2 and more than 1 mm.

Plagioclase is very rare, with only one small xenolith containing this mineral, along with green cored clinopyroxene and apatite.

Most of the xenoliths show signs of reaction with the magma where they are inserted, resulting in the formation of a rim of clinopyroxene and oxides that encloses them.

The xenolith in the Eiras do Faião sill (fig. 6.1G) and some in the Ribeira d'Ilhas plug have a granular, fine to medium grained texture that shows hints of recrystalyzation, since all the grains have sutured boundaries, are approximately equidimensional, and often show amphibole growing in clinopyroxene junctions.

The clinopyroxenes in these xenoliths can show a sieved texture with blebs of brown amphibole growing inside it. Sieve textures can be interpreted as resulting from corrosion of minerals in a magma with which they are not in equilibrium, or as a consequence of incipient partial melting. In some cases, clinopyroxenes can also display oxide exsolution lamelae along cleavage planes.

In some of the coarser grained xenoliths and in most of the xenocrysts, the amphiboles are dotted with small oxide and sulphide inclusions, giving them a darker, unclear aspect.

Gabbroic to dioritic and syenitic xenoliths containing plagioclase and K feldspar were also reported by Palácios (1985) in the Eiras do Faião sill, but were not sampled in this study. The same author also sampled only one peridotitic xenolith in the LCV that contained olivine showing deformation bands, with the remaining minerals being clinopyroxe and oxides.

6.1.12 Summary and discussion

The petrographic descriptions made above allow for the inference of a simplified crystallization order in the observed rocks, leaving out some of the more specific mineral assemblages (fig. 6.3).

The first phases to crystallize would then be Cr-Al rich spinels (Cr_2O_3 35-7 %, Al_2O_3 19-5 %, see 6.2.5) followed by olivine, in which they are often included. Olivine is an important constituent in most basic rocks but does not occur in the more evolved basic rocks (e.g. some of the Sintra, Sines and Monchique gabbros) and in the intermediate rocks.

They are followed by Fe-Ti oxides and clinopyroxenes, with the latter showing inclusions of all the previously mentioned these minerals. Fe-Ti oxide and

clinopyroxene crystallization will continue throughout the evolution of these rocks, while Cr-Al spinel is only found in the more basic, undifferentiated terms.

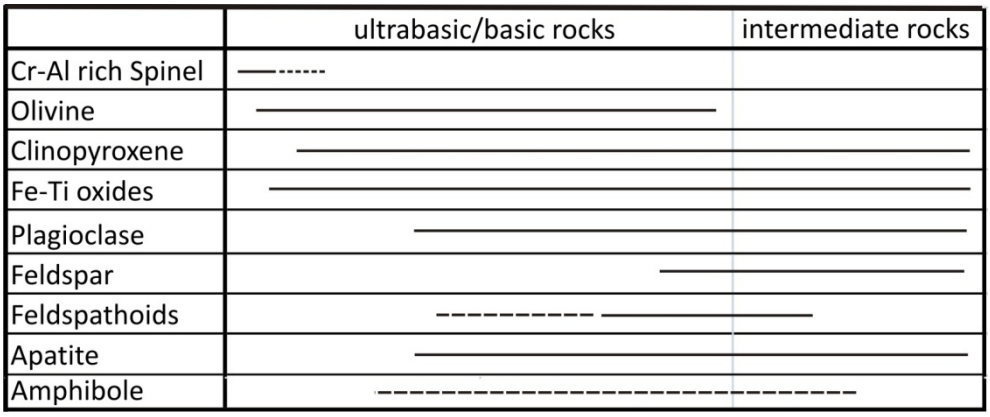

Fig. 6.3: Diagram showing a simplified crystallization order for the studied samples.

Amphibole might be the fourth phase to crystallize in the basaltic rocks. These minerals sometimes show inclusions of olivine, Fe-Ti oxides and clinopyroxene in the basic porphyritic rocks. But in the gabbros amphibole crystallization should be preceded by plagioclase since in these rocks amphibole distinctively shows plagioclase inclusions.

Apatite should start to crystallize approximately at the same time as plagioclase and amphibole since it is often found in the matrix of basaltic rocks and in inclusions on amphibole found in gabbros.

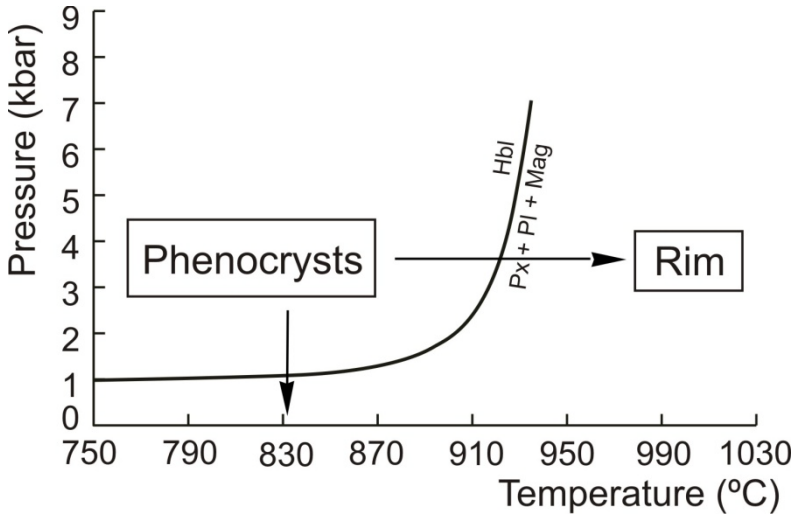

Fig. 6.4: Conditions under which hornblende grains can form pyroxene + plagioclase + Fe-Ti oxides rims. The solid line shows the stability field of hornblende after (Rutherford and Hill, 1993). Adapted from Plechov et al., 2008.

Feldspar appears relatively late in some of the gabbros but its crystallization continues in the intermediate rocks.

The existence of amphibole phenocrysts reacting with the liquid resulting on the formation of rims of oxides, plagioclase and clinopyroxene in the basal lava flows of the LVC (e.g. Negrais) might be caused by pressure release and dehydration during ascension and eruption, which led to the destabilization of the amphibole (fig. 6.4). Given that in some cases the amphibole did not have time to fully react and complete the transformation into these products, it can be speculated that the ascension and eruption of these magmas was relatively fast, in a scale of days (e.g. Rutherford and Hill, 1993; Rutherford and Devine, 2003).

Alternatively, amphibole destabilization can also occur isobarically, during the recharge of a magma chamber with a more basic, hotter magma (e.g. Ruthford and Devine, 2003; Plechov et al., 2008). The recharging liquid can also be drier, leading to further destabilization of the hydrated minerals (e.g. Reagan et al., 1987). The distinction between these two hypotheses for amphibole rim formation will be discussed in further detail in section 6.2.

Amphibole is also found to be frequently associated with apatite in xenocrysts (with the apatites occurring as inclusions in the amphibole) and xenoliths. This association has been interpreted by some authors as resulting from the crystallization of carbonatitic or alkaline silicic carbonated magmas at mantle depths (Wass, 1979; O'Reilly and Griffin, 2000).

The presence of xenoliths, whose textures show evidence for recrystallization, and in the case of the sieve textured clinopyroxenes, even partial melting, supports the notion that these might have formed in deeper magma chamber or conduit. They were later remobilized by a new, hotter magma pulse where they reequilibrated and perhaps even underwent partial melting due to heating and decompression during ascension.

Accordingly, the observation of both recrystallization in xenoliths and reaction rims around amphibole xenocrysts is evidence for reequilibration and adjustment to lower pressure and/or higher temperature conditions.

Finally, the simultaneous existence of two different kinds of clinopyroxene in the same magma, as observed in several of the intrusive rocks, might be an indicator of magma mixing and therefore, a complex pre-installation history (e.g.

Duda and Schminke, 1985; Dobosi, 1989; Dobosi and Fodor, 1992; Martins, 1999; Pilet et al., 2002), and shall be discussed in more detail in the mineral chemistry section (6.2).

6.2. Mineral Chemistry

The chemical characterization of the main petrographic phases of the sampled lithologies was done by Electronic Microprobe Analysis in the Laboratório de Microssonda Electrónica of the Centro de Geologia da Universidade de Lisboa under the technical supervision and orientation of Dr. Pedro Celestino Reis.

The analyses were performed on polished thin sections using a JEOL JXA 8200 electron microprobe. An acceleration voltage of 15 kV and a beam current of 25 nA were used. The electron beam was focused to 5 μm diameter. Typical uncertainties are below 2% for the major oxides.

The analyzed elements in each mineral group were calibrated using the standards indicated in table 1 in annex IV.

The more relevant lithologies in most of the sampled occurrences were chosen for analysis, with the addition of a sample from the Monchique nepheline syenites in order to compare the composition of their green clinopyroxenes with the green cores recognized in the clinopyroxenes of some mafic rocks (see section 6.1).

6.2.1 Olivine

In the studied rocks, olivine is a major constituent of basalts, as well as of some of the lamprophyres, where it occurs as a phenocryst phase. It is also present in some of the gabbros. The structural formula of the analyzed olivines was calculated on a basis of 4 oxygens.

The chemical variation of the olivine mineral group can be described as a solid solution series between forsterite, an Mg rich component (Fo: Mg_2SiO_4), and fayalite, the Fe rich component (Fa: Fe_2SiO_4). It shows a tendency for increasing the fayalite contents with differentiation, whereas the more Fo rich compositions are thought to be products of crystallization from less evolved magmas characterized by lower Mg/(Mg + Fe ratios.

Compositional variations in this mineral are described using the forsterite (Fo = 100 × [Mg/(Mg + Fe)]) contents as a differentiation index, as shown in figs. 6.5-6.

Olivines from basalts show some compositional variation, with the cores of phenocrysts being more Fo rich (Fo > 85%) than their rims, than the microphenocrysts and than the matrix minerals. Taking into consideration that $\boldsymbol{D_{Mg}^{ol/liq}}$ (with D being the partition coefficient, in this case between Mg and the olivine-liquid pair $D_{Mg} = \boldsymbol{C_{Mg}^{ol}/C_{Mg}^{liq}}$) tends to increase with decreasing temperature (e.g Roeder and Emslie, 1970), such compositional evolution is interpreted as a result of progressive Mg depletion in the liquid with olivine crystallization in a cooling magmatic system.

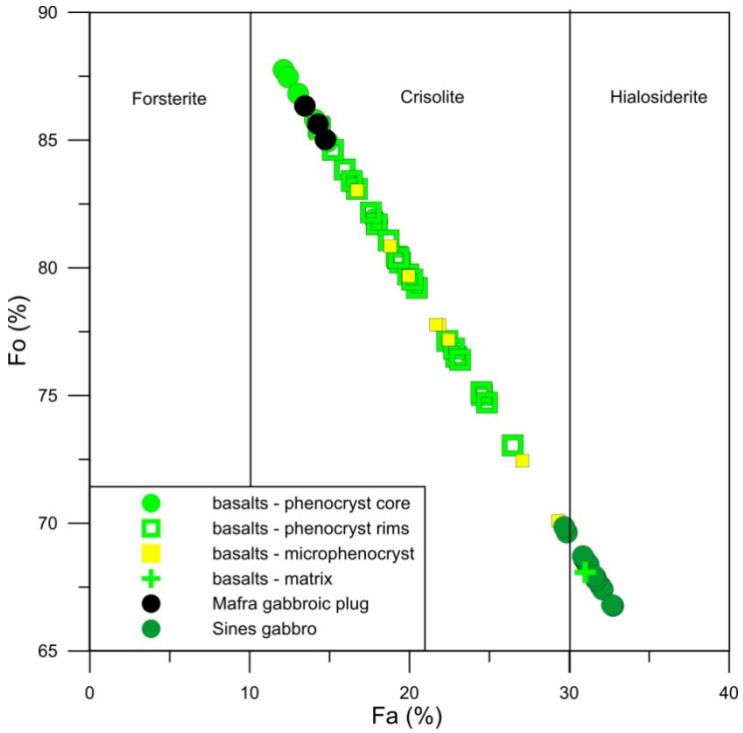

Fig. 6.5: classification of the analyzed olivines according to their abundances in forsterite (Fo – Mg_2SiO_4) and fayalite (Fe_2SiO_4).

The olivines in the Mafra gabbroic plug also show relatively high Fo contents (> 83%), while the ones in the Sines gabbro show the lower Fo and higher Fa contents in all of the analyzed rocks, reflecting crystallization from a less Mg rich, more evolved liquid.

In general, MnO contents increase with decreasing forsterite contents while NiO and SiO_2 decrease (fig. 6.6). CaO contents of olivines show two distinct trends: the first one characterized by the progressive increase of CaO with decreasing Fo and is seen in the LVC's rocks and in the Mafra gabbro, while a second trend is discernable in the Sines gabbro and in crystals with Fo < 73%, marked by a decrease in CaO.

The decrease in NiO agrees with progressive depletion in this element in the liquid due to earlier olivine and clinopyroxene crystallization.

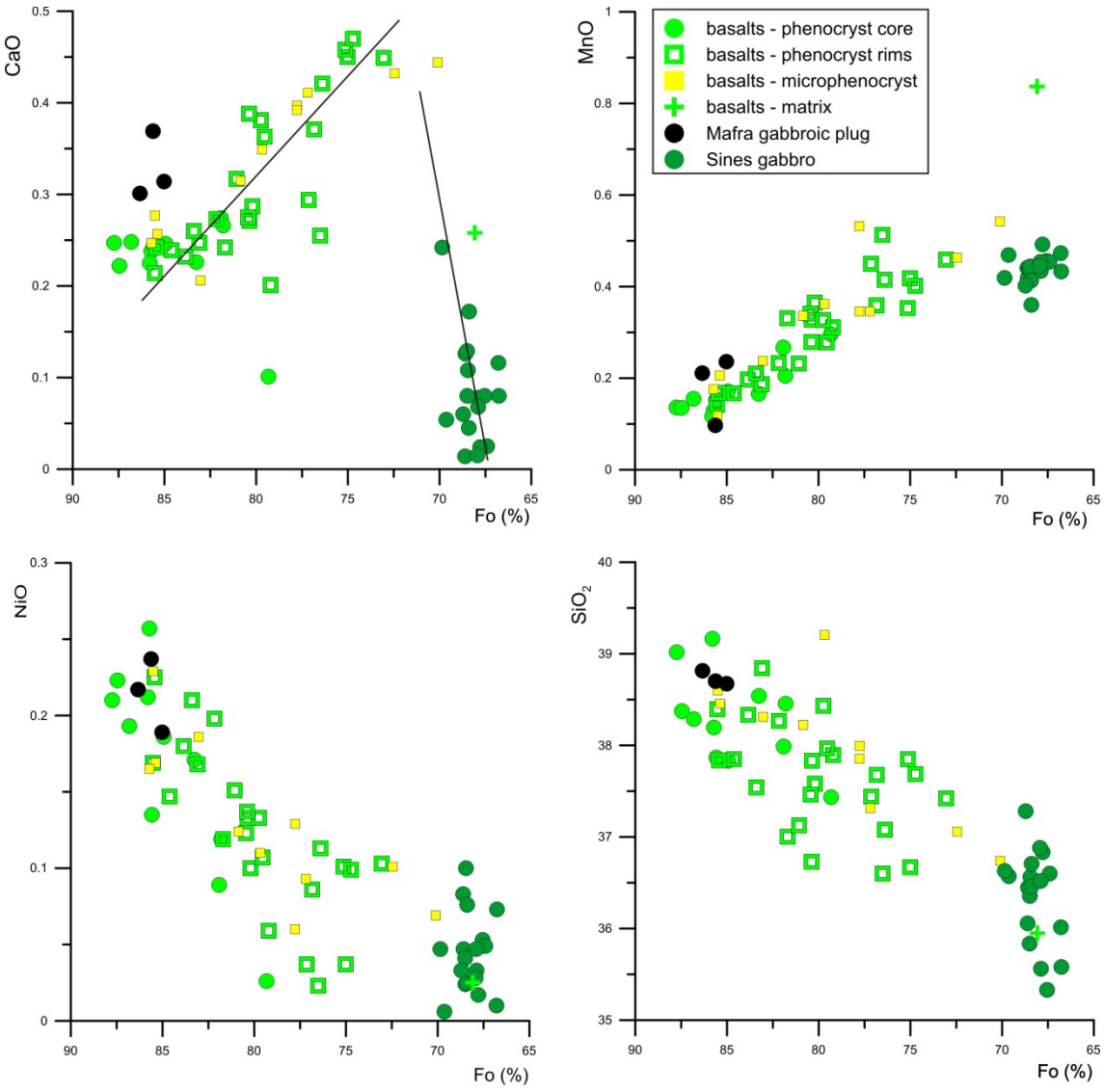

Fig. 6.6: Variation of the concentrations of CaO, MnO, NiO and SiO_2 with the content in Forsterite (Fo) for the analysed olivines.

During olivine crystallization the rapid reduction of the Ni contents in the melt would create space in the crystal lattice of olivine, which can lead to increasing Ca substitution. However, the crystallization of Ca-rich clinopyroxene and plagioclase would result in the depletion of Ca in the residual melt, which is probably the reason for the decrease in CaO contents observed in olivine below $\approx Fo_{73}$. Therefore, the notorious decrease in CaO seen in the Sines gabbro is likely to be the result of continuing olivine

crystallization after the onset of clinopyroxene and/or plagioclase crystallization and removal, since these minerals incorporate more CaO.

The rise in MnO in the olivine composition with decreasing Fo in the basalts is related to the higher availability of this incompatible element in more evolved liquids and due to the increasing compatibility of Mn in more Fa rich olivines (e.g. Beattie et al., 1991). The lack of a Mn increase in the more Fa rich olivines from the Sines gabbros is probably due to reduced Mn availability caused by its removal from the melt by the precipitation of a more Mn rich Fe-Ti oxides (MnO 0.7-1.2%).

The distribution coefficient for the Fe/Mg ratio between olivine and liquid ($\boldsymbol{Kd^{ol-liq}_{Fe/Mg}} = (\boldsymbol{X^{ol}_{Mg}/X^{ol}_{Fe}}) * (\boldsymbol{X^{liq}_{Fe}/X^{liq}_{Mg}})$, where $\boldsymbol{X}$ is the molar fraction) was also calculated, assuming the whole rock analysis as representative of the liquid from which the olivines crystallized, and that this liquid would have a Fe^{3+}/Fe^{2+} ratio of 0.2 (Middlemost, 1989 in Rollinson, 1993). The $\boldsymbol{Kd^{ol-liq}_{Fe/Mg}}$ value is independent of temperature and pressure variations and is of approximately 0.3 ± 0.03 for situations where the olivine is in equilibrium with the composition of the magmatic liquid (Roeder and Emslie, 1970; Beattie et al., 1991).

Assuming that there is equilibrium and $\boldsymbol{Kd^{ol-liq}_{Fe/Mg}}$ = 0.3 ± 0.03, the composition of the possible olivine-liquid pairs can be calculated using the following expression:

$$\boldsymbol{Kd^{ol-liq}_{Fe/Mg}} = \left[(\mathbf{1} - \boldsymbol{Fo_{ol}}) * \boldsymbol{Mg\#_{liq}}\right] * [\boldsymbol{Fo_{ol}} * (\mathbf{1} - \boldsymbol{Mg\#_{liq}})]$$

where $\boldsymbol{Mg\#_{liq}} = \frac{\boldsymbol{MgO_{liq}}}{(\boldsymbol{MgO_{liq}+FeO_{liq}})}$ and $\boldsymbol{Fo_{ol}}$ is the calculated forsterite content of the olivines.

The resulting curves were plotted on fig. 6.7 together with the analyzed rock-mineral pairs.

Most of the calculated $\boldsymbol{Kd^{ol-liq}_{Fe/Mg}}$ values were different from the expected average of 0.3 ± 0.03 predicted for olivines in equilibrium with the host magma (Roeder and Emslie, 1970). The higher values correspond mostly to the ones observed in the rims of phenocrysts and in matrix crystals and occur in the samples from the LVC's Monte Serves neck, the Ribeira d'Ilhas plug, and especially the Sines gabbro. The lower values

occur only in the Negrais lava flow of the LVC and are typically found in crystal cores (fig. 6.7). The only olivines that show $\boldsymbol{Kd}_{\boldsymbol{Fe/Mg}}^{\boldsymbol{ol-liq}}$ values indicative of equilibrium between the crystal and the host liquid are some of the crystals present in the Monte Serves neck, the Ribeira d'Ilhas plug and the Negrais flow.

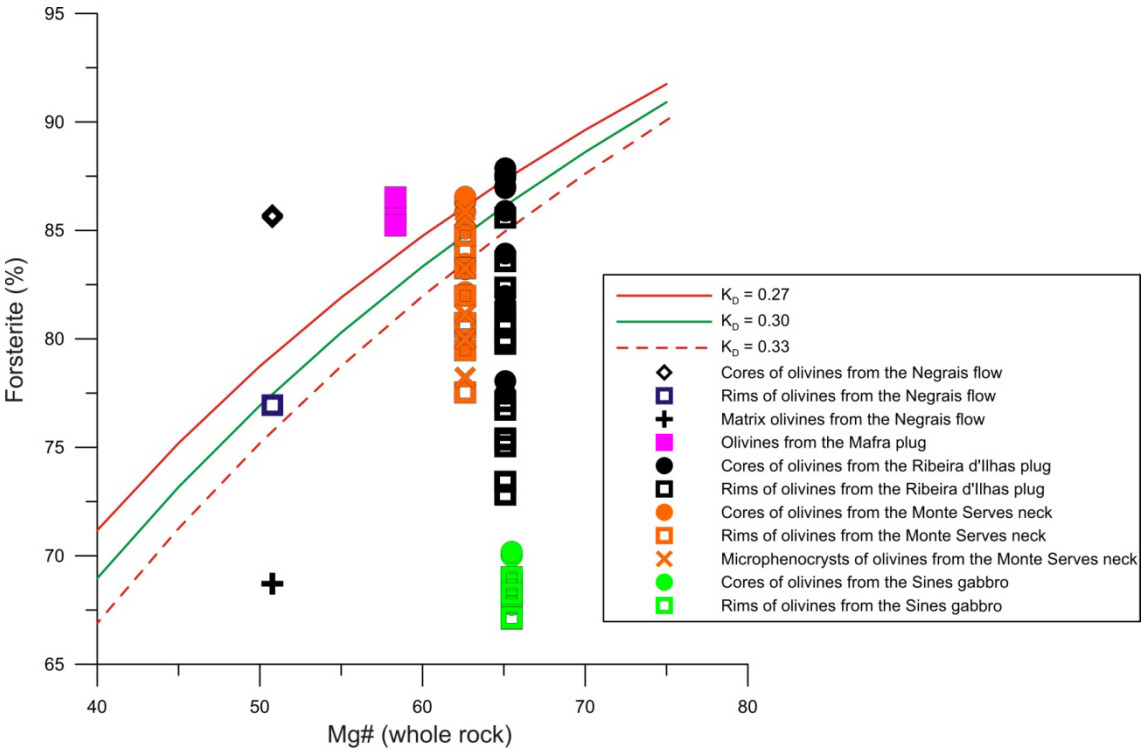

Fig. 6.7: Fosterite contents of the olivines vs. whole rock composition. Also represented is the variation of the forsterite content in olivines with the changing Mg# of a magmatic liquid for rocks with $\boldsymbol{Kd}_{\boldsymbol{Fe/Mg}}^{\boldsymbol{ol-liq}}$ values between 0.27 and 0.33.

The higher than expected $\boldsymbol{Kd}_{\boldsymbol{Fe/Mg}}^{\boldsymbol{ol-liq}}$ values mean that the olivine is richer in FeO than it would be observed if this mineral was in equilibrium with a liquid whose composition is equivalent to the whole rock analysis. These higher than expected $\boldsymbol{Kd}_{\boldsymbol{Fe/Mg}}^{\boldsymbol{ol-liq}}$ observed in some rocks might be due to the analyzed whole rock composition not being representative of the liquid composition from which the olivines crystallized. This may happen if either previous crystallization of other phases such as spinel, clinopyroxene or even olivine changed the FeO/MgO of the liquid or due to an increase of MgO in the liquid by to accumulation and consequent resorption of MgO-rich olivine.

Alternatively, the whole rock composition can be biased towards more MgO-rich contents, reflecting the "input" from the olivine crystals in the analysed samples,

which would consequentially change FeO/MgO of the whole rock and assumed liquid composition. This can be significant in samples that show evidence for important crystal accumulation, such as the Sines gabbro.

There is also the possibility that the observed whole rock composition reflects the mixing of magmas with different Fe/Mg ratios, but although some of the crystals are rounded, which might taken to be an indication of post crystallization reaction, the lack of reverse zoning in the olivines apparently rules out this hypothesis.

The accumulation of olivine, causing the whole rock analysis not to be representative of the liquid from which the analyzed olivines precipitated seems the most reasonable explanation for the very high $\boldsymbol{Kd_{Fe/Mg}^{ol-liq}}$ values observed for the olivines in the Sines gabbro. The presence of macroscopic layering in the outcrops where this lithology was sampled, and the textural and geochemical characteristics of these rocks (see sections 4.1.7 and 6.1.7) support their formation by accumulation processes.

As for the lower than expected $\boldsymbol{Kd_{Fe/Mg}^{ol-liq}}$ and consequent higher forsterite values observed in the Mafra gabbro and some of the cores of crystals in the Negrais flow, they indicate that these olivines are more magnesian than expected in a rock with that Mg#. These high $\boldsymbol{Kd_{Fe/Mg}^{ol-liq}}$ values are usually calculated for crystal cores and might be due to the early crystallization of some olivine cores in the ascending magmas that were not immediately separated from the liquid, which later crystallized as the Mafra gabbro and the basalts. The hypothesis that these crystals/cores precipitated from an earlier, more primitive magma is not supported by the absence of reverse zoning in the crystals.

According to Roeder and Emslie (1970) it is possible to estimate the crystallization temperature of olivines in equilibrium with the liquid, by knowing the distribution coefficient for Mg between the olivine and the magmatic liquid ($\boldsymbol{D_{Mg}^{ol-liq}}$) using the expression:

$$\log D_{Mg}^{ol-liq} = \frac{3740}{T} - 1.87$$

where T is the temperature in Kelvins.

Beattie (1993) proposed a different, theorectically more precise method for the calculation of the saturation temperature for olivine, given that it takes into account

several compositional effects. It is based on non regular solid solution models for silicate melts, integrates several thermodynamic characteristics of the crystal-melt pair and is supposed to have an error of approximately 10º K. The equation used to determine the temperature values is:

$$T^{ol} = \frac{\frac{\Delta H_M^{ol}}{R} + \left(P - 10^5\right) * \frac{\Delta V_M^{ol}}{R}}{\frac{\Delta S_M^{ol}}{R} + 2lnD_{Mg}^{Ol-L} + 2ln1.5C_{NM}^{L} + 2ln3C_{SiO2}^{L} - (NF)}$$

where T^{ol} is the temperature of saturation of olivine in K, R is the gas constant, P the pressure in Pa, ΔH_M^{ol}, ΔS_M^{ol} and ΔV_M^{ol} the enthalpy, entropy and volumes of fusion of the M component in olivine, D_{Mg*}^{Ol-L} the partition coefficient between melt and olivine for Mg, C_{SiO2}^{L} to the molar fraction of SiO_2 in the melt, C_{NM}^{L} the molar fraction of Network Modifying cations (NM = FeO, MgO, MnO and CaO) in the melt and NF to the molar fraction of the Network Forming cations [NF = 7/2*ln(1-$C_{AlO1.5}^{L}$) + 7*ln (1- C_{ATiO2}^{L})].

D_{Mg}^{ol-liq} was calculated according to the method developed by Beattie (1993), which allows the determination of this value with the data relative to the melt phase alone:

$$D_{Mg}^{ol-liq} = \frac{\psi^{ol} - \sum_{M=1}^{n} B_M^{ol} C_{MgO}^{liq}}{\sum_{M=1}^{n} A_M^{ol} C_{MgO}^{liq}}$$

Where ψ^{ol} is the molar proportion of cations in the M site of olivines (0.666), C_{MgO}^{liq} is the molar concentration of MgO in the liquid, and A_M^{ol} and B_M^{ol} are empirical constants given in Beattie (1993).

D_{Ni}^{ol-liq} was also determined using the method devised by Beattie et al. (1991) where $D_{Ni}^{ol-liq} = A_{Ni}^{ol-liq} * D_{Mg}^{ol-liq} + B_{Ni}^{ol-liq}$, where A_{Ni}^{ol-liq} and B_{Ni}^{ol-liq} are empirical constants given in Beattie et al. (1991).

The results obtained for each of the occurrences where olivine was found to be in equilibrium with the magma is summarized in table 6.1.

The calculated D_{Ni}^{ol-liq} shows good agreement between the values obtained from the compositions of the magma and crystals and the ones computed using the equations proposed by Beattie et al. (1991), except for the MgO and Ni poorer sample, where the

calculated D is much higher than the measured one (table 6.1). The equations derived to describe the variation of $\boldsymbol{D_{Ni}^{ol-liq}}$ with MgO concentrations in the liquid (Hart and Davis, 1978; Mata, 1996) do not predict a decrease in this value with decreasing MgO in the liquid, and neither does the equation by Beattie et al. (1991) that relates $\boldsymbol{D_{MgO}^{ol-liq}}$ with $\boldsymbol{D_{Ni}^{ol-liq}}$, so this low value might be an artifact caused by the low Ni contents of the analyzed rim of olivine, whose composition is most likely not in equilibrium with the whole rock composition that was assumed to represent the liquid phase.

The calculated temperatures correspond to olivine saturation temperatures at 1 bar and should reflect the temperature of the magma during the onset of olivine crystallization at surface conditions.

Average temperatures calculated for the saturation temperatures of olivine vary between a maximum of 1278º C in the Ribeira d'Ilhas plug and a minimum of 1154 ºC in the Negrais flow, showing lower temperatures in the extrusive lava flow than in the intrusives, as would be expected, as shown in table 6.1.

Table 6.1: Average $\boldsymbol{Kd_{Fe/Mg}^{ol-liq}}$, measured and calculated $\boldsymbol{D_{Mg}^{ol-liq}}$ (Beattie, 1993), $\boldsymbol{D_{Ni}^{ol-liq}}$ (Beattie et al., 1991) and temperatures for olivine saturation calculated according to Roeder and Emslie (1970) and Beattie (1993) for the crystals that show equilibrium with the melt in basaltic rocks.

Occurrence	Ribeira d'Ilhas plug	Negrais flow	Monte Serves neck
Sample	RM 37	RM 43	RM 66
Average $\boldsymbol{Kd_{Fe/Mg}^{ol-liq}}$	0.30	0.31	0.28
Average measured $\boldsymbol{D_{Mg}^{ol-liq}}$	4.02	5.48	4.19
$\boldsymbol{D_{Mg}^{ol-liq}}$ calculated according to Beattie, 1993	3.89	5.61	3.91
T °C, Roeder and Emslie, 1970, measured $\boldsymbol{D_{Mg}^{ol-liq}}$	1238.8	1160.4	1227.6
T °C, Roeder and Emslie, 1970, calculated $\boldsymbol{D_{Mg}^{ol-liq}}$	1247.3	1154.8	1246.0
T °C, Beattie, 1993, measured $\boldsymbol{D_{Mg}^{ol-liq}}$	1267.2	1178.2	1238.5
T °C, Beattie, 1993, calculated $\boldsymbol{D_{Mg}^{ol-liq}}$	1278.4	1171.0	1262.3
$\boldsymbol{D_{Ni}^{ol-liq}}$measured	9.3	5.3	11.1
$\boldsymbol{D_{Ni}^{ol-liq}}$calculated according to Beattie et al., 1991	9.8	14.7	10.4

The measured and calculated $\boldsymbol{D_{Mg}^{ol-liq}}$ values are in good agreement, as are the temperatures calculated using the Roeder and Emslie (1970) and Beattie (1993) geothermometers. Although the geothermometer defined by Beattie (1993) tends to

produce higher temperatures, both of them generate similar results with a maximum difference of 30º C between the temperatures obtained with the two thermometers.

As was previously noted by Mata (1996), the similarity between the values obtained using these two very different equations reflects the dominance of the $\boldsymbol{D_{Mg}^{ol-liq}}$ value in the calculations, with the crystallization temperature being almost an inverse linear function of $\boldsymbol{log\, D_{Mg}^{ol-liq}}$, whereas the other compositional and thermodynamic parameters will have little importance on the final values obtained for the olivine saturation temperature.

6.2.2 Clinopyroxene

As was previously described in section 6.1, clinopyroxenes are one of the more abundant and petrographically diverse minerals present in the studied rocks, showing several types of zonation and color, sometimes even within the same sample (e.g. figs. 6.1, 6.8).

These minerals are also one of the main phases present in the rare ultramafic xenoliths, and can therefore provide valuable information about the nature of the magma from which they precipitated. Consequently, the clinopyroxenes from the xenoliths found in samples from the Fontanelas seamount and Eiras do Faião sill were also analyzed.

The structural formula for the analyzed pyroxenes was calculated on a basis of 6 oxygens, with Fe^{2+} and Fe^{3+} being calculated according to Droop (1987).

They are mostly Quadrilateral Ca-Mg-Fe clinopyroxenes (fig. 6.9a, c), and only a few of the crystals fall in the Ca-Na clinopyroxene field (fig. 6.9a, c), according to the classification of Morimoto (1988).

These Ca-Na pyroxenes correspond to aegirine-augites and are found in the Monchique nepheline syenites and as green cores in the clinopyroxenes of a lamprophyre dyke from Loulé (C-20).

On the triangular Ferrosilite (Fs - $Fe_2Si_2O_6$) – Enstatite (Es - $Mg_2Si_2O_6$) – Wollastonite (Wo - $Ca_2Si_2O_6$) diagram (fig. 6.9b, d), most of the samples plot on the augite and diopside fields, with only a few of the cores of the green cored

clinopyroxenes in the Eiras do Faião tephritic sill and in the lavas of the Fontanelas seamount plotting on the hedenbergite field.

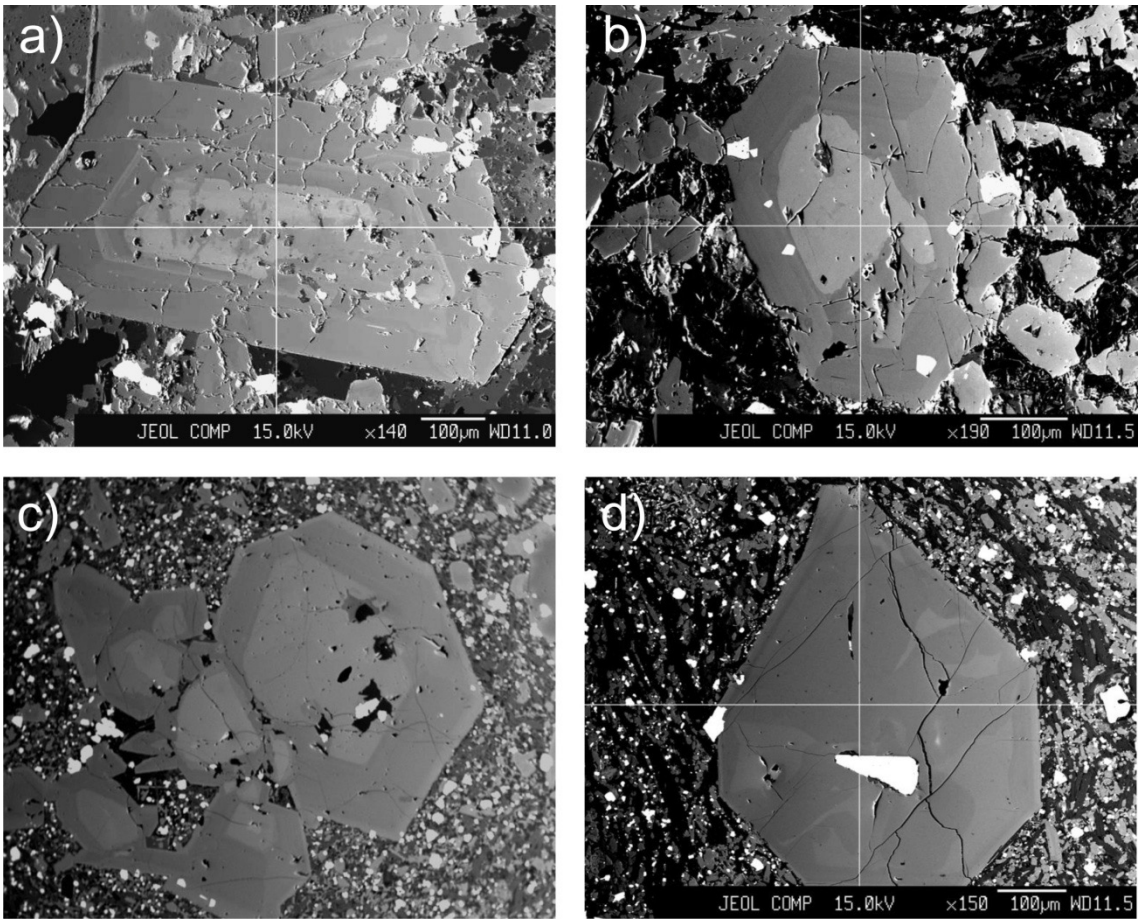

Fig. 6.8: Backscatter electron images of clinopyroxene phenocrysts in basic porphyritic rocks: a) green cored clinopyroxene in Loulé lamprophyre (C-20); b) green cored clinopyroxene in the Malveira da Serra sill (RM 25); c) composite green cored clinopyroxene in the Ribeira d'Ilhas plug (RM 36); clinopyroxene (Clinopyroxene) phenocrysts in the Negrais flow, with oxide inclusion.

Some samples show Wo > 50% and plot on the wollastonite field, but actually correspond to diopsides. The increase of Wo is an artifact caused by the incorporation of non Quad components (e.g. aegirine $NaFe^{3+}Si_2O_6$) in the structure of the clinopyroxenes that formed in silica undersaturated magmas.

In general, as differentiation progresses, the samples seem to become more depleted in Mg, evolving towards compositions more enriched the Fs and Wo molecules, which will also incorporate other non Quad components.

The Sintra gabbro and the more evolved Montelevar sill seem to show two distinct kinds of clinopyroxene with contents in Wo and Fs.

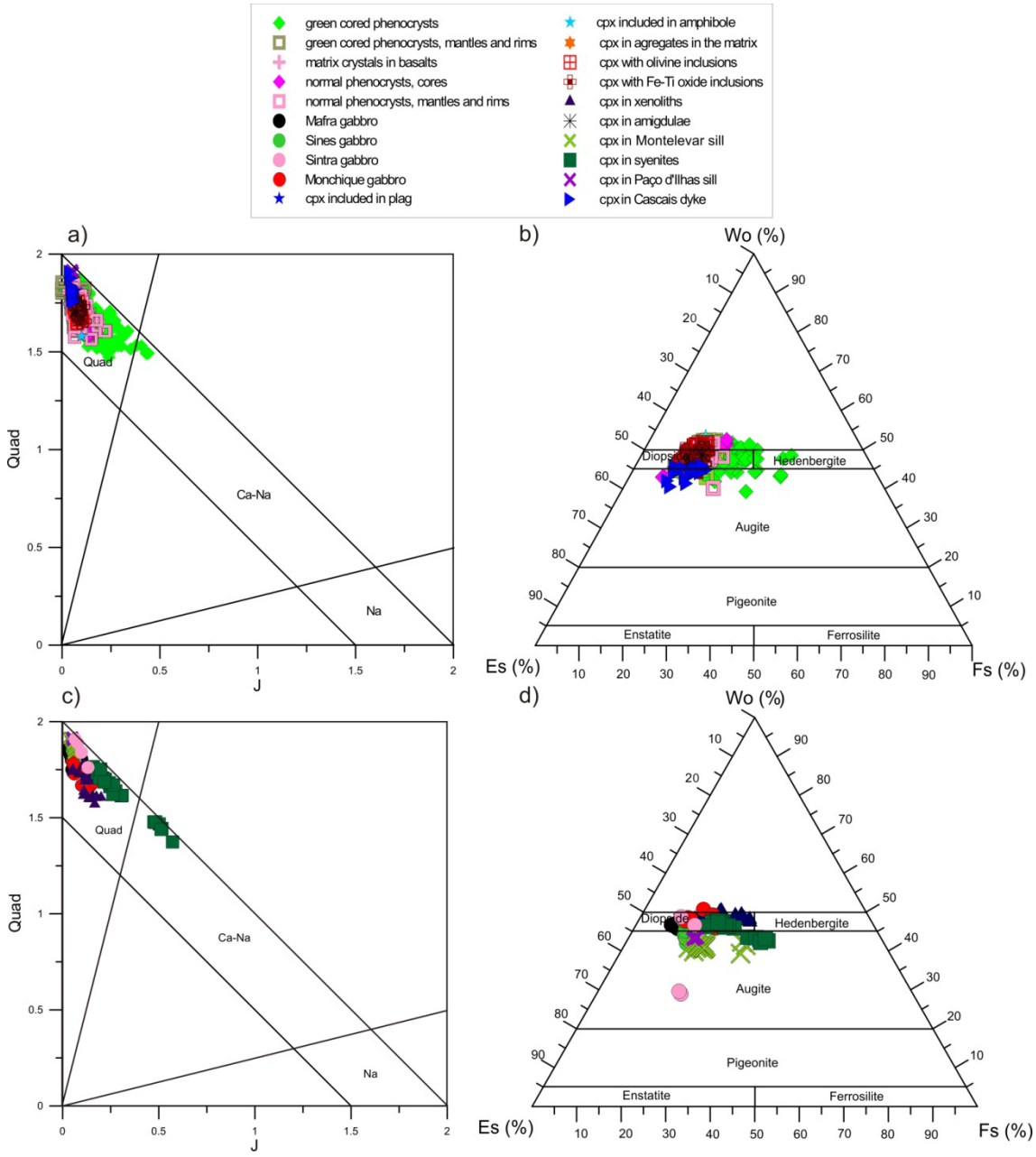

Fig. 6.9: a, c) Quad (Ca+Mg+Fe^{2+} a.p.f.u.) versus J (2*Na a.p.f.u.) diagram of Morimoto (1988) and, b,d) triangular Ferrosilite (Fe), Enstatite (Es), Wollastonite (Wo) classification diagram the analysed clinopyroxenes in porphyritic (a,b) and granular (c,d) samples.

As was previously described in section 6.1, some samples contain clinopyroxenes with a specific type of zoning, showing a green core surrounded by a colorless to pink mantle and rim (e.g. figs. 6.1, 6.8), as well as the more common Clinopyroxenes that show a colorless to pink core, with the rims showing a more intense shade of the same color. In order to investigate the differences in the chemical

compositions of these cores, a series of profiles were made across normally zoned and green cored crystals. Two representative compositional profiles are pictured in fig. 6.10.

By analyzing the compositional profiles of each of these groups of clinopyroxenes, we can observe that the crystals with normal zoning (fig. 6.10) possess a core richer in MgO and Cr_2O_3 with the rims being progressively enriched in Al_2O_3, TiO_2, FeO, and to a lesser degree in Na_2O in relation to the core. This is the result of a progressive depletion of the liquid in MgO and Cr_2O_3 due to the simultaneous crystallization of spinel and olivine, and consequential raise in Al_2O_3, TiO_2, FeO and Na_2O.

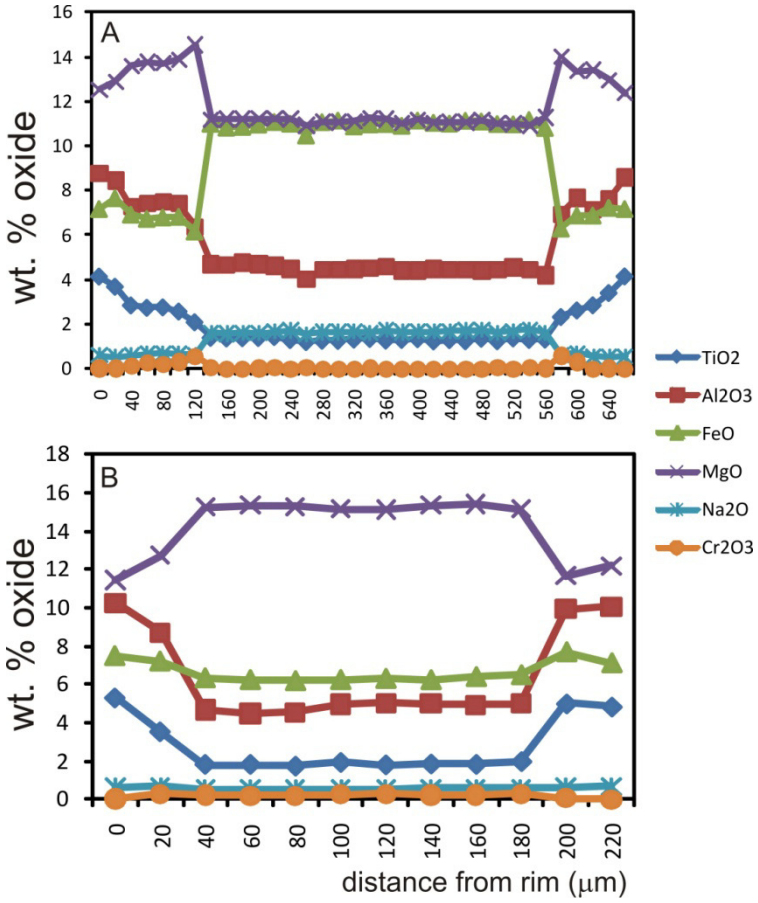

Fig. 6.10: Examples profiles across clinopyroxenes with reverse (top, green cored clinopyroxene in Ribeira d'Ilhas plug) and normal (bottom, pink cored clinopyroxene in Ribeira d'Ilhas plug) zonation in clinopyroxenes.

On the other hand, the zonation pattern is reversed in the green cored clinopyroxenes. The cores are richer in FeO and Na_2O and depleted in MgO, Cr_2O_3, Al_2O_3 and TiO_2 in relation to the mantles and rims. As the analysis progress towards the

rims of these crystals there is an abrupt transition in the abundances of most elements from the green core to the colorless to pink mantle, where the clinopyroxenes becomes more MgO, Cr_2O_3, Al_2O_3 and TiO_2 rich and FeO and Na_2O poor, showing similar compositions to the cores in the normally zoned crystals. As the rim of the mineral approaches, however, FeO, Al_2O_3 and TiO_2 increase and MgO and Cr_2O_3 decrease, in the same way to what happens in a normally zoned clinopyroxene, due to the ongoing crystallization of spinel and olivine that causes the concentrations of these elements to decrease in the liquid.

These green cored, reversely zoned clinopyroxenes are found in the porphyritic basic rocks and their peculiar zonation appears to have formed when a basic, MgO and Cr_2O_3 rich magma mixed and entrained green crystals precipitated from a more evolved, FeO and Na_2O rich but MgO, Cr_2O_3 and TiO_2 depleted liquid. This episode was responsible for the partial resorption of the green clinopyroxenes and the growth of more primitive, Cr_2O_3, MgO and TiO_2 rich and Na_2O, FeO poor mantles. After the homogenization of the mixed liquid, the pyroxenes continued to grow, with the compositions of the rims evolving towards higher TiO_2, Na_2O, Al_2O_3 and lower MgO, Cr_2O_3 as crystallization progressed.

The simultaneous existence of these reversely zoned phenocrysts in the same samples with normally zoned ones puts forward that mixing and hybridization processes between magmas in different states of evolution taking place at depth can be regarded as an important process in generating the petrological diversity observed in the basic alkaline rocks of the WIM, as it has been proposed for other intraplate alkaline provinces (e.g. Duda and Schminke, 1985; Dobosi, 1989; Dobosi and Fodor, 1992; Ho et al., 2000; Sachs and Hansteen, 2000; Pilet et al., 2002, Marchev et al., 2006). This issue will be addressed in more detail later in this section and in the summary of this chapter (6.2.6).

The compositional variations with Mg# for some major elements of in the clinopyroxenes present in basic porphyritic rocks are displayed in figs. 6.11 to 6.14.

From the observation of fig. 6.11, it is shown that the green cores show significantly different compositions from the other clinopyroxenes found in the same rocks. They are systematically richer in FeO and Na_2O but generally poorer in TiO_2, MgO, Cr_2O_3 and sometimes even in CaO and Al_2O_3, than the normally zoned pink

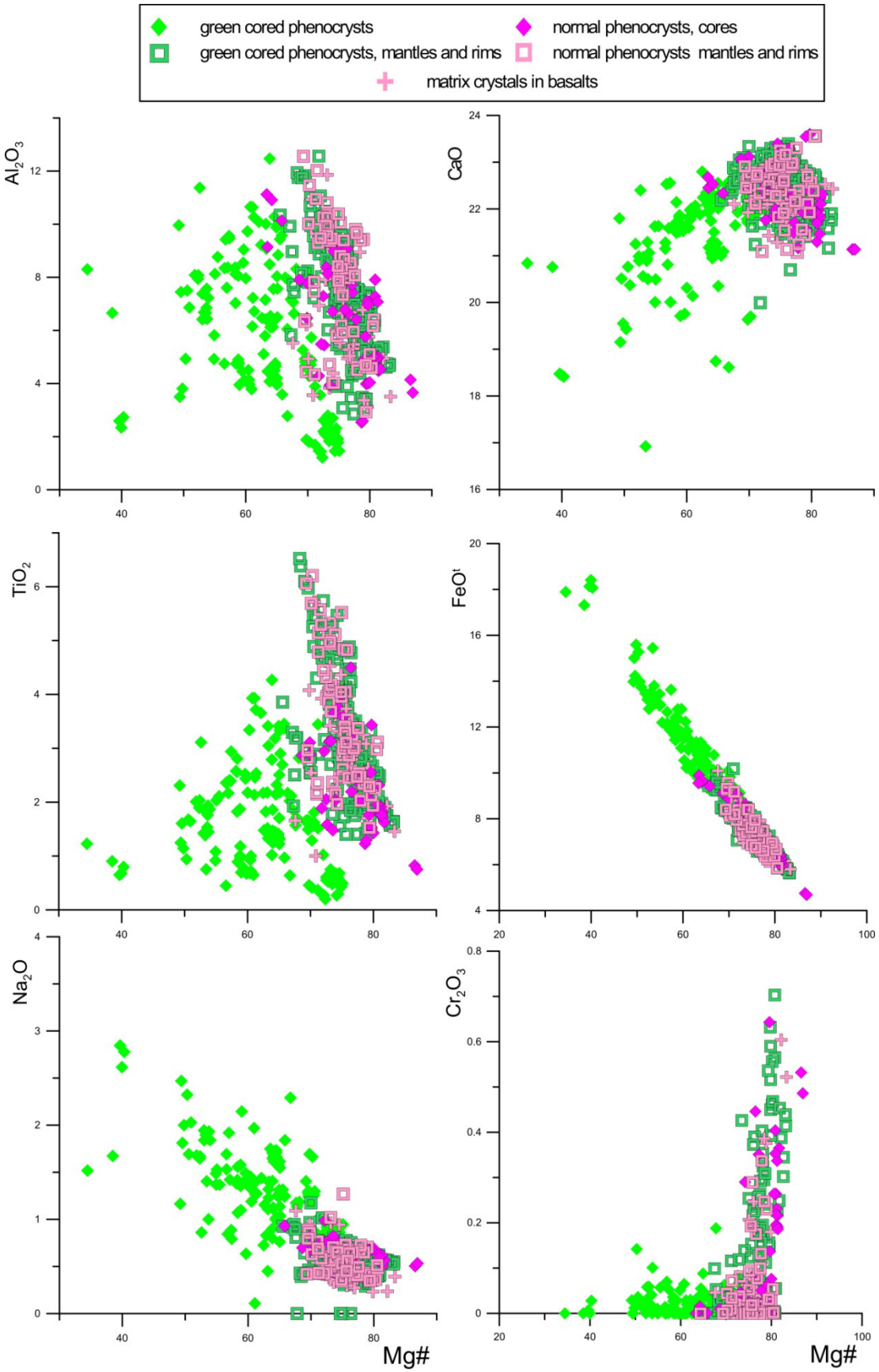

Fig. 6.11: Al_2O_3, CaO, TiO_2, FeO^t, Na_2O, Cr_2O_3 content variation with Mg# in the clinopyroxenes present as phenocrysts and matrix phases in porphyritic basic rocks.

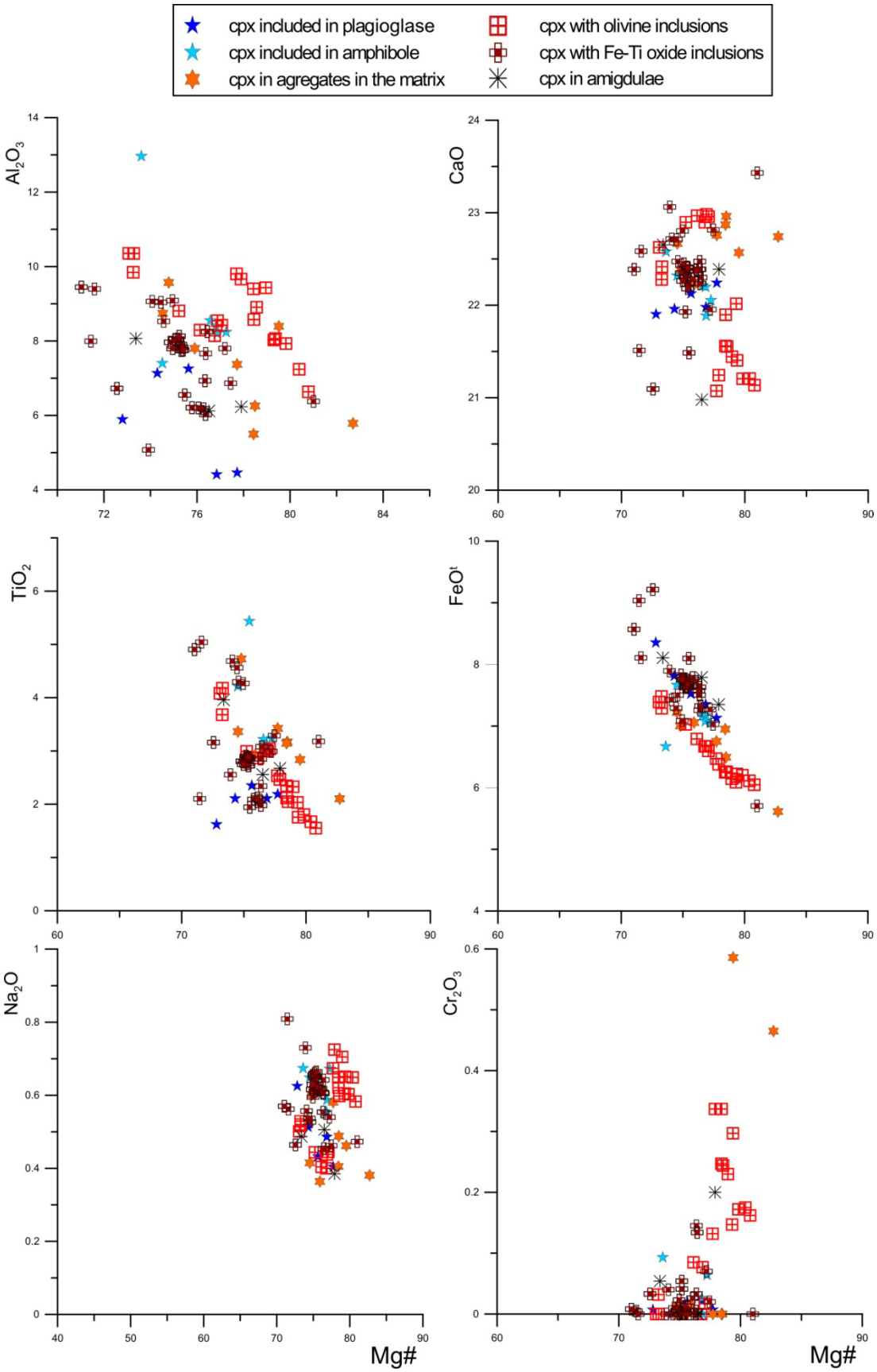

Fig. 6.12: Al_2O_3, CaO, TiO_2, FeO^t, Na_2O, Cr_2O_3 content variation with Mg# in the clinopyroxenes present as inclusions in phenocrysts, occurring as in aggregates and amigdulae or showing inclusions of olivine or abundant Fe-Ti oxides.

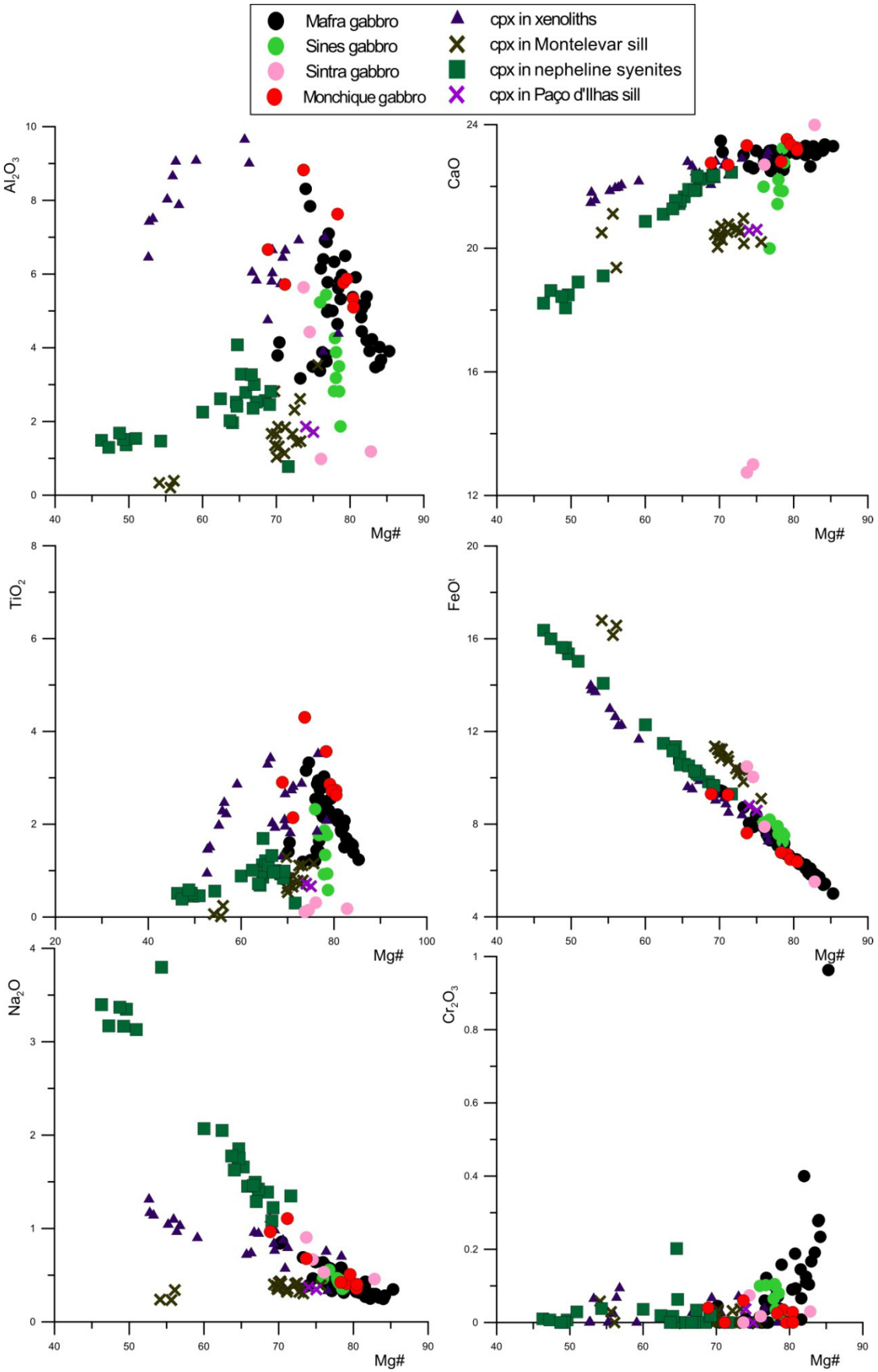

Fig. 6.13 Al_2O_3, CaO, TiO_2, FeO^t, Na_2O, Cr_2O_3 content variation with Mg# in the clinopyroxenes present in uncontaminated intrusive rocks and in the xenoliths.

clinopyroxenes that occur as phenocrysts and matrix phases in the same rocks. However, and confirming the conclusions drawn from the compositional profiles across green cored crystals, the rims of the green cored crystals show similar compositions to the cores and rims of the normally zoned pink clinopyroxene and matrix crystals, suggesting that these rims crystallized from a magma similar to the one from which the remaining phenocrysts formed, while the cores originated from a liquid with a different, more evolved composition.

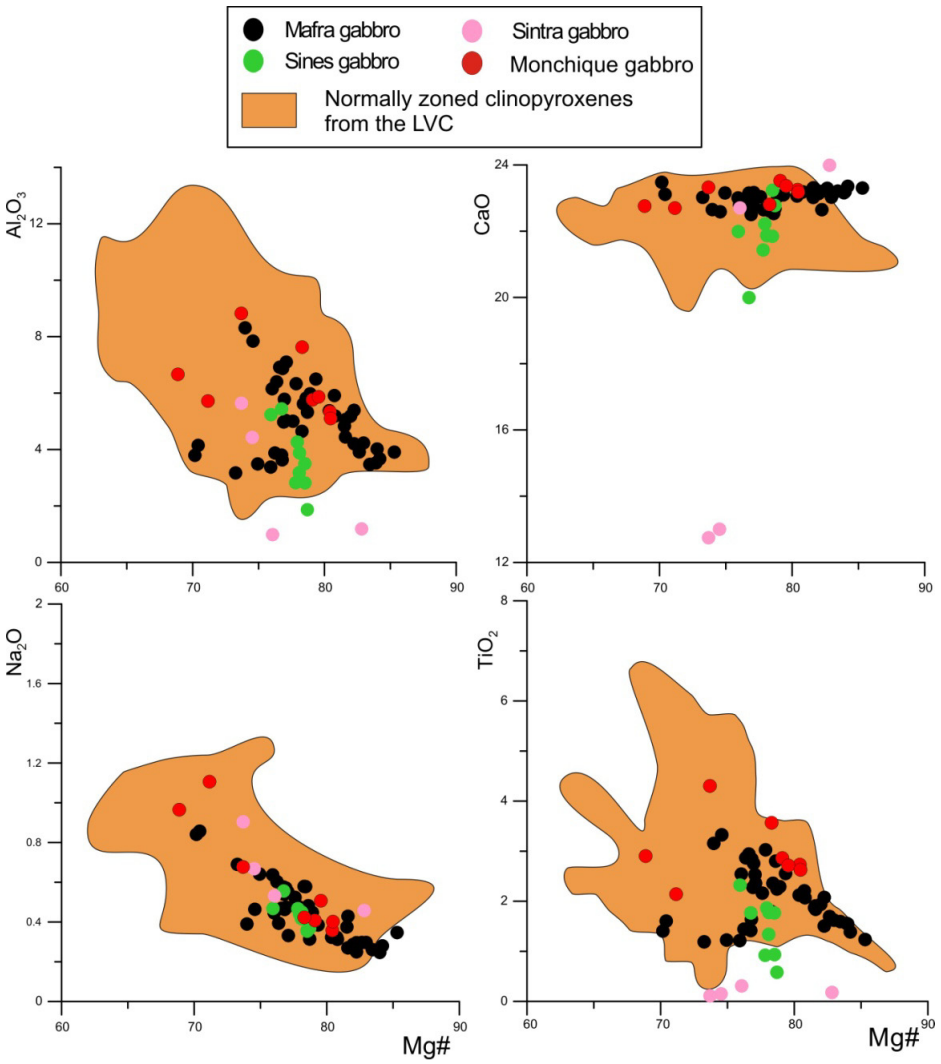

Fig. 6.14: Al_2O_3, CaO, TiO_2 and Na_2O, content variation with Mg# in the clinopyroxenes present in the alkaline basic intrusive rocks of the WIM.

The crystals present in the basic porphyritic rocks as inclusions in phenocrysts, occurring in aggregates and amigdulae or showing inclusions of olivine or abundant Fe-Ti oxides show are represented separately since it is possible that these many types of

occurrence could present significant differences in elemental abundances. Nonetheless, they show compositional ranges identical to the normally zoned clinopyroxenes, suggesting similar crystallization conditions for these phases (fig. 6.12). The higher Mg#, Cr_2O_3 and lower FeO^t and TiO_2 shown by the clinopyroxenes with olivine inclusions, as well as by the ones that occur as aggregates, can indicate that these represent earlier crystallization products from the same or a similar liquid.

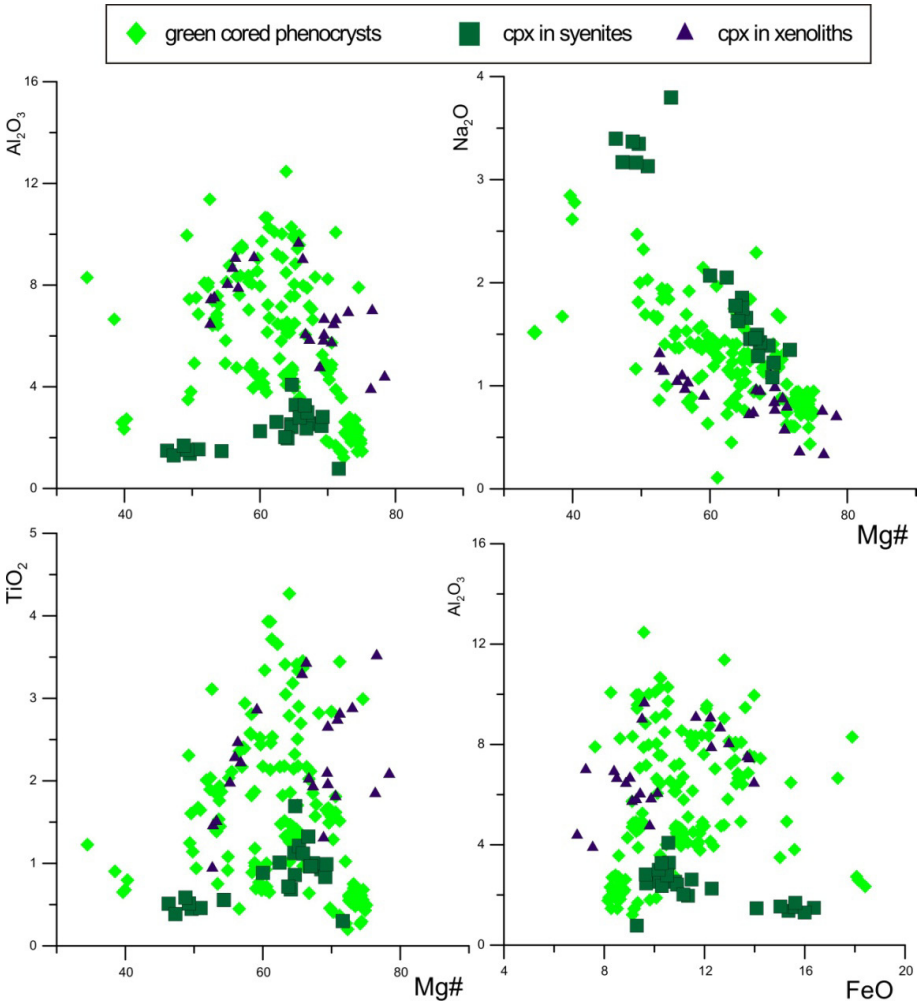

Fig. 6.15: content variations of Al_2O_3 TiO_2 and Na_2O with Mg#, and of Al_2O_3 with FeO^t in the clinopyroxenes present in the xenoliths, Monchique nepheline syenites and in the green cores of reversely zoned clinopyroxenes occurring in basic porphyritic rocks.

The clinopyroxenes found in the uncontaminated intrusive granular lithologies (Mafra, Sintra, Sines and Monchique gabbros, Monchique nepheline syenites and xenoliths) show a narrower compositional range (figs. 6.9 and 6.13) than those found in the basic porphyritic rocks. Some of these, such as in the case of the Mafra, Monchique and Sines gabbros, show compositional affinities with the diopsides and Ti-augites

observed in the porphyritic basaltic rocks, hinting that they might have crystallized from a similar parental liquid (fig 6.14). The Sintra gabbros, however, show clinopyroxenes that are more depleted in TiO_2 and in some cases CaO than the ones found in the basic rocks from the LVC and in the remaining intrusive complexes.

On the other hand, the more FeO rich, green colored clinopyroxenes in the xenoliths and nepheline syenites from Monchique seem to show some affinities with the green clinopyroxene cores found in the basic porphyritic rocks (figs. 6.13 and 6.15). However, the aegirine-augites from the Monchique nepheline syenites tend to be more enriched in Na_2O, at certain Mg#, and show lower TiO_2, CaO and Al_2O_3 concentrations than the green cores in basic porphyritic rocks (fig. 6.15), arguing that the green cores found in the basic porphyritic rocks in the WIM did not form in a similar nepheline syenite magma at upper crustal pressure and temperature conditions.

The clinopyroxenes in the xenoliths show more diverse compositions than those in the nepheline syenites, but are similar to the crystals observed in some of the green cores (fig. 6.15), hinting for a similar origin for the cores in the reversely zoned clinopyroxenes and the clinopyroxenite and hornblendite xenoliths that are present in the same outcrops at times (e.g. Ribeira d'Ilhas plug, Eiras dos Faião sill, Fontanelas seamount). However, not all of the green cores in reversely zoned clinopyroxenes are similar in composition to the clinopyroxenes in the xenoliths, namely the more CaO, Al_2O_3 and TiO_2 depleted and Na_2O, FeO rich, which probably formed from a more evolved melt.

If the clinopyroxenes in the xenoliths and in the green cores are in fact related, this implies that the green cores precipitated at depth from a magma, which also generated the xenoliths by crystallization and accumulation processes. The green cores and xenoliths must have been remobilized and mixed with an ascending, more primitive basaltic liquid where their partial resorption and the formation of their more primitive clinopyroxene rims took place.

The contaminated Montelevar and Paço d'Ilhas sills and one of the dykes in Cascais dyke show clinopyroxene compositions that reflect the degree of evolution of the rocks that contain them (fig. 6.16). The Cascais dyke is a hawaiite and thus is less evolved than the rocks that constitute both of the sills (mostly mugearitic to benmoreitic compositions) and its clinopyroxenes show compositions similar to the normally zoned clinopyroxenes present in the basic porphyritic rocks of the LVC (fig. 6.16).

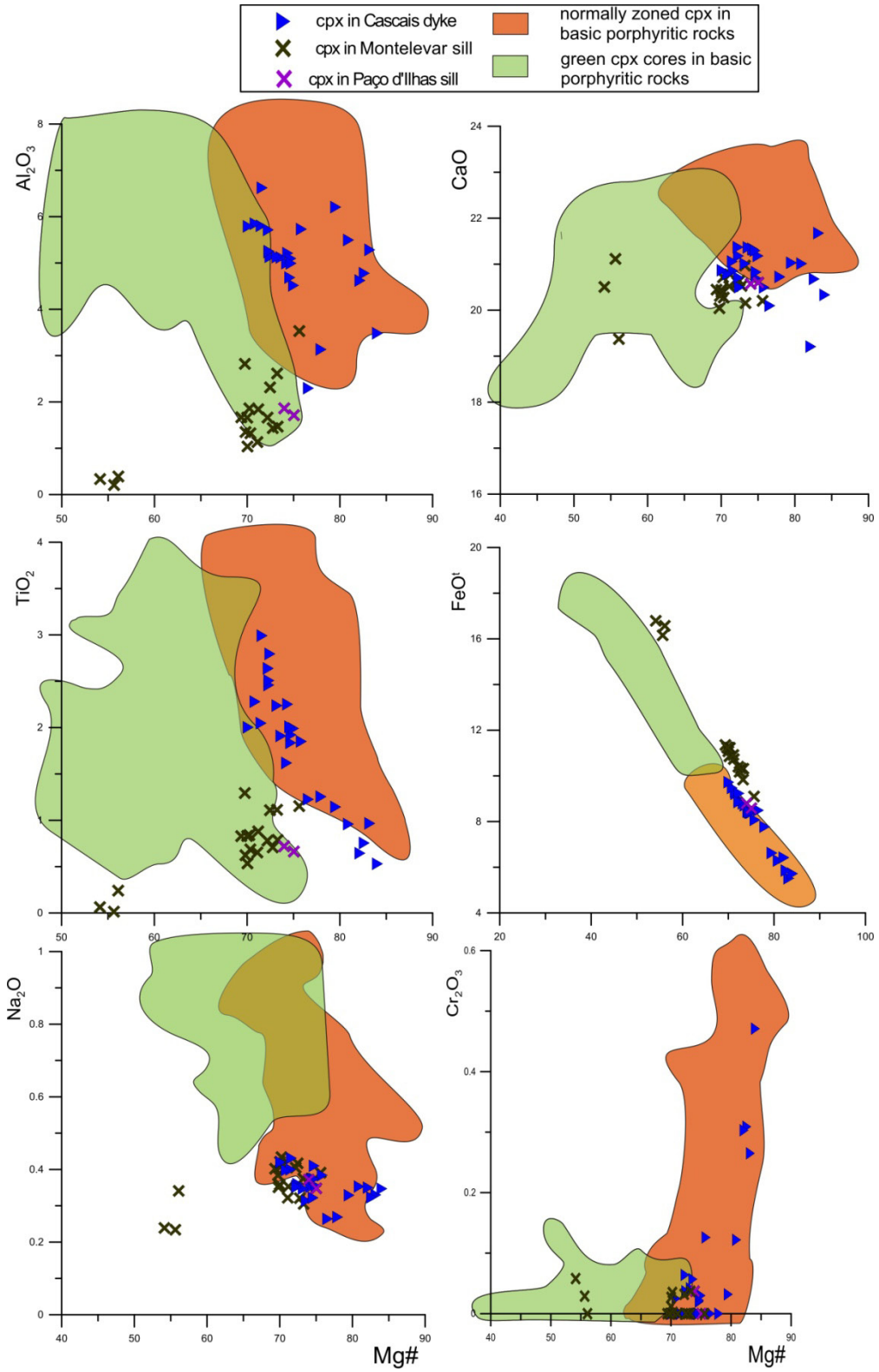

Fig. 6.16: Al_2O_3, CaO, TiO_2, FeO^t, Na_2O, Cr_2O_3 content variation with Mg# in the clinopyroxenes present in the contaminated Paço d'Ilhas and Montelevar sills and Cascais dyke (sample RM 90).

The clinopyroxenes in the more evolved and Si-rich Paço d'Ilhas and Montelevar sills are poorer in MgO, TiO_2, Cr_2O_3 and Al_2O_3, but richer in SiO_2 and FeO^t (fig. 6.16).

The intermediate Montelevar sill seems to show two different clinopyroxene populations, with distinct contents in FeO^t, Al_2O_3 and TiO_2 (fig. 6.16).

The clinopyroxenes from these sills, although showing similar contents in some elements, do not show the same optical and chemical characteristics as the clinopyroxenes found in the green cores and therefore these cores cannot have crystallized from similar intermediate, contaminated liquids in upper crustal pressure and temperature conditions.

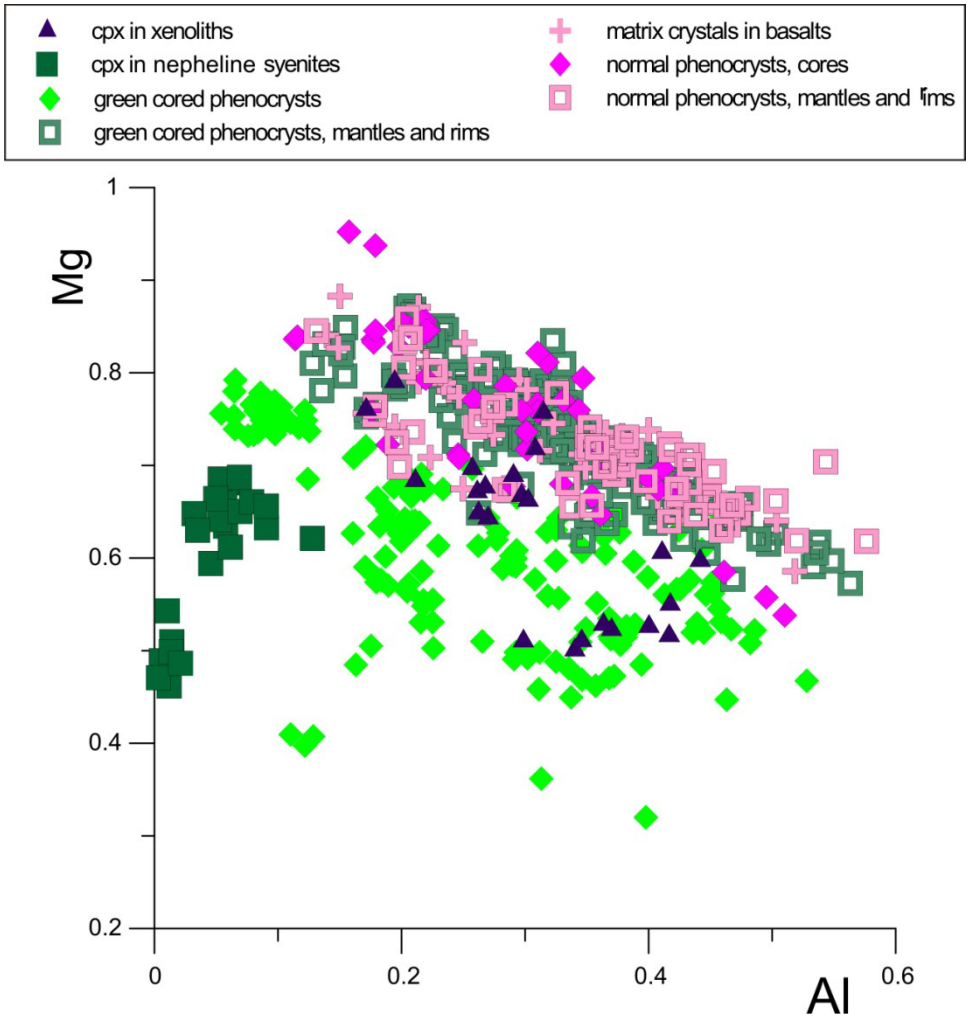

Fig. 6.17: Al vs. Mg (a.p.f.u.) contents for the several types of clinopyroxenes from the Monchique nepheline syenites, the xenoliths and the porphyritic basic rocks.

It is clear from figure 6.17, that the green cores in the reversely zoned clinopyroxenes are clearly distinct in terms of Mg and Al composition from their rims, from the other clinopyroxenes (mostly Clinopyroxenes) that occur in the same basic porphyritic rocks and from the green clinopyroxenes from the Monchique nepheline syenites. They do, however, show some affinities with the ones found in the xenoliths, again suggesting a common origin for these cores and the clinopyroxenes in the xenoliths.

These green clinopyroxene cores and the clinopyroxenes found in the xenoliths must have therefore formed from a more evolved, Mg depleted liquid, but that was enriched in Na_2O and FeO. This liquid is not compatible with the basanitic liquid that hosts the reversely zoned clinopyroxenes and from which their Clinopyroxene rims and the other clinopyroxenes crystallized, neither with the nepheline syenite where the green clinopyroxenes from Monchique formed, so it should have had some intermediate composition between these two extremes.

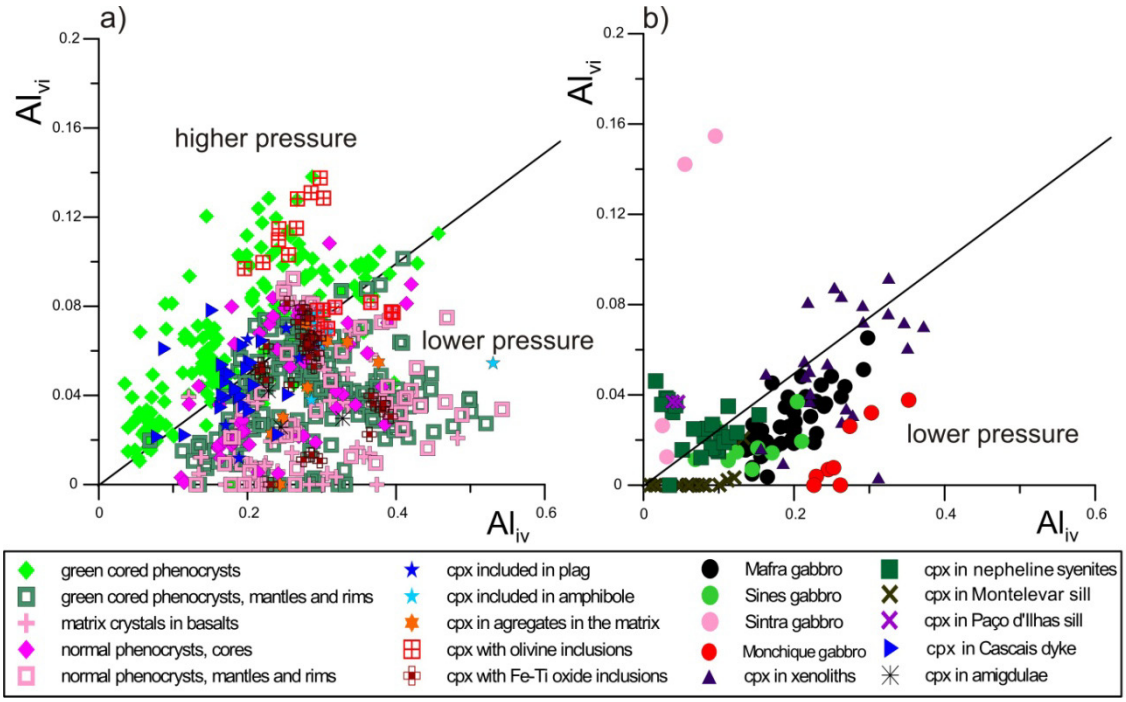

Fig. 6.18: Al_{iv} vs. Al_{vi} (a.p.f.u.) contents for the clinopyroxenes from the porphyritic basic rocks (a) and from the granular intrusives (b). Pressure fields from Aoki and Shiba (1973).

Clinopyroxenes with higher amounts of Al (a.p.f.u. - atoms per formula unit) in octahedral coordination (Al^{vi}), and therefore higher Al^{vi}/Al^{iv} ratios (> 0.25), are formed

at higher pressures, where more jadeitic molecule ($NaAlSi_2O_6$) is incorporated into the clinopyroxenes (Aoki and Shiba 1973; Wass, 1979).

As can be seen of fig. 6.18a, the samples showing higher amounts of Al^{vi} are the green cores and the pyroxene with olivine inclusions. In the case of the clinopyroxenes with olivine inclusions, it is likely that they crystallized at higher depths, at an early stage in the magma crystallization history, and shortly after the olivine they involve, and were later brought to shallower depths.

As for the green cored clinopyroxenes, the fact that the most of them plot in the high pressure field comes to reinforce the possibility of their derivation from crystallization in a deeper conduit or chamber. Also, the majority of the analysis in rims and mantles plots well into the low pressure field, as a result of their more superficial origin. This indicates that the more evolved green cores crystallized at higher depths than their more primitive rims.

Intrusive granular rocks plot mostly in the low pressure field (fig. 6.18b), as expected due to their relatively shallow intrusion depth.

Some of the clinopyroxenes from the more evolved Montelevar and Paço d'Ilhas sills, Monchique syenites and a few samples from the Sintra gabbro plot in the high pressure field, but this is likely to be a consequence of their higher SiO_2 content which means that most of the Al present in their structure will be in octahedral coordination (Al^{vi}) since most of the tetrahedral positions will be occupied by Si, which will consequently generate higher Al^{vi}/Al^{iv} ratios.

Several clinopyroxenes from the xenoliths also plot in the higher P field which is another indication of crystallization at higher pressures, as was the case with the green cored clinopyroxenes.

The positive correlation for Ti and Al_{iv} (a.p.f.u.) is an indicator of the importance of the $(Mg, Fe^{2+})^{M1} + 2Si^{T} \rightarrow Ti^{M1} + 2Al^{T}$ (Ti-Tschermakite) substitutions in the evolution of the series (fig. 6.19). This substitution is common in the more SiO_2 undersaturated magmas given that the crystallizing clinopyroxenes incorporate more Ti and Al in order to compensate for the lower Si contents.

The matrix crystals, normally zoned phenocrysts and the rims of the green cored clinopyroxenes present in basic porphyritic rocks show Al_{iv}/Ti ratios of approximately 3 (fig. 6.19d), as do most of the gabbroic rocks in the intrusive complexes. The green cores and the clinopyroxenes in the xenoliths, as well as the Monchique nepheline

syenite show a different evolution trend, characterized by values closer to 4 for this same ratio (fig. 6.19d), since they contain less Ti.

The more evolved magmas, such as the ones represented by the Montelevar sill and Monchique nepheline syenite (fig. 6.19b), crystallized clinopyroxenes with higher Al_{iv}/Ti contents, similar to those shown by some of the green cores on clinopyroxenes in basic porphyritic rocks and by some of the pyroxenes in xenoliths as well, although the latter can show both higher Ti and Al contents.

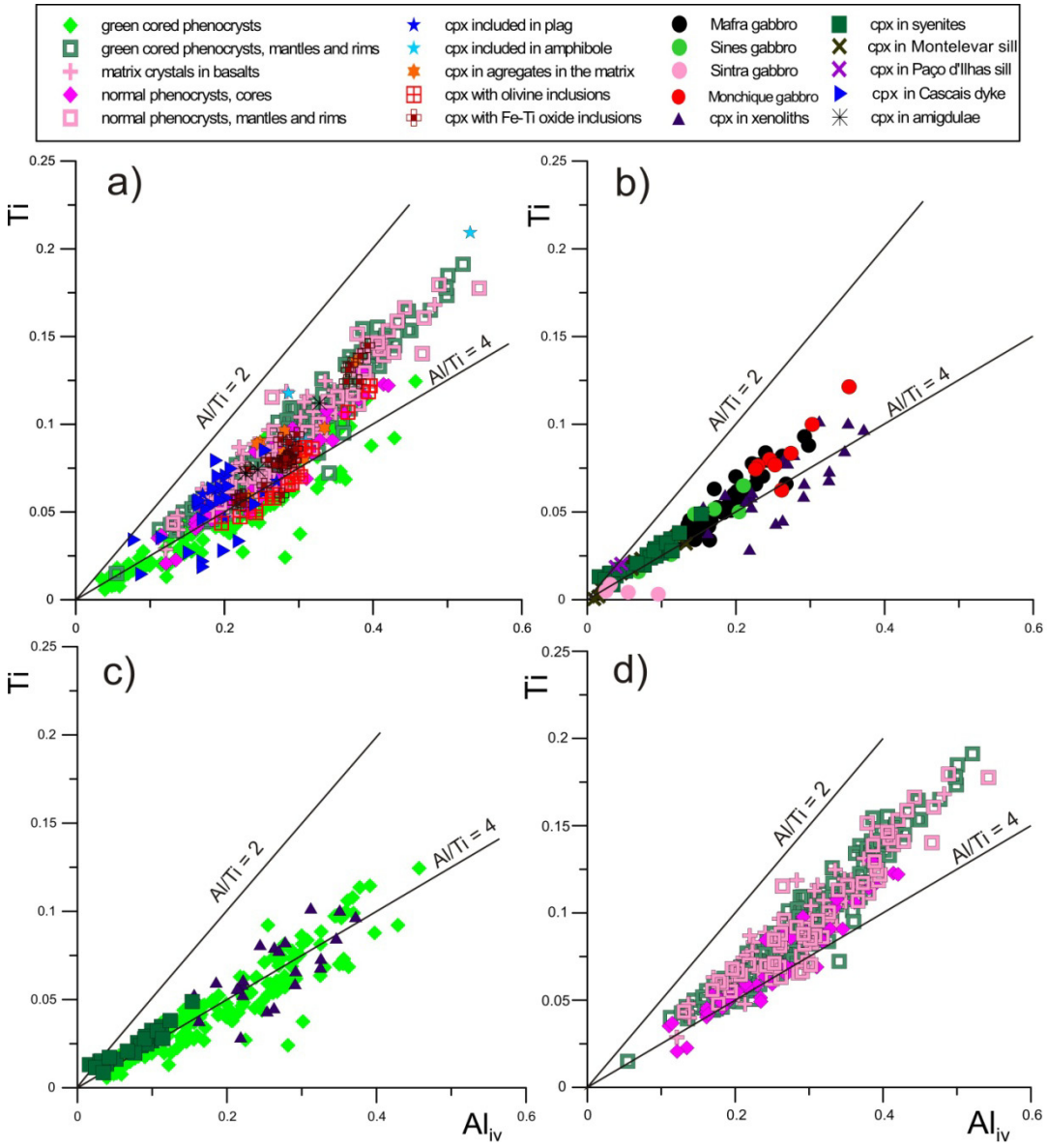

Fig. 6.19: Variation of the amounts of Ti with Al_{iv} (a.p.f.u.) for all the analyzed samples: a) all clinopyroxenes present in basic porphyritic rocks; b) all clinopyroxenes in granular intrusive rocks; c) green cores of reversely zoned clinopyroxenes, pyroxenes in the Monchique nepheline syenite and xenoliths; d) normally zoned clinopyroxenes and rims and mantles of the reversely zoned clinopyroxenes in the basic porphyritic rocks.

Lower Al/Ti ratios have also been related to high pressure crystallization conditions (Thompson, 1974). Given this, the lower Al/Ti in the green cores compared with their rims points (fig. 6.19c,d) towards the existence of two separate phases of mineral formation: an initial crystallization phase at high pressure, when the cores formed, and a second one at lower pressure during which the more primitive rims and mantles formed, which is in agreement with the information obtained from the Al_{iv} vs Al_{vi} diagram. Magma mixing and high pressure crystallization will be discussed in further detail in section 6.2.6, integrating data from other mineral phases present in these rocks.

Given that the Al_{iv}/Ti ratio is almost always higher than 2 (fig. 6.19), other kind of substitutions must take place in the clinopyroxenes in order to maintain the charge balance.

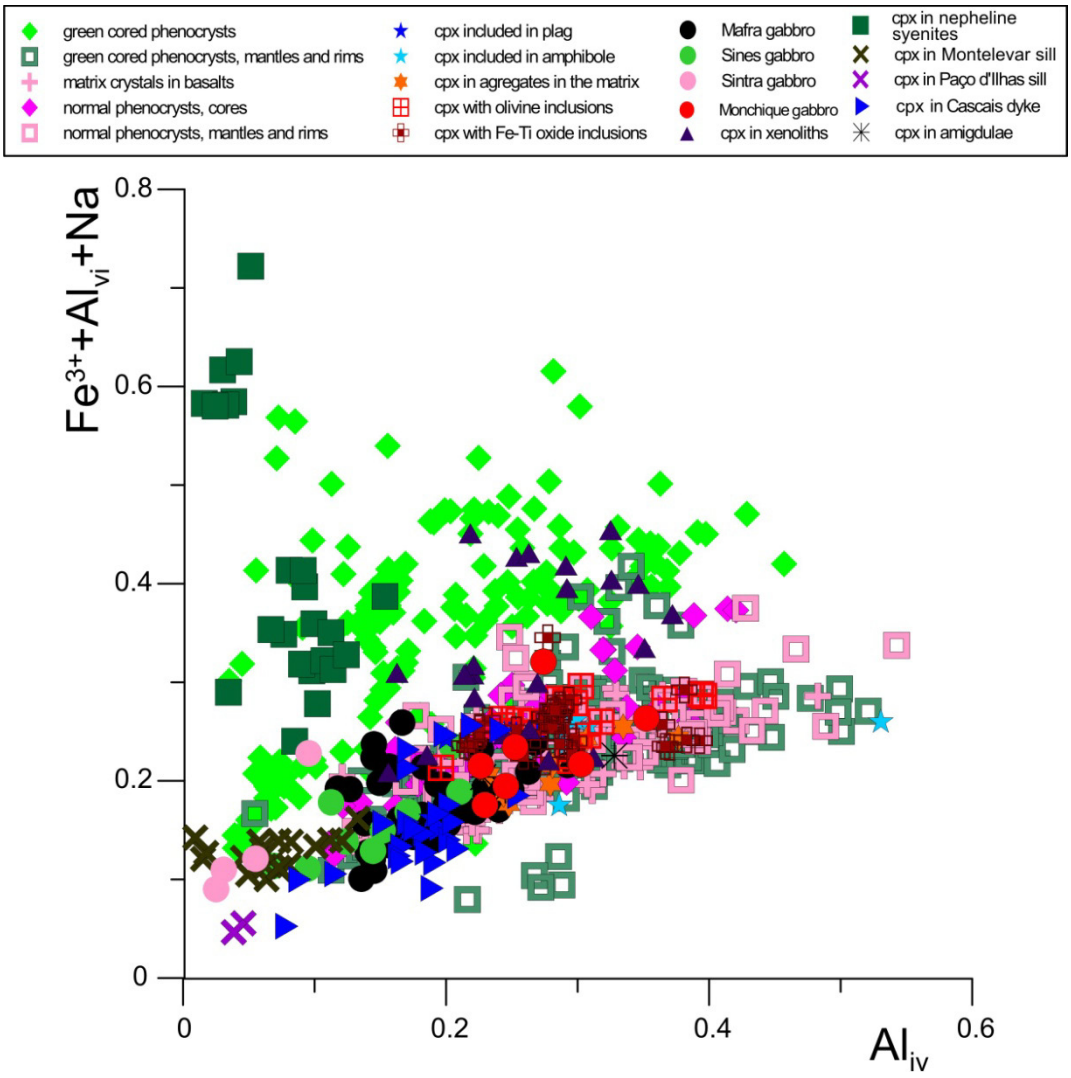

Fig. 6.20: Variation of the amounts of Fe^{3+}+Al_{vi} +Na with Al_{iv} (a.p.f.u.) for all the analyzed samples.

As can be seen on fig. 6.20, the analyzed clinopyroxenes show relatively high values of trivalent ions Al^{3+}_{vi}, Fe^{3+} (a.p.f.u.), and also of monovalent ions such as Na^{+}, to compensate for the charge deficiency caused by the incorporation of Al^{3+} in the tetrahedral position, illustrating the importance of the $Ca^{M2} + (Mg, Fe^{2+})^{M1} + Si^{T} \rightarrow 2Na^{M2} + (Fe^{3+}, Al)^{M1} + Al^{T}$ substitutions, especially in the green cores, Monchique nepheline syenites and xenoliths, which also show the lower Al_{iv}/Ti ratios.

An effort was made to use the structural single pyroxene geobarometer developed by Nimis (1995, 1999) to try and quantify any possible differences in the crystallization depth of the different types of clinopyroxene cores, but the results yielded mostly negative pressure values, even in the clinopyroxenes that plot in the high pressure field of Wass (1979).

This may be due to the construction of this geobarometer being based on changes of unit cell and M1 volumes with pressure, which means that it can be error prone in crystals with high Fe^{3+}/Fe^{2+} values, as is the case in some of the green cores. High Fe^{3+} can lead to a change in the distribution of Fe^{2+} between the M1 and M2 sites and of Fe^{3+} in M1. This causes a change in the M1–O and M2–O bond lengths, and thus a change in the site volumes that is independent from pressure (Bindi et al., 1999). Also, the presence of water in the magma and later low pressure reequilibration of the green cores and xenoliths with the magma might have led to the lower than expected pressure values that are often equivalent to the ones obtained for the matrix crystals.

Another possible cause for the absence of results using the Nimis (1995, 1999) geobarometer is the inability to obtain an accurate, independent estimate for the crystallization temperature of the clinopyroxenes, since this is a temperature dependent geobarometer.

6.2.3 Plagioclase, feldspars and feldpathoids

The analyzed rocks contain, besides the expected plagioclase and feldspars, several types of feldspathoids like nepheline and analcime. Nepheline is present as a matrix phase in one of the lamprophyric dykes of Loulé (C-20) and as a major constituent of the Monchique nepheline syenites, while analcime was found as a matrix constituent in the basic Lomba dos Pianos and Malveira da Serra sills, in the Mafra

gabbro, the intermediate phono-tephritic Eiras do Faião and in the evolved Monchique nepheline syenites.

The structural formula for the analyzed plagioclase and feldspars was calculated in a 32 oxygens basis.

As for the feldspars and plagioclases, they can be classified and described according to the abundances of each of the terms of the three end member solid solution they form between anorthite (An - $CaAl_2Si_2O_8$) and albite (Ab - $NaAlSi_3O_8$) and orthoclase (Or – $KAlSi_3O_8$).

According to the high temperature feldspar nomenclature (e.g. Deer et al., 1966), they can be classified as either anorthite (An_{100-90}), bitownite (An_{90-70}), labradorite (An_{70-50}), andesine (An_{50-30}), oligoclase (An_{30-10}), albite (Ab_{100-90}), anorthoclase ($Ab_{90-60,}$ $Or_{<40}$), sanidine or microcline/orthoclase (Or_{40-100}), (if they crystallize at higher temperatures in volcanic rocks the term sanidine is used, while the terms microcline/ orthoclase are employed for lower temperature crystallization in intrusive rocks).

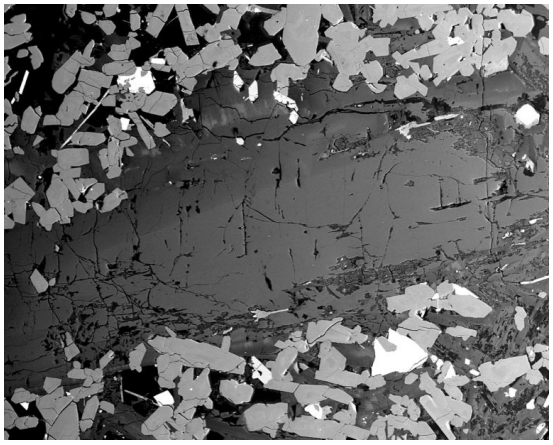

Fig. 6.21: Backscatter electron image of a rare plagioclase phenocryst surrounded by a matrix of clinopyroxene, Fe-Ti oxides and plagioclase on a sample from the Monte Serves neck of the LVC.

On the basaltic rocks, the cores in the rare plagioclase phenocrysts vary mostly between bitownite and labradorite (An_{74-50}), with their rims showing compositions within the same range. The matrix phases are mostly labradorite to andesine (An_{55-38}) in the Ribeira d'Ilhas plug and show a range from labradorite to oligoclase (An_{67-23}) in the basalts of the LVC.

The basic Lomba dos Pianos sill seems to possess two different populations of phenocrysts with cores with An_{75-65} and An_{46-52}. The rims of these phenocrysts cover a

wide compositional range, from bitownites to oligoclase (An_{73-29}) with one the phenocrysts actually being rimmed by anorthoclase ($An_5Ab_{57}Or_{39}$). The population with lower An contents might have a xenocrystic origin, since the minerals in the matrix shows higher anorthite contents (An_{68-63}) than these labradorite-andesine cores.

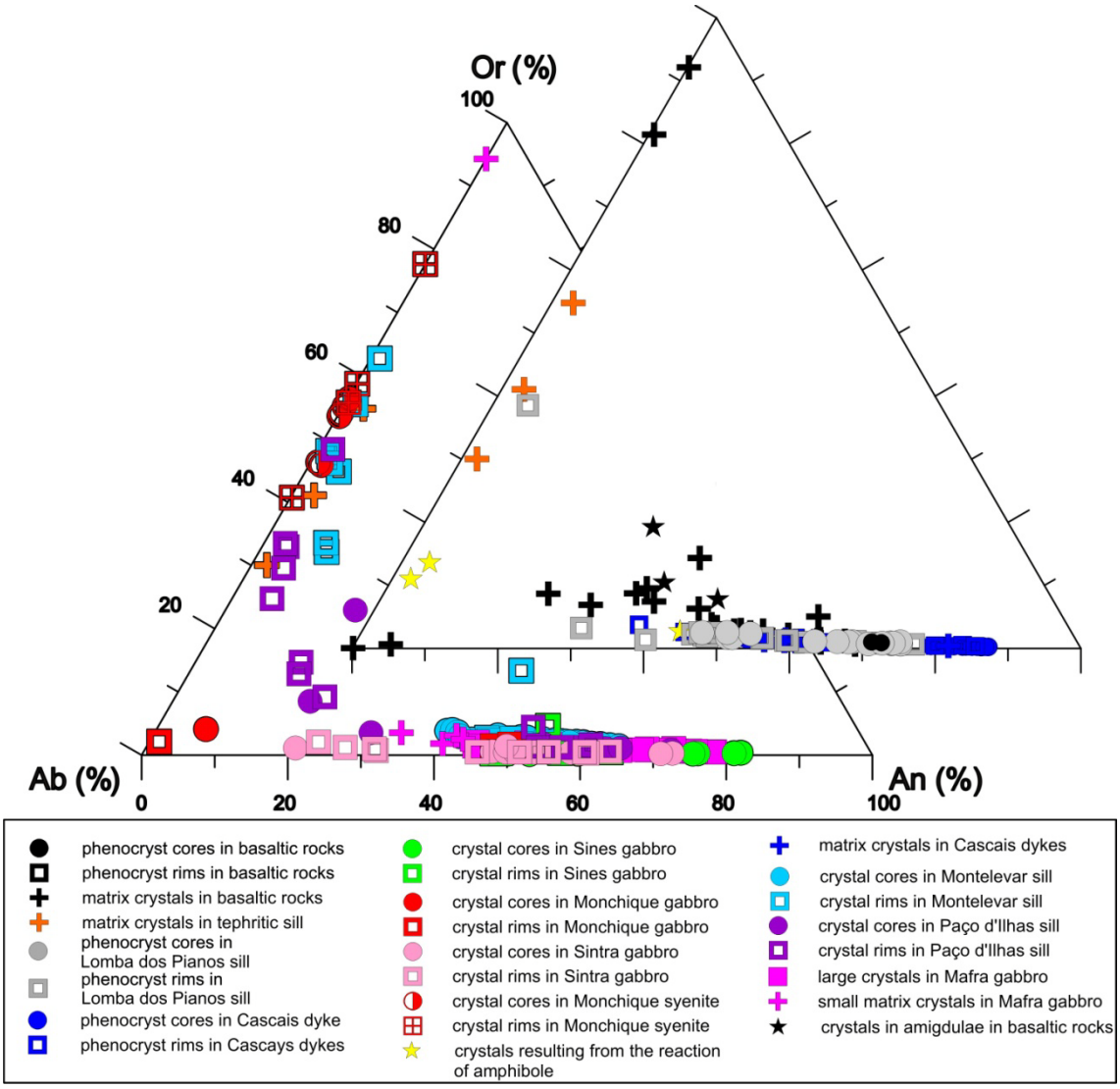

Fig. 6.22: Anorthite-albite-orthoclase (An-Ab-Or) ternary diagram showing the variability exhibited by plagioclase and feldspar crystals in the basaltic (in the front) and granular (in the background) rocks of Late Cretaceous age.

The hawaiite that forms the Cascais dyke (sample RM 90) also seems to have two different phenocryst populations, one with An contents between An_{87-82} and the other between An_{68-52}, with the rims showing a wider range of compositions (An_{79-37}), while the matrix crystals show compositions with a more reduced An_{62-56} range. This

dyke also shows the more An rich plagioclases in the entire dataset, despite being more evolved than the basaltic rocks gabbros.

The matrix crystals within the basic Malveira da Serra sill and Loulé dykes, both of which show lamprophyric affinities, range in composition from labradorite to oligoclase (An_{69-23}). Rare albite (Ab_{99-94}) was also identified as a matrix phase. Sanidine is also present in the matrix of Loulé lamprophyre C-20 (Or_{92-82}).

The crystals that occur in amygdulae in the Ribeira d'Ilhas plug are andesines (An_{46-31}), with compositions similar to the matrix crystals.

The plagioclases that form in the reaction rims of brown amphiboles in the basaltic liquid are more sodic, classifying either as andesines ($An_{44}Ab_{54}$) or anorthoclases ($An_3Ab_{86-82}Or_{14-11}$).

The phono-tephritic Eiras do Faião sill shows only alkaline feldspars (anorthoclase and microcline) in the matrix ($Ab_{68-42}Or_{55-30}$), while the mugearitic Montelevar sill shows mostly plagioclase (andesine to labradorite) cores (An_{65-40}), which can have either andesine to labradorite (An_{54-46}) or alkaline feldspar ($Ab_{58-36}Or_{63-32}$ sanidine and anorthoclase) rims.

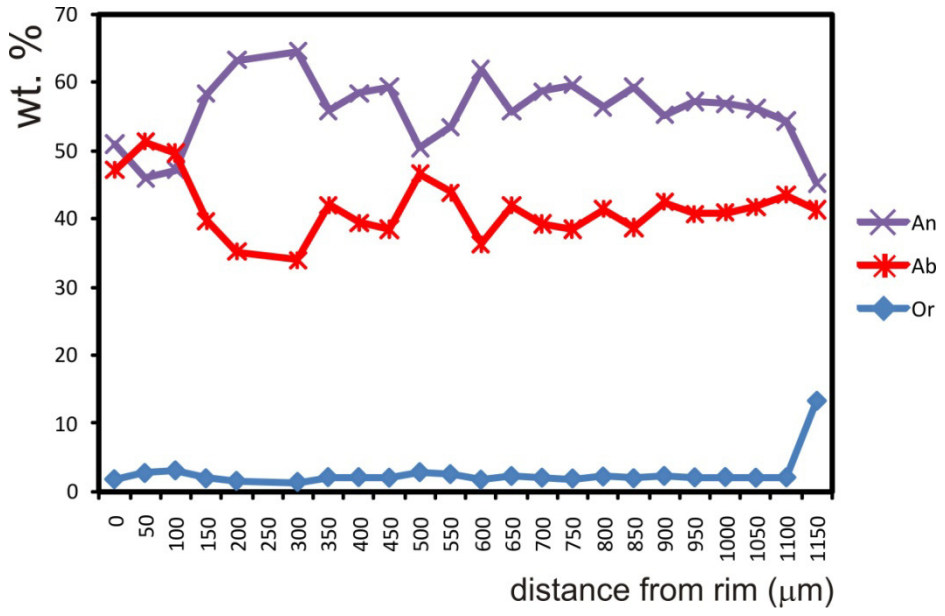

Fig. 6.23: Compositional profile across a plagioclase crystal with oscillatory zoning from the Montelevar sill.

Some of the plagioclase crystals in the Montelevar sill show oscillatory zoning, with alternating bands of more An enriched with more Ab rich layers (fig. 6.23). This

type of zoning can be produced by convection of a plagioclase crystal in a stratified magma chamber where the more evolved an more basic melts are located in different levels of the chamber, or reflect the injections of pulses of hotter, more mafic magma into a chamber of intermediate composition (e.g. Ginibre et al., 2002 and references therein). Alternatively, decompression crystallization in the sill can release latent heat which would then heat the magma and increase the An contents of plagioclase (Blundy et al., 2006).

The intermediate Paço d'Ilhas sill shows crystals with cores whose compositions vary mainly between labradorite and rarer bitownite (An_{72-51}). Also present are rare anorthoclase cores (An_{18} Ab_{59} Or_{23}). The rims of these crystals vary between labradoritic (An_{58-54}) and andesinic (An_{29-20}) and from anorthoclase (An_{15-3} Ab_{72-63} Or_{33-14}) to orthoclase/microcline (Or_{48} Ab_{50}) compositions.

The crystals from the Sintra gabbro have oligoclase (An_{27-23}), and andesine-labradorite-bitownite (An_{72-47}) cores, with their rims covering the same compositional spectrum (An_{70-20}).

In the Sines gabbros, the cores of the plagioclases range from bitownites to labradorites (An_{82-50}), while their rims are labradoritic to slightly andesinic (An_{64-48}). On the gabbroic rocks present in Monchique, both sodic ($An_{7-1}Ab_{97-89}$ albite and oligoclase) and more calcic (An_{51-47} andesine-labradorite) plagioclase cores and rims were identified. In the Monchique nepheline syenites, however, all of the analysed crystal cores and rims are K rich feldspars (Or_{77-41}).

In the Mafra gabbro the larger plagioclase crystals show compositions ranging from bitownite to andesine (An_{78-45}), while the smaller "matrix" crystals are more Na-rich andesines (An_{50-34}) or even potassic feldspar (Or_{94}).

The amount of anorthite (An) in plagioclase is related with the temperature of the magmatic system (e.g. Blundy and Wood, 1991, Bindeman et al., 1998). Also, the distribution coefficient D for a certain element in plagioclases with compositions within the An_{40-80} range is very dependent on both their An content and the crystallization temperature of the plagioclase, according to the expression below, proposed by Blundy and Wood (1991), Bindeman et al. (1998):

$$\boldsymbol{RT\ln(D) = X * An + Y}$$

where R is the gas constant (8.314 $JK^{-1}mol^{-1}$), T the temperature in K, An the molar anortite content 'X' is the slope and 'Y' the intercept in an $RT\ln(D)$ vs. An plot.

So as the An content in plagioclase is controlled by temperature and liquid composition (e.g. Blundy and Wood, 1991, Bindeman et al., 1998), and is well correlated against the MgO content of the melt (Bédard, 2006), by knowing the An content of plagioclase crystals, it is possible to estimate the MgO content of the liquid contemporary to crystallization, and afterwards estimate the temperature of the melt in a plagioclase saturated system using the following expressions (Bédard, 2006):

$$\boldsymbol{An} = \boldsymbol{X} * \boldsymbol{MgO} + \boldsymbol{Y} \text{ (for dry melts)}$$

$$\boldsymbol{An} = \boldsymbol{X} * \boldsymbol{ln}\,(\boldsymbol{MgO}) + \boldsymbol{Y} \text{ (for hydrous melts)}$$

$$\boldsymbol{T} = \frac{\mathbf{10\,000}}{(\boldsymbol{X} * \mathbf{ln}(\boldsymbol{MgO}) + \boldsymbol{Y})}$$

With An being the molar anorthite content, MgO being the melt's MgO content (in wt %) and T the temperature in ºC. X and Y are the slope and the Y axis intercept, respectively, of the fitting line for the regression of the interrelation of plagioclase An-content, melt composition and temperature, for wet and dry systems. X and Y vary according to the table below (Bédard, 2006).

Table 6.3: values for the X and Y parameters to use in the equations of Bédard (2006).

for dry melts:	**X**	X std-error	**Y**	Y std-error
MgO < 1% (T_{min})	0.50206	0.09061	0.1009	0.10362
MgO > 1%	0.04448	0.00158	0.42132	0.07065
for wet melts (T_{max})	0.10639	0.00444	0.57229	0.13285

After the melt's MgO content is estimated, it is possible to calculate the temperature of crystallization of the plagioclase crystals.

The temperatures obtained by this method in several of the analyzed rocks are displayed in table 6.4.

The highest average temperatures were obtained for the crystals with the higher An contents present as phenocrysts in the Lomba dos Pianos sill and Cascais

dyke, as well as in the cores of the crystals of the Mafra and Sines gabbro (1091, 1266, 1118 and 1068 ºC, respectively) reflecting higher crystallization temperatures for plagioclase in these magmas.

All of the analyzed matrix crystals reflect lower crystallization temperatures (880-1043ºC), as expected, since they correspond to the latest crystallizing phases in these rocks and probably formed during rapid cooling events.

Table 6.4: Temperatures obtained for the plagioclase crystals in the studied samples using the method proposed by Bédard (2006).

Sample	Location/Occurrence		An mol	T [°C] min	T [°C]	T [°C] max
RM 9	Lomba dos Pianos sill	Phenocryst cores I	70.6	963.2	1091.4	1268.4
RM 9	Lomba dos Pianos sill	Phenocryst cores II	50.5	823.0	911.4	1026.8
RM 9	Lomba dos Pianos sill	Phenocryst rims	58.0	876.5	980.3	1119.7
RM 9	Lomba dos Pianos sill	Matrix crystals	66.0	926.4	1043.3	1202.4
RM 36	Ribeira d'Ilhas plug	Matrix crystals	48.9	813.4	899.3	1011.1
RM 36	Ribeira d'Ilhas plug	Crystals in amigdulae	46.3	798.2	880.3	986.5
RM 37	Ribeira d'Ilhas plug	Matrix crystals	48.8	813.9	900.1	1012.5
RM 43	Negrais lava flow	Matrix crystals	57.6	870.2	971.4	1106.5
RM 66	Monte Serves neck	Matrix crystals	63.3	911.2	1024.5	1178.2
RM 90	Cascais dyke	Phenocryst cores I	84.8	1093.9	1266.8	1518.7
RM 90	Cascais dyke	Phenocryst cores II	61.0	892.1	999.3	1143.5
RM 90	Cascais dyke	Phenocryst rims	62.8	910.4	1024.1	1179.1
RM 90	Cascais dyke	Matrix crystals	62.3	902.5	1013.0	1162.5
RM 50	Montelevar sill	Crystals in trachyte	52.4	836.0	928.2	1049.4
PI 08	Paço d'Ilhas sill	Crystal cores	60.4	888.3	994.4	1137.0
PI 08	Paço d'Ilhas sill	Crystal rims	22.0	693.7	754.1	830.4
RM 11	Sintra gabbro	Crystal cores I	56.6	863.1	962.5	1094.7
RM 11	Sintra gabbro	Crystal cores II	25.2	695.4	754.5	828.0
RM 11	Sintra gabbro	Crystal rims	55.6	856.3	953.7	1083.0
RM 83	Mafra gabbro	Crystal cores	73.0	983.5	1118.2	1306.0
RM 83	Mafra gabbro	Crystal rims	49.9	819.9	907.5	1022.0
RM 83	Mafra gabbro	Small crystals	47.2	804.3	888.1	996.9
RM 101	Sines gabbro	Crystal cores	67.4	944.7	1068.7	1239.9
RM 101	Sines gabbro	Crystal rims	54.8	850.1	945.6	1072.0
Mon 84	Monchique gabbro	Crystal cores	50.4	820.2	910.1	1028.1
Mon 84	Monchique gabbro	Crystal rims	48.4	808.3	895.1	1008.4

T [°C] min, T [°C] T [°C] max as in table 6.3.

The intermediate Montelevar sill, Monchique, Sines and Sintra gabbros and the rims of the other intrusive rocks, all show crystallization temperatures around 900ºC, reflecting their crystallization in slowly cooling intrusive environments, which allowed for growth to take place at lower temperatures.

The temperatures obtained for the phenocrysts cores II of the Lomba dos Pianos sill and Cascais dykes are lower (911 and 1000ºC) than the ones obtained for the rims, type I phenocrysts and even matrix crystals (1043 and 1013ºC), reinforcing the idea that these might be xenocrysts incorporated into the magma or have resulted from the mixing of a more evolved, cooler magma, with a hotter and more primitive melt.

The existence of crystal cores with different An contents, and the consequent variation in crystallization temperatures obtained in the plagioclases of the Sintra gabbro, however, might be caused by different processes, such as secondary crystallization of more albite rich plagioclase during hydrothermal alteration, or the absence of the sampling of all the intermediate plagioclase compositions during analysis.

As for the feldpathoids present and analyzed in these rocks, they include analcite in the matrix of the Eiras do Faião, Lomba dos Pianos and Malveira da Serra sills, in the Mafra gabbro and in the Monchique nepheline syenite.

Table 6.5: representative analysis of the feldspathoids present in alkaline rocks from the WIM

mineral	analcite	analcite	nepheline	nepheline
occurrence	Lomba dos Pianos sill	Malveira da Serra sill	Loulé dyke	Monchique nepheline sienyte
type	matrix	matrix	matrix	crystal core
SiO_2	57.78	56.61	39.93	46.41
TiO_2	0.00	0.02	0.00	0.04
Al_2O_3	22.98	23.00	33.17	30.65
FeO	0.04	0.13	0.20	0.59
MgO	0.00	0.00	0.00	0.00
CaO	0.31	0.63	0.18	0.25
Na_2O	12.97	12.90	24.72	15.93
K_2O	0.03	0.03	0.00	5.14
SrO	0.00	0.00	0.00	0.00
BaO	0.01	0.00	0.00	0.00
Total	94.13	93.30	98.20	99.00

Nepheline was analyzed in the matrix of the Loulé lamprophyre C20 and in the Monchique nepheline syenite.

Representative analyses of these two minerals are displayed in table 6.5.

6.2.4 Amphibole

In the studied rocks amphiboles can occur as normally or reversely (fig. 6.24a) zoned phenocrysts rocks or more rarely as matrix components in basic porphyritic rocks. They are often a major constituent of gabbroic rocks, where they poikilitically involve the other mineral phases. They are also a major component in the xenoliths and can be found as large xenocrysts in basaltic plugs and flows, often showing signs of destabilization and dehydration (fig. 6.24b).

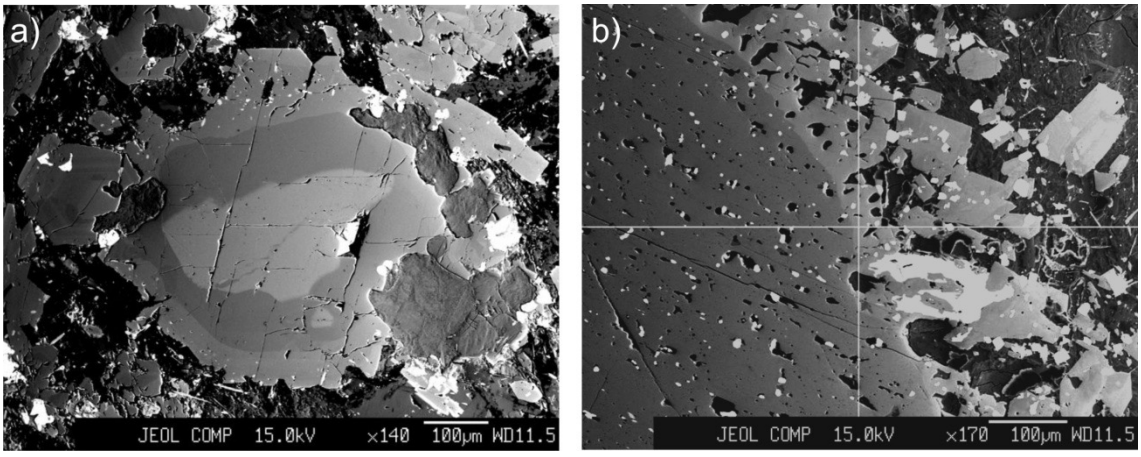

Fig. 6.24: Backscatter electron image of amphibole phenocrysts. a) amphibole phenocrysts showing reverse zoning in the Malveira da Serra sill (RM 25); b) amphibole xenocryst showing a reaction rim of clinopyroxene and several oxide and sulphide inclusions on the Ribeira d'Ilhas plug (RM 36).

The structural formula for the analyzed amphiboles was calculated on an anhydrous base, with 13 cations, including Ca, K and Na.

These minerals are relatively homogenous in terms of composition and classify as calcic amphiboles (hornblendes, *s.l.*), namely pargasites and more frequently as kaersutites (Leake, 1997; fig 6.25).

The pargasites occur in many of the analyzed types, such as crystals in the Sintra gabbro, the cores in the phenocrysts in the basic Malveira da Serra sill and Fontanelas seamount lavas, but also as xenocrysts reacting with the host magma in the Ribeira d'Ilhas basaltic (*s.l.*) plug.

Two green amphiboles formed by late hydrothermal alteration from the Sintra gabbro classify as magnesio-hornblendes (Na+K < 0.5) and are clearly not related to the remaining analyzed suite (fig. 6.25).

Also noticeable in fig. 6.25 is that amphiboles from the Sintra gabbro seem to show systematically lower contents in Ca and Na+K and higher Si and Fe (a.p.f.u.) that the remaining analyzed amphiboles.

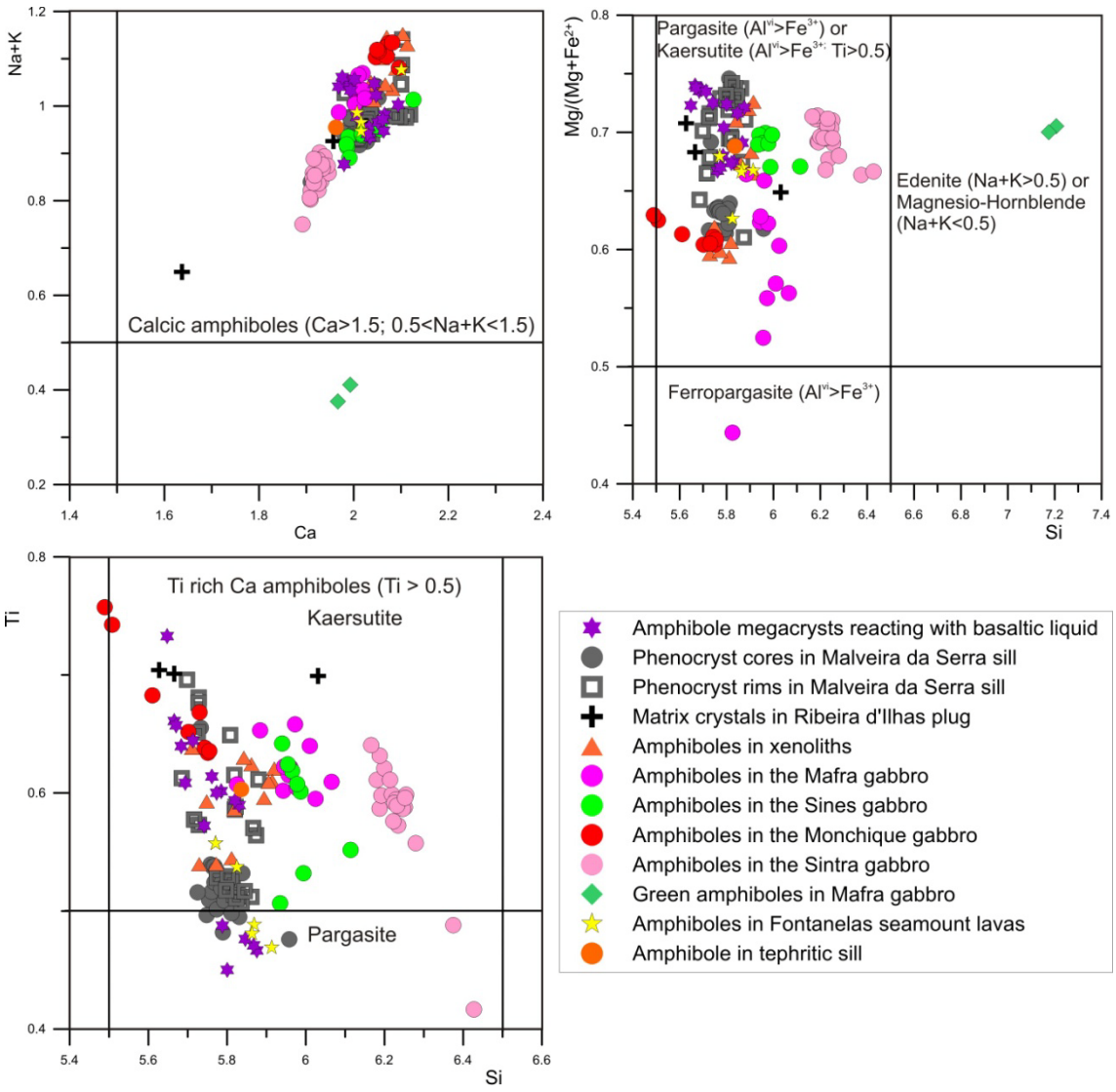

Fig. 6.25: Amphibole classification diagrams according to Leake et al. (1997).

Amphiboles in the other gabbros show relatively homogenous compositions within each gabbro, with the ones in the Mafra and Monchique gabbro being more evolved, rich in K_2O, TiO_2, FeO and MnO and poorer in MgO and Na_2O than the amphiboles in the Sines gabbro. By comparison, amphiboles from the Sintra gabbro

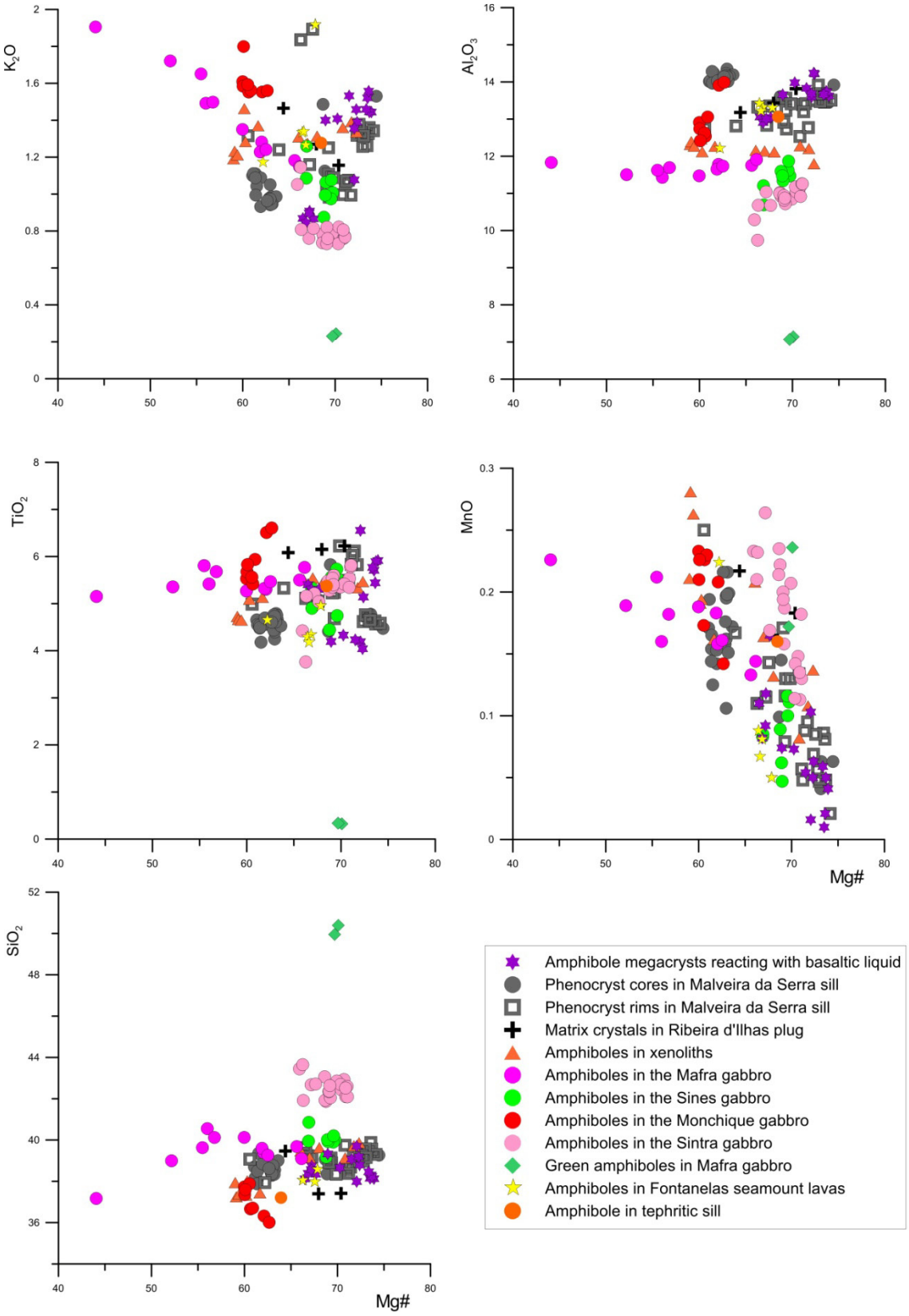

Fig. 6.26: K_2O, Al_2O_3, TiO_2, MnO, SiO_2 content variation with Mg# in the amphiboles present in the intrusive rocks.

show systematically lower contents in CaO, Al_2O_3 and K_2O and higher SiO_2 and FeO than the remaining analyzed amphiboles, thus they appear to have formed from a different, more evolved magma, enriched in SiO_2 and FeO but with less abundant alkali and TiO_2 contents.

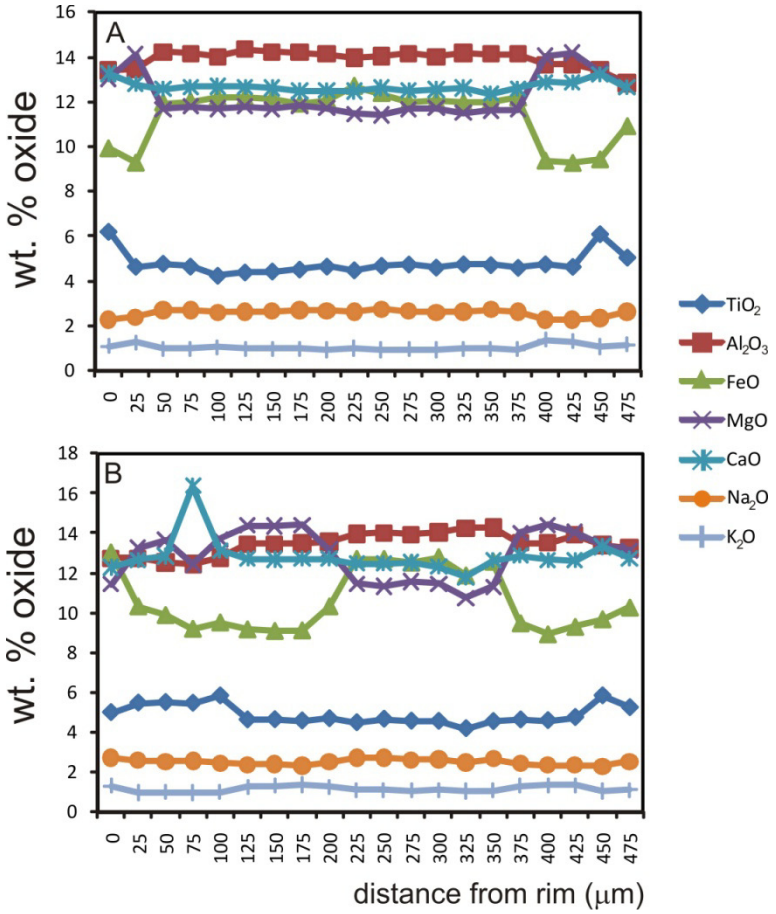

Fig. 6.27: Representative compositional profiles across reversely zoned (A and B) amphiboles from the Malveira da Serra sill (RM 25).

The differences in amphibole composition between gabbros do not mirror the differences in the abundance of the same elements in the whole rock geochemistry of these rocks, so they should reflect either late crystallization and growth, possibly from a residual intercumulus liquid, or accumulation of crystals forming from an evolving melt within a magma chamber. These hypotheses would render the composition of the whole rock analysis unrepresentative of the liquid from which the amphiboles formed.

Two types of cores can be identified in the amphiboles from the Malveira da Serra sill (figs. 6.26 and 6.27). One is more FeO, Na_2O, Al_2O_3 and MnO rich, but MgO, TiO_2 and K_2O poor than the other.

The more MgO rich cores correspond to normally zoned amphibole phenocrysts while the MgO poor cores belong to reversely zoned amphiboles as can be observed in the profiles shown in fig. 6.27. Reversely zoned clinopyroxenes were also identified in this sill (see 6.2.3 in this section).

In the normally zoned crystals, the rims show lower MgO, but are enriched in TiO_2, K_2O, FeO and Na_2O relative to the core, a trend also observed in clinopyroxenes and compatible with the progressive crystallization and removal of olivine.

In the reversely zoned crystals, the rim first shows a lighter brown color and a more MgO, and TiO_2 rich and Al_2O_3, MnO and FeO depleted composition. As one progresses towards the dark brown core, there is an abrupt change to lower MgO and TiO_2 values and higher FeO, MnO and Al_2O_3 contents (fig. 6.27), concurrent with the normal evolution trends shown by a basic magma experiencing fractional crystallization.

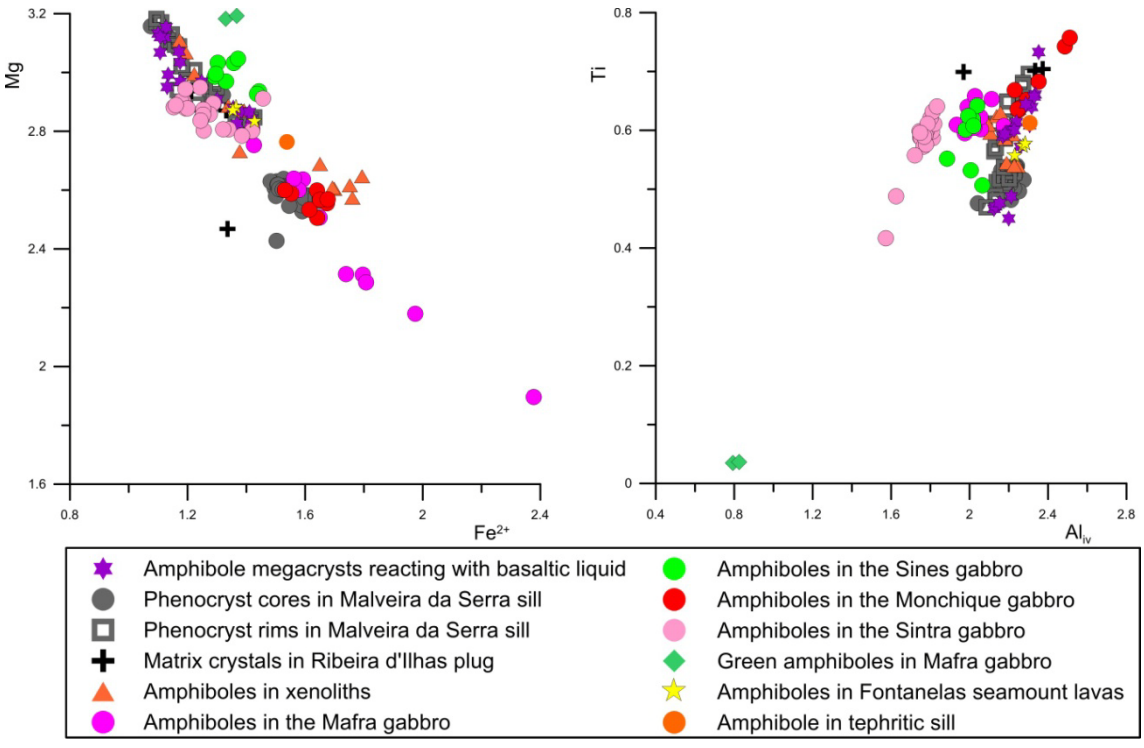

Fig. 6.28: K_2O, Al_2O_3, TiO_2, MnO, SiO_2 content variation with Mg# in the amphiboles present in the intrusive rocks.

The reverse zonation seen on some of the amphiboles from the Malveira da Serra sill, together with the same kind of zonation observed in clinopyroxenes in this and other intrusions, argues again for the existence of magma mixing and homogenization between a more evolved and a more primitive liquid at depth, prior to the installation of this sill.

Amphiboles from the Fontanelas seamount show compositions similar to the ones found in other porphyritic basic rocks.

The xenocrysts that reacted with the basaltic melt and developing reaction rims of clinopyroxene, oxides and sometimes plagioclase (see fig. 6.1 and section 6.1 for more details) show compositions similar to the rims and cores of the normally zoned phenocrysts in the Malveira da Serra sill. This sill corresponds to an intrusive basic rock where amphibole appears to be stable, but where it also shows evidence for the existence magma mixing previous to installation at upper crustal depths. This suggests that the development of the reaction rims in amphiboles discussed in section 6.1.12 might be attributed to decompression and dehydration of the amphiboles, associated to the devolatilization of the magma, rather than to magma mixing.

The amphibole xenocrysts show small differences in composition among themselves, namely in terms of K_2O and MgO contents. The retrograding amphiboles in the Lomba dos Pianos sill show the lowest MgO and K_2O values, and the ones in the Negrais flow have the highest MgO and K_2O contents, while the crystals in the Ribeira d'Ilhas plug have intermediate compositions between these two. These heterogeneities are probably a result of the crystallization of these minerals from magmas with slightly different compositions and degrees of evolution.

The xenoliths show amphiboles with a range of compositions that overlap either the gabbros or the cores of reversely zoned amphiboles from the Malveira da Serra sill, implying formation from a liquid with similar characteristics.

The more common types of substitutions in these rocks seem to be simple Mg for Fe^{2+} and Ti for Mg or Fe^{2+} in the octahedral position (fig. 6.28) and also Al for Si in the tetrahedral position if Ti is incorportated in M1, indicating important coupled Ti-tschermakite substitution ($(Mg, Fe^{2+})^{M1} + 2Si^{T} \rightarrow Ti^{M1} + 2Al^{T}$), similarly to what what was observed for the clinopyroxenes.

The amphibole-plagioclase geothermometer for silica undersaturated rocks developed by Holland and Blundy (1994) was applied to the studied rocks where mineral chemistry data was available for plagioclase and amphibole pairs occurring in equilibrium. Since this geothermometer is pressure dependent and no pressure estimate is available for the crystallization of these amphiboles, the temperatures were calculated using pressures of 1, 2, 5 and 10 kbar. The expression that yields the equilibrium temperature between amphibole and plagioclase is:

$$T = \frac{7.78 + Y_{ab-an} - 33.6X_{Na}^{M4} - (66.8 - 2.92P) * X_{Al}^{M2} + 78.5X_{Al}^{T1} + 9.4X_{Na}^{A}}{0.0721 - R * \ln\left(\frac{27 * X_{Na}^{M4} * X_{Si}^{T1} * X_{an}^{plag}}{64 * X_{Ca}^{M4} * X_{Al}^{T1} * X_{ab}^{plag}}\right)}$$

where T is the temperature in Kelvin, P is the pressure in kbar, the X_i^n terms represent the molar fraction of a species (or component) *i* in phase (or crystallographic site) *n*, and $Y_{ab\text{-}an}$ = 3 kJ if $X_{ab} > 0.5$, or $Y_{ab\text{-}an} = 12*(2X_{ab}-1)+3$ kJ if $X_{ab} < 0.5$.

Table 6.6: Temperatures obtained for the amphibole-plagioclase pair using the Holland and Blundy (1994) geothermometer.

				P= 1 kbar	P= 2 kbar	P= 5 kbar	P= 10 kbar
Occurrence	Sample	type of amphibole	type of plagioclase	T ° C	T ° C	T ° C	T ° C
Lomba dos Pianos sill	RM 9	reacting amphiboles	An rich plagioclase phenocrysts	1000.0	1001.8	1007.1	1015.9
Ribeira d'Ilhas plug	RM 36	rim of reacting amphiboles	matrix crystals	900.6	904.0	914.0	930.8
Ribeira d'Ilhas plug	RM 36	crystals in amigdulae	crystals in amigdulae	883.8	887.0	896.4	912.1
Mafra gabbro	RM 83	poikiltic amphibole	plagioclase rims	1011.3	1011.9	1013.9	1017.3
Mafra gabbro	RM 83	amphibole rims	matrix crystals	932.9	933.4	934.8	937.2
Sines gabbro	RM 101	amphiboles surrounding cpx	plagioclase cores	1034.3	1034.2	1033.9	1033.4
Sines gabbro	RM 101	amphiboles surrounding cpx	plagioclase rims	990.4	990.3	990.0	989.6
Monchique gabbro	Mon 84	amphibole cores	plagioclase cores	997.8	998.0	998.3	998.9
Monchique gabbro	Mon 84	amphibole rims	plagioclase rims	978.5	979.0	980.5	983.1
Sintra gabbro	RM 11	amphibole cores	plagioclase cores	910.6	912.6	918.4	928.0
Sintra gabbro	RM 11	amphibole rims	plagioclase rims	882.1	884.2	890.6	901.3
Sintra gabbro	RM 11	green amphiboles	plagioclase rims	630.4	636.5	654.8	685.2

The results are shown in table 6.6. In the intrusive rocks, the higher temperatures were obtained for the Sines, Mafra, and Monchique gabbros (1030-980 ºC at 1 kbar) and the basic Lomba dos Pianos sill (≈1000 ºC, assuming both the amphiboles and plagioclase phenocrysts crystallized in equilibrium), than in the Sintra gabbro (910-880 ºC at 1 kbar) and in the Ribeira d'Ilhas basaltic plug (900-800 ºC at 1 kbar).

The amphiboles are a late phase in many of the gabbros, since they envelop most of the other minerals present in these rocks, so these low crystallization temperatures were expected. Even lower temperatures were obtained for the Ribeira d'Ilhas plug since the amphiboles in this rock occur in amigdulae and represent the crystallization products of the last remaining fraction of melt.

The late hydrothermal green amphiboles in the Sintra gabbro show the lowest crystallization temperatures (≈ 630 ºC), supporting the hypothesis that they formed in secondary, subsolidus conditions after the crystallization of the remaining assemblage.

Amphibole geobarometry using Al in amphibole geobarometers was not applicable to these samples since they are calibrated for silica saturated magmas (e.g. Hollister et al., 1987; Johnson and Rutherford, 1989; Schmidt, 1992; Anderson and Smith, 1995) where Al incorporation in amphibole is controlled by pressure, while in silica undersaturated rocks such as these, the Al contents in amphibole are also dependent in the availability of Si.

6.2.5 Oxides

The majority of the oxides present in basic igneous rocks are Fe-Ti oxides, along with rare Cr spinel.

The structural formula for the spinels (magnetite, chromite and ulvospinel) was calculated in a 32 oxygens basis, while for the ilmenites these were calculated on a 6 oxygens basis.

The results obtained for these analyses are displayed in ternary diagrams in accordance to their TiO_2, FeO and Fe_2O_3 abundances (fig. 6.30). Also represented are the lines corresponding to the high temperature hematite (Fe_2O_3)-ilmenite($FeTiO_3$), and

magnetite(Fe_3O_4)-ulvospinel(Fe_2TiO_4) solid solutions defined by Buddington and Lindsley (1964).

Most of the analyzed samples are titanomagnetites and plot close to the line that defines the magnetite-ulvospinel solid solution (fig. 6.30), indicating they contain significant amounts of Ti and variable quantities of Fe^{2+} and Fe^{3+}. This high abundance of titanomagnetite and the relative scarcity of magnetite-ilmenite exsolution features in the oxides present in the basic porphyritic rocks argue for rapid cooling of most of these magmas.

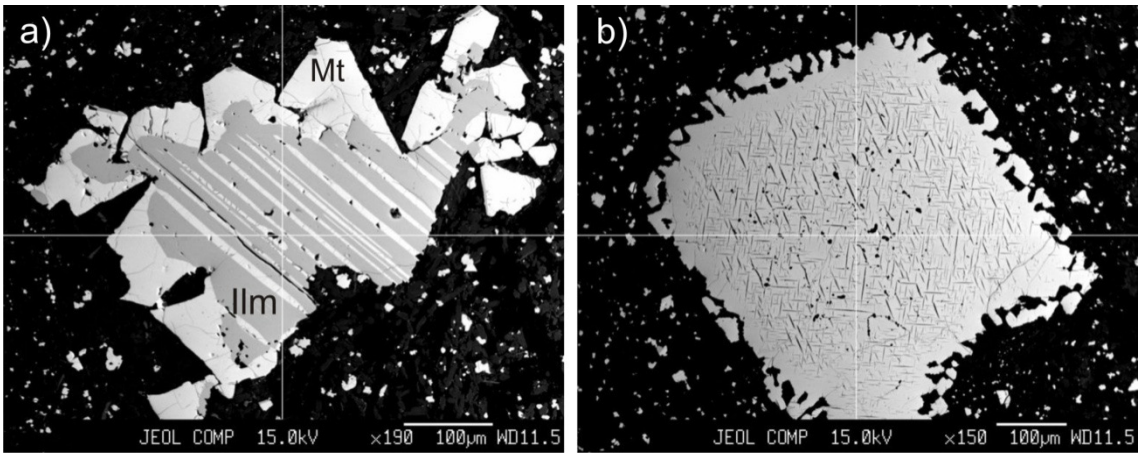

Fig. 6.29: backscatter electron images of: a) crystal of ilmenite (darker) showing magnetite exsolution and rim; b) exsolution of pleonaste (black rods) and ilmenite from magnetite, in the Negrais flow (RM 43).

In the studied samples, ilmenites are, in general, much rarer than Ti-magnetites and occur either as exsolution lamellae in magnetite (e.g. fig. 6.29) or more rarely as isolated crystals in the silica saturated sills (Paço d'Ilhas and Montelevar).

The scarcity of ilmenite is a common situation in silica undersaturated rocks, since their low silica activity ($\boldsymbol{a_{SiO2}}$) favours the incorporation of Ti in clinopyroxenes, forming Clinopyroxene and inhibiting the formation of ilmenite (Verhoogen, 1962), whose crystallization is also strongly dependent on the magma's TiO_2 content (e.g. Toplis and Carrol, 1995). According to Charmichael et al. (1974) and Mata and Munhá (2004), the reactions that expresses the control of $\boldsymbol{a_{SiO2}}$and $\boldsymbol{a_{TiO2}}$ over the formation of these minerals are:

$$2FeTiO_3 + 2\ CaAl_2Si_2O_8 \leftrightarrow 2CaTiAl_2O_6 + Fe_2SiO_4 + 3SiO_2$$

ilmenite plagioclase pyroxene olivine silica

$$2FeTiO_3 + Fe_2SiO_4 \leftrightarrow 2Fe_2TiO_4 + SiO_2$$

ilmenite olivine spinel melt

On silica undersaturated melts, the reaction will progress towards the end members in the right. If silica is added to the system increasing $\boldsymbol{a_{SiO2}}$, then the reaction products will be driven to the left end member. Consequently, the presence of ilmenite in the SiO_2 saturated sills is likely to be an effect of addition of silica to the system, probably as a consequence of assimilation of SiO_2 rich crustal lithologies.

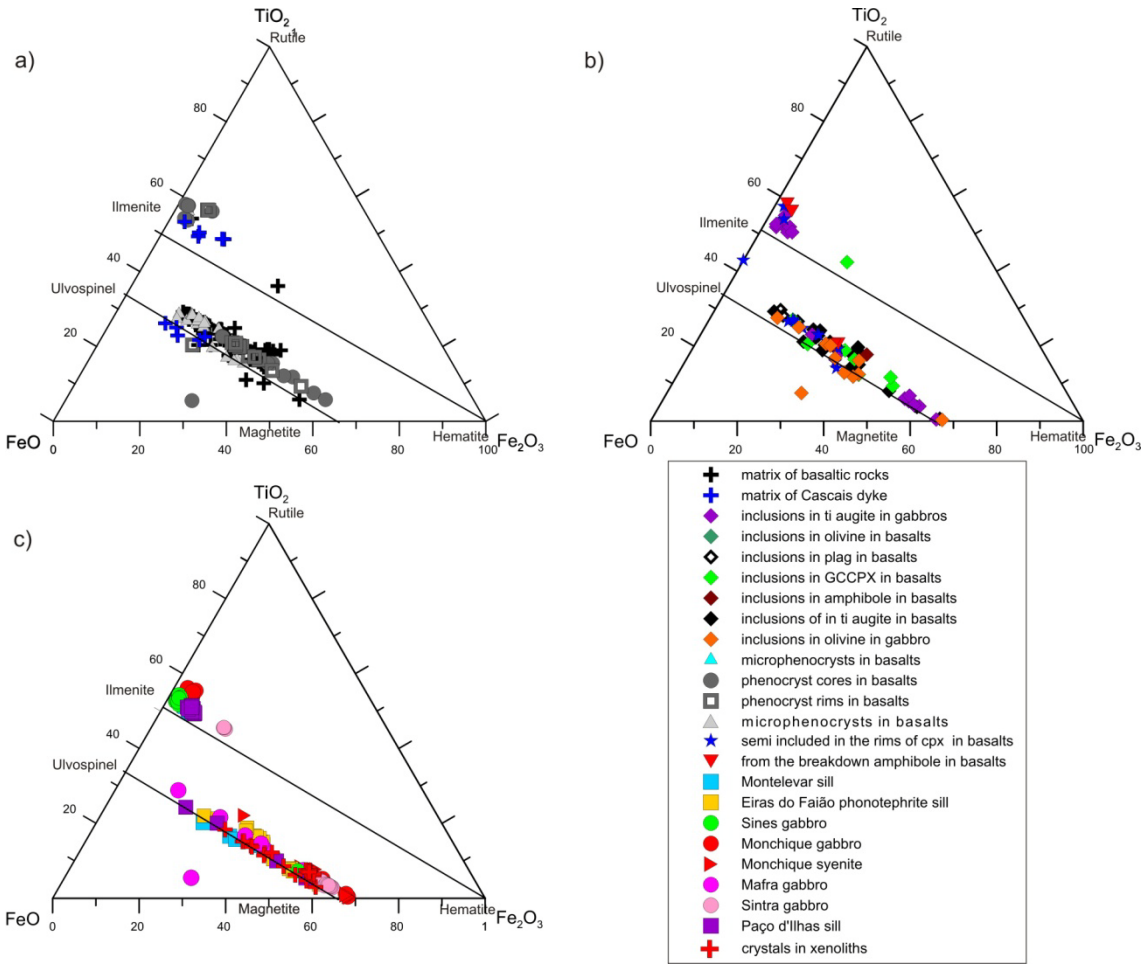

Fig. 6.30: Ternary diagram showing the analyzed oxide samples from: a) basic porphyritic rocks; b) inclusions in minerals, breakdown of amphiboles in basaltic rocks and; c) from the granular intrusives. Lines representing the high temperature (1300 ºC, 1 atm) magnetite-ulvospinel and hematite-ilmenite solid solutions from Buddington and Lindsley (1964).

Chromite and chromian titanomagnetite were also identified and analyzed. They occur more frequently as inclusions in olivines, but can also be found as matrix crystals in the basaltic Ribeira d'Ilhas plug and as one of the opaque phases present in the Mafra

gabbro. Chromites have 16-35% Cr_2O_3, 10-18% Al_2O_3 and 3.5-10.4% MgO. Chromian titanomagnetites (Cr_2O_3 7-13%; Al_2O_3 5-19%; TiO_2 8-16%) are rare but can be found as matrix crystals and phenocrysts (total of 4 analyses) in basic porphyritic rocks.

In the basic porphyritic rocks (fig. 6.30a), phenocrysts, microphenocrysts and matrix crystals mostly plot in the magnetite-ulvospinel solid solution line, and are therefore mainly titanomagnetites (TiO_2 35-6 %). Exsolution between titanomagnetite and ilmenite was observed in some phenocrysts as can be observed in fig. 6.29.

Ilmenite can occur sporadically as a matrix phase in these rocks, but it is always associated with titanomagnetite exsolution.

The oxide inclusions present in the silicate minerals of the basic porphyritic rocks (fig. 6.30b) display compositions similar to the matrix and phenocrystic phases, corresponding mostly to titanomagnetites (TiO_2 5-24 %), but in some cases ilmenites and magnetites resulting from the exsolution of titanomagnetite were also identified.

The types of oxide inclusions observed in silicated minerals are listed below:

- The majority of the analyzed chromian spinels (Cr_2O_3 7-35%; Al_2O_3 5-18%) occur as inclusions in olivine, but can also be found in Clinopyroxene, meaning that this was one of the first phases to crystallize and to be removed from the melt.
- Inclusions in olivines found in basalts and gabbros have mostly Cr-rich (7-35%) spinel inclusions although some titanomagnetites and magnetites can also be observed in olivines from the Sines gabbro (fig. 6.30c), that have the lowest forsterite contents of all the analyzed olivines (Fo < 70%).
- Plagioclases have Ti-rich titanomagnetite inclusions while the ones present in amphibole are more Fe^{3+} rich.
- The minerals found partially included in the rims of clinopyroxene crystals are titanomagnetites and have compositions that are very similar to the oxides found in the matrix.
- Within the same reaction rim, the oxides that result from the reaction of amphibole with the host magma are either ilmenites or titanomagnetites, suggesting that the amphiboles break down to two distinct oxide phases, one accommodating mostly FeO and some TiO_2 and the other contains higher amounts of both Fe_2O_3 and TiO_2. This suggests variable oxygen fugacity conditions during amphibole breakdown.

- Green cored clinopyroxenes and the Paço d'Ilhas sill have the more Fe_2O_3 rich titanomagnetite inclusions, with the former even showing one inclusion with Fe^{3+} rich ilmenite.

While the oxides present in the basic porphyritic rocks are mostly titanomagnetites, the ones present in the gabbros can be either titanomagnetites or crystals containing magnetite with exsolved ilmenite lamellae. These exsolved crystals are substantially more common in the intrusives (Sintra, Sines and Monchique gabbros, Paço d'Ilhas sill, fig. 6.30c), since slower cooling facilitates this process.

The Monchique and Sines gabbros show predominantly magnetites and ilmenites, indicating slow cooling conditions.

The Mafra gabbro has two different oxide phases, one with a larger size with chromium spinel cores (Cr_2O_3 > 30%) and titanomagnetite rims, and a smaller one made out exclusively of titanomagnetite.

Ilmenites and magnetites from the Sintra gabbro are the more Fe_2O_3 rich of the oxides present in the gabbroic rocks, indicating equilibration with more oxidizing conditions.

The phonotephritic Eiras do Faião sill shows more or less Ti rich titanomagnetites (3-20%) while in the intermediate Montelevar sill the oxide phases are both titanomagnetite and ilmenite, with the titanomagnetite (TiO_2 13.6-18.1 %) sometimes exsolving from the ilmenite. The intermediate Paço d'Ilhas sill shows both titanomagnetite and ilmenite crystals, with exsolution features present in some of them.

The Monchique nepheline syenites show only magnetites and titanomagnetites (TiO_2 3-20 %) and hence must have formed from a more Ti depleted liquid.

The Fe-Ti oxides present in the xenoliths (fig. 6.30c) are Fe^{3+} rich magnetites and titanomagnetites, which is in accordance with crystallization from a more oxidated and evolved melt.

According to experimental work (Hill and Roeder, 1974) and empirical observations (e.g. Mata and Munhá, 2004), the existence of spinels with a compositional spectrum ranging from chromite to chromian titanomagnetite and titanomagnetite in the basic porphyritic rocks suggests that crystallization took place under relatively high oxygen fugacity (fO_2) conditions, at least above the NNO (Ni-Ni oxide) buffer.

These relatively high oxygen fugacity conditions detected in the earlier spinels, suggests that the oxidizing conditions might have been inherited from a mantle source that had been previously metasomatized by an oxidizing agent (e.g. Mata and Munhá, 2004).

It is usually agreed that during magmatic evolution, the minerals from the ulvospinel-magnetite solid solution should show a trend in the direction of Fe^{3+}enrichment and Ti depletion with increasing differentiation, in response to falling temperature (e.g. Charmichael et al., 1974; Haggerty, 1976). However, in the studied basaltic porphyritic rock this does not seem to be the case, with the later phases such as matrix crystals, microphenocrysts and inclusions in plagioclase showing higher TiO_2 contents that earlier phases like the phenocryst cores (fig 6.30).

This trend can be the result of the progressive decrease of the oxygen fugacity conditions with increasing differentiation (Mata, 1996). At higher fugacities the reaction below will form the products on the right, meaning that Fe-rich spinels will crystallize incorporating a large portion of the available Fe^{3+}.As fO_2 and temperature decrease and TiO_2 concentrations in the melt increase, the Ti-rich ulvospinel molecule will enter the spinel's structure in higher amounts since there is less available Fe^{3+} and D_{Ti} increases with decreasing temperatures (Mata, 1996; Mata and Munhá, 2004).

$$\underset{\text{ulvospinel}}{3Fe_2TiO_4} + \underset{\text{gas}}{O_2} \leftrightarrow \underset{\text{magnetite}}{2Fe_3O_4} + \underset{\text{magma}}{3TiO_2}$$

$$\underset{\text{plagioclase}}{CaAl_2Si_2O_8} + \underset{\text{spinel}}{2Fe_3O_4} + \underset{\text{melt}}{2TiO_2} \leftrightarrow \underset{\text{pyroxene}}{CaTiAl_2O_6} + \underset{\text{olivine}}{Fe_2SiO_4} + \underset{\text{spinel}}{Fe_2TiO_4} + \underset{\text{melt}}{O_2}$$

Oxygen fugacity measures the chemical potential of oxygen in the form of adjusted pressure. It relates to the redox conditions of the magmas, which at a fixed T are more oxidizing at higher fugacities, and more reducing at lower fugacities. The variation of oxygen fugacity conditions with temperature can be described using redox buffers, which correspond to assemblages of minerals or compounds that constrain oxygen fugacity as a function of temperature.

Oxygen fugacities (expressed as log fO_2) and blocking temperatures of equilibration for the rocks that showed magnetite-ilmenite pairs were calculated applying the ILMAT program by Lepage (2003) that uses the geothermobarometer of

Andersen and Lindsley (1985) with the Mol % of ulvospinel and ilmenite being calculated according to Lindsley and Spencer (1982).

The results are compiled in table 6.7 and fig. 6.31 and show log fO_2 values varying between -27.7 in the basaltic Negrais lava flow and -13.10 in the Sintra gabbro with the accompanying blocking temperatures ranging from 500ºC in the Negrais flow plug to 850ºC in the Ribeira d'Ilhas basaltic plug.

Table 6.7: oxygen fugacities and blocking temperatures obtained for the magnetite-ilmenite pairs in the studied rocks using the ILMAT software (Lepage, 2003) and the geothermobarometer of Andersen and Lindsley (1985)

Sample		Mol Ulv %	Mol Ilm %	temp (ºC)	log fO_2
RM43 zoned phenocryst	Negrais flow	55.52	98.06	565.48	-24.23
RM43 zoned phenocryst	Negrais flow	54.28	98.64	499.63	-27.72
RM43 zoned phenocryst	Negrais flow	54.47	97.88	581.28	-23.45
RM43 rim of amphibole	Negrais flow	54.04	97.86	582.39	-23.39
RM36 rim of amphibole	Ribeira d'Ilhas plug	53.55	92.85	850.44	-13.83
RM50 zoned crystal	Montelevar sill	57.10	95.43	762.81	-16.57
RM50 zoned crystal	Montelevar sill	41.62	93.25	776.46	-15.30
RM101 zoned crystal	Sines gabbro	21.08	98.10	542.62	-25.02
RM101 zoned crystal	Sines gabbro	15.98	97.95	546.38	-24.60
RM101 zoned crystal	Sines gabbro	14.69	96.84	594.55	-21.59
RM101 zoned crystal	Sines gabbro	14.69	97.65	559.94	-23.66
MON84 zoned crystal	Monchique gabbro	1.50	94.95	546.46	-20.45
MON84 zoned crystal	Monchique gabbro	3.39	95.01	582.09	-19.85
MON84 zoned crystal	Monchique gabbro	14.67	95.38	640.41	-19.11
RM 11 zoned crystal	Sintra gabbro	12.0	83.3	768.33	-13.16
RM 11 zoned crystal	Sintra gabbro	13.6	83.5	776.52	-13.10
RM 11 zoned crystal	Sintra gabbro	10.8	82.9	762.31	-13.20
RM 11 zoned crystal	Sintra gabbro	8.2	83.5	741.06	-13.52
RM 11 zoned crystal	Sintra gabbro	9.0	83.6	746.83	-13.46

Most of the samples plot along the FMQ (fayalite-magnetite-quartz) and NNO redox buffers, or below the previous. The most oxidizing conditions appear to have occurred in the Sintra gabbro, which shows higher fugacities than the NNO buffer, and to a lesser degree in the Montelevar sill and Monchique gabbro, while the more reducing conditions were recorded in the LVC and Sines gabbros.

The more oxidizing conditions detected in the Sintra gabbro agree with the more Fe_2O_3 rich contents of their magnetites and ilmenites and could be related to subsolidus equilibration during a secondary alteration phase in more oxidizing conditions. However, the high temperature of equilibrium is not in agreement with this hypothesis, since it is≈ 100º C higher than the one obtained for the crystallization of secondary amphibole.

Blocking temperatures for the LVC lava flows are surprisingly low, both in the phenocrysts and the matrix, indicating slow cooling in the sampled basal flow, probably as a result of covering and isolation from rapid cooling by subsequent lava flows of the LVC's lava pile.

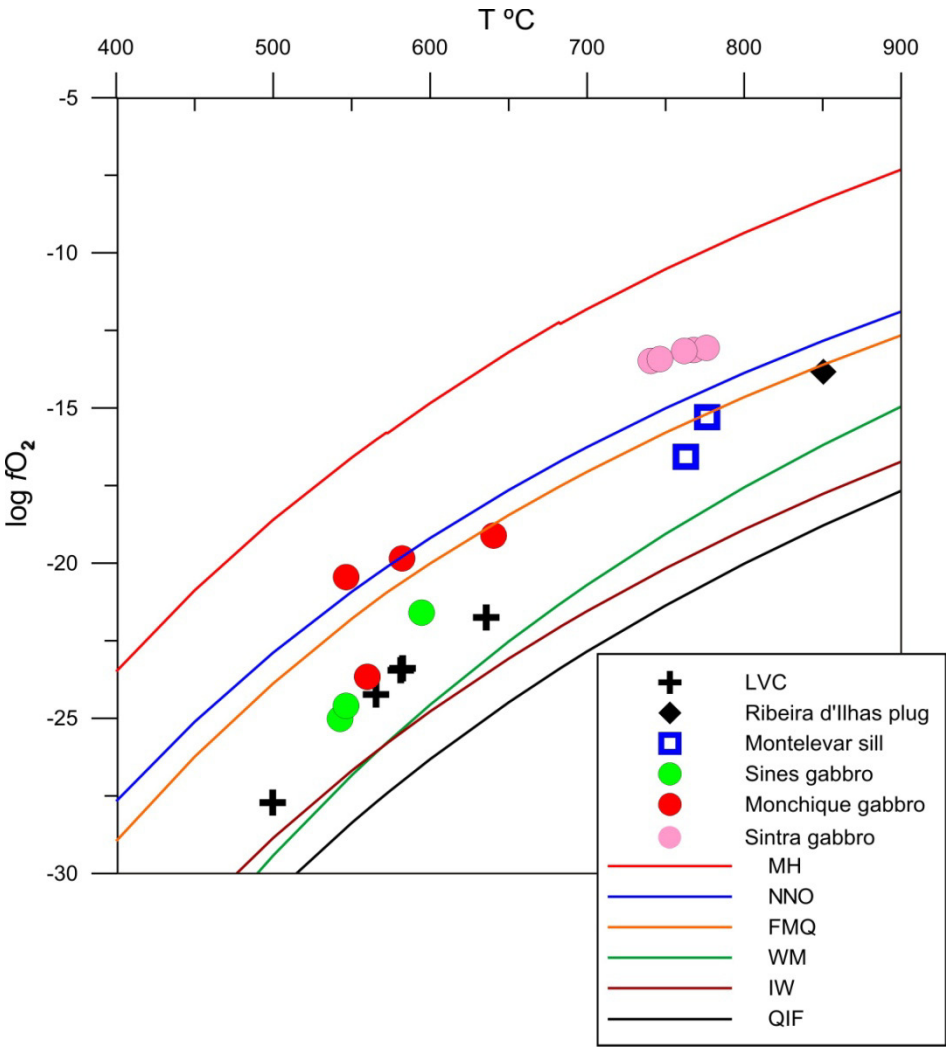

Fig. 6.31: Log oxygen fugacity vs. temperature at 1 bar pressure for the analyzed samples and common buffer assemblages, plotted from algorithms (Frost in Lindsley, ed., 1991) (MH, magnetite-hematite; NNO, Nickel-nickel oxide; FMQ, fayalite-magnetite-quartz; WM, wustite-magnetite; IW, iron-wustite; QIF, quartz-iron-fayalite)

Equilibrium temperatures for the formation of the magnetite-ilmenite pairs in the reaction rims of amphiboles in the Negrais flow and Ribeira d'Ilhas plug are quite low, with the amphiboles in the Negrais flow showing the lowest value. This may be caused by later subsolidus equilibration in the Negrais flow, or correspond to a primary feature, with the reactions in amphibole in the Negrais flow taking place at lower temperatures than the ones in the Ribeira d'Ilhas plug.

The higher blocking temperatures for the intermediate Montelevar sill and basaltic Ribeira d'Ilhas plug are likely a result of faster cooling in these relatively thinner intrusives, when compared to the Sines and Monchique igneous complexes and even to the LVC's lava pile.

In general, most of the blocking temperatures are quite low, which indicates that the formation of magnetite from ilmenite probably took place during subsolidus oxidation, by exsolution of a previously existing homogenous phase (titanomagnetite), which is supported by the observation of trellis lamellae in many of the exsolved crystals (e.g. fig. 6.29).

6.2.6 Micas

Brown to reddish micas are present in a small fraction of the analyzed rocks, occurring mostly as phenocrysts in one of the lamprophyric Loulé dykes, as an accessory phase in the matrix of the Eiras do Faião phonotephritic sill, in the Monchique syenites and the Sintra gabbro and even more infrequently in the basaltic rocks.

The structural formula for the analyzed micas was calculated on an anhydrous base, with 22 oxygens.

Most of the analyzed micas are Mg rich phlogopites with the exception of the micas in the Monchique nepheline syenite, the two more Fe rich rims in one of the phenocrysts in the Loulé lamprophyre, and one crystal in the Eiras do Faião phonotephrite and Paço d'Ilhas sills that are classified as biotites.

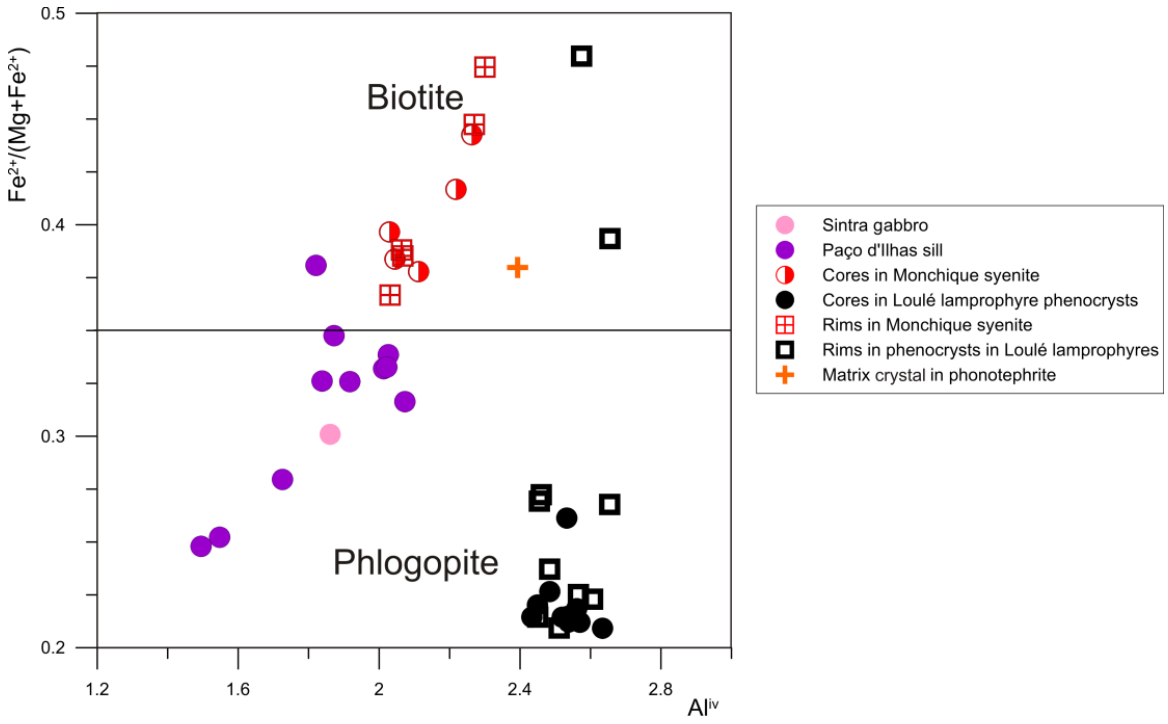

Fig. 6.32: classification of the mica minerals, according to Rieder et al., (1998).

The crystals in the nepheline syenites usually form a compositionally separate group that is more FeO, MnO, K_2O and F rich, indicating crystallization from a more evolved liquid. Meanwhile, the remaining analyzed crystals formed from more basic magmas are enriched in MgO, TiO_2, BaO and Na_2O (fig. 6.33) relative to the ones found in the nepheline syenites.

Mica compositions in the studied rocks seem to show a tendency for a progressive TiO_2, Na_2O, BaO and Al_2O_3 decrease and a K_2O, and MnO increase with decreasing Mg#, i.e. with increasing differentiation (fig. 6.33).

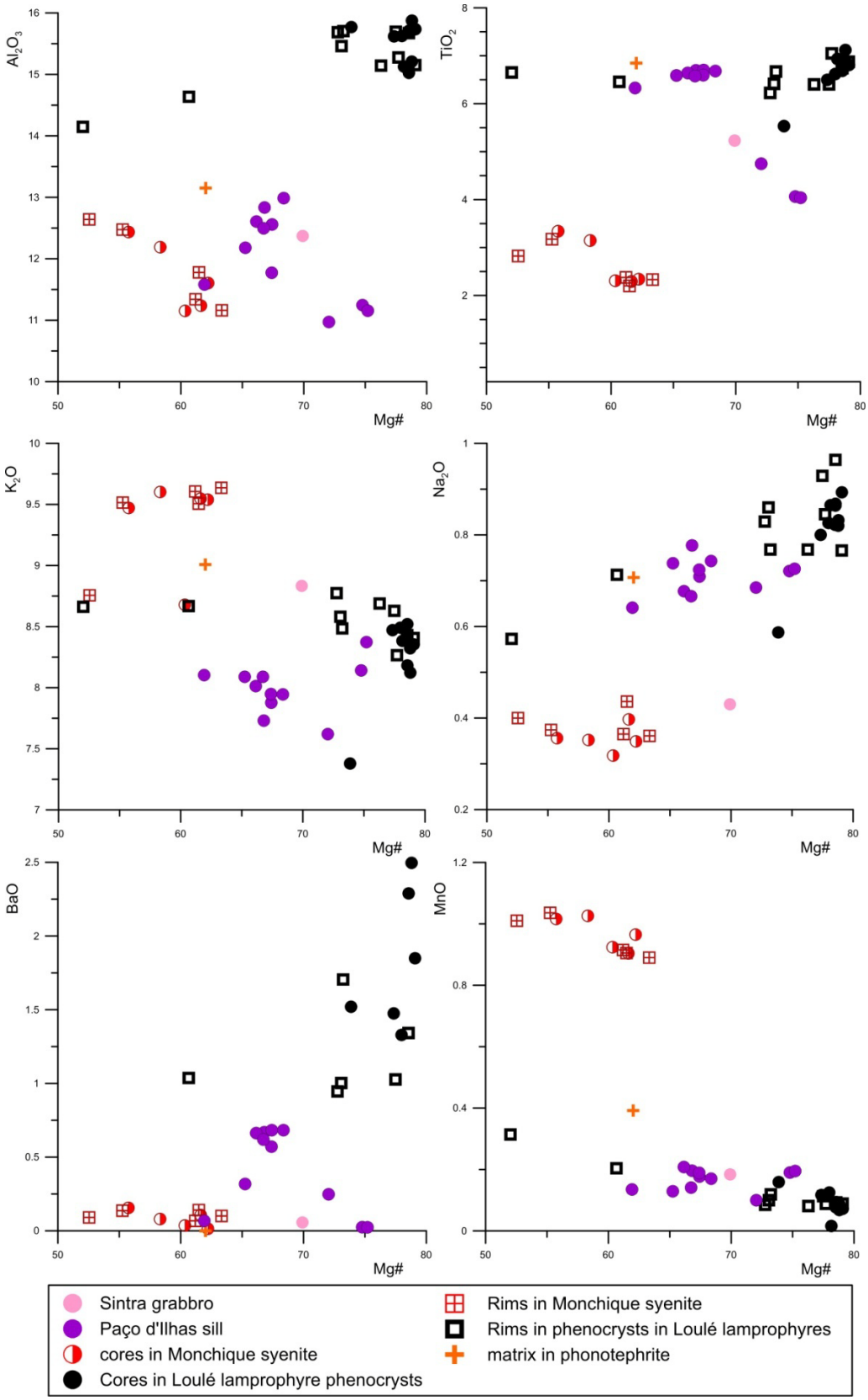

Fig. 6.33: Al_2O_3, TiO_2, K_2O, Na_2O, BaO and MnO variation with Mg# for the analyzed micas.

6.2.7 Summary and discussion

From the mineral chemistry data described above, it is possible to make several inferences concerning the processes responsible for the evolution and differentiation of the alkaline magmas of the WIM.

Using the geothermometers of Roeder and Emslie (1979) and Beattie (1993), the olivine saturation was calculated to have occurred at temperatures between 1250 and 1150 ºC, for the Ribeira d'Ilhas plug and Negrais lava flow, respectively.

The precipitation and removal of olivine led to the decrease of Mg and Ni and an increase of FeO^t in the residual melt, which is reflected in the crystallization sequence of the olivines.

The decreasing amounts of CaO and MnO in the olivines with increasing Fa contents are associated to the onset of the crystallization of clinopyroxene, plagioclase and possibly Fe-Ti oxides.

The importance of crystal accumulation processes in the genesis of some of the alkaline rocks of the WIM was reinforced by the observation that for some of the studied samples (e.g. Sines and Mafra gabbros), their $\boldsymbol{Kd}^{\boldsymbol{ol-liq}}_{\boldsymbol{Fe/Mg}}$ value did not reflect equilibrium between the composition of the olivines and the rock where they were included. Therefore, the whole rock compositions of these occurrences cannot be considered as representatives of the liquids from which the olivines precipitated.

In general, the clinopyroxene compositions evolve towards terms that are more enriched in FeO and Na_2O, while becoming progressively depleted in MgO. At around Mg# < 70 the TiO_2 and Al_2O_3 contents of clinopyroxenes start to decrease, probably due to decreasing contents in the melt caused by onset of crystallization and removal of titanomagnetite and plagioclase.

Clinopyroxene phenocrysts often show reverse zoning, with the cores possibly crystallizing at higher pressures (see fig. 6.18), suggesting the mixture between a more evolved and a more basic magma at depth, both of alkaline nature and thus possibly genetically related (e.g. Duda and Schminke, 1985; Dobosi, 1989; Dobosi and Fodor, 1992; Pilet et al., 2002).

Plagioclase and feldspars predictably evolve from more An rich compositions in the more basic rocks to more Ab and Or rich terms in the more siliceous lithologies.

The studied plagioclases appear to have crystallized between approximately 1200º C, for the terms richer in An, and 800 ºC, for the crystals poorer in An (see table 6.4). However, it must be emphasized that the highest obtained temperatures (T_{max}) are likely to overestimate the crystallization temperatures for plagioclase since these are higher than some of the olivine saturation temperatures and olivine is one of the first crystallizing phases in the studied rocks (see 6.1.12).

Some of the basic porphyritic rocks contain two distinct plagioclase core populations in their phenocrysts. One showing higher An contents in the cores than in the rims, while the other can show lower amounts of anorthitic in the core molecule than its rim and even the matrix phases.

The most common oxides present in the rocks of the WIM are titanomagnetites that coexist with less abundant early chromian spinels (chromites and chromian titanomagnetites) as well as ilmenites and magnetites, most of which resulting from the exsolution of titanomagnetites.

The oxygen fugacities and blocking temperatures calculated for the magnetite-ilmenite pairs in these rocks suggest that in most cases these went through later subsolidus equilibration and exsolution at temperatures around 500-650º C. The obtained fO_2 values point towards conditions close to the NNO and FMQ buffers. These data are in accordance with fO_2 contemporaneous of the crystallization of chromite in the LVC ($\log fO_2$ = -8.5 at 1200ºC) as calculated by D'Orey and Palácios (1986).

The Sintra gabbro shows the more oxidating conditions of all the studied occurrences, with fO_2 values above the FMQ buffer, which is in agreement with the results obtained by Palácios et al. (1995) for this complex. This intrusive complex also shows widespread signs for late hydrothermal subsolidus alteration, namely the presence of secondary low temperature amphibole, feldspar, chlorite and epidote, which might have led the ilmenites and magnetites to reequilibrate under more oxidizing conditions.

The Fe-Ti oxides present in the xenoliths are mostly Fe^{3+}-rich titanomagnetites that show a compositional range indicative of crystallization from a relatively evolved and oxidized melt. Also, their composition is similar to the one shown in the oxides that occur as inclusions in the green cores of clinopyroxenes, pointing to a common origin.

The amphiboles present in the sampled rocks are mainly Ti rich kaersutites and pargasites. They appear as late phases that envelop earlier clinopyroxenes, oxides,

apatites and other crystals, as normally or reversely zoned phenocrysts, seldom as matrix phases and more rarely as xenocrysts or as a major component in the rare xenoliths.

The equilibrium temperatures for the amphibole-plagioclase pairs in the gabbroic and volcanic rocks are between 880 and 1040º C, confirming that this equilibrium is achieved relatively late in the crystallization history of these rocks.

The compositional similarities between the minerals present in the amphibole rich xenoliths and as xenocrysts and the ones that constitute the normal crystallization products of the analyzed rock suite suggest that in some cases, some of these might have formed from a common parental melt (e.g. amphibole megacrysts), while others must have derived from a more evolved but compositionally related magma (e.g. green cores in the clinopyroxenes).

The xenoliths can therefore be interpreted as cognate aggregates resulting from in depth crystallization from a hydrated, basic to intermediate alkaline magma or alternatively, as residues of wall rock assemblages in equilibrium with a similar melt.

Kaersutite is a common phase both in the xenoliths and xenocrysts. According to experimental data, this mineral is stable at depths corresponding to the lithospheric mantle (e.g. Irving and Frey, 1984; Pilet et al., 2010) and corresponds to a *liquidus* phase between 21 and 11 kbar (Merril and Wyllie, 1975), and again at pressures under 2 kbar in hydrous basic alkaline magmas with low FeO^t/TiO_2 (Johnson et al., 1989), which is equivalent to depths of approximately 70 to 37 km and 7 km, respectively (considering an average density of 3000 kg/m^3 for the overlying crust and mantle). More recently, Irving and Green (2008) proposed that amphibole megacrysts are only stable up to 15 kbar (≈ 50 km) in hydrous basic to intermediate liquids.

Due to their larger size, monomineralic nature, ubiquitous reaction rims and reduced range in composition, showing values comparable to the ones observed in other amphibole crystals, it is implied that the kaersutite xenocrysts could represent the products of high pressure crystallization of a similar basic, hydrous alkaline melt. They precipitated as individual crystals from that melt in the interior of a deep conduit or chamber, and did not aggregate into xenoliths. As the magmas ascended and the pressure dropped, the volatiles exsolved, and the amphibole xenocrysts became unstable and started developing the observed reaction rims, as discussed in section 6.1.12.

The existence of reversely zoned clinopyroxenes, amphiboles and plagioclase supports the occurrence of magma mixing preceding the installation of the rocks that contain them.

In the case of magmas showing green cored clinopyroxenes, this mixing event must have taken place at high depths, as is indicated by the seemingly high pressure nature of these cores (fig. 6.18), when a basic magma encountered a more evolved, FeO, alkali, and P_2O_5 enriched melt from which the green cores crystallized. This resulted in the homogenization of the different melts and consequential partial resorption of the more evolved green clinopyroxenes as well as in the development of more primitive (higher Mg#) rims during magma ascension, generating their reverse zoning. The quantity of basic, primitive liquid must have been much larger than the more evolved melt it mixed with since the resulting liquid is still of ultrabasic to basic nature.

It is also possible that the observed reversely zoned amphiboles result from the same mixing process, since they occur simultaneously with the green cored clinopyroxenes in the Malveira da Serra sill, which means that this more evolved magma would also be volatile rich.

The rare reversely zoned plagioclase phenocrysts could also be the product of high pressure crystallization and later mixing with a more primitive magma, as was suggested for the plagioclase megacrysts found in basic alkaline rocks in Scotland (Upton et al., 1999, 2009).

The existence of high pressure fractionation in the LVC's magmatic plumbing system is also supported by the existence of a high pressure paragenesis in the Suímo dyke outcrop consisting of megacrysts of olivine (Fo≈ 91), amphibole, garnet (pyrope), clino and orthopyroxene and spinel (Palácios, 1985). According to Rankenburg et al. (2004) the simultaneous presence of garnet and clinopyroxene with compositions similar to the ones observed in this dyke suggests crystallization from a basic melt pressures above 21 kbar (≈ 70 km). There is, however, the possibility that this paragenesis might represent xenocrystic material from mantle peridotites.

Moreover, green cored clinopyroxenes, amphibole megacrysts, and xenoliths are often present simultaneously in the outcrops of basic porphyritic rocks from the second pulse of Late Cretaceous alkaline magmatic activity. This suggests that these might be crystallization products from the same melt from which the green cored clinopyroxenes formed. In this case, the green cores, the evolved amphibole cores and the megacrysts

would represent phases crystallizing in the middle of the chamber or conduit, while the xenoliths containing minerals with similar compositions could represent cumulus or wall rock assemblages previously crystallized from that same magma chamber (fig. 6.34), similarly to what was proposed by Marchev et al. (2006) for the same type of assemblages observed in lamprophyric dykes in the Rhodopes. The absence of olivine and plagioclase from those cumulus assemblages could be due to either incomplete sampling of the ultramafic xenoliths and/or caused by suppression of plagioclase and olivine crystallization in a hydrous magma at high pressure conditions. Such conditions greatly reduce the stability of plagioclase, olivine and garnet, leading to enhanced crystallization of calcic clinopyroxene and amphibole instead (e.g. Danyushevsky, 2001; Müntener et al., 2001).

Such magma chambers are thought to be located at the depth where ascending magmas became neutraly buoyant, which can happen in boundaries between layers with strong density contrasts, such as the crust-mantle boundary (e.g. Duda and Schmicke, 1985; Marchev et al., 2006; Davis et al., 2007) or within the lower crust, at depths corresponding to the Conrad discontinuity (e.g. Duda and Schmicke, 1985; Sachs and Hansteen, 2000). Magmas stagnated at such depth could then start to crystallize and evolve, generating the xenoliths by accumulation of crystals fractionated from a basic melt and later the green pyroxenes from a more evolved liquid that resulted from the fractionation and removal of the phases present in the xenoliths.

This evolved magma could correspond to the differentiation product of a liquid generated during an earlier pulse of alkaline magmatic activity. Both the WIM and many other continental intraplate locations where reversely zoned clinopyroxene and amphibole phenocrysts occur along with amphibole clinopiroxenite xenoliths seem to have experienced several pulses of basic alkaline activity previous to the emplacement or extrusion of the rocks that contain the reversely zoned crystals and xenoliths (e.g. Cantal lavas in the Massif Central, Pilet et al., 2002; magmatism in the Panonian Basin, Dobosi, 1989, Dobosi and Jenner, 1999; West Eiffel, Duda and Schmincke, 1985; Hocheifeld, Jung et al., 2006). It is thus suggested that the parental liquids from which the xenoliths and xenocrysts formed correspond to magmas from the earlier pulses of alkaline activity that stagnated at high depths, probably due to unfavorable stress fields that limited the propagation of conduits to the surface.

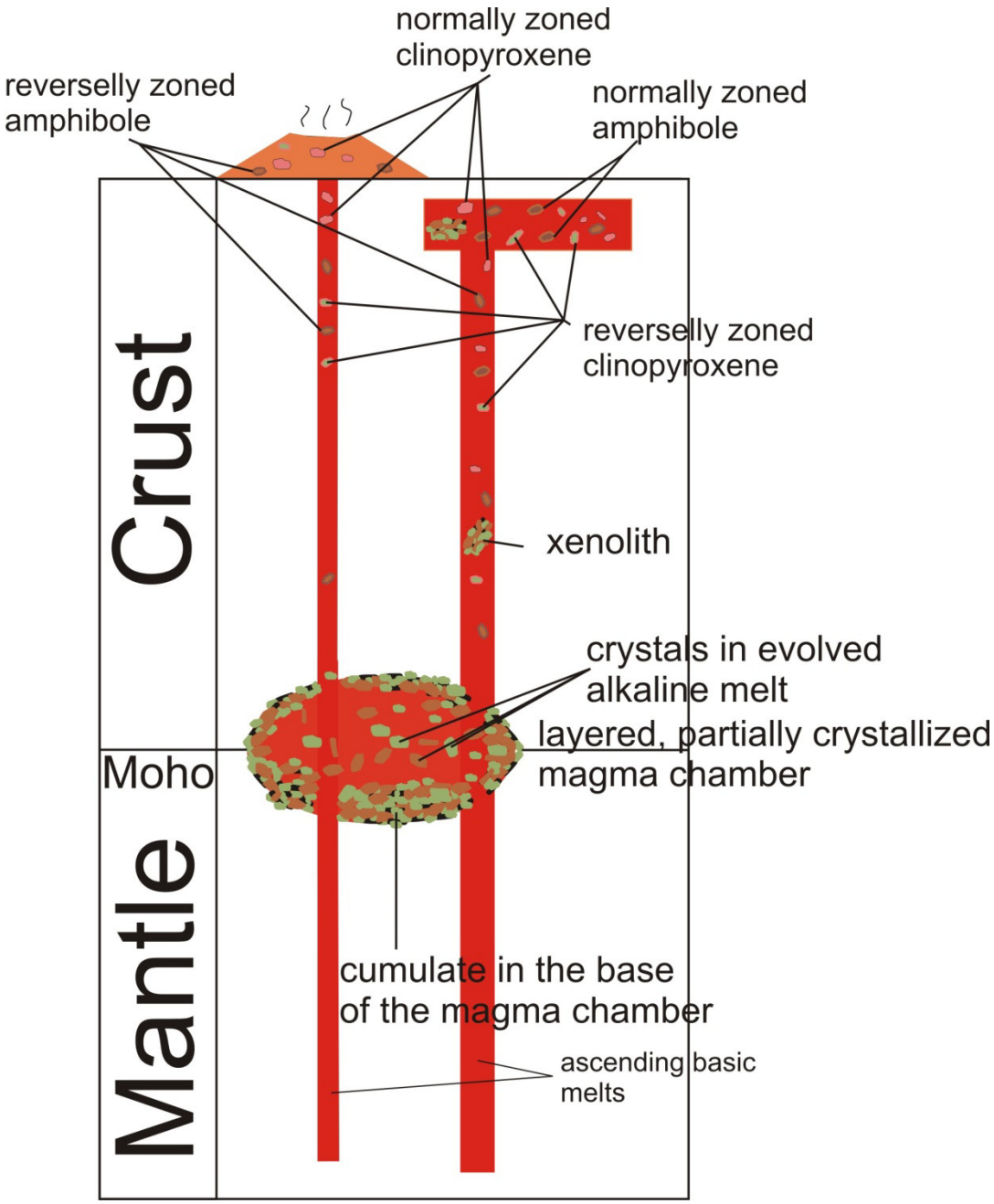

Fig. 6.34: Schematic representation of a possible mechanism for the formation of the reversely zoned crystals and xenoliths. Initial magma accumulation (first magma pulse) in a magma chamber at high depth starts to fractionate and evolve. When a second pulse of more basic magma passes through the chamber it remobilizes accumulated crystals (xenoliths) and isolated crystals that are suspended in an evolved melt. These crystals will react with the basic melt and develop rims that are more primitive than their cores, thus generating the reversely zoned crystals. Adapted from Duda and Schminke (1985).

A phonotephritic to tephrophonolitic liquid has been identified in glass inclusions found in green clinopyroxenes, titanite and Fe-Ti oxides in clinopyroxenite xenoliths (Sachs and Hansteen, 2000) that are similar to the ones found in the Late

Cretaceous alkaline rocks of the WIM and has been interpret as the parental liquid from which those xenoliths formed.

The mixing and homogenization of a basic, primitive magma with small portions of a more evolved, volatile rich liquid would lead to the formation of melt that retains its basic nature but suffered a small reduction in density and an increase in volatile content when compared with the original basic liquid. This could result in the pressurization of the system, leading to rapid ascension and installation of the magmas.

A volatile rich magma also has the potential to exsolve those volatiles during ascension and decompression, generating explosive eruptions such as the ones that happened before every effusive phase in the LVC, resulting in the formation of the pyroclastic deposits.

It is therefore suggested that the mixing of basic alkaline magmas with more evolved magmas of alkaline nature at depth could have been an important factor leading to the ascension and eruption of some of the basic alkaline magmas of the WIM.

It should be noted that some authors proposed that the xenoliths and xenocrysts containing green clinopyroxene and amphibole with composition similar to the ones present in the analyzed rocks are in fact part of disaggregated metasomatic veins present within the lithospheric mantle that formed as a result of the action of siliceous, volatile rich (CO_2 and H_2O) mantle melts (e.g. Pilet et al., 2005, 2008; Niu, 2008; Irving and Green, 2008; Upton et al., 2009). These melts can correspond to liquids with a basanite to hawaiite composition and other products of their differentiation (Irving and Green, 2008; Pilet et al., 2010), previously generated from very low amounts of partial fusion of slightly enriched peridotites in the asthenosphere (e.g. Pilet et al., 2005, 2008; Niu, 2008). They would precipitate clinopyroxene and amphibole rich assemblages by percolative fractional crystallization (Pilet et al., 2005, 2010; Irving and Green, 2008) while advancing through the lithospheric mantle.

The occurrence of apatite associated with amphibole in xenoliths and as xenocrysts, similarly to what is observed in the alkaline rocks of the WIM, has also been interpreted as the result of in depth crystallization of alkaline silicic carbonated magmas (e.g. O'Reilly and Griffin, 2000), however, the determination of the chemical composition of apatite is necessary in order to confirm this hypothesis.

According to Pilet et al. (2008) the melting of these metasomatic hornblendite to pyroxenite veins along with variable amounts of surrounding peridotite can generate

liquids with a compositional array ranging from nephelinite to alkali basalt with variably enriched geochemical signatures. However, it is not possible to unequivocally determine whether these metasomatic amphibole bearing veins are a precursor or a consequence of alkaline magmatism (Pilet et al., 2010).

Considering the arguments presented above, the xenocrysts and xenoliths observed in the studied rocks of the WIM could be interpreted as being part of the mantle assemblage that melted in order to generate the alkaline magmatism that took place in the Late Cretaceous in the WIM, or be the result of crystallization and accumulation processes that occurred at depth during earlier phases of alkaline magmatism. Yet, in order to properly evaluate these hypothesis, additional detailed mineral chemistry studies are necessary, including the determination of trace element and isotopic composition of individual mineral phases that occur simultaneously as xenoliths, xenocrysts and as normally zoned phenocrysts and matrix phases.

7. Geochemistry and petrogenesis

In this chapter the main elementar and isotopic characteristics of the studied Late Cretaceous alkaline rocks and their genetic implications are discussed.

The samples were prepared for analysis at the Departamento de Geologia da Universidade de Lisboa. They were hydraulically crushed, in order to ensure the removal of all the signs of alteration, then reduced in size using a jaw crusher and afterwards powdered in an agate swing mill.

Concentrations for major and trace elements were obtained at Actlabs Ancaster, Ontario, Canada. Major elements were analyzed using Inductively Coupled Plasma Mass Spectrometry (ICP-MS) after alkaline dissolution with lithium metaborate/tetraborate followed by nitric acid dissolution (except for Ni, Cu and Zn measurements that were performed after acid digestion).

Samples were prepared and analyzed in a batch system. Each batch contained a method reagent blank, certified reference material and 17% replicates. Samples were mixed with a flux of lithium metaborate and lithium tetraborate and fused in an induction furnace. The melt was immediately poured into a solution of 5% nitric acid containing an internal standard and mixed continuously until completely dissolved (≈ 30 minutes).

The fused sample was diluted and analyzed by Perkin Elmer Sciex ELAN 6000, 6100 or 9000 ICP-MS. Three blanks and five controls (three before sample group and two after) were analyzed per group of samples. Duplicates were fused and analyzed every 15 samples. The instrument was recalibrated every 40 samples. Calibration was performed using seven prepared USGS and CANMET certified reference materials. One of the seven standards was used during the analysis for every group of ten samples. The prepared sample solution was spiked with internal standards to cover the entire mass range.

The calculated reproducibility is ≈ 1 relative % for major elements and 5 relative % for trace, rare earth elements (REE) and high field strength elements (HFSE). The accuracy of the analyses, evaluated by analyzing international standards, is generally better than 10 relative-%. More information on the procedure, precision and accuracy of the Actlabs analyses can be found at http://www.actlabs.com.

7.1. Major and trace element geochemistry

The distinction between major and trace elements is based on fundamental differences in geochemical behavior. A "major" element is an essential constituent of the minerals making up a rock and changing the concentrations of these elements can lead to changes in the phase assemblage. Typically, these are expressed under oxide form and are: SiO_2, Al_2O_3, MgO, MnO, FeO, CaO, Na_2O, K_2O and also Cr_2O_3, and NiO for mantle rocks. The major elements in magmas are by definition compatible, and most of them are well buffered by the residual minerals.

Trace elements, on the other hand, replace a few atoms of the major elements in the crystal structures, without affecting the phase assemblage significantly, so their abundances are usually lower than 0.01% or 1000 part per million (ppm). They are accessory in many petrogenetic processes, and they are therefore useful as tracers of such processes. During solid-phase transformations, they will redistribute themselves locally between the newly formed mineral phases but, during melting or magmatic evolution, they are partitioned to a greater or lesser degree into the melt. Thus trace element signatures of magmatic rocks carry information about the composition of the source and the nature of their melting and evolution processes.

The partitioning of trace elements between crystalline and liquid phases is usually described by a partition coefficient D, which is a simple ratio of two concentrations at chemical equilibrium:

$$\boldsymbol{D^i} = \frac{\boldsymbol{C_s^i}}{\boldsymbol{C_l^i}}$$

where $\boldsymbol{D^i}$ is the partition coefficient of trace element *i*, $\boldsymbol{C_s^i}$ and $\boldsymbol{C_l^i}$ are the concentrations (by weight) of this element in the solid and liquid phases, respectively.

Goldschmidt (1954) recognized that the distribution of trace elements in minerals is strongly controlled by ionic radius and charge. The partition coefficient of a given trace element between solid and melt can be quantitatively described by the elastic strain this element causes by its presence in the crystal lattice. When this strain is large because of the large differences in sizes between lattice space and ionic radius, the partition coefficient becomes small, and the element is partitioned into the liquid.

Many trace elements have values of D < 1, because they differ substantially either in ionic radius and/or charge, from the atoms of the major elements they should replace in the crystal lattice and as a consequence remain in the melt. Due to this, they are called incompatible. In opposition, trace elements such as Sr in plagioclase, Ni in olivine, and Sc in clinopyroxene fit into their host crystal structures, therefore being compatible for those specific minerals, becoming useful in detecting processes where the fractionation of these phases is involved.

Incompatible trace elements are often divided into two major groups, according to ionic radius and charge, which define their field strenght. High Field Strength elements (HFSE) are small cations with high ionic charges (e.g. Zr, Hf, Th, Nb, Ta, U, and the Rare Earth Elements (REE) or lanthanides), and are not easily incorporated in the more common silicate minerals.

Large Ion Lithophile elements (LILE) such as Cs, Rb, K, Ba, Sr, have larger ionic radiuses and lower ionic potential, and have a tendency to be more compatible in some minerals. They are also more easily mobilized by hydrous fluids, being more mobile in alteration and metassomatic processes than HFSE.

Trace elements with very low partition coefficients may vary by three orders of magnitude in the melt, depending on the degree of melting of the source. The concentration of such elements is inversely proportional to the melt fraction F, because the melt contains, essentially, the entire budget of this trace element and if there is a larger amount of melt available, the concentration of trace elements will become more "diluted". Another consequence of highly incompatible behavior of trace elements is that if the mineral in the source that contains most of the chemical budget for a certain element (e.g. Zr in zircon) is exhausted during melting, their concentration ratios in the melt become constant, independently of melt fraction, and will be identical to the respective ratio in the mantle source.

7.1.1. Classification and Major element geochemistry

After recalculation to 100% on a volatile free basis, all of the sampled rocks, even the ones with cumulate textures, fall within the alkaline field in the TAS (Total Alkalis versus Silica, fig. 7.1), considering the compositional division between the alkaline and sub-alkaline series defined by MacDonald (1968).

Both extrusive and intrusive rocks are plotted in the TAS diagram, as well as in the other graphs used to characterize the geochemistry and evaluate the compositional evolution of the studied samples. This was done in order to allow a comparison between the basic alkaline extrusive and intrusive occurrences and to try and distinguish any significant variation between them. The number of studied complexes within a relatively large area advises some caution when interpreting these diagrams since it is not realistic to assume that all the rocks are cogenetic and have evolved in identical ways, even if, in some cases, their age and possibly even parental magmas might be similar.

The samples from the ultrabasic (SiO_2 < 45%) Foz da Fonte sill classify as tephrites since olivine does not occur in this rock.

The Paço d'Ilhas sill is not so straightforwardly classified due to its layered nature, with its samples showing a considerable compositional range. The basic samples (45 < SiO_2 < 52 %), that represent layers where more mafic minerals have accumulated, fall within the basalt field. However, the more evolved of the intermediate (52 < SiO_2 < 63 %, Na_2O-2 > K_2O) layers plot well into the benmoreite field and correspond to the more evolved samples in the dataset. The mesocratic layers that constitute most of the sill actually plot in the mugearite field.

The studied flows and necks from the LVC are ultrabasic to basic rocks that classify as basanites (Ol > 10 %) and alkali basalts (Lexim neck), with the plugs also falling on the basanite field. The sills integrated in this complex show more evolved compositions, ranging from hawaiites (Lomba dos Pianos) to mugearites (Montelevar and Anços), benmoreites (Anços). The Eiras do Faião sill shows a distinct, more alkali.rich and SiO_2 undersaturated, phonotephritic composition, unlike the other nearby sills that are also included in the LVC.

The three different dykes from the Cascais region plot in different fields of the TAS diagram. The porphyritic basalt from Bafureira beach falls within the alkaline basalt field, the dyke that outcrops in the Parede beach can be classified as a tephrite and the one collected in Poça beach plots in the hawaiite field.

The Malveira da Serra sill is also classified as a tephrite since it lacks olivine.

The two sampled Loulé dykes are both ultrabasic lamprophyric rocks and plot in the foidite field, but the monchiquite C-20 shows a much higher amount of alkalis than the olivine phyric C-12-1.

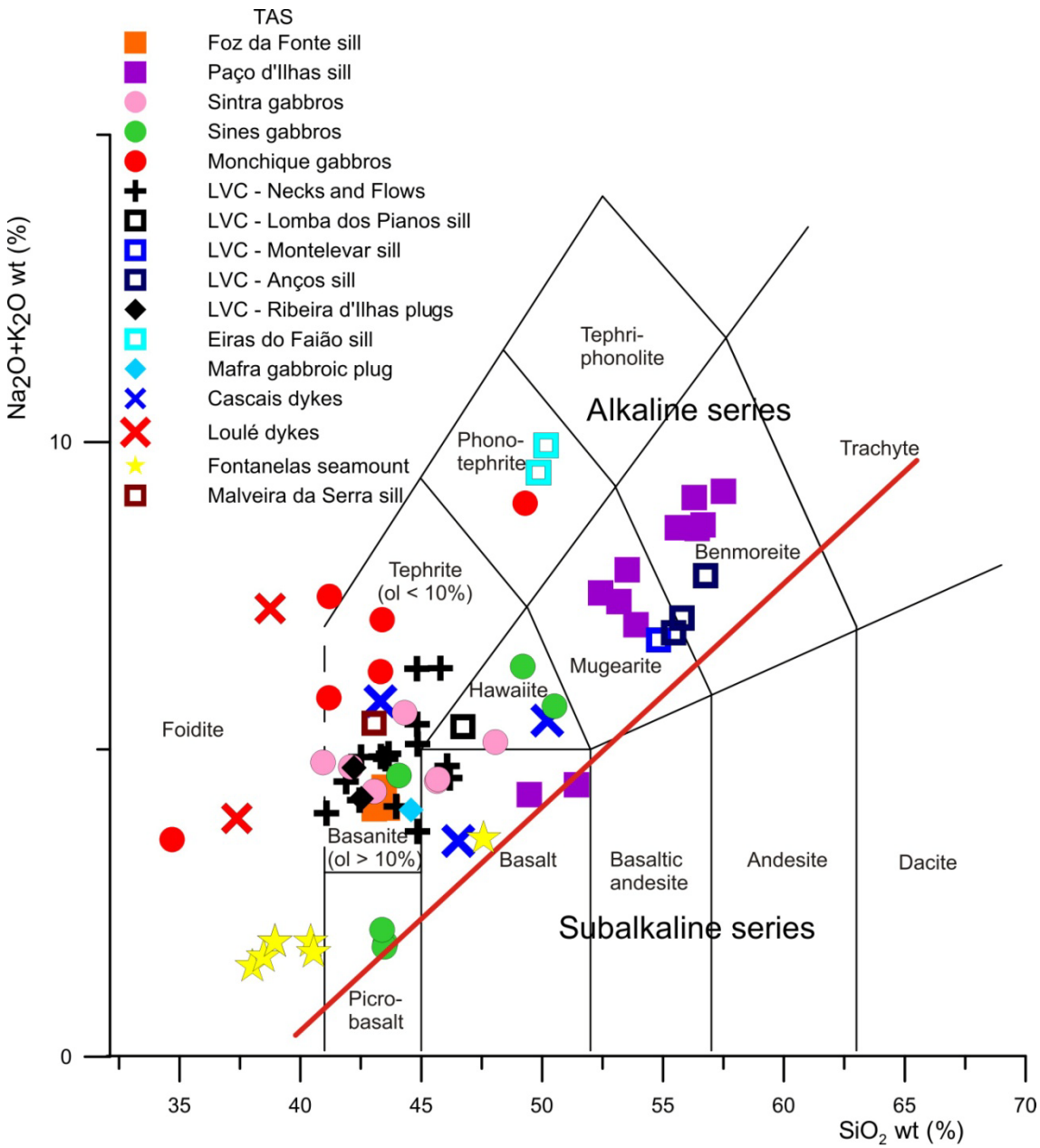

Fig. 7.1: Total Alkalis versus Silica diagram for the studied samples, after LeBas et al. (1986). Line dividing the alkaline and sub-alkaline series from MacDonald (1968).

Most of the samples from the Fontanelas seamount are very altered, and contain a high amount of vesicles filled with secondary alteration products (sometimes over 40% of the volume of the sample). Although they were subject to leaching in 1.5N HCl before being sent out for analysis, their Loss On Ignition (LOI) values were still very high (6.5-10%), so caution must be taken while trying to classify them and interpreting their whole rock geochemical data. The lavas from this seamount are mostly ultrabasic rocks and fall in the foidite field, except for one sample that plots on the alkali basalt field. They are all alkaline but it is possible that their total alkalis content is not

representative of its original value due to alkali removal or addition during alteration. The high degree of alteration of the samples does not allow further classification of the foidites as nephelinites or leucitites.

As for the granular rocks represented in fig. 7.1, the gabbroic plug present in Mafra falls on the basanite/tephrite field, alongside a lot of samples from the LVC, Sintra, Sines, Monchique and the Foz da Fonte sill.

The basic intrusive rocks from Sintra plot on the basanite/tephrite fields as well, with the diorite being slightly more evolved and falling in the hawaiite field.

In its turn, the mafic intrusives from Sines show larger scatter in the TAS diagram. The ultrabasic rocks from the Pedras Negras outcrop plot on the picrobasalt field, reinforcing the idea introduced in section 6.1 that these are in fact products of accumulation processes. One of the samples from the amphibole rich gabbro from the southern gabbro outcrops plots on the basanite/tephrite field near the Sintra gabbros, while the other sample from the same outcrop and the diorite fall in the more evolved hawaiite field, with the diorite being the more silica rich rock in this group.

Compared with the basic rocks from other intrusive complexes, the mafic rocks from Monchique are more alkali rich for a given SiO_2 content. On the TAS diagram one sample is ultrabasic and plots near one of the Loulé samples on the foidite field, although it is even more SiO_2 poor. The other samples fall in the basanite/tephrite field with the more SiO_2 rich one even plotting on the phonotephritic field.

Another feature evident in the TAS diagram is the existence of two different magmatic evolution trends. One progresses towards silica oversaturared compositions and is clearly more important, as it includes most of the analyzed samples as well as other rocks of the same age that were not sampled in this study (e.g. Sintra granite and syenite, Sines syenite, rhyolites from the LVC). This trend illustrates evolution from a silica undersaturated basanitic parent towards silica saturation, originating the benmoreites of the Anços sill and eventually culminating in rocks of rhyolitic or granitic composition (not shown, see Palácios, 1985, and Matos Alves, 1964).

The other trend is SiO_2 undersaturated and it also departs from a possible basanitic parent but progresses towards silica undersaturated compositions represented by the tephriphonolites of the Monchique complex and of the Eiras do Faião sill, culminating in the nepheline syenites (not shown) that form the larger part of the Monchique igneous complex (e.g. Valadares, 2004).

Looking at a broader context, the trend towards silica oversaturated compositions seems to dominate in the Late Cretaceous alkaline magmatism of the WIM, being common to the LVC (Palácios, 1985), the Sintra igneous complex where the granites and syenites make up most of the outcropping area (e.g. Matos Alves, 1964), the Sines igneous complex where quartz bearing syenites are found (e.g. Canilho, 1972) and even some of the seamounts that constitute the MTR contain SiO_2 saturated rocks (Merle et al., 2006).

Most of the samples integrate the potassic series defined by Middlemost (1975) for basic alkali rocks, although all the basic samples of the Sintra igneous complex, the amphibole rich gabbros in the Sines complex, a few samples from the LVC and one from Paço d'Ilhas all plot in the sodic series field (fig. 7.2). However, their positioning in the sodic series can be due to the accumulation of Na-rich phases such as plagioclase or amphibole.

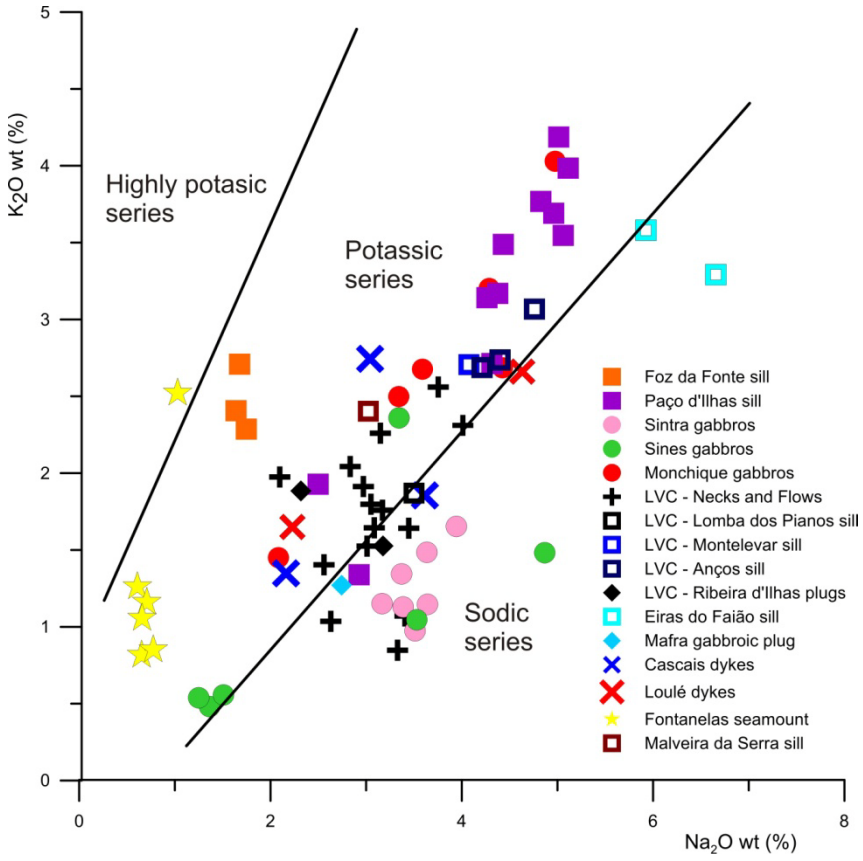

Fig. 7.2: Classification diagram for the alkaline basalt series after Middlemost (1975).

Only one sample from the Fontanelas seamount (AT692E) falls in the highly potassic series field, but the higher potassium content in this sample might be due to

secondary addition of K during alteration. K addition from seawater has already been reported in submarine basalts from the MTR (Merle et al., 2009) meaning that a similar process is behind the high K in the Fontanelas seamount.

The Mg# [Mg# = 100 x (MgO/(MgO+FeO)), with FeO being calculated according to the Fe_2O_3/FeO ratios recommended by Middlemost (1989)] for these rocks varies between 70.2 for dyke C-12-1 in Loulé and 34.7 one of the felsic layers in the Paço d'Ilhas sill, averaging at 54 in the basic and ultrabasic rocks (SiO_2 < 52%), which is somewhat lower than expected for basic and ultrabasic alkaline igneous rocks. This suggests that these magmas have undergone significant fractional crystallization in a deeper, unexposed part of the magmatic plumbing system before eruption or emplacement.

Major elements are plotted against SiO_2 in figure 7.3, with SiO_2 being used as an indicator of magmatic differentiation.

Owing to their relatively wide geographical (e.g. figs. 4.1, 4.2) and chronological (94-72 Ma, see section 5) distribution, as well as diverse modes of occurrence, the studied rocks cannot be considered cogenetic. In this perspective, the binary plots presented from here onwards and containing all of the studied samples are only used as tool to identify possible common processes affecting the evolution of these rocks and emphasize similarities or differences detected between each of the different occurrences.

In the studied rocks, MgO, FeO, TiO_2 and CaO all decrease with increasing SiO_2 contents, while Al_2O_3, Na_2O and K_2O increase. P_2O_5 shows very scattered concentration values that seem to be characterized by an initial increase, followed by a significant decrease for SiO_2 > 45%, which can be interpreted as resulting from apatite fractionation.

Some deviations from the apparent trends are probably the consequence of the already discussed crystal accumulation processes. These can justify the higher MgO in some of the Sines gabbros, as well as in the porphyritic basalts of LVC's flows and necks and in the case of the porphyritic dykes from Cascais due to olivine accumulation (fig. 7.3). The high FeO^T and TiO_2 values found in the more basic samples in the Paço d'Ilhas sill (fig. 7.3) can also be attributed to the accumulation of Fe rich mafic minerals such as Fe-Ti oxides and clinopyroxene in the mafic layers.

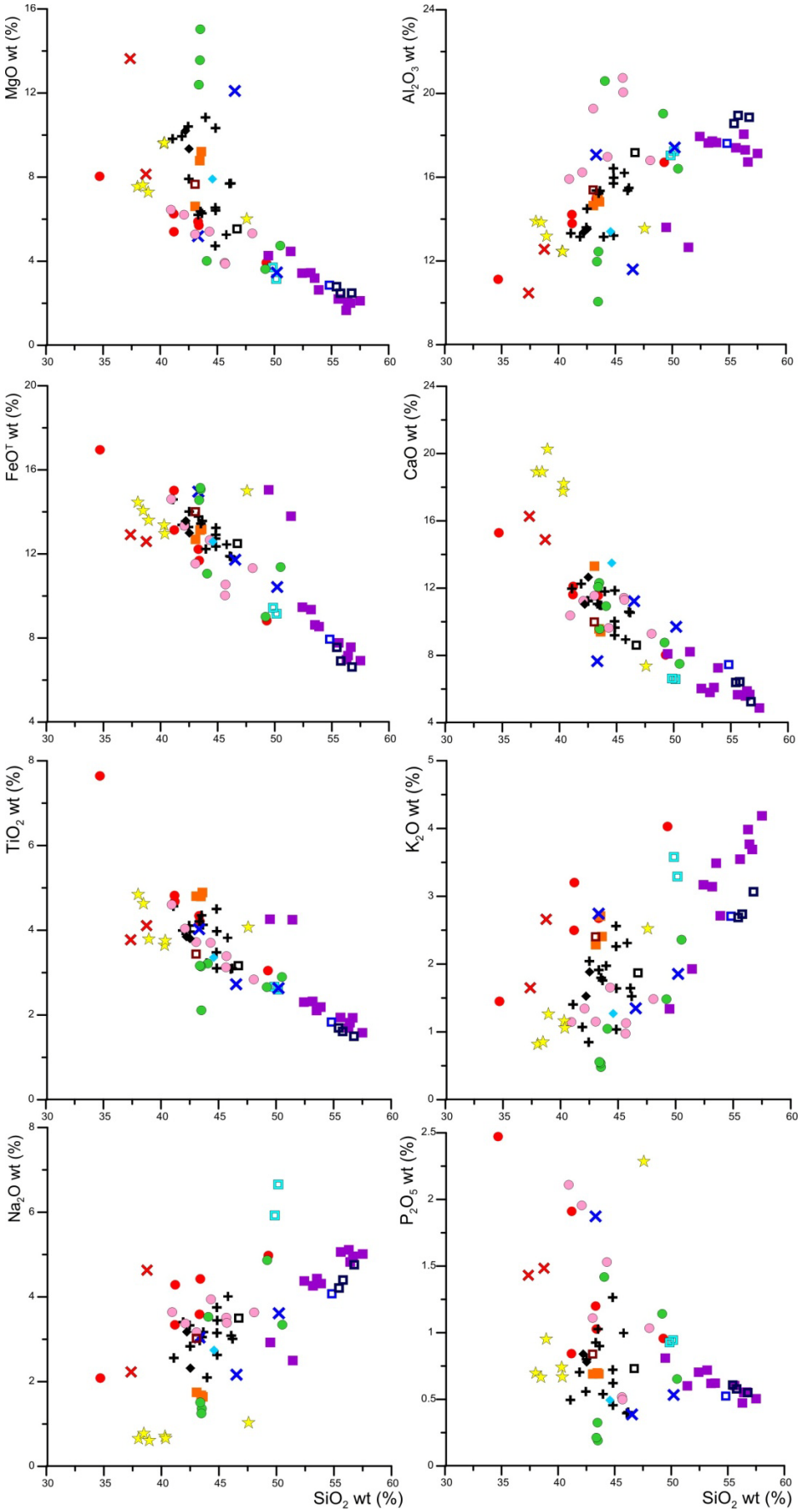

Fig. 7.3: Plots of selected major elements versus SiO_2 content for the analyzed samples. Legend as in figs. 7.1 and 7.2.

Al_2O_3 also shows some spread (fig. 7.3), with a few samples from the basic rocks in Sintra and from the Vasco da Gama beach in Sines being more enriched in Al than other rocks with the same SiO_2 content. On the other hand, the samples from Pedras Negras in Sines, the mafic layers from the Paço d'Ilhas sill and the porphyritic basaltic dyke from Cascais show lower than expected Al contents. These opposite behaviors of the same element, sometimes in the same intrusive (Sines) are probably due to plagioclase removal during fractional crystallization creating the Al_2O_3 deficit in some samples (Pedras Negras gabbro in Sines, mafic layers in Paço d'Ilhas) while its accumulation led to Al_2O_3 excess in other samples (Azóia and Praia Vasco da Gama gabbros in Sintra and Sines, respectively).

CaO seems to decrease with increasing SiO_2 (fig. 7.3). However, the high CaO values in the samples from the Fontanelas seamount can be related to secondary alteration processes that added carbonate, and consequently CaO to these rocks.

The scatter observed in the plots of Na_2O, K_2O and P_2O_5 against SiO_2 (fig. 7.3) might be caused by either to fractionation and accumulation processes, or due to differences in source composition that originated magmas which could possess different concentrations of Na, K and P. Also, crustal contamination processes can influence the amount of alkalies present in the melt since these elements can be very abundant in crustal rocks. The importance of the contamination processes will be discussed in section 7.3.2

Samples that carry feldspathoids (basic rocks from Monchique, Eiras do Faião sill, Loulé dykes) usually have higher alkali contents and often correspond to the highest K_2O and Na_2O contents for a given SiO_2 value observed in the diagrams. Plagioclase and feldspar accumulation in the gabbroic rocks can produce similar effects, with their removal causing the lower K_2O and Na_2O contents observed in the mafic cumulates such as the Pedras Negras gabbro in Sines and the mafic layers in the Paço d'Ilhas sill.

As for P_2O_5, samples such as the Sintra, Monchique and the Sines Vasco da Gama beach gabbros clearly show signals of apatite accumulation, which justifies the high P_2O_5 contents in these rocks. The low contents of P_2O_5 in the Pedras Negras gabbro in Sines seem, again, to be due to accumulation of P poor phases like olivine and clinopyroxene.

In more general terms, the decrease in MgO, FeO and TiO_2 can explained by the crystallization and removal of mafic minerals such as olivine, clinopyroxene, Fe-Ti

oxides and amphibole. Clinopyroxene and amphibole also incorporate significant CaO and their removal, coupled with CaO rich plagioclase, can also explain the decrease in this oxide with increasing silica contents.

Al_2O_3 clearly increases up to values around 55% SiO_2 and from then onwards seems to show a slight decrease with increasing SiO_2, probably due to the removal of crystallizing plagioclase

The generalized increase in Na_2O, K_2O, and SiO_2 can be justified by the relative enrichment in these elements caused by removal of MgO, FeO, TiO_2, CaO and even Al_2O_3 by crystallization of olivine, clinopyroxene, plagioclase and Fe-Ti oxides. None of those minerals is particularly rich in those elements so their fractionation does not contribute to the decrease of their concentrations in the residual liquids.

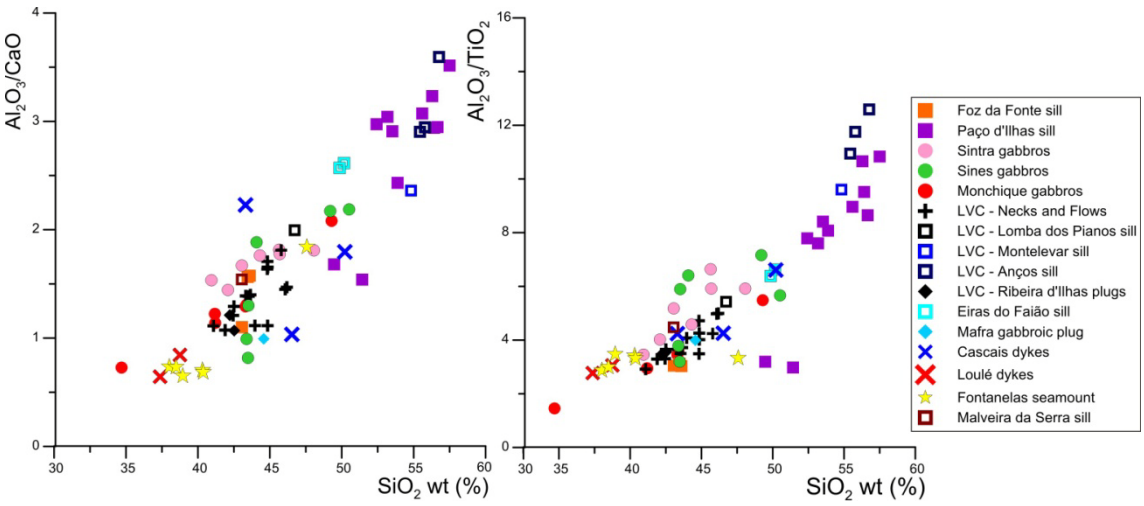

Fig. 7.4: Plots Al_2O_3/CaO and Al2O3/TiO_2 versus SiO_2 content for the analyzed samples.

The Al_2O_3/CaO ratio increases from nearly chondritic towards supercondritic values (chondrites≈ 1.23, Palme and O'Neill, 2003) with increasing silica contents, which argues for the importance of clinopyroxene and plagioclase removal on the evolution of the magmatic liquids since these remove show low Al_2O_3/CaO.

In their turn, the Al_2O_3/TiO_2 ratios (fig. 7.4) are lower than the ones found in chondrites (18.5-22.4, Palme and O'Neill, 2003), meaning that these magmas are enriched in Ti relative to a primordial source. Also, as seen on fig. 7.4, this ratio increases with increasing differentiation. That is a consequence of crystallization and removal of Fe-Ti oxides and clinopyroxene that remove TiO_2 from the liquid, confirming the importance of the fractionation of these minerals in the evolution of

these magmas. Crystal accumulation seems to be responsible for some deviations from the general trend observed by the samples from Sines, Sintra and Paço d'Ilhas.

7.1.2. Trace element geochemistry

As was mentioned before, certain trace elements see their concentrations decrease with progressive crystallization and removal of minerals. These elements possess ionic radius and valence similar to the more abundant major elements and can therefore substitute these major elements and integrate the crystal structure of some specific mineral(s). They are referred to as compatible trace elements and show D > 1 for the phases in which they are compatible (table 7.1).

Table 7.1: Partition coeffiecients (D) for selected minerals and elements in basaltic (s.l.) rocks according to the data available on GERM database (www.earthref.org, Matsui et al., 1977; Takashi, 1978; Okamoto, 1979; Villemant et al., 1981; Lemarchand et al., 1987; Nielsen, 1992; Beattie, 1994; Latourrette et al., 1995; Esperanza et al., 1997; Zack and Brumm, 1998; Bindeman et al., 1998; Green et al., 2000; Adam and Green, 2006).

	D									
	Ni		Cr		V		Sc		Sr	
	Min	Max	Min	Max	Min	Max	Min	Max	Min	Max
Olivine	2.86	47	0.64	1.18	0.15	0.23	0.22	0.32	$1.5E^{-05}$	0.01
Clinopyroxene	2.5	10	8.49	26	3.1	5.7	1.63	3.62	0.104	0.2
Magnetite	31	65		153	0.02	6.85	0.67	1.96		
Ilmenite		3.8		6		11	0.58			
Plagioclase	0.04	0.5	0.08	0.6	0.01	0.27	0.04	0.1	2.7	10
Amphibole	16	18	0.21	7	3.4	5.7	1.59	2.86	0.298	0.42

Within the analyzed samples, compatible trace element correspond to Ni, Cr, V, Sc and to a lesser degree, Sr. The variation in their concentrations will be caused mostly by the precipitation and removal of minerals identified as phenocryst phases (see section 6.2) such as olivine (Ni), clinopyroxene (Cr, V, Sc, Ni) , Fe-Ti oxides (V, Sc, Ni, Cr), plagioclase (Sr) and others, but one cannot discard source heterogeneity as a possible cause of diversity in the observed concentrations for these elements. They are plotted against Mg# instead of SiO_2 in fig. 7.5 since this index allows for a relative expansion of the X axis values in what respects basic rocks, facilitating the detection of early processes that involve the crystallization of mafic minerals which accommodate some of these compatible elements.

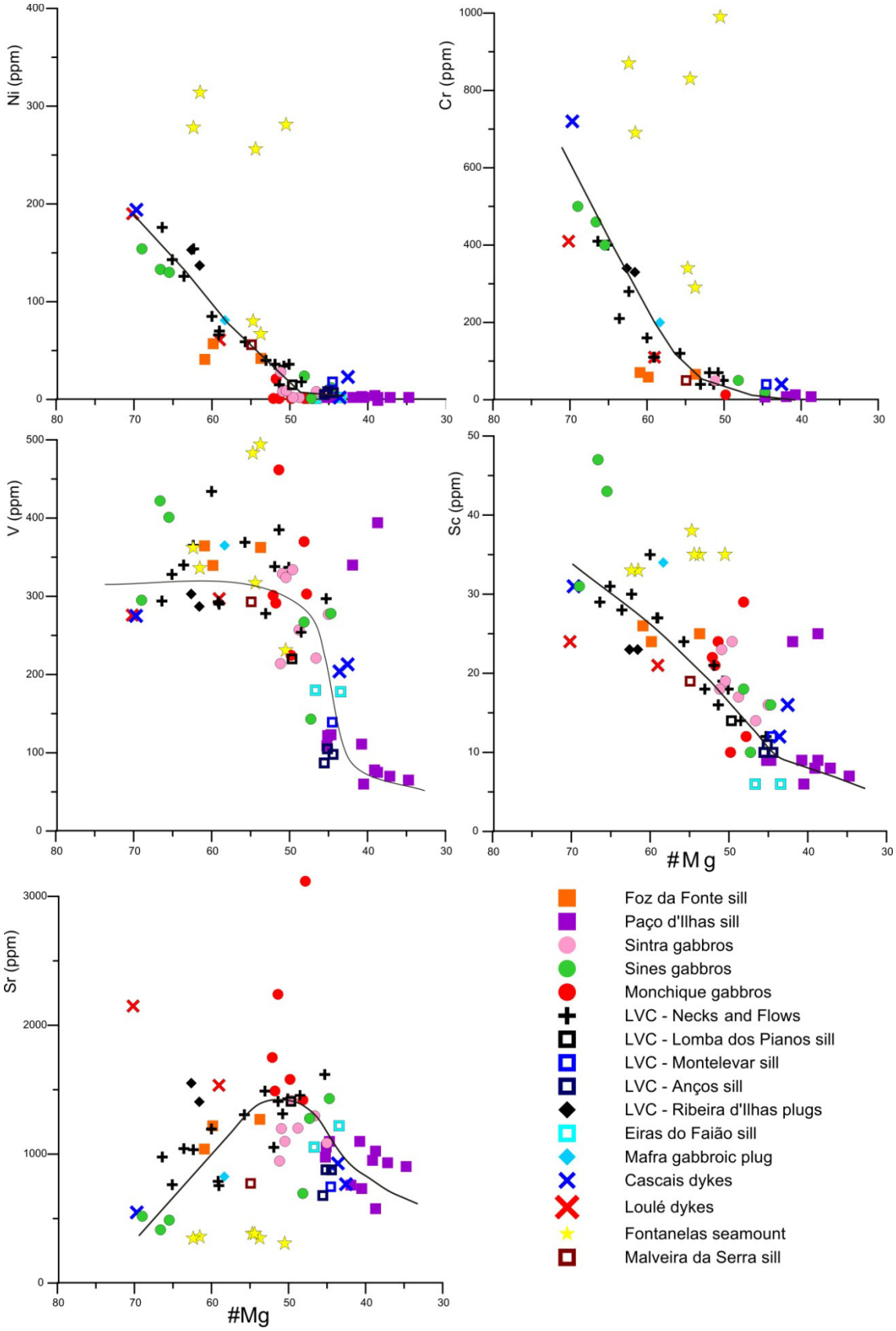

Fig. 7.5: Plots of selected compatible trace elements versus Mg# for the analyzed samples. Given that the plotted samples are not cogenetic, the drawn lines are simply indicative of what may be interpreted as a general evolutionary tendency of the Late Cretaceous alkaline magmas.

Ni is strongly compatible in olivine, clinopyroxene and Fe-Ti oxides and is often used as an indicator for olivine fractionation since this is usually the more abbundant early crystallizing phase in basic alkaline magmas (tab. 7.1). As is observed in fig. 7.5, the Ni contents are usually low, rarely surpassing 200 ppm, and decrease very rapidly with decreasing Mg#, pointing towards early removal of olivine. The samples from the Fontanelas seamount are an exception to this case, as they show Ni contents up to 314 ppm.

Cr is also strongly compatible in clinopyroxene, amphibole and especially spinel (tab. 7.1), and shows a behavior similar to Ni, decreasing quickly with decreasing Mg# (fig. 7.5), also arguing for the early removal of these phases. Again, the lavas from the Fontanelas seamount are the samples with the highest Cr contents.

It is noticeable that none of the analyzed samples fit the criteria that define primary magmas (i. e. magmas which are products of mantle melting and have not been modified by fractional crystallization or interaction with country rock during ascension, and are characterized by: Mg# > 68, Ni > 320 ppm, Cr > 1000 ppm, e.g. Frey et al., 1978), implying that, as was previously proposed, these magmas must have undergone important spinel, olivine and probably clinopyroxene fractionation in depth prior to eruption or installation.

V is very compatible in Fe-Ti oxides such as magnetite and ilmenite and slightly less so in clinopyroxene and amphibole (tab. 7.1). In fig. 7.5, V also shows a negative correlation with decreasing Mg for values lower than 55 Mg#, as a consequence of the removal of Fe-Ti oxides and clinopyroxenes from then onwards. For Mg# values higher than 55 the samples show more or less scattered but relatively stable V values, reflecting either source heterogeneity or accumulation. The previously discussed mafic cumulate layers of the Paço d'Ilhas sill, and Sines Pedras Negras gabbro show higher V values than samples with similar Mg# due to their cumulate nature, while other samples from the basic rocks in Monchique or the Fontanelas seamounts might show higher V abundances due to source enrichment since they do not show any clear petrographic signs of crystal accumulation.

Sc is mainly compatible in clinopyroxene and also with magnetite and amphibole. It shows a negative correlation with decreasing Mg# arguing for an important role for early clinopyroxene and magnetite removal in the evolution of the alkaline series. The same samples that fell out of the main trend in the V vs. Mg# diagram also plot out of the main trend here, due to the same processes of accumulation

(Paço d'Ilhas, Sines). The positioning of the less evolved samples from Monchique and Fontanelas probably reflects their origin from a distinct source or from a similar source that was affected by lower degrees of partial melting.

Sr is only compatible in plagioclase and its concentration in the melt should lower with the progressive crystallization and removal of this mineral. Plotted against Mg# the Sr concentrations seem to increase until Mg#≈ 50 and start to decrease from then onwards, marking the initiation of removal of plagioclase from the system. The samples from the Fontanelas seamount show homogeneously low Sr values for all samples, due to either removal of this mobile element during seawater alteration, or during the leaching that these samples were subject to prior to analysis. Some samples from Monchique and Loulé show unusually high Sr values probably due to being derived from a more Sr enriched source or even due to resulting from lower degrees of partial melting of a source similar to the other basic alkaline rocks.

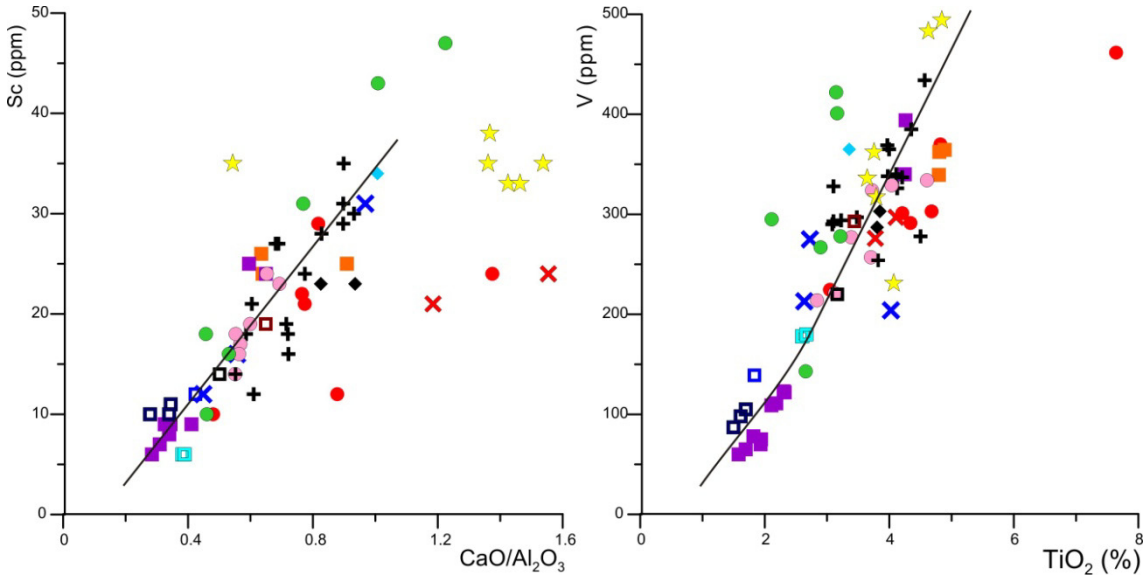

Fig. 7.6: Plots of CaO/Al_2O_3 vs. Sc for and TiO_2 vs. V for the analyzed samples. Legend as in fig. 7.5.

The strong correlation between the TiO_2 and V contents of the studied rocks confirms the importance of Ti-rich clinopyroxene and especially Fe-Ti oxides (up to 5% V_2O_3 and 54% TiO_2, see annex IV) in controlling the distribution of these elements.

Sc and the CaO/Al_2O_3 ratio also show a strong correlation, arguing that these values are both controlled by the crystallization of clinopyroxene. Samples from the Fontanelas seamount show higher CaO/Al_2O_3 values probably due to secondary CaO

addition during alteration, while the rocks from Monchique and Loulé seem to be enriched in CaO.

7.1.2.1 Primitive mantle normalized multielemental diagrams

Whenever trace elements possess ionic radius or valences that do not allow them to integrate the structures of the more common minerals crystallizing from a silicate magma, their concentration in the residual liquid will tend to increase with differentiation. These are known as incompatible trace elements.

Primitive mantle normalized multielemental diagrams, or spider diagrams, are a quick way to visualize and characterize the abundance and variation of incompatible trace elements in igneous rocks. They allow for the display of many elements, whose concentration is normalized to a primitive mantle composition (Palme and O'Neill, 2003), facilitating the detection of relative enrichments and/or depletions in relation to this composition. For the discussion of trace element signatures it is important to remind that the trace element contents of plutonic rocks may not be the best representatives of the compositions of their parental melts due to the likely occurrence of crystal removal and accumulation processes which may modify these signatures, although some of their original compositional features can still be distinguishable.

Given that geochronological data allowed the identification of two separate pulses of magmatism within the Late Cretaceous alkaline magmatism (Miranda et al., 2009, see section 5), and since changes in incompatible trace element concentrations can be a useful tool in detecting differences between magmas of similar composition, the samples from both groups will be presented separately when appropriate.

Below, the primitive mantle normalized spider diagrams and chondrite (Palme and O'Neill, 2003) normalized Rare Earth Element (REE) diagrams for individual or groups of major occurrences are represented and will be discussed separately (figs. 7.7 and 7.8), in order to facilitate the interpretation of the obtained results.

In general, all samples belonging to the second and more recent pulse of alkaline activity in the WIM (75-72 Ma, Miranda et al., 2009, this study) are incompatible element enriched and in most cases, the more basic samples show negative K, P, Hf and Zr anomalies.

In the south, the 72 Ma Loulé dykes and basic rocks from the Monchique igneous complex show similar patterns, with negative anomalies in K, Zr, Hf and sometimes even Ti and P (fig. 7.7).

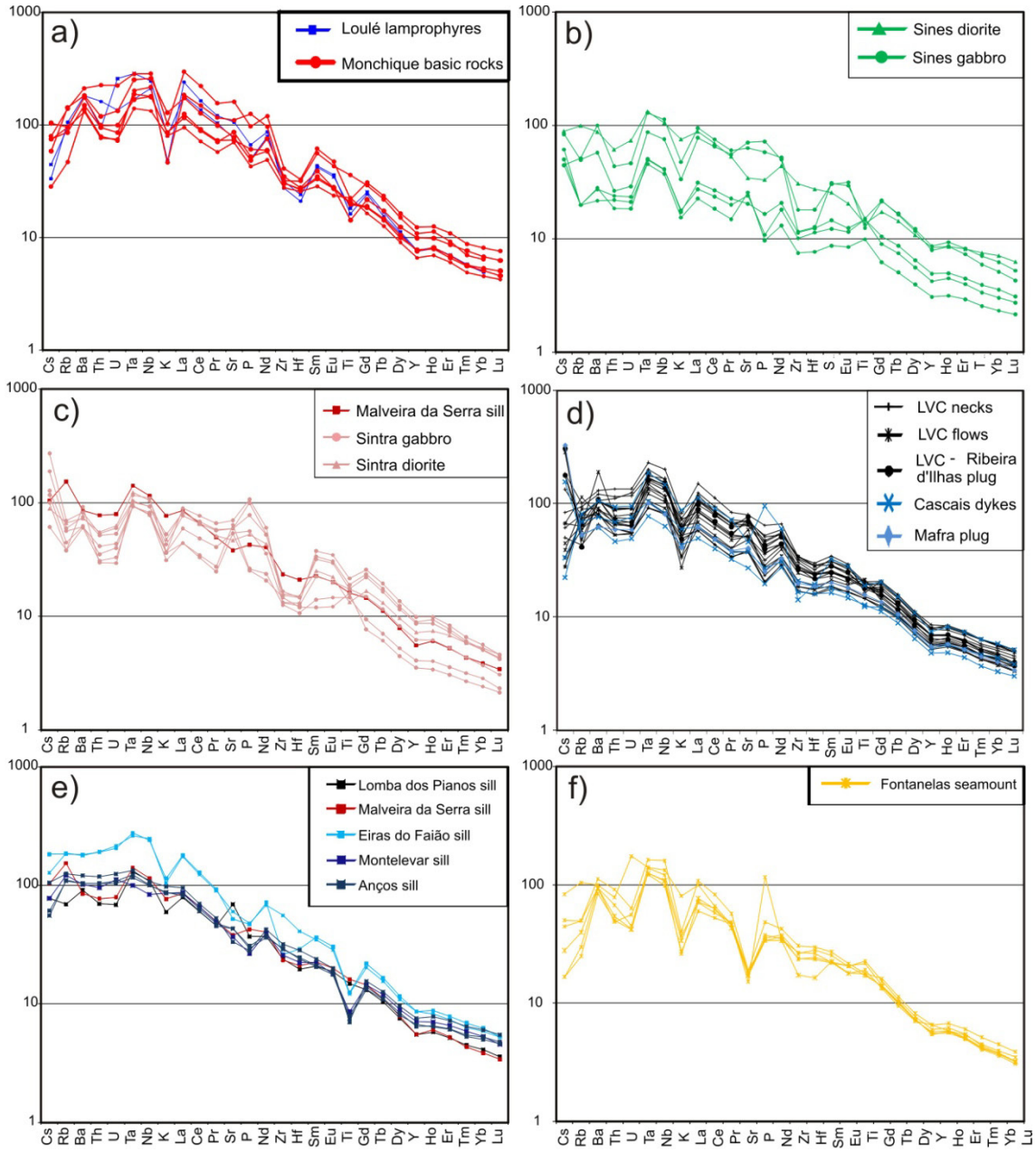

Fig. 7.7: Primitive upper mantle normalized (Palme and O'Neill, 2003) multielemental plots for the rocks of the second pulse of Late Cretaceous alkaline igneous activity (75-72 Ma).

In the Sines igneous complex, the basic rocks are not as enriched as in Monchique. The cumulate nature of the Pedras Negras gabbro is reflected on their trace element abundance patterns, with these being the least trace element enriched samples, which also show a small positive Ti anomaly due to the accumulation of Fe-Ti oxides and Clinopyroxene. Otherwise, they show the same negative K, P, Zr and Hf anomalies as observed in the basic rocks from Monchique.

The Vasco da Gama beach amphibole rich gabbros are more trace element enriched and display more pronounced K, Hf and Zr negative anomalies and are missing the negative P anomaly probably due to accumulation of apatite. Also, they show a small negative Ti anomaly that might be consequence of the accumulation of Ti rich phases in the Pedras Negras gabbro. The higher incompatible element abundances in this gabbro supports the view that these samples represent a higher part of the magma chamber where the residual, more evolved liquid resulting from the progressive removal of mafic minerals to form cumulates such as the Pedras Negras gabbro gathered.

The spidergram for the Sines diorite shows a smoother patern with less pronounced or inexistent negative anomalies in K, Zr, Hf and Ti but with small negative anomalies in Sr and P, probably due to the removal of plagioclase and apatite, respectively.

The basic rocks from the Sintra igneous complex show trace element abundances and patterns similar to the ones observed in the Sintra and Sines complexes, with negative K, Zr and Hf anomalies, sometimes also showing negative Ti as well. P can show a positive anomaly due to the accumulation of apatite in some of these rocks.

The gabbros from the Peninha outcrop show more enriched signatures and negative Ti and positive P anomalies, while the ones from the Azóia outcrop show the opposite behavior, i.e. positive Ti and negative P anomalies. This suggests that these gabbroic outcrops represent different zones in the magma chamber. In this perspective, the Azóia gabbros could correspond to a deeper level where Ti rich oxides accumulated and the Peninha gabbro to a higher level of the same chamber where the residual, Ti depleted and incompatible element enriched liquid accumulated.

The diorite shows a pattern with an enrichment level intermediate between both the gabbro outcrops.

The Malveira da Serra sill is plotted with the basic rocks from the Sintra complex since some authors proposed that it might be a precursor of the installation of this complex (e.g. Kullberg and Kullberg, 2000). It shows a similar spidergram to these and other Late Cretaceous alkaline rocks, but with smaller K, Zr and Hf negative anomalies and with a small Sr negative anomaly.

Necks, flows and plugs from the LVC and Cascais dykes all show similar incompatible element patterns between themselves and with the same pronounced negative K anomalies but with smaller P, Zr and Hf anomalies. One of the Cascais dykes shows a positive P anomaly, as a result of the abundance of apatite in the sample.

Ti varies between having no anomaly and showing small negative or positive anomalies, probably due to the removal or accumulation of Fe-Ti oxides and Clinopyroxene.

The sills associated with the LVC and the Sintra igneous complex have basic (Lomba dos Pianos, Malveira da Serra) to more evolved (Eiras do Faião, Montelevar, Anços) compositions and show incompatible trace element patterns that reflect the processes responsible for that evolution.

The phonotephritic Eiras do Faião sill shows the more enriched character of all the sills, where the same negative K, P, Zr and Hf anomalies seen in the more basic rocks are observed, as well as a pronounced negative Ti anomaly probably caused by the removal of Fe-Ti oxides and Clinopyroxenes .

The intermediate Anços and Montelevar sills show similar spidergrams, with absent or very small negative K, Zr and Hf anomalies, while having pronounced negative Ti and P anomalies due to the removal of Fe-Ti oxides and Clinopyroxenes, and apatite.

The basic Lomba dos Pianos sill show spidergrams more similar to the other basic rocks in the province, with small negative K, Zr and Hf anomalies and but is distinguished by a positive Sr anomaly probably due to the abbundance of plagioclase phenocrysts in the sill.

Incompatible trace element patterns for the Fontanelas seamount have slightly different trace element patterns than the onshore basic samples. All of the samples show a pronounced negative, K and Sr anomalies. The Sr anomaly was probably caused by the Sr removal during the replacement of plagioclase in the matrix by secondary alteration products. These alteration products might have kept some of the Sr but were totally or partially removed during the leaching with HCl these samples were subject to prior to analysis. The K anomaly is common to all of the Late Cretaceous rocks and might be related to retention in the source, but there is also the possibility that it might have been enhanced by the alteration and/or leaching, as was previously discussed for Sr. Only one sample from Fontanelas shows a negative Zr and Hf anomaly and another one shows a spike in P, probably due to the important occurrence of apatite in inclusions in amphibole.

Considering the uncontaminated nature of these basic and ultrabasic magmas (further developed in section 7.3.2), demonstrated by the absence of Ta and Nb troughs, and considering that the crystallization and removal of phases that might cause the

depletion of these incompatible trace elements did not occur, these negative anomalies are likely to be caused by retention of these elements in residual mantle phases.

The residual phases responsible for the retention and consequent negative anomalies on the multielemental diagrams of rocks from the second pulse of alkaline magmatic activity might have formed during a metasomatic episode and correspond to K-rich amphibole or phlogopite, for K (e.g. Class and Goldstein, 1997), apatite in the case of P (e.g. O'Reilly and Griffin, 2000), and eventually baddeleyite or zircon for Zr and Hf (Andronikov and Foley, 2002; Kerr et al., 2010). These phases would either remain as a part of the mantle source during the small degree of partial melting that characterizes the generation of basic and ultrabasic alkaline magmas or equilibrate with them before their ascension and installation at crustal levels.

Small Ti negative anomalies are also visible in some samples, arguing for early removal of this element by the crystallization of Fe-Ti oxides, respectively or due to source retention in Ti rich minerals.

The nature and origin of these anomalies, their possible causes and implications for the composition and evolution history of the mantle source will be discussed in detail in section 7.4.

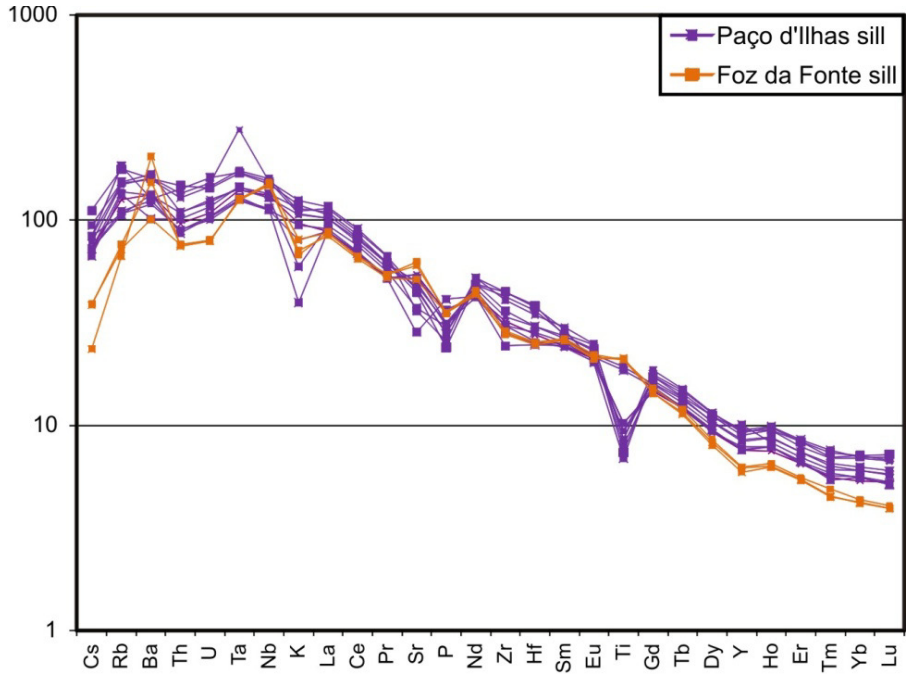

Fig. 7.8: Primitive upper mantle normalized (Palme and O'Neill, 2003) multielemental plots for the ≈ 90 Ma alkaline igneous rocks.

The older intrusions (Foz da Fonte and Paço d'Ilhas sills), that belong to the first pulse of magmatic activity in the WIM (94-88 Ma, Miranda et al., 2009, this study), show multielemental plots that are distinct from the ones seen on the c. 72 Ma rocks (fig. 7.8). They have no systematic Zr and Hf anomalies and possess less important or absent K anomalies. Among the Paço d'Ilhas samples, the more evolved samples show negative Ti anomalies due to the removal of Fe-Ti oxides and clinopiroxene to the basic layers.

Accordingly, the basic layers possess small negative anomalies for K and Sr. These anomalies may have been generated by the removal of plagioclase and K feldspar into the leucocratic layers by flotation of these less dense crystals, as suggested by Mahmoudi (1991). This is in agreement with the observed macroscopic layering in this sill.

7.1.2.2 Rare Earth Element abbundances

The REE (Rare Earth Elements) compositions are more homogeneous, with all the samples showing fractionated chondrite normalized REE patterns, being enriched in LREE (Light REE) and MREE (Medium REE) over HREE (Heavy REE) (La_N/Yb_N = 48.9 – 8.8; Tb_N/Yb_N = 3.4-1.9) suggesting the influence of residual garnet during melting events since HREE are significantly more compatible than MREE in garnet than in the melt (e.g. McKenzie and O'Nions, 1991; Adam and Green, 2006). The REE patterns of each of the sampled occurrences (fig. 7.9) will be discussed in more detail below.

No systematic differences are observed between rocks from both pulses of Late Cretaceous alkaline igneous activity.

The southern Monchique and Loulé samples are among the most fractionated (fig. 7.9a), with $(La/Yb)_N$ ranging from 48.9 to 22.9. The patterns in the Loulé lamprophyres have a steeper slope and can cut across the curves of some of the basic Monchique samples, suggesting the derivation from a more enriched source or a source with higher amounts of residual garnet.

On the other hand, the Sines gabbros and diorite are among the least fractionated (fig. 7.9b), with the Pedras Negras samples ($(La/Yb)_N$ = 15.2-8.8) being the least REE enriched of all the analyzed samples, probably as a result of their origin as cumulates of relatively REE depleted phases, such as olivine. Some of the samples from Sines, along with some of the Sintra gabbros ($(La/Yb)_N$ = 18.4-14.9) show small positive Eu

anomalies (Eu/Eu* 0.97-1.28) possibly due to the accumulation of Eu retaining plagioclase (fig. 7.9c).

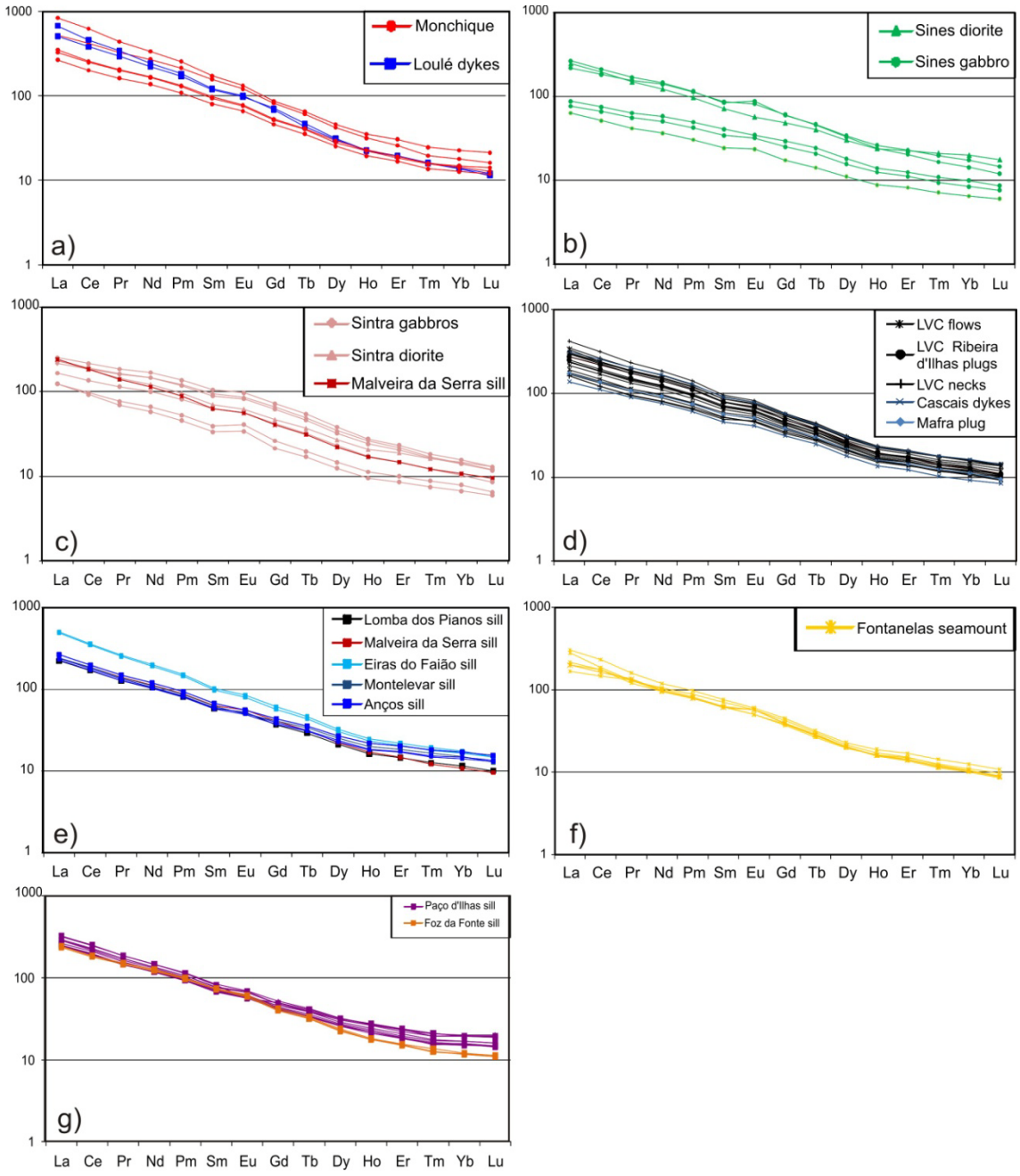

Fig. 7.9: Chondrite normalized (Palme and O'Neill, 2003) REE variation diagrams for all the studied occurrences.

Samples from the LVC necks and flows, Cascais dykes and Mafra gabbroic plug all show similar LREE enriched patterns ($(La/Yb)_N$ = 26.1-13.3, fig. 7.9d). However, the Eiras do Faião sill shows some of the more enriched and fractionated compositions of the complex ($(La/Yb)_N$ = 29.6-28.7), while the more basic Lomba dos Pianos sill has

REE patterns similar to the basalts. The more evolved Anços and Montelevar sills are slightly more enriched in HREE ($(La/Yb)_N$ = 16.3-15.7; fig. 7.9e) which show mostly flat patterns, unlike the gently oblique basic samples.

The Fontanelas seamount shows the same LREE enriched patterns ($(La/Yb)_N$ = 25.3-16.6; fig. 7.9f), as the samples from Paço d'Ilhas and Foz da Fonte sills ($(La/Yb)_N$ = 20.8-14.7; fig. 7.9g), which belong to the first pulse of alkaline magmatic activity.

The more evolved Paço d'Ilhas samples are also more HREE enriched showing the same flat HREE slopes observed in other more differentiated sills.

The relatively flat HREE patterns observed in the more evolved samples translate into low $(Gd/Lu)_N$ ratios (2.4-3.16 for the more evolved sills against 5.99-3.2 for the remaining samples, fig. 7.10c) and can be interpreted as an indicator of the influence of crustal contamination processes as an evolution mechanism for these rocks, since the continental crust is more HREE enriched and shows flatter HREE patterns and consequentially lower $(Gd/Lu)_N$ ratios (1.54-1.61, Rudnick and Gao, 2003). Further indicators for the occurrence of crustal contamination processes will be discussed in section 7.3.2.

Crystal fractionation does not seem to change the $(La/Yb)_N$ of the samples since Yb_N increases but $(La/Yb)_N$ ratios remain the same (fig. 7.10a).

However, crystal fractionation and accumulation are responsible for some minor negative and positive Eu anomalies, respectively (fig. 7.9). Specifically the slightly positive anomalies in some of the Sintra and Sines gabbros due to plagioclase accumulation and the negative Eu anomalies in the Paço d'Ilhas sill, Sines diorite and in one of the basic rocks from Monchique caused by the removal of this mineral.

Most of the samples show Eu/Eu* values of approximately 1.1 (with $Eu^* = \sqrt{(Sm_N x Gd_N)}$; Rollinson, 1993), corresponding to a small positive Eu anomaly (fig. 7.10b). A correlation between lower Eu/Eu* and Sr/Nd is also observed, suggesting that the small negative Eu anomalies formed due to crystal fractionation and removal of plagioclase from the liquid in some of the Paço d'Ilhas sill, Sines diorite, Monchique and Montelevar sill (fig. 7.10b). This process also lowered the Sr/Nd ratio, since Sr is preferentially incorporated in plagioclase. Plagioclase accumulation is responsible for the higher Eu/Eu* and Sr/Nd values of some of the Sintra and Sines gabbros and also of the plagioclase rich Lomba dos Pianos sill.

Plagioclase removal, however, seems to have played a relatively small role in controlling the evolution of these magmas since there are not many samples with low

Eu anomalies and low Sr/Nd coupled with Eu/Eu*. Also, Al_2O_3 continues to increase with increasing SiO_2 for most of the samples (fig. 7.3), except some of the layered Paço d'Ilhas sill.

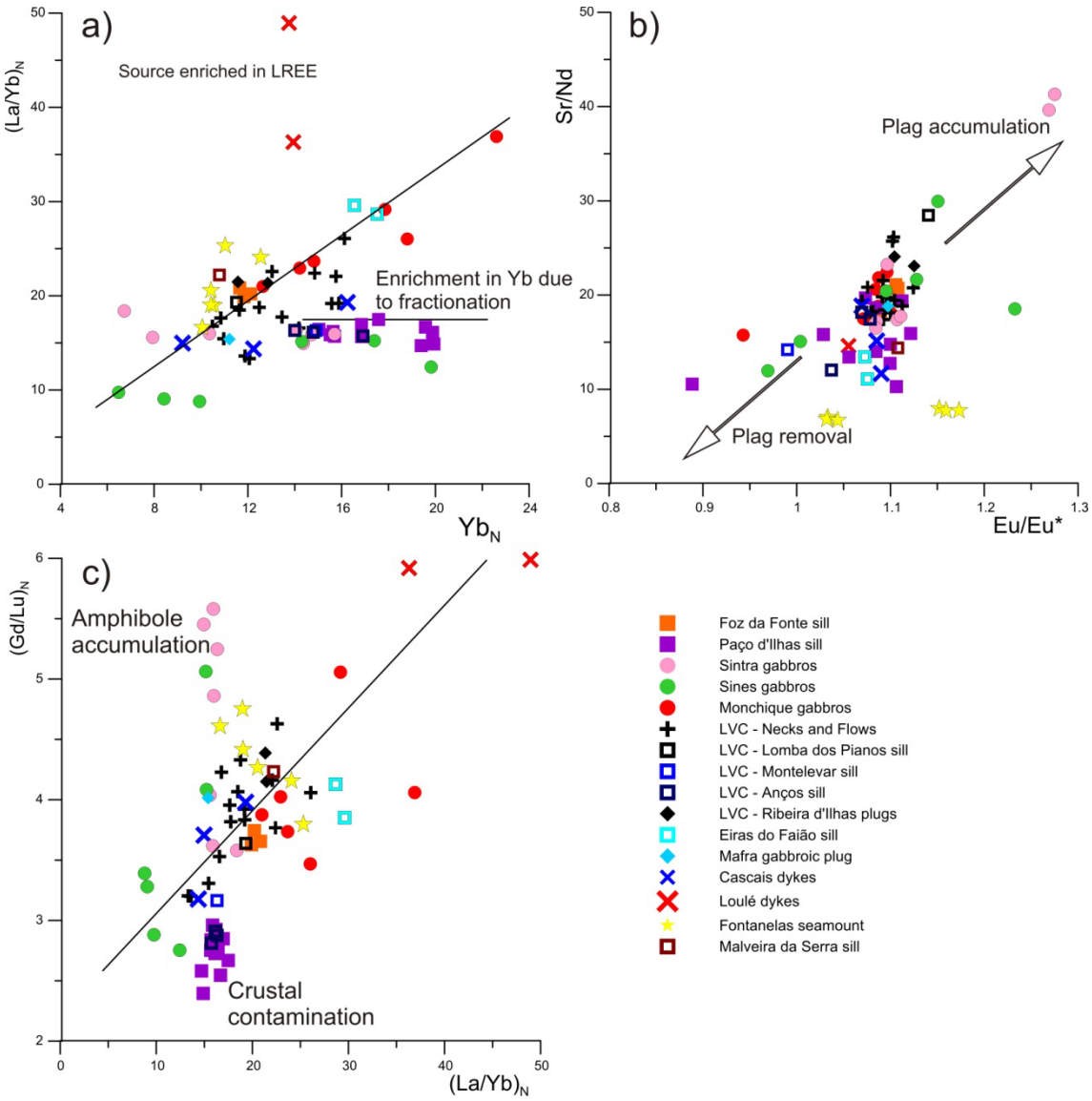

Fig. 7.10: a) Yb_N vs. $(La/Yb)_N$, b) Eu/Eu* vs. Sr/Nd, c) $(La/Yb)_N$ vs. $(Gd/Lu)_N$ diagrams for the studied samples.

The Middle REEs (MREEs) are more compatible with amphibole and depletion in MREE, such as Gd, in relation to LREE or HREE is usually associated with amphibole crystallization and removal. Although apatite is also REE compatible, removal of this mineral does not fractionate REE.

As was stated above, $(La/Yb)_N$ ratios are not greatly affected by crystal fractionation, so deviations from the main trend in the $(La/Yb)_N$ vs $(Gd/Lu)_N$ diagram

should be caused by amphibole accumulation if they plot towards higher values of $(Gd/Lu)_N$ for a certain $(La/Yb)_N$ value or by crustal contamination if the opposite is observed. The amphibole rich Peninha and Praia Vasco da Gama gabbros in the Sintra and Sines igneous complexes, respectively, seem to show signs of amphibole accumulation, while the lower $(Gd/Lu)_N$ ratios of the more evolved Paço d'Ilhas and Anços sills seem to be related to crustal contamination processes.

7.2. Radiogenic Isotope geochemistry

Sr and Nd isotope analyses were carried out at the Laboratório de Geologia Isotópica of the Universidade de Aveiro, in collaboration with Prof. Maria do Rosário Azevêdo and under the technical supervision of Eng. Sara Ribeiro. Rb, Sr, Sm and Nd contents were previously determined by ICP-MS at Actlabs Ancaster, Ontario, Canada. A 2% error in values given for the concentration of these elements was assumed in order to calculate the errors in $^{87}Rb/^{86}Sr$ and $^{147}Sm/^{144}Nd$.

All the intervening reagents in the preparation of the samples were distilled by sub-boilling, and the water produced by a Milli-Q Element (Millipore) apparatus.

The samples were mostly unaltered, but whenever trace amounts of secondary carbonate were present, the powders were leached in 1N acetic acid (CH_3COOH) according to the following method, adapted from Weiss and Frey (1996): a) the sample is weighed into an acid washed Savillex© beaker; b) 10 mL of 1N acetic acid are added; c) the suspension is ultra-sonicated for 10 minutes; d) the supernatant is decanted; e) steps b to d are repeated until reaction stops and the supernatant is clear and pale yellow to colorless. In the case of the very altered pillow lavas from the Fontanelas seamount, the amount of carbonate present as a secondary phase that replaces igneous minerals or as vesicle fillings was so significant that the powders were leached according to this same procedure, but with 2.5 HCl instead of acetic acid. The residue is then thoroughly washed in water and dried in a hot plate before digestion.

The samples were digested at 200 ºC during a 3 days period in Teflon Parr® acid digestion bombs containing 2 mL HF and 1 mL HNO_3. Afterwards, the residue is dried and then redissolved with 3ml HCl 6N in the digestion bombs during 1 night.

The elements to analyse were purified using conventional ion chromatography technique. In a first phase, for Sr and REE separation, the samples were dissolved and loaded in quartz columns containing AG8 50W Bio-Rad cation exchange resin (200-400 mesh) using HCl 2.5N as eluent for Sr and HCl 6N for REE. After, for Nd purification, the REE residue is evaporated in a hot plate, redissolved in 0.2 N HCl, and placed in a smaller quartz column containing Ln Resin (100-150 μm)–IChroM.

The isotopic analysis for Sr and Nd were performed on a VG SECTOR 54 multicollector Thermal Ionization Mass Spectrometer (TIMS). Sr was loaded on a single Ta filament with H_3PO_4, whereas Nd was loaded with HCl on a Ta outer side filament, in a triple filament arrangement. Data were acquired at dynamic mode with peak measurements at 1-2V to ^{88}Sr and 0.8-1.5V to ^{144}Nd. Sr and Nd isotopic ratios were corrected for mass fractionation relative to $^{88}Sr/^{86}Sr=0.1194$ and $^{146}Nd/^{144}Nd=0.7219$. This study took place over two years, during which the SRM-987 standard gave an average value between 0.7102562 ± 46 (N=23; conf. lim.=95%) and 0.710243 ± 10 and (N=14; conf. lim.=95%) for $^{87}Sr/^{86}Sr$, while the $^{143}Nd/^{144}Nd$ value for the JNdi-1 standard varied between 0.512105 ± 4 (N=18; conf. lim.=95%) and 0.512098 ± 5 (N=14; conf. lim.=95%). $^{143}Nd/^{144}Nd$ data are normalized to La Jolla standard. The average levels of blanks were in the range 0.25-1.0 ng for Sr and 0.5-1ng for Nd.

Pb isotopic ratios were conducted at the Department of Petrology (FALW), Vrjie Universiteit, Amsterdam, Netherlands, in collaboration with Dr. Jane Chadwick. All samples were treated in the same manner as standards and blanks using standard chemical separation techniques (after Pin, 1994). All errors are reported as 2σ.

Prior to dissolution, the samples containing secondary carbonate were leached with 6N HCl according to the procedure in Weiss and Frey (1996).

Leached samples were then washed with MilliQ water and dried. These and the non leached samples, all weighing approximately 200 mg, were then placed in a Teflon beaker together with 2 mL 40% HF dist. and 0.8 mL conc. HNO_3.The beakers were then placed on a hot plate at 150 ºC for 2-3 days while they were disgested. HNO_3 was added until the sampled was completely destroyed. The sample was later dissolved in 6N HCl and left on the hot plate for 2-5 days.

Afterwards, this solution was split in two identical aliquots, one for the determination of elementar concentrations of Pb, U and Th which was diluted 5000 times in 5% HNO_3 and the other for the acquisition of the isotopic ratios.

0.7 N HBr was later added to the aliquot intended for isotopic analysis in order to release the Pb. This solution was then centrifuged at 12000 RPM for 4 minutes, transferred to a C-Tube and then pippeted into previously washed 0.15 mL glass columns with AGIx8 (200-400 mesh) ion exchange resin, where the Pb fraction was recovered using HBr and HCl.

Elementar Pb, U and Th were analyzed in a Quadrupole Thermo X-Series II ICP-MS. Samples were prepared using a modified version of the method described by Turner et al. (1999). Detection limits and analytical precision ranged from <100 ppb to <1 ppt, and relative analytical precision was typically approximately 2 to 5% (one standard deviation). See Eggins et al. (1997) for an in-depth description of the method used.

Pb isotopes were analysed by standard–sample bracketing using a Thermo Finnigan Neptune multi-collector ICP-MS. All analyses were conducted using a Cetac AX-100 autosampler, in combination with a Cetac Aridus nebuliser to introduce samples into the MC-ICP-MS. The wash-out time between analyses was 3 min, and uptake time 2 min. A total of 5 blocks of 20 cycles were measured, with integration times of 4 s per cycle. Levels of 201Hg were always less than 0.05mV.

For each measurement, the average of the two bracketing machine blanks was subtracted before calculation of the Pb isotopic ratios. The blank levels varied between sessions with intensities of 1.5–3.0 mV on ^{208}Pb. Variable blank correction always introduced fewer uncertainties than the error from counting statistics in the concentration range of our solutions.

A 100 ppb solution of NIST SRM-981 standard gave 16.9367 ± 10, 15.4950 ± 10 and 36.7147 ± 23 (2σ, n= 3) for $^{206}Pb/^{204}Pb$, $^{207}Pb/^{204}Pb$ and $^{208}Pb/^{204}Pb$, respectively. The values of Baker et al. (2004) were used for normalisation. For the BHVO standard, these ratios yielded 18.76084 ± 10, 15.6281 ± 10 and 38.7385 ± 22 for $^{206}Pb/^{204}Pb$, $^{207}Pb/^{204}Pb$ and $^{208}Pb/^{204}Pb$, respectively (2σ, n=2). Full procedure Pb blank solutions were in the order of 0.05 ppb, corresponding to 150 pg Pb. Data reduction was done offline, following the formula for sample–standard bracketing (Albarède et al., 2004). The calculation of error propagation was performed using relative errors (%). All errors given on Pb isotopic ratios are 2

standard deviations (absolute). A detailed description of the method applied can be found in Elburg et al. (2005).

7.2.1 Introduction

Intraplate continental alkaline magmas have to cross thick continental lithosphere before they are erupted or emplaced at shallow depths. Therefore, besides carrying information about their original source, these magmas can also provide clues about the nature of the crust and lithospheric mantle they cut through, as well as information concerning the processes that control their evolution during the ascent to the surface. Long-lived radioactive isotopes are powerful tools for such studies, since they can be used as tracers for mantle and crustal magma generation, evolution and even mixing processes.

Isotope ratios for long lived isotopic reservoir, such as any sort of isolated volume of the mantle, are a linear function of their parent/daughter ratio (e.g. Rb/Sr in the $^{87}Rb \rightarrow {}^{87}Sr$ system) and a nearly linear function of time or geological age of the system. When this mantle domain undergoes equilibrium partial melting, the melt inherits the isotopic ratio of the entire system. Consequently, radiogenic isotope ratios are powerful tracers of the parent–daughter ratios of mantle sources of igneous rocks and of their evolution in time. If isotope data from several other long lived decay systems are combined (e.g $^{147}Sm \rightarrow {}^{144}Nd$, $^{235}U \rightarrow {}^{207}Pb$, $^{238}U \rightarrow {}^{206}Pb$, $^{232}Th \rightarrow {}^{208}Pb$ etc), a better image of source chemistry and history can be constructed, since different isotopic systems have different geochemical properties that lead to the development of distinct parent-daughter isotope ratios on major reservoirs. For example, Sr and Rb are both incompatible, but with $\boldsymbol{D_{Rb} < D_{Sr}}$, and concentrate in mantle melts, consequentially the mantle domains affected by magmatic extraction have a low Rb/Sr ratio and evolved towards low $^{87}Sr/^{86}Sr$. However, Sm/Nd ratios are higher in the mantle, while differentiated crustal rocks are enriched in the slightly more incompatible Nd relative to Sm, so the mantle rocks usually show higher $^{143}Nd/^{144}Nd$ ratios than crustal rocks, especially the more differentiated ones, which have low $^{143}Nd/^{144}Nd$. In summary, most of the differences in isotopic composition are a result of ancient chemical fractionation events and the consequent time integrated evolution under different parent/daughter ratios.

It is generally much easier to measure the ratio of two isotopes than the absolute abundance of one. We therefore measure the ratio of, for example, ^{87}Sr to a non-radiogenic isotope, which by convention is ^{86}Sr. In this work, these ratios will be used, together with some incompatible trace element ratios, as tracers of mantle sources, crust–mantle interaction processes, and mantle melting processes, with the aim of understanding the petrogenesis of the Late Cretaceous alkaline rocks of the WIM.

Another possible way of representing isotopic ratios is through the Epsilon (ε) notation, that describes the deviations of several isotopic ratios from the ones attributed to the Chondritic Uniform Reservoir (CHUR – an approximation of the isotopic values on the chondritic solar system, before planetary differentiation took place (DePaolo and Wasserburg, 1976), at the time (t) of rock formation. This value is given by the following equation:

$$\varepsilon Nd(t) = [(^{143}Nd/^{144}Nd)_{sample(t)}/ (^{143}Nd/^{144}Nd)_{CHUR(t)}-1] \times 10000$$

Epsilon units usually correspond to larger numbers and are therefore a more easily understood representation of the initial isotopic ratios, rendering comparisons between different rocks an easier task.

7.2.2 Results

The studied samples show relatively low $^{87}Sr/^{86}Sr_i$ (0.703005 to 0.704884) and high εNd_i (and high $^{143}Nd/^{144}Nd$) values (5.8 to2.8) that plot on the depleted quadrant of the $^{87}Sr/^{86}Sr_i$ vs. εNd_i diagram (fig. 7.11), showing lower values of $^{87}Sr/^{86}Sr_i$ than Bulk Earth and higher εNd_i than the CHUR, except for the sample from the Lomba dos Pianos sill that is distinctively more enriched in $^{87}Sr/^{86}Sr_i$. These values suggest a time integrated depletion in Rb and Nd relative to Sr and Sm, respectively, which is in contrast with the previously mentioned trace element enriched nature of these rocks.

The majority of the basic samples that do not present any evidence for contamination by crustal lithologies show a narrow Sr and Nd isotopic range and plot mostly between the HIMU and FOZO components ($^{87}Sr^{87}Sr/^{86}Sr_i$ 0.7030-0.7037; εNd_i 5.7 – 3.7, fig. 7.10-11). Meanwhile, some of the more evolved samples (Paço d'Ilhas sill, Anços sill) and one basic dyke (basalt dyke from Cascais) define a trend towards more radiogenic Sr isotopic ratios and lower εNd ($^{87}Sr/^{86}Sr_i$ up to 0.7049 and εNd_i as low as 3.1, fig. 7.10-12), probably as a result of contamination by crustal lithologies.

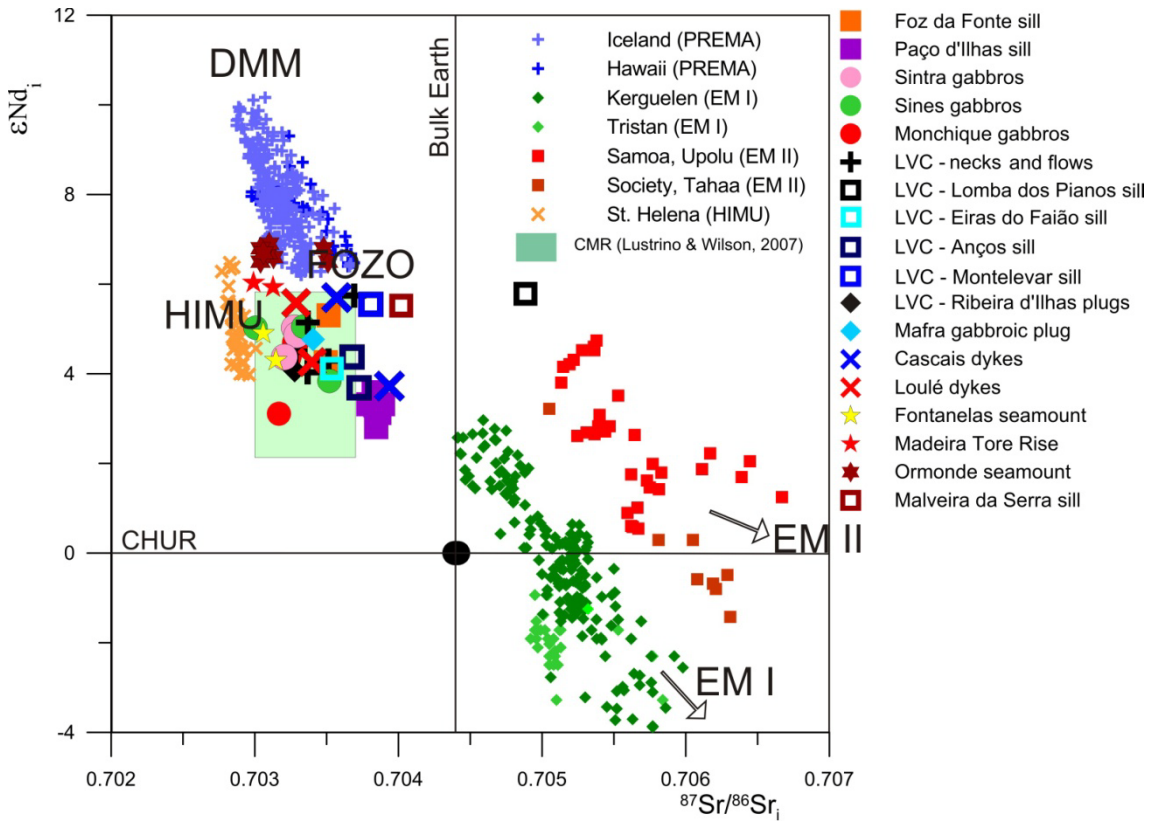

Fig. 7.11: Sr-Nd isotopic plot comparing locations representative of different mantle end-member compositions and the Common Mantle Reservoir (CMR, Lustrino and Wilson, 2007) with the Late Cretaceous intraplate alkaline magmatism of the West Iberian Margin. Data for the ocean island that represent the different mantle end members from the GEOROC database (http://georoc.mpch-mainz.gwdg.de/georoc/). For more information on mantle components, see section 3.

It is possible to observe two trends diverging from the central cluster of values ($^{87}Sr/^{86}Sr_i$ 0.703-0.7037; εNd_i 5.7-3.7, figs. 7.11-12). One trend is defined by the Malveira da Serra, Montelevar and Lomba dos Pianos sills and is characterized by an $^{87}Sr/^{86}Sr_i$ increase while εNd_i remains unaltered. In the second trend, represented by the Paço d'Ilhas and Anços sills and one of the Cascais dykes, $^{87}Sr/^{86}Sr_i$ increases simultaneously as εNd_i decreases (fig. 7.11-12). These two trends are probably the result of contamination by crustal lithologies with different isotopic and trace element abundances, and will be discussed in more detail later in section 7.3.2. They do not seem to reflect secondary alteration and the addition of secondary carbonated material since the samples were leached with acetic acid, which successfully removed that secondary carbonated fraction in the Foz da Fonte and Anços sills (fig. 7.13).

A tentative explanation for the observed inconsistency between the enriched trace element signatures and depleted Sr and Nd isotopic composition shown by the Late Cretaceous alkaline rocks of the WIM is that the trace element enrichment of the source could be attributed to a mantle metasomatism event that possibly occurred

shortly before the generation of these magmas, adding incompatible trace elements to the source while not affecting its originally depleted isotopic composition. Since this enrichment took place shortly before magma generation, the source for these rocks did not have sufficient time to evolve into a more significantly enriched and heterogenous isotopic composition. Such a metasomatic agent could have been a liquid derived from very low amounts of partial melting from a relatively isotopically depleted reservoir, such as the asthenospheric mantle, or the first melt fractions of an ascending mantle plume, as is suggested by several authors for other cases of intraplate alkaline magmatism (e.g. Niu, 2008; Pilet et al., 2008, 2010; Martins et al., 2010) and seems to be supported by mineral chemistry data presented in section 6.2. Evidence provided by trace element geochemistry for the existence of metasomatic mantle processes will be discussed in section 7.4.

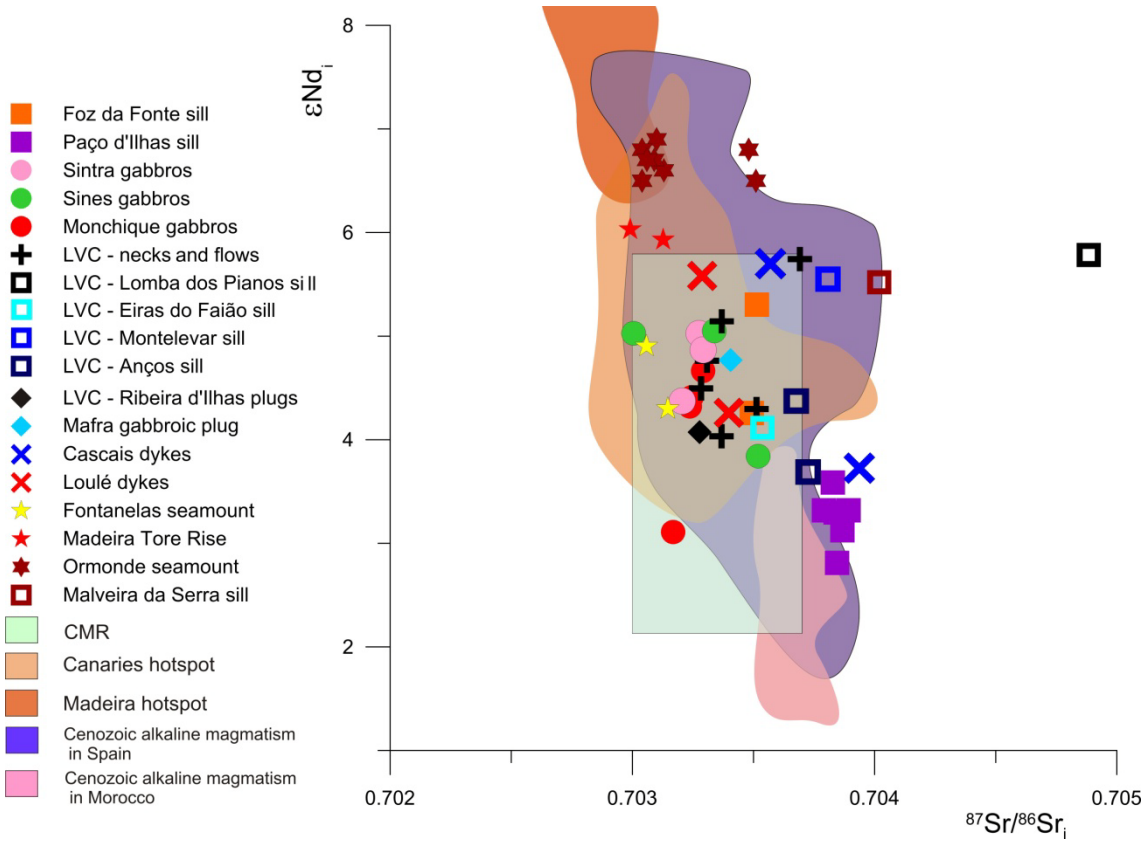

Fig. 7.12: Sr-Nd isotopic plot comparing the compositions of the CMR, Madeira and Canaries hotspots and of the Cenozoic Moroccan and Spanish alkaline intraplate magmatic activity with the Late Cretaceous intraplate alkaline magmatism of the West Iberian Margin. Data for the CMR, the Madeira and Canaries hotspots, Spanish and Moroccan cenzoic magmatism from Lustrino and Wilson (2007).

The samples from the nearby Late Cretaceous Ormonde seamount (≈ 67 Ma) and Madeira-Tore Rise (≈ 80-100 Ma) show even more depleted Nd isotopic compositions, with higher εNd_i values, but on the other hand show a similar $^{87}Sr/^{86}Sr_i$ range (fig. 7.11).

In most cases, the uncontaminated basic Late Cretaceous Alkaline rocks from the WIM also plot in the same fields defined by the Common Mantle Reservoir (CMR, a mantle reservoir defined as a common source component for the rocks of the circum-Mediterranean anorogenic Cenozoic igneous province by Lustrino and Wilson, 2007), the Canaries mantle plume and Cenozoic alkaline magmatism occurred in Spain.

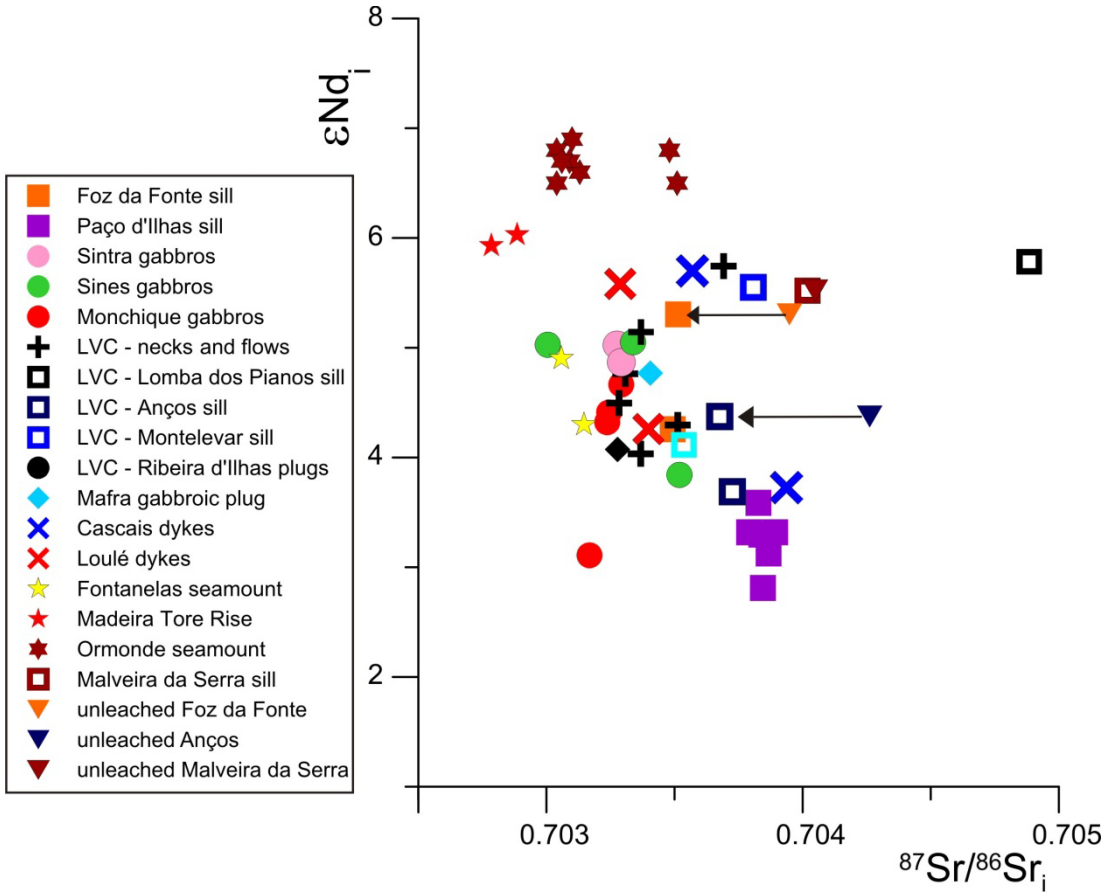

Fig. 7.13: Sr-Nd isotopic values for the analyzed samples, including the unleached and leached Foz da Fonte, Malveira da Serra and Anços sills. The leaching process resulted in a significant decrease of $^{87}Sr/^{86}Sr$.

Pb isotopes show $^{206}Pb/^{204}Pb_i$ (18.827-19.564) compositions that are more enriched than DMM and most of the samples with EM component signatures, but less enriched than HIMU (figs. 7.14 and 7.15). $^{207}Pb/^{204}Pb_i$ values (15.567-15.634) define a compositional array close to the Northern Hemisphere Reference Line (NHRL, a trend defined by the basalts from the Mid Atlantic Ridge basalts and ocean islands of the northern Atlantic, Hart, 1984) and EM II (fig. 7.14), while $^{208}Pb/^{204}Pb_i$ (38.603-39.948) shows values trend close to the NHRL between EM II and HIMU, except for the samples from the Fontanelas seamount who show higher $^{208}Pb/^{204}Pb_i$ values. The origin

of such high $^{208}Pb/^{204}Pb_i$ in the Fontanelas seamount will be addressed in detail in section 7.5.2.

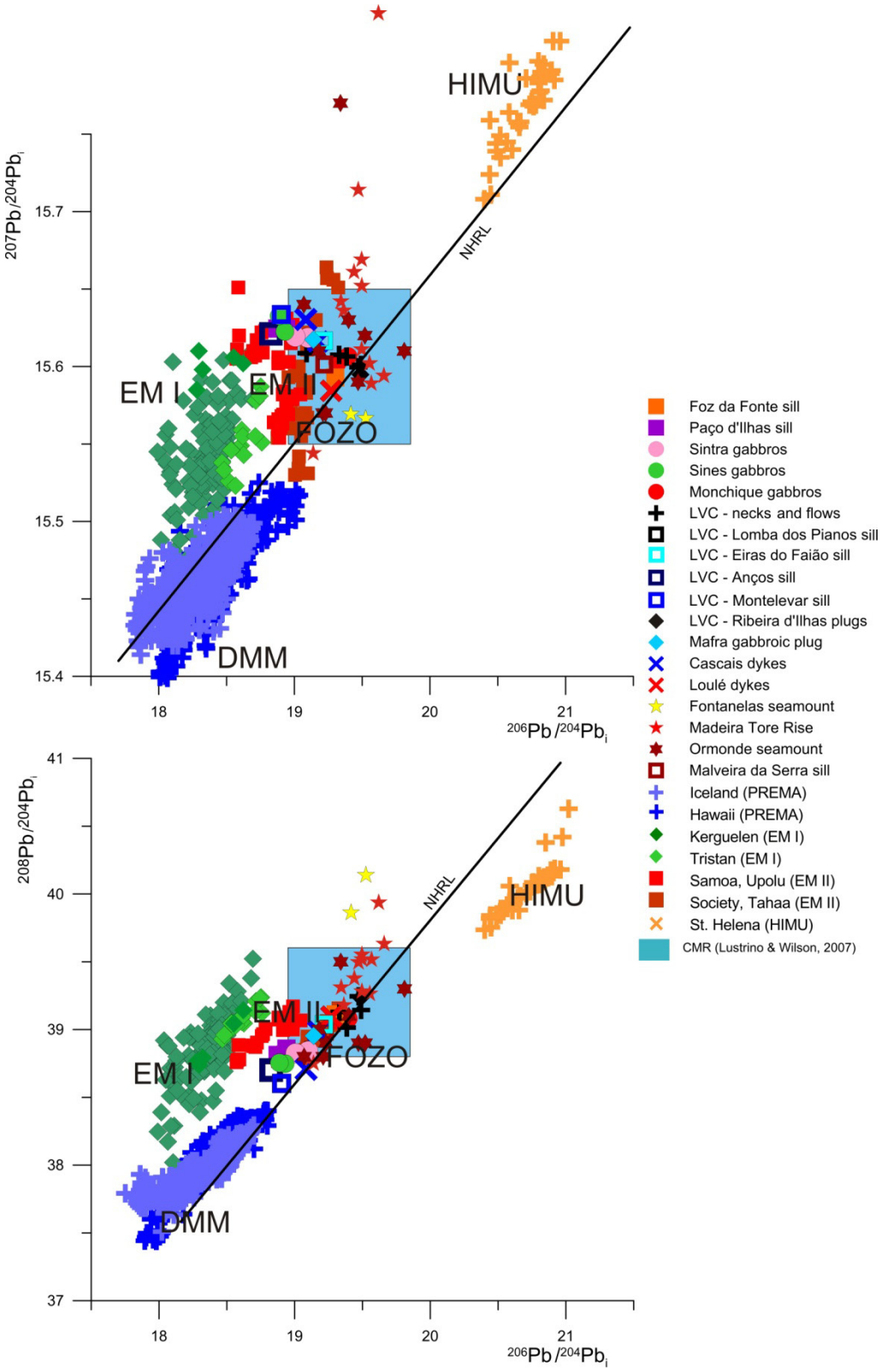

Fig. 7.14: Pb-Pb isotopic plots comparing mantle end-member compositions and CMR (Lustrino and Wilson, 2007) with the Late Cretaceous intraplate alkaline magmatism of the West Iberian Margin. Data for the ocean island that represent the different mantle end members from the GEOROC database.

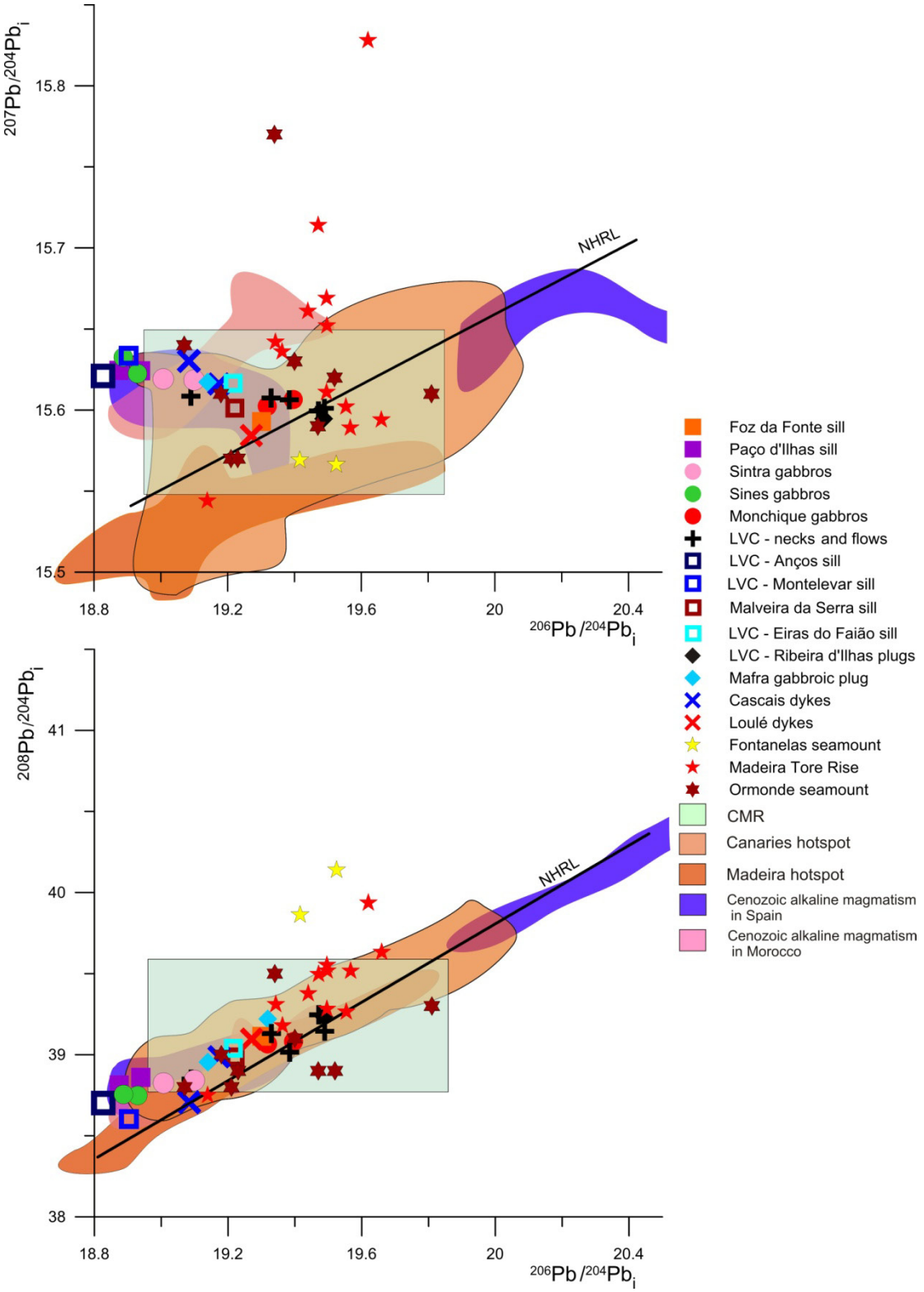

Fig. 7.15: Pb-Pb isotopic plots comparing the compositions of the CMR, Madeira and Canaries hotspots and of the Cenozoic Moroccan and Spanish alkaline intraplate magmatic activity with the Late Cretaceous intraplate alkaline magmatism of the West Iberian Margin. Data for the CMR, the Madeira and Canaries hotspots, Spanish and Moroccan cenzoic magmatism from Lustrino and Wilson (2007).

The more basic samples cluster around $^{206}Pb/^{204}Pb_i$ 19.564-19.20, $^{207}Pb/^{204}Pb_i$ 15.609-15.580 and $^{208}Pb/^{204}Pb_i$ 39.245-39.00 values, along the NHRL. The more

evolved rocks, along with the gabbros from Sintra and Sines, show Pb isotopic signatures that plot progressively away from the NHRL, towards higher $^{207}Pb/^{204}Pb_i$ (max. 15.634) and lower$^{206}Pb/^{204}Pb_i$ (min. 18.827) and $^{208}Pb/^{204}Pb_i$ (min. 38.603), which is likely to be related to crustal contamination, a process which will be discussed in detail in section 7.3.2.

The basic samples also plot near some samples from the Madeira Tore rise and, more consistently, the Ormonde seamount (fig. 7.14 and 7.15). However, the compositions of these two submarine features tend to show more enriched Pb isotopic values, including much higher $^{207}Pb/^{204}Pb_i$.

They also fall within the fields defined by the CMR and Canaries hotspots, with some of the more evolved samples and gabbros trending towards Pb isotopic compositions that plot into the fields defined by other intraplate continental alkaline occurrences in the region such as the Moroccan and Spanish Cenozoic alkaline magmatism (fig. 7.15).

This might indicate that similar evolution mechanisms, such as crustal contamination, characterized the evolution of the magmas in all these provinces. One of the seamounts of the MTR and some of the samples from the Ormonde peak on the Gorringe bank seem to show composition affinities with the samples from the Madeira hotspot, falling into or near the field they define in the diagrams.

On the Pb-Sr and Pb-Nd isotopic spaces (figs. 7.16 and 7.17) the studied samples also plot in between a more depleted PREMA like reservoir and the high U/Pb HIMU, near FOZO. Some of the evolved samples show a trend towards EM type compositions. These correspond to the more evolved and possibly contaminated samples which plot closer to the EM II domain.

Samples from the basic rocks present in the Sines and Sintra complexes show distinct behaviors from their basic counterparts in the WIM as is shown by the Pb-Pb, Pb-Sr and Pb-Nd diagrams (figs. 7.14-17). They plot along with the more evolved and possibly contaminated samples in the Pb-Pb isotopic space and show intermediate compositions in the Pb-Sr and Pb-Nd diagrams with more basic and evolved rocks in the Pb-Sr and Pb-Nd diagrams.

Comparing our results with the alkaline rocks of similar age present in the region (fig. 7.17), it is discernible that they show, in general, consistently lower Nd and in most cases higher Sr isotopic ratios than the nearby Madeira-Tore rise and Ormonde

seamount for similar $^{206}Pb/^{204}Pb$ values. Again, the more evolved rocks tend to show isotopic signatures similar to the ones shown by the Cenozoic alkaline magmatism present in Spanish territory. Some of the basic samples plot in the fields defined by samples from the Canaries hotspot.

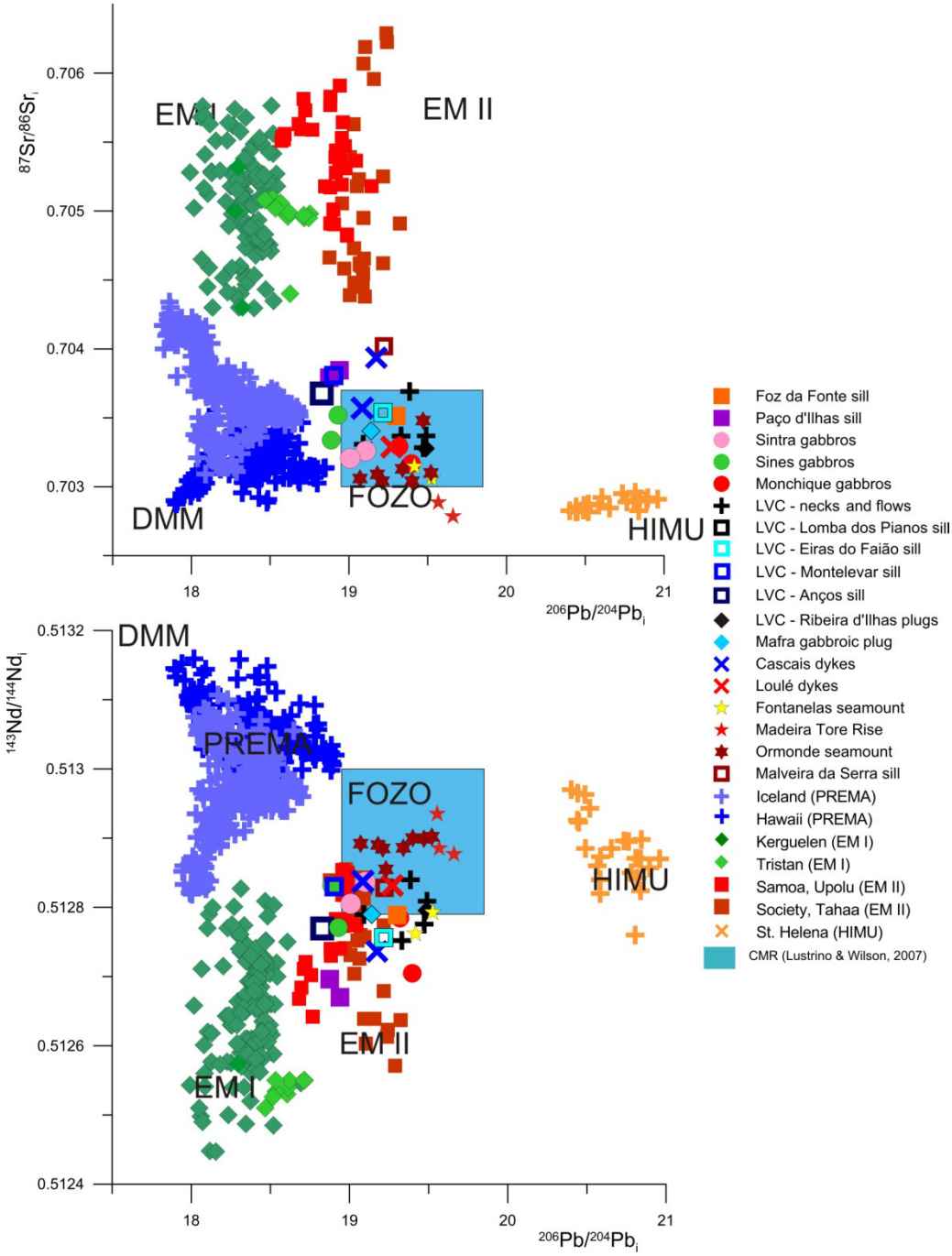

Fig. 7.16: $^{206}Pb/^{207}Pb$ vs. $^{87}Sr/^{86}Sr$ and $^{206}Pb/^{207}Pb$ vs. $^{143}Nd/^{144}Nd$ plots comparing mantle end-member compositions and CMR with the Late Cretaceous intraplate alkaline magmatism of the West Iberian Margin. Data for the CMR from Lustrino and Wilson (2007), and for the ocean island that represent the different mantle end members from the GEOROC database.

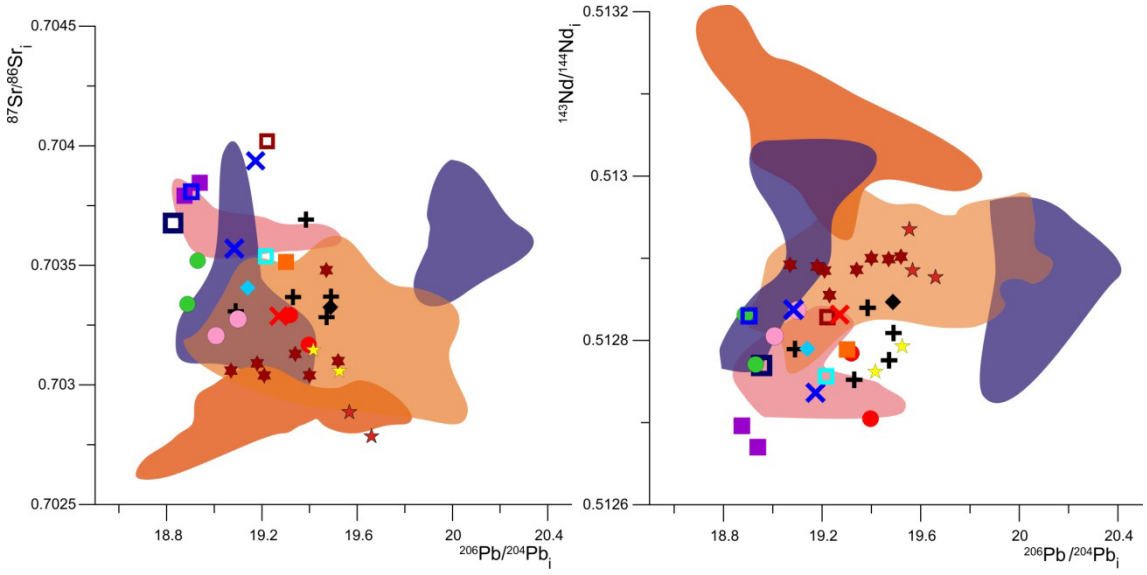

Fig. 7.17: $^{206}Pb/^{207}Pb$ vs. $^{87}Sr/^{86}Sr$ and $^{206}Pb/^{207}Pb$ vs. $^{143}Nd/^{144}Nd$ plots comparing the compositions of the CMR, Madeira and Canaries hotspots and of the Cenozoic Moroccan and Spanish alkaline intraplate magmatic activity with the Late Cretaceous intraplate alkaline magmatism of the West Iberian Margin. Data for the CMR, the Madeira and Canaries hotspots, Spanish and Moroccan cenzoic magmatism from Lustrino and Wilson (2007). Legend as in fig. 7.14.

These results seem to indicate that the studied rocks originated from a source with a Sr Nd time integrated isotopic depletion, suggesting the involvement of a sublithospheric source that is slightly more enriched than the asthenospheric mantle sampled in the Mid Ocean Ridges (DMM component) but with different, less radiogenic compositions than the EM and HIMU components.

Meanwhile, the Pb isotopic composition of the same rocks is quite radiogenic and argues for a source with higher time integrated U/Pb ratios than the depleted asthenospheric mantle or the EM mantle components.

The source for the Late Cretaceous alkaline magmas of the WIM could reside either in a mantle plume component or at the metasomatized lithospheric mantle. These hypothesis will be address in more detail in section 7.5.

One sample from a basaltic dyke in Cascais (RM 64) shows a rather enigmatic isotopic signature, having higher $^{87}Sr/^{86}Sr_i$ and lower εNd_i than other basic rocks in the region, while showing similar radiogenic Pb ratios. This could be either due to crustal contamination by a more enriched crustal lithology or to a lithospheric contribution during the generation of this dyke. This subject will de approached in more detail below.

7.3 Magmatic evolution processes

Parental magmas tend to generate more evolved, silica rich liquids through differentiation processes such as fractional crystallization, assimilation/crustal contamination and mixing with other melts.

The influence of these processes in the composition and evolution of the Late Cretaceous Alkaline rocks from the WIM is discussed in this section.

7.3.1 Fractional Crystallization

As was previously mentioned on the major and trace element characterization of the samples, the fractional crystallization and removal and/or accumulation of olivine, clinopyroxene, Fe-Ti oxides, and in some cases even plagioclase and apatite, seems to have had an important role in the evolution of the alkaline magmatic suites observed on the West Iberian Margin.

Some of the evidence for the importance of crystal accumulation has already been discussed in the petrographical characterization of the samples (section 6.1) and during the geochemical description of the studied samples (sections 7.1 and 7.2). Its effects are also evident from the observation of figures 7.1-4 and 7.7-10 and generally result in marked enrichements or depletions in a certain element that is abundant in a given mineral. Samples are usually enriched in such an element if that mineral has accumulated in the studied rock or depleted if it has been extensively removed from the melt.

As the rocks sampled in this study have different ages, and are not from a single intrusion or complex, it cannot be assumed that crystal fractionation affected these intrusions in the same way, since fractionating assemblages should vary. Therefore, in order to illustrate the role of crystal fractionation on the variability of the alkaline magmas from the WIM, the modeling effort will be concentrated on the LVC and associated minor intrusions (see section 2.3), since this complex was more extensively sampled.

As was already mentioned, primary rocks are absent in the LVC as well as from the other sampled occurrences. This is by itself evidence for the importance of fractional crystallization processes in the evolution of the rocks from the WIM, and argues for the existence of deeper chambers where fractionation of at least olivine, chromian spinel and maybe even clinopyroxene and other phases (e.g. amphibole, apatite) took place.

In order to model the crystal fractionation processes in the rocks from the LVC and try to evaluate the role of this process in the differentiation of these magmas, sample RM 69 was selected as being representative of the parental composition from which most of the rocks associated with this complex might have evolved. This sample has relatively high MgO, Ni and Cr concentrations and Mg# (MgO 9.98 %, Ni 143 ppm, Cr 400 ppm and Mg# 65.1) and shows no signs that its composition was controlled by crystal accumulation. Other samples with higher contents in Ni, Cr and MgO can be found among the sampled LVC rocks, but their compositions and textures shows evidence for modification by important crystal accumulation.

The amount of fractional crystallization of a certain mineral phase or assemblage necessary to generate the observed compositional spectrum can be modeled using the Rayleigh law, which describes the case where crystals are removed from the melt instantly after crystallization (e.g. Rollinson, 1993). The equation that describes Rayleigh/fractional crystallization is:

$$\frac{C_l}{C_0} = F^{(D-1)}$$

Where C_l is the concentration of an element in the remaining magmatic liquid, C_0 is the concentration of the same element in the initial magma, F is the remaining melt fraction and D is the partition coefficient between the crystallizing mineral(s) and the magmatic liquid.

This can be rewritten as:

$$C_l = \left(F^{(D-1)}\right) * C_0$$

This will give the concentration on an element of known D in the remaining liquid after a certain amount (1-F) of the fractional crystallization of a given mineral or mineral assemblage.

K is not a stoichiometric element relatively to any of the minerals thought to have fractionated in the LVC, it behaves incompatibly, and does not show much variation between samples with a given SiO_2 content, so it was chosen to be the differentiation proxy plotted in the X axis of the diagrams used to evaluate the role of the fractional crystallization process.

Overall, the evolution of the concentrations for the compatible trace elements (Ni, Cr, Sc, V) from basanitic to intermediate terms is in agreement with the fractional

crystallization of an assemblage of clinopyroxene (55%) + olivine (20%) + plagioclase (17.5%) + magnetite (7.5%) (fig. 7.18).

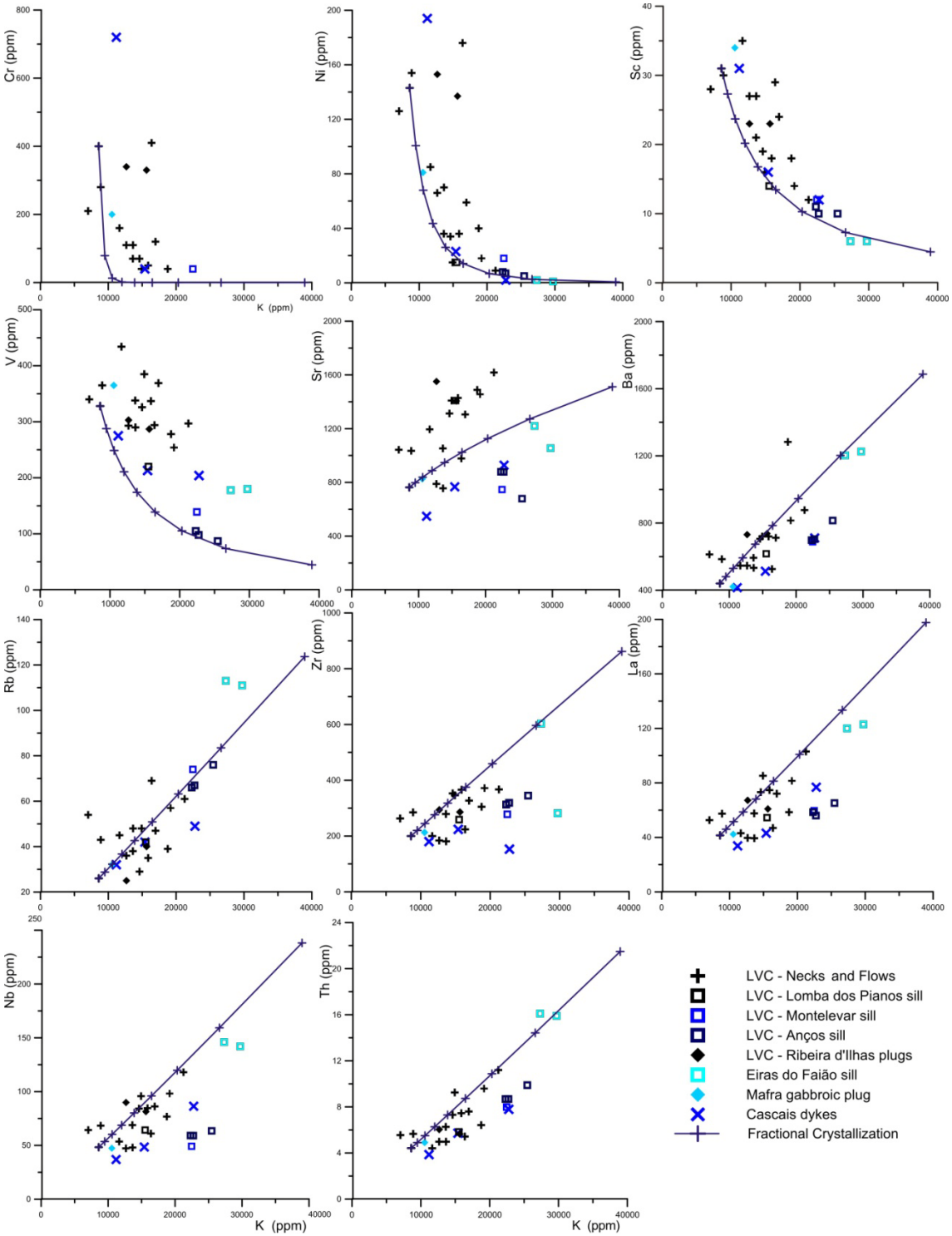

Fig. 7.18: Plots of K vs. selected trace elements showing the samples from the LVC and associated ocurrences and the trend defined by the fractionation of an assemblage of clinopyroxene (55%) + olivine (20%) + plagioclase (17.5%) + magnetite (7.5%). Each tick mark corresponds to 10% increment of the crystallized mass.

Sr shows a different behavior, becoming compatible in some of the more evolved samples, like the Anços and Montelevar sills. Some of the incompatible trace elements, such as Rb and Ba, also seem to follow a trend compatible with the fractional crystallization of that same assemblage. Still, not all of the samples plot near the modeled trend for the more incompatible Zr, La, Nb and Th (fig. 7.18).

In some cases this seems to be due to the choice of a relatively enriched initial composition for the parental liquid used in this modeling, since the remaining samples sometimes appear to define evolution trends parallel to the modeled one. However, the more evolved, silica saturated Anços and Montelevar sills, seem to define a different trend, oblique to the calculated one, characterized by a less pronounced enrichment in incompatible trace elements. This implies that fractional crystallization is not the only mechanism controlling the evolution of this rock suite.

These results must be regarded with caution and only as giving a general idea of the crystal fractionation processes affecting the LVC, as its accurate interpretation must take into account:

1) the possible occurrence of distinct parental magmas (mantle source heterogeneity and/or several distinct melting events);
2) the fact that, as shown before (see section 6), the fractionating phase(s) can change during the evolutionary process;
3) the existence of assimilation and contamination processes.

If we apply the same calculated fractional crystallization trend to the entire data set in order to encompass all of the studied samples, one can observe the existence of similar trends to the ones identified for the LVC (fig. 7.19), indicating that that these magmas might have evolved through the fractionation of relatively similar mineral assemblages.

In fig. 7.19 it is noticeable that the Sr concentration for the Anços, Montelevar and especially the Paço d'Ilhas sill show a considerable divergence from the main trend observed for the evolution of Sr with K, showing a compatible behaviour. To explain this change in behavior it is necessary to model the crystal fractionation of a different crystal assemblage (fig. 7.19) with with plagioclase (50%), clinopyroxene (30%), amphibole (10%) and magnetite (10%) (green trend in fig. 7.19).

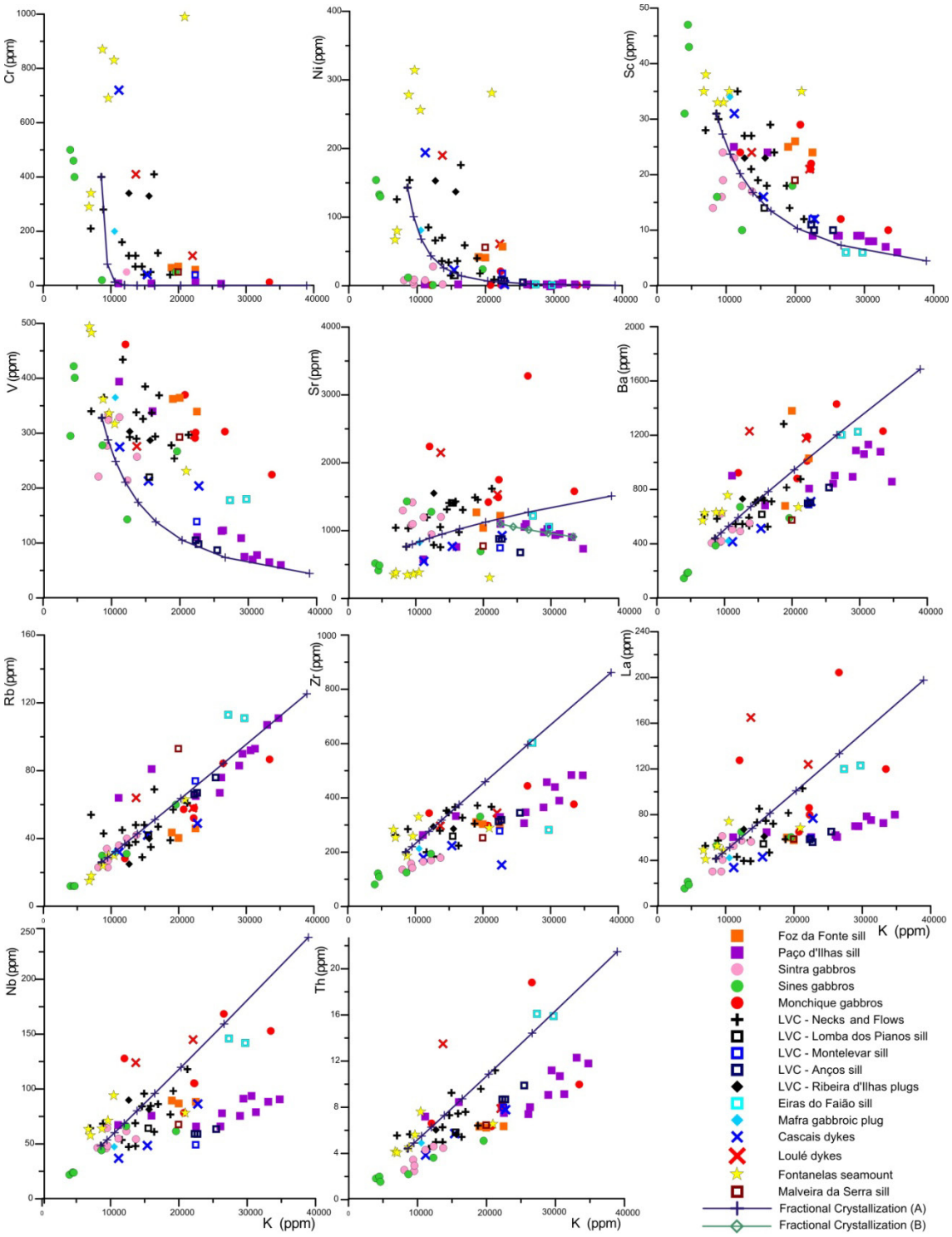

Fig. 7.19: Plots of K vs. selected trace elements showing all the collected samples and the trend defined by the fractionation of an assemblage of: (A) clinopyroxene (55%) + olivine (20%) + plagioclase (17.5%) + magnetite (7.5%) and (B) plagioclase (50%), clinopyroxene (30%), amphibole (10%) and magnetite (10%). Each tick mark corresponds to 10% increment of the crystallized mass.

It should be noted that the modeled fractional crystallization curve requires the crystallization of nearly 80% of the original basanitic liquid in order to reproduce the

observed geochemical evolution (figs. 7.18 and 7.19), which seems to be a very high value and can also be considered as suggestive of the existence of other processes controlling the evolution of these rocks. However, if only the LVC is considered, the remaining 20% of the liquid are roughly in the same proportion of evolved rocks present in this complex.

Table 7.2: Partition coeffiecients (K_d) for the minerals used in fractional crystallization modelling according to the data available on GERM database (www.earthref.org, Philpotts and Schnetzler 1970; Paster et al., 1974; Sun et al., 1974; Matsui et al., 1977; Mysen, 1978; Takashi, 1978; Okamoto, 1979; Shimizu, 1980; Kravuchuk et al. 1981; Villemant et al., 1981; Dostal et al., 1983; Lemarchand et al., 1987; McKenzie and O'Nions, 1991; Nielsen, 1992; Adam et al., 1993; Beattie, 1993, 1994; Hart and Dunn, 1993; Dalpe and Baker, 1994; Latourrette et al., 1995; Esperanza et al., 1997; Zack and Brumm, 1998; Bindeman et al., 1998; Green et al., 2000; Adam and Green, 2006; Aignertorres et al., 2007).

mineral	clinopyroxene	olivine	amphibole	plagioclase	magnetite
K	0.0072	0.0056	0.78	0.301	0.045
Sc	3.62	0.32	1.59	0.04	1.96
V	3.1	0.15	3.4	0.1	6.85
Cr	8.49	1.3	0.1	0.08	153
Ni	2.6	2.86	16	0.04	31
Rb	0.011	0.04	0.34	0.058	0.11
Sr	0.2	0.0000154	0.298	2.536	
Zr	0.123	0.06	0.31	0.003	0.71
Nb	0.0077	0.01	0.159	0.01	0.01
Ba	0.22	0.05	0.46	0.183	0.028
La	0.0536	0.00053	0.039	0.065	0.015
Th	0.012	0.0000024	0.009	0.05	0.1

In summary, fractional crystallization is an important process in the evolution of the Late Cretaceous alkaline magmas of the WIM, as demonstated by the modeling of the evolution of the samples associated with the LVC through the crystallization and removal of an assemblage of clinopyroxene (55%) + olivine (20%) + plagioclase (17.5%) + magnetite (7.5%). The remaining samples of the studied Late Cretaceous alkaline rocks plot close to the line defined by this model but the more evolved terms define a trend that is oblique to the obtained fractional crystallization curve. This and the some elemental and isotopic characteristics of the more evolved samples suggest that, besides fractional crystallization, these rocks should have been under the influence of other processes during their evolution, such as crustal contamination.

7.3.2 Crustal Contamination

The absence of samples that might correspond to primary magmatic liquids among the basic alkaline rocks of the WIM argues for the occurrence of stagnation in magma chambers and important fractional crystallization before these magmas reached the upper crustal levels.

Such a setting is also compatible with a scenario where crustal rocks or melts can be assimilated or mixed with the ascending magmas, contaminating the mantle melts and changing their isotopic and trace element signature, since stagnation and crystallization of basic magmas will provide the country rock with the heat necessary for its fusion and subsequent mixing with the basic magmas (e.g. DePaolo et al., 1981; Reiners et al., 1995; Spera and Bohrson, 2001; Bohrson and Spera, 2001). This hypothesis is addressed below.

7.3.2.1 Trace element and isotopic evidences for contamination

The most obvious indication for the existence of crustal contamination as an important petrogenetic process is the variation of the isotopic ratios with increasing silica, i.e. with magmatic evolution. In fig. 7.19a-e it is visible that $^{87}Sr/^{86}Sr$ and $^{207}Pb/^{204}Pb$ increase, but $^{143}Nd/^{144}Nd$, $^{206}Pb/^{204}Pb$ and $^{208}Pb/^{204}Pb$ decrease with increasing SiO_2. This is a strong indicator for increasing assimilation of siliceous crustal material with continuing crystallization.

Some samples, however, show high $^{87}Sr/^{86}Sr$ and relatively unchanged εNd_i and Pb isotopic ratios while having low SiO_2 contents (Lomba dos Pianos and Malveira da Serra sills and a basaltic dyke from Cascais, see also figs 7.11 to 7.13), which argues for the existence of another type of possibly SiO_2-poor contaminant.

Although none of the analyzed samples shows Nb and Ta negative anomalies which are classic indicators of contamination by crustal material, which is depleted in these elements (Rudnick and Gao, 2003), the observed increase in Th/La, Zr/Nb and K/Nb towards values closer to crustal compositions with increasing SiO_2 (fig. 7.20) cannot be explained by fractional crystallization processes alone, which would result on the persistence of the same values for incompatible trace element ratios from basic to acid terms. Thus, the input from a contaminant with higher Zr/Nb, Th and K and lower

La and Nb than the original magmas is required to cause an increase of these ratios with magmatic evolution.

The continental crust has higher Th/La (Upper Continental Crust 0.34; Lower Continental Crust 0.15; Rudnick and Gao, 2003), Zr/Nb (UCC = 16.1; LCC 13.6; Rudnick and Gao, 2003) and K/Nb (UCC = 1937; LCC 1012; Rudnick and Gao, 2003) and is the most likely contaminant of these magmas.

Nb/U decreases with increasing silica (fig. 7.21) to values below those associated with oceanic ocean island basalts linked to mantle plumes or the asthenosphere (47 ± 10; Hoffman et al., 1986), which is also in agreement with contamination of these samples by crustal lithologies with lower Nb/U (UCC = 4.44; LCC 25.0; Rudnick and Gao, 2003).

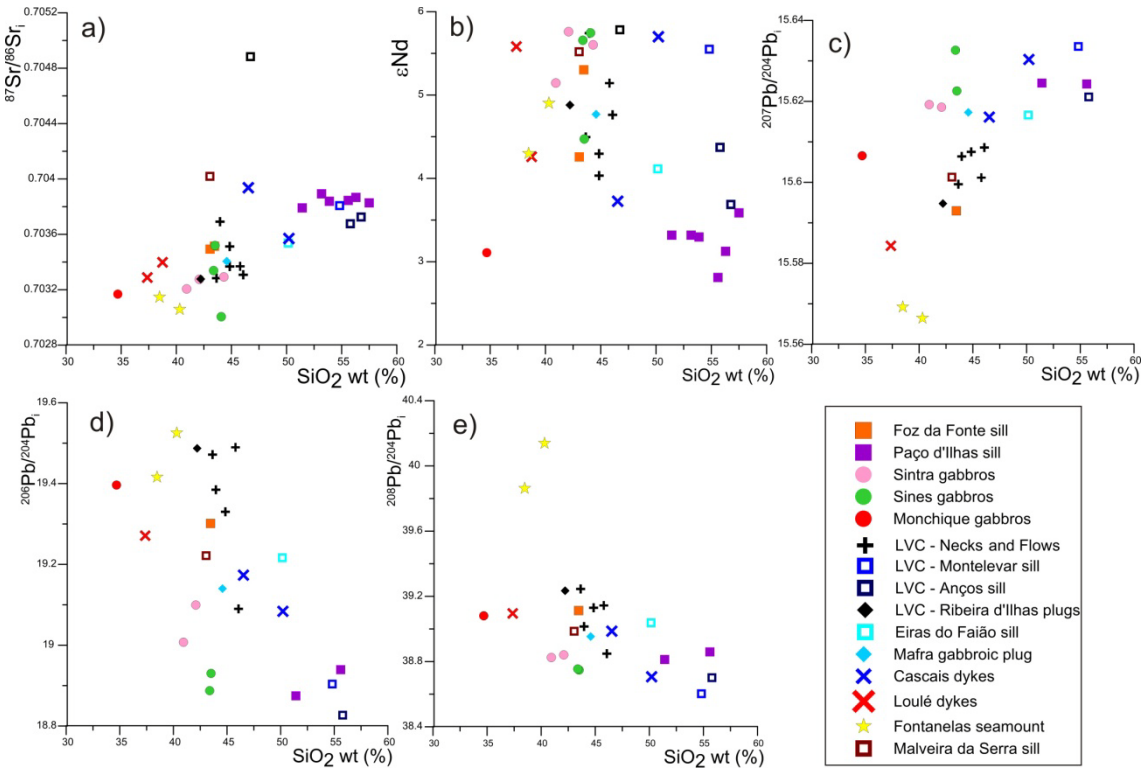

Fig. 7.20: Plots of SiO_2 vs. isotopic ratios showing changes with increasing silica contents.

Some samples have higher Nb/U than ocean basalts (fig. 7.21), probably due to the removal of U during alteration by aqueous fluids since most of these high values occur in the Sintra, Sines and Monchique intrusive complexes, where late hydrothermal alteration is observed, or in the extensively seawater altered pillow lavas of the Fontanelas Seamount.

The higher contents in HREE, low values of $(Gd/Lu)_N$ (fig. 7.10,) and flatter HREE profiles (fig. 7.9) discussed in section 7.1.2 also argue for significant crustal assimilation in the more evolved samples, especially the sills of intermediate composition.

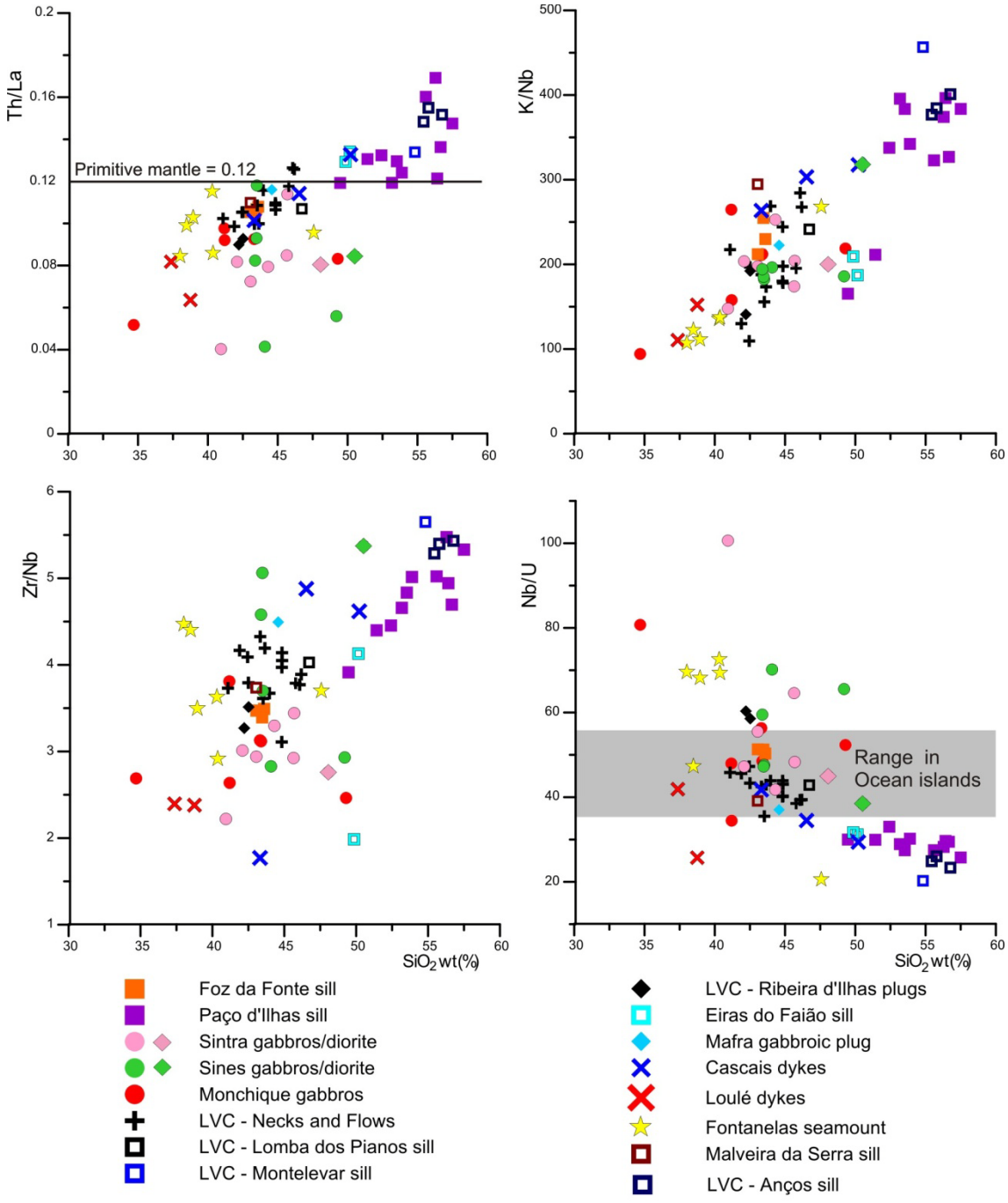

Fig. 7.21: Plots of SiO_2 vs. Th/La, K/Nb, Zr/Nb and Nb/U for the studied samples. The more SiO_2 rich samples show progressively higher Th/La, K/Nb and Zr/Nb and lower Nb/U reflecting the progressive contamination of these rocks by crystal lithologies. See text for discussion.

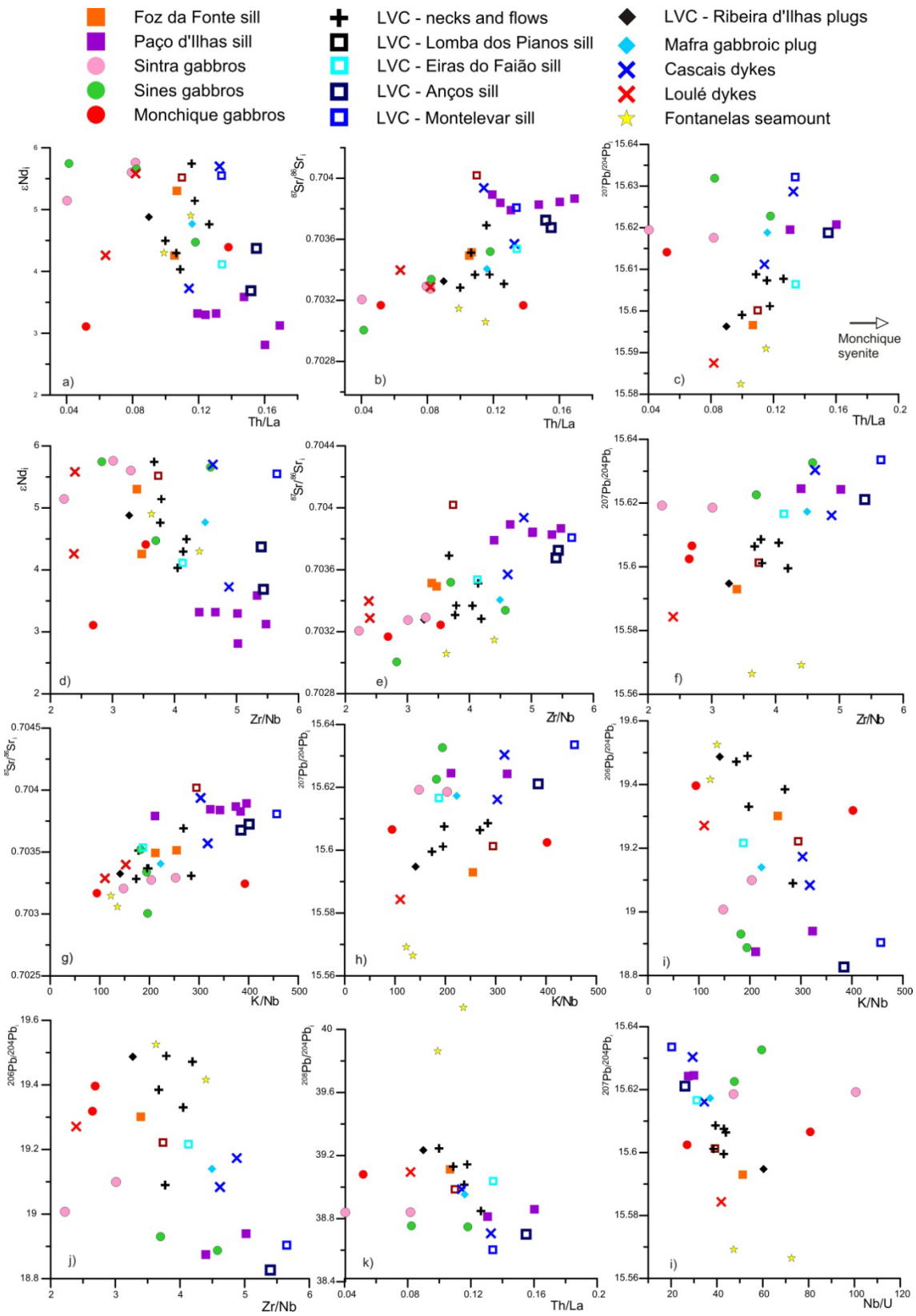

Fig. 7.22: Plots of trace element ratios Th/La, K/Nb, Zr/Nb and Nb/U vs. isotopic ratios of the analyzed samples. See text for discussion.

Increasing Th/La, K/Nb and Zr/Nb, and decreasing Nb/U also correlate with increasing $^{87}Sr/^{86}Sr_i$ (fig. 7.22), which is in accordance with the contamination of the initial basic magmas by a crustal lithology with high time integrated Rb/Sr.

εNd_i values decrease with increasing Th/La and with decreasing Nb/U but show more complex relations with K/Nb and Zr/Nb, hinting that there might be some heterogeneity in the composition of the contaminants that were assimilated by these magmas (fig. 7.22).

The Pb isotopic composition of these rocks evolves towards less radiogenic $^{206}Pb/^{204}Pb_i$ and $^{208}Pb/^{204}Pb_i$ compositions with increasing Th/La, K/Nb and Zr/Nb and decreasing Nb/U. $^{207}Pb/^{204}Pb_i$ shows the opposite behavior, increasing towards higher Th/La, K/Nb and Zr/Nb and lower Nb/U (fig. 7.21). The high $^{207}Pb/^{204}Pb$ suggests that this crustal contaminant is quite old due to its enrichement in ^{207}Pb. This is because the half life of ^{235}U is relatively short ($^{235}U \rightarrow {}^{207}Pb$ 0.7038 x 10^9 a) when compared with the half life of ^{238}U ($^{238}U \rightarrow {}^{206}Pb$ 4.468 x 10^9 a), so high ^{207}Pb coupled with low ^{206}Pb values must have been generated relatively early in the Earth's history, when ^{235}U was more abundant.

From the data presented above, the more contaminated rocks seem to correspond to the intermediate sills (Anços, Montelevar, Paço d'Ilhas), with the diorites from the Sintra and Sines igneous complex and the Cascais dykes (including basaltic sample RM64) also showing evidence for some crustal contribution to their composition (figs. 7.20 and 7.21).

The samples from the Sintra and Sines igneous complexes deserve special attention since they have higher $^{207}Pb/^{204}Pb_i$ and lower $^{206}Pb/^{204}Pb_i$ and $^{208}Pb/^{204}Pb_i$ than the other basic samples and are an exception to the general observed variations, showing apparently contaminated Pb isotopic ratios but relatively uncontaminated trace element, Nd and Sr isotope signatures (figs. 7.14-15 and 7.20-22). This could mean that the Pb isotopic signatures either reflect the contamination by a lithology with similar Sr and Nd isotopic signatures but distinct Pb isotopic ratios or that the contaminated Pb signature in these rocks might be an artifact created by the secondary hydrothermal alteration that affected these intrusions (see section 6.1). Since Pb is present in low concentrations in the rocks of the alkaline complexes (3.1-4.7 ppm), but high temperature, Cl rich hydrothermal fluids might show high contents in Pb (e.g. Simonetti and Bell, 1994), it is possible that the hydrothermal fluids might have introduced significant radiogenic Pb. It is possible that the Pb and a portion of the hydrothermal

fluids originated from within the surrounding sedimentary rocks which could contain more radiogenic lead. However, it is necessary that these fluids contained significantly less Sr and Nd than the Sintra and Sines gabbros, so that hydrothermal alteration at low water:rock ratios (<< 1) resulted in unchanged Sr and Nd isotopic ratios (e.g. Tepley and Davidson, 2003) while being responsible for a more contaminated isotopic Pb signature.

Alternatively, this secondary process might simply have resulted in changes in the U/Pb and U/Th ratios, leading to inadequate correction for U decay and incorrect initial Pb isotopic ratios. U, along with Pb, could have been leached from the rock during the hydrothermal alteration phase, while less mobile Th should have remained unaltered. However, the simultaneous changes in all the Pb isotopic ratios and the low measured $^{206}Pb/^{204}Pb$ and $^{208}Pb/^{204}Pb$ and high $^{206}Pb/^{204}Pb$ suggest this is not the most likely case.

Recapitulating, the data indicate that most of the more evolved terms in the analyzed rocks interacted with a crustal contaminant rich in SiO_2, Th, K, $^{87}Sr/^{86}Sr$ and $^{207}Pb/^{204}Pb$, but depleted in La, Nb, $^{143}Nd/^{144}Nd$, $^{206}Pb/^{204}Pb$ and $^{208}Pb/^{204}Pb$.

A smaller group of samples, represented by the Lomba dos Pianos, Malveira da Serra and Montelevar sills, seems to have assimilated a contaminant with high $^{87}Sr/^{86}Sr$ but which apparently contained low amounts of Nd and Pb, since the isotopic ratios of these elements do not appear to have been affected by this event.

7.3.2.2 Quantifying crustal contamination by AFC

The samples displaying the stronger indications of contamination (the more evolved sills and dykes present in the Lisbon region, as well as the diorites from the Sintra and Sines complexes, figs. 7.19-21) intrude the Mesozoic siliciclastic, carbonate and evaporitic sediment cover of the Lusitanian basin (e.g. Kullberg, 2000) in the upper crust and had to cut through the Ossa Morena zone mafic to felsic plutons and metassediments of the middle and lower crust (Capdevila and Mougenot, *in* Boilot and Winterer (eds.), 1988). The contaminants assimilated by the studied rocks are most likely to correspond to either acid igneous rocks or metassediments in the Paleozoic Ossa Morena Zone (OMZ) and/or sediments in the Lusitanian Basin (LB) that either resulted from the erosion of lithologies in the OMZ and Central Iberian Zone (CIZ) or from precipitation of carbonate from Mesozoic Atlantic waters. The contaminant can also be a mix of sediments from the different Paleozoic terranes, and therefore show

different signatures in accordance to the proportion in which each of these terranes are represented.

Assimilation of crustal rocks can take place simultaneously with fractional crystallization, in a mechanism known as Assimilation and Fractional Crystallization (AFC, DePaolo, 1981). The equation that describes the behavior of trace elements during such a processes was derived by DePaolo (1981) and corresponds to:

$$\frac{C_L}{C_o} = f' + \frac{r}{r-1+D} * C_a/C_o(1-f')$$

where C_L , C_o and C_a correspond to the concentration of a trace element in question in the residual melt, the parental liquid and the assimilant, respectively. D is the bulk distribution coefficient for that same element, *r* the ratio of the assimilation rate to the ratio of the crystallization rate and f' is given by: $f' = F^{-(r-1+D)/(r-1)}$, where F is the fraction of melt remaining.

The evolution of isotopic ratios during such a process is also described by DePaolo (1981) and given by the following equation:

$$e_L^c = e_L^0 + (e^c - e_L^0) * (1 - \left(\frac{c_L^0}{c_L}\right) * f')$$

where e_L^c, e_L^0 and e^c , are the isotopic ratios of the residual melt, of the parental magma and of the contaminant, respectively. c_L^0 is the concentration of the trace element whose isotopic ratios is being addressed in the parental magma while c_L^0 is the concentration of that same element in the contaminant.

These equations allow the modeling of the behavior of trace elements and isotopic ratios during AFC but are rather simplistic, assuming constant distribution coefficients and assimilation to crystallization ratios for the entirety of the process, which is unrealistic. They also fail to integrate any estimate of the volume of crustal contribution and disregard the thermal constrains of the AFC process, which is a serious flaw since the energy to heat and melt the country rock comes from the intruding magma and its crystallization, and is therefore a function of its composition (e.g. Reiners et al., 1995; Spera and Bohrson, 2001; Bohrson and Spera, 2001).

Several possible contaminants were used to test if they fitted the evolution trend of the geochemical signatures of the more contaminated rocks in the West Iberian Margin, namely metassediments and granitoids from both the OMZ and CIZ, and carbonates from the LB.

The compositions of these contaminants are averages of the existing analysis from rocks belonging to each of the different Paleozoic terranes (**OMZ metassediments**: Borrego, 2009; Chaminé et al., 2000; Chichorro et al., 2008; Pereira et al., 2006; 2007; **OMZ granitoids**: Brandés et al., 2004; Chichorro et al., 2008; Lopez-Guijarro, et al., 2008; Moita et al., 2009; Montero et al., 1999; Pereira et al., 2007; Pin et al., 2008; Priem et al., 1986; **CIZ metassediments**: Bea et al., 2003; Ugidos et al., 1997 Lopez-Guijarro, et al., 2008**; CIZ granitoids**: Antunes et al., 2007; Azevedo and Nolan, 1998; Casquet et al., 2001; Dias et al., 2002; Gomes and Neiva, 2005; Martins et al., 2009; Neiva et al., 2009; Silva et al., 2000; Vale Aguado et al., 2006; Villaseca et al., 1998; 2009); the isotopic composition of the **Lusitanian basin carbonates** was calculated using the Nd and Sr isotopic composition values for the Atlantic seawater (McArthur et al., 2001; Stille et al., 1996) while their elementar Sr composition was assumed to correspond to an average Phanerozoic carbonate (Condie, 1991) and for Nd and other trace elements, a composition corresponding to the average of the values reported in Plank and Langmuir (1998) and Gao et al. (1998).

The effect of AFC processes in the Pb isotopic signature of the studied rocks was not evaluated due to the lack of data for any of the possible contaminants.

Also, the composition of the contaminant(s) for rocks with such a wide geographical distribution and showing different modes of occurrence is expected to be isotopically heterogeneous and so the models presented here are only indicative of possible scenarios that could have occurred during the evolution of the Late Cretaceous alkaline magmas of the WIM.

The results yielded by this method, using the D values as the ones indicated in table 7.4 and an *r* value of 0.3, which is approximately the value calculated by Taylor (1980) for a typical upper crustal case, are displayed in fig. 7.23.

They show that some of the more enriched isotopic and trace element signatures can be obtained by assimilation of a crustal rock with a composition similar to the one found in the metassediments of the OMZ, along with the 40% crystallization of the same paragenesis modeled in for fractional crystallization (see section 7.3.1). However, the Sr-Nd signatures of the samples with lowest $^{144}Nd/^{143}Nd$ as well as those that show both high $^{144}Nd/^{143}Nd$ and $^{87}Sr/^{86}Sr$ cannot be reproduced by assimilation of such a lithology.

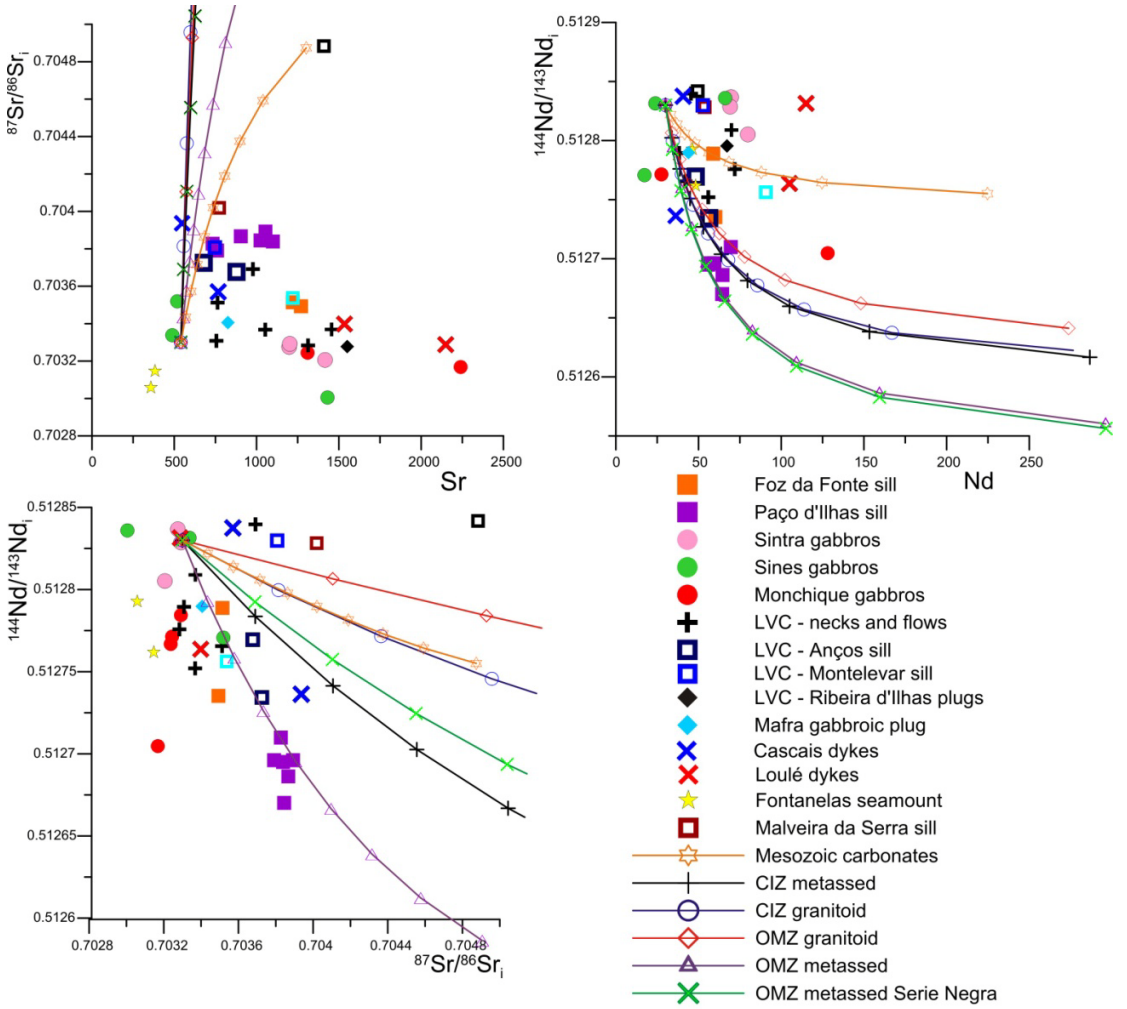

Fig. 7.23: $^{87}Sr/^{86}Sr$ vs. $^{144}Nd/^{143}Nd$, Sr vs. $^{87}Sr/^{86}Sr$ and Nd vs. $^{144}Nd/^{143}Nd$ diagrams for the studied samples with the lines of compositional variation for the AFC modelling of several different contaminants. Each of the marks in the contamination lines represents a 0.1 increase in F or a 10% decrease in the remaining melt fraction. See text for discussion.

The other tested contaminants seem to be unable to replicate the observed compositional features, producing changes in $^{87}Sr/^{86}Sr$ that are not accompanied by the necessary decrease in $^{144}Nd/^{143}Nd$ to in order to generate isotopic signatures similar to the ones observed in the alkaline rocks of the WIM.

7.3.2.2 Quantifying crustal contamination by EC-AFC

The equations that allow the modeling of the behavior of trace elements and isotopic ratios during AFC are rather simplistic, assuming constant distribution coefficients and assimilation to crystallization ratios for the entirety of the process, which is unrealistic. They also fail to integrate any estimate of the volume of crustal contribution and disregard the thermal constrains of the AFC process, which is a serious

flaw since the energy to heat and melt the country rock comes from the intruding magma and its crystallization, and is therefore a function of its composition (e.g. Reiners et al., 1995; Spera and Bohrson, 2001; Bohrson and Spera, 2001).

Energy Constrained Assimilation and Factional Crystallization (EC-AFC; Spera and Bohrson, 2001) is an alternative method to model the AFC process that self consistently balances thermal energy conservation, species and mass while also tracking compositional variations generated in the anatetic melt as country rock undergoes partial melting. It integrates the the effects of energy conservation and country rock partial melting into the geochemical evolution of an open system magma reservoir, effectively linking them (Bohrson and Spera, 2001).

This kind of model allows for the rate of assimilation and composition of the anatetic melt produced by the fusion of crustal material to change with time, as the temperature of the country rock increases by heat transfer from the magma and with the heat produced during crystallization (Bohrson and Spera, 2001), thus creating a more realistic approach than traditional AFC models that only account for mass, species and chemical variations at a fixed assimilation rate (DePaolo, 1981). However, EC-AFC models use fixed magma-mineral distribution coefficients which means that these are constant during the entire melt evolution, which is still not realistic.

The EC-AFC calculations were done using an Excel spreadsheet provided by Spera and Bohrson (2001). The thermal and geochemical input parameters used in the modeling of EC-AFC at upper crustal conditions are displayed in tables 7.3 and 7.4 and the results on figs 7.24-25. The EC-AFC process is deduced to have occurred in the upper crustal levels since the most contaminated samples correspond to the more evolved sills, which were emplaced into the upper crust. As such, the thermal parameters are the same as those used for a standard upper crustal case in Bohrson and Spera (2001), except for the carbonate assimilant which are from Chadwick et al. (2007).

As the observed magmas all show evidence for the existence of some fractional crystallization prior to emplacement, the compositional parameters for the initial parental magma have been modified so that they can represent a more primitive, unfractionated composition. This composition maintains the same average Sr/Nd ratio of the WIM's basic rocks which will allow for some fractional crystallization to take place, releasing energy and heat to the country rock before the trace element values reach unrealistically high values in the modeled EC-AFC curves.

The initiation of assimilation of the wall rock is strongly dependent on thermal parameters such as the initial wall rock temperature (T_a), which can be highly variable, so in order to simulate a wider range of natural conditions, the calculations for the EC-AFC model were done for several values of T_a.

Table 7.3: Thermal parameters used for EC-AFC modeling.

Magma liquidus temperature	1280	Isobaric specific heat of magma	1484 J/kg K
Magma initial temperature	1280	Isobaric specific heat of assimilant	1370 J/kg K
Assimilant liquidus temperature	900 (siliceous) 800 (carbonates)	Crystallization enthalpy	396000 J/kg
Assimilant initial temperature	300 (a); 400 (b)	Fusion enthalpy (silicates)	270000 J/kg
Solidus temperature	900	Fusion enthalpy (carbonates)	250000 J/kg
Equilibration temperature	950		

Table 7.4: Compositional parameters used for EC-AFC modeling.

	Sr (ppm)	bulk Sr D_0	$^{87}Sr/^{86}Sr$	Nd (ppm)	bulk Nd D_0	$^{143}Nd/^{144}Nd$
Initial Magma composition	540	0.6	0.7033	30.0	0.1	0.51282
Carbonates from the Lusitanian Basin	350	0.7	0.7075	10	0.1	0.51202
ZOM granitoids	306	1.2	0.7241	22	0.1	0.51209
ZOM metassediments	114	1.2	0.7175	31	0.1	0.51196
ZOM Série Negra metassediments	150	1.2	0.7350	31	0.1	0.51195
ZCI granitoids	144	1.2	0.7468	36	0.1	0.51222
ZCI metassediments	152.8	1.2	0.7345	40.5	0.1	0.51199

As can be observed in fig. 7.24, for a contaminant with an initial temperature of 300 ºC (T_a = 300 ºC), typical of upper crustal conditions (Bohrson and Spera, 2001), the EC-AFC trends defined by the OMZ granitoids could explain the isotopic signature of the basaltic Cascais dyke with the assimilation of≈ 2% of such a contaminant, but after an unrealistic 94% crystallization of the initial liquid. In its turn, the assimilation of 2% of the Série Negra metassediments from the OMZ could generate the isotopic signature observed in the Paço d'Ilhas sample with the lowest $^{143}Nd/^{144}Nd$. However, this would occur at the same unrealistic 94% crystallization of the initial melt. Also,

none of these contaminants can reproduce the evolution of Sr and Nd concentrations in the liquid, since assimilation only takes place very late in the crystallization history.

Assuming a higher T_a of 400 ºC, the Mesozoic carbonated contaminant shows a better fit with the observed magmatic evolution of the Late Cretaceous alkaline rocks of the WIM. The assimilation of approximately 6-10% of carbonate country rock is required in order to explain the observed signatures, after 62-68% of crystallization of the original basic magma. The assimilation of such a component also agrees with the obtained trace element data.

For the same T_a value, none of the other possible siliceous contaminants can provide a good fit for the observed data, especially on the Nd vs. $^{143}Nd/^{144}Nd$ and Sr vs. $^{87}Sr/^{86}Sr$ diagrams (fig. 7.24). Since fusion temperatures and enthalpies are higher for siliceous rocks, more fractional crystallization has to take place before the silicated country rock receives enough energy to reach its fusion temperature. As a consequence, and since Nd and Sr are incompatible, the modeling process produces higher contents in these elements through fractional crystallization. This also means that $^{143}Nd/^{144}Nd$ and $^{87}Sr/^{86}Sr$ values will only start changing late in the crystallization history, when the country rock is provived with enough energy to melt, and such timing corresponds to very high Nd and Sr concentrations.

Still, if only the evolution in the isotopic compositions is considered, the assimilation of 0.6% granitoids from the OMZ could be responsible for the isotopic signature of the basaltic dyke from Cascais (fig. 7.24). The incorporation of less than 3% of a contaminant with an isotopic signature close to the CIZ granitoids or OMZ Série Negra metassediments could generate the isotopic signature of the Anços sill and maybe even the Paço d'Ilhas sill (fig. 7.24). Yet, this would only take place after over 90% crystallization of the initial liquid, which again seems too high for the generation of intermediate rocks.

However, if higher initial assimilant temperatures are considered, the amount of necessary heat transfer from fractional crystallization would be smaller and the described curves in the element vs. isotope diagrams would probably show a better fit with the actual data.This can happen at higher depths in locations where long lived magmatism and/or extension are taking place, causing the heat flux to be higher than in stable regions (e.g. Jung et al., 2006; Chadwick et al., 2007), and consequentially increase the geothermal gradient in the area. This will mean that temperatures at mid to

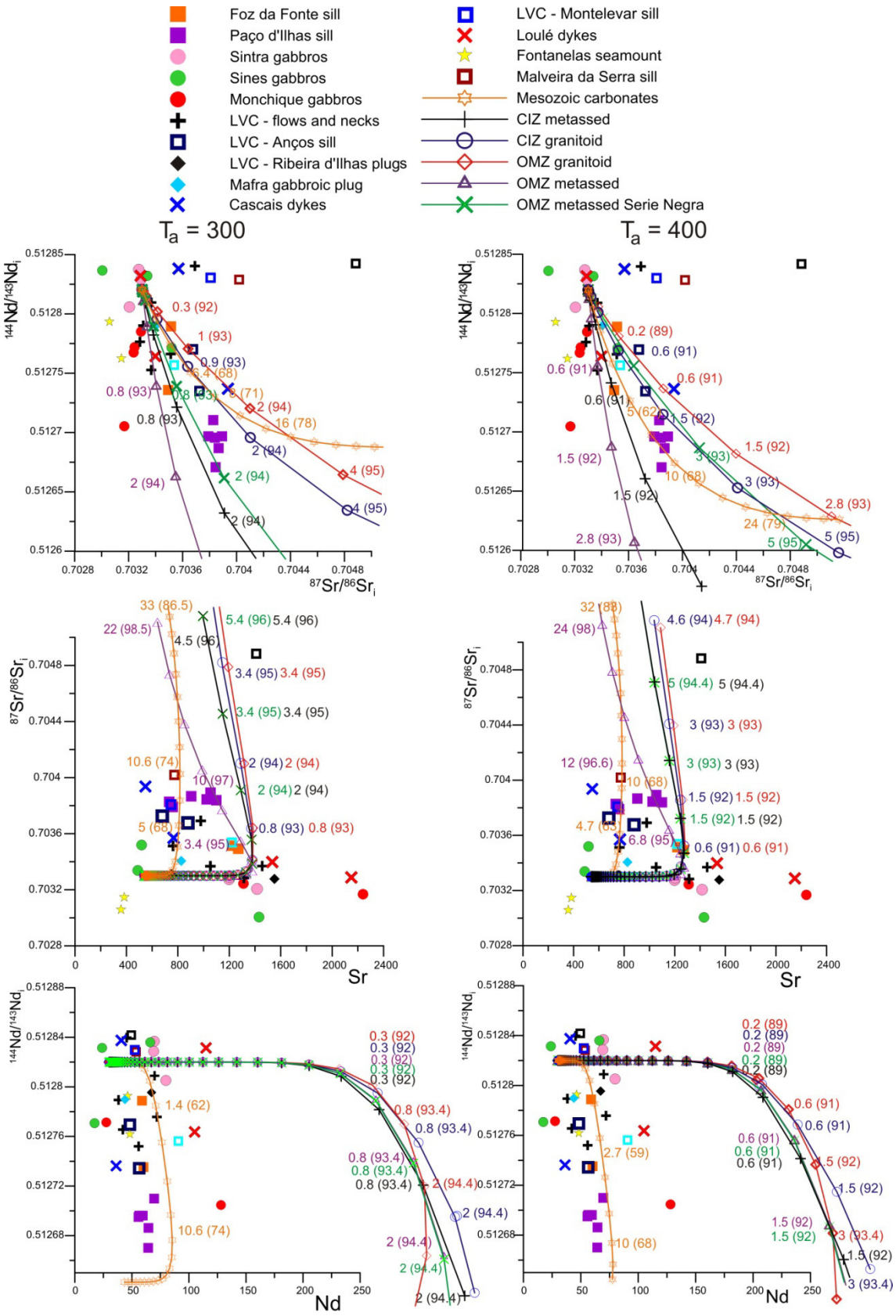

Fig. 7.24: $^{87}Sr/^{86}Sr$ vs. $^{144}Nd/^{143}Nd$, Sr vs. $^{87}Sr/^{86}Sr$ and Nd vs. $^{144}Nd/^{143}Nd$ diagrams for the studied samples with the lines of compositional variation for the EC-AFC of several different contaminants. The displayed numbers correspond to the percentage of mass of wall rock melt, with the amount of fractional crystallization that has occurred in brackets. See text for discussion.

lower crustal depths can be as high or higher than 800 ºC (Sachs and Hansteen, 2000; Jung et al., 2006).

For T_a = 800º C (fig. 7.25) the modeled trace element evolution seems to show a better fit with the observed data. Assimilation of siliceous contaminants starts at more reasonable amounts of crystallization (≤ 43%), however, the isotopic signatures of the contaminated melt do not show a good fit with the data, showing a large decrease in $^{143}Nd/^{144}Nd$ for small increases in $^{87}Sr/^{86}Sr$ (fig. 7.25).

The lack of a good fit between the EC-AFC models and the data obtained for the Late Cretaceous alkaline rocks of the WIM can also be due to the poorly constrained trace element and isotopic composition of their contaminants. These can include siliciclastic sediments combining clasts from all of the Paleozoic terranes, and possibly even sediments containing mixes of silicate clasts in carbonated cement matrixes whose isotopic signatures should be more diverse than the simple averages presented on table 7.4.

Nevertheless, when compared to the carbonates, the siliceous contaminants would require the addition of smaller amounts of material to the initial liquid in order to produce the isotopic and trace element signatures observed in the more contaminated samples given their more radiogenic Sr and empoverished Nd isotopic signatures and higher contents in incompatible elements. This makes them more likely candidates to produce this contaminated trend than a carbonated assimilant. Also, the assimilation of exclusively carbonate material does not explain the variations in $^{87}Sr/^{86}Sr$ and $^{143}Nd/^{144}Nd$ with increasing SiO_2.

The assimilation of the high amounts of carbonate, as suggested by the models (10-16%), would also lead to more undersaturated, CaO rich magmas (e.g. Barnes et al., 2005; Martins et al., 2008) and the more contaminated samples in the WIM show, in general, the lowest CaO contents while simultaneously being the more silica saturated rocks present in the region, as well as the only ones showing normative quartz (0.14-6.1% in the Paço d'Ilhas, Anços and Montelevar sills) which does not favor carbonate assimilation, but still allows the possibility of the existence of a carbonated siliciclastic contaminant.

All this favors contamination of the more evolved WIM alkaline magmas by a siliceous contaminant or at least for a major contribution from such a contaminant that may or not have a carbonate matrix. Since the studied rocks intrude sediments derived from the erosion of the siliceous OMZ and CIZ terranes, these sediments seem to be the

most likely contaminants, although fusion would have to be initiated earlier than in our EC-AFC models, which can be achieved either by lowering the fusion temperature of the assimilant (e.g. by adding volatiles) or by raising the assimilant's initial temperature.

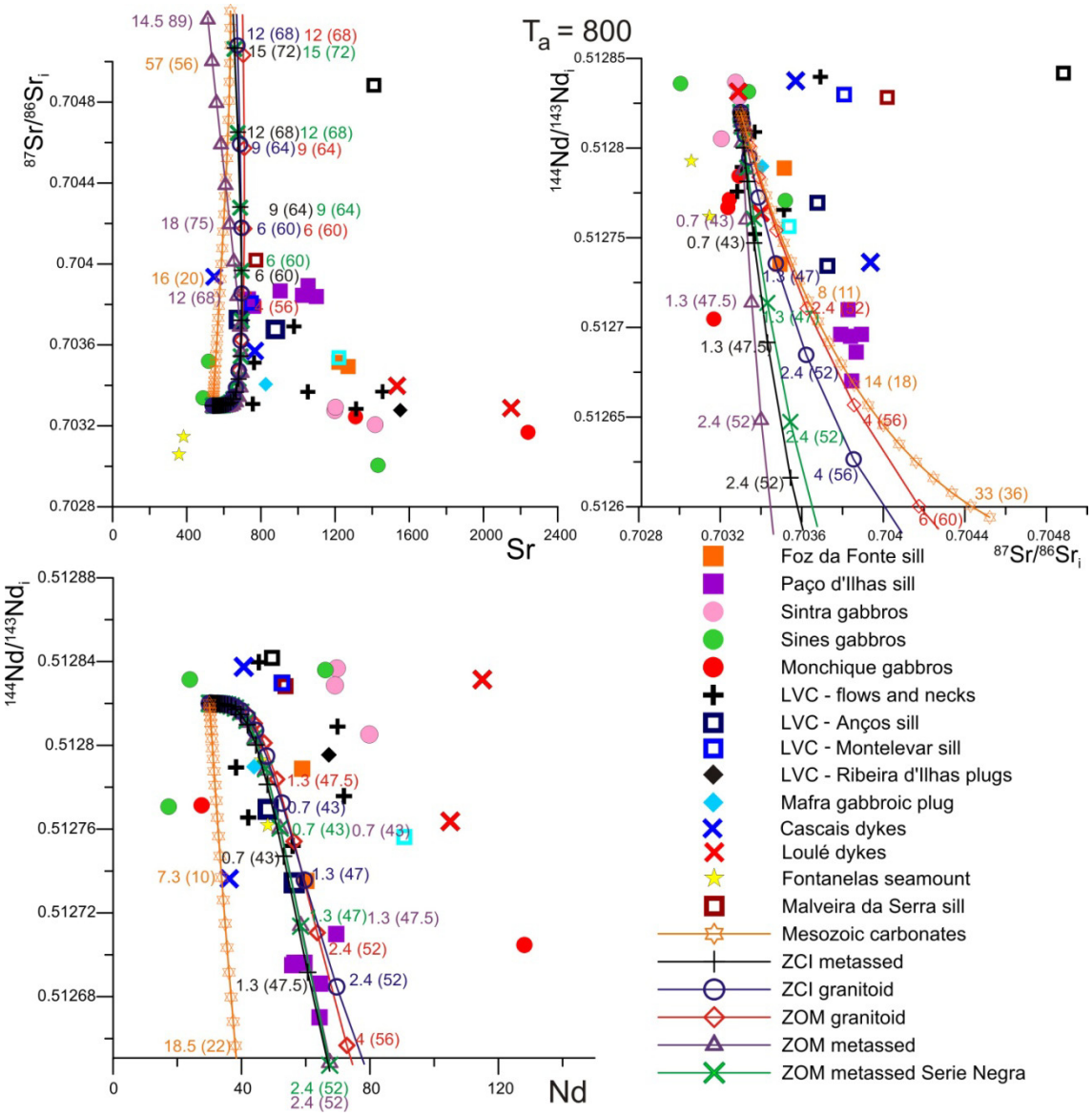

Fig. 7.25: $^{87}Sr/^{86}Sr$ vs. $^{144}Nd/^{143}Nd$, Sr vs. $^{87}Sr/^{86}Sr$ and Nd vs. $^{144}Nd/^{143}Nd$ diagrams for the studied samples with the lines of compositional variation for the EC-AFC of several different contaminants. The displayed numbers correspond to the percentage of mass of wall rock melt, with the amount of fractional crystallization that has occurred in brackets. See text for discussion.

The different contamination trend observed in the samples from the Malveira da Serra, Lomba dos Pianos and Montelevar sills is characterized by high $^{87}Sr/^{86}Sr$ and $^{143}Nd/^{144}Nd$ moving the samples towards the enriched quadrant (figs. 7.11-12 and 7.22-24). Yet the basic Lomba dos Pianos and Malveira da Serra sills do not show any

evidence for the existence of crustal contamination in their trace element signatures, although the intermediate Montelevar sill plots along the other contaminated samples (figs. 7.12, 7.23-25).

Such a trend was not reproduced using any of the modeled assimilants, so it must have originated from a different contaminant, enriched in radiogenic Sr but either with a Nd isotopic signature similar to the one shown by the parental magmas to these sills or having very low Nd contents, meaning that the assimilation of such a material would not significantly affect the magma's original $^{143}Nd/^{144}Nd$ value. This contaminant could correspond to a carbonate with low Nd concentrations or to a melt resulting from incongruent fusion of igneous or sedimentary rocks containing Rb and Sr rich phases such as biotite and feldspar. The fusion of such minerals would generate a melt enriched in radiogenic Sr but poor in Nd, driving up the Sr isotopic signature, but leaving $^{143}Nd/^{144}Nd$ unaffected.

The Lomba dos Pianos sill contains what appear to be plagioclase xenocrysts, it is possible that these might have crystallized from a magma with higher $^{87}Sr/^{86}Sr$ and possibly even lower $^{143}Nd/^{144}Nd$ values than the parental melts of the studied rocks. However, since Sr/Nd ratios in plagioclases are usually high ($\boldsymbol{D_{Sr}^{plag} > D_{Nd}^{plag}}$, Bindeman et al., 1998) and these minerals can carry a significant amount of Sr, their presence could shift the whole rock composition towards high $^{87}Sr/^{86}Sr$ while leaving $^{143}Nd/^{144}Nd$ and other trace elements relatively unaffected.

On the other hand, this hypothesis requires that the plagioclase xenocrysts derive from disagregated wall rock assemblages, or from the mixing of liquids with different compositions. In the latter case, the parental and contaminating magmas would have homogenized and consequentially originated a hybrid isotopic signature. Since both the Lomba dos Pianos and Malveira da Serra sills show evidence for magma mixing, this could be a reasonable explanation for the existence of this isotopic trend, but it still does not explain why other rocks that show evidence for magma mixing do not show similar isotopic signatures, and cannot explain the higher $^{87}Sr/^{86}Sr$ of the Montelevar sill, since there is no evidence that points towards the existence of magma mixing in the petrogenesis of that sill.

In summary, the more evolved, intermediate rocks of the WIM show evidence of contamination by a siliceous, Th, K, $^{87}Sr/^{86}Sr$ and $^{207}Pb/^{204}Pb$ rich, but La, Nb, $^{143}Nd/^{144}Nd$, $^{206}Pb/^{204}Pb$ and $^{208}Pb/^{204}Pb$ depleted assimilant.

Another trend, materialized by the Lomba dos Pianos, Malveira da Serra and Montelevar sills is characterized by an increase in $^{87}Sr/^{86}Sr$ and unchanged Nd and Pb isotopic signatures might be the result of the assimilation of carbonate material or an incongruent melt from Rb and Sr rich phases.

The apparently contaminated Pb isotopic signatures of the Sintra and Sines igneous complexes are likely to be the result of secondary hydrothermal alteration by Pb rich fluids.

The comparison between the AFC and EC-AFC models is hindered by the lack of knowledge concerning the composition of the contaminants and also by the high number of assumptions that had to be made in relation to the thermal parameters used for the EC-AFC models. Although EC-AFC seems to be a more complete and realistic method, integrating energy conservation with compositional parameters, the lack of available data for both these types of parameters can be a handicap while interpreting the obtained results. On the other hand, the more simplistic AFC curves also fail to reproduce most of the observed contamination trends.

7.3.3 Magma mixing

Magma mixing between an ultrabasic to basic and a more evolved, phonotephritic to tephrophonolitic alkaline melt was proposed in order to justify the presence of reversely zoned zone clinopyroxenes, amphiboles and plagioclase in some of the studied intrusives (e.g. the Malveira da Serra and Lomba dos Pianos sills, the Ribeira d'Ilhas plugs, the lavas from the Fontanelas seamount and the Loulé lamprophyre C-20, section 6.2.6).

Given the basic to ultrabasic nature of the rocks that appear to have gone through magma mixing events ($38 < SiO_2\% < 46.7$), the amount of intermediate alkaline liquid that mixed with the ultrabasic to basic magma must have been very small.

The range of compositions shown by liquids resulting from the mixing and homogenization of different proportions of two distinct components can be easily modeled as binary mixing, using the following equation (e.g. Faure, 1986):

$$\boldsymbol{X_m = X_a * f + X_b * (1 - f)}$$

where $\boldsymbol{X_m}$, $\boldsymbol{X_a}$ and $\boldsymbol{X_b}$ are the concentration of element *X* in the mixed melt (*m*) and in the components *a* and *b*, respectively, while $\boldsymbol{f}$ is the proportion of the component *a* in

the mix (e.g. if $\boldsymbol{f}$=0.3 there is 30% of component *a* to 70% of component *b* in the mixed liquid).

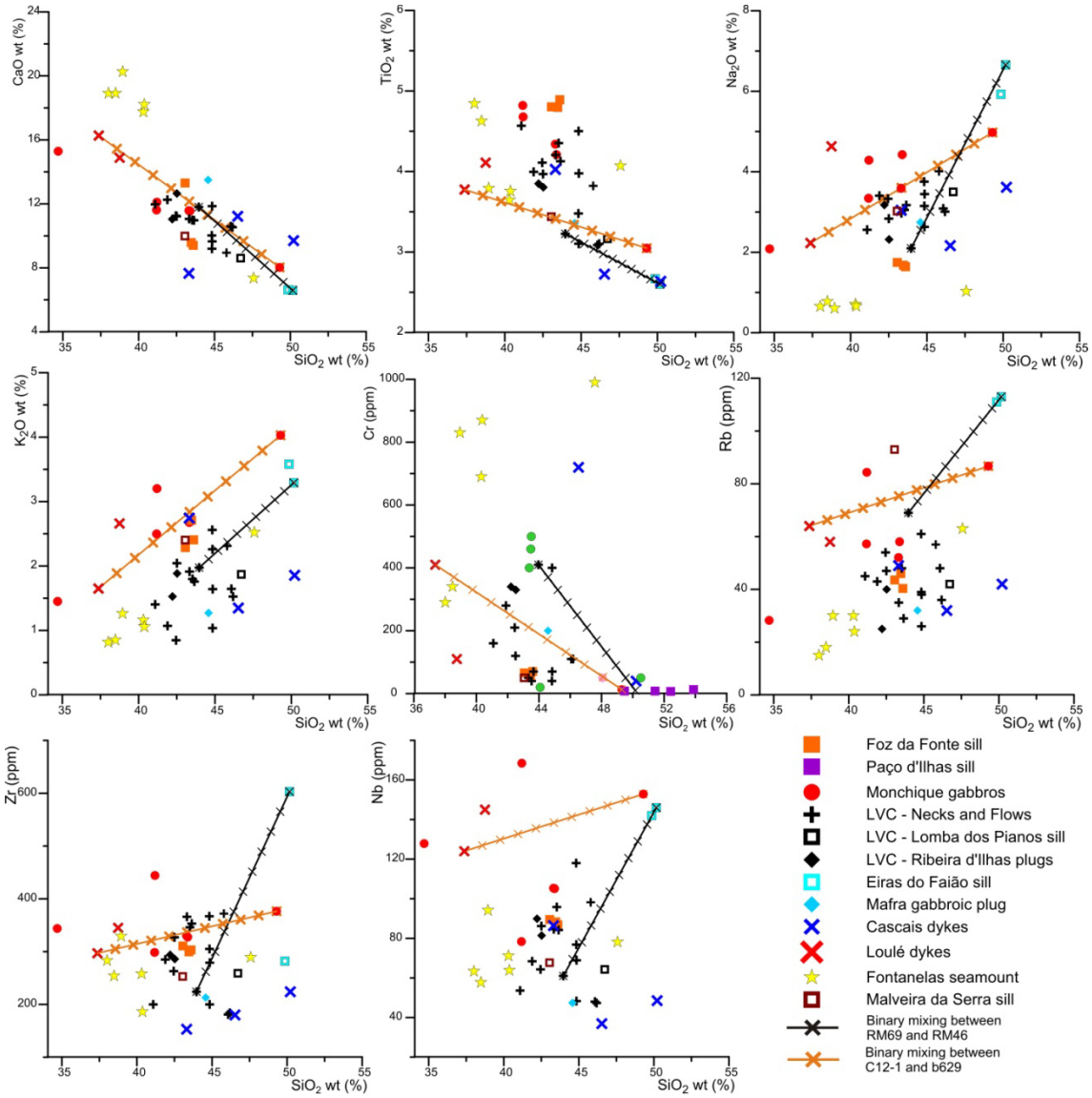

Fig. 7.26: Plots of SiO_2 vs. several major and trace elements for the studied basic rocks. Also plotted are the binary mixing lines between basic and intermediate alkaline magmas. Each of the tick marks corresponds to an increase of 10% of a component in the mix. See text for discussion.

Modeling was done using two end member compositions for either *a* and *b*, since the rocks that appear affected by this process range from ultrabasic lamprophyres in the Algarve region and hawaiites such as the Lomba dos Pianos sill. So binary mixing was calculated between a liquid with a composition equivalent to lamprophyre C-12-1(a_1) and an intermediate rock from Monchique (b_1) with a tephriphonolite

composition (sample b629). Binary mixing between basanite RM 69 (a_2) and phonotephrite RM 46 from the Eiras do Faião sill (b_2) was also carried out.

Consequently, if binary mixing was an important mechanism in the petrogenesis of the Late Cretaceous alkaline rocks of the WIM, the Malveira da Serra and Lomba dos Pianos sills, the Ribeira d'Ilhas plugs, the lavas from the Fontanelas seamount and the Loulé lamprophyre C-20 would have to plot along the calculated mixing lines.

Nonetheless, the results do not seem to reproduce the data obtained for the samples in a coherent manner for either major and trace elements (fig. 7.26), suggesting that either these were the wrong end members to use in the mixing modeling or that the process does not influence the major and trace element signature of these rocks.

In summary, the relative unimportance of binary mixing as a petrogenetic process in the WIM seems to be supported by the lack of any linear trends forming among the samples that show traces of mixing, as would be expected if this process was of higher relevance (e.g. Geldmacher et al., 1998; Meade et al., 2010). This means that the assimilation and fractional crystallization processes are of much higher importance in the evolution of the studied rocks.

7.4 Magma generation and partial melting processes

Given the evidence presented above (section 7.1), it seems that the basic rocks in the Late Cretaceous alkaline magmatic cycle of the WIM were generated by melting of an enriched mantle source, which is likely to contain garnet and other minor residual phases in addition to olivine, orthopyroxene and clinopyroxene. In this section the nature, melting extent, composition and mineralogy of this mantle source is evaluated.

Since none of the samples fulfill the criteria needed to be considered primary mantle melts (Mg# > 68, Ni > 320 ppm, Cr > 1000 ppm, cf. Frey et al., 1978), only the samples with a more primitive character and that showed only minor or no traces of fractionation were used (Mg# > 60, Ni > 50).

7.4.1 Residual mantle mineralogy

7.4.1.1 Characterization of residual mantle mineralogy

In fig. 7.27 we can observe several anomalies in the Primitive Mantle normalized multielemental diagrams for the more primitive rocks of the Late Cretaceous alkaline cycle of the WIM.

The most striking features are the previously mentioned negative K, P, Zr and Hf anomalies, but careful observation of this diagram reveals negative anomalies in Sr for the Fontanelas seamount as well as small positive anomalies of the same element in some of the rocks from the second pulse of Late Cretaceous alkaline magmatic activity. The Loulé dyke also shows a negative Ti anomaly, while some of the LVC's rocks and the Foz da Fonte sills show a small spike in this same element.

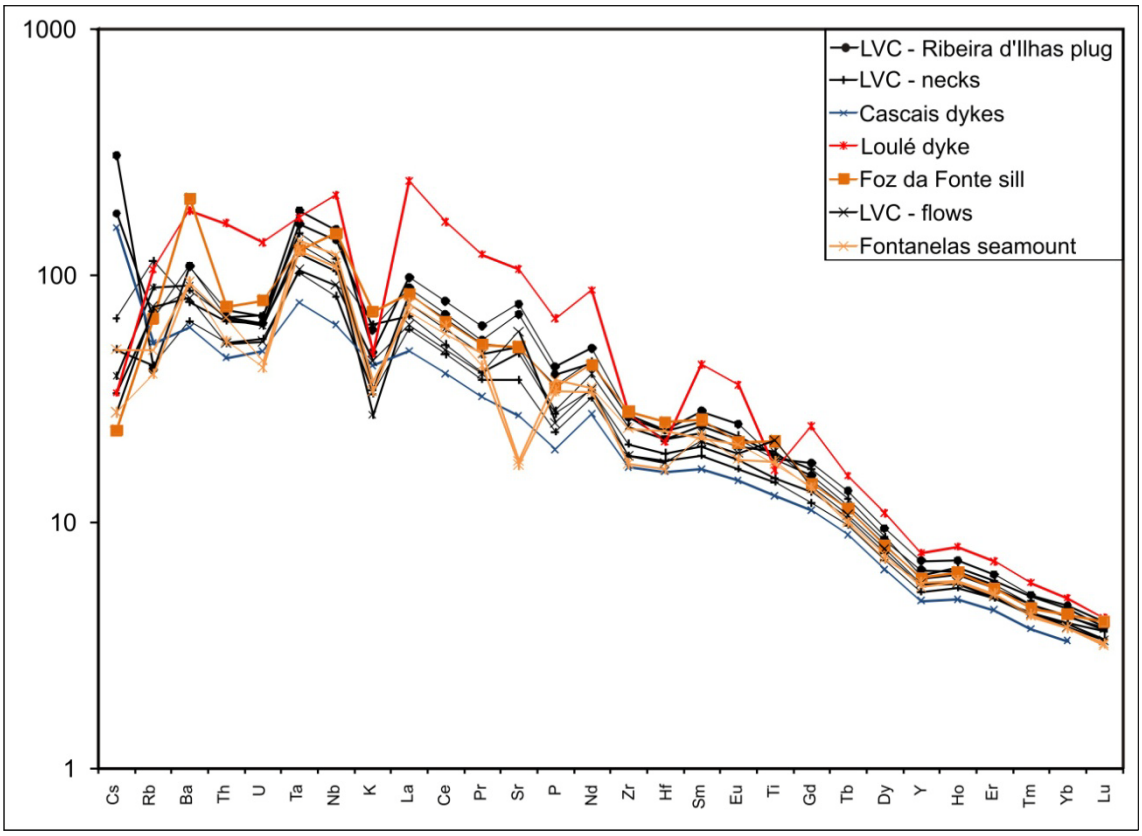

Fig. 7.27: Primitive upper mantle normalized (Palme and O'Neill, 2003) multielemental plots for the primary samples.

This type of anomalies can be caused by fractionation and accumulation of phases rich in these elements or originate from the buffering of the elemental concentrations by a residual mantle phase during melting events. As in most of these magmas, the main fractionating phases are olivine and clinopyroxene, which do not contain significant amounts of K, Sr, Zr and Hf, these anomalies should be related to the residual mineralogy present in the mantle at the time of melting.

It is therefore necessary to propose the presence of a K-rich residual mantle phase in order to explain the depletion in K relative to other similarly incompatible elements (e.g. Th, Nb, La) when normalized to primitive mantle values, resulting in the negative K anomalies observed in most of the basic rocks from the second pulse of Late Cretaceous alkaline activity in the WIM (75-72 Ma, Miranda et al., 2009, this study).

Nb, Y and K behave incompatibly during the melting of a nominally anhydrous mantle, and their concentrations should decrease with increasing amounts of partial melting of the source, becoming less enriched in the melt as a consequence of mass dilution with increasing amounts of fusion. This can be seen for Y and Nb in fig. 7.28 where, if identical source compositions are assumed, it is possible to propose that the Loulé lamprophyres were the result of smaller amounts of partial melting while the rocks from the LVC and Fontanelas seamount derived from higher degrees of melting.

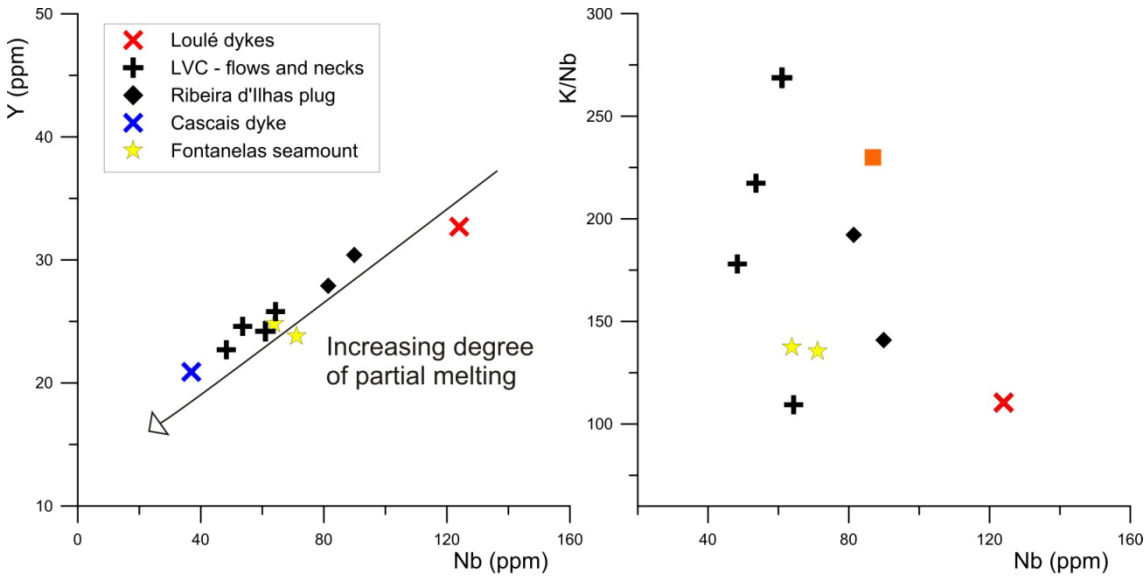

Fig. 7.28: Plots of Nb vs. Y and K/Nb for the primitive samples.

Assuming that $D_{Nb} \approx D_K$ and similar source compositions for all of the samples, K/Nb should consequentially remain constant during melting of such an anhydrous peridotitic source. However, in anhydrated mantle assemblage, K rich phases such as amphibole and phlogopite can be present, and K becomes more compatible than Nb, which is reflected by lower K/Nb ratios in the liquids generated from such a mantle and in the decreasing K/Nb values with decreasing degrees of partial melting (Class et al., 1998).

Primitive rocks from the WIM show low K/Nb values (110 – 303) when compared to the primitive mantle (442, Palme and O'Neill, 2003). Also, K/Nb seems to increase with increasing amounts of partial melting since K becomes more incompatible with the increasing melting degree, which can be associated with decreasing amounts of the K bearing mineral in the source (fig. 7.28).

This residual K rich phase could correspond to either amphibole (K richterite, kaersutite or pargasite) or phlogopite, which are common accessory phases in metassomatized mantle xenoliths (see Pearson et al., 2003 and references therein) and can fractionate incompatible elements such as K, Ba and Rb.

K is more compatible in amphibole with relation to Rb ($\boldsymbol{D_K^{amph} > D_{Rb}^{amph}}$; LaTourette et al., 1995), contrary to phlogopite ($\boldsymbol{D_K^{phlog} < D_{Rb}^{phlog}}$; LaTourette et al., 1995, Foley et al., 1996). So given that in the spidergram of fig. 7.27 and on fig. 7.29 K seems to be more compatible than Rb, and that the Rb usually shows higher primitive mantle normalized values than K, the residual K rich phase is likely to be an amphibole.

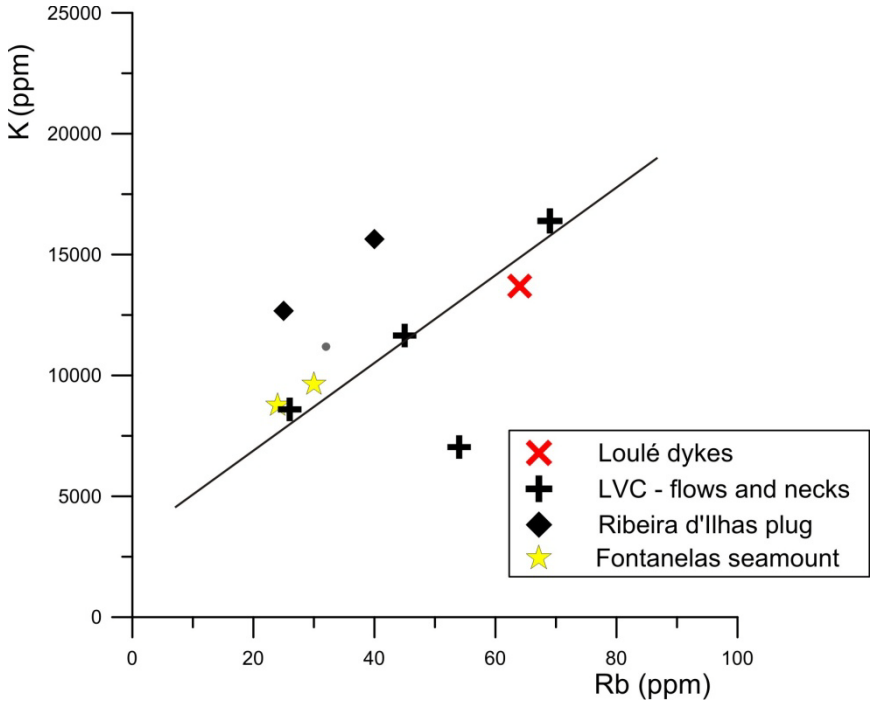

Fig. 7.29: plot Rb vs. K for the primitive samples.

In addition, during melting events Ba and Rb will behave differently if either amphibole or phlogopite are present as residual phases, given that Ba and Rb are compatible with respect to phlogopite ($\boldsymbol{D_{Ba}^{phlog}}$ = 4.1-3.1; $\boldsymbol{D_{Rb}^{phlog}}$ = 7.5-5; Adam and

Green, 2006) but moderately incompatible in amphibole ($\boldsymbol{D_{Ba}^{amph}}$ = 0.26-0.19; $\boldsymbol{D_{Rb}^{amph}}$ = 0.26-0.1, Adam and Green, 2006).

Consequently, the incompatible behavior of Ba, which decreases with decreasing Nb and partial melting degree, and the scattered values for Rb, Ba/Nb and Rb/Nb ratios with varying Nb contents (fig. 7.30) once more suggest that amphibole, rather than phlogopite, is the most likely residual K bearing phase, as these ratios are fractionated by the presence of residual phologopite during low degrees of melting (le Roex and Lanyon, 1998) and should increase with increasing melting degree and decreasing Nb.

Depletion of Zr, Hf, and Ti (fig. 7.27) relative to the middle REE elements (Sm, Eu, and Gd) also cannot be explained by partial melting of dry garnet peridotite, given that the bulk partition coefficients for Zr, Hf, and Ti between garnet peridotite and silicate melt are similar to the ones shown by MREE (Salters et al., 2002).

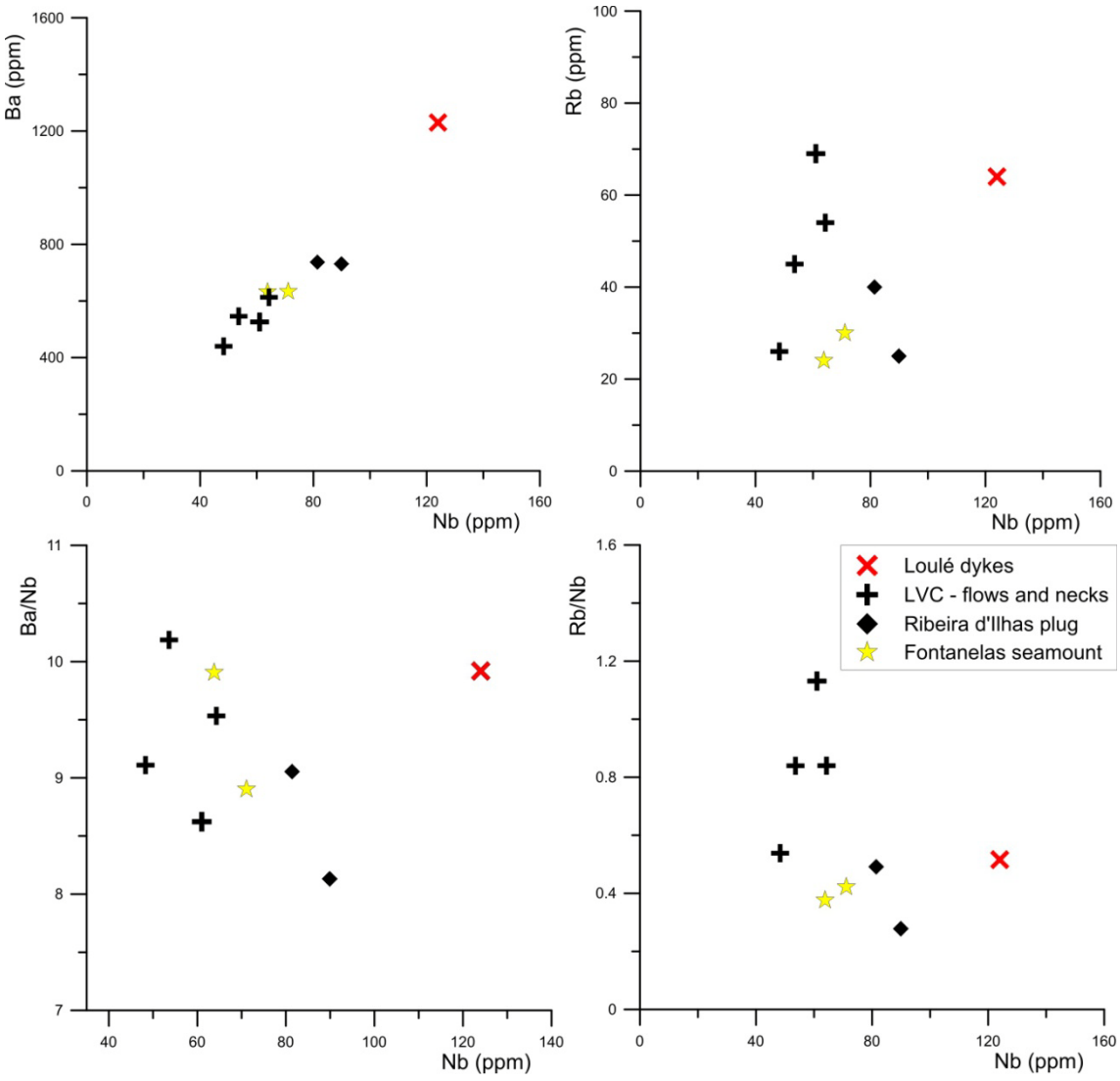

Fig. 7.30: plots of Nb vs. Ba, Rb, Ba/Nb and Rb/Nb for the primitive samples.

The negative anomalies in Zr and Hf observed in most of the basic samples from the second cycle of alkaline activity (fig. 7.30) are associated with ZrHf* below 0.75 (where ZrHf* is defined by $(Zr+Hf)_N/(Nd+Sm)_N$, Tappe et al., 2006) which corresponds to the minimum value associated with samples from the first cycle, who do not show negative Zr and Nb anomalies. The lowest ZrHf* values are found in the Loulé dykes and basic rocks from Monchique (0.37-0.46), all of which have lamprophyric affinities, and also in the amphibole rich gabbroic rocks from the Sintra and Sines intrusions (0.27-0.44).

Other basic rocks belonging to the LVC and associated dykes and sills show less pronounced Zr and Hf anomalies and consequently higher ZrHf* (0.51-0.76), while the more evolved and contaminated sills and dykes show no Zr and Hf anomaly and some of the highest ZrHf* (0.78-0.94).

The negative Zr and Hf anomalies, and consequentially low ZrHf* values, in basic and ultrabasic rocks do not appear to be related with crustal contamination processes or with crystal fractionation, since the samples, excepting the Loulé dyke, do not show any coupled variations in ZrHf* and other HFSEs, like Nb, Ta and Ti, which could be indicative of crustal contamination processes, or of the fractionation and removal of a Ti rich oxide.

Therefore these anomalies are considered to be primary features of these magmas, and associated with specific source characteristics at the time of melting. The aforementioned decoupling of the variations in Zr and Hf with other HFSEs in most of the samples also excludes the retention of these elements in a residual Ti rich oxide phase in the mantle such as rutile and ilmenite, since these minerals would fractionate all HFSE elements (McCallum and Charette, 1978; Zack and Brumm, 1998; Foley et al., 2000; Klemme et al., 2005). This means that it is possible that a Ti free, Zr and Hf rich phase existed in the mantle at the time of melting.

The more common Zr and Hf bearing phases observed in xenoliths and as xenocrysts are baddeleyite (e.g. Heaman and LeCheminant, 2001) and zircon (e.g. Kinny and Dawson, 1992; Konzett et al., 1998). Seeing that these low ZrHf* values are associated with lower than unity $(Th/Nb)_n$ ratios, the negative Zr and Hf anomalies can be indicative of the presence of residual mantle zircon instead of baddeleyite, since the Zr-site in zircon has a wider size than in baddeleyite and as such can incorporate some Th, leading to $(Th/Nb)_n < 1$ in the magmas, while $Th/Nb)_n > 1$ would be indicative of the presence of baddeleyite (Kerr et al., 2010).

The fractionation or presence of residual perovskite in the mantle can be called upon to justify the negative Ti anomaly in the Loulé dyke. This anomaly is coupled with lower Zr/Nb and higher La/Nb (Nb and Zr are also compatible in perovskite: $\boldsymbol{D_{Nb}^{per}}$ = 10-0.69; $\boldsymbol{D_{Zr}^{per}}$ = 15-2.06; $\boldsymbol{D_{Ti}^{per}}$ = 10-1.07 Kato et al., 1988; Liebske et al., 2005; see fig. 7.31).

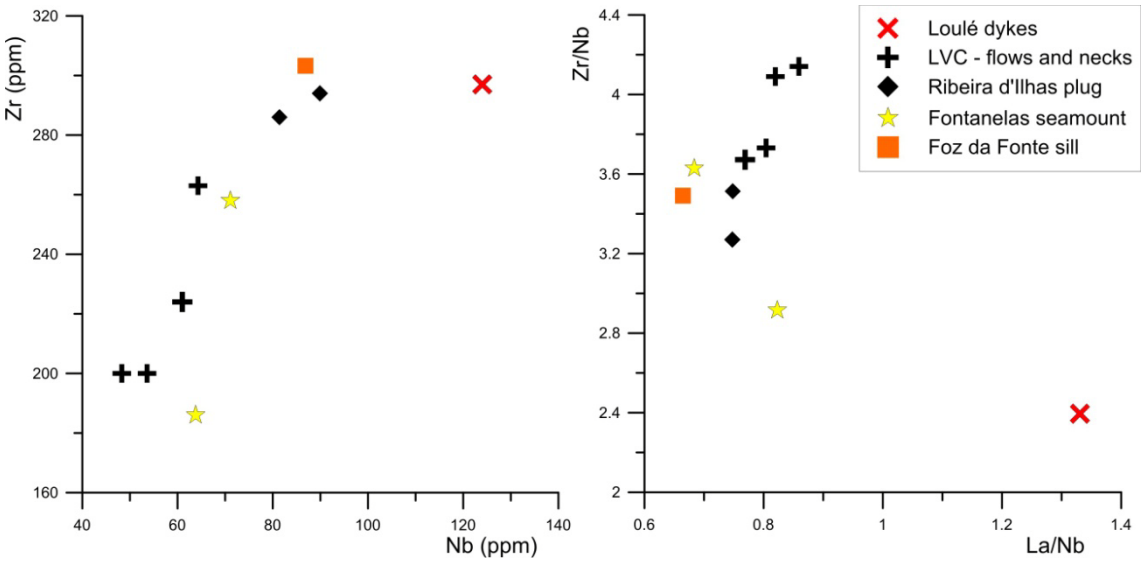

Fig. 7.31: Plots of Nb vs. Zr and La/Nb vs. Zr/Nb for the more primitive samples.

Perovskite is a common phase in ultrabasic carbonated magmas (e.g. Rock, 1977; Bédard, 1994; le Roex and Lanyon, 1998; Riley et al., 2003; Tappe et al., 2004), such as the volatile rich and carbonate bearing lamprophyres, but it has not been identified in the samples from the Loulé lamprophyres (see section 6.1.9). This phase has only rarely been recognized in mantle xenoliths (e.g. Lloyd et al., 1996; Chesley et al., 1999; Arzamastsev and Mitrofanov, 2009). However, the identification of this mineral in mantle material appears to have been wrongly attributed at times, according to Neal et al. (2001). Thus it seems more likely that the Ti anomaly is not related with residual perovskite or with the early crystallization and removal of this mineral.

7.4.1.2 On the nature of the metasomatic agent

Amphibole and zircon, as well as other phases such as phlogopite, apatite, monazite, ilmenite, rutile, are common accessory phases in mantle xenolith assemblages that have suffered carbonatitic metassomatism in many continental alkaline provinces (e.g. Rudnick et al., 1993; Yaxley et al., 1998; le Roex and Lanyon, 1998; Gorring and

Kay, 2000; Tappe et al., 2006; Zeng et al., 2010). Negative anomalies in K, P, Zr, Hf and Ti in basic and ultrabasic alkaline rocks have also been associated with the metassomatic action of carbonatitic liquids (e.g. Zeng et al., 2010), and experimentally determined partition coefficients between peridotite and carbonatite melts imply that the carbonatites are depleted in these elements (e.g. Sweeney et al., 1995; Klemme et al., 1995; Blundy and Dalton, 2000). Rudnick et al. (1993) associated the decrease in the Ti/Eu ratio with increasing La/Yb of peridotites, and in the magmas generated from their partial melting, with the occurrence of carbonatitic metasomatism. As can be seen on fig. 7.31, Ti/Eu seems to decrease on the studied samples with MgO > 7, with some of them showing values lower than the one attributed to the primitive mantle (7901, Palme and O'Neill, 2003).

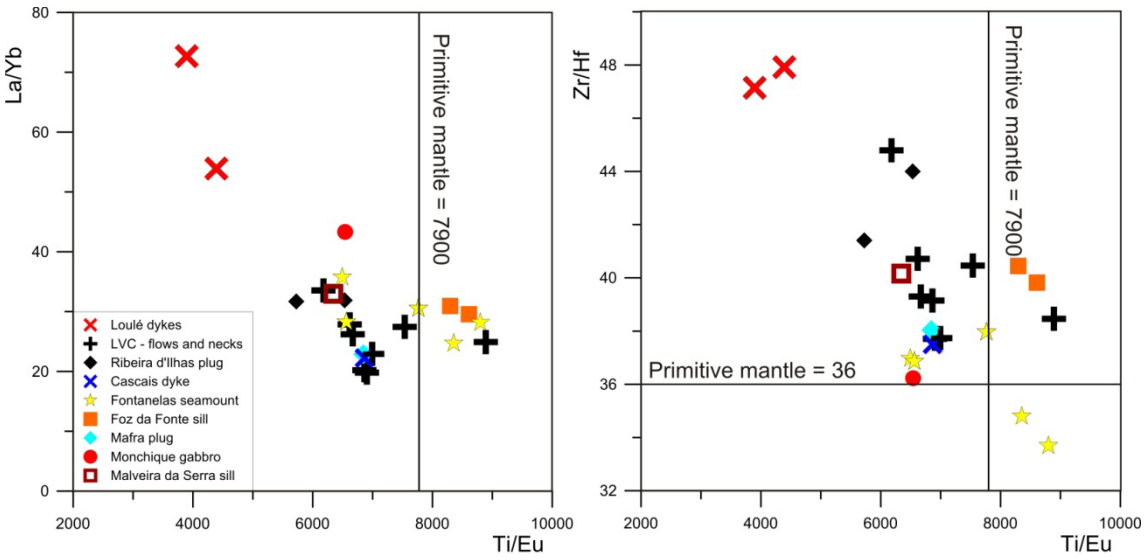

Fig. 7.32: Ti/Eu vs. La/Yb and Zr/Hf for the samples with MgO > 7. The values for primitive mantle ratios are from Palme and O'Neill (2003).

Carbonatitic metasomatism can promote the stability of Ca-rich grossular garnets (Pfänder et al. 2007; Martins et al., 2010) which have $D_{Zr}^{grt} > D_{Hf}^{grt} > 1$ (van Westrenem et al., 2001) consequentially causing lower Zr/Hf ratios in magmas generated from sources metasomatized by carbonatitic liquids containing grossular. However, in the majority of cases, relatively high Zr/Hf (36.2-47.9 in the studied samples), above the ratio shown by the primitive mantle (36, Palme and O'Neill, 2003), coupled with the lower Ti/Eu values (fig. 7.32) and high La/Yb are interpreted as a fingerprint of the action of carbonatite metasomatism (e.g. Dupuy et al., 1992; Ionov

et al., 1993; Rudnick et al., 1993; Yaxley et al., 1998; Tappe et al., 2007; Zeng et al., 2010).

From the observation of figure 7.32 it is also noticeable that the Foz da Fonte sill, which formed during the first pulse of Late Cretaceous igneous alkaline activity, does not appear to have suffered the effects of carbonatite metasomatism, which is expected since the metasomatic trace element signature is only present in samples from the second pulse.

The combination of the increase in Ti/Eu and decrease in Zr/Hf with decreasing Th (fig. 7.33) and increasing degree of melting indicates that the carbonatite metasomatized mantle is preferentially sampled in the initial stages of melting, as anticipated, since carbonation lowers the solidus of mantle peridotite. Consequentially, the carbonated mantle domains will melt before anything else and the metasomatic signature of the resulting melts will be more evident for melting events characterized by low degrees of melting (see also Mata, 1996; Mata et al., 1998). As the degree of melting increases, unmetasomatized parts of the mantle can start to melt and the carbonatitic signature becomes progressively diluted within increasing contributions from non metasomatized domains to the magma.

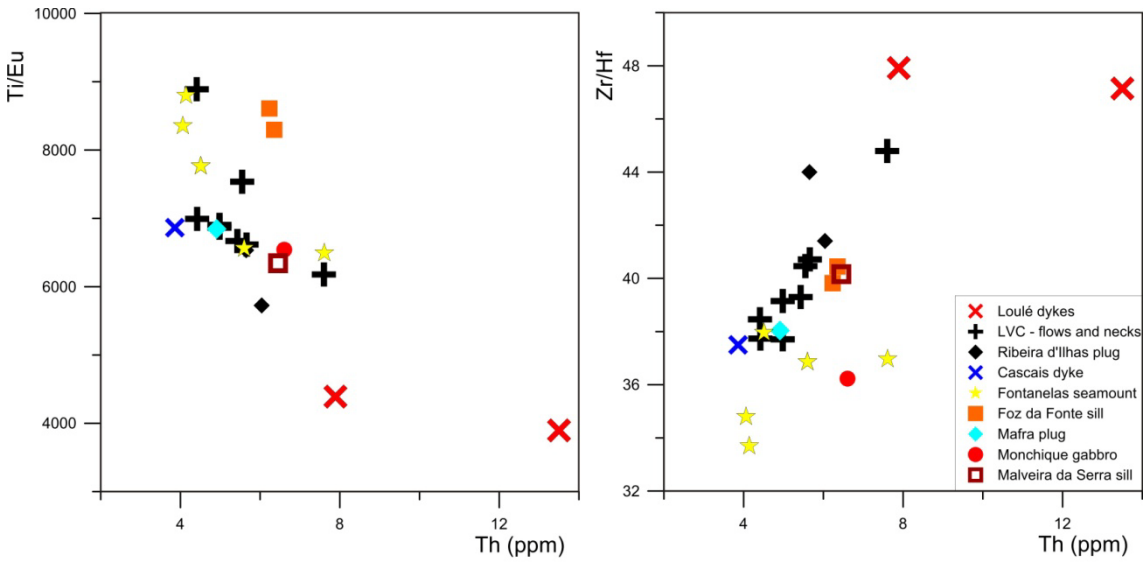

Fig. 7.33: Plots of Th vs. Ti/Eu and Zr/Hf for the samples with MgO > 7%.

The imprint of a metasomatic event by a carbonatite liquid can by itself generate the observed trace element patterns, with its negative anomalies in K, P, Zr, Hf and sometimes even Ti, but it can also lead to the formation of the minerals previously

identified as being responsible by the retention of these elements, for example amphibole (e.g. Kinny and Dawson, 1992; Yaxley et al., 1998, Zaccarini et al., 2004). The crystallization of zircon can also be associated with mantle carbonate given that zircons found in MARID (Mica, Amphibole, Rutile, Ilmenite and Diopside) xenoliths appear to have formed from interaction with carbonated and K rich silicic liquids (Kinny and Dawson, 1992; Sweeney et al., 1993; Konzett et al., 1998, 2000; Dawson et al., 2000).

The melting of carbonated peridotite will at first generate carbonatitic melts, but the nature of the generated liquids will progress gradually towards silica undersaturated siliceous compostions with increasing melting degree (e.g. Thibault et al., 1992; Hirose, 1997; Gudfinnsson and Presnall, 2005; Dasgupta et al., 2007).

Silicate and carbonate liquids can be found in close association in some mantle xenoliths (e.g. Yaxley et al., 1991; Neumann et al., 2002; Martins et al., 2010). In some cases, mixtures of these two liquids can occur as silicic carbonatite or carbonate bearing silicate melts (e.g. Neumann et al., 2002; Sisson et al., 2009). Therefore, it is likely that the source rocks for the Late Cretaceous alkaline magmatism in the WIM underwent both carbonated and siliceous metasomatism, similarly to what has been proposed by Dixon et al. (2008) for the rejuvenated stage lavas of Niihau in Hawaii. Also, the metasomatic episodes involving carbonated melts are likely to be volumetrically restricted due to the consumption of the small volumes of carbonatitic liquid during metasomatic decarbonation reactions (e.g enstatite $4MgSiO_3$ + dolomite $CaMg(CO_3)_2$ = forsterite $2Mg_2SiO_4$+ diopside $CaMgSi_2O_6$ + $2CO_2$; Yaxley, 1991).

Pilet et al. (2008) have recently proposed and alternative mechanism for the generation of enriched undersaturated alkaline rocks, involving volatile rich (H_2O+CO_2) basic alkaline siliceous liquids metasomatizing the lithosphere and forming hornblendite and hornblende clinopyroxenite veins (e.g. Coltorti et al., 2004; Pilet et al., 2008). In fact, experiemental work has shown that the partial melting of such metasomatic veins, along with interacting and additional melting of the surrounding peridotite, can be invoked to explain the major and trace element trace element concentrations of basic undersaturated alkaline magmas with compositions ranging from nephelinite to alkali basalt (fig. 7.36, Pilet et al., 2008, 2010).

Those results can also reproduce most of the features observed in spidergrams common in this type of magmas and found on the studied rocks (negative anomalies in K, P, Zr and Hf and pronounced enrichments in LREEs and Nb, fig. 7.34), except for

the negative anomaly in Ti and low Ti/Eu values found in the Loulé lamprophyre and in other ultrabasic to basic intraplate alkaline provinces (e.g. Tappe et al., 2004, 2006; Androkinov and Foley, 2002; Zeng et al., 2010). This is because the magmas generated by this kind of source are very Ti rich, given the large amounts of Ti bearing amphibole present in the source.

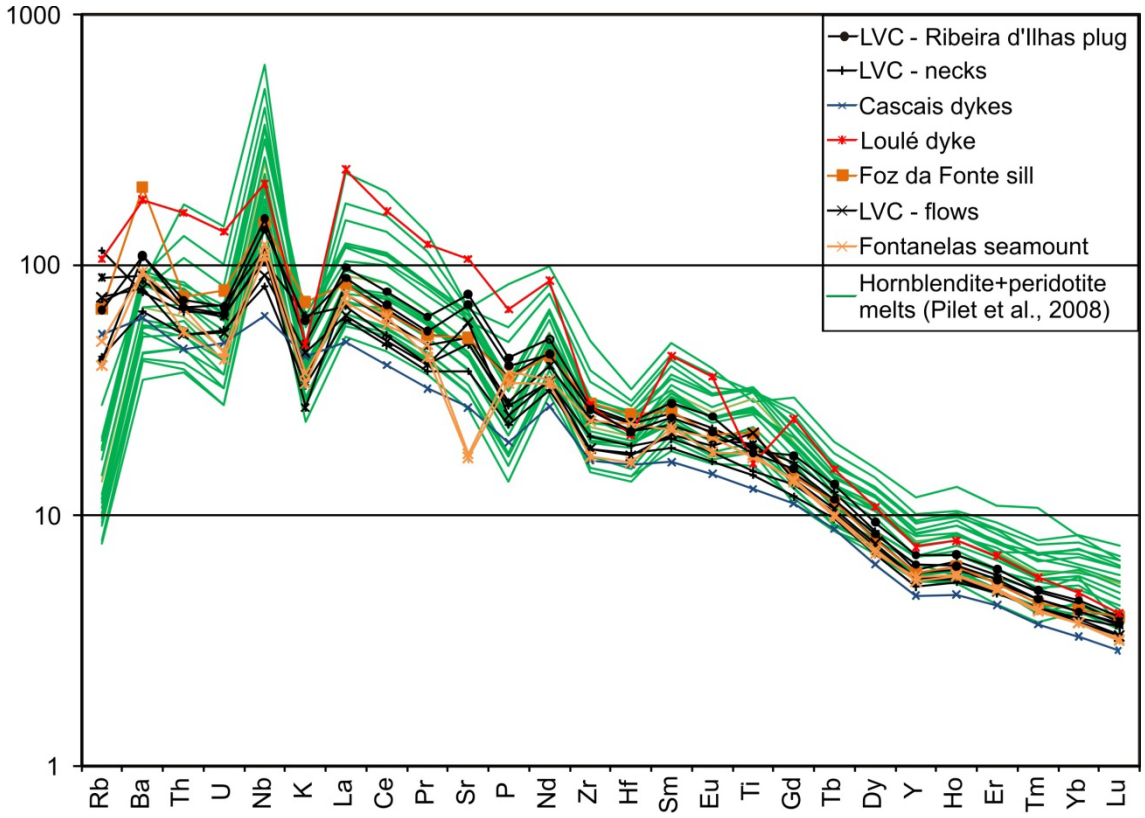

Fig. 7.34: Primitive upper mantle normalized (Palme and O'Neill, 2003) multielemental plots for the more primitive samples of the WIM and for the experimental melts obtained from hornblendite and hornblendite + peridotite sources by Pilet et al. (2008).

Other possible sources for alkaline magmatism, including silica deficient carbonated eclogite and garnet pyroxenite, have also been proposed as possible sources for basic alkaline magmas, but the melts produced from these sources are generally too poor in alkalis (Hirschman et al., 2003; Kogiso et al., 2003; Kogiso and Hirschman 2006) and cannot explain the negative Ti anomalies and high Zr/Hf ratios commonly observed in these magmas (Zeng et al., 2010) and in some of the Late Cretaceous alkaline rocks studied in this work.

In summary, trace element abundances and ratios point towards a metasomatic enrichment of the source of the alkaline magmatism present in the WIM. The

composition of such a metasomatic agent is likely to be gradational, from a carbonatitic to a volatile rich siliceous melt. However, the high Zr/Hf and low Ti/Eu point towards an important carbonatitic contribution. Carbonatite and silicate melts possess different melt structures, owing to having $\mathbf{CO_3^{2-}}$ and O^{2-} as the main coordinating or complexing anion (Klemme et al., 1995; Blundy and Dalton, 2000) and will therefore show different bulk distribution coefficients for certain elements (see also Martins et al., 2010). Experimental studies show that carbonatite melts show marked depletions in Ti in relation to LREE and MREE, resulting in low Ti/Eu (e.g. Klemme et al., 1995; Dasgupta et al., 2009). On the other hand, D values for Ti between garnet peridotite and silicate melts are similar to the ones shown by MREE (Salters et al., 2002) and generate higher Ti/Eu, as the ones seen in experimental results by Pilet et al. (2008).

Overall, high Zr/Hf and low Ti/Eu are diagnostic of an important carbonatitic component in the metasomatic agent that affected the source of some of the Late Cretaceous alkaline magmas of the WIM, resulting in the imprint of its trace element signature in the metasomatized mantle.

Evidence seems to point to carbonatitic and volatile rich (H_2O+CO_2) siliceous liquids, both of which can be generated progressively by decompression melting of a common, ascending carbonated peridotite (e.g. Gudfinnsson and Presnall, 2005; Dasgupta et al., 2006). As these two kinds of metasomatic agents have been previously identified in the subcontinental lithospheric mantle (e.g. Dautria et al., 1992; Woodland et al., 1996), it is likely that they could have both acted in the mantle underneath the West Iberian Margin producing heterogenous mantle domains.

7.4.1.3 Asthenospheric vs. Lithospheric contributions: constraints from residual mantle mineralogy

The presence of metasomatic residual amphibole is not compatible with the temperature conditions that characterize the convecting asthenosphere or associated with mantle plumes (e.g. Class and Goldstein, 1997), which implies that the magmas with negative K anomalies were at least in equilibrium with cooler, amphibole bearing lithospheric mantle.

However, the unradiogenic Sr and radiogenic Nd isotopic signature of these magmas is compatible with a sublithospheric source. This depleted signature contrasts with the observed trace element enrichment and indicates that the source must have been subject to a metasomatic event which took place shortly before the generation and

emplacement of these alkaline magmas, not giving them time to evolve into distinct isotopic signatures by radioactive decay as a reservoir separated from the convecting asthenosphere. The nature of this asthenospheric or lithospheric mantle source will be discussed in further detail in section 7.5.

It should be noted that the nature of the lithospheric mantle in the WIM can nevertheless be quite similar to the underlying asthenosphere.

As was previously discussed, rifting in the Lusitanian basin ended before the onset of the Late Cretaceous alkaline magmatism (e.g. Rasmussen et al., 1998; Kullberg, 2000; Kullberg et al., 2010). After the continental break-up and the initiation of seafloor spreading, the lithosphere and asthenosphere will return to thermal equilibrium (e.g. Ziegler and Cloetingh, 2004). The thermal anomalies induced by the upwelling asthenosphere during rifting will decay and stabilize to 65% of their maximum intensity after 60 Ma in the case of mantle plumes. For margins where amagmatic rifting took place, such as WIM, that value is reached in shorter amounts of time (Ziegler and Cloetingh, 2004).

This means that by the Late Cretaceous, which is approximately 25 Ma after the end of rifting and oceanic break-up (at 124-118 Ma, e.g. Sibuet et al., 2007), the lithosphere of the newly formed passive West Iberian Margin could have been constituted by a mix of previously existing Paleozoic subcontinental lithosphere with Mesozoic asthenosphere accreted by conductive cooling. Subsequently, in the Late Cretaceus the lower part of the lithosphere in the WIM should then have a Mesozoic age and show chemical characteristics similar to the depleted convective asthenosphere (e.g. Wilson, 1993).

Later, during the Late Cretaceous alkaline cycle, this relatively young lithospheric domain could be the site of metasomatism by carbonated and hydrated silicated melts derived from low degrees of melting of a carbonated peridotite eventually present in the asthenosphere or in an upwelling mantle plume, similarly to what is proposed by Dasgupta et al. (2006) for oceanic settings. However, the thicker continental lithosphere would prevent the formation of the more silica rich melts produced in the spinel stability field that are sampled in oceanic areas with a thinner lithosphere. It would only allow for the generation of liquids resulting from small melt fractions at higher depths, and consequentially in equilibrium with stable garnet. These incompatible element enriched low degree melts would react with the lithosphere and form discrete veins that might contain amphibole, zircon and other metasomatic

minerals, and also have a lower solidus than the surrounding lithosphere due to their hydrated and/or carbonated nature.

These veined domains could therefore be easily fused during a subsequent event, and the enriched melts generated by their fusion could mix with more depleted liquids resulting from the partial melting of the asthenosphere or surrounding lithosphere, creating the observed trace element and isotopic signatures. The metasomatic component in the final signatures, will be more or less evident depending on the proportion of melt generated from metasomatic material and from the more depleted asthenosphere in the final melt.

However, this later melting event had to be triggered by a thermal perturbation of the lithosphere, either by the arrival of hotter mantle from a plume or convecting cell or by adiabatic decompression associated with lithospheric extension. As the WIM was not under extension during the Late Cretaceous, the first option seems the more likely.

The mineral chemistry data for the xenocrysts and xenoliths presented on section 6.2 can be used as evidence for the presence of clinopyroxene, amphibole and apatite rich domains that could be a result of mantle metasomatism by silicic carbonated liquids in the subcontinental mantle lithosphere (e.g. Pilet et al., 2005; O'Reilly and Griffin, 2000). However, the pressure and consequentially the depth at which those minerals formed is still fairly unconstrained and one cannot argue without reasonable doubt that these processes took place in the subcontinental lithospheric mantle or in the lower crust.

7.4.2 Estimates for the degree of melting

Even though all of the studied samples are of alkaline nature and share some compositional affinities (see section 7.1), the variability detected in terms of trace element and even isotopic signatures indicates that the source of this Cretaceous alkaline event cannot be considered to be homogeneous. This must be taken into account when reading the next discussion, where source homogeneity can be implied.

Even if such an assumption is not strictly correct, the common characteristics shown by the studied samples are thought to validate the following discussion, in a sense that the results obtained are suitable at least for comparison purposes.

The relative amount of mantle partial melting that occurred in order to form the more primitive WIM magmas can be estimated by plotting a very incompatible element,

such as Th, versus a ratio of two other incompatible elements (e.g. Sm/Nd, Hf/Th) with the less incompatible of the two as the numerator. These very incompatible elements (Th, Nd) have very high affinities with the liquid and are enriched in small melt fractions in comparison to the other less incompatible elements. As the degree of melting of the source increases, concentration of the very incompatible elements will tend to decrease as they become more diluted in the melt.

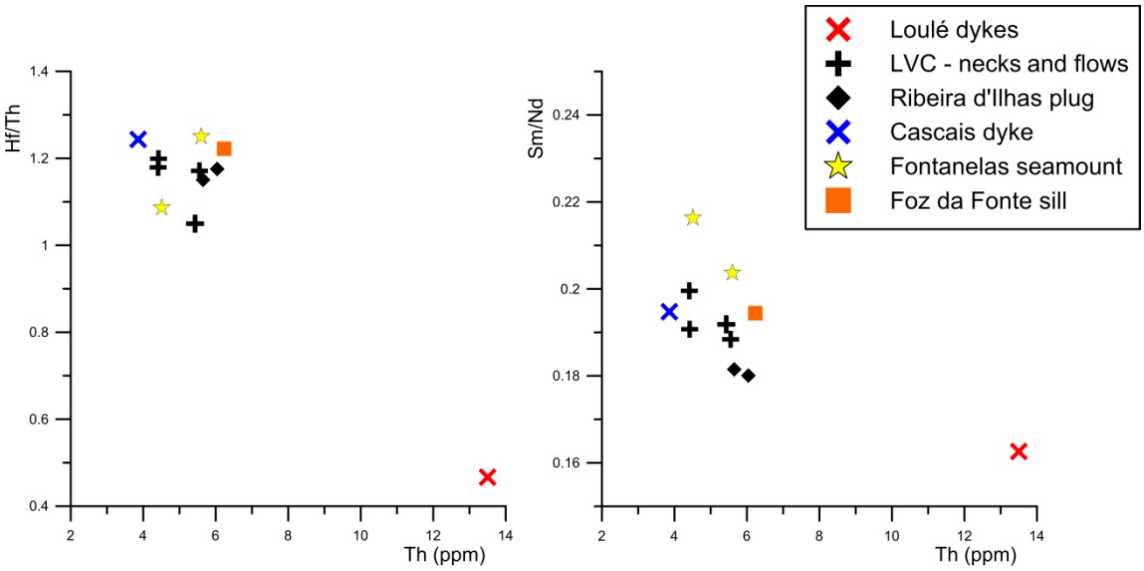

Fig. 7.35: Plot of Th vs. Hf/Th and Sm/Nd for the samples that represent more primitive magmas. Th decreases and incompatible trace element ratios increase with increasing amounts of partial melting of the source.

From fig. 7.35, we can suggest that the Loulé lamprophyric dyke is the result of the smallest amount of partial melting, while basalts from the LVC and Fontanelas seamount, the Foz da Fonte sill, the Cascais dykes and the Ribeira d'Ilhas plug all seem to be the product of similar, higher amounts of partial melting.

These conclusions are supported by fig. 7.36 where the Loulé dyke shows the higher La, La/Yb and Tb/Yb, in accordance with an origin from small degrees of partial melting, which progressively increases towards the rocks from the LVC, Fontanelas seamount, Foz da Fonte sill and Cascais basaltic dyke.

Garnets have high *D* for HREE (e.g. Adam and Green, 2006), and since all the more primitive samples show a strong REE fractionation, as was observed in fig. 7.9, with the samples having high LREE/HREE ($(La/Yb)_N$ 49 – 15.4) and MREE/HREE fractionation ($(Tb/Yb)_N$ 3.1 – 2.7) ratios, it is considered that melting took place in the presence of residual garnet.

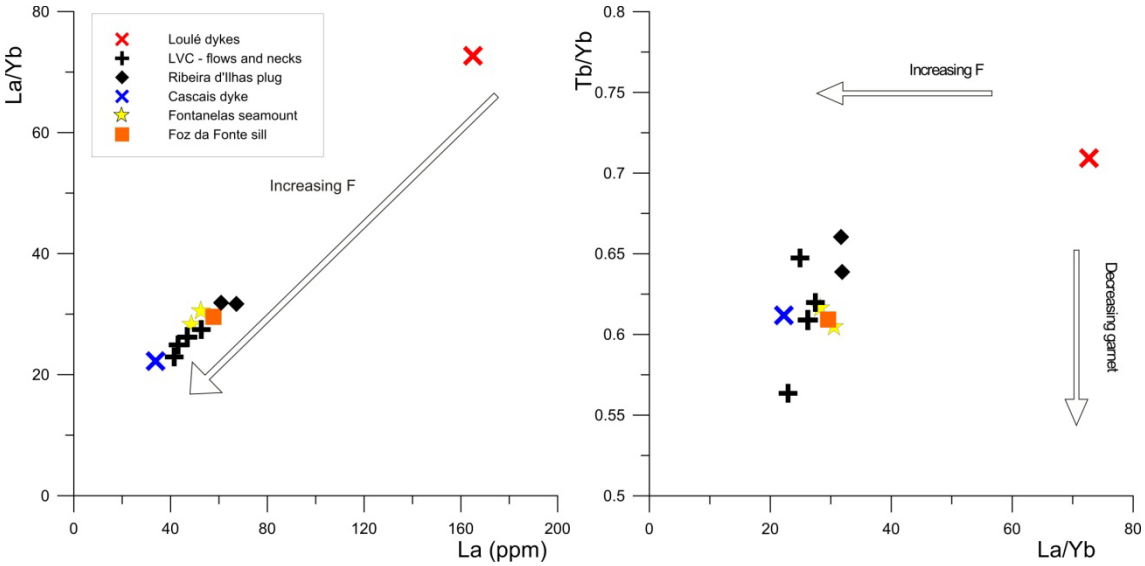

Fig. 7.36: Plots of La vs. La/b and La/Yb vs. Tb/Yb for the samples that represent primary magmas. F is the degree of partial melting of the mantle source. It increases with decreasing La/Yb and La.

As a mantle peridotite phase, garnet is stable at depths higher than 60 km where it occurs along with spinel up to 70 km and as the only Al rich phase from that depth onwards (e.g. Shen and Forsyth, 1995), meaning that the depth of melting for the alkaline rocks of the WIM was at least 60 km and likely higher.

Also, in fig. 7.36 it is observed that La and La/Yb, as well as Tb/Yb decrease with increasing degree of melting. La and Tb become more diluted in melts that result from higher partial melting fractions and furthermore because the amount of residual garnet in the mantle also decreases as the mineral is consumed during fusion, leading to a decrease of Yb retention in residual garnet and consequentially to lower La, La/Yb and Tb/Yb values.

The amount of partial melting taking place at the source of a certain magmatic event can also be quantitatively determined using the variation of the concentration of incompatible trace elements with increasing amounts of melting.

In this case, modeling was done using equilibrium batch melting. Batch or equilibrium batch melting assumes that the melt is continually reacting and equilibrating with the solid residue until extraction from the source takes place, and provides good results when compared to other mantle melting models (e.g. Feingenson et al., 1996; Spath et al., 2001). The equation that governs such a behavior was determined by Shaw (1970):

$$\frac{C_L^i}{C_o^i} = \frac{1}{D_n + F(1 - D_n)}$$

where C_L^i is the concentration of element *i* in the magmatic liquid, C_o^i is the concentration of the same element in the source rock, F is the amount of partial melt and D_n the bulk distribution coefficient between the residual solid and the magma ($\sum D_n = D_i^{min\,n-liq} \times X_{min\,n}$).

In order to account for different melt contributions from the individual solid mineral phases in proportions that are different from the ones in which they are present in the source assemblage, the batch melting equation was rewritten as follows by Shaw (1970):

$$\frac{C_L^i}{C_o^i} = \frac{1}{D_n + F(1 - P)}$$

where P is the bulk distribution coefficient for the minerals that contribute to the melt ($P = \sum p_n \times D_n$, where p_n is the normative weight fraction of a certain mineral in the melt and D_n is the mineral-melt distribution coefficient for a given trace element for that same mineral).

REEs were used to constrain the amounts of partial melting that took place in the source of the more primitive WIM magmas (Mg# > 60, Ni > 150). Since chondrite normalized patterns for REEs are strongly dependent on source composition and mineralogy, as well as on the degree of partial melting of that same source, the shape of those patterns will be controlled by the occurrence of phases whose presence is in its turn controlled by pressure/depth, such as spinel and garnet (e.g. Ellam, 1992; Kerr, 1994).

Only the more primitive and uncontaminated magma compositions were used for the elaboration of these models since these went through minimal amounts of fractional crystallization and therefore their REE concentrations have not been significantly affected by this process. For this reason the basaltic dyke from Cascais (sample RM 64) had to be left out of the process, since it appears to have been contaminated by crustal material (see section 7.3.2), although it is a fairly basic and undifferentiated rock.

Table 7.5: *D* values for the REE elements used for equilibrium batch melt modeling. Data from: Irving and Frey, 1978; McKenzie and O'Nions, 1991; Dalpe and Baker, 1994; Latourrette et al., 1995; Chazot et al., 1996; Green et al., 2000; Johnson and Schwab, 2004; Adam and Green, 2006; Shaw, 2006.

	Olv	Opx	Cpx	Grt	Amph	Spin
La	0.000053	0.0004	0.0536	0.0005	0.039	0.00002
Ce	0.0005	0.0017	0.057	0.0027	0.067	0.00003
Pr	0.0008	0.0048	0.1	0.01	0.105	0.0001
Nd	0.001	0.0068	0.14	0.028	0.142	0.0002
Sm	0.0007	0.01	0.26	0.14	0.188	0.0004
Eu	0.0016	0.013	0.31	0.19	0.35	0.0006
Gd	0.0015	0.012	0.367	0.498	0.32	0.0009
Tb	0.004	0.03	0.33	1.18	0.4	0.0012
Dy	0.0017	0.022	0.31	1.94	0.406	0.0015
Ho	0.009	0.048	0.35	2.66	0.41	0.0023
Er	0.0015	0.12	0.3	3.9	0.297	0.003
Tm	0.0091	0.071	0.33	4.24	0.36	0.0038
Yb	0.027	0.035	0.22	5	0.31	0.0045
Lu	0.024	0.004	0.31	5.5	0.3	0.0053

Table 7.6: Modal abundances and melt modes for the minerals in each of the modeled sources. Adapted from Späth et al. (2001).

	source 1		**source 2**		**source 3**	
	starting mode	**melt mode (p)**	**starting mode**	**melt mode (p)**	**starting mode**	**melt mode (p)**
Olv	0.53	0.05	0.54	0.05	0.54	0.315
Opx	0.22	0.054	0.235	0.055	0.255	0.31
Cpx	0.15	0.33	0.155	0.33	0.16	0.31
Grt	0.05	0.066	0.045	0.065	0.045	0.065
Amph	0.05	0.5	0.025	0.5	0	0

Despite of the uncertainties associated with the assumptions made regarding the trace element and mineralogical composition of the source and the weight contributions of its phases to the final melt, batch melt modeling of REE has often been used to estimate the amounts of partial melting that took place at the mantle source (e.g. Feigenson et al., 1996; Spath et al., 2001), showing good correlation with the depths and degrees of melting inferred independently from different methods.

In addition to garnet, the presence of a K-rich amphibole must be added to the residual mineralogy of the source mantle while melting was taking place for some of the samples belonging to the second phase of Late Cretaceous alkaline magmatism. The need for the presence of amphibole in the mantle source has been discussed in detail in section 7.4.1.

Table 7.7: Elemental abundances (ppm) for the REE in each of the modeled sources.

	source 1	source 2	source 3
La	3.43	2.74	2.74
Ce	7.14	5.54	5.54
Pr	1.08	0.81	0.81
Nd	5.04	3.72	3.72
Sm	1.42	0.95	0.95
Eu	0.52	0.34	0.34
Gd	1.58	1.09	1.09
Tb	0.26	0.18	0.18
Dy	1.42	1.07	1.07
Ho	0.30	0.24	0.24
Er	0.88	0.70	0.70
Tm	0.13	0.10	0.10
Yb	0.79	0.60	0.60
Lu	0.11	0.09	0.09

The obtained results can be observed in figs. 7.37 and 7.38 and the modeling parameters (source composition, used ***D*** values and source mineralogy and melting modes) are displayed in tables 7.5, 7.6 and 7.7.

Several independent sources had to be modeled in order to reproduce the chondrite normalized REE patterns presented by the analyzed samples. All these sources are LREE enriched and contain residual garnet. Amphibole was present in the modeled sources 1, 2 and 3 but not 4 since this last source was used to model the Foz da Fonte sill where residual amphibole is not supposed to be present.

The results indicate that the ultramafic Loulé lamprophyres are derived from very low amounts of partial melting (1-2%) of a more REE enriched source, with higher amounts of residual garnet and amphibole (fig. 7.37).

The source for the remaining Late Cretaceous alkaline rocks of the second pulse of magmatism present in the WIM is less REE enriched, contains smaller amounts of garnet and amphibole (table 7.6) and requires higher amounts of partial melting (3-6%) in order to generate the observed REE patterns in these samples.

The REE contents of the basaltic Cascais dyke (RM 64) cannot be modeled using any of these sources and would require an even more depleted source, with different melting modes (fig. 7.37). They are also positioned slightly off the modeled trends in fig. 7.39. Both these factors argue that small amounts of contamination by crustal materials led to small but significant changes in its REE concentrations.

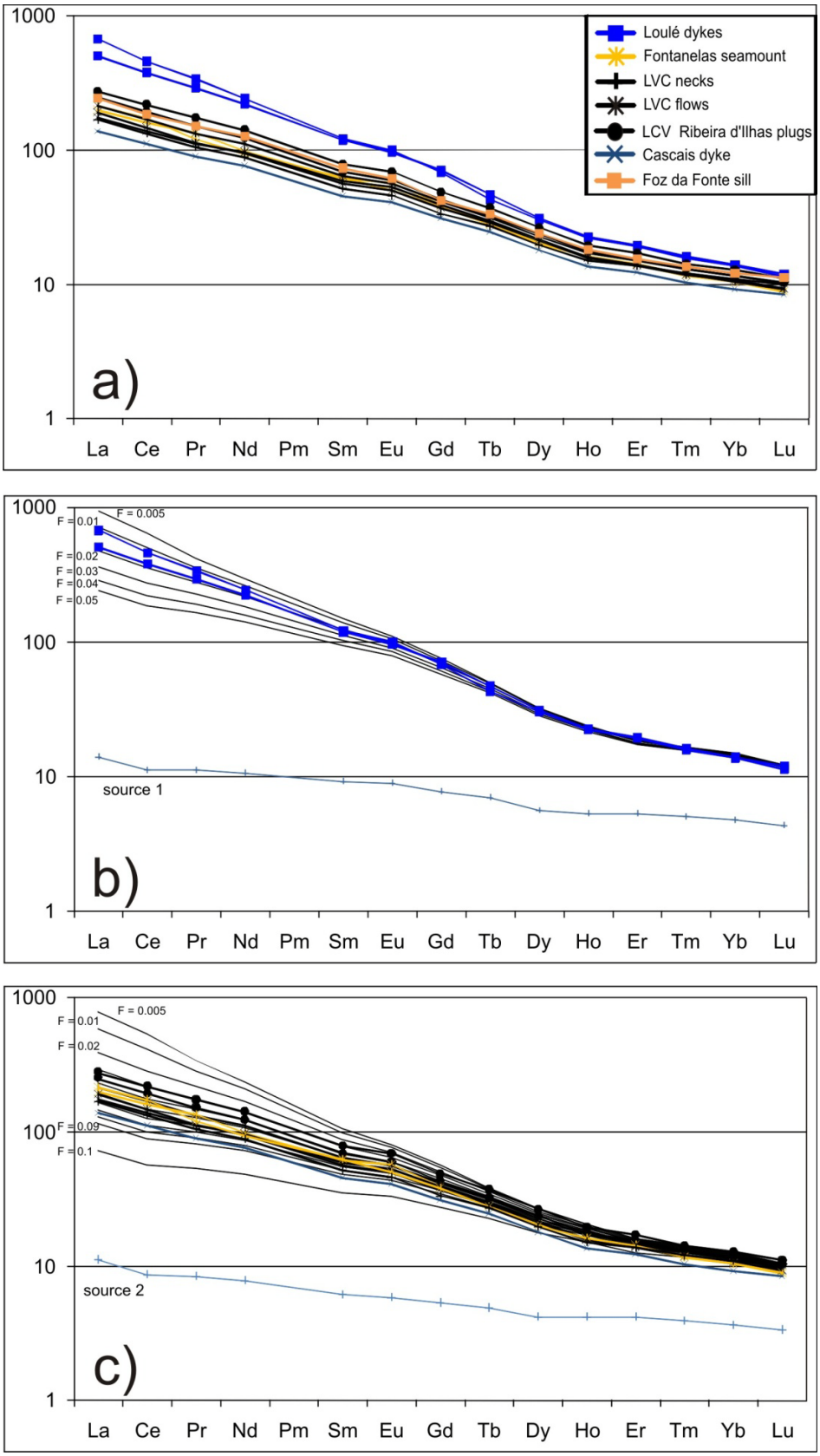

Fig. 7.37: a) Chondrite normalized (Palme and O'Neill, 2003) REE patterns for the primary samples; b and c) chondrite normalized patterns for the melts resulting from equilibrium batch melting of source 1 and source 2, respectively. F is the relative amount partial melt that occurred in each step (e.g. F =0.02 is equivalent to 2% melting of the source).

The REE patterns of the Foz da Fonte sill were modeled from the partial melting of 4-5% of an amphibole free garnet peridotite very similar to the one that generated the rocks from the LVC (source 3, table 7.6).

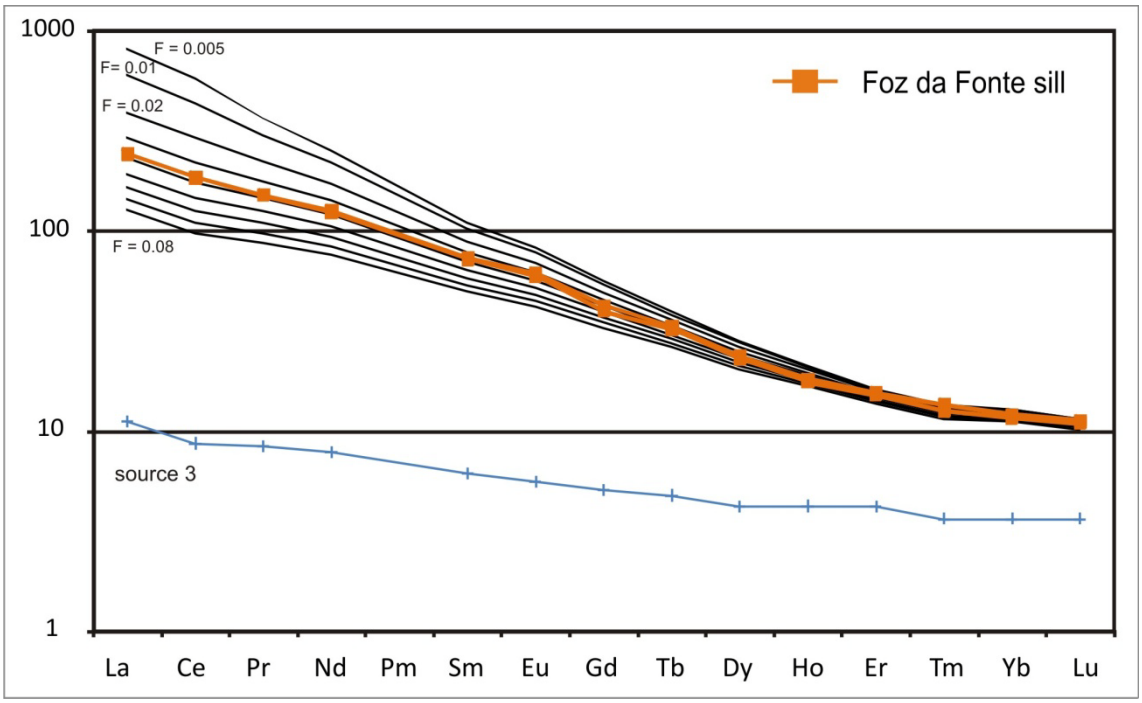

Fig. 7.38: chondrite normalized patterns for the melts resulting from equilibrium batch melting of source 3. F is the relative amount partial melt that occurred in each step (e.g. F = 0.02 is equivalent to 2% melting of the source).

The plotting of La vs. La/Yb and La/Yb vs. Sm/Yb of the modeled melting curves with the data obtained for the more primary samples (fig. 7.39) also agrees with the results proposed above, reinforcing the idea that the parameters used for the modeling are reasonable. The minor differences observed between sources 2 and 3 indicate that amphibole plays a minor role in fractionating REE since these sources are nearly equivalent except source 3, which lacks amphibole.

In fig. 7.39 are melts derived from sources equivalent to 1 and 2 but representing a shallower peridotite, with spinel instead of garnet are also plotted. It is clear from the trends generated by the melting of spinel bearing sources that garnet has to be present in order to explain the observed REE fractionation, since the melts from spinel peridotites show much lower La/Yb and Sm/Yb values.

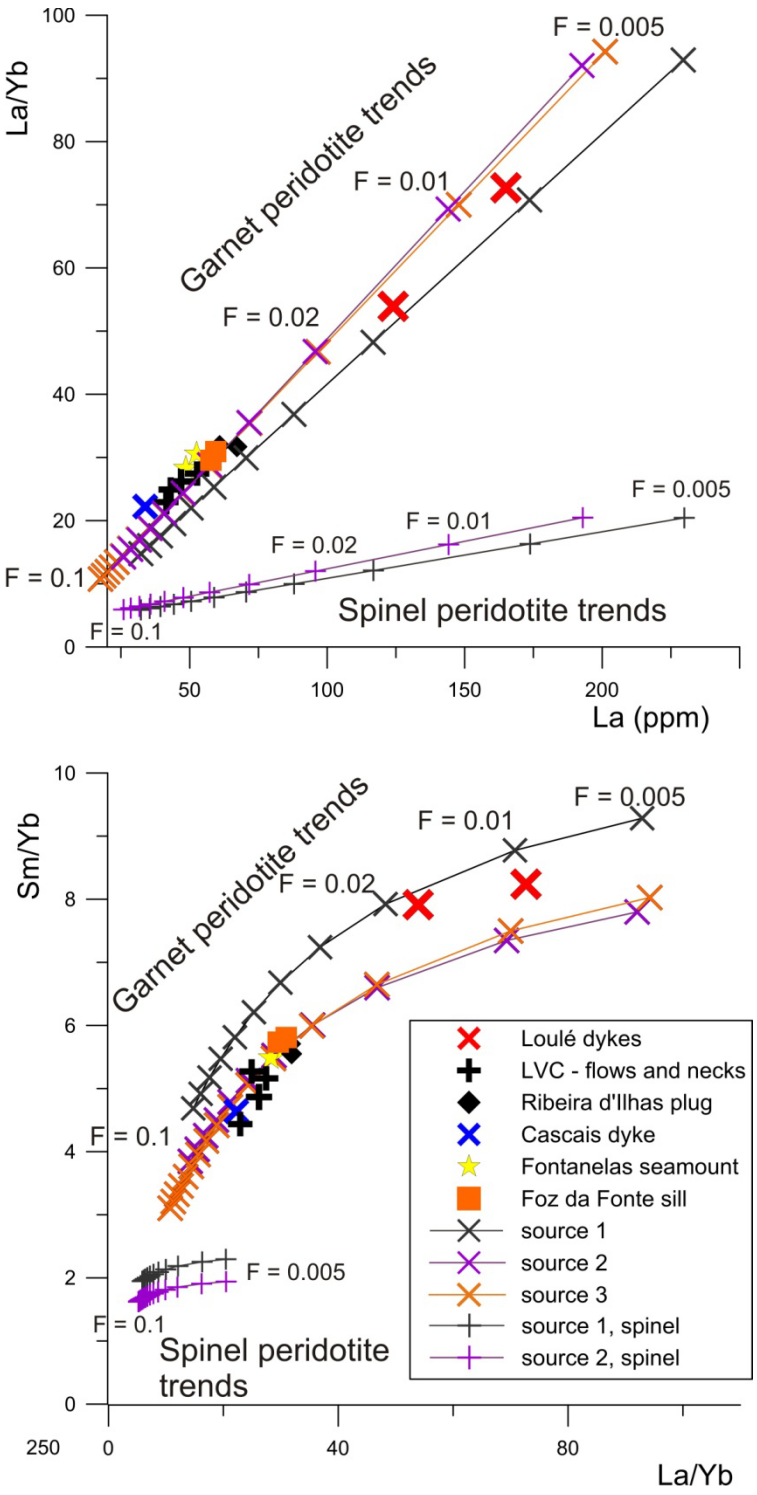

Fig. 7.39: La vs. La/Yb and La/Yb vs. Sm/Yb for the more primitive samples and batch melting curves calculated for sources 1, 2, 3 and 4 and for sources 1 and 2 where garnet was replaced by spinel. F is the relative amount partial melt that occurred in each step (e.g. F = 0.02 is equivalent to 2% melting).

7.5 Nature of the mantle source for the Late Cretaceous alkaline magmatism in the WIM

In this section, the geochemical information compiled in this work and presented by other authors who worked in the region will be discussed in order to try and evaluate the nature of the mantle source that originated the Late Cretaceous alkaline magmas of the WIM.

7.5.1 Lithospheric contribution to the Late Cretaceous alkaline magmatism of the WIM

As was documented in the previous sections, the mantle source of the Late Cretaceous alkaline magmas of the WIM shows a complex history involving metasomatic enrichment by a volatile rich carbonated to siliceous melt.

However, if one considers the age corrected isotopic compositions of the uncontaminated samples ($^{87}Sr/^{86}Sr_i$ 0.7030-0.7037; εNd_i 5.7 – 3.7; $^{206}Pb/^{204}Pb_i$ 19.564-19.20, $^{207}Pb/^{204}Pb_i$ 15.609-15.580, $^{208}Pb/^{204}Pb_i$ 39.245-39.00), these seem to show a relatively small compositional range. Given the relatively large time span (94-72 Ma) of this magmatic episode, the composition of the mantle of the WIM can be considered as being reasonably stable and homogenous over that time period, which covered two distinct pulses of magmatic activity (Miranda et al., 2009; this study). These values are also within the range of compositions previously obtained for the Monchique alkaline complex (fig. 7.40) by Bernard-Griffiths et al. (1997).

The isotopic signatures shown by the samples of the alkaline cycle of the Mesozoic magmatic activity in the WIM are notoriously different from the ones that characterize the mantle sources of the previous tholeiitic and transitional cycles, which are of Early Jurassic and Late Jurassic/Early Cretaceous ages, respectively.

The tholeiitic cycle (≈ 198 Ma, Veratti et al., 2007) is part of the Central Atlantic Magmatic province, contemporaneous with rifting in the Algarve, Santiago do Cacém and southernmost Lusitanian basins, where it has been described, and therefore related to the initial rifting of the Atlantic and Tethyan margins (e.g. Martins, 1991; Martins et al., 2008; Cebriá et al., 2003). Basic magmas from the tholeiitic cycle shows higher values for $^{207}Pb/^{204}Pb$ and $^{87}Sr/^{86}Sr$ and lower εNd, $^{206}Pb/^{204}Pb$ and $^{208}Pb/^{204}Pb$ isotopic

ratios (Messejana dolerite dyke - $^{87}Sr/^{86}Sr_i$ 0.70524 to 0.70673, εNd_i -3.4 to 0.12; $^{206}Pb/^{204}Pb$ 18.385-18.715, $^{207}Pb/^{204}Pb$ 15.616-15.641, $^{208}Pb/^{204}Pb$ 38.371-38.701 Cebriá et al., 2003; tholeiitic volcanism from the Algarve basin - $^{87}Sr/^{86}Sr_i > 0.70539$; Martins

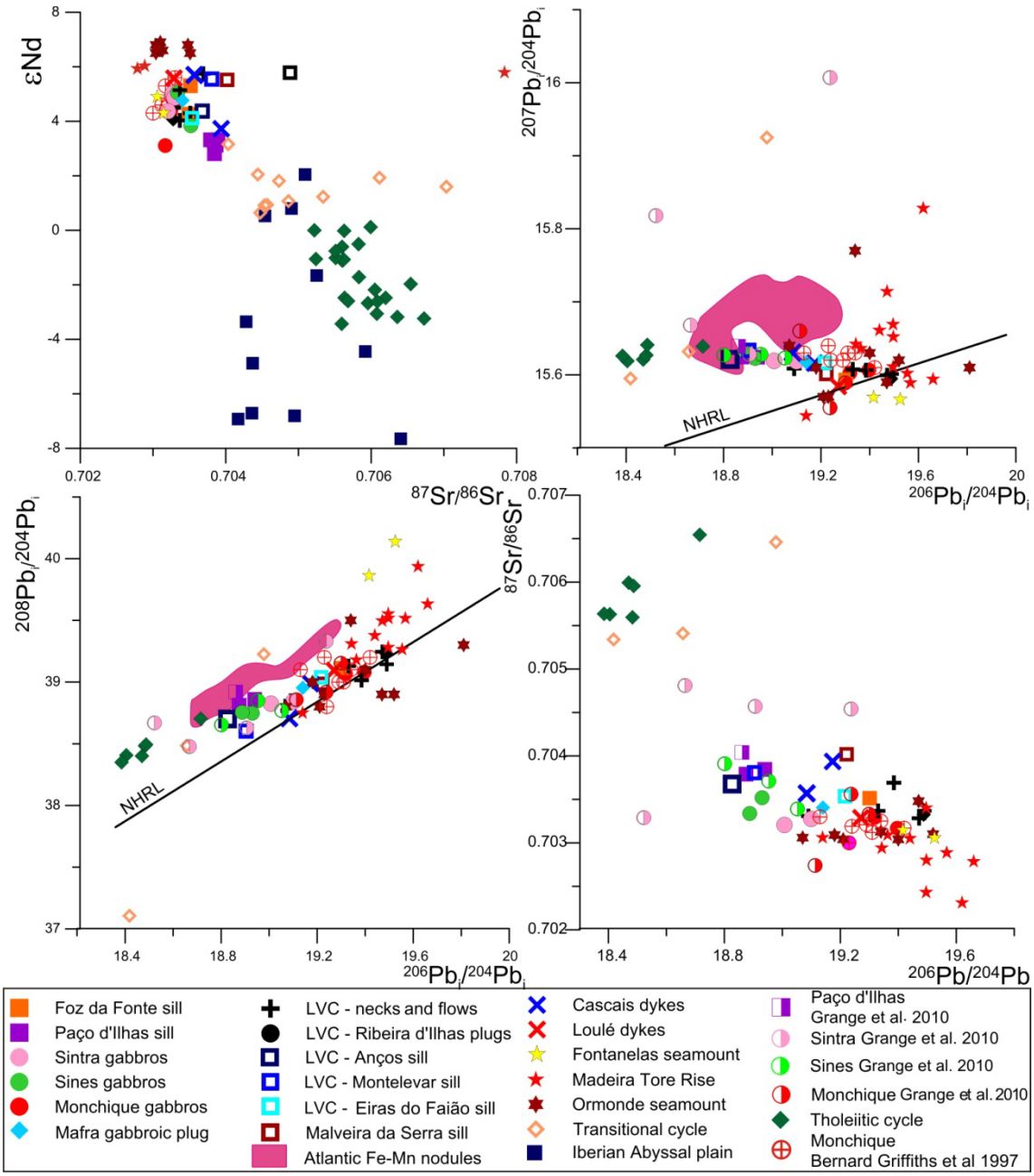

Fig. 7.40: Plots of Sr, Nd and Pb isotopic ratios for the samples from the Late Cretaceous Alkaline magmatism of the WIM, including the Madeira-Tore Rise (Geldmacher et al., 2006; Merle et al., 2006), Monchique complex and Ormonde seamount (Bernard-Griffiths et al., 1997), and the data for the onshore occurrences by Grange et al. (2010). Data for the transicional cycle from Alves (2010) and Grange et al. (2008). Data for the tholeiitic cycle from Cebriá et al., 2003 and Martins et al. (2008) and data from the intrusives in the Iberian Abyssal Plain from Chazot et al. (2005). Atlantic Fe-Mn nodules field draw from data in von Blackenburg et al. (1996), O'Nions et al. (1998) and Abouchami et al. (1999).

et al., 2008; fig. 7.40) that have been attributed to a high contribution from the lithospheric mantle (Martins et al., 2008) along with the Central Atlantic Plume material as sources for these melts (e.g. Cebriá et al., 2003).

The transitional cycle (141-146 Ma, Grange et al., 2008; Alves, 2010) outcrops only within the Lusitanian Basin and also possesses a distinct trace element and isotopic signature, with intermediate values between the Late Cretaceous alkaline magmatism and the previous tholeiitic event ($^{87}Sr/^{86}Sr_i$ 0.70403 to 0.706, εNd_i -3.16 to 0.64; $^{206}Pb/^{204}Pb$ 18.418-18.978, $^{207}Pb/^{204}Pb$ 15.595-15.632, $^{208}Pb/^{204}Pb$ 37.106-38.484; Grange et al., 2008, Alves, 2010; fig. 7.40). The isotopic and geochemical signature of the magmas from this cycle has been interpreted as to reflect partial melting of enriched metasomatized mantle domains, with the heat required for their fusion being provided by the ascending asthenosphere which occurred as a consequence of progressive extension in the Lusitanian basin during the last rifting phases (Grange et al., 2008; Alves, 2010).

From the tholeiitic (Lower Jurassic) to the transitional (Upper Jurassic/Lower Cretaceous) and finally to the alkaline cycle (Late Cretaceous) there seems to be a trend towards a more depleted Sr and Nd isotopic signature with time (figs. 7.40-41), which contrasts with the progressive enrichment in the trace element abundances and increasingly radiogenic Pb that is simultaneously observed (fig. 7.40-41).

Grange et al. (2010) sampled and analyzed the Sintra, Sines and Monchique complexes as well as the Paço d'Ilhas sill from the Late Cretaceous alkaline cycle. Based on whole rock trace element data and isotopic analysis from feldspar (Pb and Sr) and zircon (Hf) separates, these authors proposed a sublithospheric enriched DMM source that produced melts that were subsequently contaminated with variable amounts of more radiogenic subcontinental lithospheric mantle.

These authors assumed that their isotopic and trace element data did not reflect any kind of contamination from crustal lithologies and therefore was representative of the mantle sources of these magmas. This interpretation included even the more evolved samples, which in this case include granites and microgranites (Sintra), syenites (Sines) and nepheline syenites (Monchique). It is difficult to explain the generation of large volumes of felsic magma only by fractional crystallization of basic magmas in upper crustal settings without the occurrence of any kind of contamination, as they proposed for the alkaline complexes of Sintra, Sines and Monchique. In these complexes, the more evolved rocks make up most of the outcropping area, while the basic rocks are

much rarer at the surface (e.g. Matos Alves, 1964; Canilho, 1972; Clavijo and Valadares, 2003) and do not seem to be compensated by extensive volumes of mafic cumulates at depth (e.g. Kullberg et al., 2010 for Sintra). Furthermore, the isotopic data for these more evolved rocks from (Grange et al., 2010) plots along the contaminated trend defined for the more evolved rocks identified in this study (see section 7.3.2 and figs. 7.39 and 7.19-24), towards compositions that are more enriched in $^{87}Sr/^{86}Sr_i$ and $^{207}Pb/^{204}Pb$ but that show lower $^{206}Pb/^{204}Pb$ and $^{208}Pb/^{204}Pb$.

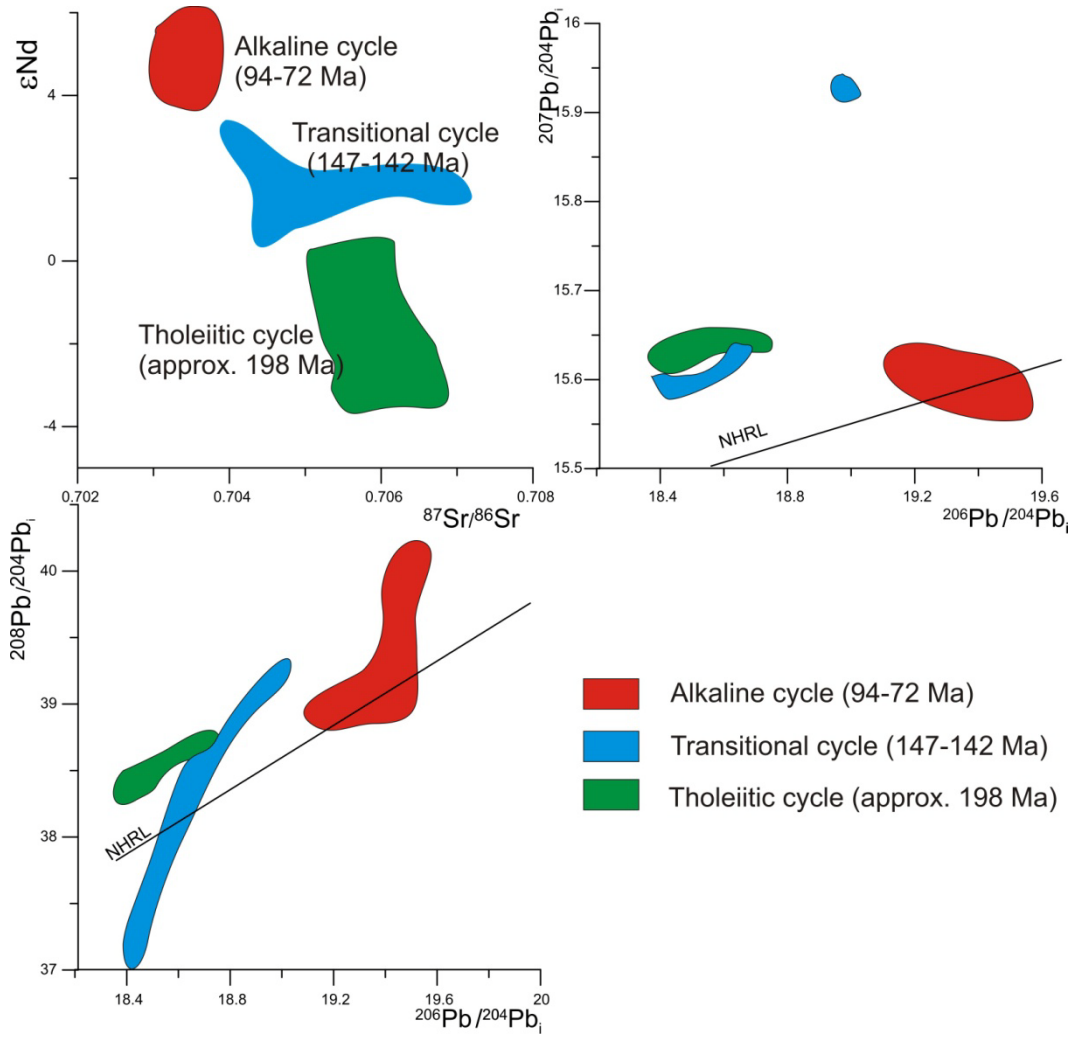

Fig. 7.41: Plots of Sr, Nd and Pb isotopic ratios for the samples from the three cycles of Mesozoic magmatic activity present in the WIM. Data for the alkaline cycle corresponds to the uncontaminated samples from this study, for the transitional cycle data are from Alves (2010) and Grange et al. (2008) and for the tholeiitic cycle from Cébria et al. (2003).

The increases in K/Nb, Th/La and coupled decrease in Nb/U with increasing silica contents seen in the more evolved and contaminated rocks in this study (see

section 7.3.2, fig. 7.21), also take place in the acid rocks sampled by Grange et al. (2010), thus pointing again towards important contamination by silica rich lithologies associated with the generation of these rocks (fig. 7.42). The marked positive Pb and negative Nb anomalies seen in the multielemental plots for the more evolved rocks (see fig. 4 in Grange et al., 2010) reinforce the conclusion that, in opposition to what is proposed by these authors, such rocks formed from magmas that have assimilated significant amounts of crustal contaminant(s) and therefore their isotopic signatures cannot be used to make inferences about the nature of their mantle source.

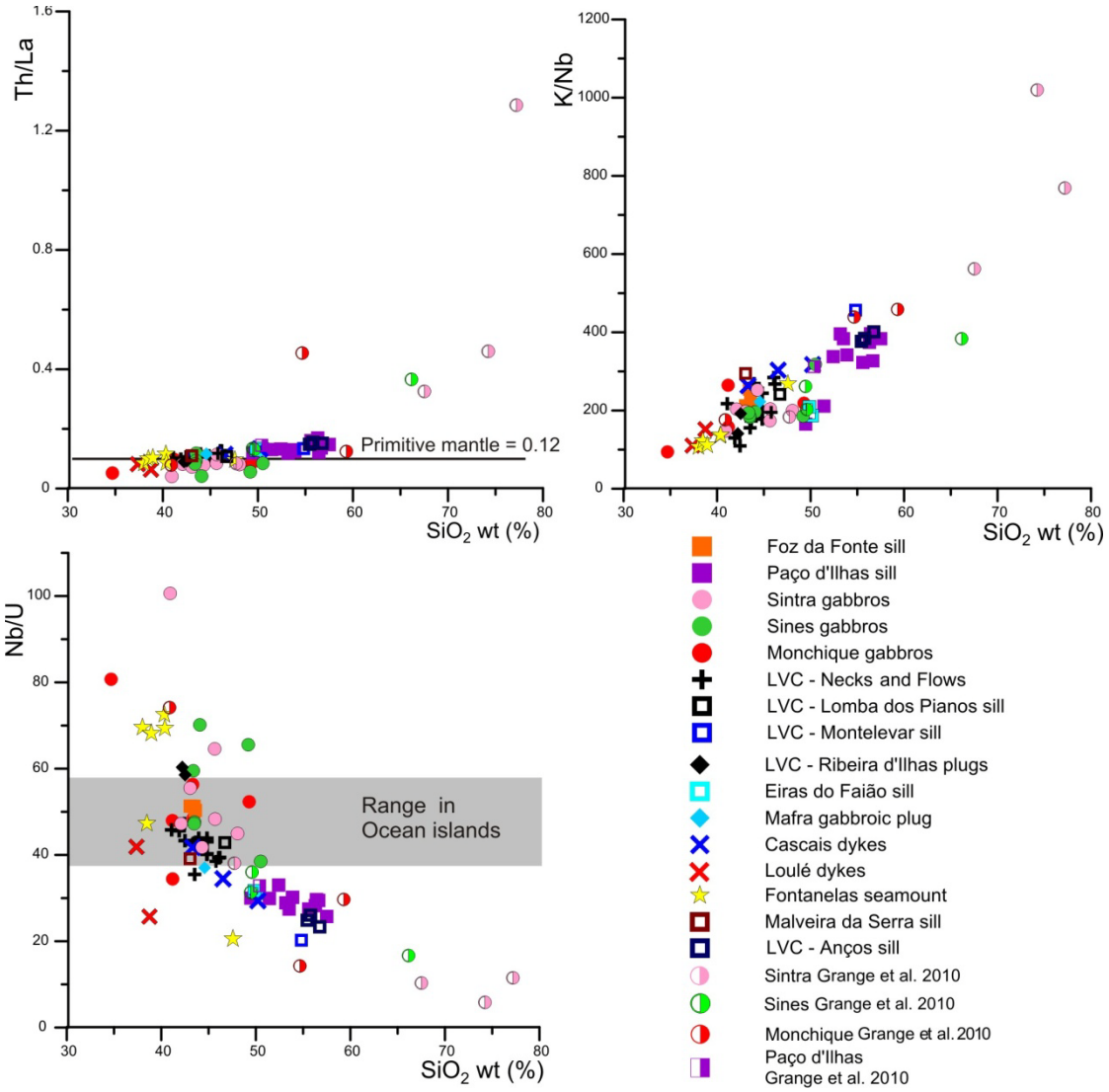

Fig. 7.42: Plots of SiO_2 vs. incompatible elements ratios Th/La, K/Nb, Zr/Nb and Nb/U for the studied samples and for the samples from Sintra, Sines, Monchique and Paço d'Ilhas collected by Grange et al (2010).

Since the samples from the Sines and Sintra "gabbro" analyzed by Grange et al. (2010) actually correspond to diorites which are already slightly contaminated (see section 7.3.2), only the samples from the Monchique gabbro can be considered as representatives of uncontaminated, but more or less fractionated mantle melts. Meanwhile the other "gabbros", the Paço d'Ilhas sill and the evolved rocks from the alkaline complexes all show evidence for important crustal contamination. The values reported by Grange et al. (2010) for the uncontaminated Monchique gabbro are $^{87}Sr/^{86}Sr_i$ = 0.70356, $^{206}Pb/^{204}Pb$ = 19.237, $^{207}Pb/^{204}Pb$ = 15.555 and $^{208}Pb/^{204}Pb$ = 38.918, which is within the range reported for the uncontaminated samples from the WIM reported in this work and by Bernard-Griffiths et al. (1997), except for slightly lower $^{207}Pb/^{204}Pb$ and $^{208}Pb/^{204}Pb$ (fig. 7.40). These authors attribute the isotopic signatures described for Monchique to an enriched DMM component derived from a deep, sublithospheric OIB like source that might correspond to a mantle plume or to the ambient astenospheric mantle enriched by a mantle plume.

The apparent decoupling of the Sr, Pb and Hf isotopic ratios detected by Grange et al. (2010) in the samples from Sintra is puzzling, but can be tentatively explained by the mixed effects of the contaminated nature of the magmas with the late stage hydrothermal event that affect this complex (see sections 6.1 and 7.3.2). Crustal contamination would lead to an increase in $^{87}Sr/^{86}Sr$, $^{207}Pb/^{204}Pb$ coupled with a decrease in $^{206}Pb/^{204}Pb$, $^{208}Pb/^{204}Pb$ and εHf. However, some samples seem to show low $^{87}Sr/^{86}Sr$, high $^{207}Pb/^{204}Pb$ and variable, but still positive εHf. On section 7.2.2 the higher $^{206}Pb/^{204}Pb$, and lower $^{207}Pb/^{204}Pb$ and $^{208}Pb/^{204}Pb$ shown in the whole rock analysis of the Sintra gabbros were attributed to the effects of late stage hydrothermal alteration by a Pb rich fluid. This hydrothermal alteration affects the feldspars and plagioclases more clearly (see section 6.1) than the other phases and so could be responsible for the more radiogenic Pb signature seen in some of the feldspar separates analyzed by Grange et al. (2010). However, the $^{87}Sr/^{86}Sr$ ratios are low and the metasomatizing fluids are not thought to contain unradiogenic Sr (see section 7.3.2).

The low $^{87}Sr/^{86}Sr_i$ in the feldspar separates from the more evolved rocks analyzed by Grange et al. (2010) might correspond to an artifact generated by overcorrection for the Rb-Sr decay in samples with high Rb/Sr ratios (1.56-5.77 for the more evolved rocks while only 0.002 to 0.2 in the basic to intermediate rocks). Any small imprecisions in the analysis of trace element concentrations in high Rb/Sr rocks or minerals leads to large error propagation in the calculation of age corrected Sr isotope

data and therefore produces less reliable $^{87}Sr/^{86}Sr_i$ values. On fig 7.43 the calculated $^{87}Sr/^{86}Sr_i$ are plotted along with the repective error bars, and it is possible to observe that the two granite samples from Sintra, (PT9A, alkali granite and PT5A, microgranite, Grange et al., 2010), display the largest error bars for the calculated $^{87}Sr/^{86}Sr_i$ and could therefore have reasonably higher isotopic ratios than the ones they are attributed in Grange et al. (2010). Such hypothetical higher $^{87}Sr/^{86}Sr_i$ would be more compatible with their contaminated nature.

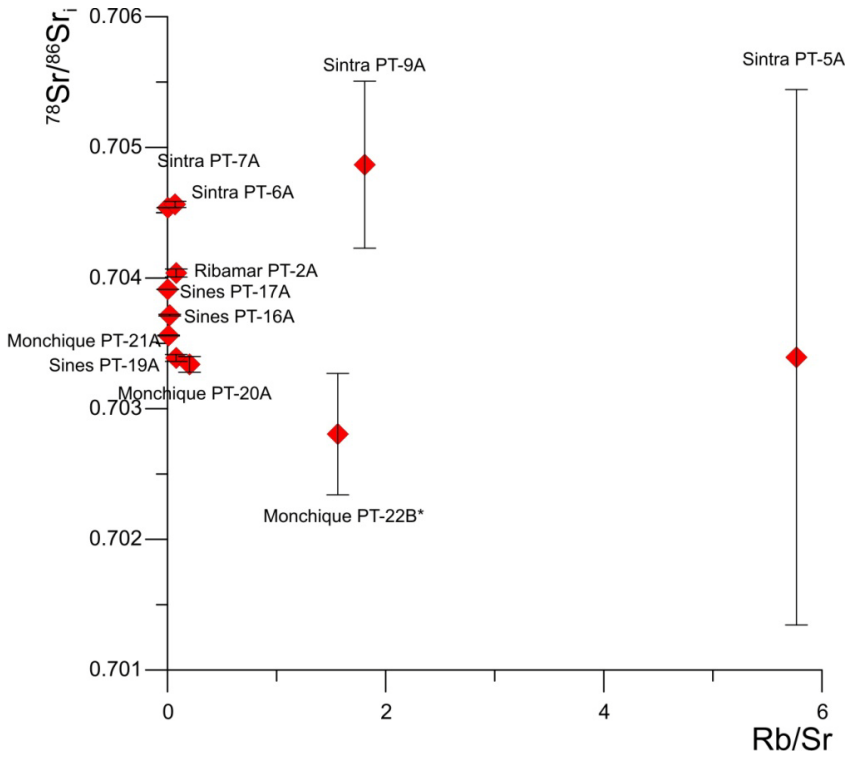

Fig. 7.43: Plot of age corrected Sr isotope ratios vs. Rb/Sr for feldspar separates analyzed by Grange et al. (2010), with error bars representing the propagated error using a ± 5 % analytical uncertainty in Rb and Sr determinations. The data shows that the uncertainties in $^{87}Sr/^{86}Sr_i$ increase with higher the Rb/Sr ratios.

A north to south increase in $^{206}Pb/^{204}Pb$ with simultaneous decrease in $^{87}Sr/^{86}Sr_i$ and $^{207}Pb/^{204}Pb$ in the occurrences studied by Grange et al. (2010) was interpreted by these authors as reflecting the progressive north to south increase in the contribution of an asthenospheric component. However, this trend is not observed on the data for uncontaminated rocks, for both the onshore and offshore occurrences (fig. 7.44). Instead, the samples show considerable scatter of isotopic ratios at whatever latitude they occur, arguing against a larger lithospheric contribution in the northern occurrences or significant variation of contribution from different components with latitude.

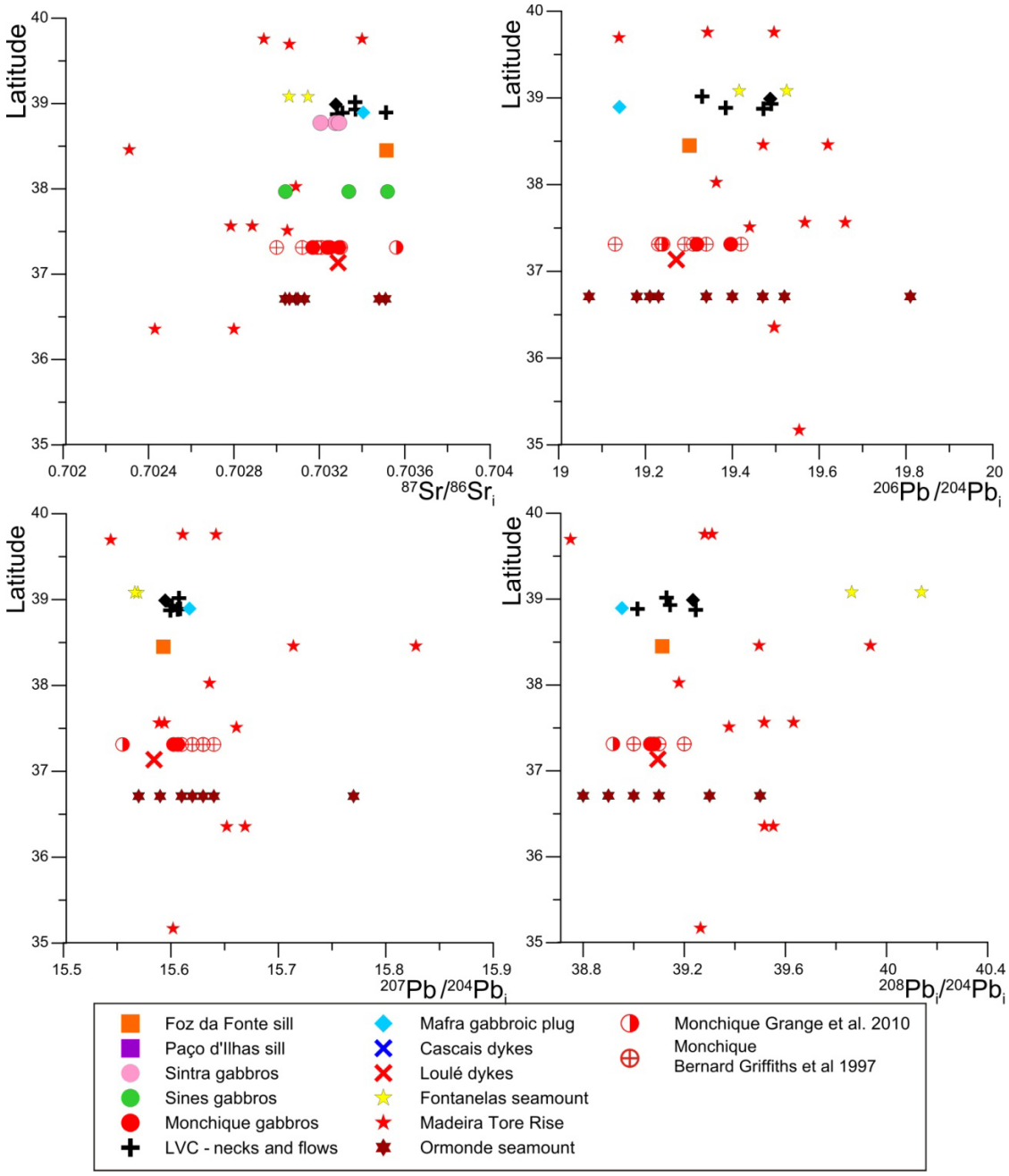

Fig. 7.44: Plots of Sr and Pb isotopic ratios vs. Latitude for the Late Cretaceous alkaline magmatism of the WIM, including the Ormonde seamount (Bernard-Griffiths et al., 1997) and the Madeira-Tore rise (Geldmacher et al., 2006; Merle et al., 2006).

Also, the use of the Cabo Ortegal Complex by Grange et al (2010) as a proxy for the subcontinental lithospheric mantle composition of the WIM can be questioned since it corresponds to a metamorphosed Lower Paleozoic ophiolite with back-arc affinities, and that shows signs of modification by subduction processes (Santos Zalduegui et al., 1996; Martinez et al., 2007). Such does not seem an adequate proxy to compare with the compositional characteristics with the subcontinental lithospheric mantle from a

Mesozoic passive margin such as the WIM. Instead, data from exposed sublithospheric mantle rocks along peridotite ridges in the Galicia banks and Iberia abyssal plain a seem to be more adequate proxy, but these show a more depleted trace element and Nd isotope signature and enriched Sr compositions (e.g. Beard et al., 2002; Chazot et al., 2005, fig.7.40). However, the Pb isotopic signature of these rocks remains undetermined except for some late pegmatitic veins of Cretaceous age that intrude those peridotites, which show rather unradiogenic lead ($^{206}Pb/^{204}Pb$ 18.65, $^{207}Pb/^{204}Pb$ 15.48 and $^{208}Pb/^{204}Pb$ 38.3, Beard et al., 2002) and cannot be the source of the old lithospheric component identified in the WIM by Grange et al. (2010) and Merle et al. (2006).

Other authors have argued that basic alkaline intraplate magmas enriched in trace elements and with radiogenic Pb and Nd relatively unradiogenic Sr can result from the melting of old recycled metasomatized lithospheric mantle (e.g. Pilet et al., 2005), of subcontinental lithospheric mantle metasomatized during previous subduction events (Finn et al., 2005; Panter et al., 2006), or even of veins that resulted from metasomatism contemporaneous of rifting and asthenospheric ascension that created high U/Pb domains (Nardini et al., 2009)

An origin within the subcontinental lithosphere for the Late Cretaceous alkaline magmas of the WIM can be rejected since the known isotopic composition for the peridotites and metasomatic veins of the continental lithosphere sampled in the Iberian Abyssal plain are markedly different from the studied magmas (fig. 7.40, Schärer et al., 1995; Seifert et al., 1997; Charpentier et al., 1998; Beard et al., 2002; Chazot et al., 2005). The metasomatic events recorded in these peridotites seem to be caused by the percolations of depleted asthenospheric melts (Charpentier et al., 1998; Beard et al., 2002; Chazot et al., 2005) mostly during the Cretaceous (138-122 Ma, Féraud et al., 1996; Schärer et al., 1995; Schärer et al., 2000; Beard et al., 2002), i. e. they are contemporaneous of the last extensional phases on the WIM and appear to be marking the transition from continental rifting to seafloor spreading. The products from this metasomatic event did not have enough time to evolve the radiogenic Pb signatures observed in the studied samples, as can be confirmed by the unradiogenic Pb isotope ratios of the gabbroic pegmatitic intrusions in site 1070 of ODP leg 173 (Beard et al., 2002).

An earlier phase of magmatism that might have affected the lithospheric mantle of the WIM is recorded in the exposed lithospheric section exposed in the ridges, but it is thought to correspond to underplating under the lower crust during a late Variscan

extensional phase at≈ 270 Ma (Whitmarsh and Wallace, 2001). However, both these metasomatic phases do not show the trace element and isotopic enriched characteristics that characterize the source of the Late Cretaceous alkaline magmas.

From the discussion above, a significant contribution of an ancient lithospheric component in the source of the alkaline rocks from the WIM can be discarded, although it is possible that there is an input from the subcontinental lithosphere that has been recently metasomatized by enriched sublithospheric melts, as seems to be indicated by the presence of residual amphibole and of a carbonatite metasomatic signature (see section 7.4.1).

7.5.2 Pb isotopic signatures in seamounts and the effects of seawater alteration and crustal contamination

Merle et al. (2006) proposed an asthenospheric source with an OIB like composition to justify the composition of the seamounts of the northern part of the MTR (Madeira-Tore Rise) and also identified a lithospheric source component enriched in $^{207}Pb/^{204}Pb$. In this study, as in Grange et al. (2010), Pb isotopic data was acquired on plagioclase and feldspar separates, which in the case of Merle et al. (2006), are assumed not to contain any initial U and to therefore reflect the initial Pb isotopic composition of the melt. This assumption might not be accurate in the case of the onshore samples due to the hydrothermal alteration event discussed above, and also in the case of the samples from the MTR due to the important seawater alteration.

Seawater alteration might remove common magmatic lead (Michard and Albaréde, 1985; Hauff et al., 2000) while simultaneously introducing some Pb from seawater (You et al., 1996) in the feldspars and plagioclases. If this alteration process occurs at relatively high temperatures (i.e. shortly after extrusion), it can be responsible for the partial albitization of the feldspars. The albitic structures can take up more secondary U and Pb (Housh and Bowring, 1991; You et al., 1996) and therefore contribute to a higher time integrated Pb isotopic signature, especially if no age correction is applied. Otherwise, radiogenic Pb can accumulate in cracks and grain boundaries (Ludwig and Silver, 1977; Housh and Bowring, 1991) or be present in oxide, sulphide or other high U/Pb mineral inclusions in the feldspars (Ludwig and Silver, 1977; Housh and Bowring, 1991; Bryce and DePaolo, 2004). Although the

excess Pb in crystal cracks and boundaries might be easily removed during leaching, if there is an important albitic component or inclusions of high U/Pb minerals in these plagioclase and feldspars, there might be an important excess Pb component that Merle et al. (2006) did not consider.

The suggestion that at least part of the anomalous Pb ratios in MTR samples are the result of alteration processes is reinforced by the observation that for the same seamount (Teresa, in Geldmacher et al., 2006 and Gago Coutinho, in Merle et al., 2006) $^{207}Pb/^{204}Pb$ values are substantially different, being lower in the leached whole rock data set ($^{207}Pb/^{204}Pb$ 15.589-15.594, Geldmacher et al., 2006) and showing higher values in the dataset based on feldspar and plagioclase separates ($^{207}Pb/^{204}Pb$ 15.661, Merle et al., 2006).

Nevertheless, it must be mentioned that the simple addition of radiogenic Pb from seawater will not produce the observed anomalous radiogenic Pb isotopic signatures in the feldspars from the MTR, since North Atlantic seawater isotopic signature tends to show lower $^{206}Pb/^{204}Pb$ and $^{208}Pb/^{204}Pb$ for the higher $^{207}Pb/^{204}Pb$ values (fig. 7.39, von Blackenburg et al., 1996; O'Nions et al., 1998; Abouchami et al., 1999), while these rocks can show simultaneously high $^{206}Pb/^{204}Pb$, $^{207}Pb/^{204}Pb$ and $^{208}Pb/^{204}Pb$.

In the oxidizing environments that characterize seawater alteration, U is present as uranyl (UO^{2+}) cations which form compounds that are highly soluble in seawater and can be introduced in igneous rocks via secondary phases during low temperature alteration (MacDougall et al., 1979, Michard and Albaréde, 1985; Chen et al., 1986; Hauf et al., 2000; Wheat et al., 2002). This can lead to increases up to 500% in the U/Pb ratios of crystalline basaltic material (Verma, 1991) and consequentially to higher $^{206}Pb/^{204}Pb$ and $^{207}Pb/^{204}Pb$ with time due to radiogenic ingrowth. Such an effect has been observed in other altered, Mesozoic submarine igneous rocks, including altered gabbros in the Iberian Abyssal plain (Seifert et al., 1997), basalts recovered in Hawaiian ODPs (Nobre Silva et al., 2009), the oceanic crust near the Canaries islands (Hoernle, 1998), and the oceanic lithosphere of the Caribbean Igneous Province (e.g. Hauff et al., 2000).

Pb is more susceptible than other elements to show increases in isotopic ratios after hydrothermal alteration due to changes in the U and Pb concentrations introduced during such events. Given the relatively shorter half lives of U isotopes when compared to other isotopic systems (e.g. $^{235}U \rightarrow t^{1/2} = 0.71 \times 10^9$ yr, $^{238}U \rightarrow t^{1/2} = 4.47 \times 10^9$ yr,

$^{232}Th \rightarrow t^{1/2} = 14 \times 10^9$ yr, $^{147}Sm \rightarrow t^{1/2} = 1.06 \times 10^{10}$ yr, $^{87}Rb \rightarrow t^{1/2} = 48.8 \times 10^9$ yr, Faure, 1986), for relatively high U/Pb, isotopic Pb ratios can become more radiogenic in relatively short time spans, as it has been recognized by Hauff et al. (2000) that associated high $^{207}Pb/^{204}Pb$ and scattered Th/U to the effects of hydrothermal alteration. So the higher $^{207}Pb/^{204}Pb$ and sometimes $^{208}Pb/^{204}Pb$ in some altered samples can be caused by a complex, open system alteration mechanism involving Pb removal, and U and radiogenic Pb remobilization from/by seawater. Meanwhile, Th has very low concentrations in seawater (≤ 0.00064 ppb, Langmuir and Herman, 1980) and is not easily removed during seawater alteration (Chen et al., 1986), so it is basically immobile and its concentration tends to increase in relation to Pb during alteration, due to Pb removal. This will result in different increases in the Pb isotopic ratios due to the effects of radiogenic ingrowth of rocks that have seen their U/Pb, Th/Pb and U/Th ratios modified by seawater alteration processes.

However, the extremely high $^{207}Pb/^{204}Pb$ in some of the samples from the MTR cannot be easily reconciled with simple time integrated decay of a "source" with a high U/Pb ratio resulting from seawater alteration. Since ^{235}U has such a short half life, it is present in very small amounts in the present day, and also was present in small amounts at the time of formation of these rocks. As a result high $^{207}Pb/^{204}Pb$ values usually indicate the presence of a very old, generally Proterozoic/Archean component with high time integrated U/Pb. Since the lithosphere in the region does not seem to incorporate ancient metasomatic veins with such age or composition (Beard et al., 2002; Chazot et al., 2005), this component could be inherited from contamination of the evolved MTR magmas by terrigenous upper crustal sediment.

Upper crustal rocks show high U/Pb ratios due to growth in volcanic arcs, where high U/Pb magmas were generated during the Archaean (e.g. Mata et al., 2007) and U addition during granulite facies metamorphism of the lower crust which removes U and adds it to its upper part (e.g. Rudnick and Goldstein, 1990). These rocks can be eroded and the resulting sediments that inherit their radiogenic Pb isotopic signatures (average of 18.93, 15.71 and 39.03 for $^{206}Pb/^{204}Pb$, $^{207}Pb/^{204}Pb$ and $^{208}Pb/^{204}Pb$ ratios, respectively, Millot et al., 2004) that will eventually end up being deposited as turbidites at high depths in the oceans, retaining the same upper crustal isotopic signatures (average $^{206}Pb/^{204}Pb$, $^{207}Pb/^{204}Pb$, and $^{208}Pb/^{204}Pb$ of 19.22, 15.78, and 39.58, respectively, Hemming and McLennan, 2001).

Since the magmas with "lithospheric" isotopic signatures in the MTR are of intermediate to acidic nature (Merle et al., 2006), it is reasonable to assume that they experienced some low pressure fractionation in relatively shallow magma chambers. Those magma chambers can be located in the interface between the ocean floor and a layer of terrigenous turbidites on top of which the seamounts built. Such a site corresponds to an important density and rigidity contrast between distinct layers, which can facilitate the stagnation of magma and the formation of planar intrusive bodies where magma can accumulate and evolve (e.g Kavanagh et al., 2005). Intrusions in Cretaceous sediments near the Tore seamount can be observed in the seismic reflection profiles done in the area (C. Roque, pers. comm. 2010) and turbiditic sediments were identified in hole 1070A of ODP Leg 173 (Whitmarsh et al., 1998), at approximately the same longitude as the Tore seamount, so it is possible that such a detritic layer is present along the remainder of the MTR and had an important role on controlling the location of the magma chambers that fed those seamounts.

If so, magmatic evolution by crystal fractionation at the MTR is likely to have been accompanied by some degree of assimilation of these sedimentary lithologies resulting from AFC processes, which might have been responsible for the observed increase in $^{207}Pb/^{204}Pb$. This is supported by the detection of old radiogenic Pb in the zircons present in these rocks (Merle et al., 2006). The relatively unchanged Sr and Hf isotopic ratios can be justified by the higher contents of these elements in the magmatic rocks relative to the sediments, which make contamination only evident after the assimilation or high amounts of contaminant. Cases of assimilation of continental sediment in oceanic environments have been previous documented in the Canaries (Thirlwall et al., 1997; Hoernle et al., 1998; Hansteen and Troll, 2003)

The modification of U/Pb and Th/Pb ratios by hydrothermal alteration can also be the cause of incorrect age corrections when calculating the initial Pb isotopic ratios in these rocks. This leads to over or undercorrections which will not reflect the initial isotopic signatures of these rocks and of the source they originated from. This might be behind the atypical Pb isotopic signatures of the Fontanelas seamount, which will be discussed below.

As it can be observed in fig. 7.45, U seems to have been mobile in the Fontanelas seamount as well as in the Loulé lamprophyres. The mobility of Pb is harder to assess since this element was only analyzed in the aliquots of the samples, some of which were leached. U-Th-Pb can be fractionated during leaching, resulting on an

artificial increase of certain parent daughter ratios, which will in their their turn lead to overestimating the amount of radioactive decay that has taken place since magma extraction and cooling (e.g. Hauff et al., 2000). However, given that the age corrected samples from Monchique from this work plot mostly within the compositional range defined by the age corrected samples from Bernard-Griffiths et al (1997), we can infer that the age correction has not been greatly overestimated for the samples collected onshore.

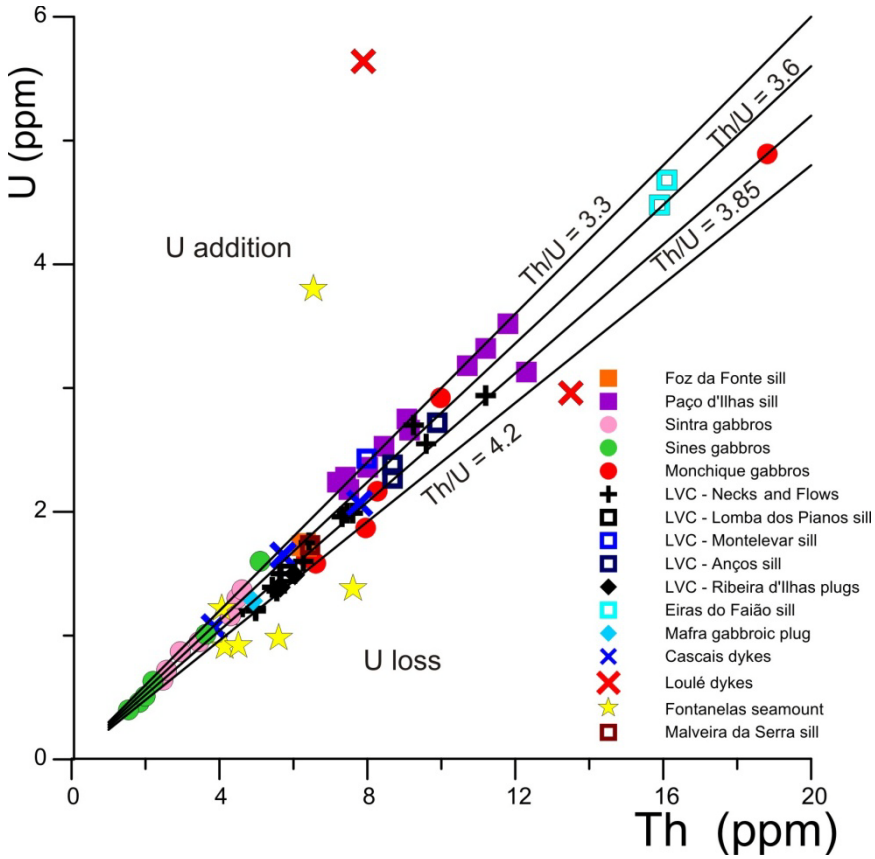

Fig. 7.45: Plot of Th vs. U for the analyzed samples. Samples that plot out of the trends defined by constant Th/U have been affected by either U loss or addition.

The more enriched isotopic signature of the Fontanelas seamount can nearly be reproduced by the radioactive decay of a basaltic rock with an age corrected isotopic signature similar to one of the basalts from the LVC (RM 43) but with much higher U/Pb, Th/Pb and Th/U, and consequentially higher $^{238}U/^{204}Pb$ and $^{232}Th/^{204}Pb$, which will lead to significantly more enriched $^{206}Pb/^{204}Pb$ and $^{208}Pb/^{204}Pb$ by radioactive decay in time. These elementar ratios might have been modified during alteration and leaching and therefore invalidate the application of the accurate age correction in these samples. Nevertheless, the $^{207}Pb/^{204}Pb$ values obtained for the Fontanelas seamount in both in the

measured and corrected ratios cannot be justified exclusively by alteration or improper age corrections so it should reflect a primary feature of the source of these rocks.

7.5.3 Nature of the sublithospheric mantle source

From the discussion above we can conclude that the isotopic composition of the uncontaminated Late Cretaceous alkaline magmas of the WIM shows characteristics that are compatible with a sublithospheric source.

These rocks have higher Sr and Pb isotope ratios but less radiogenic Nd than the DMM (average DMM: $^{87}Sr/^{86}Sr$ 0.70263, $^{143}Nd/^{144}Nd$ 0.51313, $^{206}Pb/^{204}Pb$ 18.275, $^{207}Pb/^{204}Pb$ 15.486, Workman and Hart, 2005), which is thought to represent most of the depleted asthenospheric upper mantle. They also have lower $^{87}Sr/^{86}Sr$ and higher $^{143}Nd/^{144}Nd$ than the EM 1 and 2 components (e.g. Hart et al., 1992) and lead isotopic compositions are considerably less radiogenic and lower than the ones that characterize the HIMU component (Hart et al., 1992; Hauri et al., 1994; Stracke et al., 2005).

The source thus seems to show an intermediate composition between DMM and HIMU, having lower time integrated Sm/Nd but higher Rb/Sr, U/Pb and Th/U than DMM while still having lower time integrated U/Pb and Th/U than HIMU as well as slightly higher Rb/Sr than this last component.

Such a composition is at least partially within the range defined for several other mantle components, such as the C component (Hanan and Graham, 1996), FOZO (Hart et al., 1992; Hauri et al., 1994; Stracke et al., 2005), PREMA (Zindler and Hart, 1986; Wörner et al., 1986), LVC (Hoernle et al., 1995), CMR (Lustrino and Wilson, 2007), PHEM (Farley et al., 1992). These components have been detected in OIB and intraplate continental magmatic events all over the globe and are thought to represent mixing between EM, HIMU and DMM components within the mantle (PREMA, Zindler and Hart, 1986), lower mantle material present as a mixing component in all deep mantle plumes (PREMA, FOZO and PHEM, Zindler and Hart, 1986, Hart et al., 1992, Farley et al., 1992), lower mantle containing recycled oceanic crust (C, Hanan and Graham, 1996 or FOZO, Stracke et al., 2005), enriched upwelling asthenosphere (LVC, Hoernle et al., 1995), or the local asthenospheric mantle that has been enriched by subduction or delamination processes during the Hercynian or Alpine orogenies (CMR, Lustrino and Wilson, 2007).

FOZO was at first defined from the observation of a FOcal ZOne (hence the acronym FOZO) where the compositional arrays of mantle plumes (represented by OIBs) and the depleted mantle (represented by MORBs) converge in Sr-Nd-Pb isotopic space (Hart et al., 1992; Stracke et al., 2005). This component is likely to have acquired its isotopic signature from the recycling oceanic crust to the lower mantle (Stracke et al., 2005) and is the mantle component that shows a better agreement with the observed isotopic signatures of the source of the Late Cretaceous alkaline rocks of the WIM.

Although many authors consider FOZO an idependent mantle component (e.g. Hart et al., 1992; Stracke et al., 2005), it is possible to produce an equivalent type of isotopic signature that characterizes it from the mixing and dilution of HIMU with the remaining DMM and EM components (e.g. Hoernle et al., 1991; Widom et al., 1999). A clear way of making a distinction between these two hypotheses is through the analysis of noble gas and Os isotope data since FOZO possess distinctively high $^{3}He/^{4}He$ ratios ($R/R_A \approx 45$, Ballentine et al., 2002) while HIMU shows much lower $^{3}He/^{4}He$ ($R/R_A \approx 5$, Ballentine et al., 2002). FOZO is also thought to possess unradiogenic Os signatures ($^{187}Os/^{188}Os \approx 0.128$), while HIMU presents very radiogenic Os ($^{187}Os/^{188}Os \approx 0.150$) due to its recycled nature (e.g. Hauri, 2002; Class and Goldstein, 2005).

Additionally, Piromallo et al. (2008) suggested that the widespread and relatively constant isotopic signature of Cretaceous to Quaternary magmas in the Euro-Mediterranean area, which motivated the proposal of common sublithospheric mantle reservoirs (such as the previously mentioned LVC and CMR), is the result of a large scale mantle contamination episode by the Central Atlantic Plume (CAP) that took place in the Late Cretaceous, when the CAP plume was channeled through thinned western European lithosphere. The CAP plume should presently correspond to the mantle upwelling that feeds the Canaries and Cape Verde mantle plumes (Piromallo et al., 2008).

Therefore, the geochemical data presented in this study, in accordance with what had been previously suggested for this area by Palácios (1985), Martins (1991), Bernard-Griffiths et al. (1997), Merle et al. (2006), Lustrino and Wilson (2007), Piromallo et al. (2008), and Grange et al. (2010), indicate that the source for the Late Cretaceous alkaline magmas of the WIM seems to be primarily of sublithospheric origin and to be sampling a mantle composition similar to that of the FOZO component or to a mix between HIMU, DMM and EM components.

As the sublithospheric mantle in question does not correspond to the DMM type mantle that is sampled in Mid Ocean Ridges but seems to show a FOZO like signature, it should therefore reflect a more enriched, plume like contribution. The contribution of a plume like feature for this magmatism had been previously proposed for Monchique, by Geldmacher and Hoernle (2000) who interpreted it as the result of the first pulse of activity of the Madeira plume. In the case of the Madeira-Tore rise, the Cretaceous to present magmatic activity has been attributed to the action of a large scale thermal anomaly in the Canaries-Madeira-Portugal area (Hoernle et al., 1995; Merle et al., 2006, 2009) or to complex interactions between the Canaries and Madeira hotspots, the Cretaceous Mid Atlantic Ridge (MAR) and movement along the Azores-Gibraltar fault (Geldmacher et al., 2006).Grange et al. (2010) suggested the involvement of the same mantle plume proposed by Merle et al. (2006, 2009) to justify the onshore magmatism of the Paço d'Ilhas sill as well as the Sintra, Sines and Monchique igneous complexes.

As was noticed in section 7.2 (figs. 7.12 and 7.15), most of the uncontaminated samples presented in this study, as well as many of the samples from the Madeira-Tore Rise fall within the compositional field defined by samples from locations thought to have formed due to the activity of the Canaries mantle plume.

Though one may question the validity of the comparison of initial isotopic ratios of the studied Late Cretaceous alkaline rocks of the WIM (94 to 72 Ma) with the compositional range of the Canaries and Madeira plumes which are partially defined based on the composition of significantly younger rocks.

In order to address this question diagrams where the age corrected composition of the WIM alkaline rocks is plotted along with present day samples from the Canaries and Madeira plumes (7.46a, 7.47a,c), similar to the ones previously used throughout this study, are compared with diagrams where an age correction for 80 Ma (the average age of the studied WIM rocks) was applied (fig. 7.46b and 7.47b,d) both to the studied samples and to the rocks of the Madeira and Canaries plumes. Notice that such an age correction, when applied do Canaries and Madeira plumes, allows the estimation of the isotopic composition of the magmas produced by those hotspots at the time of generation of the WIM alkaline rocks.

These figures (fig. 7.46 and 7.47) clearly show the good agreement between the two types of diagrams with both supporting the isotopic similitude between the WIM alkaline magmas and those erupted from the Canaries.

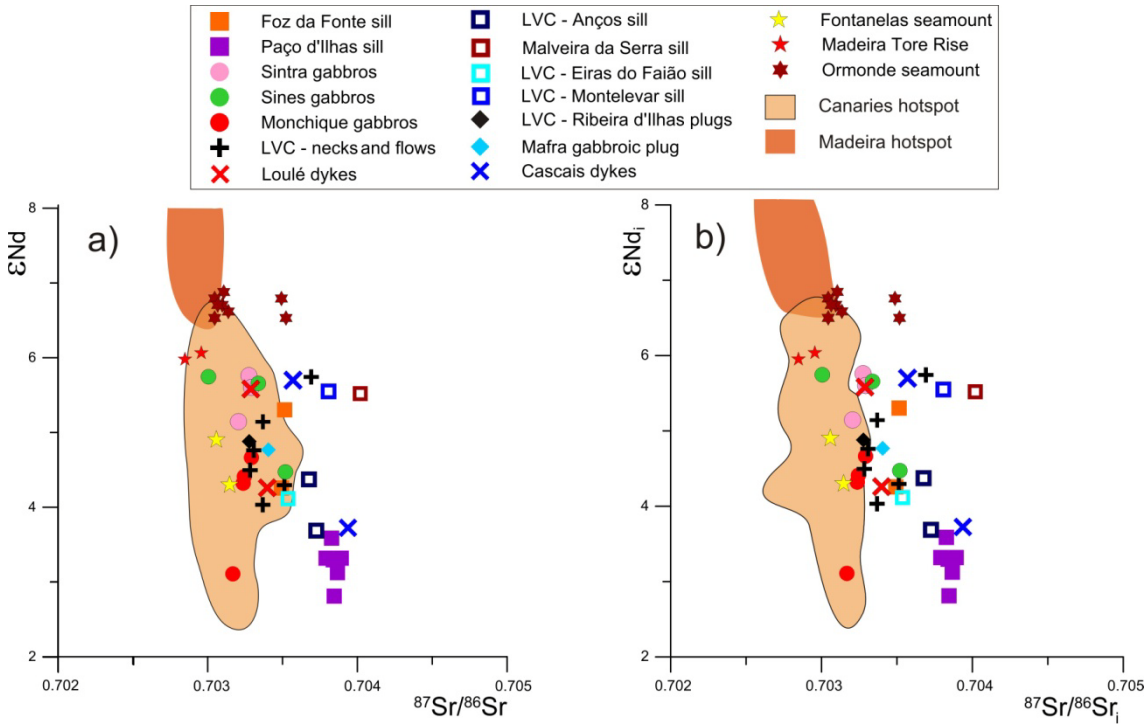

Fig. 7.46: Plots of the measured (a) and recalculated for and 80 Ma age (b) Sr and Nd isotopic compositions of the analyzed rocks and for samples from the Madeira and Canaries hotspots.

However, the Sr-Nd isotope diagram presenting recalculated compositions for 80 Ma of decay shows a significant number of samples that do not fit into the Canaries field due to somewhat more radiogenic Sr (fig. 7.46). This can be a consequence of the smaller amount of data points that include the necessary data to recalculate the isotopic compositions. Alternatively, these higher Sr and perhaps lower εNd can reflect small contributions from a lithospheric component that might correspond to the clinopyroxenites and websterites identified by Chazot et al. (2005) in the Iberian Abyssal Plain and represented in fig. 7.40. However this lithospheric contribution does not seem to affect the Pb isotopic system or the trace element contents.

Most of the samples from the MTR also plot on the same field, reinforcing the suggestion made by Geldmacher et al. (2006) that this feature might be related to the evolution of the Canaries hotspot.

It should also be noted that the samples from the Ormonde seamount and one of the samples from the MTR (Tore NW, Merle et al., 2006) and even the Fontanelas seamount seem to show compositions closer to the field defined by the samples from the Madeira hotspot (figs. 7.46 and 7.47). Given that these occurrences seem to be younger than the others near them (except for Fontanelas, whose age is still not known), it is possible that the Madeira hotspot also played a role in generating them, since this

hotspot occurs further north than the Canaries hotspot and the general direction of plate motion during the Late Cretaceous is towards the NE (e.g. Piromallo et al., 2008).

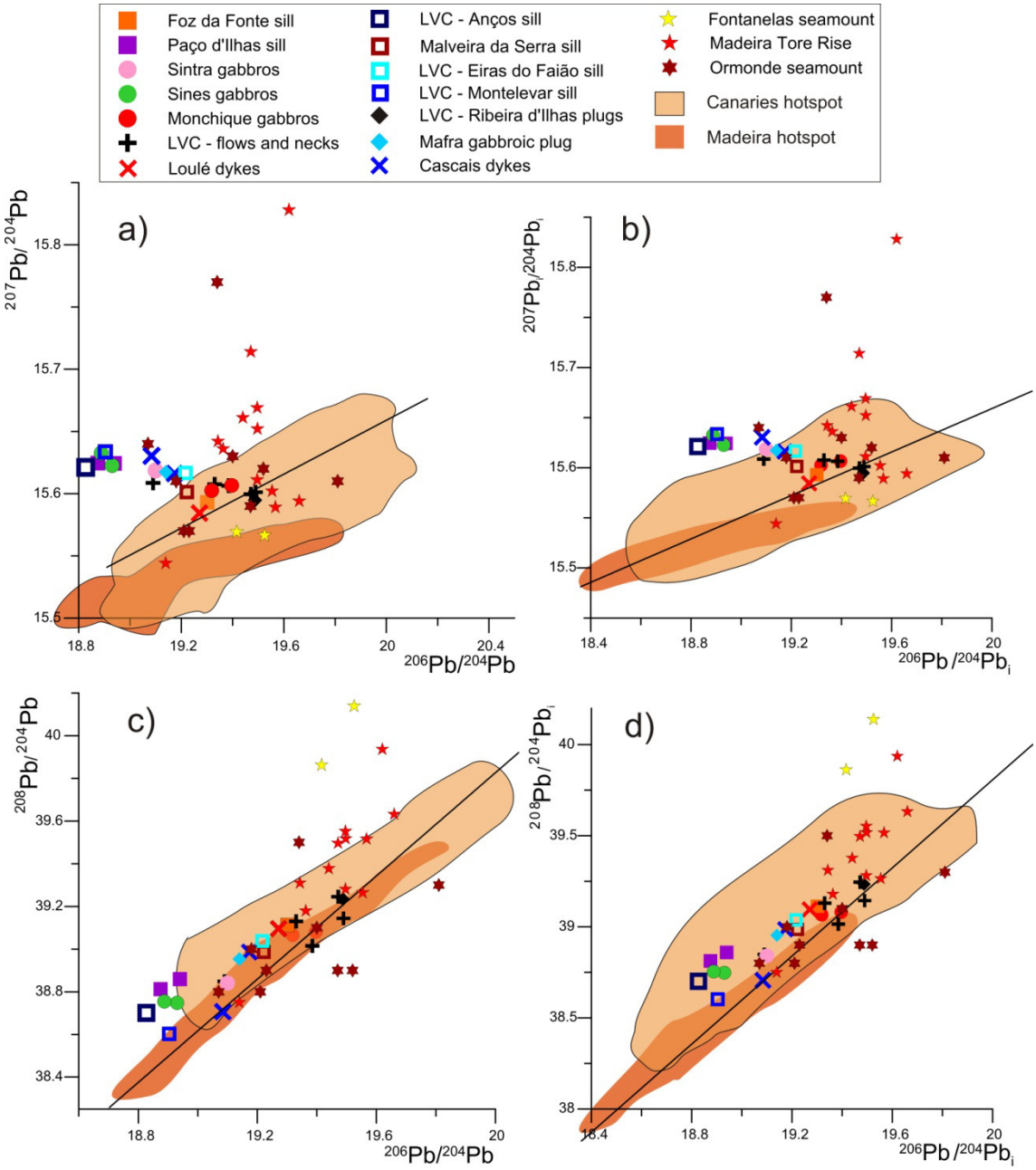

Fig. 7.47: Plots of the measured (a, c) and recalculated for and 80 Ma age (b, d) Pb isotopic compositions of the analyzed rocks and for samples from the Madeira and Canaries hotspots.

It therefore seems likely that the source that generated the Late Cretaceous Alkaline magmatism on the onshore and offshore WIM was related to the presence of a sublithospheric thermal anomaly that appears to correspond to the Canaries mantle

plume, which shows an overall composition close to the FOZO mantle component (e.g. Stracke et al., 2005).

Given that the Canaries mantle plume has been subject to numerous studies, the available data allow for the discrimination between FOZO and a mix of HIMU, DMM and the other mantle components in the source of the magmas of this mantle plume. HIMU has, however, consistently been the dominant plume component suggested in the literature (e.g. Hoernle et al., 1991; Thirlwall et al., 1997; Widom et al., 1999; Gurenko et al., 2006; Gurenko et al., 2009).

Helium isotope ratios ($^{3}He/^{4}He$ from 6.3 to 9.6 R_A; Hilton et al., 2000; Gurenko et al., 2006) are low, but can be interpreted as resulting from the contribution of an undegassed component, more consistent with the presence of diluted FOZO (Hilton et al., 2000). Alternatively, it could be the result of HIMU being diluted in a DMM component (Hilton et al., 2000). Hilton et al. (2000) favour the hypothesis where an undegassed component with high $^{3}He/^{4}He$ and radiogenic Pb (FOZO?) mixes with DMM which is degassed and has unradiogenic Pb, although this is still a controversial issue (e.g. Graham, 2002; Gurenko et al., 2006). FOZO has also been suggested to be the dominant mantle component in the Canaries mantle plume by Ignacio et al. (2006) based on the isotopic signature of carbonatites from Fuerteventura.

However, Os isotope systematics for the uncontaminated samples of the Canaries mantle plume ($^{187}Os/^{188}Os$ 0.139 – 0.151, Widom et al., 1999) support an important contribution of a radiogenic, recycled component variably mixed with shallow, depleted asthenospheric mantle, compatible with HIMU and not with FOZO (Widom et al., 1999).

Therefore, the dominant plume component in the Canaries mantle plume, and therefore in the Late Cretaceous alkaline rocks of the WIM, appears to be HIMU, which is thought to reflect the recycling of old Proterozoic (1.2 to 2.0 Ga) oceanic crust (e.g. Widom et al., 1999).

Nevertheless, the lack of a clear age progression for the alkaline magmatism of the WIM implies that the magmas had their ascension and location strongly conditioned by local stress fields, structure, and plate motions in the region during the Late Cretaceous.

The isotopic composition of the source remained relatively homogenous during the both pulses of alkaline magmatism, from 94 to 72 Ma. Nevertheless, differences in trace element composition between these two pulses point towards the presence of

residual amphibole in the source of some of the more primitive alkaline rocks from the second pulse of alkaline (75-72 Ma) activity in the WIM. This, along with other trace element characteristics of the same samples, agrees with the occurrence of metasomatism by a volatile rich (H_2O + CO_2) metasomatic agent in the source shortly before eruption. The metasomatic signature decreases with increasing degree of melting, meaning that there was not an exclusively metasomatic contribution for these magmas. The source for such a metasomatic agent might have been low degree melts from a carbonated peridotite in an ascending mantle plume or asthenospheric convection cell, as proposed in section 7.4.

Amphibole is not stable at temperature and pressure conditions that characterize the asthenosphere (e.g. Class and Goldstein, 1997) and is usually indicative of either melting of the lithospheric mantle or at least of equilibration of asthenospheric melts in the overlying metasomatized and amphibole bearing lithospheric mantle.

This metasomatism is particularly evident in the source of the ultramafic lamprophyres and must have occurred a comparatively short time before the melting event that generated them. This is because the isotopic compositions of the lamprophyres lie within the range for the other uncontaminated samples in the region (e.g. figs. 7.46 and 7.47), and thus show no evidence of the time-integrated incompatible element enrichment, resulting in more radiogenic Sr, Pb and depleted Nd signatures, that would be expected if the metasomatism was a much older event.

It is likely that the hydrous and carbonated metasomatic melts derived from the low degrees of melting from such plume quickly crystallized or were consumed during open system metasomatic processes at the base of the lithosphere during the first pulse of activity. Only the liquids resulting from higher volumes of melting from the same source, represented by the tephrites of the Foz da Fonte sill, reached the surface.

The thermal boundary layer (TBL) at the base of the lithosphere, was then metasomatized during the first pulse of alkaline magmatic activity. The metasomatized parts of this layer would have lower fusion temperatures due to their volatile rich nature and might have melted during the second pulse of activity, probably with the heat addition from other plume magmas. The melts from these metasomatic veins a contributed with their specific trace element signature to the resulting magmas. As the asthenospheric contribution increased and the metasomatized domains at the TBL were consumed during melting, the input metasomatic carbonatitic and the amphibole

signatures became more diluted and was progressively eliminated from the resulting magmas.

This mechanism accounts for both the constant isotopic signature and the differences in trace element composition observed in these pulses, whereas a different origin for both pulses would probably have to imply differences in the isotopic compositions of the lithospheric and asthenospheric components (e.g. Class and Goldstein, 1997; Class et al., 1998; Jung et al. 2006).

The heat source that melted the metasomatized lithosphere during the second pulse of alkaline activity could correspond to the Canaries plume, whose hotter center, was initially relatively far from the metasomatized domain, and might later have approached the zone of hydrated and enriched mantle lithosphere due to the motion of the Iberian plate above it.

Another hypothesis to justify the two different pulses is the involvement of the Madeira mantle plume during the second the second pulse of alkaline activity. As was discussed above, the presence of a younger (< 80 Ma, Merle et al., 2006) seamount in the Tore area with an isotopic signature close to the lavas from the Madeira hotspot (e.g. fig.7.44-45) raises the possibility for the presence of this plume near the WIM during the final stages of magmatic activity during the Late Cretaceous. The proximity of a second melting anomaly could have triggered the melting of the lithosphere that had been previously metasomatized by the action of melts from the earlier passage of the Canaries plume. However, the contribution of the Madeira mantle plume would be expected to be reflected on the isotopic composition of the melts derived from higher degrees of partial melting, which is not clear for the majority of samples from the second pulse (e.g. figs 7.46 and 7.47).

Alternatively, the identical isotopic signature in melts derived from a plume and with a metasomatic contribution could simply reflect the small degree melting and re-solidification at the leading edge of the starting head of a mantle plume, as was suggested by Kerr et al. (2010) for the signature of the sills that these authors identified as being the first representatives of the melting of the Réunion plume, in Pakistan.

7.6 Summary

The geochemical and isotopic study of the Late Cretaceous alkaline magmatism of the WIM allowed for the detailed characterization of these magmas, their evolution processes and mantle sources.

The ultrabasic to basic alkaline, trace element enriched melts seem to have originated from low degrees of partial melting (1-6%) of a trace element enriched source, located at depths equivalent to the garnet stability field (> 60 km). That source is likely to correspond to a sublithospheric, volatile rich (CO_2+H_2O) garnet lherzolite. The melts from the second pulse of Late Cretaceous alkaline activity also show some contribution from an amphibole bearing equivalent in the lithosphere. That same lithospheric lherzolite has been metasomatized by the first volatile rich (CO_2+H_2O) liquids derived from low degrees of melting from an ascending carbonated garnet lherzolite and therefore preserves most of its trace element and isotopic features. While such a metasomatic signature is only evident on the magmas from the second pulse of Late Cretaceous alkaline activity on the WIM, rocks from both pulses show similar isotopic signatures, meaning that the metasomatizing agent might have had the same source as the magmas from the first pulse.

That ascending carbonated lherzolite was probably a part of the Canaries mantle plume since the uncontaminated magmas from the WIM show isotopic compositions ($^{87}Sr/^{86}Sr_i$ 0.7030-0.7037; εNd_i 5.7 – 3.7; $^{206}Pb/^{204}Pb_i$ 19.564-19.20, $^{207}Pb/^{204}Pb_i$ 15.609-15.580, $^{208}Pb/^{204}Pb_i$ 39.245-39.00) similar to the rocks from the Canaries (see figs. 7.12, 7.15, 7.17 and 7.46-47), which is thought to represent the surface expression of a deep mantle reservoir related with the recycling of oceanic lithospheric material.

The relatively low Mg#, Ni and Cr contents of the Late Cretaceous alkaline magmas resulting from the partial melting of such sources went through early fractional crystallization events before ascending to the surface or upper crustal levels.

Trace element compositions indicate that at shallower depths, the ultrabasic to basic magmas evolved towards more silicic compositions by fractional crystallization of firstly olivine, clinopyroxene and Fe-Ti oxides, with amphibole and plagioclase gaining more importance in the more differentiated terms.

Most of the samples from the basic rocks in the igneous complexes of Sines and Sintra have their major and trace element compositions controlled by crystal accumulation processes. The recognition of the existence of such processes allowed the

identification of different levels of exposure on what probably corresponded to the same magmatic chamber in the different igneous complexes. In this case, the Pedras Negras gabbro in Sines and the Azoia gabbro in Sintra would correspond to deeper levels of the chambers, where more basic phases such as olivine and clinopyroxene precipitated, while the Praia Vasco da Gama and Peninha gabbros represent higher parts of the same intrusions, repectively, where more evolved liquid accumulated and precipitated mostly amphibole and plagioclase. A similar process had already been identified in the Paço d'Ilhas sill (Mahmoudi, 1991).

However, fractional crystallization had to be coupled with assimilation of crustal lithologies in order to explain the evolution of the isotopic and trace element signatures seen in these rocks. Two different AFC trends are observed, one that is observed mainly in basic sills and implies the assimilation of an Sr-rich yet, Nd and Pb poor, contaminant which is only reflected in changes towards more radiogenic Sr isotopic signatures ($^{87}Sr/^{86}Sr_i$ up to 0.7049 while εNd_i remains unchanged), and is likely to correspond to a carbonated lithology. The other AFC trend encompasses the majority of the more silica rich rocks and the contaminant involved should correspond to a lithology that is enriched in SiO_2, Th, K, $^{87}Sr/^{86}Sr$ (up to 0.70389) and $^{207}Pb/^{204}Pb$ (up to 15.6336 $^{207}Pb/^{204}Pb_i$), but depleted in La, Nb, $^{143}Nd/^{144}Nd$ (εNd_i down to 2.8), $^{206}Pb/^{204}Pb$ and $^{208}Pb/^{204}Pb$ (down to 18.8268 and 38.6027). These characteristics are typical of upper crustal rocks, but the exact nature of that upper crustal lithology remains unclear, although a siliciclastic sedimentary rock seems the more likely candidate.

Lead isotopic ratios in the gabbros from Sintra and Sines show values that are typical of contaminated rocks but these samples do not, however, share any of the other isotopic or trace element characteristics with the other contaminated rocks. This suggests that the unradiogenic $^{206}Pb/^{204}Pb$ and $^{208}Pb/^{204}Pb$ and radiogenic $^{207}Pb/^{204}Pb$ might have been acquired by these gabbros as the result of an hydrothermal metasomatic event that was also responsible for the crystallization of epidote, green amphibole, feldspar and carbonate in these rocks. The metasomatic fluid might have been relatively Pb rich in relation to the gabbros but comparatively Sr and Nd poor, which would justify the changes in the Pb isotopic signature but not in the Sr and Nd isotopic ratios. Given the similarity of the changes in Pb isotopic compositions between the gabbros and the upper crustal contaminant detected in the more evolved rocks, it is suggested that the fluid derived from the upper crustal country rocks that surround the

igneous complexes either by dehydration processes or simply from mobilization of interstitial pore solutions.

Magma mixing was inferred to have taken place at depth from petrographic and mineral chemistry data (see sections 6.1 and 6.2), yet it seems to have played a minor role in the evolution of the studied rocks. In fact, the modeling of mixing between the basic and intermediate end members postulated in section 6.2 failing to reproduce the observed major and trace element signatures.

8. Discussion and geodynamical implications

This section aims at establishing a connection between the geochronological, geochemical and mineral chemistry data presented and discussed in the previous sections of this manuscript and integrate them with information relative to the plate motion, the structure and tectonics of the region, in order to establish a coherent geodynamical model that explains the occurrence of the studied alkaline magmatic episode in the WIM during the Late Cretaceous.

8.1 The relationship between the alkaline magmatism in the WIM, hot mantle anomalies and plate kinematics

The alkaline magmatism that took place in the WIM during the Late Cretaceous is an important event in the history of the then recently formed passive margin. The volume of erupted material of the Madeira-Tore Rise (MTR) alone is calculated to be over 10^5 km^3 (Merle et al., 2009). The magmatism that took place between the Tore seamount and mainland Portugal and in the onshore WIM has to be added to the volume erupted in the MTR, as is also the case with the alkaline magmatism present in the other side of the Mid Atlantic Ridge (MAR), materialized by the Newfoundland seamounts. Together, these occurrences total an important volume of magmatism that spreads through three different plates (North America, Iberia/Europe and Africa) which cannot be easily reconciled with shallow magma generation mechanisms such as decompression melting along deep transfer faults or even with shallow edge driven convection, as proposed by Matton and Jébrák (2009), due to its scattered nature and the absence of cratonic lithosphere in the region.

Since the area affected by this magmatism was not undergoing contemporaneous extension, the existence of such a large volume of magma must then be related to the presence of one or several deeper, hotter and/or wetter mantle anomaly(ies) in the region during the Late Cretaceous.

Such melting anomalies are likely to originate in deeper, warmer parts of the mantle and correspond to mantle plumes as defined by Morgan (1971). Also, the isotopic signatures of the uncontaminated rocks in the region favor the hypothesis that they might have derived from relatively similar sources (e.g. Geldmacher et al., 2006; Merle et al., 2006; Grange et al., 2010; this study).

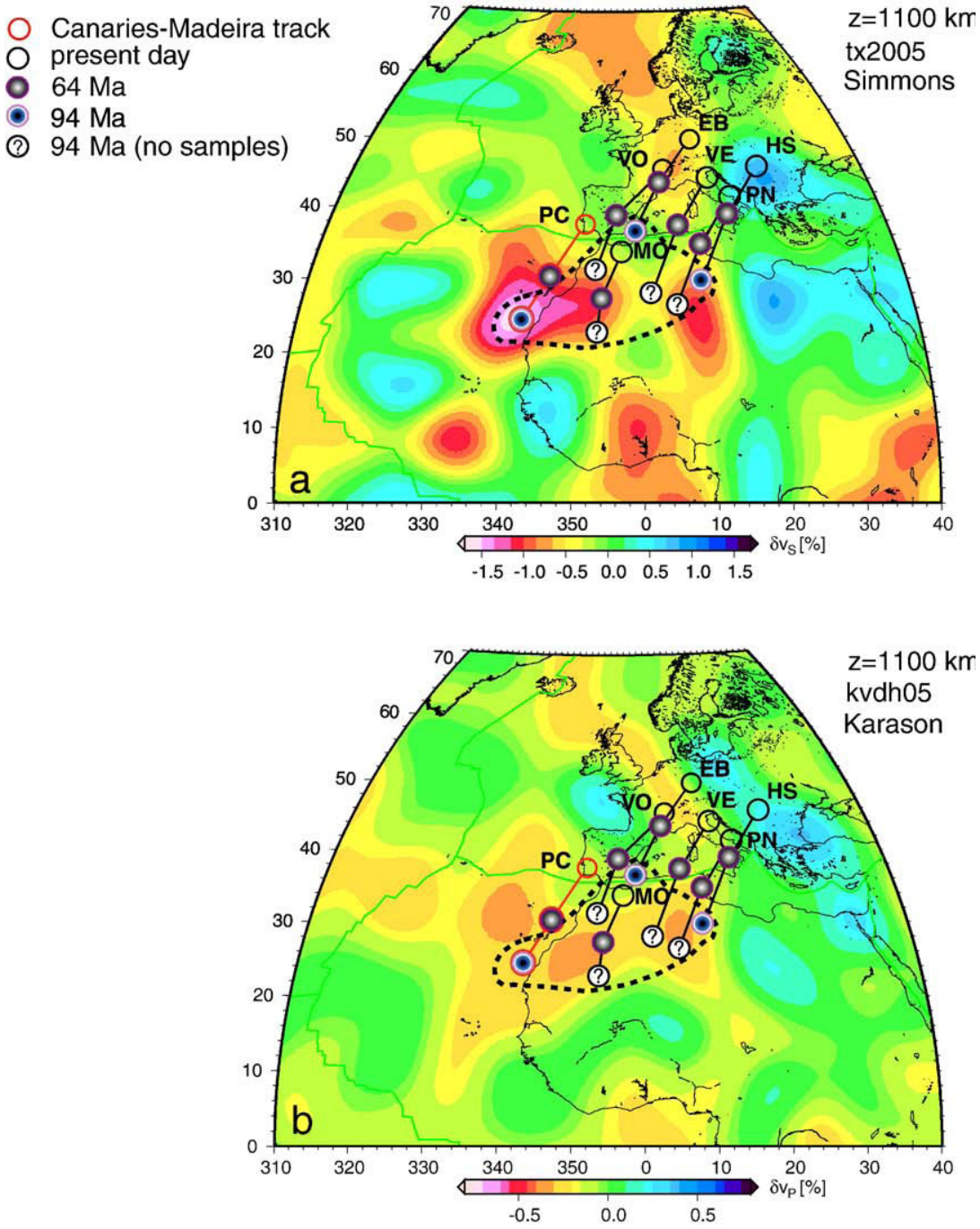

Fig. 8.1: Location of some alkaline European volcanic centers projected back in time (present day, 64 Ma and 94 Ma positions), according to absolute plate motion in Fig. 3 of Piromallo et al. (2008). Circles represent locations of some reference areas, rather than individual centers: Eifel–Bohemia (EB) and Vosges-Massif Central (VO), exhibiting long-lived and continuous activity; Portugal–Canaries (PC), Hungary–Serbia (HS), Veneto Volcanic Province (VE), Pietre Nere (PN) and Morocco (MO), circumscribing the region of older activity (N55–60 Ma). Portugal is plotted in red to acknowledge its relation to the Canaries–Madeira hotspot track (i.e. Geldmacher et al., 2005). The expected paleo-positions at 94 Ma of the remaining areas are therefore reported with a question mark. A dashed line bounds the region enclosing paleo-positions of centers which erupted oldest alkali products. Background map is given at 1100 km depth for two different global tomographic models: a) tx2005 (Simmons et al., 2006), b) Karason and van der Hilst (2001). Shear-wave (a) and P-wave (b) velocity anomalies exhibit consistent large-scale features at this depth in the lower mantle: low velocity anomalies encompassing north-western Africa and central-eastern Atlantic, in contrast to high velocity anomalies in Eastern Europe and Mediterranean and north-eastern Africa. As in Piromallo et al. (2008).

The passage of the Iberian/European plate over the regions of the mantle where the Madeira and Canaries plumes are located during the late Cretaceous has already been suggested to explain the presence of the abundant alkaline magmatism in the region. Morgan (1983) and Duncan (1984) suggested that Iberia had been positioned very near both the Madeira and Canaries plumes during the Late Cretaceous. The paleogeographical reconstitution made by Piromallo et al. (2008) also shows the Iberian region on top of the Canaries mantle plume at 94 Ma (fig. 8.1)

The Newfoundland seamounts (Duncan, 1984; Geldmacher et al., 2006), the alkaline rocks of the Ormonde peak in the Gorringe bank (Geldmacher et al., 2006), and the Monchique igneous complex (Geldmacher et al., 2000) have been attributed to the melting of Madeira plume material, while the Canaries plume has been associated with the magmatism of (at least) the southern half of the MTR (Geldmacher et al., 2006).

Other authors did not attribute this mantle anomaly to a specific plume, preferring to refer to a larger feature, such as a regional widespread mantle upwelling the Central Atlantic, resulting on a wide, long lived thermal anomaly from which smaller magmatic pulses develop (Merle et al., 2006, 2009; Grange et al., 2010). According to the authors, this feature has been generating magmatism in the Portugal-Madeira-Canaries-Azores area since the Cretaceous. Such an anomaly can correspond to the low velocity zones in the mantle identified in the mantle between the Canaries and Iberia by seismic tomography studies (e.g. Hoernle et al., 1995; Montelli, et al., 2004).

Paleomagnetic data collected on some of the onshore intrusions and compiled in table 8.1 also points towards magma cooling at paleolatitudes similar to the ones where the Madeira and Canaries plume heads (which can be up to 2000 km in diameter, e.g. Griffiths and Campbell, 1990; Campbell, 2007), are presently located (Madeira ≈ 32.6N; Canaries ≈ 27.5N), adding further strength to the relationship between these hotspots and the observed Late Cretaceous magmatism. Incidentally, these data are also compatible, within error, with magma generation taking place on smaller, hot mantle anomalies.

Additionally, the existence of uplift and erosion that is not associated with important tectonic shortening in the Lusitanian basin between the Nazaré and Arrábida faults (Proença da Cunha and Pena dos Reis, 1995; Rasmussen et al., 1998; Dinis et al., 2008), as well as thermal metamorphism and hydrothermal activity in the centre of Iberia (Casquet et al., 1992; Tritlla and Solé, 1999) pre-dating and during the onset of

the Late Cretaceous alkaline cycle support the hypothesis of the involvement of anomalously hot mantle in this event. Moreover, in the Sines region, the Late Cretaceous period of slope progradation is associated with regional tilting and thermal uplift in the central proximal part of the margin (38ºN), most likely in association with the contemporaneous alkaline magmatism (Alves et al., 2009).

Table 8.1: Compilation of paleomagnetic data for the Late Cretaceous alkaline magmatism of the WIM. *N* corresponds to the number of samples or the number of accepted sites, *D* is the magnetic declination, *I* the magnetic inclination α_{95} corresponds to the 95% confidence interval for *D* and *I* and *K* is the best-estimate of the precision parameter ***k*** for the observed distribution of site-mean Virtual Geomagnetic Poles. Paleo lat is the paleo latitude of acquisition of the Natural Remanent Magnetization, calculated using the geocentric axial dipole model where $\tan I = 2\tan \lambda$, where λ is the paleo latitude.

Study	**Occurrence**	**Published**						
		N	***D***	***I***	***Paleo lat***	**α_{95}**	***k***	**age**
Van der Voo (1969)	Sintra granite	25	359	42.5	24.6	5	34.5	80 Ma
Storetvedt et al. (1987)	Sintra granite	34	*358*	*27.3*	14.5	3.3	57	80 Ma
Storetvedt et al. (1987)	Sintra, Cabo da Roca complex	30	39.4	43.4	25.3	6.2	19	75 Ma
Van der Voo (1969)	Lisbon basalts	17	354	40.5	23.1	4.5	63.8	72 Ma
Van der Voo and Zijderveld (1971)	Lisbon basalts	33/34	352	40	22.8	3	70.4	72 Ma
Martón et al. (2004)	Ribeira d'Ilhas stock	5/7	343	40	22.8	4	367	72 Ma (?)
Ribeiro et al. (2010)	Sines	?	21.5	38.3	21.5	2.3	?	75 Ma
Ribeiro et al. (2010)	Sines	?	40.6	43	25	2.2	?	75 Ma
Storetvedt et al. (1987)	Sines	36	*41*	*41*	23.5	3.3	54	75 Ma
Van der Voo (1969)	Monchique Syenite	8	182	-37	20.6	6.5	73.6	72 Ma
Storetvedt et al. (1990)	Monchique Complex	27	181	-42	24.2	4.5	39.4	72 Ma
Gomes and Sant'Ovaia (2000)	Monchique syenite	26	190.6	-39.5	22.4	5.4	?	72 Ma
Storetvedt et al. (1990)	Salema intrusion	70	341	42	24.2	1.7	93.7	70-72Ma(?)

The distribution of alkaline magmatism within two different plates between 100 and 65 Ma is also suggestive of the presence of a mantle melting anomaly in the region. This anomaly was initially located in the American plate, generating the Newfoundland seamounts but from 95 Ma onwards seems to be located to the east of the MAR, under the WIM, where it is responsible for the formation of the MTR and the onshore WIM magmatism (fig. 8.2). The magmatism seems to progress further SW with time, which is in accordance with general plate motion towards the NE (e.g. Piromallo et al., 2008, fig. 8.1).

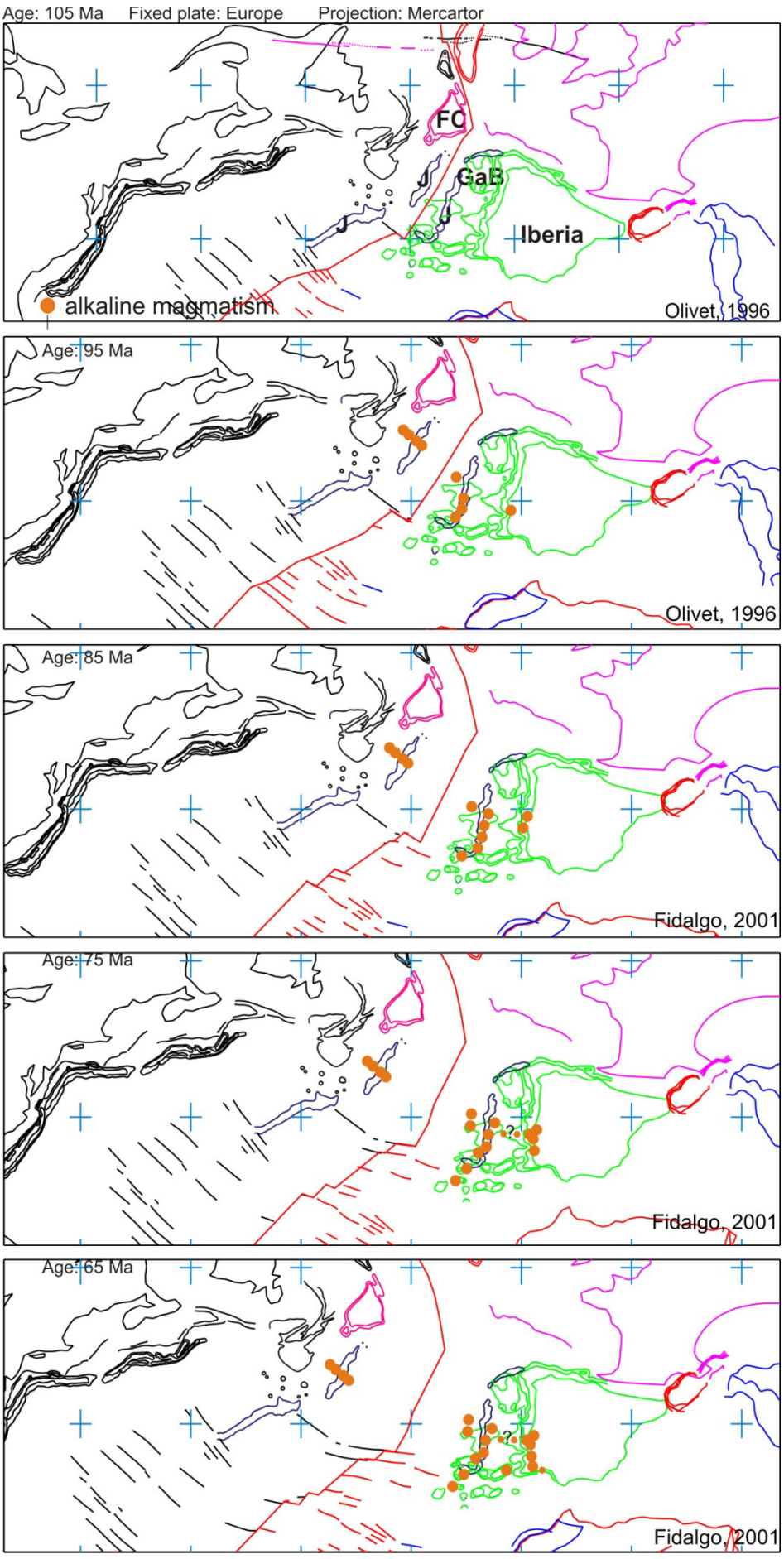
Age: 105 Ma
Fixed plate: Europe
Projection: Mercartor
FC
GaB
Iberia
alkaline magmatism
Olivet, 1996
Age: 95 Ma
Olivet, 1996
Age: 85 Ma
Fidalgo, 2001
Age: 75 Ma
Fidalgo, 2001
Age: 65 Ma
Fidalgo, 2001

Fig. 8.2: Paleogeographical reconstitution of the evolution northern Central Atlantic from 105 to 65 Ma in relation to a fixed Europe referential. Paleopoles from Olivet (1996) and Fidalgo (2001) as indicated in the figure. J – J magnetic anomaly, FC- Flemish Cap, GaB- Galicia Banks. Late Cretaceous alkaline magmatic occurrences in orange. Figure made by Maryline Moulin.

However, the lack of a clear age progression for the onshore and offshore magmatism and the similar ages obtained for the lower volume of alkaline magmatism intruding the opposite rifted and thinned margins of the Iberian plate (105-69 Ma in the Pyrenees, Basque-Cantabrian basin, Catalan ranges, and Galicia; Ancochea et al., 1992; Carracedo et al., 1999; Fabriès et al., 1998; Montigny et al., 1986, Solé et al., 2003) suggest a relationship between the Late Cretaceous magmatism and the changes in plate kinematics and seafloor spreading geometry contemporaneous with the opening of the Bay of Biscay, as well as a strong structural control on the position of the onshore magmatic occurrences, instead of a simpler model where magma generation takes place on a hot mantle plume located under the moving lithosphere.

Nevertheless, a model involving magma generation exclusively by decompression associated with plate kinematics and/or movement across lithospheric structures alone is not realistic, since these processes cannot generate the large volumes of magmas observed in the WIM. Also, the isotopic characteristics of these magmas point towards the contribution of a hot, deep sublithospheric mantle anomaly (see section 7.5.3). So it is therefore more likely that this magmatism is related to the presence of the Canaries hotspot in the mantle underneath region during the Late Cretaceous but that plate kinematics, the structure and tectonics of the WIM play a key role in controlling the timing, location and volume of some of these magmatic occurrences, as discussed on section 8.2.

8.2 The relationship between the structure of the WIM and the location of the alkaline magmatism

During the Late Cretaceous, magmatism was more abundant offshore than onshore, meaning that the less voluminous onshore magmatism must have had its location strongly controlled by local structure, horizontal plate kinematics and tectonic processes, whether it originated from a wide thermal anomaly such as a mantle plume or a more regional feature. The thicker continental lithosphere is also likely to have limited

adiabatic melting above an ascending mantle plume or convective cell, resulting in more reduced rates of magmatic productivity under continental Iberia, in relation to oceanic or ocean-continent transitional domains.

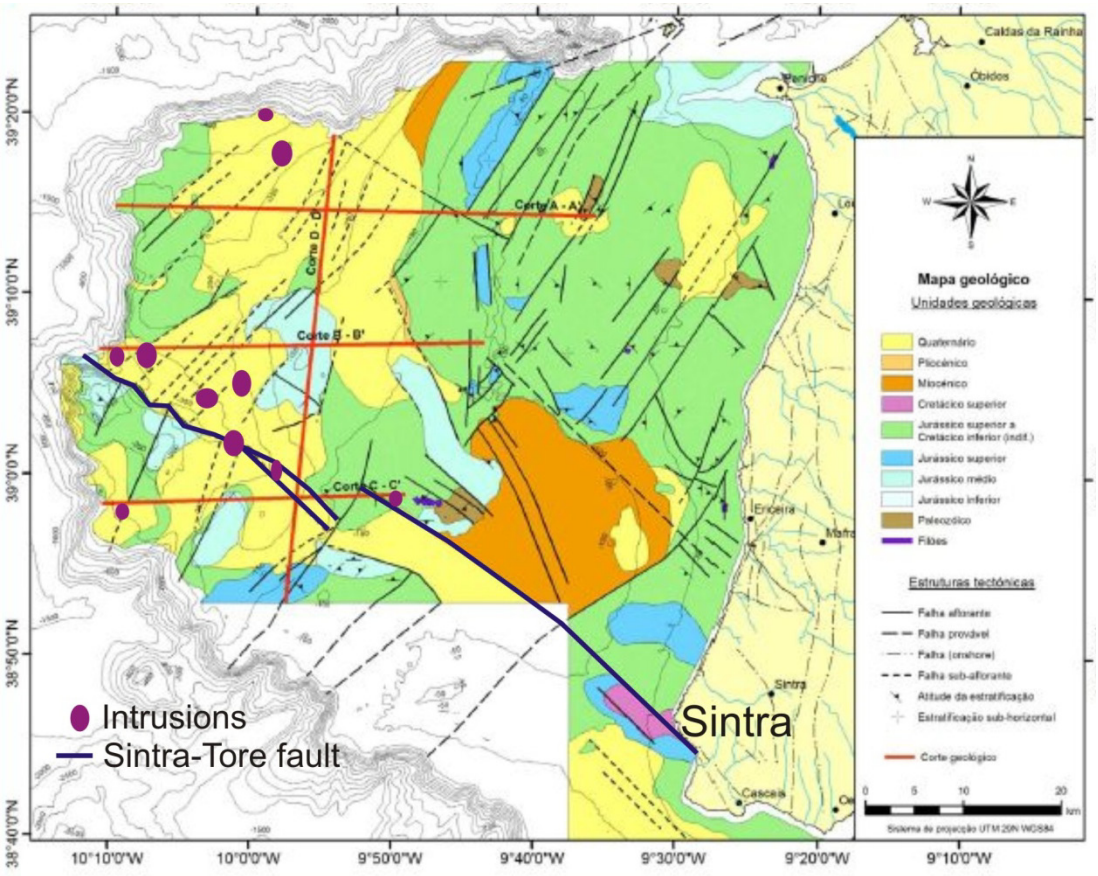

Fig. 8.3: Location of the Sintra-Tore fault and associated small intrusions in the continental shelf. Adapted from Badagola (2008).

One structure that played a major role in controlling the location of the Late Cretaceous alkaline magmatism seems to be the Sintra-Tore fault (Badagola, 2008; fig. 8.3). This structure connects the 88-80 Ma (Merle et al., 2006) Tore seamounts with the 80-75 Ma Sintra igneous complex (Storetvedt et al., 1987; Miranda et al., 2009) and corresponds to the superficial expression of a deep strike slip fault whose orientation varies between NW-SE, close to Sintra (fig. 8.3) but becomes WNW-ESE as it passes near the Fontanelas seamount and approaches the Tore seamount (fig. 8.4). Several magmatic features have been identified along its strike, including the Fontanelas seamount (fig. 8.4), as well as several small scale magmatic features identified by Badagola (2008) in the continental shelf between Sintra and Fontanelas (fig. 8.3).

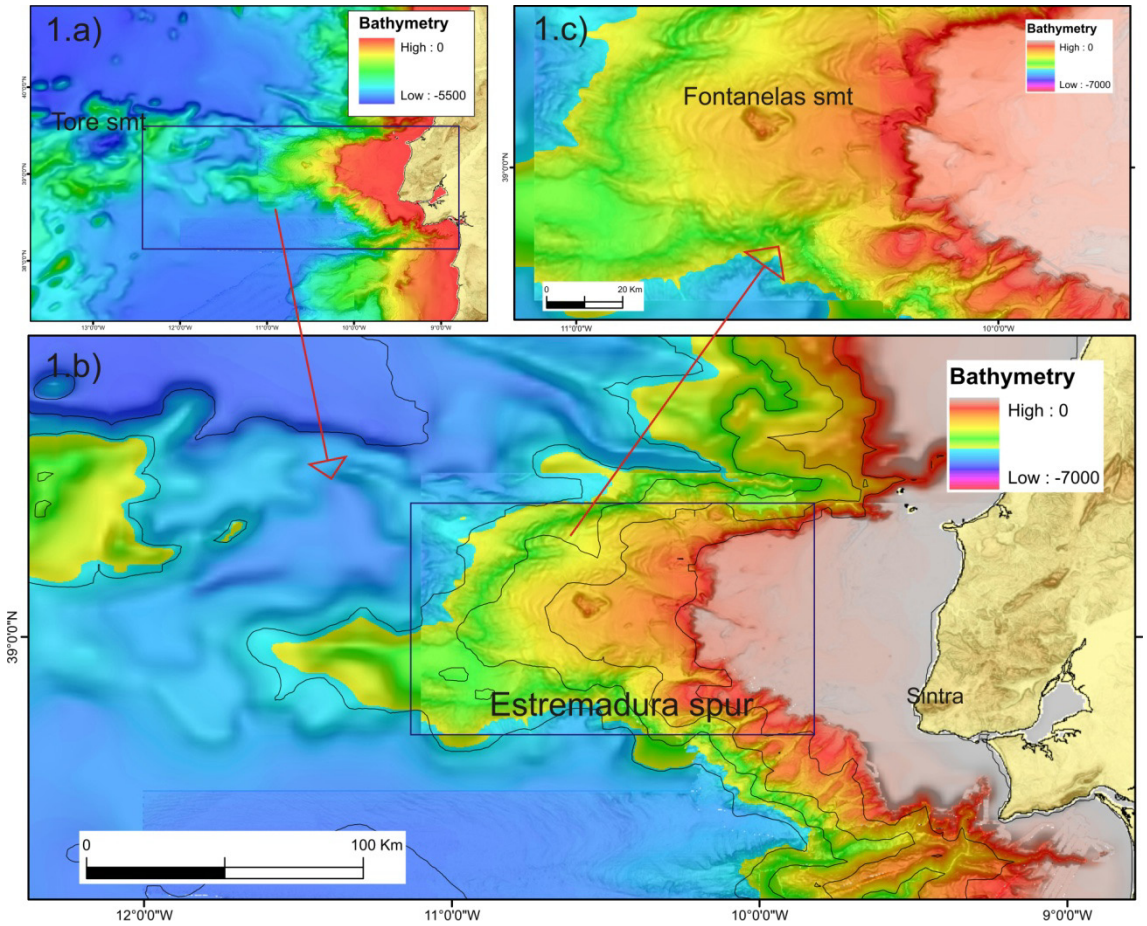
1.a)
Bathymetry
High : 0
Low : -5500
Tore smt
1.c)
Bathymetry
High : 0
Low : -7000
Fontanelas smt
0
20 Km
1.b)
Bathymetry
High : 0
Low : -7000
Estremadura spur
Sintra
0
100 Km
39°0'0"N
12°0'0"W
11°0'0"W
10°0'0"W
9°0'0"W

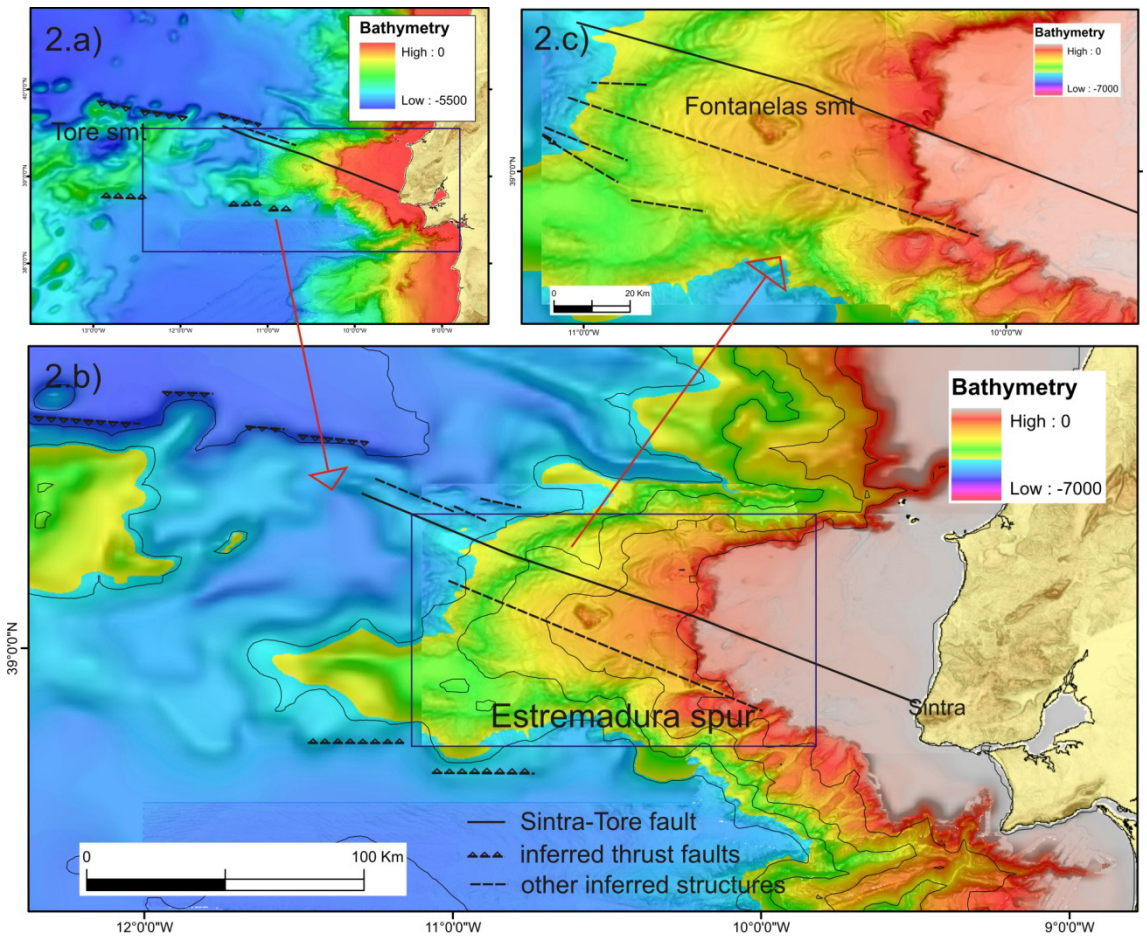
2.a)
Bathymetry
High : 0
Low : -5500
Tore smt
2.c)
Bathymetry
High : 0
Low : -7000
Fontanelas smt
0
20 Km
2.b)
Bathymetry
High : 0
Low : -7000
Estremadura spur
Sintra
Sintra-Tore fault
inferred thrust faults
other inferred structures
0
100 Km
39°0'0"N
12°0'0"W
11°0'0"W
10°0'0"W
9°0'0"W

Fig. 8.4: (1) Uninterpreted seafloor morphology of the area between the Estremadura spur and Tore seamount (a and b) and of the Fontanelas seamount (c). (2) structural interpretation of the same data. Bathymetric data from the GEBCO dataset (www.nbi.ac.uk), the SWIM compilation (Zitellini et al., 2009), the CANHOES (PDCTM/MAR/56781/2004) project. Most of the bathymetry for the Estremadura spur and the area around the Fontanelas Seamount is a courtesy ofthe EMEPC.

Several magnetic anomalies that also possibly correspond to igneous intrusions were identified further W of the Fontanelas seamount (e.g. Silva et al., 2000; fig. 2.2). They do not occur in close proximity of the Sintra- Tore fault, but can be related with other minor faults in the region with similar orientations (NW-SE to E-W, fig. 8.4)

Other important WNW-ESE to E-W trending structures were also identified between the Estremadura spur and the Tore seamount (Roque, 2009), with the present day morphology of the seamount being controlled by some of these features. These structures are mostly thrusts and backthrusts that deform sediments up to the Pliocene-Pleistocene (Roque, 2009) but have been active since at least the Cretaceous and are likely to have an even older origin, for instance, as rift related transfer faults (C. Roque, pers. comm., 2010).

The position of these important E-W structures also coincides with the proposed location for the offshore boundary between the Paleozoic terranes of the South Portuguese Zone and Ossa Morena Zone, which would correspond to the boundary between the Meguma and Avalon terranes in the conjugate Grand Banks margin (fig. 8.5, Capdevila and Mougenot, 1988; Lefort et al., 1996), which is materialized by another set of linear magnetic anomalies known as the Collector Anomaly (CA). Other geodynamic reconstitutions of the Variscan orogeny in Iberia do not necessarily agree with the model presented in fig. 8.5 (e.g. Ribeiro et al. 2007) but do not invalidate the hypothesis that is proposed in this section.

The Collector Anomaly (CA) is thought to represent the suture of the Theic ocean (e.g Lefort et al., 1996), but given its proximity with the Newfoundland seamounts and the recently recognized alkaline intrusions along the Sintra-Tore fault, it is possible that the positive magnetic anomalies in the Grand Banks margin can also correspond to Cretaceous alkaline intrusions. Such an inference is speculative since there does not seem to be a consensus over the general position of the CA (e.g. Jansa et al., 1993; Pe-Piper et al. 1994) and whether the CA was positioned further south during

the Cretaceous (e.g. Silva et al., 2000). Thus the location of the CA needs to be confirmed by detailed plate kinematics reconstructions and geomagnetism studies.

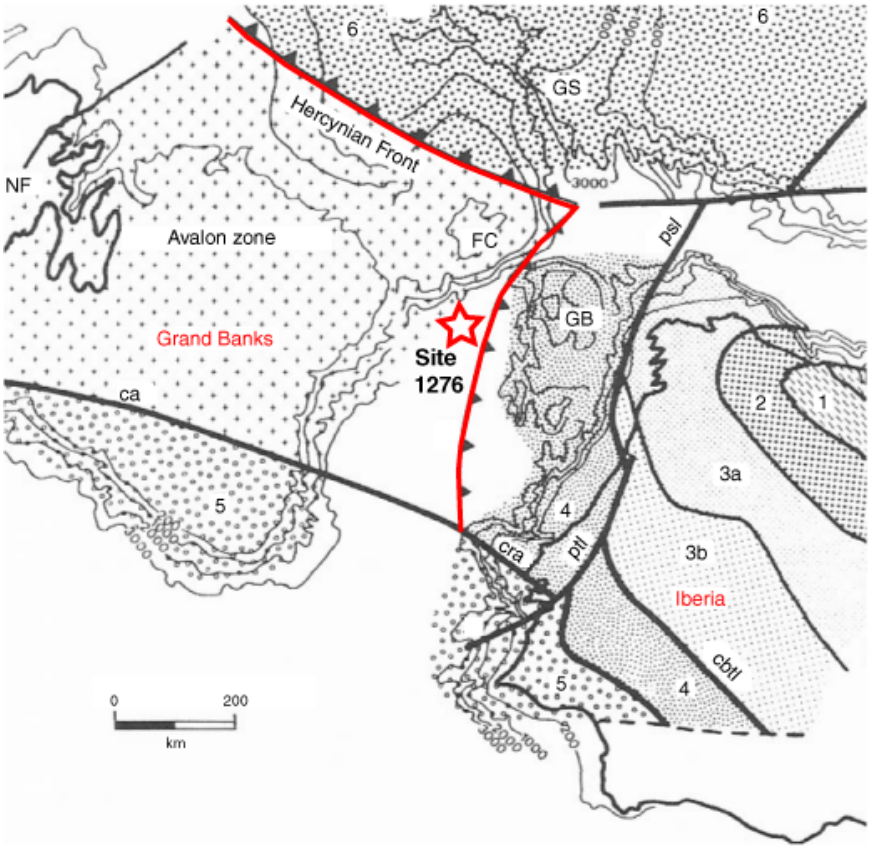

Fig. 8.5: Representation of the boundaries between different Paleozoic terranes in the Iberia-Newfoundland area before continental break-up. GB – Galicia Banks, FC – Flemish Cap, GS – Goban Spur, ca – Collector Anomaly, cra – Cabo da Roca anomaly, 1- Cantabrian Zone; 2 - West Asturian and Leonesian Zone; 3a - Galician and Castillan Subzone (Iberia) and South Armorican Zone (France); 3b - West Lusitanian and Alcudian Subzone (Iberia) and North and Central Armorican Zone (France); 3a + 3b - Central Iberian Zone (Iberia); 4 - Ossa-Morena Zone; 5 - South Portuguese Zone in Iberia and Meguma terrane in the Grand Banks; 6 – Rheno-Hercynian zone. Taken from Capdevila and Mougenot, in Boilot and Winterer (eds.), 1988.

Other features, such as the offset of the magnetic J anomaly in the Estremadura Spur region (e.g. figs. 1 and 2 in Sibuet et al., 2007; fig. 6 in Srivastava et al., 2000; fig. 1 in Withmarsh and Wallace, 2001) and the lack of peridotite ridges in the Tagus Abyssal plain in contrast with the Iberian Abyssal plain seem to indicate that the Sintra-Tore fault, as part of the Estremadura Spur, appears to be part of a very important structural boundary in the region that may have been crucial in facilitating the ascent and emplacement of the Late Cretaceous alkaline magmas in the WIM.

The recognition of the Sintra-Tore fault as an important structure of the WIM raises the question of whether other structures of the same type, or at least with the same orientation, are associated with the Late Cretaceous alkaline magmatism. For instance, the geometry of the feeders of the Sintra intrusion, deduced from AMS and gravimetric data, also point towards the existence of E-W conduits, along with others with NE-SW and NW-SE directions (Terrinha et al., 2003; Kullberg et al., 2006, 2010).

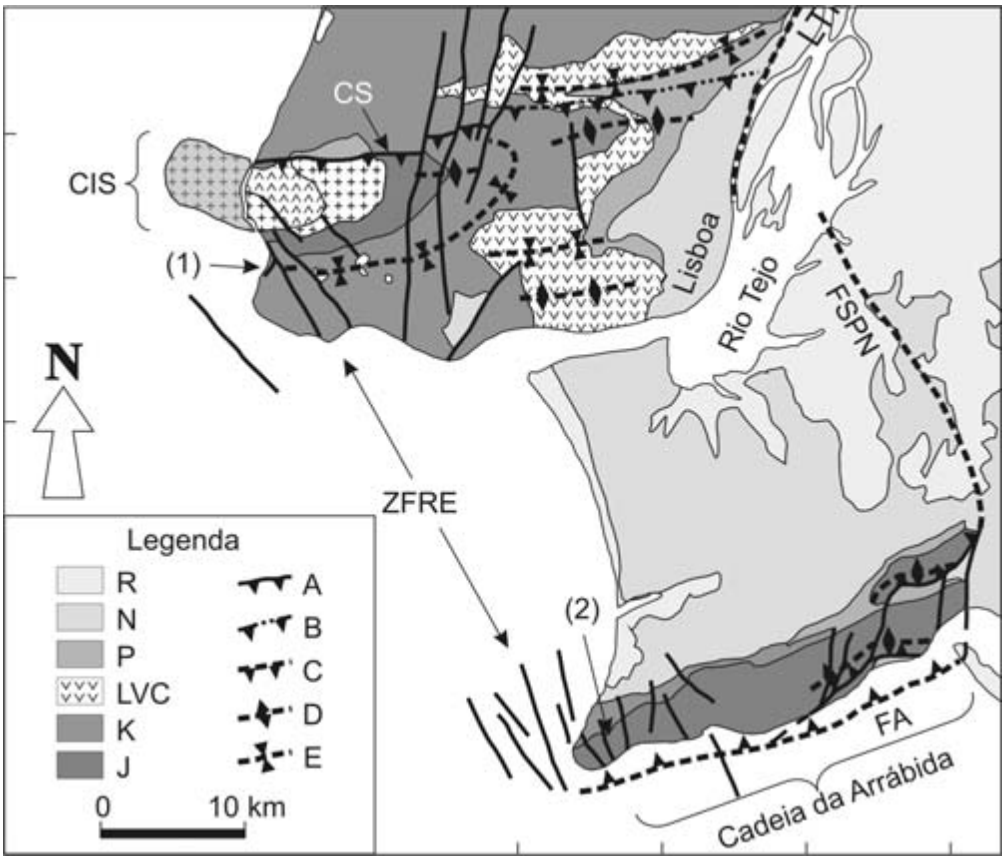

Fig. 8.6: Locationof the main structures in the Sintra-Arrábida region. J- Jurassic, K- Cretaceous, LVC – Lisbon Volcanic Complex, P – Paleogene, N – Neogene, R – recent sediments, A- Thrust, B – Blind thrust, C – inferred thrust, D – anticline, E – sincline (1) and (2) Jurassic syn-sedimentary normal faults, CIS – Sintra Igneous Complex, FA- Arrábida Fault, CS – Sintra thrust, ZFRE Cabo da Roca – Espichel fault zone. From Kullberg et al., 2006.

Also, the Sintra igneous complex, in addition to being located on the Sintra-Tore fault, is affected by a late thrust with an approximately E-W direction and is located at the intersection of these structures with other faults trending NW-SE to N-S (figs. 8.5 and 8.6). It is possible that this thrust acted earlier as a transfer or normal fault and later as a conduit for magma ascent before basin inversion took place and reactivated with the presently observed kinematic (Kullberg et al., 2006, 2010). This structure is thought

to continue towards the East, between Sintra and the Tagus river, in the form of a blind thrust whose surface expression is the fold with an E-W axis that occurs in the Loures region, where many of the LVC's flows and necks outcrop (fig. 8.6).

In the Lisbon region, the Monsanto anticline, the Torres Vedras and Tagus estuary fault are other important structures showing the same general E-W trend and are located near the region where most of the rocks from the LVC outcrop.

The alkaline Foz da Fonte and Sesimbra sills are located not too far away from the Arrábida fault, which corresponds to the southern limit of the Lusitanian basin and is interpreted as being an important, E-W oriented structure thought to have acted as a normal/transfer fault during rifting (e.g. Kullberg, 2000; Kullberg et al., 2010). However, magnetic lineation and imbrications in the Foz da Fonte sill indicate a WSW-ENE flow direction which can be indicative of the presence of a linear feeder with a NNE-SSW direction,instead of E-W (Miranda et al., 2006).

The Torres Vedras, Arrábida and Tagus estuary faults are all important structures in the region, limiting different half grabens or sub-basins inside the larger Lusitanian basin (Ribeiro et al., 1979; Rasmussen et al., 1998; Kullberg, 2000; Alves et al., 2003). They are consequentially thought to correspond to syn-rift transfer faults showing an oblique movement that were reactivated as thrust and reverse faults during the Alpine orogeny. These can therefore be considered important crustal discontinuities that might have played a large role of facilitating the ascent of the alkaline magmas during the Late Cretaceous.

The Sines igneous complex is located on the Southern border of the small Santiago do Cacém Mesozoic basin, which should contact with the surrounding Paleozoic basement through an approximately E-W fault. Furthermore, the complex is cut by structures with the roughly the same direction (e.g. Inverno et al., 1993; fig. 2.11). NNW-SSE faults, such as the Santo André fault, are also important in the region as they define the limits of the previously mentioned basin (e.g. Inverno et al., 1993)

In the southern Monchique igneous complex, Gonzalez-Clavijo and Valadares (2003) proposed that magma ascension and installation was controlled by pre existing left strike slip ENE-WSW faults, while other authors (Gomes and Pereira, 2004; Sant'Ovaia et al., 2007) argue for the existence of NW-SE feeders on the basis of AMS and paleomagnetic data. Important structures in the region include the nearby NNW-SSE Portimão fault and structures with NNE-SSW directions that offset the complex (Gonzalez-Clavijo and Valadares, 2003).

The scattered intrusions in the Algarve basin appear associated with salt diapirs (Loulé dykes), normal faults (Praia do Zavial), N-S to NNW-SSE oriented faults (Lagos region) and can even intrude E-W structures in the Western Algarve (Romariz et al., 1979; Terrinha, 1998).

The variety of different structures involved in controlling the ascent and emplacement of these magmas and acting as feeders in the larger intrusions at upper crustal levels implies that these alkaline magmas used pre-existing, possibly rift related structures to make their way up to the surface. Many of these pre-existing structures should have been inherited from existing fractures in the Variscan basement (Terrinha, 1998; Kullberg, 2000) and could therefore extend to deep crustal levels. Nevertheless, the persistent identification of E-W transfer faults associated with the Late Cretaceous magmatic products in the Lusitanian basin suggests a higher importance of these structures in controlling the ascension of the magmas. Meanwhile, the actual location of the major magmatic occurrences seems to be controlled by the intersection of such faults with other NNW-SSE or NE-SW fractures.

It has been suggested that the Sintra, Sines and Monchique complexes are connected at deeper levels (lower crust and subcontinental mantle lithosphere), by a NNW-SSE trending dextral strike slip fault related to the rotation of Iberia (Ribeiro et al., 1979; Terrinha, 1998). Alternatively, it has been put forward that the Sintra-Tore and Sintra-Sines-Monchique (SSM) faults share a common origin, related to the super-critical propagation of a lithospheric fracture resulting from a meteorite impact in the Tore Seamount area (Ribeiro et al., 1997, Ribeiro, 2002). These authors propose that the change in direction from approximately E-W to NNW-SSE is the result of the refraction of fault propagation due to changes in the thickness and rheology of the lithosphere being crossed, that progressively changes from very thinned (Tore), to thinned (Sintra) to probably unthinned (Monchique).

The existence of the Sintra-Sines-Monchique (SSM) fault is yet to be confirmed by either direct observation of indirect geophysical methods. When compared to the Sintra-Tore fault, which is observed at the surface and in seismic profiles (Badagola, 2008), the evidence for the existence of the SSM fault is not obvious. Nonetheless, a series of smaller scale fractures with the same NNW-SSE strike of the SSM fault have been identified in the Lusitanian and Algarve basins (Terrinha, 1998; Kullberg et al., 2006, 2010; fig. 8.6), and close to the Sintra and Monchique igneous complexes.

A NW-SE trending fault zone with approximately 50 km of length has been identified between the Sintra complex and the Miocene Arrábida thrust belt (Kullberg, 2000; Kullberg et al., 2006, 2010). These faults cut across the Lower Cretaceous sediments, and also the Foz da Fonte sill. Kullberg (2000) has shown that these structures were active during Mid Jurassic rifting in the Arrábida belt. Also, they are often injected with basic to intermediate dykes (the Oeiras-Cascais dykes).

The Portimão fault was mapped from the vicinities of the Monchique complex, till approximately 100 km further south, already in the offshore domain (Terrinha et al., 1999; Terrinha et al., 2009). This structure is a steep strike slip fault at present, but it was active at least since Mid Jurassic times, separating two sub-basins in the main Algarve basin (Terrinha, 1998; Terrinha et al., 1999).

These two fault zones were interpreted as the surface expression of the deeper SSM strike-slip fault that concentrated shear during the rotation of Iberia and controlled the ascent of the alkaline magmas (e.g. Terrinha, 1998; Terrinha et al., 2003; Kullberg et al., 2006, 2010).

In summary, the Late Cretaceous alkaline magmas seem to have used of a series of pre-existing structures in order to extrude or ascend to upper crustal levels, noticeably E-W to WNW-ESE, NNW-SSE and NE-SW trending faults. In the uppermost crustal levels, the intersection of these fault systems controlled the location of individual occurrences, as can be deduced from the geometry of the feeders in Sintra (Terrinha et al., 2003; Kullberg et al., 2006; 2010) and from the main structures present in the vicinities of both this and the Sines igneous complex. In its turn magma ascent in the Monchique igneous complex is thought to have taken place in reactivated Variscan WNW-ESE to NW-SE structures in the upper crust.

In the Lusitanian basin, the Estremadura spur and possibly even in the case of the Sines igneous complex, the E-W to WNW-ESE structures seem to have played a major role in controlling the ascent of these magmas. Since many of these are thought to have acted as transfer faults during rifting and also correspond to reactivated structures inherited from the Variscan orogen, they can be thought of as extending to relatively high depths in the lithosphere, at least until the lower crust and to control the magma ascent, as previously suggested by Terrinha (1998).

At the lower crust and subcontinental mantle lithosphere levels, the debate remains relatively open, in the sense that both the WNW-ESE to E-W faults in the Tore-Estremadura region and the hypothetical NNW-SSE SSM fault are viable pathways for

rising magmas, although their extension to such depths cannot be unequivocally demonstrated at present.

8.3 Towards an integrated geodynamical model for the Late Cretaceous alkaline magmatism of the WIM

The geochronological evidence for the existence of two pulses of alkaline magmatism was presented in section 5 of this work (see also Miranda et al., 2009). It was also shown that these two pulses are distinguishable in terms of trace element abundances (section 7.1), but derived from mantle source with a nearly identical sublithospheric mantle isotopic signature (sections 7.2 and 7.5).

Meanwhile, Grange et al. (2010) argued for the existence of an age progression in their dataset, with the intrusions younging towards the south. They interpret this age progression to reflect the movement of the Iberian plate above a fixed mantle plume. However, this implies that the plate has to move in from SSE to NNW between 88 and 68 Ma (Grange et al., 2010), while in fact the western part of the Iberian plate moves from NW to SE up to 80 Ma as a consequence of the opening of the Bay of Biscay (Sibuet et al., 2004), and shows an overall northwards (≈ SW to NE) motion from then onwards, as the opening of the Bay of Biscay ends and Iberia starts moving in the same direction as Europe (e.g Piromallo et al., 2008). Even if the overall SW to NE motion was predominant during the Late Cretaceous, the igneous complexes should be aligned in a NE-SW direction, while their actual alignment is NNW-SSE. Also, the interpretation by Grange et al. (2010) does not account for a younger event in the Lisbon area at 72 Ma, which could not reflect the northwards drift of Iberia above a mantle plume.

Moreover, the occurrence of magmatic of activity in the same location at different time intervals (in the Lisbon region there is alkaline magmatism at 94-88 Ma and later 75-72 Ma, with the Sintra granite intruding in between at 79 Ma), the simultaneous activity in different locations at approximately the same time (Algarve, Sines and Lisboa between 75-72), the Late Cretaceous kinematics of the Iberian plate and the absence of an age progression in the offshore WIM magmatism favor the hypothesis of the occurrence of two distinct pulses of activity on the onshore WIM instead of a simple N to S age progression.

As discussed in section 7, the enriched nature of the Late Cretaceous alkaline magmas point towards and OIB like source. This type of sources is usually located in the sublithospheric mantle and is associated with deep rooted upwelling from lower parts of this layer, in the form of mantle plumes (e.g. Morgan, 1971).

The isotopic characteristics of the uncontaminated sampled rocks ($^{87}Sr/^{86}Sr_i$ 0.7030-0.7037; εNd_i 5.7 – 3.7; $^{206}Pb/^{204}Pb_i$ 19.564-19.20, $^{207}Pb/^{204}Pb_i$ 15.609-15.580, $^{208}Pb/^{204}Pb_i$ 39.245-39.00) are compatible with a common origin between these magmas and the melts from the Canaries mantle plume. Considering that the known paleomagnetic data and paleogeographic reconstitutions indicate that Iberia was located in the vicinities of the Canaries mantle plume during the Late Cretaceous (see section 8.1), it can be argued that this hot mantle anomaly is a long living one and that it was the heat and mass source of the alkaline magmatism of the WIM.

During the first pulse of alkaline activity in the onshore WIM (94-88 Ma), the sublithospheric, plume related magmas represented by the Foz da Fonte sill were installed in the upper crust without traces of interaction with the mantle lithosphere or with the crust. In its turn, the Paço d'Ilhas sill is constituted by magmas that suffered e important assimilation of crustal material and fractional crystallization.

Samples from the second pulse (75-72 Ma) show distinct trace element patterns in relation to the first one. The differences observed between the two pulses can be related to different levels of interaction of sublithospheric plume magmas with the overlying continental mantle lithosphere as a consequence of changes observed in the Iberian plate motion. It is suggested that the lack of a metasomatic signature during the first pulse is linked to a more favorable stress field during the rotation of Iberia (up to 80 Ma, Sibuet et al., 2004), which allowed for the quick ascent of the magmas generated in an ascending plume.

The second pulse coincided with the onset of the rapid collision between the African and Iberian plates and the first recorded phases of inversion of the Mesozoic basins (e.g. Mougenot, 1980, Terrinha, 1998, Rosembaum et al., 2002) which started after the rotation had ceased. This created a less favorable stress regime and restrained the opening of fractures and quick magmatic ascent, favoring interaction with subcontinental lithosphere which either resulted in the metasomatism of its lowermost part, or allowed for the melting and incorporation of lithosphere that had been probably metasomatized during the first pulse.

The metasomatizing agents were probably the first volatile rich (H_2O+CO_2) low degree melts from the ascending Canaries plume. These early melts metasomatized the overlying subcontinental mantle, imprinting the plume signature and lowering the fusion temperatures of these rocks. It is the similarity in the isotopic signatures observed in both pulses that allows the assignment of common origins to the sublithospheric and metasomatic components.

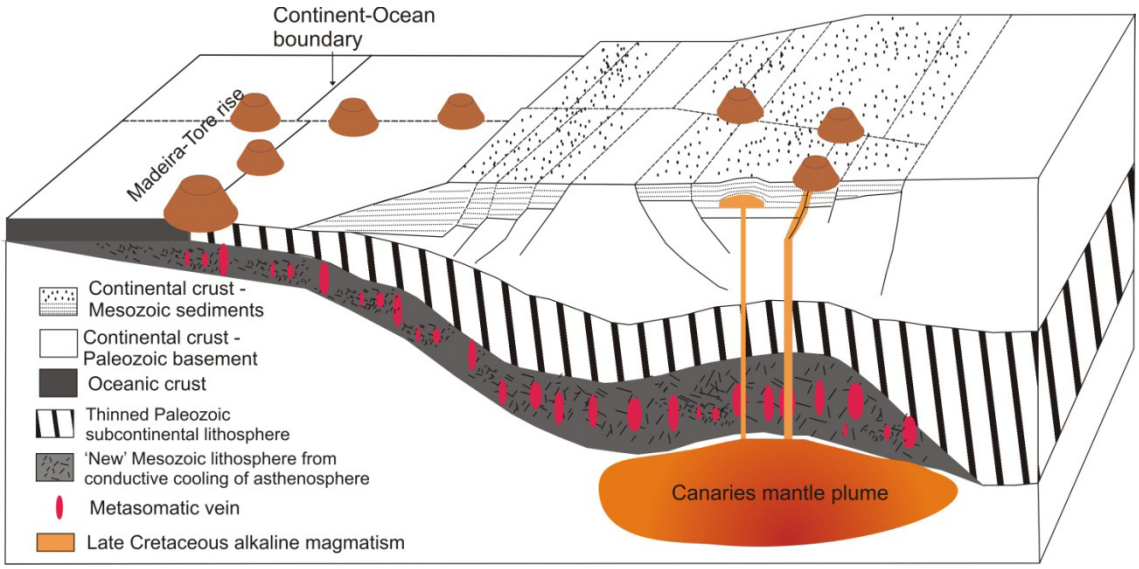

Fig. 8.7: Schematic representation of the interplay between structure and magmatism during the Late Cretaceous in the WIM. Adapted from Kullberg et al., 2010.

Later, when these rocks crossed their solidus either due to the higher proximity of the plume's hot center or to the passage of other plume derived melts, the metasomatized lithosphere started to melt, contributing to the volume of magma generated during the second pulse. The metasomatic signature is reflected only in the magmas derived from smaller amounts of partial melting, since it becomes progressively more diluted with time, as the liquids generated in the asthenosphere from the melting of the plume head increase in volume. This metasomatic signature is characterized by negative K, Zr, Hf and sometimes Ti anomalies in the multielemental diagrams, accompanied by low Ti/Eu, and high Zr/Hf.

As the magmas from the first pulse (or early magmas from the second pulse) ascended, some became trapped at depths corresponding to the upper mantle or lower crust, where they started to crystallize, among other minerals, clinopyroxene and amphibole, thus evolving from basic to at least intermediate compositions (see section 6.2).

During the second pulse of Late Cretaceous alkaline activity, some of the chambers or conduits where these magmas evolved were recharged with a more primitive batch of basanitic magma which mixed with the more evolved liquid they contained, creating the reversely zoned crystals observed in some of the Late Cretaceous alkaline rocks of the WIM (see section 6.2). During these recharge events the mixing of a hot, basic magma with a more evolved, volatile rich melt led to the pressurization and reduction in density of the basic magmas aiding the quick ascent of these magmas. The higher volatile content of the resulting magmas could have also facilitated the ascent to shallower levels, possibly leading to the extrusion of the LVC, which is characterized by the occurrence of explosive events before the onset of the effusive activity. The explosive events of the LVC can be tentatively related to decompression and devolatilization of a volatile rich magma.

Although mineral chemistry data seems to show that magma mixing is a relatively common phenomenon in the Late Cretaceous alkaline rocks of the WIM, it did not have a major influence in the isotopic or major and trace element characteristics of the rocks where it is recorded. This leads to the proposition that the mixed magmas were probably related to a common source and that only a small volume of intermediate melt mixed with the primitive basic liquid (see sections 6.2 and 7.3.3).

During their ascent, these magmas used pre-existing faults inherited from Mesozoic rifting and the Paleozoic Variscan orogeny. Many of the magmatic occurrences in the western Mesozoic basins seem to be related to WNW-ESE to E-W transfer faults that were active during rifting (fig. 8.7). Meanwhile, their exact site of emplacement seems to result from the intersection of these structures with other fault systems with NE-SW and NNW-SSE orientations.

Some of the previously mentioned E-W to WNW-ESE structures might represent major lithospheric discontinuities and acted as preferential pathways for magma ascent and emplacement, as seems to be the case with the Sintra-Tore faults, along which several intrusions are found, including the Sintra igneous complex and the Fontanelas seamount, among several other minor intrusives.

Many of these magmas did not reach the surface but instead accumulated as sills and laccoliths in upper crustal levels and evolved through combined assimilation and fractional crystallization processes. Crystal fractionation led to the formation of cumulate rocks in the larger intrusive bodies, either by gravitational settling (e.g. Pedras

Negras gabbro in the Sines complex) or by flotation processes (e.g. benmoreite/monzonite layers of the Paço d'Ilhas sill).

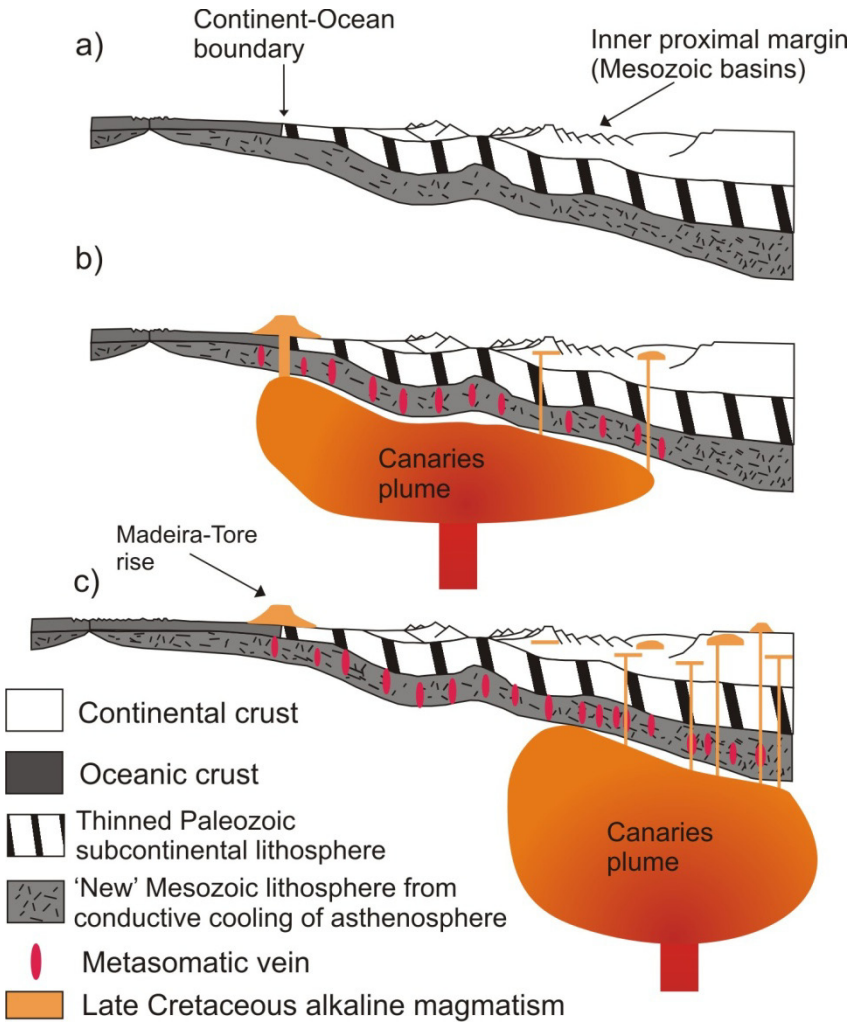

Fig. 8.8: Schematic representation of the evolution of the WIM during the Late Cretaceous. a) at 100 Ma, before the onset of magmatism; b) at≈ 88 Ma, during the first pulse of alkaline magmatic activity and c) at ≈ 75 Ma during the second pulse of alkaline magmatic activity. Adapted from Alves et al., 2009.

The energy provided by conductive cooling of the intrusions and by crystallization allowed for the assimilation of the country rock. The contaminants are thought to be of upper crustal nature and the two different contamination trends observed in the data set relate to the different nature of the assimilated material. The higher $^{87}Sr/^{86}Sr$, $^{207}Pb/^{204}Pb$ and lower $^{143}Nd/^{144}Nd$, $^{206}Pb/^{204}Pb$ and $^{208}Pb/^{204}Pb$ trend is thought to reflect contamination from siliclastic sedimentary material, while the trend that is characterized only by a rise in $^{87}Sr/^{86}Sr$ might be related to the assimilation of small amounts of Sr rich and Nd poor carbonated material. The high $^{207}Pb/^{204}Pb$ of the

siliciclastic contaminant suggests that this contaminant has inherited an old, Precambrian crustal component.

The scatter observed in the ages for both the onshore and offshore Late Cretaceous alkaline occurrences is also indicative of the importance of the plate kinematics of Iberia, pre-existing structure and the size of the hot mantle anomaly in controlling the timing and location of this magmatism (fig. 8.8). Most of the seamounts in the Madeira-Tore rise were active (103 Ma to 80 Ma, Merle et al., 2006, 2009; Geldmacher et al., 2006) during the time interval when the opening of the bay of Biscay and the rotation of Iberia took place (~118 -80 Ma, Sibuet et al., 2004). These seamounts extruded on a major lithospheric discontinuity that defines the passage from a transitional continental domain constituted mostly by exhumed peridotite, to true oceanic crust, as schematically shown on fig. 8.7 and 8.8 (e.g. Sibuet et al., 2007; Afilhado et al., 2010). During the rotation of Iberia, this discontinuity might have worked as a lithospheric strike slip fault and facilitated the ascent of the magmas along its strike, especially in areas where it intersected other structures or where small changes in its general trend might have led to the onset of transtension. The simultaneous magmatism in the Paço d'Ilhas and Foz da Fonte intrusions and possibly also in the Sintra complex (the granite intrudes at ca. 79 Ma) can be related to the channeling of plume material from the Tore area, where significant magmatism took place, through corridors of thinned lithosphere or along the E-W to WNW-ESE structures of the Estremadura spur. The Newfoundland seamounts, which erupted on the American plate but in an area where similar E-W to WNW-ESE structures might be present, show a similar age of 98 Ma (Sullivan and Keen, 1977 in Pe-Piper *et al*., 2007).

From 80 Ma to the end of the Cretaceous, the offshore magmatism in the WIM seems to be limited to the Ormonde peak of the Gorringe bank (≈ 65 Ma, Féraud *et al*., 1982, 1986) although the NW Tore seamount shows a 80.5 Ma age (Merle et al., 2006). On the other hand, this was the time when magmatism was most abundant in the onshore WIM, which might reflect the drift of Iberia over a hotter area of the mantle (fig. 8.8). The small amount of magma production in the onshore with respect to the offshore is likely to be related both to the higher thickness of the lithosphere in this region, which held back magma production by decompression, and to the contemporary tectonic regime characterized by compression due to the initiation of collision between Africa and Iberia/Europe.

As was mentioned earlier, the most likely source for the Late Cretaceous alkaline magmatism of the WIM seems to have been the Canaries mantles plume (see section 7.4), however, it remains unclear if it continued to affect the region throughout the duration of both pulses or if at some point the metasomatized lithosphere bearing the Canaries plume isotopic and trace element signature melted to generate the magmas of the second pulse. If it was the latter case, an additional heat source was necessary to melt the refertilized lithosphere. That heat source might have speculatively been the Madeira mantle plume.

9. Conclusions

After a careful analysis of the new geochronological, geochemical and mineral chemistry data and of the elaboration of a model for the geodynamic evolution of Iberia on the previous sections, this part of the manuscript will act as an extended summary of the present work and list the main conclusions from each of these sections.

Sampling:

- The sampling, analysis and study of the basaltic (s.l.) pillow lavas of the Fontanelas seamount suggest that the positive magnetic anomalies (one of which corresponds to the Fontanelas seamount) between the Tore seamount and the Sintra igneous complex could correspond to Late Cretaceus alkaline igneous occurrences.

Geochronology:

- The new age determinations, combined with previously published data, allowed to constrain the duration of the Late Cretaceous alkaline cycle to circa 22 Ma, between 94 and 72 Ma, and to define two distinct pulses of alkaline magmatic activity.

- The first of these pulses occurred between 94-88 Ma and is limited to sills in the Lisbon region (Foz da Fonte and Paço d'Ilhas). The second pulse involved a larger volume of magma and took place between 75-72 Ma. It has a wider geographical distribution (≈ 37 to 39º N) and more diverse modes of occurrence such as subvolcanic complexes (Sines, Monchique and the Cabo da Roca complex in Sintra), flows, necks, plugs, dykes and sills (LVC, Loulé lamprophyres).

- U-Pb dating of zircon separates from the Sintra granite gives an 79.2 ± 0.8 Ma age, which although equivalent, within error, to the oldest age obtained for the syenite (78.3 ± 1.9 Ma, Storetvedt et al., 1987), is still older than the other K-Ar ages obtained for these rocks (76.4 ± 1.4 and 76.1 ± 1.1 Ma, Storetvedt et al., 1987). This, combined with the observed field cross-cutting relations and geophysical data (gravimetry and AMS, Terrinha et al., 2003), allows us to speculate that the granite

corresponds to an older laccolith that is intruded by a more recent gabbro to syenite suite.

Petrography and Mineral Chemistry:

- Field, textural and mineral and whole rock chemistry data indicate that the Pedras Negras gabbro in the Sines igneous complex formed by the accumulation of mafic minerals (mostly olivine and clinopyroxene) on the bottom of a magma chamber. The Praia Vasco da Gama gabbro in the same complex should in its turn represent a higher level of the same magma chamber, which is supported by textural and whole rock geochemistry evidence. The fact that the deeper level of the magma chamber represented by the Pedras Negras gabbro outcrops at the same altitude than its shallower counterpart (Praia Vasco da Gama gabbro) can be due to the uplift on the northern block accommodated by the E-W fault that cross cuts the complex.

- Petrographic evidence shows that the earlier minerals to crystallize are Cr-rich spinels, followed by olivine and Fe-Ti oxides and then by clinopyroxene, plagioclase and amphibole.

- The precipitation and removal of olivine led to the decrease of MgO and Ni and an increase of FeO in the residual melt, which is reflected in the progressive increase of the fayalite content in the olivines. The decreasing amounts of CaO and MnO in the olivines, with increasing Fa contents, are associated to the onset of clinopyroxene, plagioclase and possibly Fe-Ti oxides crystallization.

- The importance of crystal accumulation processes in the genesis of the Sines gabbros was reinforced by the observation that their $\boldsymbol{Kd}_{Fe/Mg}^{ol-liq}$ value did not reflect equilibrium between the composition of the olivines and the analyzed whole rock composition.

- Crystallization temperatures obtained for olivine vary between 1250º C in the Ribeira d'Ilhas plug and 1150 ºC for the and Negrais lava flow. The temperatures for plagioclase crystallization ≤ 900º C for the Ribeira d'Ilhas plug

and 970º C for the Negrais flow) and for equilibrium amphibole-plagioclase pairs are lower, confirming that these are late magmatic phases.

- Most of the clinopyroxenes present in the analyzed rocks are Ca-rich diopsides and augites. In general, the clinopyroxene compositions evolve towards terms that are more enriched in FeO (ferrosilitic molecule; $Fe_2Si_2O_6$) and Na_2O, while becoming progressively depleted in MgO. Some of the more Fe-rich clinopyroxenes classify as hedenbergites and, when Na_2O rich as aegirine-augites.

- Two different types of clinopyroxene phenocrysts were identified. One with normal zoning, consisting of a pink to purple core and a rim with a darker shade of the same color. The second type shows a green core and a pink to purple rim.

- The green cored clinopyroxenes phenocrysts show reverse zoning, with the cores being more Fe^{3+}, and Na rich and Mg and Ti poor than their rims and mantles. These cores also show higher Al^{vi} which are indicative of crystallization at higher pressures. This suggests that the reverse zonation results from the mixture between a more evolved and a more basic magma at depth, both being of alkaline nature and thus possibly genetically related. The differences in composition between the green cores of the reversely zoned phenocrysts of basic rocks and the green clinopyroxenes of the Monchique nepheline syenite imply that the more evolved liquid would not be phonolitic but possibly intermediate, such as a tephri-phonolite or phono-tephrite.

- There are compositional similarities between the clinopyroxenes in the xenoliths and the green cores of the reversely zoned phenocrysts, suggesting a common origin.

- Like the clinopyroxenes, some of the plagioclases in the basic rocks also show reverse zoning, which is further evidence for the occurrence of magma mixing at depth.

- Average crystallization temperatures for plagioclases are lower than the ones obtained for olivines, which is in agreement with this mineral being a later

phase in the crystallization sequence. Crystallization temperatures for crystal cores of gabbroic rocks vary between ≈1100º C in the Mafra gabbro to 910º C in the Monchique gabbro, with Sines and Sintra showing intermediate temperatures (1070 and 960º C, respectively) and the more evolved sills showing even lower temperatures (960-900º C). Matrix crystals from basic rocks show relatively high temperatures (1040 to 900º C) as a result of their fast growth under rapid cooling conditions.

- The amphiboles found in the studied samples are mostly kaersutites and pargasites. Some show reverse zoning, providing aditional evidence for the occurrence of magma mixing processes. Secondary magnesio-horneblende occurs in the Sintra gabbros.

- Amphibole-plagioclase equilibrium temperatures are in agreement with the ones calculated for plagioclase alone and reinforce the late character of both these phases. They vary between ≈ 1010, 1030, 1000 and 910º C for the Mafra, Sines, Monchique and Sintra gabbros and 890º C in the amygdulae of the Ribeira d'Ilhas plug.

- Compositional similarities between amphibole xenocrysts, amphiboles in the xenoliths and the cores of the reversely zoned phenocrysts found in the Malveira da Serra sill suggest a common origin for these phases.

- The majority of the analyzed oxides are titanomagnetites but there are also rare, early chromian spinels, often included in olivine. In addition to these phases, some magnetite and ilmenite were identified in large exsolved crystals which are more common in the intrusive rocks. These exsolved crystals were likely originally titanomagnetites as well. The predominance of spinels from the ulvospinel-magnetite solid solution series is a consequence of the low silica activity ($\boldsymbol{a_{SiO2}}$) of the silica undersaturated alkaline magmas from which they formed. Individual ilmenite crystals are only found in the more evolved, contaminated and SiO_2 rich sills like Paço d'Ilhas and Montelevar.

- The crystallization of the earlier spinels (chromite to chromian titanomagnetite and titanomagnetites) must have taken place at relatively high

oxygen fugacity conditions, above the NNO buffer, since solid solution between aluminous and Fe-Ti spinels seems to be possible only under such conditions.

- With increasing differentiation, the spinels became richer in TiO_2, which can be attributed to a decrease in fO_2 of these low $\boldsymbol{a_{SiO2}}$ magmas. This decrease is confirmed by the values obtained for the exsolved ilmenite-magnetite pairs in the gabbros and basaltic rocks which are generally below the NNO buffer.

- The Sintra gabbros show the highest oxigen fO_2 values for the magnetite-ilmenite exsolution pairs, which is probably a result of subsolidus equilibration during the secondary alteration event that affected the gabbros in this complex.

- The calculated blocking temperatures for the exsolved ilmenite-magnetite pairs are quite low, both for the intrusive and extrusive rocks, suggesting subsolidus equilibration under relatively slow cooling conditions in both environments. Blocking temperatures vary between 500 and 600º C in the Negrais lava flow and Sines gabbro, go up to 640º C in the Monchique gabbro and 770º C in the Sintra gabbro. The highest blocking temperatures were calculated for the Montelevar sill (≈ 770º C) and for the oxides in the reaction rim of an amphibole megacryst in the Ribeira d'Ilhas plug (≈ 850º C).

- Kaersutite xenocrysts are interpreted to represent the products of high pressure crystallization (> 15 kbar) of a similar basic, hydrous alkaline melt, formed within a deep conduit or chamber, and that therefore did not aggregate into xenoliths. As the magmas ascended, the pressure dropped, and the volatiles exsolved, the amphibole xenocrysts became unstable and started developing the observed clinopyroxene+plagioclase+Fe-Ti oxide reaction rims.

- The existence of reversely zoned clinopyroxenes, amphiboles, plagioclase and xenoliths, sometimes even in the same outcrop, can be interpreted as evidence for the occurrence of magma mixing preceding the emplacement of the magmas at higher levels. All these are relatively evolved and can be interpreted as being the crystallization products from similar alkaline melts of intermediate nature.

- The magma mixing event must have taken place at high depth, given the higher Al^{vi} content of the green cores in clinopyroxenes and the stability conditions for kaersutite. Such depths are likely to correspond to boundaries between layers with strong density contrasts, such as the crust-mantle boundary or the Conrad discontinuity within the crust.

- The green clinopyroxene cores, the evolved amphibole cores and megacrysts and the evolved plagioclase cores are thought to represent phases crystallizing in the middle of the chamber or conduit that contained the more evolved magma that mixed with the basic melt. In their turn, the xenoliths containing minerals with similar compositions could represent cumulus or wall rock assemblages in that chamber or conduit that had previously crystallized from the same evolved magma and were remobilized once that chamber was recharged with the basic melt.

Elemental and Isotope Geochemistry:

- All of the sampled rocks classify as alkaline and most of them belong to the potassic series, although some of them plot in the sodic field of the classification by Middlemost (1975), mostly due to the accumulation of Na-rich phases. They are trace element enriched in relation to the primitive mantle.

- Major and trace element abundance in cumulate rocks is controlled by the respective cumulate mineral assemblage and degree of fractionation. This is more evident in intrusive rocks, such as the Sines and Sintra gabbros and the Paço d'Ilhas sill.

- The magmatic evolution follows two distinct differentiation trends from an initial ultrabasic/basic alkaline melt. The silica oversaturated trend seems to be predominant, being common to the LVC, Sintra and Sines igneous complexes, while the SiO_2 undersaturated trend only occurs in the Monchique igneous complex and is also represented by the Eiras do Faião sill, which is integrated in the LVC.

- All the samples show fractionated REE patterns, which is illustrated by high La_N/Yb_N (48.9 – 8.8) and Tb_N/Yb_N (3.4-1.9). This can be interpreted as

resulting from the presence of residual garnet during the melting events, which implies that melting must have taken place deeper than 60 km.

- The studied samples show relatively low $^{87}Sr/^{86}Sr_i$ (0.703005 to 0.704884) and high εNd_i (5.8 to2.8).

- Pb isotopes show compositions ($^{206}Pb/^{204}Pb_i$, 18.827-19.564, $^{207}Pb/^{204}Pb_i$ 15.567-15.634, $^{208}Pb/^{204}Pb_i$ 38.603-39.948) that are more enriched than DMM, but less enriched than HIMU, defining a compositional array close to the NHRL and to the FOZO component. Samples for the Fontanelas seamount show much higher $^{208}Pb/^{204}Pb_i$ values than the remaining samples, probably due to secondary alteration processes which changed the Th/Pb and U/Pb ratios of these rocks and prevented the application of proper corrections for radioactive decay.

- Basic, uncontaminated samples show a more reduced compositional range in Sr, Nd, and Pb isotopic ratios ($^{87}Sr/^{86}Sr_i$ 0.7030-0.7037; εNd_i 5.7 – 3.7; $^{206}Pb/^{204}Pb_i$ 19.564-19.20, $^{207}Pb/^{204}Pb_i$ 15.609-15.580, $^{208}Pb/^{204}Pb_i$ 39.245-39.00). There are no perceptible differences in the isotopic compositions of the rocks from the two different magmatic pulses, which means that the composition of the mantle of the WIM can be considered as being reasonably stable and homogenous between 94 and 72 Ma.

- The basic, unfractionated samples seem to have resulted from very low amounts of partial melting (1-6 %) of enriched mantle sources. The sources for the Loulé lamprophyres, Foz da Fonte sill and remaining unfractionated basic rocks (mostly from the LVC and Fontanelas seamount) are different in terms of the degree of enrichment and of residual mineralogy. The source of the lamprophyres is substantially more LREE enriched, while the Foz da Fonte sill lacks residual amphibole in its source.

- The Sr and Nd isotopic signatures of the basic uncontaminated rocks suggest a time integrated depletion in Rb and Nd relative to Sr and Sm, respectively. This is in contrast with the incompatible trace element enriched nature of these rocks. Such a discrepancy can be attributed to a mantle metasomatism event took place shortly before magma generation, which means that the isotopic ratios of this

metasomatized source did not have sufficient time to evolve into a more significantly enriched and heterogenous composition.

- The isotopic signature of uncontaminated rocks is compatible with a sublithospheric origin for these magmas. Their composition plots between the range defined by the HIMU and DMM components, near FOZO, in Sr-Nd, and Pb-Pb isotopic variation diagrams and shows similarities to the offshore occurrences of Late Cretaceous age (MTR and Ormonde).

- The uncontaminated samples show an isotopic composition that is within the range of compositions shown by samples derived from the activity of the Canaries mantle plume, suggesting that the Late Cretaceous alkaline magmas of the WIM probably resulted from the activity of the same plume. Magmas derived from this mantle plume also show FOZO like Sr, Nd and Pb isotopic signatures. However, He and Os isotopic data for samples from the Canary islands point a model involving the dilution of a HIMU plume component in the a DMM (asthenospheric?) component.

- Primitive mantle normalized multielemental diagrams confirm the trace element enriched character of these rocks and show some features that are common to all the studied samples, such as positive Nb and Ta anomalies.

- These diagrams also allowed for the identification of distinct features in the trace element patterns of the two pulses of Late Cretaceous alkaline magmatic activity. Basic samples from the second pulse show negative K, Zr, Hf and sometimes Ti anomalies, which are absent in unfractionated basic samples of the first pulse.

- These negative anomalies are thought to reflect the action of a metasomatic event which modified the original mantle mineralogy and chemical composition.

- The negative K anomalies are attributed to the presence of residual amphibole during melting, which buffered K concentrations in the resulting magmas. Amphibole is only stable at temperature conditions correspondent to the

lithospheric mantle and therefore should reflect the action of volatile rich metasomatic fluids in the lithosphere or the equilibration of magmas with metasomatized lithospheric mantle domains.

- Negative anomalies in Zr, Hf and Ti are thought to reflect the action of carbonatitic or CO_2 rich melts that metasomatized the mantle before the melting event that generated the magmas of the second pulse of Late Cretaceous alkaline activity.

- The composition of the metasomatic agent is likely to be gradational, from a carbonatitic to a volatile rich siliceous melt. However, the high Zr/Hf and low Ti/Eu at high La/Yb point towards an important carbonatitic contribution.

- The source for such a metasomatic agent might have been low degree melts from a carbonated peridotite in an ascending mantle plume, such as the Canaries mantle plume. These early melts imprinted the plume signature in the lithosphere and lowered its fusion temperature. This is supported by the similar isotopic signatures observed in both pulses, which allowed for the assignment of a common origin for the sublithospheric and for the metasomatic components.

- The contribution of metasomatized mantle to the total volume of produced melt decreases with increasing degrees of melting, as the rocks that derive from higher amounts of fusion show lower Zr/Hf, La/Yb and higher Ti/Eu. This means that the melts from the metasomatized source were progressively diluted in asthenospheric plume related melts.

- Since this metasomatic signature is only detected in rocks from the second pulse, it is likely that the metasomatic event is contemporary of the first pulse of magmatic alkaline activity (94-88 Ma) or that it occurred just before the formation of the magmas from the second pulse.

- Most of the studied samples represent somewhat fractionated magmas since they do not fit the criteria to classify as unfractionated primary magmas. This is an indicator for the existence of important fractionation at depth.

- The magmatic evolution of the samples from the LVC appears to have been controlled by assimilation and fractional crystallization (AFC) processes. The fractionating assemblage which better reproduces the evolution trend seen in these rocks is constituted by clinopyroxene (55%) + olivine (20%) + plagioclase (17.5%) + magnetite (7.5%).

- Assimilation of upper crustal lithologies is thought to have occurred concurrently with crystal fractionation in order to create the observed trace element and isotopic signatures. Two main AFC trends are observed, one characterized by the progressive increase in Th/La, Zr/Nb, K/Nb, $^{87}Sr/^{86}Sr$ and $^{207}Pb/^{204}Pb$, and decrease in $(Gd/Lu)_N$, Nb/U, $^{143}Nd/^{144}Nd$, $^{206}Pb/^{204}Pb$ and $^{208}Pb/^{204}Pb$ with increasing SiO_2. This trend seems to be common to most of the contaminated and evolved samples and is thought to reflect assimilation of an upper crustal, siliceous, rock.

- The other AFC trend is characterized by increasing $^{87}Sr/^{86}Sr$ and relatively unchanged trace element as well as εNdi and Pb isotopic ratios in the contaminated rocks, which also possess relatively low SiO_2 contents. This trend is thought to be the result of the assimilation of small amounts of Sr rich but Nd and Pb depleted contaminant, such as carbonate material.

- The gabbros of the Sintra and Sines igneous complexes show apparently contaminated Pb isotopic signatures along with uncontaminated Sr and Nd isotopic ratios. Such a signature is likely to be the result of secondary hydrothermal alteration by Pb rich fluids.

- Mineral chemistry data supports the existence of magma mixing at depth for some of the magmas of the second pulse of the Late Cretaceous alkaline activity. However, geochemical modeling seems to show that this process is of little importance in creating the petrological diversity observed in these rocks, with fractional crystallization and assimilation appearing to be the most important processes.

- The mixing and homogenization of a basic, primitive magma with small portions of a more evolved, volatile rich liquid probably led to the formation of a

melt that retained its basic nature but suffered a reduction in density and an increase in the volatile content. This resulted in the pressurization of the system, leading to rapid ascension and installation of the magmas.

- As the volatile rich magma approached the surface, the volatiles would start to exsolve due to decompression, generating explosive eruptions such as the ones that happened before every effusive phase in the LVC.

Wider geodynamical implications:

- The timing and location, and even certain geochemical characteristics of the Late Cretaceous alkaline magmatism in the WIM seems to be associated with local structure and changes in the kinematics of the Iberian plate.

- The absence of a metasomatic signature materialized by negative negative K, Zr and Hf anomalies during the first pulse of Late Cretaceous alkaline activity in the onshore WIM (94-88 Ma) could be related to a more favorable stress field during the contemporaneous rotation of Iberia which permitted the quick ascent of the magmas generated in an ascending plume.

- During the second pulse (75-72 Ma) some of the samples show a metasomatic signature characterized by negative K, Zr and Hf anomalies. The presence of such a signature is associated with the contemporaneous onset of the rapid collision between the African and Iberian plates and the initiation of inversion in the Mesozoic basins which created an unfavorable stress regime, and restraining the opening of fractures and quick magmatic ascent. This favored interaction with subcontinental lithosphere and either resulted in the metasomatism and fusion of its lowermost part, or allowed for the melting and incorporation of lithosphere metasomatized during the first pulse.

- The lack of an age progression for the Late Cretaceous alkaline magmatism of the onshore and offshore WIM suggests that this magmatism is not simply controlled by the translation of Iberia over an individual hot spot. Instead, this fact suggests that the magmatism and its emplacement is associated with various

factors, such as the changes in Iberian plate kinematics, pre-existing Variscan and Mesozoic rifting faults of and the large size of the hot mantle anomaly. The occurrence of the MTR seamounts (103 to 80 Ma) along the ocean-continent transitional domain suggests this acted as a northerly trending major deep rooted shear zone probably active during the rotation of Iberia.

- From 80 Ma to the end of the Cretaceous, the offshore magmatism in the WIM seems to be limited to the Ormonde peak of the Gorringe bank (65 Ma) although the NW Tore seamount shows a 80.5 Ma age. On the other hand, this was the time when magmatism was most abundant in the onshore WIM, which might reflect the drift of continental Iberia over an anomalous, hotter area of the mantle.

- The smaller volume magma produced in the onshore, when compared with the offshore is probably associated with the higher thickness of the lithosphere in this region, which reduced the quantity of produced magma and/or accommodated the intrusions at various levels of discontiniuties.

- During their ascension, magmas appear to have taken advantage of a series of pre-existing structures, related with the Variscan orogeny and/or with Mesozoic rifting.

- The emplacement of the magmatic bodies in upper crustal levels, occurred at the intersection of the WNW-ESE to E-W rift transfer faults with NE-SW and NNW-SSE fault systems, both of which consist of reactivations of Paleozoic fauls. Some of these WNW-ESE to E-W, which are sub-parallel to the oceanic transform faults, appear to be major lithospheric discontinuities that controlled the magma emplacement and transport along large areas, such as the Tore-Sintra fault in the Estremadura spur.

- As a corollary, it is concluded that the timing, location and certain geochemical characteristics of the Late Cretaceous alkaline magmatism in the WIM are associated with the regional crustal/lithospheric structure and changes in the kinematics of the Iberian plate and its overall motion over the Canary hot spot.

10. Suggestions for future work

- Collection of further geochronological data on the LVC, many of the small volume occurrences it is associated with (sills, plugs and dykes), the Mafra radial dyke complex, the Cascais dykes, the Fontanelas seamount and some of the basic alkaline occurrences in Algarve basin would allow for a refinement of the timing of this magmatism and dispel doubts over the occurrence of an age progression or several pulses of activity for this event, as well as provide a better frame for the relation between the Late Cretaceous alkaline magmatism of the WIM and its contemporaneous geodynamic context.

- A more complete geochronological dataset would also allow to better constrain the timing of the metasomatic processes that took place before the emplacement and extrusion of certain Late Cretaceous alkaline occurrences.

- The characteristics of this metasomatic event could be known in more detail if the more basic, uncontaminated lithologies are sampled and studied. To avoid problems with the composition of the rocks being modified by crystal accumulation, matrix separates should be prepared and analyzed instead of whole rock samples.

- Detailed mapping of the Sines and Sintra complexes and their dyke complexes in order to distinguish different facies among the already identified lithologies and understand the relation between mafic, intermediate and felsic outcrops and between these and the dykes they are intruded by. This, accompanied with further geochemical and geochronologic data, would lead to improvements in the emplacement histories and evolution mechanisms of these complexes.

- This detailed mapping would also allow for the in depth study of the crystal fractionation and accumulation processes in these complexes through whole rock and mineral chemistry analyzes, namely if the different types of gabbro really do represent different levels of the same magma chamber.

- Comprehensive sampling and mineral chemistry study of the xenoliths present in this province, namely in the Ribeira d'Ilhas plugs and Eiras do Faião sill. This would allow a better characterization of the crystallization conditions, including parental melt composition, depth and temperature. It would also provide new information on the relation between these xenoliths and the magmas where they are contained.

- Detailed mineral chemistry, including in situ trace elements and isotopic analysis made by LA-ICP-MS of the xenocrysts that show reverse zoning and are evidence for the occurrence of magma mixing at depth. This would result in a better understanding of the crystallization conditions and composition of the parental magma of these cores.

- Sampling, geochemical and geochronological analyses of the remaining seamounts between Fontanelas and Tore and of the seamounts NW of Tore between this seamount and the King's Trough. This would allow the characterization of these rocks and determine whether they are associated with the same Late Cretaceous Alkaline episode in the WIM associated with the Canaries plume, or if they are related to any other context.

- The collection of paleomagnetic data on the dated rocks would also improve the paleogeographic reconstitutions of Iberia during the Late Cretaceous and allow for a better assessment of geodynamic context contemporaneous of the studied magmatic episode.

11. References

Abouchami, W. A., Galer, S. J., Koschinsky, A. K., 1999. Pb and Nd isotopes in NE Atlantic Fe – Mn crusts : Proxies for trace metal paleosources and paleocean circulation. *Geochimica et Cosmochimica Acta*, *63,* 10, pp. 1489 -1505.

Abranches, M. C., Canilho, M. H., 1981. Estudos de geocronologia e geologia isotópica pelo método de Rubídio-Estrôncio, dos três maciços Mesozóicos Portugueses. Bol. Soc. Geol. Portugal, t. XXII, pp. 385-390.

Adam, J., Green, T.H. Sie, S.H., 1993. Proton microprobe determined partitioning of Rb, Sr, Ba, Y, Zr, Nb and Ta between experimentally produced amphiboles and silicate melts with variable F content. *Chemical Geology,* 109, pp. 29-49.

Adam, J., Green, T., 2006. Trace element partitioning between mica- and amphibole-bearing garnet lherzolite and hydrous basanitic melt: 1. Experimental results and the investigation of controls on partitioning behaviour. *Contributions to Mineralogy and Petrology*, *152,*1, pp. 1-17.

Afilhado, A., Moulin, M., Cunha, T., Lourenço, N., Neves, M. C., Pinheiro, L., Terrinha, P., Rosas, F., Matias L., Pinto de Abreu M., 2010. A Margem Oeste Portuguesa, *In* R. Dias, A. Araújo, P. Terrinha, J. C. Kullberg (Eds.) - *Geologia de Portugal no contexto da Ibéria*. Escolar Editora, in press.

Aignertorres, M., Blundy, J., Ulmer, P., Pettke, T., 2007. Laser Ablation ICPMS study of trace element partitioning between plagioclase and basaltic melts: an experimental approach. *Contributions to Mineralogy and Petrology*, 153, pp. 647-667.

Albarede, F., Telouk, P., Blichert-Toft, J., Boyet, M., Agranier, A., Nelson, B., 2004. Precise and accurate isotopic measurements using multiple-collector ICPMS. *Geochimica et Cosmochimica Acta*, 68, 12, pp. 2725-2744.

Alvaro, M. Apalategui, O., Baena, J., Balcells, R., Barnolas, A., Barrera, J.L., Bellido, F., Cueto, L., Díaz de Neira, A., Elízaga, E., Fernández-Gianotti, J. R., Ferreiro, E., Gabaldón, V., García-Sansegundo, J., Goméz, J, Heredia, N., Hernández-Urroz, J., Hernández-Samaniego, A., Lendínez, A., Levya, F., López-Olmedo, F., Lorenzo, S., Martín, L., Martín Serrano, A., Matas, J., Monteserrín, V., Nozal, F., Olive, A., Ortega, E., Piles, E., Ramírez, J., Robador, A., Roldán, F., Rodríguez, L., Ruiz, P., Ruiz, M. T., Sánchez-Carretero, R., Teixell, A., 1994. Mapa Geológico Nacional a escala 1:1.000.000. IGME, Madrid.

Alves, T., Manuppella, G., Gawthorpe, R. L., Hunt, D. W., Monteiro, J. H., 2003. The depositional evolution of diapir- and fault-bounded rift basins: examples from the Lusitanian Basin of West Iberia. *Sedimentary Geology*, *162,* 3-4, pp. 273-303.

Alves, T. M., Moita, C., Sandnes, F., Cunha, T., Monteiro, J. H., Pinheiro L. M., 2006. Mesozoic– Cenozoic evolution of North Atlantic continental- slope basins: The Peniche basin, western Iberian margin, *AAPG Bull*., 90, pp. 31 – 60.

Alves, T. M., Moita, C., Cunha, T., Ullnaess, M., Myklebust, R., Monteiro, J. H., Manupella, G., 2009. Diachronous evolution of Late Jurassic–Cretaceous continental rifting in the northeast Atlantic (west Iberian margin). *Tectonics*, *28,*4, pp. 1-32.

Alves, C., 2010. Estudo petrológico e geoquímico do magmatismo transicional na Bacia Lusitânica, Tese de Mestrado, Universidade de Lisboa, 127 p.

Ancochea, E., Huertas, M. J., Ibarrola, E., Snelling, E., 1992. Actividad magmática Cretacica en el Noroeste de la Peninsula Ibérica. *Ver. Soc. Geol. España*, 5, 3-4, pp. 65-71.

Andersen, D.J., Lindsley, D.H., 1985. New (and final!) models for the Ti-magnetite/ilmenite geothermometer and oxygen barometer. Abstract AGU 1985 Spring Meeting Eos Transactions. American Geophysical Union 66 (18), p. 416.

Anderson, J. L., Smith, D. R., 1995. The effects of temperature and oxygen fugacity on the Al-in-hornblende barometer: American Mineralogist, v. 80, pp. 549–559.

Andronikov, A.V., Foley, S.F., 2002. Trace element and Nd-Sr isotopic composition of ultramafic lamprophyres from the East Antartic Beaver Lake area. *Chemical Geology*, 175, pp. 291–305.

Antunes, I. M., Neiva, A., Silva, M., Corfu, F., 2008. Geochemistry of S-type granitic rocks from the reversely zoned Castelo Branco pluton (central Portugal). *Lithos*, 103, 3-4, pp. 445-465.

Aoki, K., Shiba, I., 1973. Pyroxenes from lherzolite inclusions of Itinome-gata, Japan. *Lithos*, 6, 1, pp. 41-51.

Armienti, P., Gasperini, D., 2007. Do we really need mantle components to define mantle composition? *Journal of Petrology,* 48, 1, pp. 693-709.

Arzamastsev, A. A., Mitrofanov, F. P., 2009. Paleozoic plume-lithospheric processes in northeastern Fennoscandia: Evaluation of the composition of the parental mantle melts and magma generation conditions. *Petrology*, *17,* 3, pp. 300-313.

Asmeron Y., Jacobsen, S., Wernicke, B., 1994. Variations in magma source regions during large-scale continental extension, Death Valley region, western United States. *Earth and Planetary Science Letters*, 125, pp. 235-254.

Assunção, C. F. T., 1937. A piroxena do filão da Falagueira (Amadora). *Bol. M. L. M. G. F. C. Lisboa*, 2ª série, 6.

Auzende, J.-M., Olivet, J.-L., Charvet, J., Le Lann, A., Le Pichon, X., Monteiro, J. H., Nicolas, A., Ribeiro, A., 1978. Sampling and observation of oceanic mantle and crust on Gorringe Bank. *Nature,* 273, pp. 45-48.

Azevedo, M. R., Nolan, J., 1998. Hercynian late-post-tectonic granitic rocks from the Fornos de Algodres area (northern Central Portugal). *Lithos*, 44, pp. 1-20.

Azevedo, M. R., Aguado, B. V., 2010. Origem e instalação de granitóides Variscos na Zona Centro Ibérica. *In* R. Dias, A. Araújo, P. Terrinha, J. C. Kullberg (Eds.) - *Geologia de Portugal no contexto da Ibéria*. Escolar Editora, in press.

Badagola, A., 2008. Evolução morfo-tectónica da plataforma continental do Esporão da Estremadura. Tese de Mestrado. Universidade de Lisboa, p. 171.

Ballentine C. J., van Keken P. E., Porcelli D., Hauri E., 2002. Numerical models, geochemistry, and the zero paradox noble gas mantle. *Phil. Trans. Roy. Soc. London A*, 360, pp. 2611–2631.

Bandrés, A., Eguiluz, L., Pin, C., Paquette, J. L., Ordonez, B., Le Fevre, B., 2004. The northern Ossa-Morena Cadomian batholith (Iberian Massif): magmatic arc origin and early evolution. *International Journal of Earth Sciences (Geologische Rundschau)*, *93*, pp. 860-885.

Barnes, C. G., Prestvik, T., Sundvoll, B., Surratt, D., 2005. Pervasive assimilation of carbonate and silicate rocks in the Hortavær igneous complex, north-central Norway. *Lithos*, *80,* 1-4, pp. 179-199.

Bea, F., Montero, P., Zinger, T., 2003. The nature, origin, and thermal infuence of the granite source layer of Central Iberia. *Journal of Geology*, *111*, pp. 579-595.

Beattie, P., Ford, C., Russell, D. 1991. Partition coefficients for olivine-melt and orthopyroxene-melt systems. *Contributions to Mineralogy and Petrology*, *109*, pp. 212-224.

Beattie, P., 1993. Olivine-melt and orthopyroxene-melt equilibria. *Contributions to Mineralogy and Petrology*, *115*, pp. 103-111.

Beattie, P. 1994. Systematics and energetics of trace-element partitioning between olivine and silicate melts: Implications for the nature of mineral/melt partitioning. *Chemical Geology*, 117, pp. 57-71.

Beattie, P., Ford, C., Russell, D., 1991. Partition coefficients for olivine-melt and orthopyroxene-melt systems. *Contributions to Mineralogy and Petrology*, *109*, pp. 212-224.

Beard, J. S., Fullagar, P., Sinha, K., 2002. Gabbroic Pegmatite Intrusions, Iberia Abyssal Plain, ODP Leg 173, Site 1070: Magmatism during a Transition from Non-volcanic Rifting to Sea-floor Spreading. *Journal of Petrology*, *43,* 5, pp. 885-905.

Bedard, J. H., 1994. Mesozoic east North American alkaline magmatism: Part 1. Evolution of Monteregian lamprophyres, Quebec, Canada. *Geochimica et Cosmochimica Acta*, *58*, pp. 95-112.

Bédard, J., 2006. Trace element partitioning in plagioclase feldspar. *Geochimica et Cosmochimica Acta*, *70,* 14, pp. 3717-3742.

Bernard-Griffiths, J., Gruau, G., Cornen, G., Azambre, B., Mace, J., 1997. Continental Lithospheric Contribution to Alkaline Magmatism: Isotopic (Nd, Sr, Pb) and Geochemical (REE) Evidence from Serra de Monchique and Mout Ormonde Complexes. *Journal of Petrology,* 38, 1, pp. 115-132.

Bernstein, S., Kelemen, P. B., Tegner, C., Kurz, M. D., Blusztajn, J., Kent Brooks, C., 1998. Post-breakup basaltic magmatism along the East Greenland Tertiary rifted margin. *Earth and Planetary Science Letters*, 160, pp. 845-862.

Beslier, M.-O., Girardeau, J., Boillot, G., 1990. Structure and kinematics of emplacement of peridotites uplifted during continental rifting results of the Galinaute dives on Galicia margin (Spain). *Tectonophysics,* 184, pp. 321-343.

Bindeman, I., Davis, I. A., Drake, M. J., 1998. Ion microprobe study of plagioclase-basalt partition experiments at natural concentration levels of trace elements. *Geochimica et Cosmochimica Acta*, *62.* 7, pp. 1175-1193.

Bindi, L., Cellai, D., Melluso, L., Conticelli, S., Morra, V., Menchetti, S., 1999. Crystal chemistry of clinopyroxene from alkaline undersaturated rocks of the Monte Vulture Volcano, Italy. *Lithos*, 46, 2, pp. 259-274.

Black, R., Lameyre, J., Bonin, B., 1985. The structural setting of alkaline complexes. *Journal of African Earth Sciences*, 3, 1-2, pp. 5-16.

von Blanckenburg, F., O'Nions, R., Heinz, J., 1996. Distribution and sources of pre-anthropogenic lead isotopes in deep ocean water from FeMn crusts. *Geochimica et Cosmochimica Acta*, *60,* 24, pp. 4957-4963.

Blundy, J. D., Wood, B. J., 1991. Crystal-chemical controls on the partitioning of Sr and Ba between plagioclase feldspar, silicate melts, and hydrothermal solutions. *Geochimica et Cosmochimica Acta*, *55*, pp. 193-209.

Blundy, J., Dalton, J., 2000. Experimental comparison of trace element partitioning between clinopyroxene and melt in carbonate and silicate systems, and implications for mantle metasomatism. *Contributions to Mineralalogy Petrology*, 139, pp. 356–371.

Blundy, J., Cashman, K., Humphreys, M., 2006. Magma heating by decompression-driven crystallization beneath andesite volcanoes. *Nature*, *443*, pp. 76-80.

Bodinier, J., Godard, M., 2003. Orogenic, ophiolitic and abyssal Peridotites. In *Treatise of Geochemistry,* 2, pp. 103-152.

Boillot, G., Féraud, G., Recq, M., Girardeau, J., 1989. Undercrusting by serpentinite beneath rifted margins. *Nature*, 341, pp. 523-525.

Bohrson, W. A., Spera, F. J., 2001. Energy-Constrained Open System Magmatic Processes II: Application of Energy-Constrained Assimilation-Fractional Crystallization (EC-AFC) model to magmatic systems. *Journal of Petrology*, 42, 5, pp. 1019-1041.

Bonhomme, M., Mendes F., Vialette, Y., 1961. Âges absolus par la méthode au strontium de granites de Sintra et de Castro daire au Portugal. *C.R. Acad. Sci. Paris*, 252, pp. 3305-3306.

Borrego, J., 2009. Cartografia Geológico-Estrutural de um sector da Zona de Ossa-Morena (Sector de Estremoz – Barrancos) e sua interpretação Tectónica. Tese de Doutoramento, Universidade de Évora, 479 p.

Brandenburg, J. P., van Keken, P. E., 2007. Deep storage of oceanic crust in a vigorously convecting mantle. Journal of Geophysical Research, 112, B06403.

Bryce, J. G., DePaolo, D. J., 2004. Pb isotopic heterogeneity in basaltic phenocrysts. Geochimica et Cosmochimica Acta, 68, 21, pp. 4453-4468.

Burke, K., Torsvik, T. H., 2004. Derivation of Large Igneous Provinces of the past 200 million years from long-term heterogeneities in the deep mantle. *Earth and Planetary Science Letters*, 227, 3-4, pp. 531-538.

Campbell, I., 2007. Testing the plume theory. *Chemical Geology*, 241, 3-4, pp. 153-176.

Canilho, M. H., 1972. Estudo geológico-petrográfico do maciço eruptivo de Sines. *Bul. Mus. Lab. Min. Geol. Fac. Ciênc. Univ. Lisboa,* 12, 2.

Canilho, M. H., Abranches, M. C., 1982. Rb-Sr geochronology of the Sines alkaline complex. *Comun. Serv. Geol. Portugal*, t. 68, 2, pp. 237-240.

Casas-Sainz, A. M., Gil-Imaz, A., 1992. Extensional subsidence, contractional folding and thrust inversion of the eastern Cameros basin, northern Spain. *Geologische Rundschau*, 86, 4, pp. 802-818.

Casquet, A., Galindo, C., Gonzalez-Casado, J. M., Alonso, A., Mas R., Rodas, M., Garcia, E., Barrenechea, J. F., 1992. El metamorfismo en la cuenca de los Cameros. Geocronologia e implicaciones tectónicas. *Geogaceta*, 11, pp. 22-25.

Capdevilla R., Mougenot, D., 1988. Pre-Mesozoic basement of the western Iberian continental margin and its place in the Variscan belt, in Boilot and Winterer (eds.), *Proc. Ocean Drill. Prog. Sci. Res*. 103, pp. 3-12.

Carmichael, I. S. E., Turner, F., Verhoogen, J., 1974. Igneous petrology. McGraw-Hill, New York, 739 pp.

Carracedo, M., Larrea, F. J., Alonso, A., 1999. Estructura y organizacion de las coladas submarinas de las lavas almohadilladas de edad Cretacica que afloran en la cordiller Vasco-Cantabrica. *Estudios Geol*., 55, pp. 209-222.

Cebriá, J. M., López-Ruiz, J., Doblas, M., Martins, L. T., Munhá, J. M., 2003. Geochemistry of the Early Jurassic Messejana-Plasencia dyke (Portugal-Spain); Implicatons on the Origin of the Central Atlantic Magmatic Province. *Journal of Petrology*, 44, 3, pp. 547-568.

Chang, Z., Vervoort, J.D., Knaack, C., McClelland, W.C., 2006. U-Pb dating of zircon by LA-ICP-MS. *Geochemistry, Geophysics, Geosystems*, 7, no. 5, p. 1-14, Q05009.

Chaminé, H., Moço, H., Rocha, L., Gomes, F., Garcia, C., Flores, C., 2000. Middle Paleozoic metacarbonates and black shales: preliminary characterization based on geochemical, mineralogical and petrological markers. *Actas IIIer Congreso Ibérico de Geoquímica*, pp. 337-341.

Charpentier, S., Kornijrob, J., Chazot, G., Cornen, G., 1998. Interaction entre lithosphere et asthenosph ere au tours de l'ouvertur oceanique : donnes isotopiques preliminaires sur la marge passive de la Galice. *C. R. Acad. Sci. Paris, Sciences de la terre et des planetes*, 326, pp. 757-762.

Casquet, C., Galindo, C., Tornos, F., Velasco, F., Canales, A. 2001. The Aguablanca Cu-Ni ore deposit (Extremadura, Spain), a case of synorogenic orthomagmatic mineralization: age and isotope composition of magmas (Sr-Nd) and ore (S). *Ore Geol. Rev*, 18, pp. 237-250.

Chazot, G., Menzies, M.A., Harte, B., 1996. Determination of partition coefficients between apatite, clinopyroxene, amphibole, and melt in natural spinel lherzolites from Yemen: Implications for wet melting of the lithospheric mantle. *Geochimica et Cosmochimica Acta* 60, (3), pp. 423-437.

Chazot, G., Charpentier, S., Kornprobst, J., Vannucci, R., Luais, B., 2005. Lithospheric mantle evolution during continental break-up: the West Iberia non-volcanic passive margin. *Journal of Petrology*, *46*, pp. 2527-2568.

Chen, J., Wasserburg, G., Vondamm, K., Edmond, J., 1986. The U-Th-Pb systematics in hot springs on the East Pacific Rise at 21°N and Guaymas Basin. *Geochimica et Cosmochimica Acta*, *50,* 11, pp. 2467-2479.

Chadwick, J. P., Troll, V. R., Morgan, D., Gertisser, R., Waight, T. E., Davidson, J. O., 2007. Carbonate Assimilation at Merapi Volcano, Java, Indonesia: Insights from Crystal Isotope Stratigraphy. *Journal of Petrology*, 48, 9, pp. 1793-1812.

Chase, C.G., 1981. Oceanic island Pb: two-stage histories and mantle evolution. *Earth Planet. Sci. Lett.*, 52, pp. 277– 284.

Chauvel, C., Hofmann, A.W., Vidal, P., 1992. HIMU-EM: the French Polynesian connection. *Earth and Planetary Science Letters*, 110, pp. 99–119.

Chesley, J., Rudnick, R. L., Lee, C., 1999. Re-Os systematics of mantle xenoliths from the East African Rift: age, structure, and history of the Tanzanian craton. *Geochimica et Cosmochimica Acta*, *63,* 7-8, pp. 1203-1217.

Chichorro, M., Pereira, M. F., Williams, I. S., Pin, C., Silva, J. B., 2008. Cambrian ensialic rift-related magmatism in the Ossa-Morena Zone (Évora–Aracena metamorphic belt, SW Iberian Massif): Sm–Nd isotopes and SHRIMP zircon U–Th–Pb geochronology. *Tectonophysics*, 461, pp. 91 - 113.

Class, C., Goldstein, S. L., 1997. Plume–lithosphere interactions in the ocean basins; constraints from the source mineralogy. *Earth and Planetary Science Letters*, 150, 3–4, pp. 245–260.

Class, C., Goldstein, S. L., 2005. Evolution of helium isotopes in the Earth's mantle. *Nature*, *436,* 7054, pp. 1107-12.

Class, C., Goldstein, S. L., Altherr, R., Bachélery, P., 1998. The Process of Plume-Lithosphere Interactionsin the Ocean Basins-the Caseof Grande Comore. *Journal of Petrology*, *39*, 5, pp. 881-903.

Clavijo, E. Valadares, V., 2003. O maciço alcalino de Monchique (SW Português): estrutura e modelo de instalação na crosta superior. *Com. Inst. Geol. e Min*., t.90 pp. 43-64.

Coltorti, M., Beccaluva, L., Bonadiman, C., Faccini, B., Ntaflos, T., Siena, F., 2004. Amphibole genesis via metasomatic reaction with clinopyroxene in mantle xenoliths from Victoria Land, Antarctica. *Lithos*, *75,* 1-2, pp. 115-139.

Condie, K. C., 1991. Another look at rare earth elements in shales, Geochimica *et Cosmochimica Acta*, 55, 9, pp. 2527-2531.

Cornen, G., 1982 - Petrology of the alkaline volcanism of Gorringe Bank (southwest Portugal). *Marine Geology,* 47, 1-2, pp. 101-130.

Cornen G., Girardeau, J., Monnier, C., 1999. Basalts, underplated gabbros and pyroxenites record the rifting process of the West Iberian Margin. *Mineral. Petrol*., 67, pp. 111-142.

Costa, C., 1980. Estudo estrutural do campo filoniano Oeiras-Cabo Raso. Relatório de Estágio Científico. *FCUL, Univ. Lisboa*.

Costa, A. A., Machado, O., 1929. Les basaltes portugais (aspects et chronologie des eruptions). *Bul. Vulc*. 19 a 22, 6º an, pp. 65-72.

Crough, S.T., 1983. Hotspot Swells, *Ann. Rev. Earth Planet. Sci.*, 11, pp. 165-193.

Daley, E.E., DePaolo, D.J., 1992. Isotopic Evidence for Contrasting Upper Crust and Lower Lithosphere Strain Histories During Extension: SE Great Basin, *Geology*, 20, pp. 104-108.

Dalpe, C., Baker, D.R., 1994. Partition coefficients for rare-earth elements between calcic amphibole and Ti-rich basanitic glass at 1.5 Gpa, 1100º C. *Mineralogical Magazine*, 58, pp. 207-208.

Danyushevsky, L. V., 2001. The effect of small amounts of H2O on crystallisation of mid-ocean ridge and backarc basin magmas. *Journal of Volcanology and Geothermal Research*, 110, 3-4, pp. 265-280.

Dasgupta, R., Hirschmann,M.M., Stalker, K., 2006. Immiscible transition from carbonate- rich to silicate-richmelts in the 3 GPameltinginterval of eclogite+CO2 and genesis of silica-undersaturated ocean island lavas. *Journal of Petrology,* 47, pp. 647–671.

Dasgupta, R., Hirschmann, M. M., Smith, N. D., 2007. Partial Melting Experiments of Peridotite + CO_2 at 3 GPa and Genesis of Alkalic Ocean Island Basalts. *Journal of Petrology*, *48*, 11, pp. 2093-2124.

Dasgupta, R., Hirschmann, M. M., McDonough, W. F., Spiegelman, M., Withers, A. C., 2009. Trace element partitioning between garnet lherzolite and carbonatite at 6.6 and 8.6 GPa with applications to the geochemistry of the mantle and of mantle-derived melts. *Chemical Geology*, 262, 1-2, pp. 57-77.

Davis, A. S., Clague, D. A., Paduan, J. B., 2007. Diverse Origins of Xenoliths from Seamounts at the Continental Margin, Offshore Central California. *Journal of Petrology*, *48,* 5, pp. 829-852.

Dautria, J.M., Dupuy, C., Takherist, D., Dostal, J., 1992. Carbonate metasomatism in the lithospheric mantle: peridotitic xenoliths from a melilititic district of the Sahara basin. *Contributions to Mineralogy and Petrology*, 111, pp. 37–52.

Dawson, J. B., Hill, P. G., Kinny, P. D., 2001. Mineral chemistry of a zircon-bearing, composite, veined and metasomatised upper-mantle peridotite xenolith from kimberlite. *Contributions to Mineralogy and Petrology*, *140*, pp. 720-733.

Deer, W. A., Howie, R. A., Zussman J., 1966. Rock-forming minerals.

DePaolo, D. J., 1981. Trace element and isotopic effects of combined wallrock assimilation and fractional crystallization. *Earth and Planetary Science Letters*, 53, pp. 189–202.

DePaolo, D. J., Wasserburg, G. J., 1976. Nd isotopic variations and petrogenetic model. *Geophysical Research Letters*, 3, pp. 249-252.

Dias, G., Simões, P., Ferreira, N., Leterrier, J., 2002. Mantle and Crustal Sources in the Genesis of Late-Hercynian Granitoids (NW Portugal): Geochemical and Sr-Nd Isotopic Constraints. *Gondwana Research*, *5,* 2, pp. 287-305.

Dinis, J.L., Rey, J., Cunha, P.P., Callapez, P., Pena dos Reis, R., 2008. Stratigraphy and allogenic controls of the western Portugal Cretaceous: an updated synthesis *Cretaceous Research*, 29, 5-6, pp. 772-780.

Dixon, J., Clague, D. A., Cousens, B., Monsalve, M. L., Uhl, J., 2008. Carbonatite and silicate melt metasomatism of the mantle surrounding the Hawaiian plume: Evidence from volatiles, trace elements, and radiogenic isotopes in rejuvenated-stage lavas from Niihau, Hawaii. *Geochemistry Geophysics Geosystems*, *9,* 9.

Dobosi, G., 1989. Clinopyroxene zoning patterns in the young alkali basalts of Hungary and their petrogenetic significance t. *Mineralogy and Petrology*, *101*, pp. 112-121.

Dobosi, G., Fodor, R. V., 1992. Magma fractionation, replenishment, and mixing as inferred from green-core clinopyroxenes in Pliocene basanite, southern Slovakia. *Lithos*, *28,* 2, pp. 133-150.

Dobosi, G., Jenner, G. A., 1999. Pyroxene megacrysts from the Nograd volcanic province, Petrologic implications of trace element variation in clinopyroxene megacrysts from Nograd volcanic province, north Hungary: a study by laser ablation microprobe-inductively coupled plasma-mass spectrometry. *Lithos*, *46*, pp. 731-749.

Dostal, J., Dupuy, C., Carron, J.P., Dekerneizon, M.L. and Maury, R.C., 1983. Partition-Coefficients of Trace-Elements - Application to Volcanic-Rocks of St-Vincent, West-Indies. *Geochimica et Cosmochimica Acta*, 47, 3, pp. 525-533.

Dostal, J., Owen, J. V., 1998. Cretaceous alkaline lamprophyres from NE Czech Republic: geochemistry and petrogenesis. *Geol. Rundsch*., 87, pp. 67-77.

D'Orey, F., Palácios, P., 1986. Chromian spinels in the basalts from the Lisbon volcanic complex (Portugal) and their petrogenetic implications. *Ciências da Terra*, 8, pp. 191-202.

Droop, G. T., 1987. A general equation for estimating Fe3+ concentrations in ferromagnesian silicates and oxides from microprobe analyses, using stoichiometric criteria. *Mineralogical Magazine*, 51, 3, pp. 431-435.

Duda, A., Schmincke, H., 1985. Polybaric differentiation of alkali basaltic magmas: evidence from green-core clinopyroxenes (Eifel, FRG). *Contributions to Mineralogy and Petrology*, *91*(4), pp. 340-353.

Duggen, S., Hoernle, K. A., Hauff, F., Bouabdellah, M., Thirlwall, M. F., 2009. Flow of Canary mantle plume material through a subcontinental lithospheric corridor beneath Africa to the Mediterranean. *Geology*, 37, 3, pp, 283-286.

Dunn, A. M., Reynolds, P. H., Clarke, D., Ugidos J., 1998. A comparison of the age and composition of the Shelburne dyke, Nova Scotia, and the Messejana dyke, Spain. *Can. J. Earth Sci*, 35, 10, pp. 1110-1115.

Dupuy, C., Liotard, J.M., Dostal, J., 1992. Zr/Hf fractionation in intraplate basaltic rocks: Carbonate metasomatism in the mantle source. *Geochimica et Cosmochimica Acta*, 56, 6, pp. 2417-2423.

Duncan, R. A. 1984. Age Progressive Volcanism in the New England Seamounts and the Opening of the Central Atlantic Ocean. *Journal of Geophysical Research*, *89,* B12, pp. 9980-9990.

Eggins, S. M., Woodhead, J. D., Kinsley, L. P. J., Mortimer, G. E., Sylvester, P., McCulloch, M. T., Hergt, J. M., Handler, M. R., 1997. A simple method for the precise determination of > 40 trace elements in geological samples by ICPMS using enriched isotope internal standardization. *Chemical Geology*, 134, 4, pp. 311-326.

Elburg, M., Vroon, P., van der Wagt, B., Tchalikian, A., 2005. Sr and Pb nisotopic composition of five USGS glasses (BHVO-2G, BIR-1G, BCR-2G, TB-1G, NKT-1G). *Chemical Geology* 223, pp. 196-207.

Elkins Tanton, L. T., Hager, B. H., 2000. Melt intrusion as a trigger for lithospheric foundering and the eruption of the Siberian flood basalts. *Geophysical Research Letters*, 27, 23, pp. 3927-3940.

Ellam, R. M., 1992. Lithospheric thickness as a control on basalt geochemistry. *Geology*, 20, pp. 153-156.

Esperanza, S., Carlson, R.W., Shirey, S.B. and Smith, D., 1997. Dating crust-mantle separation: Re-OS isotopic study of mafic xenoliths from central Arizona. *Geology,* 25, pp. 651-654.

Fabries J., Lorand J.-P., Bodinier, J.-L., 1998. Petrogenetic evolution of orogenic lherzolite massifs in the central and western Pyrenees. *Tectonophysics*, 292, 1-2, pp. 145-167.

Falloon T. J., Green D. H., 1990. Solidus of carbonated fertile perido- tite under fluid-saturated conditions. *Geology*, 18, pp. 198–199

Farley, K., Natland, J., Craig, H., 1992. Binary mixing of enriched and undegassed (primitive?) mantle components (He, Sr, Nd, Pb) in Samoan lavas. *Earth and Planetary Science Letters*, *111,* 1, pp. 183-199.

Feigenson, M. D., Patino, L. C., Carr, M. J., 1996. Constraints on partial melting imposed by rare earth element variations in Mauna Kea basalts. *Journal of Geophysical Research*, 101, pp. 11815–11829.

Féraud, G., Gastaud, J., Auzende, J.-M., Olivet, J.-L., Cornen, G., 1982. $^{40}Ar/^{39}Ar$ ages for the alkaline volcanism and basement of the Gorringe Bank, North Atlantic Ocean, *Earth and Planetary Science Letters*.,57, pp. 211-226.

Féraud, G., York, D., Mével, C., Cornen, G., Hall, C., Auzend, J., 1986. Additional ^{40}Ar-^{39}Ar dating of the basement and alkaline volcanisme of Gorringe Bank (Atlantic Ocean). *Earth and Planetary Science Letters*, 79, pp. 255-269.

Ferreira, M. R. P., Macedo, C. R., 1979. K-Ar ages of the Permian-Mesozoic basaltic activity in Portugal. *Abstracts VI Europ. Col. Geochron., Cosmochron. and Isotope Geology,* Norway, pp. 26-27.

Ferreira, M. P.; Macedo, C. R.; Ferreira, J. F., 1988. K-Ar Geochronology in the Selvagens, Porto Santo and Madeira Islands (Eastern Central Atlantic): A 30 m.y. Spectrum of Submarine and Subaerial Volcanism. *Abstracts of the Lunar and Planetary Science Conference*, 19, p. 325.

Ferreira, M. P.; Macedo, C. R.; Ferreira, J. F., 1988. K-Ar Geochronology in the Selvagens, Porto Santo and Madeira Islands (Eastern Central Atlantic): A 30 m.y. Spectrum of Submarine and Subaerial Volcanism. *Abstracts of the Lunar and Planetary Science Conference*, 19, p. 325.

Fidalgo Gonzáles, L., 2001. La cinématique de l'Atlantique Nord : la question de la déformation intraplaque. Thèse de doctorat, Univ. de Bretagne Occidentale, Brest, 2, 260 p., http://archimer.ifremer.fr/doc/2001/sup-1205.pdf**.**

Finn, C. Müller, D., Panter, K., 2005. A Cenozoic diffuse alkaline magmatic province (DAMP) in the southwest Pacific without rift or plume origin. *Geochemistry Geophysics Geosystems*, *6,* 2.

Fodor, R. V., Mukasa, S. B., Sial, A. N., 1998. Isotopic and trace element indications of lithospheric and asthenospheric components in Tertiary alkalic basalts , NE Brazil. *Lithos*, 43, pp. 197-217.

Foley, S., 1992. Vein-plus-wall-rock melting mechanisms in the litho- sphere and the origin of potassic alkaline magmas. *Lithos*, 28, pp. 435-453.

Foley, S., Jackson, S., Fryer, B., Greenouch, J., Jenner, G., 1996. Trace element partition coefficients for clinopyroxene and phlogopite in an alkaline lamprophyre from Newfoundland by LAM-ICP-MS. *Geochimica et Cosmochimica Acta*, *60,* 4, pp. 629-638.

Foley, S.F., Barth, M.G., Jenner, G.A., 2000. Rutile/melt partition coefficients for trace elements and an assessment of the influence of rutile on the trace element characteristics of subduction zone magmas. *Geochimica et Cosmochimica Acta*, 64, 5, pp. 933-938.

Frey, F. A., Green, D. H., Roy, S. D., 1978. Integrated models of basalt petrogenesis: a study of quartz tholeiites to olivine melilitites from south eastern Australia utilizing geochemical and experimental petrological data. *Journal of Petrology*, 19, pp. 463–513.

Furman, T., 1995. Melting of metasomatized subcontinental lithosphere: undersaturated mafic lavas from Rungwe, Tanzania. *Contrib. Mineral. Petrol*., 122, pp. 97-115.

Furman, T., Graham, D., 1999. Erosion of lithospheric mantle beneath the East African Rift system: geochemical evidence from the Kivu volcanic province. *Lithos*, 48, pp. 237-262.

Gao, S., Luo, Zhang, T-C., Zhang, B., Han, Y., Zhao, Z., Hu, Y., 1998. Chemical composition of the continental crust as revealed by studies in East China, *Geochimica et Cosmochimica Acta*, 62, 11, pp. 1959-1975.

Galdeano, A., Moureau, M., Pozzi, J., Berthou, P. Y., Malod J. A., 1989. New paleomagnetic results from Cretaceous sediments near Lisboa (Portugal) and implications for the rotation of Iberia. *Earth and Planetary Science Letters*, 92, pp. 95-106.

Geldmacher, J., Hoernle, K., 2000. The 72 Ma geochemical evolution of the Madeira hotspot (eastern North Atlantic): recycling of Paleozoic *Earth and Planetary Science Letters*, *183*, pp. 73-92.

Geldmacher, J., Haase, K. M., Devey, C. W. & Garbe-Schoenberg, C. D., 1998. The petrogenesis of Tertiary cone- sheets in Ardnamurchan, NW Scotland; petrological and geochemical constraints on crustal contamination and partial melting. *Contributions to Mineralogy and Petrology*, 131, pp. 196-209.

Gelmacher, J., van den Bogaard, J. P., Hoernle, K., Schminke, H. U., 2000. The $^{40}Ar/^{39}Ar$ age dating of the Madeira Archipelago and hotspot track (eastern North Atlantic). *Geochemistry, Geophysics, Geosystems*, 1, 2.

Geldmacher, J., Hoernle K.,. Bogaard, P. v. d, Duggen, S., Werner, R. 2005. New $^{40}Ar/^{39}Ar$ age and geochemical data from Seamounts in the Canary and Madeira volcanic provinces, *Earth Planetary Science Letters*, 237, pp. 85–101.

Geldmacher, J., Hoernle, K., Klügel, A., Bogaard, P., Wombacher, F., Berning, B., 2006. Origin and geochemical evolution of the Madeira-Tore Rise (eastern North Atlantic). *Journal of Gephysical Research*, 111, B9, B09206.

Gibson, S., Thompson, R., Dickin, A., Leonardos, O., 1995. High Ti and Low Ti mafic potassic magmas: Key to plume lithosphere interactions and continental flood basalt genesis. *Earth and Planetary Science Letters*, 136, pp. 49-165.

Ginibre, C., Kronz, A., Wörner, G., 2002. High-resolution quantitative imaging of plagioclase composition using accumulated backscattered electron images: new constraints on oscillatory zoning. *Contributions to Mineralogy and Petrology*, *142*, pp. 436-448.

Goldschmidt, V. M., 1954. Geochemistry. Clarendon Press, Oxford.

Gomes, C. S. R., Sant'Ovaia, H. 2000. Marcas de paleomagnetismo no maciço de Monchique. In: *Livro de Resumos da 6a Conferéncia do GGET 2000, Grupo de Geologia Estrutural e Tectónica,* Universidade de Évora, 59 pp.

Gomes, C., Pereira, L., 2004. Paleomagnetismo do Maciço de Monchique (Sul de Portugal): implicações tectónicas. *Cadernos Lab. Xeologico de Laxe*, 29, pp. 291-297.

Gomes, M., Neiva, A. 2005. Geochemistry of granitoids and their minerals from Rebordelo–Agrochao area, northern Portugal. *Lithos*, *81*, pp. 235 - 254.

Gong, Z., Langereis, C. G., Mullender, T.A.T. 2008. The rotation of Iberia during the Aptian and the opening of the Bay of Biscay. *Earth Planetary Science Letters*, 273, pp. 80–93.

Gonzalez-Clavijo, E., Valadares, V., 2003. O Maciço Alcalino de Monchique (SW Portugal): estrutura e modelo de instalação na crosta superior. Com. Inst. Geol. Min., 90, pp. 43-64.

Gorring, M. L., Kay, S. M. 2000. Carbonatite metasomatized peridotite xenoliths from southern Patagonia: implications for lithospheric processes and Neogene plateau magmatism. *Contributions to Mineralogy and Petrology*, *140*, pp. 55-72.

Gradstein, F.M., Ogg, J.G., and Smith, A.G., Agterberg, F.P., Bleeker, W., Cooper, R.A., Davydov, V., Gibbard, P., Hinnov, L.A., House, M.R., Lourens, L., Luterbacher, H.P., McArthur, J., Melchin, M.J., Robb, L.J., Shergold, J., Villeneuve, M., Wardlaw, B.R., Ali, J., Brinkhuis, H., Hilgen, F.J., Hooker, J., Howarth, R.J., Knoll, A.H., Laskar, J., Monechi, S., Plumb, K.A., Powell, J., Raffi, I., Röhl, U., Sadler, P., Sanfilippo, A., Schmitz, B., Shackleton, N.J., Shields, G.A., Strauss, H., Van Dam, J., van Kolfschoten, T., Veizer, J., and Wilson, D., 2004. A Geologic Time Scale 2004. Cambridge University Press, p. 589.

Graham, D. W., 2002. Noble Gas Isotope Geochemistry of Mid-Ocean Ridge and Ocean Island Basalts: Characterization of Mantle Source Reservoirs. D. Porcelli, C. J. Ballentine and R. Wieler (editors), *Reviews in Mineralogy and Geochemistry*, *47,* 1, pp. 247-317.

Grange, M., Schärer, U., Cornen, G., Girardeau, J., 2008. First alkaline magmatism during Iberia-Newfoundland rifting. *Terra Nova*, *20,* 6, pp. 494-503.

Grange, M., Scharer, U., Merle, R., Girardeau, J., Cornen, G. 2010. Plume-Lithosphere Interaction during Migration of Cretaceous Alkaline Magmatism in SW Portugal: Evidence from U-Pb Ages and Pb-Sr-Hf Isotopes. *Journal of Petrology*, *in press.*

Green T.H., Blundy J.D., Adam J., Yaxley G.M., 2000. SIMS deter- mination of trace element partition coefficients between garnet, clinopyroxene and hydrous basaltic liquids at 2–7.5 GPa and 1080–1200ºC. *Lithos*, 53, pp. 165–187

Griffiths, R. W., Campbell, I. H., 1990. Stirring and structure in mantle starting plumes, *Earth and Planetary Science Letters*, 99, 1-2, pp. 66-78.

Gudfinnsson, G. H., Presnall, D. C., 2005. Continuous Gradations among Primary Carbonatitic, Kimberlitic, Melilititic, Basaltic, Picritic, and Komatiitic Melts in Equilibrium with Garnet Lherzolite at 3-8 GPa. *Journal of Petrology*, *46,* 8, pp. 1645-1659.

Gurenko A.A., Hoernle K.A., Hauff F., Schmincke H.-U., Han D., Miura Y.N., Kaneoka I., 2006. Major, trace element and Nd–Sr–Pb–O– He–Ar isotope signatures of shield stage lavas

from the central and western Canary Islands: insights into mantle and crustal processes. *Chemical Geology*, 233, pp. 75–112

Gurenko, A., Hoernle, K., Sobolev, A. V., Hauff, F., Schmincke, H., 2009. Source components of the Gran Canaria (Canary Islands) shield stage magmas: evidence from olivine composition and Sr–Nd–Pb isotopes. *Contributions to Mineralogy and Petrology*, *159,* 5, pp. 689-702.

Haggerty, S.E., 1976. Opaque mineral oxides in terrestrial igneous rocks. In: Oxide Minerals. (D. Rumble, ed.). Mineralogical Society of America, *Reviews in Mineralogy*, Vol. 3.

Hanan, B. B., Graham, D. W., 1996. Lead and helium isotope evidence from oceanic basalts for a common deep source of mantle plumes, *Science*, 272, pp. 991–995.

Hansteen, T., Troll, V. 2003. Oxygen isotope composition of xenoliths from the oceanic crust and volcanic edifice beneath Gran Canaria (Canary Islands): consequences for crustal contamination of ascending magmas. *Chemical Geology*, *193,* 3-4, pp. 181-193.

Harmand, C., Cantagrel, J.-M., 1984. Le volcanisme alcalin Tertiaire et Quaternaire du Moyen Atlas Maroc : chronologie K-Ar et cadre geodynamique. *Journal of African Earth Sciences,* 2, 1, pp. 51–55.

Harry, D., Leeman, P., 1995. Partial melting of melt metasomatized subcontinental mantle and the magma source potential of the lower lithosphere. *Journal of Gephysical Research*, 100, B7, pp. 255-269.

Harry, D. L., Bowling, J. C., 1999. Inhibiting magmatism on nonvolcanic rifted margins. *Geology*, 27, 19, pp. 895-898.

Hart, S. R., Davis, K., 1978. Nickel partitioning between olivine and silicate melt. *Earth and Planetary Science Letters*, 40, 2, pp. 203-219.

Hart, S. R., 1984. A large-scale isotope anomaly in the Southern Hemisphere mantle. *Nature*, 309, pp. 753–757.

Hart, S. R., Hauri, E. H., Oschmann, L. A., Whitehead, J. A., 1992. Mantle plumes and entrainment-Isotopic evidence, *Science*, 256, pp. 517–520.

Hart, S., Dunn, T. 1993. Experimental cpx/melt partitioning of 24 trace elements. *Contributions to Mineralogy and Petrology*, 113, pp. 1-8.

Hart, S.R., Blusztajn, J., 2006. Age and geochemistry of the mafic sills, ODP Site 1276, Newfoundland margin. *Chem. Geol*., 235, 3–4, pp. 222–237.

Hauff, F., Hoernle, K., Schmidt, A., 2003. Sr-Nd-Pb composition of Mesozoic Pacific oceanic crust (Site 1149 and 801, ODP Leg 185): Implications for alteration of ocean crust and the input into the Izu-Bonin-Mariana subduction system. *Geochemistry Geophysics Geosystems*, *4,* 8.

Hauri, E. H., Whitehead, A., Hart, R. 1994. Fuid dymanics and geochemical aspects of entrainement in mantle plumes. *Journal of Geophysical Research*, *99,* B12, 24275-24300.

Hauri, E.H., 2002. Osmium isotopes and mantle convection. Philos. *Trans. R. Soc. Lond*., A 360, pp. 1–12.

Hawkesworth, C.J., Mantovani, M.S.M., Taylor, P.N., Palacz, Z., 1986. Evidence from the Paraña ossouth Brazil for a continental contribution to DUPAL basalts. *Nature*, 322, pp. 356–359.

Hawkesworth, C. J., Kempton, P. D., Rogers, N. W., Ellam, R., van Carlsten, P., 1990. Continental mantle lithosphere and shallow level enrichement processes in the Earh's mantle. *Earth and Planetary Science Letters*, 96, pp. 256-268.

Hawkesworth, C. J., Gallagher, K., 1993. Mantle hotspots, plumes and regional tectonics as causes for intraplate magmatism. *Terra Nova*, 5, pp. 552-559.

Heaman, L. M., LeCheminant, A. N., 2001. Anomalous U-Pb systematics in mantle-derived baddeleyite xenocrysts from Ile Bizard: evidence for high temperature radon diffusion?, *Chemical Geology*, 172, 1-2, pp. 77-93.

Hemming, S., McLennan, S., 2001. Pb isotope compositions of modern deep sea turbidites. *Earth and Planetary Science Letters*, *184,* 2, pp. 489-503.

Hill, R., Roeder, P., 1974. The crystallization of spinel from basaltic liquid as a function of oxygen fugacity. *Journal of Geology*, 82, pp. 709–729.

Hilton, D.R., Macpherson, C.G., Elliott, T.R., 2000. Helium isotope ratios in mafic phenocrysts and geothermal fluids from La Palma, the Canary Islands (Spain): implications for HIMU mantle sources. *Geochim. Cosmochim. Acta,* 64, pp. 2119–2132.

Hirose, K., Kushiro, K., 1993. Partial melting of dry per- idotites at high pressure: determination of compositions of melts segregated from peridotite using aggregates of diamond. *Earth Planet. Sci. Lett.*, 114, pp. 477-489.

Hirose, K., 1997. Partial melt compositions of carbonated peridotite at 3 GPa and role of CO 2 in alkali-basalt magma generation. *Geophysical Research Letters*, *24*, pp. 2837-2840.

Hirschmann, M. M., Kogiso, T., Baker, M. B., & Stolper, E. M., 2003. Alkalic magmas generated by partial melting of garnet pyroxenite. *Geology*, *31,* 6, pp. 481-484.

Ho, K., Chen, J., Smith, A., Juang, W., 2000. Petrogenesis of two groups of pyroxenite from Tungchihsu, Penghu Islands, Taiwan Strait: implications for mantle metasomatism beneath SE China. *Chemical Geology*, 167, 3-4, pp. 355-372.

Hoernle, K., 1998. Geochemistry of Jurassic Oceanic Crust beneath Gran Canaria (Canary Islands): Implications for Crustal Recycling and Assimilation. *Journal of Petrology*, *39,* 5, pp. 859-880.

Hoernle, K., Tilton, G. Schmincke, H.-U., 1991. Sr–Nd–Pb isotopic evolution of Gran Canaria: evidence for shallow enriched mantle beneath the Canary Islands. *Earth and Planetary Science Letters*, 106, pp. 44–63.

Hoernle, K., Zhang, Y.-S., Graham, D., 1995. Seismic and geochemical evidence for large scale mantle upwelling beneath the eastern Atlantic and western and central Europe. *Nature*, 374, pp. 34-39.

Hofmann, A. W., 1988. Chemical differentiation of the Earth: the relationship between mantle, continental crust, and oceanic crust*, Earth and Planetary Science Letters*, 90, 3, pp. 297-314.

Hofmann, A. W., 2003. Sampling Mantle Heterogeneity through Oceanic Basalts: Isotopes and Trace Elements. In *Treatise of Geochemistry, 2,* pp. 61-101.

Hofmann, A. W., White, W. M., 1980. The role of subducted oceanic crust in mantle evolution, Carnegie Inst. Washington, 79, pp. 477–483.

Holland, T., Blundy, J., 1994. Non-ideal interactions in calcic amphiboles and their bearing on amphibole-plagioclase thermometry. *Contributions to Mineralogy and Petrology*, *116*, pp. 433-447.

Hollister, L. S., Grissom, G. C., Peters, E. K., Stowell, H. H., Sisson, V. B., 1987. Confirmation of the empirical correlation of Al in hornblende with pressure of solidification of calc-alkaline plutons. *American Mineralogist*, 72, pp. 231–239.

Housh, T., Bowring, S. 1991. Lead isotopic heterogeneities within alkali feldspars: Implications for the determination of initial lead isotopic compositions. *Geochimica et Cosmochimica Acta*, 55, 8, pp. 2309-2316.

Humphreys, E. R., Niu, Y., 2009. On the composition of ocean island basalts (OIB): The effects of lithospheric thickness variation and mantle metasomatism. *Lithos*, *112,* 1-2, pp. 118-136.

Ingamells, C. O., Engels, J. C., 1976. Preparation, analysis and sampling constants for a biotite. Nat. Bur. Stand. Spec. Pub., 422, pp. 401-419.

Ignacio, C., Munoz, M., Sagredo, J., Fernandezsantin, S., Johansson, A., 2006. Isotope geochemistry and FOZO mantle component of the alkaline–carbonatitic association of Fuerteventura, Canary Islands, Spain. *Chemical Geology*, 232, 3-4, pp. 99-113.

Inverno, C. M. C., Manupella, G., Zbyszewski, G., Pais, J., Ribeiro, M. L., 1993. Notícia explicativa da Folha 42-C Santiago do Cacém. Serviços Geológicos de Portugal, Lisboa, p.75.

Ionov, D. A., Dupuy, C., O'Reilly, S. Y., Kopylova, M. G., Genshaft, Y. S., 1993. Carbonated peridotite xenoliths from Spitsbergen: implications for trace element signature of mantle carbonate metasomatism. *Earth and Planetary Science Letters*, *119*, pp. 283-297.

Irving, A.J., Frey, F.A., 1978. Distribution of Trace-Elements between Garnet Megacrysts and Host Volcanic Liquids of Kimberlitic to Rhyolitic Composition. *Geochimica et Cosmochimica Acta*, 42, pp. 771-787

Irving, A. J., Frey, F. A., 1984. Trace element abundances in megacrysts and their host basalts: Constraints on partition coefficients and megacryst genesis. *Geochimica et Cosmochimica Acta*, *48*, pp. 1201-1221.

Irving, A. J., Green, D. H., 2008. Phase Relationships of Hydrous Alkalic Magmas at High Pressures: Production of Nepheline Hawaiitic to Mugearitic Liquids by Amphibole-Dominated Fractional Crystallization Within the Lithospheric Mantle. *Journal of Petrology*, *49,* 4, pp. 741-756.

Jackson, M. G., Hart, S. R., Koppers, A., Staudigel, H., Konter, J., Blusztajn, J., Kurz, M., Russel, J., 2007. The return of subducted continental crust in Samoan lavas. *Nature*, 448*,* pp. 684-7.

Jansa, L. F., Pe-Piper, G., Loncarevic, B. D., 1993. Appalachian basement and its intrusion by Cretaceous dykes, offshore southeast Nova Scotia, Canada. *Can. J. Earth Sci.*, 30, 12, pp. 2495–2509.

Johnson, M. C., Rutherford, M. J. 1989. Experimental calibration of the aluminum-in-hornblende geobarometer with application to Long Valley caldera (California) volcanic rocks. *Geology*, *17*, pp. 837-841.

Johnson, M. C., Rutherford, M. J., Hess, P. C., 1989. Experimental study of igneous kaersutite stability with application to SNC petrogenesis. Abstracts of the Lunar and Planetary Science Conference XX, pp. 472-473.

Johnson, A., Schwab, B. 2004. Constrainst on clinopyroxene/melt partitioning REE, Rb, Sr, Ti, Cr, Zr, and Nb during mantle melting: First insights from direct peridotite melting experiments at 1.0 GPa . *Geochimica et Cosmochimica Acta*, 68, pp. 4949-4962.

Juarez, M. T., Lowrie, W., Osete, M. L., Melendez, G., 1998. Evidence of widespread Cretaceous remagnetization in the Iberian Range and its relation with the rotation of Iberia. *Earth and Planetary Science Letters*, 160, pp. 729-743.

Jung, C., Jung, S., Hoffer, E., Berndt, J. 2006. Petrogenesis of Tertiary Mafic Alkaline Magmas in the Hocheifel, Germany. *Journal of Petrology*, 47*,* 8, pp. 1637-1671.

Kaiser, E., 1914. Der Eläolithsyenitlakkolith der Serra de Mochique im südlichen Portugal.*N. J. Min. Geol. Paläont*., 39, pp. 225-268.

Kárason, H., van der Hilst, R.D., 2001. Tomographic imaging of the lowermost mantle with differential times of refracted and diffracted core phases (PKP, Pdiff). *J. Geophys. Res*. 106 (B4), pp. 6569–6588.

Karner, G.D., Shillington, D.J., 2005. Basalt sills of the U reflector, Newfoundland Basin: a serendipitous dating technique. *Geology*, 33, 12, pp. 985–988.

Kavanagh, J., Menand, T., Sparks, R., 2006. An experimental investigation of sill formation and propagation in layered elastic media. *Earth and Planetary Science Letters*, *245,* 3-4, pp. 799-813.

Kato, T., Ringwood, A.E., Irifune, T., 1988. Experimental-Determination of Element Partitioning between Silicate Pervoskites, Garnets and Liquids - Constraints on Early Differentiation of the Mantle. *Earth and Planetary Science Letters*, 89, 1, pp. 123-145.

Keen, C. E., Courtney, R. C., Dehler, S. A., Williamson, M., 1994. Decompression melting at rifted margins: comparison of model predictions with the distribution of igneous rocks on the eastern Canadian margin. *Earth and Planetary Science Letters*, 121, pp. 403-416.

Kerr, A. C., 1994. Lithospheric thinning during the evolution of continental large igneous provinces: A case study from the North Atlantic Tertiary province. *Geology*, 22, pp.1027-1030.

Kerr, A. C., Khan, M., Mahoney, J., Nicholson K., Hall, C. M., 2010. Late Cretaceous alkaline sills of the south Tethyan suture zone, Pakistan: Initial melts of the Reunion hotspot? *Lithos*, 117, 1-4, pp. 161-171.

Keshav, S., Gudfinnsson, G. H., Sen, G., Fei, Y., 2004. High- pressure melting experiments on garnet clinopyroxenite and the alkalic to tholeiitic transition in ocean-island basalts. *Earth and Planetary Science Letters* 223, pp. 365-379.

King, S. D., Anderson, D. L., 1998. Edge-driven convection. *Earth and Planetary Science Letters*, 160, pp. 289-296.

King, S. D., Ritsema, J., 2000. African hot-spot volcanism: small scale convection in the upper mantle beneath cratons. *Science*, 290, pp. 1137-1139.

Kinny, P. D., Dawson, J. B., 1992. A mantle metasomatic injection event linked to late Cretaceous kimberlite magmatism. *Nature* 360, pp. 726 – 728.

Klemme, S., van Der Laan, S. R., Foley, S. F., Gunther, D., 1995. Experimentally determined trace and minor element partitioning between clinopyroxene and carbonatite melt under upper mantle conditions. *Earth and Planetary Science Letters*, *133,* 3-4, pp. 439-448.

Klemme, S., Gunther, D., Hametner, K., Prowatke, S., Zack, T., 2006. The partitioning of trace elements between ilmenite, ulvospinel, armalcolite and silicate melts with implications for the early differentiation of the moon. *Chemical Geology*, 234, pp. 251-263.

Kogiso, T., Hirschmann, M.M., Frost, D.J., 2003. High-pressure partial melting of garnet pyroxenite: possible mafic lithologies in the source of ocean island basalts. *Earth and Planetary Science Letters,* 216, pp. 603–617.

Kogiso, T., Hirschmann, M.M., 2006. Partial melting experiments of bimineralic eclogite and the role of recycled mafic oceanic crust in the genesis of ocean island basalts. *Earth and Planetary Science Letters*, 249, pp. 188–199.

Konzett, J., Armstrong, R. A., Sweeney, R. J., Compston, W., 1998. The timing of MARID metasomatism in the Kaapvaal mantle: An ion probe study of zircons from MARID xenoliths *Earth and Planetary Science Letters*, 160, 1-2, pp. 133-145.

Konzett, J., Armstrong, R. A., Gunther, D., 2000. Modal Metasomatism in the Kaapvaal Craton Lithosphere: Constraints on Timing and Genesis from U-Pb Zircon Dating of Metasomatized Peridotites and MARID-type Xenoliths. *Contrib. Mineral. Petrol.*, *139*, pp. 704-719.

Kravuchuk, I.K., Chernysheva, I., Urosov, S., 1981. Element distribution between plagioclase and groundmass as an indicator for crystallization conditions of the basalts in the southern vent of Tolbachik. *Geochemistry International*, 17, pp. 18-24.

Kullberg, J., 2000. Evolução tectónica Mesozóica da Bacia Lusitâniana. Universidade Nova de Lisboa, Tese de Doutoramento, 361 p.

Kullberg, M. C., Kullberg, J. C., 2000. Tectónica da região de Sintra. *Memórias de Geociências*, Museu Nac. Hist. Nat. Univ. Lisboa, 2, pp.1-34.

Kullberg, J. C., Terrinha, P., Pais, J., Reis R. P., Legoinha P., 2006. Arrábida e Sintra: dois exemplos de tectónica pós.rifting da bacia Lusitaniana. *In* R. Dias, A. Araújo, P. Terrinha, J. C. Kullberg (Eds.), *Geologia de Portugal no contexto da Ibéria*. Univ. Évora, 418 p.

Kullberg, J. C., Rocha, R. B., Soares, A. F., Rey, J., Terrinha, P., Azerêdo, A. C., Callapez, P., Duarte, L. V., Kullberg, M. C., Martins, L., Miranda, R., Alves, C., Mata, J., Madeira, J., Mateus, O., Moreira, M., 2010. . A Bacia Lusitaniana: Estratigrafia, Paleogeografia e Tectónica *In* R. Dias, A. Araújo, P. Terrinha, J. C. Kullberg (Eds.) *Geologia de Portugal no contexto da Ibéria*. Escolar Editora, *in press*.

Larsen, L. M., Pedersen, A. K., Sundvoll, B., Frei, R., 2003. Alkali Picrites formed by melting of old metassomatized lithospheric mantle: Manîtdlat member, Vaigat formation, Paleocene of West Greenland. *Journal of Petrology*, 44, 1, pp. 3-38.

Latourrette, T., Hervig, R.L., Holloway, J.R., 1995. Trace-Element Partitioning between Amphibole, Phlogopite, and Basanite Melt. *Earth and Planetary Science Letters,* 135, 1-4, pp. 13-30.

Leal, N., 1990. O maciço eruptivo de Sintra – novos dados de natureza petrográfica e geoquímica. *Faculdade de Ciências da Universidade de Lisboa, Portugal. Tese de Mestrado.*

Leal, N., 1991. Caracterização geoquímica do maciço eruptivo de Sintra. Conjecturas de ordem petrogenética baseadas em dados geoquímicos. *Geociências,* Univ. de Aveiro, 6, pp. 1-2.

Lefort, J. P., Salmia, A., Miller, H., 1996. Age and mode of emplacement of the collector anomaly, (Canada): Is it the northwestern boundary of Gondwana? *Journal of Geodynamics*, 21, 2, pp. 177-190.

Lemarchand, F., Villemant, B., Calas, G., 1987. Trace element distribution coefficients in alkaline series. *Geochim. Cos-mochim. Acta 51*, pp. 1071–1081.

le Roex, A., Lanyon, R., 1998. Isotope and Trace Element Geochemistry of Cretaceous Damaraland Lamprophyres and Carbonatites, Northwestern Namibia: Evidence for Plume-Lithosphere Interactions. *Journal of Petrology*, *39,* 6, pp. 1117-1146.

Lopez-Guijarro, R., Armendariz, M., Quesada, C., Fernandez-Suárez, J., Murphy, J. B., Pin, C., 2008. Ediacaran–Palaeozoic tectonic evolution of the Ossa Morena and Central Iberian zones (SW Iberia) as revealed by Sm–Nd isotope systematics. *Tectonophysics*, *461*, pp. 202-214.

Ludwig, K., Silver, L., 1977. Lead-isotope inhomogeneity in Precambrian igneous K-feldspars. Geochimica et Cosmochimica Acta, 41, 10, pp. 1457-1471.

Ludwig, K. R., 2000. Users Manual for Isoplot/Ex, version 2.45, a geochronological toolkit for Microsoft Excel. Berkeley Geochronology Center. Special Publication 1a, p. 43.

Lustrino, M., 2005. How delamination and detachment of lower crust can influence basaltic magmatism. *Earth Science Reviews*, 72, 1-2, pp. 21-38.

Lustrino, M., Wilson, M., 2007. The circum-Mediterranean anorogenic Cenozoic igneous province. *Earth Science Reviews*, 81, pp. 1-65.

Langmuir, D., Herman, J. S., 1980. The mobility of thorium in natural waters at low temperatures. *Geochimica et Cosmochimica Acta*, *44,* 11, pp. 1753-1766.

Leake, B. E., 1997. Nomenclature of Amphiboles: Report of the subcommittee on Amphiboles of the International Mineralogical Association, Comission on new minerals and mineral names. *The Canadian Mineralogist*, *35*, pp. 219-246.

Leal, N., 1990. O maciço eruptivo de Sintra – novos dados de natureza petrográfica e geoquímica. *Faculdade de Ciências da Universidade de Lisboa, Portugal. Tese de Mestrado.*

Le Bas, M. J., Lemaitre, R. W., Streckeisen, A. Zanettin, B., 1986. A chemical classification of volcanic-rocks based on the total alkali silica diagram. *Journal of Petrology,* 27, pp. 745-750.

Lepage, L. D., 2003. ILMAT : an Excel worksheet for ilmenite – magnetite geothermometry and geobarometry. *Computers & Geosciences*, *29*, pp. 673-678.

Liebske, C., Corgne, A., Frost, D.J., Rubie, D.C., Wood, B.J., 2005. Compositional effects on element partitioning between Mg-perovskite and silicate melts. *Contributions to Mineralogy and Petrology*, 149, pp. 113-128.

Liégeois, J-P., Nenhallou, A., Azzouni-Sekkal, Yahiaoui, R., Bonin, B., 2005. The Hoggar swell and volcanism: Reactivation of the Precambrian Tuareg shield during Alpine convergence and West African Cenozoic *volcanism in Foulger, G. R., Natland, J. H., Presnall, D. C., Anderson, D. L., eds, Plates, Plumes and Paradigms*, Geological Society of America.

Lindsley, D.H., Spencer, K.J., 1982. Fe–Ti oxide geothermome- try: Reducing analyses of coexisting Ti-magnetite (Mt) and ilmenite (Ilm) abstract AGU 1982 Spring Meeting Eos Transactions. American Geophysical Union 63 (18), 471.

Lloyd, F. E., Edgar, a. D., Ragnarsdottir, K. V., 1996. LREE distribution in perovskite, apatite and titanite from South West Ugandan xenoliths and kamafugite lavas. *Mineralogy and Petrology*, *57,* 3-4, pp. 205-228.

Lustrino, M. & Wilson, M., 2007. The circum-Mediterranean anorogenic Cenozoic igneous province. *Earth Science Reviews*, 81, pp. 1-65.

MacDonald, G. A., 1968. Composition and origin of Hawaiian lavas. In: Coats, R. R., Hay, R.L., Anderson, C.A. (eds.), Studies in volcanology: a memoir in honour of Howel Williams. *Geol. Soc. Amer. Mem*., 116, pp. 477-522.

MacDonald, R., Rogers, N. W., Fitton, J. G., Black, S., Smith, M., 2001. Plume-Lithosphere interactions in the generation of the basalts of the Kenya Rift, East Africa. *Journal of Petrology*, 42, n. 5, pp. 877-900.

MacDougall, J.D., Finkel, R.C., Carlson, J. Krishnaswami, S., 1979. Isotopic evidence for Uranium exchange during low temperature alteration of oceanic basalts, *Earth and Planetary Science Letters*, 42, pp. 27-34.

MacIntyre, R. M., Berger, G. W., 1982. A note on the geochronology of the Iberian Alkaline Province. *Lithos*, 15, pp. 133-136.

Mahmoudi, A., 1991. Quelques intrusions alcalines et basiques du Cretacé superieur au Portugal. *These de Doctorat. Univ. Nancy I.*

Maia, A., Gonçalves, J., 2006. Análise e caracterização de um evento tectono-magmático no Complexo Vulcânico de Lisboa. Relatório da disciplina de projecto, FCUL, p. 36.

Malod, J. A., Murillas, J., Kornprobst, J., Boillot, G., 1993. Oceanic lithosphere at the edge of a Cenozoic active continental margin (northwestern slope of Galicia Bank, Spain). *Tectonophysics*, 221, 2, pp. 195-206.

Marchev, P., Arai, Shoji, and Vaselli, Orlando, Cumulate xenoliths in Oligocene alkaline basaltic and lamprophyric dikes from the eastern Rhodopes, Bulgaria: Evidence for the existence of layered plutons under the metamorphic core complexes, in Dilek, Y., and Pavlides, S., eds., *Postcollisional tectonics and magmatism in the Mediterranean region and Asia: Geological Society of America Special Paper* 409, pp. 237–258.

Martinez, S. S., Arenas, R., Andonaegui, P. Martinez Catalan, R. R., Pearce, J., 2007. Geochemistry of two associated ophiolites from the Cabo Ortegal Complex (Variscan belt of NW Spain). *Geological Society of America Memoirs 2007*, 200, pp. 445-467.

Martins, L., 1991. Actividade Ígnea Mesozóica em Portugal. *Faculdade de Ciências da Univeridade de Lisboa, Tese de Doutoramento.*

Martins, L. T., 1999. Cretaceous Alkaline Magmatism in Algarve Littoral (South Portugal): a Basanite-Lamprophyre rock suite. *Geolines*, 9, pp. 84-91.

Martins, L.T., Olivença, I., 1998. Contribuição para o conhecimento petrogenético do maciço eruptivo de Sines. *Actas do V Congresso Nacional de Geologia. Comum. I. G. M., 84, B182-185.*

Martins, L., Madeira, J., Youbi, N., Munhá, J., Mata, J., Kerrich, R., 2008. Rift-related magmatism of the Central Atlantic magmatic province in Algarve, Southern Portugal. *Litho*s, 101(1-2), pp. 102-124.

Martins, H., Sant'Ovaia, H., Noronha, F., 2009. Genesis and emplacement of felsic Variscan plutons within a deep crustal lineation, the Penacova-Régua-Verín fault: An integrated geophysics and geochemical study (NW Iberian Peninsula). *Lithos*, *111*, pp. 142-155.

Martins, S., Mata, J., Munhá, J., Mendes, M. H., Maerschalk, C., Caldeira, R.,Matielli, N., 2010. Chemical and mineralogical evidence of the occurrence of mantle metasomatism by carbonate-rich melts in an oceanic environment (Santiago Island, Cape Verde). *Mineralogy and Petrology*, 99*,* 1-2, pp. 43-65.

Martón, E., Abranches, M. C., Pais, J., 2004. Iberia in the Cretaceous: new paleomagnetic results from Portugal. *Journal of Geodynamics*, *38,* 2, pp. 209-221.

Mata, J., 1996. Petrologia e Geoquímica das Lava da Ilha da Madeira. PhD Thesis, Universidade de Lisboa, 471 pp.

Mata, J., Kerrich, R., MacRae, N., Wu, T., 1998. Elemental and isotopic (Sr, Nd, and Pb) characteristics of Madeira Island basalts: evidence for a composite HIMU - EM I plume fertilizing lithosphere. *Canadian Journal of Earth Sciences*, 35, 9, pp. 980-997.

Mata, J., Munha, J., 2004. Madeira Island alkaline lava spinels: petrogenetic implications. *Mineralogy and Petrology*, pp. 85-111.

Mata, J., Kerrich, R., Gonçalves, M. A., 2007. Earth's mantle Th/U and U/Pb evolution in the Archean. *Geochimica et Cosmochimica Acta*, 71, 15, A635.

Matos Alves, C. A., 1964. Estudo petrológico do maciço eruptivo de Sintra. *Revista da Faculdade de Ciências de Lisboa*, XII, 2º série, C, pp. 123-289.

Matos Alves, C. A., Macedo, J. R., Serralheiro, A., 1972. Novos conhecimentos sobre as *soleiras* de *Anços-Montelavar*. *Rev. Fac. Ciên. Lisboa*, 2ª série. C, XVII (1º), pp. 19-43.

Matsui, Y., Onuma, N., Nagasawa, H., Higuchi, H., Banno, S., 1977. Crystal structure control in trace element partition between crystal and magma. *Tectonics,* 100, pp. 315-324.

Matton, G., Jébrak, M., 2009. The Cretaceous Peri-Atlantic Alkaline Pulse (PAAP): Deep mantle plume origin or shallow lithospheric break-up? *Tectonophysics*, 469, pp. 1-12.

McArthur, J.M., Howarth, R.J., Bailey, T.R., 2001. Strontium Isotope Stratigraphy: LOWESS Version 3: Best fit to the Marine Sr-Isotope Curve for 0-509 Ma and Accompanying Look-Up Table for Deriving Numerical Age. *Journal of Geology* 109, pp. 155-170.

McCallum, I.S., Charette, M.P., 1978. Zr and Nb partition coefficients: implications for the genesis of mare basalts, kreep, and sea floor basalts. *Geochimica et Cosmochimica Acta*, 42, pp. 859-869.

McDonough, W. F., 1990. Constraints on the composition of the continental lithospheric mantle. *Earth and Planetary Science Letters*, 101, pp. 1-18.

McKenzie D., O'Nions R. K., 1991. Partial melt distributions from inversion of rare earth element concentrations. Journal of Petrology, 32, pp. 1021– 1091.

Meade, F. C., Chew, D. M., Troll, V. R., Ellam, R. M., Page, L. M., 2010. Magma Ascent along a Major Terrane Boundary: Crustal Contamination and Magma Mixing at the Drumadoon Intrusive Complex, Isle of Arran, Scotland. *Journal of Petrology*, *in press*.

Merle, R., Schärer, U., Cornen, G., Girardeau, J., 2006. Cretaceous seamounts along the continent-ocean transition of the Iberian Margin: U-Pb ages and Pb-Sr-Hf isotopes. *Geochimica et Cosmochimica Acta*, 70, pp. 4950-4976.

Merle, R., Jourdan, F., Marzoli, a., Renne, P. R., Grange, M., Girardeau, J., 2009. Evidence of multi-phase Cretaceous to Quaternary alkaline magmatism on Tore-Madeira Rise and neighbouring seamounts from $^{40}Ar/^{39}Ar$ ages. *Journal of the Geological Society*, 166, (5), pp. 879-894.

Merrill, R.B., Wyllie, P.J., 1975. Kaersutite and kaersutite eclogite from Kakanui, New Zealand, water excess and water deficient melting to 30 Kb. *Geol. Soc. Am. Bull*., 86, pp. 555-570.

Michard, A., Albaréde, F. 1985. Hydrothermal Uranium uptake at ridge crests. *Nature*, 317, pp. 244-246.

Middlemost, E. A., 1975. The Basalt Clan. *Earth Science Reviews*, *11*, pp. 337-364.

Middlemost, E. A. K., 1989. Iron oxidation ratios, norms and the classification of volcanic rocks. *Chemical Geology*, 77, 1, pp. 19-26.

Millot, R., Allègre, C., Gaillardet, J., Roy, S., 2004. Lead isotopic systematics of major river sediments: a new estimate of the Pb isotopic composition of the Upper Continental Crust. *Chemical Geology*, *203,* 1-2, pp. 75-90.

Miranda R. L., Jorge Pinto A., Tavares Martins L., Palácios T., 2005. Novos dados Geoquímicos em filões da Região Lisboa-Cascais,. *Livro de Actas VIII Congresso de Geoquímica/ XIV Semana da Geoquímica*, 1, pp. 173-176.

Miranda, R., Moreira, M., Valadares, V., Terrinha, P., Kullberg, J. C., 2006. Magmatic flow pattern of the Foz da Fonte sill (Upper Cretaceous) by AMS: implications for the understanding of the last cycle of mesozoic magmatic activity in the West Iberian Margin. *Abstracts of the Lasi II: Physical geology of subvolcanic systems: Laccoliths, Sills, and Dykes*., K. Thompson (ed.), *Visual Geosciences*, DOI 10.1007/s10069-006-0002-z, pp. 48-50.

Miranda, R., Valadares, V., Terrinha, P., Mata, J., Azevedo, M.R., Gaspar, M., Kullberg, J.C., Ribeiro, C. 2009. Age constraints on the Late Cretaceous alkaline magmatism on the West Iberian Margin. *Cretaceous Research*, 30, 3, pp. 575-586.

Moita, P., Santos, J. F., Pereira, M., 2009. Layered granitoids: Interaction between continental crust recycling processes and mantle-derived magmatism Examples from the Évora Massif (Ossa–Morena Zone, southwest Iberia, Portugal). *Lithos*, *111*, pp. 125-141.

Monteiro, J. H., 1984. Geologia da area imersa, in J. T. Oliveira (Coord.), Carta Geológica de Portugal, Escala 1:200000, Notícia Explicativa da Folha 7. Serviços Geológicos de Portugal, Lisboa, pp. 69-73.

Montero, P., Salman, K., Zinger, T., 1999. Rb-Sr and single zircon grain $^{207}Pb/^{206}Pb$ chronology of the Monesterio granodiorite and related migmatites.Evidence for a late Cambrian melting event in the Ossa Morena Zone. *Estudios Geologicos*, *8*, pp. 3-8.

Montelli, R., Nolet, G., Dahlen, F.A., Masters, G., Engdahl, E.R., Hung, S.H., 2004. Finite-frequency tomography reveals a variety of plume in the mantle. *Nature*, 303, pp. 338–343.

Montigny, R., Azambre, B., Rossy, M., Thuizat, R., 1986. Kr-Ar study of cretaceous magmatism and metamorphism in the Pyrenees: age and length of rotation of the Iberian Peninsula. *Tectonophysics,* 129, pp. 257–273.

Moreau. M. G., Berthou, J. Y., Malod, J.-A., 1997. New paleomagnetic data from the Algarve (Portugal): fast rotation of Ibéria between the Hauteverian and the Aptian, *Earth and Planetary Science Letters,* 146, pp. 689-701.

Morgan, J. W., 1971. Convection plumes in the lower mantle. *Nature*, 230, pp. 42–43.

Morgan, J. W., 1983. Hotspot tracks and the early rifting of the Atlantic. *Tectonophysics*, 94, pp. 123–139.

Morimito, N., 1988. Petrology Nomenclature of Pyroxenes. *Mineralogy and Petrology*, *39*, pp. 55-76.

Mougenot, D., 1980. Une phase de compression au Crétacé terminal à l'Ouest du Portugal : quelques arguments. Soc. geol. Port., Lisboa, homenagem ao Prof. C. Teixeira.

Mougenot, D., 1989. Geologia da Margem Portuguesa. *Instituto Hidrográfico, pp. 259, Portugal.*

Müntener, O., Kelemen, P.B. Grove, T.L., 2001. The role of H_2O during crystallization of primitive arc magmas under uppermost mantle condition and genesis of igneous pyroxenites: an experimental study. *Contributions to Mineralogy and Petrology*, 141, pp. 643-658.

Müntener, O., Manastschal, G., 2006. High degrees of melt extraction recorded by spinel hazburgite of the Newfoundland margin: the role of inheritance and consequences for the evolution of the southern North Atlantic. Earth and Planetary Science Letter, *Earth and Planetary Science Letters*, 252, 3-4, pp. 437-452

Mysen, B. 1978. Experimental determination of nickel partition coefficients between liquid, pargasite and garnet peridotite minerals and concentration limits of behavior according to Henry's Law at high pressure and temperature. *American Journal of Science*, 278, pp. 217-243.

Nardini, I., Armienti, P., Rocchi, S., Dallai, L., Harrison, D., 2009. Sr-Nd-Pb-He-O Isotope and Geochemical Constraints on the Genesis of Cenozoic Magmas from the West Antarctic Rift. *Journal of Petrology*, *50,* 7, pp. 1359-1375.

Neal, C. R., Haggerty, S. E., Sautter, V., 2001. "Majorite" and "silicate perovskite" mineral compositions in xenoliths from Malaita. *Science*, *292*, p. 1015a.

Neiva, A., Williams, I., Ramos, J. F., Gomes, M., Silva, M., Antunes, I., 2009. Geochemical and isotopic constraints on the petrogenesis of Early Ordovician granodiorite and Variscan two-mica granites from the Gouveia area, central Portugal. *Lithos*, *111, 3-4, pp. 186-202.*

Neumann, E., Wulff-Pedersen, E., Pearson, N. J., Spencer, E. A., 2002. Mantle Xenoliths from Tenerife (Canary Islands): Evidence for Reactions between Mantle Peridotites and Silicic Carbonatite Melts inducing Ca Metasomatism. *Journal of Petrology*, *43,*5, pp. 825-857.

Neves, M. C., Terrinha, P., Afilhado, A., Moulin, M., Matias, L., Rosas, F., 2009. Response of a multi-domain continental margin to compression: study from seismic reflection - refraction and numerical modelling in the Tagus Abyssal Plain. *Tectonophysics*, 468, 1-4, pp. 113-130.

Nielsen, R.L., 1992. BIGD: a FORTRAN program to calculate trace-element partition coefficients for natural mafic and intermediate composition magmas. *Computers and Geosciences*, 18, pp. 773-788.

Nimis, P., 1995. A clinopyroxene geobarometer for basaltic systems based on crystal-structure modeling. *Contributions to Mineralogy and Petrology*, *121*, pp. 115-125.

Nimis, P., 1999. Clinopyroxene geobarometry of magmatic rocks, Part 2. Structural geobarometers for basic to acid, tholeiitic and mildly alkaline magmatic systems. *Contributions to Mineralogy and Petrology*, *135*, pp. 62-74.

Niu, Y., O'Hara, M. J., 2003. Origin of ocean island basalts: a new perspective from petrology, geochemistry, and mineral physics considerations. *J. Geophys. Res.*, *108,* (B4), 2209.

Niu, Y. 2008. The Origin of Alkaline Lavas. *Science*, 320, pp. 883-884.

Nobre Silva, I. G., Weis, D., Barling, J., Scoates, J. S., 2009. Leaching systematics and matrix elimination for the determination of high-precision Pb isotope compositions of ocean island basalts. *Geochemistry Geophysics Geosystems*, *10,* 8, pp. 1-23.

Nogueira, C. R., Moreira, M., Terrinha, P., 2003. Fluxo magmático em diques do cortejo radial de Mafra. *Ciências da Terra, Vol Especial V, VI Congresso Nacional de Geologia, p. 53.*

Nogueira, C. R., 2008. Fluxo magmático em diques do Cortejo Radial de Mafra (sector NW), Bacia Lusitaniana, Portugal. Tese de Mestrado em Geologia, FCUL, pp. 202.

Odin, G. S., and 35 collaborators, 1982. Interlaboratory standards for dating purposes. Numerical dating in stratigraphy. (Odin, G. S., ed), 123-149, Wiley and Sons, Chichester.

Okamoto, K. 1979. Geochemical study on magmatic differentiation of Asama Volcano, central Japan. *Journal of the Geological Society of Japan*. 85,8, pp. 525-535.

Oliveira, J. T., 1990. Stratigraphy and syn-sedimentary tectonism in the South Portuguese Zone. In: Dallmeyer, R. D. & Martinez Garcia, E. (Eds.), Pre Mesozoic Geology of Iberia. Springer, pp. 334-347.

Oliveira, J. T., Pereira, E., Ramalho, M., Antunes, M. T., Monteiro, J. H., 1992. Carta Geológica de Portugal. Escala 1:500 000. *Serv. Geol. Port*., (Lisboa).

Olivet, J.-L., 1996. La cinématique de la plaque iberique. *Bulletin Centres Recherche et Exploracion-Producion Elf Aquitaine*, 20, pp. 131-195.

O'Nions, R., Frank, M., von Blanckenburg, F., Ling, H. 1998. Secular variation of Nd and Pb isotopes in ferromanganese crusts from the Atlantic, Indian and Pacific Oceans. *Earth and Planetary Science Letters*, *155,* 1-2, pp. 15-28.

O'Reilly, S., Griffin, W. L., 2000. Apatite in the mantle: implications for metasomatic processes and high heat production in Phanerozoic mantle. *Lithos*, 53, 3-4, pp. 217-232.

Palácios, T.P., 1985. Petrologia do Complexo Vulcânico de Lisboa. *Faculdade de Ciências da Universidade de Lisboa, Portugal, Tese de Doutoramento, p. 260.*

Palácios, T., Matos Alves, C.A., Leal N, Munhá, J., 1995. Mineralogia química do Maciço Eruptivo de Sintra, *Ext. Abs., IV Cong. Nac. Geol., Porto, Mem. 4, Univ. Porto - Fac. Ciênc. Mus. Lab. Min. Geol., pp. 775-779.*

Palácios, T., Matos Alves, C., Munhá, J., Leal, N., 1999. Geoquímica das Terras Raras nas rochas granulares do maciço eruptivo de Sintra. Actas do II Congresso/XI Semana da Geoquímica, Lisboa, pp. 353-354.

Palme, H., O'Neil, H. St. C., 2003. Cosmochemical Estimates of Mantle Composition. *Treatise on Geochemistry*, 2, pp. 1-38.

Panter, K. S., Blusztajn, J., Hart, S. R., Kyle, P. R., Esser, R., McIntosh, W., 2006. The Origin of HIMU in the SW Pacific: Evidence from Intraplate Volcanism in Southern New Zealand and Subantarctic Islands. *Journal of Petrology*, *47,* 9, pp. 1673-1704.

Paster, T.P., Schauwecker, D.S. and Haskin, L.A., 1974. The behavior of some trace elements during solidification of the Skaergaard layered series. *Geochimica et Cosmochimica Acta,* 38, 10, pp. 1.549-1.577.

Pearson, D. G., Nowell, G. M., 2002. The continental lithospheric mantle: characteristics and significance as a mantle reservoir. *Phil. Trans. Royal Soc. London*, A360, pp. 2383-2410.

Pearson, D. G., Canil, D., Shirey, S. B., 2003. Mantle samples included in volcanic rocks: xenoliths and diamonds. *In: Treatise of Geochemistry, Carlson, R.W. (Ed.),vol 2: The Mantle and Core*, pp. 171-275.

Peirce, C., Barton, P. J., 1991. Crustal structure of the Madeira-Tore Rise, eastern North Atlantic – results of a DOBS wide-angle and normal incidence seismic experiment in the Josephine Seamount region. *Geophys. J. Int*., 106, pp. 357-378.

Pe-Piper, G., Jansa, L.F., Palacz, Z., 1994, Geochemistry and regional signifi cance of the Early Cretaceous bimodal basalt-felsic associations on Grand Banks, eastern Canada. *Geological Society of America Bulletin*, 106, pp. 1319–1331.

Pe-Piper, G., Piper, D. J., Jansa, L. F., de Jonge, A., 2007. Early Cretaceous opening of the North Atlantic Ocean: Implications of the petrology and tectonic setting of the Fogo Seamounts off the SW Grand Banks, Newfoundland. *GSA Bulletin*, *119,* 5-6, pp. 712-724.

Pereira, M. F., Chichorro, M., Linnemann, U., Eguiluz, L., Silva, J. B., 2006. Inherited arc signature in Ediacaran and Early Cambrian basins of the Ossa-Morena Zone (Iberian Massif, Portugal): paleogeographic link with European and North African Cadomian correlatives. *Precambrian Research*, *144*, pp. 297-315.

Pereira, M. F., Brandão Silva, J., Chichorro, M., Moita, P., Apraiz, A., Ribeiro, C., 2007. Crustal growth and deformational processes in the northern Gondwana margin: Constraints from the Évora Massif (Ossa-Morena zone, southwest Iberia, Portugal). *Geological Society of America Special Paper*, *423*, pp. 333-358.

Pfander, J., Munker, C., Stracke, a., Mezger, K., 2007. Nb/Ta and Zr/Hf in ocean island basalts — Implications for crust–mantle differentiation and the fate of Niobium. *Earth and Planetary Science Letters*, *254,* 1-2, pp. 158-172.

Philpotts, J.A. and Schnetzler, C.C., 1970. Phenocryst-matrix partition coefficients for K, Rb, Sr and Ba, with applications to anorthosite and basalt genesis. *Geochimica et Cosmochimica Acta,* 34, 3, pp. 307-322

Pinheiro, L. M., Wilson, R. C. L., Pena dos Reis, R., Whitmarsh, R., Ribeiro, A., 1996. The western Ibéria margin: a geophysical and geological overview. *Proceedings of the Ocean Drilling Program, Scientific Results*, 149, Whitmarsh, R., Sawyer, D., Klaus, A., Masson, D., (Eds.).

Pilet, S., Hernandez, J., Villemant, B., 2002. Evidence for high silicic melt circulation and metasomatic events in the mantle beneath alkaline provinces : the Na ± Fe-augitic green-core pyroxenes in the Tertiary alkali basalts of the Cantal massif (French Massif Central). *Mineralogy and Petrology*, *76*, pp. 39-62.

Pilet, S., Hernandez, J., Sylvester, P., Poujol, M., 2005. The metasomatic alternative for ocean island basalt chemical heterogeneity. *Earth Planet. Sci. Lett.*, *236*, 148-166.

Pilet, S., Baker, M. B., Stolper, E. M., 2008. Metasomatized lithosphere and the origin of alkaline lavas. *Science*, *320,*, pp. 916-9.

Pilet, S., Ulmer, P., Villiger, S., 2010. Liquid line of descent of a basanitic liquid at 1 . 5 Gpa : constraints on the formation of metasomatic veins. *Contributions to Mineralogy and Petrology*, *159,* 5, pp. 621-643.

Pin, C., Briot, D., Bassin, C., Poitrasson, F., 1994. Concomitant separation of strontium and samarium-neodymium for isotopic analysis in silicate samples, based on specific extraction chromatography. *Analytica Chimica Acta*, 298, pp. 209-217.

Pin, C., Fonseca, P., Paquette, J., Castro, P., Matte, P., 2008. The ca. 350 Ma Beja Igneous Complex: A record of transcurrent slab break-off in the Southern Iberia Variscan Belt? *Tectonophysics*, 461, pp. 356-377.

Piromallo, C., Gasperini, D., Macera, P., Faccena, C., 2008. A late Cretaceous contamination episode of the European-Mediterranean mantle. *Earth and Planetary Science Letters,* 268, pp. 15-27.

Planck, T., C. H. Langmuir, 1998. The chemical composition of subducting sediment and its consequences for the crust and mantle. *Chemical Geology*, 145, pp. 325–394.

Plechov, P. Y., Tsai, A. E., Shcherbakov, V. D., Dirksen, O. V., Mag, P. P., 2008. Opacitization Conditions of Hornblende in Bezymyannyi Volcano Andesites (March 30 , 1956 Eruption). *Petrologyia*, 16, 1, pp. 21-37.

Price, S., Brodie, J., Whitman, A., Kent, R., 1997. Mid Tertiary rifting and magmatism in the Trail O region, East Greenland. *Journal of the Geological Society of London*, 154, pp. 419-434.

Priem, H.N.A., Boelrijk, N.A.I.M., Hebeda, E.H., Schermerhorn, L.J.G., 1986. Isotopic ages of the Alcáçovas orthogneiss and the Beja Porphyries, South Portugal. *Comunicações dos Serviços Geológicos de Portugal,* t. 72, pp. 3–7.

Proença da Cunha, P., Pena dos Reis, R., 1995. Cretaceous sedimentary and tectonic evolution of the northern sector of the Lusitanian Basin **(**Portugal**).** *Cretaceous Research*, *16, 2-3,* pp. 155-170.

Ramalho, M., Rey, J., Zbyszewski, G., Matos Alves, C.A., Palacios, T.,Moitinho de Almeida, F., Costa, C., Kullberg, M.C., 2001. Notícia explicativa da Folha 34-C Cascais. *Serv. Geol. Portugal*, 104 p.

Rankenburg, K., Lassiter, J. C., Brey, G., 2004. Origin of megacrysts in volcanic rocks of the Cameroon volcanic chain – constraints on magma genesis and crustal contamination. *Contributions to Mineralogy and Petrology*, *147*, pp. 129-144.

Rasmussen, E., Lomholt, S., Andersen, C., Vejbaek, O., 1998. Aspects of the structural evolution of the Lusitanian Basin in Portugal and the shelf and slope area offshore Portugal. *Tectonophysics*, *300,* 1-4, pp. 199-225.

Reagan, M. K., Gill, J. B., Malavassi, E., & Garcia, M. O., 1987. Changes in magma composition at Arenal volcano, Costa Rica, 1968-1985: Real time monitoring of open system differentiation. *Bulletin of Volcanology*, *49*, pp. 415-434.

Reiners, P.W., Neilson, B. K., Ghiorso,M. S., 1995. Assimilation of felsic crust by basalticmagma: thermal limits and extents of crustal contamination of mantle-derived magmas. *Geology*, 23, pp. 563-566.

Reiners, P. W., 2002. Temporal-compositional trends in intraplate basalt eruptions: Implications for mantle heterogeneity and melting processes. *Geochemistry Geophysics Geosystems*, 3, 2.

Ribeiro, A., M.T. Antunes, M.P. Ferreira, R. Rocha, A. Soares, G. Zbyszewski, F. Moitinho de Almeida, 1979. *Introduction à la géologie générale du Portugal*, Serv. Geol. Portugal, 114p.

Ribeiro, A., Kullberg, M. C., Kullberg, J. C., Manuppella G., Phipps S., 1990. A review of Alpine tectonics in Portugal: Foreland detachment in basement and cover rocks. *Tectonophysics*, 184 3-4, pp. 357-366.

Ribeiro, A., M. Miranda, P. Terrinha, M.C. Kullberg, E.A. Silva and J.C. Kullberg, Is the Sintra-Sines-Monchique Fracture (200 km) a segment of the meteorite impact Tore-Guadalquivir Fracture (600 km)?. *Terra Nova, 9, Abstract Supplement N°1, p. 177,EUG 9.*

Ribeiro, A. 2002. Soft Plate and Impact Tectonics. *Springer-Verlag. Berlin Heidelberg*

Ribeiro, P., Silva, P., Kratinová, Z., Marques, F., Henry, B., 2010. A new paleomagnetic study of the Cretaceous Sines massif (SW Portugal). Abstract book of the 12th Castle Meeting on Paleo, Rock and Environmental Magnetism.

Rieder, M. et al., 1998. Nomenclature of the micas. *The Canadian Mineralogist*, *36*, pp. 41-48.

Riley, T. R., Leat, P. T., Storey, B. C., Parkinson, I. J., Millar, I. L., 2003. Ultramafic lamprophyres of the Ferrar large igneous province: evidence for a HIMU mantle component. *Li*thos, *66*, pp. 63 - 76.

Rocchi, S., Armienti, P., D'Orazio, M., Tonarini, S., Wijbrans, J., Di Vincenzo, G., 2002. Cenozoic magmatism in the western Ross Embayment: Role of mantle plume versus plate dynamics in the development of the West Antartic Rift System. *Journal of Geophysical Research*, 107, B9.

Rock, N. M. S., 1976. Fenitisation around the Monchique alkaline complex, Portugal. *Lithos*, *9,* 4, pp. 263-279.

Rock, N. M. S., 1977. The nature and origin of lamprophyres: some definitions, distinctions and derivations. *Earth Sciences Review*, *13*, pp. 123-169.

Rock, N.M.S., 1982. The Late Cretaceous alkaline igneous province in the Iberian Peninsule, and its tectonic significance. *Lithos,* 15, pp. 111-131.

Rock, N. M. S., 1986. The Nature and Origin of Ultramafic Lamprophyres: Alnöites and Allied Rocks. *Journal of Petrology*, 27, 1, pp. 155-196.

Roeder, P. L., Emslie, R. F., 1970. Olivine-Liquid Equilibrium. *Contributions Mineralogy Petrology*, *29*, pp. 275-289.

Rollinson, H., 1993. Using Geochemical Data: Evaluation, Presentation, Interpretation. Harlow (Longman), 352 pp.

Romariz, C., Almeida C., Silva, M. O., 1979. Contributions to the geology of Algarve (Portugal).II - Volcanic structures in Eastern Algarve (Portugal), *Bol. do Museu e Laboratório Mineralógico e Geológico da Fac. de Ciências de Lisboa*, 16, 1, pp. 253-263.

Roque, C., Terrinha, P., Lourenço, N., Pinto de Abreu M., 2009. Morphostructure of the Tore seamount and evidences of recent tectonic activiy (West Iberian Margin). Nuevas contribuiciones al Margen Ibérico Atlantico 2009 (Flor Rodriguez, G., Gallastegui, J., Flor Blanco, G., Martin Llaneza, J., eds.), Universidad de Oviedo, pp. 33-36.

Rosembaum, G., Lister, G., Duboz, C., 2002. Relative motions of Africa, Iberia and Europe during th2 Alpine orogeny. *Tectonophysics*, 359, pp. 117-129.

Rudnick, R., Goldstein, S., 1990. The Pb isotopic compositions of lower crustal xenoliths and the evolution of lower crustal Pb. *Earth and Planetary Science Letters*, *98,* 2, pp. 192-207.

Rudnick, R. L., Mcdonough, W. F., Chappell, B. W., 1993. Carbonatite metasomatism in the northern Tanzanian mantle: petrographic and geochemical characteristics. *Earth and Planetary Science Letters*, *114*, pp. 463-475.

Rudnick, R. L., Gao, S., 2003. Composition of the continental crust. In: Holland HD, Turekian KK (eds.) Treatise on Geochemistry 3. The crust. Elsevier, Pergamon, Oxford, pp. 1–64.

Russell, S. M., Whitmarsh, R. B., 2003. Magmatism at the west Iberia non volcanic rifted continental margin: evidence from analyses of magnetic anomalies. *Geophys. J. Int*., 154, pp.706-730.

Rutherford, M. J., Hill, P. M., 1993. Magma Ascent Rates From Amphibole Breakdown - An Experimental Study Applied to the 1980-1986 Mount St . Helens Eruptions. *Journal of Geophysical Research*, 98, pp. 667-685.

Rutherford, M. J., Devine, J. D., 2003. Magmatic Conditions and Magma Ascent as Indicated by Hornblende Phase Equilibria and Reactions in the 1995 ± 2002 Soufrie Hills Magma. *Journal of Petrology*, *44,* 8, pp. 1433-1454.

Sachs, P. M., Hansteen, H. T., 2000. Pleistocene underplating and metasomatism of the lower continental crust: A xenolith study. *Journal of Petrology*, *41,* 3, pp. 331-356.

Santos Zalduegui, J. F., Schrarer, U., Ibarguchi, J. I., Girardeau, J., 1996. Origin and evolution of the Paleozoic Cabo Ortega ultramafic-mafic complex (NW Spain): U-Pb, Rb-Sr and Pb-Pb isotope data. *Chemical Geology*, *129*, pp. 281-304.

Sant'Ovaia, H., Gomes, C.R., Pereira L.G., 2007. Emplacement of the Monchique alkaline massif (SW Portugal): Microstructures and magnetic fabric constraints. *Geochimica et Cosmochimica Acta, Goldschmidt Conference Abstract* vol. A.,A876.

Salters, V.J.M., Longhi, J.E., Bizimis, M., 2002. Near mantle solidus trace element partitioning at pressures up to 3.4 GPa. *Geochem. Geophys. Geosyst*. 3.

Saunders A., Storey, M., Kent, R., Norry, M., 1992. Consequences of plume-lithosphere interactions. In Storey, B. C., Alabaster, T., Pankhurst, R. J. (eds), *Magmatism and the causes of continental break-up*, *Geological Society special publication,* n. 68, pp. 41-60.

Schärer, U., Kornprobst, J., Beslier, M., Boillot, G., Girardeau, J., 1995. Gabbro and related rock emplacement beneath rifting continental crust: U-Pb geochronological and geochemical constraints for the Galicia passive margin (Spain). *Earth and Planetary Science Letters*, *130,* 1-4, pp. 187-200.

Schärer U., Girardeau, J., Cornen, G., Boillot, G., 2000. 138-121 Ma asthenospheric magmatism prior to continental break-up in the North Atlantic and geodynamic implications*. Earth and Planetary Science Letters*, 181, pp. 555-572.

Schmidt, M. W., 1992. Amphibole composition in tonalite as a function of pressure : an experimental calibration of the Al-in-hornblende barometer. *Contributions to Mineralogy and Petrology*, pp. 304-310.

Serralheiro, A., 1978. Contribuição para a actualização do conhecimento do Complexo Vulcânico de Lisboa. Departamento de geologia da Universidade de Lisboa, p. 39.

Seifert, K. E., Chang, C., Brunotte, D. A., 1997. Evidence from Ocean Drilling Program Leg 149 mafic igneous rocks for oceanic crust in the Iberia Abyssal Plain zone Drilling Program transition (OCT) on the Iberia Abyssal Plain and its role in the opening of the Atlantic Ocean. *Journal of Geophysical Research*, *102,* (B4), pp. 7915-7928.

Shaw, D.M. 1970. Trace element fractionation during anatexis. Geochimica et Coschimica Acta, 34, pp. 237-243.

Shaw, D. M., 2006. Trace elements in magmas – a theoretical treatment. Cambridge University Press, 243 p.

Shen, Y., Forsyth, D. W., 1995. Geochemical constraints on initial and final depths of melting beneath mid-ocean ridges. *Journal of Geophysical Research*, 100(B2), pp. 2211-2237.

Shimizu, H., 1980. Experimental study on rare-earth element partitioning in minerals formed at 20 and 30kb for basaltic systems. *Geochemical Journal*, 14, (4), pp. 185-202.

Sibuet, J., Srivastava, S. P., Spakman, W., 2004. Pyrenean orogeny and plate kinematics. *Journal of Geophysical Research*, *109*, B08104.

Sibuet, J. C., Srivastava, S., Manatschal, G., 2007. Exhumed mantle forming transitional crust in the Newfoundland-Iberia rift and associated magnetic anomalies, J. *Geophys. Res.*, *112*, 101029.

Silva E. A., Miranda, J. M., Luís, J. F., Galdeano, A., 2000.Correlation between the Palaeozoic structures from West Iberian and Grand Banks margins using inversion of magnetic anomalies. *Tectonophysics,* 321, 1, pp. 57-71.

Silva, M., Neiva, A., Whitehouse, M., 2000. Geochemistry of enclaves and host granites from the Nelas area, central Portugal. *Lithos*, *50*, pp. 153-170.

Simonetti, A., Bell, K., 1994. Isotopic and Geochemical Investigation of the Chilwa Island Carbonatite Complex , Malawi : Evidence for a Depleted Mantle Source Region , Liquid Immiscibility , and Open-System Behaviour. *Journal of Petrology*, *35,* 6, pp. 1597-1621.

Simmons, N.A., Forte, A.M., Grand, S.P., 2006. Constraining mantle flow with seismic and geodynamic data: a joint approach. *Earth Planet. Sci. Lett*. 246, pp. 109–124.

Sisson, T. W., Kimura, J., Coombs, M. L., 2009. Basanite–nephelinite suite from early Kilauea: carbonated melts of phlogopite–garnet peridotite at Hawaii's leading magmatic edge. *Contributions to Mineralogy and Petrology*, *158,* 6, pp. 803-829.

Sleep, N.H., 1990. Hotspots and mantle plumes: Some phenomenology. *J. Geophys. Res*., 95, pp. 6715–6736.

Solé, J., Pi, T., Enrique, P., 2003. New data on the Late Cretaceous alkaline magmatism of the northeast Iberian Peninsula. *Cretaceous Research,* 24, pp. 135-140.

Sparks, R., Wadge, G., 1975. Geological and Geochemical studies of the Sintra alkaline igneous complex, Portugal. *Bull. Volc*., 39, 3, pp. 385-406.

Späth, A., Le Roex, A., Opiyo-Akech, N., 2001. Plume-Lithosphere interaction and the origin of Continental Rift related alkaline volcanism – the Chyulu Hills volcanic province, S Kenya. *Journal of Petrology*, 42, 4, pp. 765-787.

Srivastava, S. P., Sibuet, J. C., Cande, S., Roest, W. R., Reid, I. D., 2000. Magnetic evidence for slow seafloor spreading during the formation of the Newfoundland and Iberian margins, Earth Planet. *Earth and Planetary Sci. Letters*, *182*, pp. 61-76.

Stapel, G., Cloetingh, S., Pronk, B., 1996. Quantitative subsidence analysis of the Mesozoic evolution of the Lusitanian basin (western Iberian margin). *Tectonophysics*, 266, pp. 493-507.

Stille, P., Steinmann, M., Riggs, S., 1996. Nd isotope evidence for the evolution of the paleocurrents in the Atlantic and Tethys Oceans during the past 180 Ma. *Earth and Planetary Science Letters*, 144, pp. 9-19.
Storetvedt, K.M., Mogstad, H., Abranches, M.C., Mitchell, J.G., Serralheiro, A., 1987. Paleomagnetism and isotopic age data from Upper Cretaceous igneous rocks of W Portugal; geological correlation and plate tectonic aspects. *Geophys. J.R. astr. Soc*., 88, pp. 241-263.

Storetvedt, K.M., Mitchell, J.G., Abranches, M.C., Oftedahi, S., 1990. A new kinematic model for Iberia; further palaeomagnetic and isotopic age evidence. *Physics of the Earth and Planetary Interiors,* 62, 1-2, pp. 109-125.

Storetvedt, K.M., Martón, M., Abranches, M.C., Rother, K., 1999. Alpine remagnetization and tectonic rotations in the French Pyrenees. *Geol. Rundsch*., 87, pp. 658-647.

Storey, M., Pedersen, A. K., Stecher, O., Bernstein, S., Larsen, H. C., Larsen, L. M., Baker, J. A., Duncan, R. A., 2004. Long lived post breakup magmatism along the East Greenland margin: Evidence for shallow-mantle metassomatism by the Iceland plume. *Geology*, 32, n. 2, pp. 173-176.

Stracke, A., Hofmann, A. W., Hart, S. R. 2005. FOZO, HIMU, and the rest of the mantle zoo. *Geochemistry, Geophysics, Geosystems*, *6.*

Sweeney, R. J., Thompson, A. B., Ulmer, P., 1993. Phase relations of a natural MARID composition and implications for MARID genesis, lithospheric melting and mantle metasomatism. *Contributions to Mineralogy and Petrology*, *115*, pp. 225-241.

Sweeney, R.J., Prozesky, V., Przybylowicz, W., 1995. Selected trace and minor element partitioning between peridotite minerals and carbonatite melts at 18–46 kbar pressure. *Geochim. Cosmochim. Acta*, 59, pp. 3671–3683.

Roex, A. P., Spath, A., Opiyo-Akech, N., 2001. Plume–Lithosphere Interaction and the Origin of Continental Rift-related Alkaline Volcanism—the Chyulu Hills Volcanic Province, Southern Kenya. *Journal of Petrology*, *42,* 4, pp. 765-787.

Spera, F. J., & Bohrson, W. A., 2001. Energy-constrained open-system magmatic processes I: General model and energy-constrained assimilation and fractional crystallization (EC-AFC) formulation. *Journal of Petrology*, *42*, pp. 999-1018.

Stille, P., Steinmann, M., Riggs, S. R., 1996. Nd isotope evidence for the evolution of the paleocurrents in the Atlantic and Tethys Oceans during the past 180 Ma, *Earth and Planetary Science Letters*, 144, 1-2, pp. 9-19.

Sullivan, K.D., Keen, C.E., 1977. Newfoundland Seamounts—petrology and geochemistry. In Baragar, W.R.A., Coleman, L.C., and Hall, J.M. (Eds), Volcanic Regimes of Canada. Geol. *Assoc. Can. Spec. Pap*., 16, pp. 461–476.

Sun, C.-O., Williams, R.J. and Sun, S.-S., 1974. Distribution coefficients of Eu and Sr for plagioclase-liquid and clinopyroxene-liquid equilibria in oceanic ridge basalt; an experimental study. *Geochimica et Cosmochimica Acta*, 38, 9, 1, pp. 415-1,433.

Takahashi, E., 1978. Partitioning of Ni^{2+}, Co^{2+}, Fe^{2+}, Mn^{2+} and Mg^{2+} between Olivine and Silicate Melts - Compositional Dependence of Partition-Coefficient. *Geochimica et Cosmochimica Acta*, 42, 12, pp. 1,829-1,844.

Tappe, S., Jenner, G. A., Foley, S. F., Heaman, L., Besserer, D., Kjarsgaard, B. A., 2004. Torngat ultramafic lamprophyres and their relation to the North Atlantic Alkaline Province. *Lithos*, *76*, pp. 491 - 518.

Tappe, S., Foley, S. F., Jenner, G. A., Heaman, L. M., Kjarsgaard, B. A., Romer, R. L., 2006. Genesis of ultramafic lamprophyres and carbonatites at Aillik Bay, Labrador: A consequence of incipient lithospheric thinning beneath the North Atlantic craton. *Journal of Petrology*, *47,* 7, pp. 1261-1315.

Taylor, H. P., 1980. The effects of assimilation of country rocks by magmas on $^{18}O/^{16}O$ and $^{87}Sr/^{86}Sr$ systematics in igneous rocks. *Earth and Planetary Science Letters*, *47*, pp. 243-254.

Tepley, F. J., Davidson, J. P., 2003. Mineral-scale Sr-isotope constraints on magma evolution and chamber dynamics in the Rum layered intrusion, Scotland. *Contributions to Mineralogy and Petrology*, 145, 5, pp. 628-641.

Terrinha, P., 1998. Structural Geology and Tectonic Evolution of the Algarve Basin, South Portugal. *Imperial College, University of London, PhD Thesis.*

Terrinha, P. Dias, R.P., Ribeiro A., Cabral, J., 1999. The Portimão fault, Algarve basin, south Portugal, *Comun. Inst. Geol. Miner*., 86, pp. 107–120.

Terrinha, P., Aranguren, A., Kullberg, M. C., Pueyo, E., Kullberg, J. C., Casas Sainz, A. M., Rillo, C., 2003. Complexo ígneo de Sintra - um modelo de instalação constrangido por novos dados de gravimetria e ASM. *Ciências da Terra, Vol Especial V, VI Congresso Nacional de Geologia*, p. 58-59.

Terrinha, P., Matias, L., Vicente, J., Duarte, J., Luís, J., Pinheiro, L., Lourenço, N., Diez, S., Rosas, F., Magalhães, V., Valadares, V. ,Zitellini, N., Mendes Víctor, L. and MATESPRO Team, 2009. Morphotectonics and Strain Partitioning at the Iberia-Africa plate boundary from multibeam and seismic reflection data. *Marine Geology*, 267, 3-4, pp. 156-174.

Thibault, Y., Edgar, A. D., Lloyd, F. E., 1992. Experimental investigation of melts from a carbonated phlogopite lherzolite: Implications for metasomatism in the continental lithospheric mantle. *American Mineralogist*, *77*, pp. 784-794.

Thirlwall, M. F., Jenkins, C., Vroon, P. Z., Mattey, D. P., 1997. Crustal interaction during construction of ocean islands: Pb-Sr-Nd-O isotope geochemistry of the shield basalts of Gran Canaria, Canary Islands. *Chemical Geology*, 135, I3-4, pp. 233-262.

Thompson, R.N., 1974. Some high pressure pyroxenes. *Mineralogical Magazine*, 39, pp. 768-787.

Thompson, R., Ottley, C., Smith, P., Pearson, D. G., Dickin, A., Morrison, M., Leat, P. T., Gibson, A., 2005. Source of the Quaternary alkalic basalts, picrites and basanites of the Potrillo volcanic field, New Mexico, USA: lithosphere or convecting mantle? *Journal of Petrology*, 46, 8, pp. 1603-1643.

Toplis, M. J., Carrol, R., 1995. An experimental study of the influence of oxygen fugacity in Fe-Ti oxide stability, phase relations, and mineral-melt equilibria un Ferro-Basaltic systems. *Journal of Petrology*, *36,* 5, pp. 1137-1170.

Tritlla, J., Solé, J., 1999. A newly dated Cretaceous hydrothermal event in the Iberian Ranges(Eastern Spain) and its significance within the Mesozoic thermal history in the Iberian Peninsula. *Ore Geology Reviews,* 15, pp. 243–259.

Tucholke, B.E., and Sibuet, J.-C., 2007. Leg 210 synthesis: tectonic, magmatic, and sedimentary evolution of the Newfoundland-Iberia rift. In Tucholke, B.E., Sibuet, J.-C., and Klaus, A. (Eds.), *Proc. ODP, Sci. Results*, 210, College Station, TX (Ocean Drilling Program), pp. 1–56.

Turner, S.P., Platt, J.P., George, R.M.M., Kelley, S.P., Pearson, D.G., Nowell, G.M., 1999. Magmatism Associated with Orogenic Collapse of the Betic-Alboran Domain, SE Spain. Journal of Petrology, 40, pp. 1011-1036.

Ugidos, J. M., Valladares, M. I., Recio, C., Rogers, G., Fallick, A., Stephens, W. E., 1997. Provenance of Upper Precambrian-Lower Cambrian shales in the Central Iberian Zone, Spain: evidence from a chemical and isotopic study. *Chemical Geology*, *136*, pp. 55-70.

Upton, B., 1999. Megacrysts and Associated Xenoliths: Evidence for Migration of Geochemically Enriched Melts in the Upper Mantle beneath Scotland. *Journal of Petrology*, *40,* 6, pp. 935-956.

Upton, B., Finch, A., Slaby, E., 2009. Megacrysts and salic xenoliths in Scottish alkali basalts : derivatives of deep crustal intrusions and small-melt fractions from the upper mantle. *Mineralogical Magazine*, *73*, 6, pp. 943-956.

Valadares, V., 2004. O Complexo Alcalino de Monchique – novos dados de cartografia, geoquímica e geocronologia. *Faculdade de Ciências da Universidade de Lisboa, Portugal, Tese de Mestrado.*

Vaugham, A. P. M., Scarrow, J. H., 2003. K-rich mantle metasomatism control of location and initiation of lithospheric strike-slip faulting. *Terra Nova*, 15, n. 3, pp. 163-169.

Verati, C., Rapaille, C., Féraud,G., Marzoli,A.,Bertrand,H.,Youbi,N., 2007. $^{40}Ar/^{39}Ar$ ages and duration of the Central AtlanticMagmatic Province volcanism in Morocco and Portugal and its relation to the Triassic–Jurassic boundary. *Palaeogeography, Palaeoclimatology, Palaeoecology*, 244, pp. 308–325.

Verhoogen, J. 1962. Distribution of titanium between silicates and oxides in igneous rocks. *American Journal of Science*, 260, pp. 211-220.

Verma, S. 1992. Seawater alteration effects on REE, K, Rb, Cs, Sr, U, Th, Pb and Sr-Nd-Pb isotope systematics on MORB. *Geochemical Journal*, 26, pp. 159-177.

Villaseca, C., Barbero, L., Rogers, G., 1998. Crustal origin of Hercynian peraluminous granitic batholiths of Central Spain: petrological, geochemical and isotopic (Sr, Nd) constraints. *Lithos*, *43*, pp. 55-79.

Villaseca, C., Bellido, F., Perez-Soba, C., Billström, K., 2009. Multiple crustal sources for post-tectonic I-type granites in the Hercynian Iberian Belt. *Mineralogy and Petrology*, *96*, pp. 197-211.

Villemant, B., Jaffrezic, H., Joron, J.L. and Treuil, M., 1981. Distribution Coefficients of Major and Trace-Elements - Fractional Crystallization in the Alkali Basalt Series of Chaine-Des-Puys (Massif Central, France). *Geochimica et Cosmochimica Acta*, 45, 11, pp. 1997-2016.

Vogt, P. R., 1991. Bermuda and Appalachian–Labrador rises. *Geology*, 19, pp. 41–44.

van der Voo, R., 1969. Paleomagnetic evidence for the rotation of the Iberian peninsula. *Tectonophysics*, *7,* 1, pp. 5-56.

van der Voo, R., Zijderveld, J.D.A., 1971. Renewed palaeomagnetic study of the Lisbon volcanics and implications for the rotation of the Iberian Peninsula. *J. Geophys. Res.* 76, pp. 3913–3921.

Wass, S., 1979. Multiple origins of clinopyroxenes in alkali basaltic rocks. *Lithos*, 12, pp. 115-132.

Watson S., MacKenzie, D., 1991. Melt Generation by Plumes: A Study of Hawaiian Volcanism, *Journal of Petrology*, 32, 3, pp. 501-537.

Weaver, B.L., 1991. Trace element evidence for the origin of ocean island basalts. *Geology*, 19, pp. 123-126.

Weis, D., F. A. Frey, 1996. Role of the Kerguelen Plume in generating the eastern Indian Ocean seafloor, *J. Geophys. Res*., 101, B6, 13,381–13,849.

van Westrenen, W., Blundy, J. D., Wood, B. J., 2001. High field strength element/rare earth element fractionation during partial melting in the presence of garnet: Implications for identification of mantle heterogeneities. *Geochemistry Geophysics Geosystems*, *2,* 7.

Wheat, C., Mottl, M., Rudnicki, M., 2002. Trace element and REE composition of a low-temperature ridge-flank hydrothermal spring. *Geochimica et Cosmochimica Acta*, *66,* 21, pp. 3693-3705.

White, R. S., 1992. Crustal structure and magmatism of North Atlantic continental margins. *Geological Society of London Journal*, 149, pp. 841-854.

White, R.S., McKenzie, D., 1989. Magmatism at rift zones: the generation of volcanic continental margins and flood basalts. *J. Geophys. Res*., 94, 7685–7729.

Whitmarsh, R.B., Beslier, M.-O., Wallace, P.J., 1998. *Proc. ODP, Init. Repts*., 173, pp. 265-294.

Whitmarsh, R.B., Wallace, P.J., 2001. The rift-to-drift development of the west Iberia nonvolcanic continental margin: a summary and review of the contribution of Ocean Drilling Program Leg 173. In Beslier, M.-O., Whitmarsh, R.B., Wallace, P.J., and Girardeau, J. (Eds.), *Proc. ODP, Sci. Results*, 173, pp. 1–36.

Widom, E., Hoernle, K., Shirey, S. B., Schmincke, H. -U., 1999. Os Isotope Systematics in the Canary Islands and Madeira: Lithospheric Contamination and Mantle Plume Signatures. *Journal of Petrology*, *40,* 2, pp. 279-296.

Willbold, M., Stracke, A., 2006. Trace element composition f mantle end-members: implications for recycling of oceanic and upper and lower continental crust. *Geochem. Geophys. Geosyst*, *7,* 4.

Wilson, M., 1989. Igneous Petrogenesis: a global tectonic approach. *Chapman and Hall*, p. 466.

Wilson, M. 1993. Magmatism and the geodynamics of basin formation. *Sedimentary Geology*, *86*, pp. 5-29.

Wilson, M., Downes, H., 1992. Mafic alkaline magmatism associated with the European Cenozoic rift system, *Tectonophysics*, 208, 1-3 , pp. 173-182.

Woodland, A. B., Komprobst, J., Mcpherson, E., Menzies, M. A., 1996. Metasomatic interactions in the lithospheric mantle: petrologic evidence from the Lherz massif, French Pyrenees. *Chemical Geology*, *134*, pp. 83-112.

Workman, R. K., Hart, S. R., Jackson, M., Regelous, M., Farley, K., Blusztanjn, J., Kurz, M., 2004. Recycled metasomatized lithosphere as the origin of the Enriched Mantle II (EM2) end-member: Evidence from the Samoan Volcanic Chain. *Geochemistry Geophysics Geosystems*, *5,* 4, pp. 1-44.

Workman, R., Hart, S., 2005. Major and trace element composition of the depleted MORB mantle (DMM). *Earth and Planetary Science Letters*, *231,* 1-2, pp. 53-72.

Wright, J. B., 1969. Re-interpretation of a mixed petrographic province – the Sintra intrusive complex (Portugal) and related rocks. *Geol. Rundsch*., Bd. 48, pp. 539-565.

Yang, H.J., Frey, F.A., Clague, A., 2003. Constrains on the source components of lavas forming the Hawaiian north arch and Honolulu volcanics. *Journal of Petrology*, 44, 4, pp. 603-627.

Yaxley, G.M., Crawford, A.J., Green, D.H., 1991. Evidence for carbonatite metasomatism in spinel peridotite xenoliths from western Victoria, Australia. *Earth and Planetary Science Letters* 107, pp. 305–317.

Yaxley, G. M., Green, D. H., Kamenetsky, V., 1998. Carbonatite metasomatism in the southeastern Australian lithosphere. J*ournal of Petrology*, *39,* 11-12, pp. 1917-1930.

York, D., 1969. Least squares fitting of a straight line with correlated errors. *Earth and Planetary Science Letters*, 5, p. 320.

You, C.-F., Castillo, P.R., Gieskes, J.M., Chan, L.H., Spivack, A.J., 1996. Trace element behavior in hydrothermal experi- ments: Implications for fluid processes at shallow depths in subduction zones. *Earth Planet. Sci. Lett*., 140, pp. 41-52.

Zaccarini, F., Stumpfl, E. F., Garuti, G., 2004. Zr–Th–U minerals in chromitites of the Finero complex, Western Alps, Italy: evidence for carbonatite-type metasomatism in a subcontinental mantle plume. *The Canadian Mineralogist*, *42*, pp. 1825-1845.

Zack T., Brumm R., 1998. Ilmenite/liquid partition coefficients of 26 trace elements determined through ilmenite/clinopyroxene parti- tioning in garnet pyroxenites. Seventh *International Kimberlite Conference, Cape Town*, pp. 986–988.

Zbyszewski, G., Moitinho d'Almeida, F., Torre de Assunção,C., 1955. Notícia explicativa da Carta geológica de Portugal, 1/50 000 Folha 30-C, Torres Vedras. Serv. Geol. Port., p. 33.

Zeng, G., Chen, L., Xu, X., Jiang, S., Hofmann, A. W., 2010. Carbonated mantle sources for Cenozoic intra-plate alkaline basalts in Shandong, North China. *Chemical Geology*, *273,* 1-2, pp. 35-45.

Ziegler, P., Cloetingh, S., 2004. Dynamic processes controlling evolution of rifted basins. *Earth-Science Reviews*, *64,* 1-2, pp. 1-50.

Zindler, A. Hart S., 1986. Chemical Geodynamics. *Annual review of earth and planetary sciences*, 14, pp. 493-571.

Zitellini, N., Gràcia, E., Matias, L., Terrinha, P., Abreu, M. A., DeAlteriis, G., Henriet, J. P., Dañobeitia, J. J., Masson, D. G., Mulder, T., Ramella, R., Somoza, L., Diez, S., 2009. The quest for the Africa-Eurasia plate boundary west of the Strait of Gibraltar. *Earth and Planetary Science Letters*, 280, 1-4, pp. 13-50.

Annexes

The annexes that accompany this work, contain:

Annex I: Geographical coordinates of the sample locations.

Annex II: Whole rock geochemistry

Annex III: Sr, Nd and Pb Isotope geochemistry

Annex IV: Mineral Chemistry

Annex V: CIPW normative compositions

Annex I: Sample locations

Table I.1: Geographical coordinates of the collected samples

Sample	Latitude	Longitude	Sampling location
RM 1	38.89149377	-9.17860957	Torre da Besueira, quarry
RM 2	38.89149377	-9.17860957	Torre da Besueira, quarry
RM 3	38.89149377	-9.17860957	Torre da Besueira, quarry
RM 4	38.89252969	-9.31129795	Penedo do Lexim
RM 5	38.89252969	-9.31129795	Penedo do Lexim
RM 6	38.89252969	-9.31129795	Penedo do Lexim
RM 7	38.89125679	-9.30485262	Lexim
RM 8	38.89125679	-9.30485262	Lexim
RM 9	38.89311768	-9.43836469	Lomba dos pianos, abandoned quarry
RM 10	38.89311768	-9.43836469	Lomba dos pianos, abandoned quarry
RM 11	38.77338078	-9.46211200	Sintra, Peninha gabbro outcrop
RM 12	38.77338078	-9.46211200	Sintra, Peninha gabbro outcrop
RM 13	38.77338078	-9.46211200	Sintra, Peninha gabbro outcrop
RM 14	38.77338078	-9.46211200	Sintra, Peninha gabbro outcrop
RM 15	38.77338078	-9.46211200	Sintra, Peninha gabbro outcrop
RM 16	38.77338078	-9.46211200	Sintra, Peninha gabbro outcrop
RM 17	38.77338078	-9.46211200	Sintra, Peninha gabbro outcrop
RM 18	38.79263934	-9.46973331	Sintra, Peninha gabbro outcrop
RM 19	38.79263934	-9.46973331	Almoçageme, crossroads between Cruzamento Rua dos Casais-Caminho do Loureiro
RM 20	38.77252008	-9.48444246	Almoçageme, crossroads between Cruzamento Rua dos Casais-Caminho do Loureiro
RM 21	38.77252008	-9.48444246	Sintra, Azoia gabbro outcrop
RM 22	38.77252008	-9.48444246	Sintra, Azoia gabbro outcrop
RM 23	38.77252008	-9.48444246	Sintra, Azoia gabbro outcrop
RM 24	38.76136512	-9.46532876	Sintra, Azoia gabbro outcrop
RM 25	38.75016916	-9.44935834	Malveira-Biscaia Diorite, road between Azóia and Malveira da Serra
RM 26	39.01841828	9.22444343	Malveira da Serra sill, Malveira da Serra
RM 27	39.01841828	9.22444343	Serra do Socorro, top of vent
RM 28	39.01642923	-9.22702267	Serra do Socorro, top of vent
RM 29	39.01187697	-9.22648330	Serra do Socorro, contact with country rock
RM 30	39.01187697	-9.22648330	São Sebastião near the football field
RM 31	38.97689371	-9.16721962	São Sebastião near the football field
RM 32	38.97689371	-9.16721962	Alqueidão sill, São Geraldo chappel
RM 33	38.98572128	-9.15143387	Alqueidão sill, São Geraldo chappel
RM 34	39.06171223	-9.22347598	Alqueidão sill, Alqueidão fort
RM 35	39.05475015	-9.22634834	Runa; near Figueiredo
RM 36	38.98958645	-9.42151073	Runa; near quarry outside of Figueiredo
RM 37	38.98958645	-9.42151073	Ribeira de Ilhas, southern plug
RM 38	38.81208785	-9.19781127	Ribeira de Ilhas, central plug
RM 39	38.82312611	-9.20345810	Montemor; near the antennas
RM 40	38.86462277	-9.20938539	Montemor; geodesic mark
RM 41	38.86462277	-9.20938539	Ponte de Lousa, basal LVC layer

Sample	Latitude	Longitude	Sampling location
RM 42	38.87470562	-9.28517373	Ponte de Lousa, basal LVC layer
RM 43	38.87470562	-9.28517373	Negrais, near the football field
RM 44	38.87470562	-9.28517373	Negrais, near the football field
RM 45	38.87470562	-9.28517373	Negrais, near the football field
RM 46	38.87485427	-9.35760785	Negrais, near the football field
RM 47	38.87485427	-9.35760785	Eiras do Faião, near geodesic mark
RM 48	38.87065675	-9.35523608	Eiras do Faião, near geodesic mark
RM 49	38.86725372	-9.32805498	Near Cabrela
RM 50	38.86725372	-9.32805498	Montelevar, construction site next to cemetery
RM 51	38.87993028	-9.31298620	Montelevar, construction site next to cemetery
RM 52	38.68410681	-9.35010322	Anços, near sightseeing spot
RM 53	38.68410681	-9.35010322	Parede, Praia do Sanatório
RM 54	38.68609272	-9.35709214	Parede, Praia do Sanatório
RM 55	38.87292612	-9.31079641	Praia da Parede
RM 56	38.87267083	-9.31061530	Anços
RM 57	38.89541274	-9.23563431	Anços
RM 58	38.89499516	-9.23746750	Montemuro, contact with country rock
RM 59	38.85457930	-9.20836841	Montemuro, top
RM 60	38.86201564	-9.21942364	Moninhos, next to abandoned windmill
RM 61	38.86356120	-9.22997344	Bolores, above contact with limestones
RM 62	38.68563521	-9.35404101	Bolores, above contact with limestones
RM 63	38.68973585	-9.36356008	Praia da Parede
RM 64	38.69165599	-9.36603358	Praia das Avencas
RM 65	38.89391196	-9.09079114	Praia da bafureira
RM 66	38.89534686	-9.09190897	Monte Serves, top
RM 67	38.87616631	-9.31849315	Monte Serves, base
RM 68	38.87616631	-9.31849315	Rebanque quarry,Anços sill
RM 69	38.88572390	-9.13872429	Rebanque quarry,Anços sill
RM 70	38.88510252	-9.13711726	Fanhões
RM 71	38.87810758	-9.15384035	Fanhões
RM 72	38.87830102	-9.15442816	Ribeira de Fanhões valley
RM 73	38.87860817	-9.15534320	Ribeira de Fanhões valley
RM 74	38.88337358	-9.18713853	Ribeira de Fanhões valley
RM 75	38.80295661	-9.35896257	Roadcut between Montachique and Malhapão
RM 76	38.80320997	-9.36170197	Sintra-Algueirão roadcut in the acess to IC30
RM 77	38.76072497	-9.46068158	Sintra-Algueirão roadcut in the acess to IC30
RM 78	38.76820865	-9.46333192	Quarry in a limestone stoped block inside the diorite
RM 79	38.81252962	-9.18622294	Peninha, "pyroxene syenite"
RM 80	38.81252962	-9.18622294	Ramada, construction site
RM 81	38.93525112	-9.33294052	Ramada, construction site
RM 82	38.93108219	-9.33854069	Mafra, roadcut next to GDM football field
RM 83	38.93066513	-9.33217172	Near Almada, outside of Mafra

Sample	Latitude	Longitude	Sampling location
RM 84	38.81307792	-9.18664949	Next to the Carrefour supermarket, Mafra
RM 85	38.81473435	-9.18778146	Ramada, construction site
RM 86	38.81403807	-9.18595516	Ramada, construction site
RM 87	38.70150306	-9.39126610	Ramada, construction site
RM 88	38.70169168	-9.39165051	Praia da Poça
RM 89	38.70203709	-9.39472954	Praia da Poça
RM 90	38.70187473	-9.39569265	Between Praia da Poça and Praia do Tamariz
RM 91	38.75495499	-9.38885144	Between Praia da Poça and Praia do Tamariz
RM 92	38.90676194	-9.29328984	Roadcut between Sintra and Cascais, near the Linhó prision
RM 93	38.91153496	-9.27398817	Vent near the Mafra trains station
RM 94	38.90944207	-9.27235942	Funchal vent
RM 95	37.95094722	-8.86287778	Sines diorite, south of the Vasco da Gama beach
RM 96	37.95166667	-8.86356111	Sines gabbro, Praia Vasco da Gama
RM 97	37.95412778	-8.86608611	Sines gabbro, Praia Vasco da Gama
RM 98	37.95412778	-8.86608611	Sines gabbro, Praia Vasco da Gama
RM 99	37.96800278	-8.87742778	Sines gabbro, Ponta do Sal
RM 100	37.96800278	-8.87742778	Sines gabbro, Ponta do Sal
RM 101	37.96779167	-8.87809722	Sines gabbro, Ponta do Sal
RM 102	38.81234722	-9.18733611	Ramada construction site
RM 103	38.85483889	-9.17797778	Near Matos geodesic mark
RM 104	38.85825833	-9.45205000	Magoito beach
PI 1-11	38.99936667	-9.40196944	Abandoned quarry in Paço d'Ilhas
FF 2-4	38.45097500	-9.20160833	Foz da Fonte beach
C-12-1	37.13562778	-8.00619444	Loulé salt mine
C 20	37.13562778	-8.00619444	Loulé salt mine

Annex II: Whole rock geochemistry

Table II.1: whole rock major and trace element geochemical data for the studied samples. nd – non detected.

occurrence	Foz da Fonte sill	Foz da Fonte sill	Foz da Fonte sill	Paço d'Ilhas sill	Paço d'Ilhas sill	Paço d'Ilhas sill	Paço d'Ilhas sill	Paço d'Ilhas sill
sample ref.	FF 2	FF 3	FF 4	PI01	Pl02	PI03	PI04	PI05
SiO_2 (%)	39.93	40.41	40.43	52.51	49.95	45.82	53.11	49.45
Al_2O_3	13.58	13.74	13.94	16.44	17.1	12.60	15.68	16.2
Fe_2O_3 (tot)	11.77	12.21	12.22	7.34	9.02	13.94	7.09	7.84
MnO	0.146	0.139	0.157	0.193	0.143	0.164	0.22	0.179
MgO	6.13	8.54	8.17	2.08	3.27	3.95	1.88	2.42
CaO	12.34	8.72	8.91	5.35	5.75	7.50	5.32	6.66
Na_2O	1.62	1.52	1.56	4.78	4.17	2.71	4.65	3.96
K_2O	2.12	2.23	2.52	3.35	3.02	1.24	3.46	2.49
TiO_2	4.45	4.53	4.46	1.83	2.20	3.95	1.81	2.01
P_2O_5	0.64	0.64	0.65	0.57	0.67	0.75	0.52	0.57
LOI	6.29	5.83	5.90	4.7	4.79	7.62	6.06	6.74
Total	99.0	98.5	98.9	99.1	100.1	100.2	99.8	98.5
Sc (ppm)	25.0	26.0	24.0	9.0	9.0	25.0	8.0	9.0
V	362.4	364.5	339.4	75.0	123.0	394.0	70.0	111.0
Ni	42	41	57	n.d.	2	2	2	3
Cr	66.0	70.5	58.7	n.d.	7.0	8.0	n.d.	13.0
Ga	21.2	20.9	21.0	21.0	21.0	19.0	21.0	20.0
Ge	1.6	1.3	1.3	1.4	1.5	1.4	1.4	1.1
Rb	43.6	40.4	46.0	90.0	76.0	64.0	92.0	65.0
Sr	1270	1040	1220	1024	1099	577	933	1099
Y	27.4	25.9	27.0	39.2	33.1	33.3	40.2	34.2
Zr	310.9	303.3	299.7	458.0	347.0	263.0	440.0	330.0
Nb	89.5	86.9	88.3	91.2	77.9	67.2	93.7	65.8
Cs	0.7	0.4	0.7	1.4	1.3	1.3	1.5	1.5
Ba	679.7	1380.0	1030.0	1088.0	903.0	902.0	1061.0	807.0
La	60.0	57.7	59.5	69.9	60.5	60.3	78.5	60.4
Ce	118.6	115.8	118.9	144.0	122.0	123.0	158.0	124.0
Pr	14.6	14.2	14.7	16.5	14.0	14.0	17.9	14.1
Nd	60.2	57.6	58.9	64.3	56.7	56.1	69.5	55.8
Sm	11.37	11.20	11.17	12.00	10.40	10.50	12.90	10.30
Eu	3.59	3.41	3.47	3.99	3.40	3.47	4.04	3.30
Gd	8.65	8.15	8.18	9.85	8.39	8.75	10.60	8.57
Tb	1.26	1.19	1.21	1.50	1.27	1.29	1.58	1.26
Dy	6.07	5.69	5.86	7.89	6.58	6.74	8.18	6.59
Ho	1.03	1.00	1.00	1.50	1.19	1.25	1.55	1.25
Er	2.59	2.50	2.52	3.65	3.02	3.12	3.88	3.04
Tm	0.35	0.32	0.32	0.50	0.40	0.39	0.50	0.41
Yb	2.00	1.95	1.92	3.20	2.48	2.56	3.28	2.59
Lu	0.29	0.28	0.28	0.48	0.38	0.37	0.48	0.38
Hf	7.63	7.62	7.41	10.90	8.30	7.40	10.40	7.70
Ta	4.98	5.05	5.09	11.03	5.62	5.04	6.97	4.97
Th	6.33	6.23	6.35	11.20	8.01	7.19	10.70	7.50
U	1.74	1.73	1.72	3.32	2.36	2.24	3.18	2.18
#Mg	0.50	0.57	0.56	0.35	0.41	0.35	0.33	0.37
$(La/Yb)_N$	20.2	19.9	20.8	14.7	16.4	15.9	16.1	15.7

occurrence	Paço d'Ilhas sill	Paço d'Ilhas sill	Paço d'Ilhas sill	Paço d'Ilhas sill	Paço d'Ilhas sill	Paço d'Ilhas sill	Loulé lamproph.	Loulé lamproph.
sample ref.	PI06	PI07	PI08	PI09	PI10	PI11	C-20	C-12-1
SiO_2 (%)	50.27	52.41	49.62	50.94	53.56	53.3	36.56	34.2
Al_2O_3	16.67	16.81	12.21	16.87	15.96	16.35	11.85	9.58
Fe_2O_3 (tot)	8.84	6.49	13.31	8.21	6.45	6.77	11.88	11.82
MnO	0.142	0.157	0.164	0.182	0.155	0.195	0.183	0.229
MgO	3.26	1.55	4.31	3.04	1.97	1.95	7.68	12.48
CaO	5.48	5.2	7.93	5.80	4.54	5.56	14.04	14.89
Na_2O	4.03	4.76	2.41	4.22	4.67	4.56	4.37	2.04
K_2O	2.97	3.71	1.86	3.32	3.9	3.56	2.51	1.51
TiO_2	2.19	1.58	4.10	2.01	1.47	1.72	3.88	3.46
P_2O_5	0.68	0.44	0.58	0.59	0.47	0.52	1.4	1.31
LOI	5.53	6.12	3.94	4.97	6.1	5.9	6.01	6.98
Total	100.1	99.2	100.4	100.1	99.2	100.4	100.4	98.5
Sc (ppm)	9.0	7.0	24.0	9.0	6.0	8.0	21.0	24.0
V	122.0	65.0	340.0	109.0	60.0	78.0	297.0	276.0
Ni	2	2	2	2	2	4	61	190
Cr	n.d.	n.d.	8.0	n.d.	n.d.	n.d.	110.0	410.0
Ga	19.0	21.0	21.0	20.0	21.0	20.0	19.0	16.0
Ge	1.5	1.5	1.4	1.3	1.6	1.7	1.3	1.2
Rb	67.0	107.0	81.0	83.0	111.0	93.0	58.0	64.0
Sr	1054	904	760	977	733	952	1534	2149
Y	33.1	40.9	43.9	36.4	41.5	37.0	33.7	32.7
Zr	307.0	484.0	333.0	365.0	483.0	390.0	345.0	297.0
Nb	65.9	88.4	75.7	75.5	90.6	78.9	145.0	124.0
Cs	1.3	2.0	1.2	1.3	1.5	1.7	0.8	0.6
Ba	844.0	1079.0	682.0	894.0	858.0	1131.0	1178.0	1230.0
La	62.1	72.7	64.7	70.0	80.0	75.3	124.0	165.0
Ce	126.0	147.0	134.0	140.0	162.0	152.0	243.0	293.0
Pr	14.2	16.7	15.1	15.7	18.0	16.7	28.1	32.7
Nd	56.5	64.5	59.6	61.8	69.5	64.4	105.0	115.0
Sm	10.80	11.70	11.00	11.40	12.60	11.70	18.20	18.70
Eu	3.41	3.81	3.58	3.48	3.28	3.72	5.61	5.81
Gd	8.55	9.85	9.00	9.38	10.10	9.13	14.50	13.90
Tb	1.30	1.45	1.35	1.44	1.55	1.40	1.76	1.61
Dy	6.79	7.89	7.05	7.37	8.15	7.44	7.94	7.71
Ho	1.25	1.51	1.31	1.38	1.57	1.39	1.29	1.26
Er	3.08	3.86	3.25	3.45	3.96	3.45	3.25	3.21
Tm	0.42	0.53	0.44	0.46	0.54	0.47	0.42	0.41
Yb	2.58	3.29	2.78	2.78	3.23	2.90	2.30	2.27
Lu	0.36	0.51	0.41	0.41	0.49	0.43	0.31	0.29
Hf	7.50	11.50	8.50	9.10	11.30	9.10	7.20	6.30
Ta	5.19	6.79	5.81	5.65	6.81	5.80	11.50	6.82
Th	7.41	12.30	8.45	9.07	11.80	9.14	7.89	13.50
U	2.28	3.13	2.53	2.75	3.52	2.66	5.64	2.96
#Mg	0.41	0.31	0.38	0.41	0.37	0.35	0.55	0.67
$(La/Yb)_N$	16.2	14.9	15.7	17.0	16.7	17.5	36.3	49.0

occurrence	Monchique basic rocks	Monchique basic rocks	Monchique basic rocks	Monchique basic rocks	Monchique basic rocks	Monchique basic rocks	Monchique ne-syenite
sample ref.	b 468 B	b 468 A	b 84 A	b 84 B	b 132	b 629	s 598
SiO_2 (%)	33.97	39.89	40.55	42.24	42.65	48.94	55.73
Al_2O_3	10.89	13.35	14	14.59	14.85	16.59	20.83
Fe_2O_3 (tot)	16.60	12.72	14.79	11.92	11.49	8.76	3.27
MnO	0.25	0.279	0.208	0.23	0.213	0.202	0.109
MgO	7.87	5.23	6.16	5.74	5.61	3.9	0.78
CaO	14.97	11.72	11.44	11.29	11.36	7.97	2.06
Na_2O	2.04	4.15	3.29	3.50	4.35	4.94	7.70
K_2O	1.42	3.1	2.46	2.61	2.64	4	6.78
TiO_2	7.48	4.53	4.75	4.23	4.14	3.03	0.88
P_2O_5	2.42	1.85	0.83	1.17	1.01	0.95	0.14
LOI	0.77	2.16	1.05	1.49	1.52	0.7	2.12
Total	98.7	99.0	99.5	99.0	99.8	100.0	100.4
Sc (ppm)	24.0	12.0	29.0	21.0	22.0	10.0	2.0
V	461.6	302.9	369.9	291.3	301.1	224.5	58.9
Ni	n.d.	n.d.	n.d.	21	1	n.d.	n.d.
Cr	n.d.	n.d.	n.d.	n.d.	n.d.	13.0	n.d.
Ga	21.5	21.7	22.2	19.8	21.6	22.1	28.2
Ge	1.0	1.2	1.5	1.1	1.5	1.9	1.1
Rb	28.3	84.4	57.2	52.1	58.1	86.7	214.2
Sr	2240	3280	1420	1490	1750	1580	1290
Y	47.5	53.9	28.8	33.0	33.9	43.2	14.0
Zr	343.8	444.2	298.5	329.5	327.6	376.5	377.0
Nb	127.9	168.5	78.4	105.3	105.1	152.9	142.4
Cs	0.5	1.4	1.3	1.3	1.9	1.1	3.6
Ba	923.3	1430.0	881.4	1010.0	1190.0	1230.0	866.8
La	127.6	204.4	65.0	85.9	79.9	119.9	68.9
Ce	265.7	396.6	127.6	163.2	158.7	227.7	102.9
Pr	31.4	42.1	15.6	19.7	19.1	26.8	9.1
Nd	128.1	159.1	65.0	79.2	78.0	100.3	28.4
Sm	24.08	26.50	12.29	14.91	14.31	16.81	4.09
Eu	7.00	7.66	3.81	4.50	4.40	4.45	1.23
Gd	16.58	17.58	9.35	10.76	10.50	12.40	2.64
Tb	2.28	2.45	1.32	1.54	1.50	1.81	0.42
Dy	10.65	11.66	6.43	7.47	7.07	8.82	2.40
Ho	1.79	1.99	1.10	1.29	1.26	1.56	0.47
Er	4.28	5.07	2.78	3.18	3.06	4.01	1.41
Tm	0.50	0.63	0.35	0.41	0.40	0.55	0.22
Yb	2.95	3.73	2.09	2.44	2.34	3.10	1.42
Lu	0.41	0.54	0.30	0.36	0.32	0.45	0.22
Hf	9.49	9.84	7.70	8.10	7.96	8.27	6.41
Ta	8.11	11.38	5.60	7.54	6.75	10.11	6.11
Th	6.61	18.81	6.35	7.95	8.27	9.98	17.52
U	1.58	4.89	1.63	1.87	2.17	2.92	5.28
#Mg	0.47	0.44	0.44	0.48	0.48	0.46	0.31
$(La/Yb)_N$	29.2	36.9	21.0	23.7	22.9	26.0	32.7

occurrence	Monchique basic rocks	Monchique basic rocks	Monchique basic rocks	Monchique basic rocks	Monchique basic rocks	Monchique basic rocks	Monchique ne-syenite
sample ref.	b 468 B	b 468 A	b 84 A	b 84 B	b 132	b 629	s 598
SiO_2 (%)	33.97	39.89	40.55	42.24	42.65	48.94	55.73
Al_2O_3	10.89	13.35	14	14.59	14.85	16.59	20.83
Fe_2O_3 (tot)	16.60	12.72	14.79	11.92	11.49	8.76	3.27
MnO	0.25	0.279	0.208	0.23	0.213	0.202	0.109
MgO	7.87	5.23	6.16	5.74	5.61	3.9	0.78
CaO	14.97	11.72	11.44	11.29	11.36	7.97	2.06
Na_2O	2.04	4.15	3.29	3.50	4.35	4.94	7.70
K_2O	1.42	3.1	2.46	2.61	2.64	4	6.78
TiO_2	7.48	4.53	4.75	4.23	4.14	3.03	0.88
P_2O_5	2.42	1.85	0.83	1.17	1.01	0.95	0.14
LOI	0.77	2.16	1.05	1.49	1.52	0.7	2.12
Total	98.7	99.0	99.5	99.0	99.8	100.0	100.4
Sc (ppm)	24.0	12.0	29.0	21.0	22.0	10.0	2.0
V	461.6	302.9	369.9	291.3	301.1	224.5	58.9
Ni	n.d.	n.d.	n.d.	21	1	n.d.	n.d.
Cr	n.d.	n.d.	n.d.	n.d.	n.d.	13.0	n.d.
Ga	21.5	21.7	22.2	19.8	21.6	22.1	28.2
Ge	1.0	1.2	1.5	1.1	1.5	1.9	1.1
Rb	28.3	84.4	57.2	52.1	58.1	86.7	214.2
Sr	2240	3280	1420	1490	1750	1580	1290
Y	47.5	53.9	28.8	33.0	33.9	43.2	14.0
Zr	343.8	444.2	298.5	329.5	327.6	376.5	377.0
Nb	127.9	168.5	78.4	105.3	105.1	152.9	142.4
Cs	0.5	1.4	1.3	1.3	1.9	1.1	3.6
Ba	923.3	1430.0	881.4	1010.0	1190.0	1230.0	866.8
La	127.6	204.4	65.0	85.9	79.9	119.9	68.9
Ce	265.7	396.6	127.6	163.2	158.7	227.7	102.9
Pr	31.4	42.1	15.6	19.7	19.1	26.8	9.1
Nd	128.1	159.1	65.0	79.2	78.0	100.3	28.4
Sm	24.08	26.50	12.29	14.91	14.31	16.81	4.09
Eu	7.00	7.66	3.81	4.50	4.40	4.45	1.23
Gd	16.58	17.58	9.35	10.76	10.50	12.40	2.64
Tb	2.28	2.45	1.32	1.54	1.50	1.81	0.42
Dy	10.65	11.66	6.43	7.47	7.07	8.82	2.40
Ho	1.79	1.99	1.10	1.29	1.26	1.56	0.47
Er	4.28	5.07	2.78	3.18	3.06	4.01	1.41
Tm	0.50	0.63	0.35	0.41	0.40	0.55	0.22
Yb	2.95	3.73	2.09	2.44	2.34	3.10	1.42
Lu	0.41	0.54	0.30	0.36	0.32	0.45	0.22
Hf	9.49	9.84	7.70	8.10	7.96	8.27	6.41
Ta	8.11	11.38	5.60	7.54	6.75	10.11	6.11
Th	6.61	18.81	6.35	7.95	8.27	9.98	17.52
U	1.58	4.89	1.63	1.87	2.17	2.92	5.28
#Mg	0.47	0.44	0.44	0.48	0.48	0.46	0.31
$(La/Yb)_N$	29.2	36.9	21.0	23.7	22.9	26.0	32.7

occurrence	LVC vent	LVC vent	LVC vent	LVC vent	LVC vent	LVC vent	LVC vent	LVC vent	LVC vent
sample ref.	RM 1	RM 3	RM 4	RM 28	RM 29	RM 30	RM 66	RM 92	RM 57
SiO_2 (%)	45.39	45.73	42.38	43.99	43.59	41.4	43.3	41.08	44.98
Al_2O_3	15.14	15.34	14.83	15.67	15.97	14.12	12.76	12.90	15.92
Fe_2O_3 (tot)	11.72	11.75	13.09	12.99	12.38	13.65	11.93	13.12	12.23
MnO	0.168	0.165	0.209	0.182	0.218	0.193	0.171	0.189	0.196
MgO	7.58	7.63	6.2	6.29	4.6	7.71	9.98	9.75	5.17
CaO	10.44	10.44	10.7	9.47	9.75	10.93	11.45	12.02	8.79
Na_2O	3.04	2.98	2.97	3.38	3.65	2.76	2.54	3.34	3.94
K_2O	1.62	1.51	1.75	1.61	2.49	1.99	1	1.05	2.27
TiO_2	3.04	3.07	4.24	3.90	3.38	3.87	3.00	3.92	3.75
P_2O_5	0.39	0.4	1	0.61	1.23	0.78	0.44	0.69	0.98
LOI	0.78	0.97	1.98	1.18	1.62	1.62	2.58	1.54	1.26
Total	99.3	100.0	99.3	99.3	98.9	99.0	99.1	99.6	99.5
Sc (ppm)	27.0	27.0	16.0	21.0	12.0	24.0	31.0	30.0	14.0
V	290.0	293.0	385.0	338.0	297.0	369.0	328.0	365.0	254.0
Ni	70	66	15	36	9	59	143	154	18
Cr	110.0	110.0	40.0	70.0	< 20	120.0	400.0	280.0	n.d.
Ga	20.0	20.0	24.0	24.0	28.0	25.0	19.0	21.0	25.0
Ge	1.3	1.3	1.4	1.3	1.4	1.3	1.3	1.2	1.4
Rb	48.0	36.0	48.0	38.0	61.0	47.0	26.0	43.0	57.0
Sr	756	789	1409	1053	1618	1306	763	1035	1456
Y	25.1	24.5	34.5	29.6	37.2	30.0	22.7	26.6	33.9
Zr	181.0	184.0	346.0	279.0	367.0	327.0	200.0	285.0	372.0
Nb	48.0	47.3	95.8	68.9	118.0	86.2	48.3	68.4	98.2
Cs	0.5	0.6	1.1	1.2	3.3	2.4	0.9	0.6	1.5
Ba	533.0	546.0	720.0	593.0	877.0	712.0	440.0	585.0	815.0
La	39.4	39.6	85.2	57.6	103.0	72.1	41.5	57.4	81.5
Ce	77.3	77.8	168.0	116.0	200.0	143.0	85.2	119.0	152.0
Pr	9.2	9.1	19.4	13.7	22.5	16.8	10.2	14.3	17.7
Nd	38.3	38.0	77.7	55.9	87.8	67.4	42.1	59.5	69.9
Sm	7.87	7.62	14.00	10.60	14.80	12.10	8.03	11.00	12.30
Eu	2.68	2.71	4.52	3.57	4.73	3.85	2.66	3.62	4.00
Gd	7.10	7.12	11.70	9.07	11.80	10.00	6.80	9.32	10.50
Tb	1.06	1.06	1.65	1.31	1.64	1.37	1.02	1.30	1.42
Dy	5.36	5.31	7.88	6.45	7.96	6.55	4.98	6.17	6.97
Ho	0.94	0.93	1.34	1.10	1.33	1.08	0.86	1.04	1.22
Er	2.51	2.50	3.46	2.92	3.47	2.81	2.28	2.69	3.18
Tm	0.33	0.33	0.45	0.40	0.46	0.38	0.31	0.36	0.42
Yb	1.99	1.96	2.60	2.34	2.66	2.15	1.81	2.06	2.45
Lu	0.28	0.28	0.35	0.32	0.36	0.27	0.26	0.27	0.35
Hf	4.80	4.70	7.80	7.10	8.90	7.30	5.30	7.00	8.50
Ta	3.69	3.65	7.97	5.51	9.21	6.61	4.10	5.92	6.98
Th	4.98	4.98	9.25	6.27	11.20	7.60	4.42	5.66	9.59
U	1.22	1.20	2.70	1.60	2.94	1.99	1.20	1.50	2.55
#Mg	0.55	0.55	0.47	0.48	0.41	0.52	0.61	0.58	0.44
$(La/Yb)_N$	13.3	13.6	22.1	16.6	26.1	22.6	15.4	18.8	22.4

occurrence	LVC flow	LVC flow	LVC flow	LVC flow	LVC flow	LVC flow	Lomba dos Pianos sill	Malveira da Serra sill
sample ref.	RM 7	RM 42	RM 43	RM 69	RM 71	RM 80	RM 9	RM 25
SiO_2 (%)	39.81	42.58	42.68	43.19	42.85	41.07	44.72	41.02
Al_2O_3	12.91	15.1	15.01	12.92	15.01	13.16	16.44	14.67
Fe_2O_3 (tot)	14.14	13.54	13.27	12.02	12.34	12.85	11.96	13.35
MnO	0.166	0.221	0.216	0.169	0.171	0.174	0.177	0.172
MgO	9.52	6.1	6.14	10.65	6.26	10.07	5.3	7.3
CaO	11.6	10.87	10.73	11.59	8.79	10.89	8.24	9.52
Na_2O	2.48	2.92	3.10	2.06	3.01	3.22	3.35	2.88
K_2O	1.36	1.88	1.72	1.94	2.16	0.82	1.79	2.29
TiO_2	4.43	4.13	4.04	3.17	4.30	3.98	3.03	3.28
P_2O_5	0.48	0.91	0.88	0.53	0.69	0.54	0.7	0.8
LOI	2.32	1.3	1.37	1.76	3.66	2.75	4.1	3.8
Total	99.2	99.6	99.2	100.0	99.2	99.5	99.8	99.1
Sc (ppm)	35.0	18.0	19.0	29.0	18.0	28.0	14.0	19.0
V	434.0	337.0	326.0	294.0	278.0	340.0	220.0	293.0
Ni	85	36	34	176	40	126	15	56
Cr	160.0	50.0	70.0	410.0	40.0	210.0	n.d.	50.0
Ga	20.0	25.0	25.0	19.0	22.0	20.0	21.0	21.0
Ge	1.3	1.4	1.4	1.2	1.3	1.3	1.2	1.2
Rb	45.0	35.0	29.0	69.0	39.0	54.0	42.0	93.0
Sr	1195	1429	1313	978	1489	1043	1409	773
Y	24.6	34.7	34.9	24.2	29.9	25.8	24.2	24.2
Zr	200.0	366.0	353.0	224.0	305.0	263.0	259.0	253.0
Nb	53.6	84.6	84.2	61.0	76.8	64.3	64.3	67.7
Cs	0.5	3.2	5.1	1.2	0.8	0.7	1.4	1.9
Ba	546.0	720.0	706.0	526.0	1283.0	613.0	617.0	575.0
La	43.1	74.7	73.2	46.9	58.5	52.7	54.5	58.7
Ce	88.6	153.0	149.0	93.6	119.0	108.0	108.0	118.0
Pr	10.8	18.2	17.8	10.9	14.1	12.9	12.3	13.4
Nd	45.7	73.5	71.9	45.4	57.9	52.6	49.5	53.7
Sm	9.12	13.30	13.30	8.71	10.70	9.91	8.93	9.73
Eu	3.08	4.43	4.26	2.90	3.59	3.27	3.05	3.25
Gd	7.98	11.30	10.90	7.56	9.26	8.46	7.48	8.26
Tb	1.12	1.57	1.54	1.09	1.29	1.19	1.09	1.17
Dy	5.50	7.49	7.42	5.32	6.33	5.75	5.37	5.62
Ho	0.90	1.29	1.27	0.89	1.10	0.97	0.92	0.96
Er	2.33	3.39	3.32	2.29	2.87	2.51	2.41	2.44
Tm	0.30	0.45	0.45	0.30	0.38	0.33	0.32	0.31
Yb	1.73	2.62	2.57	1.79	2.22	1.92	1.90	1.78
Lu	0.24	0.37	0.35	0.24	0.30	0.26	0.26	0.24
Hf	5.20	8.50	8.40	5.70	7.20	6.50	5.90	6.30
Ta	4.21	6.81	6.72	4.90	6.23	5.36	5.19	5.65
Th	4.41	7.45	7.31	5.43	6.42	5.55	5.83	6.45
U	1.17	1.99	1.96	1.39	1.75	1.36	1.50	1.73
#Mg	0.56	0.46	0.47	0.63	0.49	0.60	0.46	0.51
$(La/Yb)_N$	16.8	19.2	19.2	17.6	17.7	18.5	19.3	22.2

occurrence	Eiras do Faião sill	Eiras do Faião sill	Montelevar sill	Anços sill	Anços sill	Anços sill	Ribeira d'Ilhas plug	Ribeira d'Ilhas plug
sample ref.	RM 46	RM 47	RM 50	RM 55	RM 67	RM 68	RM 36	RM 37
SiO_2 (%)	48.31	46.78	53.27	55.70	53.84	54.01	39.26	41.21
Al_2O_3	16.61	15.99	17.12	18.51	18.03	18.35	12.49	13.06
Fe_2O_3 (tot)	8.82	8.86	7.72	6.50	7.34	6.69	12.00	13.25
MnO	0.213	0.214	0.119	0.133	0.077	0.093	0.172	0.197
MgO	3.04	3.48	2.78	2.44	2.71	2.4	8.63	9.96
CaO	6.35	6.22	7.25	5.15	6.21	6.23	11.68	10.78
Na_2O	6.41	5.56	3.96	4.67	4.09	4.26	2.14	3.1
K_2O	3.17	3.36	2.63	3.01	2.61	2.65	1.74	1.49
TiO_2	2.51	2.50	1.78	1.47	1.65	1.56	3.51	3.76
P_2O_5	0.91	0.87	0.51	0.54	0.59	0.56	0.72	0.82
LOI	4.29	4.94	3.42	2.77	3.08	2.85	6.51	1.31
Total	100.6	98.8	100.6	100.9	100.2	99.7	98.9	98.9
Sc (ppm)	6.0	6.0	12.0	10.0	11.0	10.0	23.0	23.0
V	178.0	180.0	139.0	87.0	105.0	98.0	287.0	303.0
Ni	2	1	18	5	8	7	137	153
Cr	n.d.	n.d.	40.0	< 20	n.d.	n.d.	330.0	340.0
Ga	29.0	27.0	25.0	24.0	23.0	24.0	20.0	22.0
Ge	1.3	1.5	1.2	1.3	1.2	1.1	1.2	1.3
Rb	113.0	111.0	74.0	76.0	66.0	67.0	40.0	25.0
Sr	1220	1055	747	679	879	878	1406	1551
Y	37.6	37.7	31.1	33.0	28.2	29.2	27.9	30.4
Zr	603.0	282.0	278.0	345.0	313.0	319.0	286.0	294.0
Nb	146.0	142.0	49.2	63.5	59.2	59.1	81.4	89.9
Cs	2.3	3.3	1.4	1.9	1.1	1.0	3.2	5.5
Ba	1203.0	1226.0	688.0	815.0	698.0	704.0	737.0	731.0
La	120.0	123.0	59.6	65.2	58.5	56.0	60.9	67.2
Ce	221.0	229.0	118.0	125.0	114.0	109.0	124.0	140.0
Pr	24.3	25.0	13.3	14.3	12.9	12.3	14.7	16.8
Nd	90.7	95.1	52.6	56.4	50.4	48.3	58.4	67.2
Sm	15.00	15.70	9.63	10.30	9.13	8.85	10.60	12.10
Eu	4.63	4.93	2.89	3.24	3.01	2.87	3.49	4.03
Gd	11.60	12.50	8.26	8.85	7.97	7.60	8.80	9.90
Tb	1.63	1.74	1.26	1.33	1.17	1.15	1.22	1.40
Dy	7.75	8.25	6.36	6.81	5.96	5.70	5.99	6.70
Ho	1.31	1.40	1.12	1.24	1.04	1.02	1.00	1.11
Er	3.43	3.65	3.05	3.36	2.87	2.84	2.58	2.84
Tm	0.46	0.50	0.42	0.46	0.39	0.38	0.33	0.36
Yb	2.73	2.89	2.46	2.79	2.44	2.31	1.91	2.12
Lu	0.38	0.38	0.33	0.39	0.34	0.33	0.26	0.28
Hf	12.30	8.70	6.70	8.50	7.40	7.20	6.50	7.10
Ta	10.50	11.10	3.99	5.37	4.90	4.66	6.44	7.33
Th	16.10	15.90	7.98	9.89	8.68	8.68	5.65	6.04
U	4.68	4.48	2.43	2.72	2.38	2.27	1.39	1.49
#Mg	0.39	0.43	0.40	0.41	0.41	0.40	0.58	0.59
$(La/Yb)_N$	29.6	28.7	16.3	15.7	16.1	16.3	21.5	21.3

occurrence	Cascais dyke	Cascais dyke	Cascais dyke	Sintra gabbro	Sintra gabbro	Sintra gabbro	Sintra gabbro	Sintra gabbro	Sintra gabbro
sample ref.	RM 52	RM 64	RM 90	RM 11	RM 16	RM 17	RM 20	RM 22	RM 23
SiO_2 (%)	39.31	44.53	47.1	41.33	43.15	40.36	44.98	44.92	42.28
Al_2O_3	15.49	11.10	16.34	15.94	16.53	15.69	20.44	19.72	18.93
Fe_2O_3 (tot)	13.58	11.22	9.78	13.1	12.33	14.4	9.88	10.37	11.33
MnO	0.127	0.153	0.144	0.171	0.173	0.202	0.148	0.14	0.13
MgO	4.71	11.58	3.25	6.1	5.27	6.36	3.87	3.81	5.18
CaO	6.95	10.74	9.1	11.04	9.38	10.23	11.26	11.11	11.34
Na_2O	2.76	2.07	3.39	3.31	3.84	3.59	3.46	3.33	3.11
K_2O	2.49	1.29	1.74	1.32	1.61	1.13	0.96	1.11	1.13
TiO_2	3.65	2.61	2.47	3.97	3.61	4.54	3.08	3.33	3.66
P_2O_5	1.7	0.37	0.5	1.92	1.49	2.08	0.51	0.49	1.09
LOI	8.72	4.60	6.4	0.92	1.26	1.09	1.86	2.28	1.9
Total	99.5	100.3	100.2	99.1	98.6	99.7	100.4	100.6	100.1
Sc (ppm)	12.0	31.0	16.0	23.0	17.0	24.0	14.0	16.0	19.0
V	204.0	275.0	213.0	329.0	257.0	334.0	221.0	277.0	324.0
Ni	2	194	23	8	2	2	8	6	9
Cr	< 20	720.0	40.0	n.d.	n.d.	n.d.	n.d.	n.d.	n.d.
Ga	22.0	17.0	21.0	22.0	23.0	23.0	22.0	23.0	23.0
Ge	1.1	1.4	1.1	1.4	1.4	1.4	1.0	1.2	1.3
Rb	49.0	32.0	42.0	36.0	42.0	23.0	23.0	34.0	27.0
Sr	928	548	767	1198	1202	1416	1297	1086	1099
Y	32.4	20.9	23.0	38.8	37.7	43.2	17.8	15.4	27.1
Zr	153.0	180.0	224.0	165.0	179.0	143.0	136.0	158.0	142.0
Nb	86.4	36.9	48.5	54.8	54.3	64.4	46.5	45.9	48.3
Cs	0.4	2.8	0.6	3.4	4.9	1.1	1.8	2.3	2.1
Ba	711.0	415.0	513.0	505.0	553.0	622.0	406.0	413.0	420.0
La	76.8	33.8	43.1	52.6	56.3	61.3	30.3	30.3	40.6
Ce	161.0	71.2	86.4	117.0	122.0	137.0	61.7	58.9	86.6
Pr	19.4	8.7	10.0	15.4	15.6	17.8	7.4	6.7	11.0
Nd	79.5	36.2	40.7	69.7	69.1	79.8	31.4	27.4	47.3
Sm	13.90	7.05	7.77	14.50	13.70	16.20	6.03	5.15	9.64
Eu	4.53	2.38	2.57	4.95	4.76	5.61	2.37	1.97	3.25
Gd	11.60	6.37	6.94	13.40	12.60	14.70	5.35	4.37	8.51
Tb	1.58	0.93	1.04	1.84	1.73	2.04	0.74	0.64	1.21
Dy	7.68	4.55	5.11	8.76	8.20	9.68	3.72	3.17	5.85
Ho	1.30	0.77	0.90	1.48	1.37	1.57	0.64	0.54	0.98
Er	3.41	2.04	2.40	3.59	3.39	3.87	1.66	1.42	2.45
Tm	0.46	0.26	0.33	0.43	0.42	0.47	0.23	0.19	0.31
Yb	2.68	1.52	2.02	2.37	2.32	2.59	1.31	1.11	1.71
Lu	0.36	0.21	0.27	0.31	0.30	0.33	0.17	0.15	0.22
Hf	5.80	4.80	5.60	4.40	4.40	3.90	3.20	3.60	3.70
Ta	7.50	3.09	4.18	4.01	4.15	4.65	3.76	3.74	3.70
Th	7.79	3.86	5.72	4.30	4.47	2.47	2.57	3.45	2.94
U	2.07	1.07	1.65	1.16	1.30	0.64	0.72	0.95	0.87
#Mg	0.40	0.66	0.39	0.47	0.45	0.45	0.42	0.41	0.46
$(La/Yb)_N$	19.3	15.0	14.4	14.9	16.3	15.9	15.6	18.4	16.0

occurrence	Sintra gabbro	Sintra diorite	Sines diorite	Sines gabbro	Sines gabbro	Sines gabbro	Sines gabbro	Sines gabbro	Mafra gabbro
sample ref.	RM 23	RM 24	RM 95	RM 96	RM 98	RM 99	RM 100	RM 101	RM 83
SiO_2 (%)	42.28	46.94	50.31	43.83	49.13	43.41	42.8	42.84	44.19
Al_2O_3	18.93	16.41	16.34	20.48	19.01	12.42	9.9	11.82	13.29
Fe_2O_3 (tot)	11.33	11.06	11.33	11	9	15.03	14.91	14.38	12.48
MnO	0.13	0.2	0.192	0.145	0.166	0.2	0.189	0.181	0.177
MgO	5.18	5.2	4.72	3.99	3.62	15	13.35	12.24	7.84
CaO	11.34	9.07	7.47	10.87	8.75	9.55	12.12	11.92	13.38
Na_2O	3.11	3.55	3.33	3.51	4.86	1.36	1.23	1.49	2.72
K_2O	1.13	1.45	2.35	1.04	1.48	0.48	0.53	0.55	1.26
TiO_2	3.66	2.77	2.89	3.20	2.65	2.11	3.10	3.12	3.33
P_2O_5	1.09	1.01	0.65	1.41	1.14	0.19	0.32	0.21	0.49
LOI	1.9	1.71	0.70	1.16	0.84	0.43	0.92	0.85	1.27
Total	100.1	99.4	100.3	100.6	100.7	100.2	99.4	99.6	100.4
Sc (ppm)	19.0	18.0	18.0	16.0	10.0	31.0	47.0	43.0	34.0
V	324.0	214.0	267.0	278.0	143.0	295.0	422.0	401.0	365.0
Ni	9	28	24	12	1	154	133	130	81
Cr	n.d.	50.0	50.0	20.0	n.d.	500.0	460.0	400.0	200.0
Ga	23.0	23.0	23.0	25.0	24.0	15.0	17.0	17.0	21.0
Ge	1.3	1.7	1.2	1.3	1.2	1.1	1.4	1.2	1.3
Rb	27.0	40.0	60.0	30.0	31.0	12.0	12.0	12.0	32.0
Sr	1099	947	695	1431	1277	518	413	488	826
Y	27.1	31.5	36.4	34.6	37.6	13.4	21.5	18.4	24.1
Zr	142.0	170.0	331.0	125.0	194.0	81.0	122.0	109.0	213.0
Nb	48.3	61.6	61.6	44.2	66.2	21.9	24.1	23.8	47.4
Cs	2.1	1.6	1.6	1.5	0.8	0.9	0.8	1.1	5.9
Ba	420.0	492.0	590.0	387.0	672.0	146.0	184.0	189.0	421.0
La	40.6	57.3	60.4	53.1	64.9	15.5	21.4	18.7	42.3
Ce	86.6	116.0	124.0	116.0	134.0	32.8	47.7	42.1	87.0
Pr	11.0	13.8	14.3	14.9	16.2	4.0	6.1	5.4	10.4
Nd	47.3	57.4	58.1	66.1	68.9	17.3	27.4	23.9	43.9
Sm	9.64	10.80	11.00	13.30	13.00	3.74	6.25	5.27	8.66
Eu	3.25	3.60	3.30	4.74	5.08	1.37	2.01	1.86	2.94
Gd	8.51	9.53	9.84	12.40	12.20	3.54	5.99	5.11	7.74
Tb	1.21	1.38	1.50	1.71	1.75	0.53	0.91	0.78	1.12
Dy	5.85	6.84	7.65	8.31	8.67	2.81	4.60	3.97	5.42
Ho	0.98	1.18	1.35	1.36	1.48	0.50	0.79	0.71	0.92
Er	2.45	3.15	3.77	3.39	3.82	1.36	2.07	1.85	2.40
Tm	0.31	0.42	0.54	0.42	0.50	0.18	0.28	0.24	0.32
Yb	1.71	2.43	3.27	2.36	2.87	1.07	1.64	1.39	1.85
Lu	0.22	0.33	0.45	0.31	0.37	0.15	0.22	0.19	0.24
Hf	3.70	4.50	8.20	3.80	5.40	2.30	3.70	3.40	5.60
Ta	3.70	4.93	5.29	3.48	5.16	1.82	2.02	1.98	4.04
Th	2.94	4.61	5.10	2.20	3.63	1.83	1.99	1.54	4.91
U	0.87	1.37	1.60	0.63	1.01	0.46	0.51	0.40	1.28
#Mg	0.46	0.47	0.44	0.41	0.43	0.65	0.63	0.62	0.54
$(La/Yb)_N$	16.0	15.9	12.4	15.2	15.2	9.8	8.8	9.1	15.4

occurrence	Fontanelas seamount	Fontanelas seamount	Fontanelas seamount	Fontanelas seamount	Fontanelas seamount	Fontanelas seamount	Fontanelas seamount
sample ref.	AT 690A	AT 690B	AT 691A	AT 692E	AT 693P1	AT 693P2	AT 693E
SiO_2 (%)	34.94	35.28	35.2	44.35	46.88	36.48	37.46
Al_2O_3	12.77	12.69	11.91	12.63	14.78	11.27	11.55
Fe_2O_3 (tot)	13.29	12.89	12.29	13.98	11.44	12.1	12.02
MnO	0.158	0.166	0.168	0.578	0.183	0.233	0.216
MgO	6.93	6.99	6.58	5.6	8.56	8.68	8.94
CaO	17.38	17.34	18.31	6.86	11.77	16.06	16.9
Na_2O	0.6	0.71	0.55	0.96	2.13	0.64	0.61
K_2O	0.75	0.78	1.14	2.35	0.15	1.05	0.98
TiO_2	4.45	4.24	3.43	3.80	1.31	3.30	3.49
P_2O_5	0.64	0.61	0.86	2.13	0.1	0.67	0.62
LOI	6.73	6.67	10.02	6.53	2.96	8.52	7.07
Total	98.6	98.4	100.5	99.8	100.3	99.0	99.9
Sc (ppm)	35.0	38.0	35.0	35.0	33.0	33.0	43.0
V	494.0	483.0	317.0	231.0	336.0	362.0	341.0
Ni	67	80	256	281	314	278	163
Cr	290.0	340.0	830.0	990.0	690.0	870.0	340.0
Ga	21.0	18.0	18.0	15.0	15.0	16.0	16.0
Ge	1.9	2.1	2.7	1.8	1.5	1.6	1.4
Rb	15.0	18.0	30.0	63.0	30.0	24.0	5.0
Sr	349	383	383	307	358	346	145
Y	26.0	24.1	28.6	28.5	23.8	24.8	22.2
Zr	283.0	254.0	329.0	289.0	258.0	186.0	65.0
Nb	63.3	57.7	94.1	78.1	71.1	63.8	2.1
Cs	0.3	0.3	0.8	1.5	0.9	0.5	0.4
Ba	570.0	626.0	756.0	669.0	633.0	632.0	9.0
La	49.0	41.0	74.0	68.4	48.6	52.5	2.5
Ce	112.0	93.4	148.0	118.0	103.0	111.0	8.3
Pr	12.3	12.6	15.4	12.5	13.0	11.6	1.5
Nd	49.7	48.2	56.2	45.8	46.3	44.7	8.2
Sm	10.90	9.61	11.70	9.47	9.43	9.67	2.75
Eu	3.30	3.32	3.50	2.89	3.33	2.90	1.21
Gd	8.74	8.07	9.18	7.56	7.98	7.81	3.70
Tb	1.13	1.08	1.19	0.99	1.06	1.04	0.65
Dy	5.47	5.15	5.83	5.01	5.22	5.04	3.96
Ho	0.98	0.89	1.07	0.92	0.91	0.92	0.81
Er	2.55	2.30	2.80	2.49	2.34	2.38	2.43
Tm	0.31	0.29	0.37	0.32	0.30	0.30	0.36
Yb	1.74	1.66	2.07	1.82	1.72	1.72	2.10
Lu	0.23	0.22	0.28	0.25	0.23	0.23	0.30
Hf	8.40	7.30	8.90	7.90	7.00	4.90	2.20
Ta	5.02	4.87	6.50	5.62	5.52	5.02	0.11
Th	4.14	4.06	7.61	6.54	5.60	4.51	0.15
U	0.91	1.22	1.38	3.80	0.98	0.92	0.04
#Mg	0.50	0.51	0.50	0.43	0.58	0.58	0.59
$(La/Yb)_N$	19.0	16.6	24.1	25.3	19.0	20.6	0.8

Table II.2 - Recalculated whole rock major element composition in volatile free base

occurrence	Foz da Fonte sill	Foz da Fonte sill	Foz da Fonte sill	Paço d'Ilhas sill	Paço d'Ilhas sill	Paço d'Ilhas sill	Paço d'Ilhas sill	Paço d'Ilhas sill	Paço d'Ilhas sill	Paço d'Ilhas sill	Paço d'Ilhas sill	Paço d'Ilhas sill
sample ref.	FF 2	FF 3	FF 4	PI01	Pl02	PI03	PI04	PI05	PI06	PI07	PI08	PI09
SiO2 (%)	43.06	43.60	43.46	55.60	52.42	49.47	56.65	53.88	53.18	56.29	51.42	53.52
Al2O3	14.64	14.82	14.99	17.41	17.95	13.60	16.73	17.65	17.63	18.06	12.65	17.72
Fe2O3	12.69	13.17	13.14	7.77	9.47	15.05	7.56	8.54	9.35	6.97	13.79	8.63
MnO	0.16	0.15	0.17	0.20	0.15	0.18	0.23	0.20	0.15	0.17	0.17	0.19
MgO	6.61	9.21	8.78	2.20	3.43	4.26	2.01	2.64	3.45	1.66	4.47	3.19
CaO	13.31	9.41	9.58	5.66	6.03	8.10	5.68	7.26	5.80	5.59	8.22	6.09
Na2O	1.75	1.64	1.68	5.06	4.38	2.93	4.96	4.31	4.26	5.11	2.50	4.43
K2O	2.29	2.41	2.71	3.55	3.17	1.34	3.69	2.71	3.14	3.98	1.93	3.49
TiO2	4.80	4.89	4.80	1.94	2.30	4.26	1.93	2.19	2.32	1.69	4.25	2.11
P2O5	0.69	0.69	0.70	0.60	0.70	0.81	0.55	0.62	0.72	0.47	0.60	0.62
Total	100.00	100.00	100.00	100.00	100.00	100.00	100.00	100.00	100.00	100.00	100.00	100.00

occurrence	Paço d'Ilhas sill	Paço d'Ilhas sill	Loulé lamprophyres	Loulé lamprophyres	Monchique basic rocks	Monchique basic rocks	Monchique basic rocks	Monchique basic rocks	Monchique basic rocks	Monchique basic rocks	Monchique ne-syenite	LVC neck
sample ref.	PI10	PI11	C-20	C-12-1	b 468 B	b 468 A	b 84 A	b 84 B	b 132	b 629	s 598	RM 1
SiO2 (%)	57.50	56.41	38.75	37.37	34.69	41.20	41.18	43.31	43.38	49.30	56.71	46.07
Al2O3	17.13	17.30	12.56	10.47	11.12	13.79	14.22	14.96	15.11	16.71	21.20	15.37
Fe2O3	6.92	7.17	12.59	12.92	16.95	13.14	15.02	12.22	11.69	8.82	3.33	11.90
MnO	0.17	0.21	0.19	0.25	0.26	0.29	0.21	0.24	0.22	0.20	0.11	0.17
MgO	2.11	2.06	8.14	13.64	8.04	5.40	6.26	5.89	5.71	3.93	0.79	7.69
CaO	4.87	5.88	14.88	16.27	15.29	12.11	11.62	11.58	11.56	8.03	2.10	10.60
Na2O	5.01	4.83	4.63	2.23	2.08	4.29	3.34	3.59	4.42	4.98	7.84	3.09
K2O	4.19	3.77	2.66	1.65	1.45	3.20	2.50	2.68	2.69	4.03	6.90	1.64
TiO2	1.58	1.82	4.11	3.78	7.64	4.68	4.82	4.34	4.21	3.05	0.89	3.09
P2O5	0.50	0.55	1.48	1.43	2.47	1.91	0.84	1.20	1.03	0.96	0.14	0.40
Total	100.00	100.00	100.00	100.00	100.0	100.0	100.0	100.0	100.0	100.0	100.0	100.0

occurrence	LVC neck	LVC neck	LVC neck	LVC neck	LVC neck	LVC neck	LVC neck	LVC flow	LVC flow	LVC flow	LVC flow	LVC flow	LVC flow
sample ref.	RM 4	RM 28	RM 29	RM 30	RM 66	RM 92	RM 57	RM 7	RM 42	RM 43	RM 69	RM 71	RM 80
SiO2 (%)	43.53	44.85	44.82	42.51	44.84	41.89	45.79	41.08	43.33	43.65	43.96	44.83	42.45
Al2O3	15.23	15.98	16.42	14.50	13.21	13.16	16.21	13.32	15.37	15.35	13.15	15.70	13.60
Fe2O3	13.44	13.24	12.73	14.01	12.36	13.38	12.45	14.59	13.78	13.57	12.24	12.91	13.28
MnO	0.21	0.19	0.22	0.20	0.18	0.19	0.20	0.17	0.22	0.22	0.17	0.18	0.18
MgO	6.37	6.41	4.73	7.92	10.34	9.94	5.26	9.82	6.21	6.28	10.84	6.55	10.41
CaO	10.99	9.65	10.03	11.22	11.86	12.26	8.95	11.97	11.06	10.97	11.80	9.20	11.26
Na2O	3.05	3.45	3.75	2.83	2.63	3.41	4.01	2.56	2.97	3.17	2.10	3.15	3.33
K2O	1.80	1.64	2.56	2.04	1.04	1.07	2.31	1.40	1.91	1.76	1.97	2.26	0.85
TiO2	4.35	3.98	3.48	3.97	3.10	4.00	3.82	4.57	4.21	4.13	3.23	4.50	4.11
P2O5	1.03	0.62	1.26	0.80	0.46	0.70	1.00	0.50	0.93	0.90	0.54	0.72	0.56
Total	100.0	100.0	100.0	100.0	100.0	100.0	100.0	100.0	100.0	100.0	100.0	100.0	100.0

occurrence	LVC neck	Lomba dos Pianos sill	Malveira da Serra sill	Eiras do Faião sill	Eiras do Faião sill	Montelevar Sill	Anços sill	Anços sill	Anços sill	Ribeira d'Ilhas plug	Ribeira d'Ilhas plug	Cascais dyke	Cascais dyke
sample ref.	RM 3	RM 9	RM 25	RM 46	RM 47	RM 50	RM 55	RM 67	RM 68	RM 36	RM 37	RM 52	RM 64
SiO2 (%)	46.18	46.72	43.05	50.16	49.85	54.82	56.76	55.44	55.78	42.52	42.21	43.31	46.53
Al2O3	15.49	17.18	15.40	17.25	17.04	17.62	18.86	18.56	18.95	13.53	13.38	17.07	11.60
Fe2O3	11.87	12.50	14.01	9.16	9.44	7.94	6.62	7.56	6.91	13.00	13.57	14.96	11.72
MnO	0.17	0.18	0.18	0.22	0.23	0.12	0.14	0.08	0.10	0.19	0.20	0.14	0.16
MgO	7.71	5.54	7.66	3.16	3.71	2.86	2.49	2.79	2.48	9.35	10.20	5.19	12.10
CaO	10.54	8.61	9.99	6.59	6.63	7.46	5.25	6.39	6.43	12.65	11.04	7.66	11.22
Na2O	3.01	3.50	3.02	6.66	5.92	4.07	4.76	4.21	4.40	2.32	3.18	3.04	2.16
K2O	1.52	1.87	2.40	3.29	3.58	2.71	3.07	2.69	2.74	1.88	1.53	2.74	1.35
TiO2	3.10	3.16	3.44	2.60	2.67	1.83	1.50	1.70	1.61	3.80	3.85	4.03	2.73
P2O5	0.40	0.73	0.84	0.94	0.93	0.52	0.55	0.61	0.58	0.78	0.84	1.87	0.39
Total	100.0	100.0	100.0	100.0	100.0	100.0	100.0	100.0	100.0	100.0	100.0	100.0	100.0

occurrence	Sintra gabbro	Sintra gabbro	Sintra gabbro	Sintra gabbro	Sintra gabbro	Sintra gabbro	Sintra diorite	Sines diorite	Sines gabbro	Sines gabbro	Sines gabbro	Sines gabbro
sample ref.	RM 11	RM 16	RM 17	RM 20	RM 22	RM 23	RM 24	RM 95	RM 96	RM 98	RM 99	RM 100
SiO2 (%)	42.09	44.31	40.94	45.65	45.69	43.05	48.06	50.51	44.08	49.20	43.51	43.48
Al2O3	16.23	16.97	15.91	20.74	20.06	19.28	16.80	16.41	20.60	19.04	12.45	10.06
Fe2O3	13.34	12.66	14.61	10.03	10.55	11.54	11.33	11.38	11.06	9.01	15.06	15.15
MnO	0.17	0.18	0.20	0.15	0.14	0.13	0.20	0.19	0.15	0.17	0.20	0.19
MgO	6.21	5.41	6.45	3.93	3.88	5.27	5.32	4.74	4.01	3.63	15.03	13.56
CaO	11.24	9.63	10.38	11.43	11.30	11.55	9.29	7.50	10.93	8.76	9.57	12.31
Na2O	3.37	3.94	3.64	3.51	3.39	3.17	3.64	3.34	3.53	4.87	1.36	1.25
K2O	1.34	1.65	1.15	0.97	1.13	1.15	1.48	2.36	1.05	1.48	0.48	0.54
TiO2	4.04	3.71	4.60	3.12	3.39	3.72	2.84	2.90	3.22	2.66	2.11	3.15
P2O5	1.96	1.53	2.11	0.52	0.50	1.11	1.03	0.65	1.42	1.14	0.19	0.33
Total	100.0	100.0	100.0	100.0	100.0	100.0	100.0	100.0	100.0	99.9	100.0	100.0

occurrence	Cascais dyke	Mafra gabbro	Fontanelas seamount	Fontanelas seamount	Fontanelas seamount	Fontanelas seamount	Fontanelas seamount	Fontanelas seamount	Fontanelas seamount	Sines gabbro
sample ref.	RM 90	RM 83	AT 690A	AT 690B	AT 691A	AT 692E	AT 693P1	AT 693P2	AT 693E	RM 101
SiO2 (%)	50.21	44.58	38.01	38.48	38.95	47.58	40.31	40.37	48.16	43.38
Al2O3	17.42	13.41	13.89	13.84	13.18	13.55	12.45	12.45	15.18	11.97
Fe2O3	10.43	12.59	14.46	14.06	13.60	15.00	13.37	12.95	11.75	14.56
MnO	0.15	0.18	0.17	0.18	0.19	0.62	0.26	0.23	0.19	0.18
MgO	3.46	7.91	7.54	7.62	7.28	6.01	9.59	9.63	8.79	12.39
CaO	9.70	13.50	18.91	18.91	20.26	7.36	17.75	18.21	12.09	12.07
Na2O	3.61	2.74	0.65	0.77	0.61	1.03	0.71	0.66	2.19	1.51
K2O	1.86	1.27	0.82	0.85	1.26	2.52	1.16	1.06	0.15	0.56
TiO2	2.64	3.36	4.84	4.63	3.79	4.07	3.64	3.76	1.35	3.16
P2O5	0.53	0.49	0.70	0.67	0.95	2.28	0.74	0.67	0.10	0.21
Total	100.0	100.00	100.00	100.00	100.00	100.00	100.00	100.00	100.00	100.0

Annex III: Sr, Nd and Pb Isotope geochemistry

Table 1: Sr, Rb, Sm and Nd trace element data and measured and calculated initial Sr and Nd isotopic composition for the analyzed samples.

Occurrence	sample ref.	Age	Sr	Rb	$^{87}Rb/^{86}Sr$	Error (2σ)	$^{87}Sr/^{86}Sr$	Error (2 σ)	$^{87}Sr/^{86}Sr_i$	Nd	Sm	$^{147}Sm/^{144}Nd$	Error (2 σ)	$^{143}Nd/^{144}Nd$	Error (2 σ)	$^{143}Nd/^{144}Nd$	εNd_i
Foz da Fonte sill	FF 2	94	1270	44	0.100	0.003	0.703627	0.000038	0.70349	60.2	11.4	0.115	0.003	0.512806	0.000012	0.51274	4.3
Foz da Fonte sill	FF 4	94	1220	46	0.109	0.003	0.703660	0.000027	0.70351	58.9	11.2	0.115	0.003	0.512860	0.000016	0.51279	5.3
Paço d'Ilhas sill	PI01	88	1024	90	0.254	0.007	0.704159	0.000056	0.70385	64.3	12.0	0.113	0.003	0.512734	0.000011	0.51267	2.8
Paço d'Ilhas sill	PI05	88	1099	65	0.171	0.005	0.704051	0.000075	0.70384	55.8	10.3	0.112	0.003	0.512759	0.000023	0.51270	3.3
Paço d'Ilhas sill	PI06	88	1054	67	0.184	0.005	0.704120	0.000099	0.70389								
Paço d'Ilhas sill	PI07	88	904	107	0.342	0.010	0.704290	0.000052	0.70387	64.5	11.7	0.110	0.003	0.512749	0.000018	0.51269	3.1
Paço d'Ilhas sill	PI08	88	760	81	0.308	0.009	0.704172	0.000027	0.70379	59.6	11.0	0.112	0.003	0.512760	0.000012	0.51270	3.3
Paço d'Ilhas sill	PI10	88	733	111	0.438	0.012	0.704369	0.000054	0.70383	69.5	12.6	0.110	0.003	0.512772	0.000012	0.51271	3.6
Sintra gabbro	RM 11	74	1198	36	0.087	0.003	0.703382	0.000027	0.70328	69.7	14.5	0.125	0.003	0.512887	0.000013	0.51284	5.8
Sintra gabbro	RM 16	74	1202	42	0.101	0.003	0.703400	0.000027	0.70329	69.1	13.7	0.120	0.003	0.512896	0.000012	0.51283	5.6
Sintra gabbro	RM 20	74	1297	23	0.051	0.001	0.703260	0.000035	0.70321	31.4	6.0	0.116	0.003	0.512862	0.000015	0.51281	5.1
Sines gabbro	RM 96	74	1431	30	0.061	0.002	0.703070	0.000027	0.70301	66.1	13.3	0.122	0.003	0.512896	0.000012	0.51284	5.7
Sines gabbro	RM 99	75	518	12	0.067	0.002	0.703591	0.000028	0.70352	17.3	3.7	0.131	0.004	0.512835	0.000021	0.51277	4.5
Sines gabbro	RM 101	75	448	12	0.077	0.002	0.703421	0.000035	0.70334	23.9	5.3	0.133	0.004	0.512897	0.000011	0.51283	5.7
Monchique gabbro	b 468 B	72	2240	28	0.036	0.001	0.703205	0.000052	0.70317	128.0	24.0	0.113	0.003	0.5127581	0.000013	0.51270	3.1
Monchique ne-syenite	s 598	72	1290	214	0.480	0.013	0.703783	0.000055	0.70329	28.0	4.0	0.086	0.002	0.512825116	0.000012	0.51278	4.7

occurrence	sample ref.	Age	Sr	Rb	$^{87}Rb/^{86}Sr$	Error (2σ)	$^{87}Sr/^{86}Sr$	Error (2 σ)	$^{87}Sr/^{86}Sr_i$	Nd	Sm	$^{147}Sm/^{144}Nd$	Error (2 σ)	$^{143}Nd/^{144}Nd$	Erro (2 σ)	$^{143}Nd/^{144}Nd$	εNd_i
Loulé lamprophyre	C-12-1	72	2149	64	0.086	0.002	0.703486	0.000027	0.70340	115.0	18.7	0.098	0.003	0.512847	0.000018	0.5127€	4.3
Loulé lamprophyre	C-20	72	1534	58	0.109	0.003	0.703400	0.000027	0.70329	105.0	18.2	0.105	0.003	0.512813	0.000014	0.5128З	5.6
LVC neck	RM 1	72*	756	48	0.184	0.005	0.703496	0.000031	0.70331	38.3	7.9	0.124	0.004	0.512848	0.000015	0.5127९	4.8
LVC neck	RM 28	72*	1053	38	0.104	0.003	0.703479	0.000035	0.70337	55.9	10.6	0.115	0.003	0.512806	0.000013	0.5127Ƽ	4.0
LVC neck	RM 57	72*	1456	57	0.113	0.003	0.703485	0.000023	0.70337	69.9	12.3	0.106	0.003	0.512859	0.000010	0.51281	5.1
LVC neck	RM 66	72*	763	26	0.099	0.003	0.703613	0.000042	0.70351	42.1	8.0	0.115	0.003	0.512820	0.000017	0.51277	4.3
LVC flow	RM 43	72*	1313	29	0.064	0.002	0.703349	0.000028	0.70328	71.9	13.3	0.112	0.003	0.512828	0.000015	0.5127Ɛ	4.5
LVC flow	RM 69	72*	978	69	0.204	0.006	0.703900	0.000028	0.70369	45.4	8.7	0.116	0.003	0.512894	0.000019	0.51284	5.7
Mafra gabbro	RM 83	75*	826	32	0.112	0.003	0.703520	0.000030	0.70341	43.9	8.7	0.119	0.003	0.512846	0.000015	0.5127९	4.8
Lomba dos Pianos sill	RM 9	75*	1409	42	0.086	0.002	0.704972	0.000030	0.70488	49.5	8.9	0.109	0.003	0.512893	0.000014	0.51284	5.8
Malveira da Serra sill	RM 25	72*	773	93	0.348	0.010	0.704375	0.000027	0.70402	53.7	9.7	0.110	0.003	0.51288	0.000010	0.5128З	5.5
Eiras do Faião sill	RM 46	72*	1220	113	0.268	0.008	0.703811	0.000032	0.70354	90.7	15.0	0.100	0.003	0.512803	0.000014	0.5127€	4.1
Montelevar sill	RM 50	72*	747	74	0.287	0.008	0.704101	0.000028	0.70381	52.6	9.6	0.111	0.003	0.512882	0.000013	0.5128З	5.6
Anços sill	RM 55	72*	679	76	0.324	0.009	0.704057	0.000028	0.70373	56.4	10.3	0.110	0.003	0.512786	0.000013	0.5127З	3.7
Anços sill	RM 68	72*	878	67	0.221	0.006	0.703903	0.000027	0.70368	48.3	8.9	0.111	0.003	0.512822	0.000010	0.51277	4.4
Ribeira d'Ilhas plug	RM 37	72*	1551	25	0.047	0.001	0.703325	0.000035	0.70328	67.2	12.1	0.109	0.003	0.512847	0.000009	0.5128(	4.9
Cascais dyke	RM 64	72*	548	32	0.169	0.005	0.704110	0.000023	0.70394	36.2	7.1	0.118	0.003	0.512792	0.000016	0.51274	3.7
Cascais dyke	RM 90	72*	767	42	0.158	0.004	0.703732	0.000027	0.70357	40.7	7.8	0.115	0.003	0.512892	0.000022	0.51284	5.7
Fontanelas seamount	AT 690B	72*	383	18	0.136	0.004	0.703291	0.000027	0.70315	48.2	9.6	0.121	0.003	0.512821	0.000021	0.5127€	4.3

occurrence	sample ref.	Age	Sr	Rb	$^{87}Rb/^{86}Sr$	Error (2σ)	$^{87}Sr/^{86}Sr$	Error (2 σ)	$^{87}Sr/^{86}Sr_i$	Nd	Sm	$^{147}Sm/^{144}Nd$	Error (2 σ)	$^{143}Nd/^{144}Nd$	Erro (2 σ)	$^{143}Nd/^{144}Nd$	εNd_i
Fontanelas seamount	AT 693P1	72*	358	30	0.242	0.007	0.703316	0.000031	0.70306	46.3	9.4	0.123	0.003	0.512853	0.000016	0.51279	4.9

* Ages from previous works, as discussed in section 5.

Table 2: U, Th and Pb trace element data and measured and calculated initial isotopic Pb composition for the analyzed samples.

occurrence	sample	Age	Pb	U	Th	$^{206}Pb/^{204}Pb$	$^{207}Pb/^{204}Pb$	$^{208}Pb/^{204}Pb$	$^{238}U/^{204}Pb$ μ	$^{232}Th/^{204}Pb$ ω	$^{232}Th/^{238}U$ κ	$^{206}Pb/^{204}Pb_i$	$^{207}Pb/^{204}Pb_i$	$^{208}Pb/^{204}Pb_i$
Foz da Fonte sill	FF 4	94	3.88	1.43	4.04	19.6548(12)	15.6099(10)	39.4414(24)	24.06	70.49	2.93	19.3013	15.5930	39.1129
Paço d'Ilhas sill	PI01	88	11.43	2.37	10.02	19.1236(11)	15.6331(10)	39.1154(23)	13.39	58.66	4.38	18.9395	15.6243	38.8594
Paço d'Ilhas sill	PI08	88	6.88	1.72	5.86	19.0971(11)	15.6352(9)	39.0611(21)	16.19	56.92	3.52	18.8746	15.6245	38.8127
Sintra gabbro	RM 11	74	3.36	1.07	5.31	19.3378(12)	15.6299(10)	39.2299(25)	20.64	106.04	5.14	19.0995	15.6186	38.8409
Sintra gabbro	RM 17	74	4.69	0.67	3.04	19.1144(11)	15.6243(10)	38.9833(23)	9.27	43.21	4.66	19.0073	15.6192	38.8248
Sines gabbro	RM 99	75	3.12	0.48	2.56	19.0474(13)	15.6281(12)	38.9513(28)	10.02	54.68	5.46	18.9302	15.6226	38.7481
Sines gabbro	RM 101	75	3.78	0.32	1.74	18.9510(12)	15.6357(11)	38.8682(24)	5.43	30.60	5.63	18.8874	15.6326	38.7545
Monchique gabbro	b 468 B	72	6.35	1.58	6.61	19.7395(12)	15.6229(11)	39.6754(25)	30.55	166.65	5.45	19.3964	15.6066	39.0807
Monchique ne-syenite	s 598	72	29.71	6.75	30.03	19.4848(11)	15.6104(10)	39.3087(22)	14.81	68.05	4.59	19.3185	15.6025	39.0659
Loulé dyke	C-12-1	72	6.48	3.53	17.63	19.6726(11)	15.6034(10)	39.7545(23)	35.75	184.68	5.17	19.2710	15.5843	39.0955
LVC neck	RM 1	72*	3.80	1.12	6.12	19.3054(12)	15.6188(10)	39.2337(25)	19.20	108.02	5.63	19.0899	15.6086	38.8485
LVC neck	RM 28	72*	5.11	1.78	7.89	19.5870(12)	15.6197(10)	39.5027(25)	22.79	104.38	4.58	19.3303	15.6075	39.1300
LVC neck	RM 57	72*	5.93	2.55	11.71	19.8073(12)	15.6162(10)	39.6229(25)	28.27	134.16	4.75	19.4897	15.6012	39.1441
LVC flow	RM 43	72*	5.34	1.88	7.34	19.7315(11)	15.6119(10)	39.5050(22)	23.08	93.09	4.03	19.4717	15.5995	39.2454
LVC flow	RM 69	72*	3.83	1.49	7.67	19.6711(12)	15.6200(10)	39.4984(24)	25.50	135.49	5.31	19.3847	15.6064	39.0149
Mafra gabbro	RM 83	75*	6.40	1.56	7.14	19.3184(11)	15.6258(10)	39.2210(23)	15.88	74.90	4.72	19.1400	15.6173	38.9537
Malveira da Serra sill	RM 25	72*	3.41	1.62	4.35	19.5694(12)	15.6178(11)	39.2921(26)	30.96	85.78	2.77	19.2217	15.6013	38.9860
Eiras do Faião sill	RM 46	72*	5.44	3.09	7.39	19.6331(11)	15.6364(10)	39.3657(23)	37.10	91.78	2.47	19.2164	15.6166	39.0381

occurrence	sample	Age	Pb	U	Th	$^{206}Pb/^{204}Pb$	$^{207}Pb/^{204}Pb$	$^{208}Pb/^{204}Pb$	$^{238}U/^{204}Pb$ μ	$^{232}Th/^{204}Pb$ ω	$^{232}Th/^{238}U$ κ	$^{206}Pb/^{204}Pb_i$	$^{207}Pb/^{204}Pb_i$	$^{208}Pb/^{204}Pb_i$
Montelevar	RM 50	72*	7.75	2.12	10.87	19.1016(10)	15.6430(9)	38.9364(21)	17.61	93.53	5.31	18.9038	15.6336	38.6027
Anços sill	RM 68	72*	9.28	1.64	7.14	18.9546(102)	15.6272(10)	38.8835(22)	11.38	51.11	4.49	18.8268	15.6211	38.7011
Ribeira d'Ilhas plug	RM 37	72*	4.29	1.68	7.01	19.7756(12)	15.6084(11)	39.6298(25)	25.68	110.81	4.32	19.4873	15.5948	39.2343
Cascais dyke	RM 64	72*	2.25	0.75	2.03	19.4168(25)	15.6277(20)	39.2033(50)	21.67	60.81	2.81	19.1734	15.6161	38.9863
Cascais dyke	RM 90	72*	5.96	1.36	8.50	19.2500(12)	15.6382(11)	39.0475(24)	14.79	95.54	6.46	19.0839	15.6304	38.7066
Fontanelas seamount	AT 690B	72*	0.43	0.16	0.68	19.6952(44)	15.5824(35)	40.2491(90)	24.87	108.47	4.36	19.4159	15.5692	39.8620
Fontanelas seamount	AT 693P1	72*	0.15	0.10	0.96	20.0420(85)	15.5910(66)	41.7398(175)	45.15	447.93	9.92	19.5251	15.5664	40.1384

* Ages from previous works, as discussed in section 5.

Annex IV: Mineral chemistry

Table IV.a: Standards used for the calibration of the measurements in each element.

	Analyzed minerals					
	Olivine	**Pyroxene**	**Amphibole**	**Oxides**	**Plagioclase**	**Micas**
Si	almandine	pirope/almandine	almandine	almandine	plagioclase	almandine
Ti	kaersutite	rutile/kaersitite	kaersutite	rutile	kaersutite/rutile	kaersutite
Al	almandine	almandine/chlorite	chlorite	plagioclase	plagioclase	almandine
Fe	almandine	pirope/almandine	almandine	haematite	almandine	almandine
Mn	bustamite	bustamite	bustamite	bustamite	bustamite	bustamite
Mg	almandine	almandine/diopside	diopside	periclase	almandine	almandine
Ca	almandine	anhydrite/apatite	almandine	apatite	plagioclase	almandine
Na	tugtupite	albite	albite	albite	plagioclase	albite
K	sanidine	biotite	biotite		sanidine	sanidine
Cr	chromium ox	chromium ox	chromium ox	chromium ox		chromium ox
Ni	nickel silicate					
V				V B 1 ????		
Zn		willemite	willemite	willemite		willemite
Ba				benitoite	benitoite	benitoite
Sr					celestite	
Rb						????
F		fluorite	fluorite			apatite
Cl						tugtupite

Table IV.1: Electron microprobe analysis to Olivines

Occurrence	Ribeira d'Ilhas plug																			
Sample	rm 37 b1a	rm 37 b1a	rm 37 b1a	rm 37 b1a	rm 37 b1b	rm 37 b1b	rm 37 b1c	rm 37 b1c	rm 37 b1d	rm 37 b1d	rm 37 b1e	rm 37 b1e	rm 37 b2a	rm 37 b2a	rm 37 b2b	rm 37 b2b	rm 37 b2b	rm 37 b2c	rm 37 b4a	rm 37 b4a
Type	PC	PC	PR	PR	PC	PR	MPC	MPR	MPC	MPR	PC	PR	MPC	MPR	PC	PM	PR	MPC	PC	PR
SiO2	38.54	38.45	38.33	38.84	37.43	37.89	38.60	37.86	38.46	38.22	37.99	37.44	38.70	39.21	38.83	37.85	37.83	38.31	38.20	37.58
TiO2	0.03	0.03	0.02	0.02	0.00	0.00	0.05	0.08	0.04	0.05	0.03	0.05	0.03	0.06	0.03	0.02	0.05	0.03	0.03	0.05
Al2O3	0.04	0.03	0.02	0.04	0.00	0.01	0.04	0.02	0.03	0.02	0.03	0.05	0.04	0.04	0.05	0.06	0.02	0.04	0.07	0.04
Cr2O3	0.09	0.11	0.06	0.05	0.07	0.10	0.14	0.04	0.06	0.13	0.07	0.07	0.10	0.07	0.08	0.10	0.08	0.07	0.05	0.10
FeO	16.33	16.40	15.59	16.38	19.69	19.61	14.24	20.55	14.19	18.38	17.35	18.50	13.78	18.99	13.63	14.83	18.53	16.22	13.87	18.48
MnO	0.17	0.16	0.20	0.19	0.30	0.31	0.12	0.53	0.21	0.34	0.27	0.33	0.18	0.36	0.19	0.17	0.33	0.24	0.13	0.37
MgO	46.01	45.59	45.97	45.68	43.02	42.58	47.54	41.40	47.14	44.32	44.77	43.05	46.98	42.57	48.07	46.28	43.31	45.19	47.12	42.83
NiO	0.17	0.13	0.18	0.17	0.03	0.06	0.23	0.06	0.17	0.12	0.09	0.08	0.17	0.11	0.23	0.15	0.13	0.19	0.26	0.10
CaO	0.23	0.22	0.23	0.25	0.10	0.20	0.28	0.39	0.26	0.32	0.27	0.30	0.25	0.35	0.31	0.24	0.27	0.21	0.24	0.29
Total	101.6	101.1	100.6	101.6	100.6	100.8	101.2	100.9	100.5	101.9	100.9	99.8	100.2	101.8	101.4	99.7	100.5	100.5	100.0	99.8
Structural formula (a.p.f.u.)																				
Si	0.963	0.966	0.965	0.970	0.960	0.970	0.960	0.972	0.963	0.962	0.962	0.964	0.969	0.988	0.961	0.959	0.966	0.968	0.961	0.967
Ti	0.001	0.001	0.000	0.000	0.000	0.000	0.001	0.001	0.001	0.001	0.001	0.001	0.001	0.001	0.001	0.000	0.001	0.001	0.001	0.001
Al	0.001	0.001	0.000	0.001	0.000	0.000	0.001	0.001	0.001	0.001	0.001	0.001	0.001	0.001	0.001	0.002	0.001	0.001	0.002	0.001
Cr	0.002	0.002	0.001	0.001	0.002	0.002	0.003	0.001	0.001	0.003	0.001	0.001	0.002	0.001	0.002	0.002	0.002	0.001	0.001	0.002
Fe (ii)	0.341	0.344	0.328	0.342	0.422	0.420	0.296	0.441	0.297	0.387	0.367	0.398	0.289	0.400	0.282	0.314	0.396	0.343	0.292	0.398
Mn	0.004	0.003	0.004	0.004	0.006	0.007	0.002	0.012	0.004	0.007	0.006	0.007	0.004	0.008	0.004	0.004	0.007	0.005	0.003	0.008
Mg	1.714	1.707	1.725	1.700	1.645	1.624	1.762	1.585	1.759	1.663	1.690	1.652	1.754	1.599	1.774	1.748	1.649	1.702	1.767	1.643
NiO	0.003	0.003	0.004	0.003	0.001	0.001	0.005	0.001	0.003	0.003	0.002	0.002	0.003	0.002	0.004	0.003	0.003	0.004	0.005	0.002
CaO	0.012	0.012	0.013	0.013	0.006	0.011	0.015	0.022	0.014	0.017	0.015	0.016	0.013	0.019	0.016	0.013	0.015	0.011	0.013	0.016
Endmembers																				
Fo%	83.26	83.07	83.85	83.09	79.33	79.21	85.51	77.78	85.38	80.85	81.92	80.30	85.72	79.68	86.11	84.62	80.37	83.03	85.71	80.20
Fa%	16.57	16.76	15.95	16.71	20.36	20.46	14.37	21.66	14.41	18.80	17.81	19.35	14.10	19.94	13.69	15.21	19.29	16.72	14.15	19.41
Tp%	0.17	0.17	0.20	0.19	0.31	0.33	0.12	0.57	0.21	0.35	0.28	0.35	0.18	0.38	0.19	0.17	0.35	0.25	0.13	0.39

P - phenocryst, C - Core, R - Rim, M - Micro, Mx - matrix, man - Mantle

Table IV.1: Electron microprobe analysis to Olivines

Occurrence	Ribeira d'Ilhas plug						LVC flow					LVC neck						
Sample	rm 37 b4b	rm 37 b4b	rm 37 b5a	rm 37 b5a	rm 37 b5b	rm 37 b5b	rm 43 b2a	rm 43 b2a	rm 43 b2b	rm 43 b2b	rm 43 b5c	rm 66 b1a	rm 66 b1a	rm 66 b1a	rm 66 b1a	rm 66 b1b	rm 66 b1b	rm 66 b1b
Type	PC	PR	PC	PR	PC	PR	PR	PC	PC	PR	Mx	PC	PC	PR	PR	PC	Pman	PR
SiO2	38.53	37.46	37.83	37.44	37.32	37.00	38.40	37.87	38.15	36.60	35.95	39.02	39.54	38.43	37.97	39.16	38.27	37.68
TiO2	0.02	0.07	0.00	0.05	0.04	0.06	0.04	0.05	0.01	0.03	0.12	0.00	0.01	0.02	0.01	0.00	0.00	0.01
Al2O3	0.02	0.03	0.02	0.03	0.03	0.03	0.02	0.08	0.05	0.03	0.08	0.04	0.03	0.03	0.04	0.05	0.04	0.03
Cr2O3	0.11	0.11	0.05	0.13	0.10	0.06	0.14	0.11	0.07	0.08	0.08	0.10	0.09	0.09	0.12	0.08	0.07	0.09
FeO	13.15	18.53	14.53	20.19	15.98	17.27	13.87	13.87	13.96	21.27	28.31	12.31	12.74	19.44	19.74	14.16	17.43	21.81
MnO	0.10	0.34	0.17	0.45	0.20	0.33	0.14	0.15	0.13	0.51	0.84	0.14	0.09	0.33	0.28	0.12	0.23	0.36
MgO	47.44	43.54	46.49	39.08	45.23	44.07	46.46	46.69	46.52	39.81	34.87	49.99	49.63	43.66	43.65	48.39	45.67	41.26
NiO	0.24	0.12	0.19	0.04	0.14	0.12	0.17	0.14	0.12	0.02	0.03	0.21	0.18	0.13	0.11	0.21	0.20	0.09
CaO	0.22	0.28	0.25	0.29	0.23	0.24	0.21	0.24	0.22	0.26	0.26	0.25	0.24	0.38	0.36	0.23	0.27	0.37
Total	99.82	100.48	99.53	97.71	99.25	99.17	99.45	99.19	99.23	98.60	100.52	102.05	102.56	102.50	102.28	102.39	102.19	101.69
Structural formula (a.p.f.u.)																		
Si	0.966	0.959	0.959	0.992	0.956	0.955	0.970	0.960	0.966	0.968	0.965	0.954	0.962	0.966	0.958	0.961	0.957	0.966
Ti	0.000	0.001	0.000	0.001	0.001	0.001	0.001	0.001	0.000	0.001	0.002	0.000	0.000	0.000	0.000	0.000	0.000	0.000
Al	0.001	0.001	0.001	0.001	0.001	0.001	0.001	0.002	0.001	0.001	0.002	0.001	0.001	0.001	0.001	0.002	0.001	0.001
Cr	0.002	0.002	0.001	0.003	0.002	0.001	0.003	0.002	0.001	0.002	0.002	0.002	0.002	0.002	0.002	0.001	0.001	0.002
Fe (ii)	0.276	0.397	0.308	0.447	0.342	0.373	0.293	0.294	0.296	0.470	0.636	0.252	0.259	0.408	0.417	0.291	0.364	0.468
Mn	0.002	0.007	0.004	0.010	0.004	0.007	0.003	0.003	0.003	0.011	0.019	0.003	0.002	0.007	0.006	0.002	0.005	0.008
Mg	1.774	1.661	1.757	1.543	1.727	1.696	1.749	1.765	1.756	1.570	1.396	1.822	1.800	1.635	1.643	1.770	1.702	1.577
NiO	0.005	0.003	0.004	0.001	0.003	0.002	0.003	0.003	0.003	0.000	0.001	0.004	0.004	0.003	0.002	0.004	0.004	0.002
CaO	0.012	0.015	0.013	0.017	0.012	0.013	0.012	0.013	0.012	0.014	0.015	0.013	0.012	0.021	0.020	0.012	0.015	0.020
Endmembers																		
Fo%	86.46	80.44	84.94	77.14	83.29	81.70	85.53	85.58	85.47	76.51	68.08	87.74	87.34	79.75	79.54	85.80	82.17	76.84
Fa%	13.44	19.20	14.88	22.36	16.51	17.95	14.32	14.26	14.39	22.92	30.99	12.12	12.57	19.92	20.17	14.09	17.59	22.78
Tp%	0.10	0.36	0.18	0.50	0.21	0.35	0.15	0.16	0.14	0.56	0.93	0.14	0.09	0.34	0.29	0.12	0.24	0.38

Table IV.1: Electron microprobe analysis to Olivines

Occurrence	LVC neck																			
Sample	rm 66 b1c	rm 66 b1c	rm 66 b2a	rm 66 b2a	rm 66 b2a	rm 66 b2a	rm 66 b2a	rm 66 b2a	rm 66 b2b	rm 66 b2b	rm 66 b2b	rm 66 b2b	rm 66 b3a	rm 66 b3a	rm 66 b3a	rm 66 b3a	rm 66 b3b	rm 66 b3b	rm 66 b3c	rm 66 b3c
Type	MPC	MPR	PC	PC	Pman	Pman	PR	PR	PC	PC	PR	PR	PC	PC	PR	PR	MPC	MPR	PC	PR
SiO2	37.32	37.06	38.04	38.37	37.84	37.54	36.73	36.67	38.28	38.29	37.08	37.13	38.83	38.46	37.85	37.69	38.00	36.74	38.28	37.42
TiO2	0.03	0.03	0.00	0.00	0.04	0.03	0.00	0.01	0.04	0.00	0.00	0.01	0.04	0.01	0.06	0.02	0.01	0.06	0.02	0.05
Al2O3	0.02	0.01	0.03	0.05	0.03	0.03	0.02	0.03	0.05	0.04	0.02	0.06	0.03	0.02	0.04	0.05	0.04	0.12	0.07	0.02
Cr2O3	0.10	0.08	0.09	0.12	0.10	0.11	0.10	0.10	0.10	0.11	0.10	0.09	0.07	0.08	0.13	0.09	0.11	0.09	0.10	0.07
FeO	21.69	25.38	12.64	12.58	14.42	16.40	18.80	23.25	13.06	13.14	22.28	18.56	15.98	17.62	23.60	23.65	20.99	26.84	18.05	24.64
MnO	0.35	0.46	0.16	0.14	0.17	0.21	0.28	0.42	0.11	0.16	0.42	0.23	0.13	0.21	0.35	0.40	0.35	0.54	0.17	0.46
MgO	41.83	38.12	49.78	49.75	48.00	46.82	43.87	39.87	49.18	49.08	41.22	45.15	46.81	44.95	40.60	39.89	41.87	36.02	44.82	38.17
NiO	0.09	0.10	0.22	0.22	0.23	0.21	0.14	0.04	0.18	0.19	0.11	0.15	0.17	0.12	0.10	0.10	0.13	0.07	0.15	0.10
CaO	0.41	0.43	0.23	0.22	0.24	0.26	0.39	0.45	0.24	0.25	0.42	0.32	0.24	0.27	0.46	0.47	0.40	0.44	0.27	0.45
Total	101.84	101.67	101.19	101.45	101.06	101.61	100.32	100.83	101.24	101.25	101.65	101.70	102.30	101.72	103.19	102.35	101.90	100.92	101.92	101.38
Structural formula (a.p.f.u.)																				
Si	0.956	0.967	0.942	0.946	0.945	0.942	0.945	0.957	0.948	0.948	0.955	0.940	0.962	0.965	0.963	0.968	0.968	0.973	0.961	0.975
Ti	0.001	0.001	0.000	0.000	0.001	0.001	0.000	0.000	0.001	0.000	0.000	0.000	0.001	0.000	0.001	0.000	0.000	0.001	0.000	0.001
Al	0.001	0.000	0.001	0.001	0.001	0.001	0.001	0.001	0.001	0.001	0.001	0.002	0.001	0.001	0.001	0.002	0.001	0.004	0.002	0.001
Cr	0.002	0.002	0.002	0.002	0.002	0.002	0.002	0.002	0.002	0.002	0.002	0.002	0.001	0.002	0.003	0.002	0.002	0.002	0.002	0.001
Fe (ii)	0.465	0.554	0.262	0.260	0.301	0.344	0.404	0.507	0.270	0.272	0.480	0.393	0.331	0.370	0.502	0.508	0.447	0.594	0.379	0.537
Mn	0.008	0.010	0.003	0.003	0.004	0.004	0.006	0.009	0.002	0.003	0.009	0.005	0.003	0.004	0.008	0.009	0.007	0.012	0.004	0.010
Mg	1.598	1.483	1.837	1.829	1.788	1.751	1.682	1.551	1.815	1.812	1.583	1.704	1.729	1.682	1.541	1.527	1.590	1.423	1.678	1.483
NiO	0.002	0.002	0.004	0.004	0.005	0.004	0.003	0.001	0.004	0.004	0.002	0.003	0.003	0.002	0.002	0.002	0.003	0.001	0.003	0.002
CaO	0.023	0.024	0.012	0.012	0.013	0.014	0.021	0.025	0.013	0.013	0.023	0.017	0.013	0.014	0.025	0.026	0.022	0.025	0.015	0.025
Endmembers																				
Fo%	77.19	72.45	87.39	87.46	85.44	83.40	80.39	75.02	86.94	86.81	76.40	81.07	83.82	81.80	75.14	74.72	77.77	70.10	81.43	73.05
Fa%	22.45	27.05	12.45	12.41	14.39	16.39	19.32	24.54	12.95	13.03	23.17	18.69	16.05	17.98	24.49	24.85	21.87	29.30	18.39	26.45
Tp%	0.36	0.50	0.16	0.13	0.17	0.21	0.29	0.45	0.11	0.16	0.44	0.24	0.13	0.21	0.37	0.43	0.37	0.60	0.18	0.50

Table IV.1: Electron microprobe analysis to Olivines

Occurrence	Mafra gabbro			Sines gabbro																
Sample	rm 83 b1a	rm 83 b1a	rm 83 b1b	rm101 b2a	rm101 b2a	rm101 b2b	rm101 b2b	rm101 b2c	rm101 b2c	rm101 b1a	rm101 b1a	rm101 b1a	rm101 b1a	rm101 b1b	rm101 b1b	rm101 b1c	rm101 b1c	rm101 b1d	rm101 b1d	rm101 b1d	rm101 b1d
Type	C	C	C	C	R	C	R	C	R	C	C	R	R	R	C	C	R	C	C	R	R
SiO2	38.70	38.67	38.81	36.45	35.56	36.06	35.84	36.36	35.33	36.56	36.46	36.71	35.58	37.28	36.60	36.52	36.01	36.57	36.63	36.83	36.88
TiO2	0.01	0.02	0.03	0.02	0.03	0.04	0.03	0.04	0.03	0.02	0.04	0.03	0.00	0.01	0.02	0.03	0.04	0.04	0.02	0.03	0.04
Al2O3	0.10	0.01	0.06	0.01	0.00	0.00	0.00	0.02	0.04	0.00	0.03	0.00	0.00	0.00	0.00	0.02	0.01	0.02	0.01	0.00	0.00
Cr2O3	0.25	0.07	0.09	0.09	0.07	0.09	0.07	0.07	0.07	0.09	0.09	0.04	0.09	0.09	0.08	0.09	0.08	0.11	0.07	0.06	0.08
FeO	14.10	14.80	13.67	28.47	28.73	28.56	28.48	28.46	29.24	28.47	28.63	28.38	29.49	28.67	29.38	29.00	29.62	27.50	27.24	28.86	29.08
MnO	0.10	0.24	0.21	0.42	0.43	0.44	0.44	0.44	0.46	0.44	0.41	0.36	0.43	0.40	0.45	0.45	0.47	0.47	0.42	0.49	0.45
MgO	47.42	47.90	49.20	35.39	34.58	35.57	35.28	35.24	34.68	35.21	35.28	34.88	33.73	35.82	34.61	34.95	33.96	35.98	35.96	34.65	35.10
NiO	0.24	0.19	0.22	0.05	0.03	0.08	0.04	0.02	0.05	0.10	0.03	0.08	0.07	0.03	0.05	0.05	0.01	0.01	0.05	0.02	0.03
CaO	0.37	0.31	0.30	0.13	0.08	0.01	0.13	0.08	0.08	0.11	0.05	0.17	0.08	0.06	0.03	0.07	0.12	0.05	0.24	0.02	0.02
Total	101.3	102.2	102.6	101.03	99.52	100.86	100.31	100.73	99.97	101.00	101.00	100.64	99.48	102.37	101.22	101.17	100.32	100.74	100.63	100.96	101.67
Structural formula (a.p.f.u.)																					
Si	0.961	0.955	0.951	0.971	0.966	0.964	0.964	0.971	0.958	0.974	0.972	0.980	0.970	0.978	0.976	0.973	0.972	0.972	0.974	0.982	0.977
Ti	0.000	0.000	0.001	0.000	0.001	0.001	0.001	0.001	0.001	0.000	0.001	0.001	0.000	0.000	0.000	0.001	0.001	0.001	0.000	0.001	0.001
Al	0.003	0.000	0.002	0.000	0.000	0.000	0.000	0.001	0.001	0.000	0.001	0.000	0.000	0.000	0.000	0.001	0.000	0.001	0.000	0.000	0.000
Cr	0.005	0.001	0.002	0.002	0.002	0.002	0.002	0.002	0.001	0.002	0.002	0.001	0.002	0.002	0.002	0.002	0.002	0.002	0.001	0.001	0.002
Fe (ii)	0.293	0.306	0.280	0.634	0.652	0.638	0.640	0.636	0.663	0.634	0.638	0.634	0.672	0.629	0.655	0.646	0.669	0.611	0.606	0.643	0.644
Mn	0.002	0.005	0.004	0.009	0.010	0.010	0.010	0.010	0.010	0.010	0.009	0.008	0.010	0.009	0.010	0.010	0.011	0.011	0.009	0.011	0.010
Mg	1.756	1.764	1.796	1.406	1.400	1.417	1.414	1.404	1.402	1.398	1.402	1.389	1.371	1.401	1.376	1.389	1.367	1.426	1.426	1.377	1.386
NiO	0.005	0.004	0.004	0.001	0.001	0.002	0.001	0.001	0.001	0.002	0.001	0.002	0.002	0.001	0.001	0.001	0.000	0.000	0.001	0.000	0.001
CaO	0.020	0.017	0.016	0.007	0.005	0.001	0.007	0.005	0.005	0.006	0.003	0.010	0.005	0.003	0.001	0.004	0.007	0.003	0.014	0.001	0.001
Endmembers																					
Fo%	85.62	85.02	86.34	68.59	67.88	68.61	68.50	68.49	67.55	68.46	68.41	68.39	66.77	68.71	67.41	67.90	66.79	69.64	69.86	67.79	67.94
Fa%	14.28	14.74	13.45	30.95	31.63	30.90	31.01	31.03	31.95	31.05	31.14	31.21	32.75	30.85	32.09	31.60	32.68	29.85	29.68	31.67	31.57
Tp%	0.10	0.24	0.21	0.46	0.48	0.48	0.48	0.48	0.50	0.49	0.45	0.40	0.49	0.44	0.50	0.50	0.53	0.52	0.46	0.55	0.49

Table IV.2: Electron microprobe analysis to clinopyroxenes

Occurrence	Lomba dos Pianos sill																			
sample	RM 9 B1a	RM 9 B1b	RM 9 B1c	RM 9 B1d	RM 9 B1e	RM 9 B1f	RM 9 B2a	RM 9 B2b	RM 9 B2b	RM 9 B2b	RM 9 B2b	RM 9 B2b	RM 9 B2b	RM 9 B2b	RM 9 B2b	RM 9 B2b	RM 9 B2c	RM 9 B2d	RM 9 B3a	RM 9 B3a
type	Mx	Iplag	Iplag	Iplag	Iplag	Iplag	Mx	PR	PR	GC	GC	GC	GC	GC	GC	GC	GC	PR	PR	PC
SiO2	49.19	45.58	45.26	47.09	47.50	48.25	48.15	48.90	45.56	51.79	51.37	51.92	51.43	51.77	51.63	51.49	46.43	46.70	47.54	49.61
TiO2	1.00	2.11	2.35	1.62	2.19	2.11	2.13	1.75	2.85	0.43	0.37	0.29	0.27	0.20	0.30	0.27	2.04	2.46	2.03	1.23
Al2O3	3.56	7.13	7.25	5.89	4.46	4.41	4.81	3.45	7.75	1.78	1.69	1.46	1.44	1.21	1.46	1.83	6.72	5.78	4.50	2.54
Cr2O3	0.00	0.00	0.02	0.01	0.01	0.02	0.04	0.00	0.00	0.03	0.00	0.03	0.00	0.00	0.00	0.03	0.02	0.00	0.01	0.00
FeO	9.06	7.81	7.52	8.35	7.13	7.35	7.43	7.51	7.68	8.15	9.34	9.20	9.19	9.12	8.52	8.49	7.91	7.90	7.17	7.12
MnO	0.47	0.12	0.16	0.23	0.21	0.21	0.14	0.20	0.10	0.28	0.32	0.34	0.31	0.33	0.29	0.28	0.16	0.15	0.16	0.21
MgO	12.35	12.66	13.10	12.54	13.95	13.69	14.07	14.08	12.50	13.64	12.92	13.13	13.32	13.39	13.87	13.67	12.62	13.05	14.21	14.73
CaO	22.23	21.96	22.13	21.90	22.24	21.98	21.88	22.08	22.03	22.22	22.07	22.27	22.35	22.38	22.55	22.26	21.86	21.83	22.40	21.92
Na2O	0.70	0.51	0.43	0.63	0.40	0.49	0.38	0.53	0.38	0.76	0.62	0.61	0.61	0.61	0.59	0.94	0.56	0.45	0.41	0.42
K2O	0.00	0.01	0.00	0.00	0.00	0.00	0.01	0.02	0.00	0.01	0.00	0.00	0.00	0.00	0.00	0.01	0.00	0.00	0.00	0.02
F	0.00	0.00	0.01	0.00	0.03	0.00	0.00	0.00	0.09	0.03	0.00	0.01	0.00	0.00	0.00	0.00	0.00	0.21	0.10	0.00
Tot	98.62	98.02	98.22	98.31	98.13	98.57	99.08	98.56	98.96	99.10	98.71	99.28	98.99	99.06	99.21	99.28	98.38	98.50	98.46	97.84
Structural formula (a.p.f.u.)																				
Tet																				
Si	1.88	1.75	1.73	1.80	1.81	1.83	1.81	1.86	1.73	1.95	1.95	1.96	1.95	1.96	1.95	1.94	1.77	1.78	1.81	1.89
Al	0.12	0.25	0.27	0.20	0.19	0.17	0.19	0.14	0.27	0.05	0.05	0.04	0.05	0.04	0.05	0.06	0.23	0.22	0.19	0.11
Oct																				
Al	0.04	0.07	0.06	0.07	0.01	0.03	0.03	0.01	0.07	0.03	0.03	0.03	0.02	0.01	0.01	0.02	0.07	0.04	0.01	0.00
Fe3+	0.11	0.15	0.16	0.13	0.12	0.09	0.09	0.11	0.10	0.08	0.07	0.06	0.09	0.09	0.10	0.13	0.12	0.10	0.14	0.10
Cr	0.00	0.00	0.00	0.00	0.00	0.00	0.00	0.00	0.00	0.00	0.00	0.00	0.00	0.00	0.00	0.00	0.00	0.00	0.00	0.00
Ti	0.03	0.06	0.07	0.05	0.06	0.06	0.06	0.05	0.08	0.01	0.01	0.01	0.01	0.01	0.01	0.01	0.06	0.07	0.06	0.04
Fe2+	0.18	0.10	0.08	0.14	0.11	0.15	0.14	0.13	0.15	0.18	0.23	0.23	0.20	0.20	0.17	0.14	0.13	0.15	0.08	0.12
Mn	0.02	0.00	0.01	0.01	0.01	0.01	0.00	0.01	0.00	0.01	0.01	0.01	0.01	0.01	0.01	0.01	0.01	0.00	0.01	0.01
Mg	0.70	0.72	0.75	0.71	0.79	0.77	0.79	0.80	0.71	0.77	0.73	0.74	0.75	0.76	0.78	0.77	0.72	0.74	0.81	0.84
Ca	0.91	0.90	0.91	0.90	0.91	0.89	0.88	0.90	0.90	0.90	0.90	0.90	0.91	0.91	0.91	0.90	0.89	0.89	0.91	0.89
Na	0.05	0.04	0.03	0.05	0.03	0.04	0.03	0.04	0.03	0.06	0.05	0.04	0.04	0.04	0.04	0.07	0.04	0.03	0.03	0.03
K	0.00	0.00	0.00	0.00	0.00	0.00	0.00	0.00	0.00	0.00	0.00	0.00	0.00	0.00	0.00	0.00	0.00	0.00	0.00	0.00
#Mg	70.86	74.29	75.63	72.80	77.73	76.84	77.14	76.98	74.37	74.89	71.16	71.80	72.11	72.35	74.37	74.17	73.99	74.66	77.95	78.67
Wo %	44.29	42.07	41.39	42.74	42.86	43.45	42.40	43.09	42.95	47.31	47.16	47.06	44.54	44.75	44.39	43.90	42.62	42.75	42.27	42.85
En %	42.74	47.90	49.88	45.80	48.24	46.15	47.31	47.22	45.50	41.51	39.30	39.60	42.52	42.30	44.18	45.51	46.36	45.96	49.65	48.03
Fs %	12.97	10.04	8.73	11.46	8.89	10.40	10.29	9.69	11.54	11.18	13.54	13.34	12.94	12.95	11.43	10.59	11.02	11.28	8.08	9.12

P - phenocryst, C - Core, R - Rim, M - Micro, Mx - matrix, man - Mantle, M- megacryst, I - inclusion, GC - green core, anf- amphibole, Xen - crystal in xenolith, AR - amphibole reaction rim, Ag - cpx in aggregate, Am - amygdule, Ox - cpx with abbundant oxide inclusions, plag - plagioclase

Table IV.2: Electron microprobe analysis to clinopyroxenes

Occurrence	Lomba dos Pianos sill																			
	RM 9	RM 9	RM 9	RM 9	RM 9	RM 9	rm9	rm9	rm9	rm9	rm9	rm9	rm9	rm9	rm9	rm9	rm9	rm9	rm9	rm9
sample	B3b	B4a	B4b	B4b	B4b	B4b	b5a	b5b	b5b	b5b	b5b	b5b	b5b	b5b	b5b	b5b	b5b	b5b	b5b	b5b
type	PC	Mx	PR	PC	PC	PR	Mx	PR	PR	PR	GC	GC	GC	GC	GC	GC	GC	GC	GC	GC
SiO2	49.73	49.14	47.26	49.46	49.67	48.96	49.73	47.55	49.58	43.47	50.64	49.63	50.67	50.53	49.65	50.15	49.00	48.45	50.43	50.97
TiO2	1.29	1.52	1.88	1.42	1.40	1.62	1.70	2.07	1.64	3.33	0.61	0.68	0.59	0.63	0.75	0.70	1.02	1.29	0.61	0.53
Al2O3	2.59	3.12	5.54	3.48	2.85	3.42	3.37	4.30	3.40	7.90	2.17	2.70	2.28	2.46	2.72	2.79	3.57	4.28	2.62	2.15
Cr2O3	0.00	0.00	0.02	0.04	0.00	0.00	0.00	0.02	0.03	0.00	0.01	0.03	0.02	0.00	0.02	0.04	0.00	0.00	0.08	0.00
FeO	7.10	6.78	7.09	7.25	7.44	6.77	6.99	7.39	6.77	7.98	8.37	8.32	8.49	8.64	8.57	8.45	8.58	8.93	8.85	8.34
MnO	0.22	0.18	0.23	0.11	0.21	0.18	0.17	0.20	0.15	0.12	0.48	0.43	0.40	0.43	0.41	0.38	0.39	0.42	0.46	0.42
MgO	14.84	14.85	13.68	15.11	14.30	14.66	14.80	14.00	14.62	12.58	13.60	13.30	13.22	13.18	13.13	12.97	12.39	11.81	13.12	13.48
CaO	22.13	22.07	22.08	21.41	21.77	22.33	22.11	21.96	22.17	21.73	21.97	22.11	22.33	22.15	22.20	22.07	22.25	21.98	22.20	21.98
Na2O	0.35	0.40	0.55	0.32	0.37	0.41	0.42	0.50	0.41	0.42	0.82	0.78	0.78	0.75	0.76	0.72	0.85	0.88	0.81	0.72
K2O	0.01	0.00	0.00	0.00	0.01	0.01	0.01	0.01	0.01	0.00	0.01	0.00	0.01	0.00	0.00	0.00	0.00	0.00	0.02	0.00
F	0.00	0.08	0.00	0.00	0.05	0.00	0.10	0.07	0.00	0.00	0.06	0.07	0.08	0.00	0.00	0.00	0.01	0.00	0.00	0.00
Tot	98.35	98.12	98.39	98.64	98.16	98.39	99.36	98.03	98.81	97.53	98.71	98.03	98.82	98.81	98.21	98.27	98.08	98.06	99.26	98.63
Structural formula (a.p.f.u.)																				
Tet																				
Si	1.89	1.87	1.80	1.86	1.89	1.85	1.86	1.82	1.87	1.68	1.92	1.90	1.92	1.92	1.90	1.91	1.88	1.86	1.91	1.93
Al	0.11	0.13	0.20	0.14	0.11	0.15	0.14	0.18	0.13	0.32	0.08	0.10	0.08	0.08	0.10	0.09	0.12	0.14	0.09	0.07
Oct																				
Al	0.00	0.00	0.04	0.02	0.02	0.01	0.01	0.01	0.02	0.04	0.02	0.02	0.03	0.03	0.02	0.04	0.04	0.05	0.03	0.03
Fe3+	0.10	0.11	0.14	0.09	0.07	0.11	0.09	0.14	0.08	0.17	0.12	0.14	0.11	0.11	0.14	0.09	0.13	0.11	0.13	0.09
Cr	0.00	0.00	0.00	0.00	0.00	0.00	0.00	0.00	0.00	0.00	0.00	0.00	0.00	0.00	0.00	0.00	0.00	0.00	0.00	0.00
Ti	0.04	0.04	0.05	0.04	0.04	0.05	0.05	0.06	0.05	0.10	0.02	0.02	0.02	0.02	0.02	0.02	0.03	0.04	0.02	0.02
Fe2+	0.13	0.11	0.09	0.14	0.17	0.10	0.13	0.10	0.13	0.09	0.14	0.13	0.16	0.17	0.14	0.18	0.15	0.17	0.15	0.17
Mn	0.01	0.01	0.01	0.00	0.01	0.01	0.01	0.01	0.00	0.00	0.02	0.01	0.01	0.01	0.01	0.01	0.01	0.01	0.01	0.01
Mg	0.84	0.84	0.78	0.85	0.81	0.83	0.83	0.80	0.82	0.73	0.77	0.76	0.75	0.75	0.75	0.74	0.71	0.68	0.74	0.76
Ca	0.90	0.90	0.90	0.86	0.89	0.91	0.89	0.90	0.89	0.90	0.89	0.91	0.91	0.90	0.91	0.90	0.91	0.90	0.90	0.89
Na	0.03	0.03	0.04	0.02	0.03	0.03	0.03	0.04	0.03	0.03	0.06	0.06	0.06	0.06	0.06	0.05	0.06	0.07	0.06	0.05
K	0.00	0.00	0.00	0.00	0.00	0.00	0.00	0.00	0.00	0.00	0.00	0.00	0.00	0.00	0.00	0.00	0.00	0.00	0.00	0.00
#Mg	78.85	79.61	77.48	78.79	77.41	79.41	79.07	77.17	79.39	73.75	74.34	74.04	73.52	73.13	73.20	73.23	72.02	70.22	72.55	74.24
Wo %	42.91	42.70	42.34	41.41	43.44	43.01	42.95	42.21	43.49	40.84	43.51	43.46	44.49	44.17	43.69	44.52	44.60	44.69	43.61	44.29
En %	47.98	48.99	49.19	48.81	45.73	48.83	47.82	48.89	47.29	49.44	45.67	46.12	44.06	43.96	45.28	43.32	43.67	42.16	44.66	43.93
Fs %	9.11	8.31	8.47	9.79	10.84	8.16	9.24	8.90	9.22	9.72	10.82	10.42	11.46	11.87	11.03	12.16	11.73	13.15	11.74	11.78

Table IV.2: Electron microprobe analysis to clinopyroxenes

Occurrence	Lomba dos Pianos sill																			
	rm9	rm9	rm9	rm9	rm9	rm9	rm9	rm9	rm9	rm9	rm9	rm9	rm9	rm9	rm9	rm9	rm9	rm9	rm9	rm9
sample	b5b	b5b	b5b	b5b	b5b	b5b	b5b	b6a	b6a	b6a	b6a	b6a	b6a	b6a	b6a	b6a	b6a	b6a	b6a	b6a
type	GC	GC	GC	PR	PR	PR	PR	PR	PR	PR	GC	GC	GC	GC	GC	GC	GC	GC	GC	GC
SiO2	50.97	50.57	51.14	45.46	47.54	47.78	49.56	51.12	51.01	50.98	50.59	50.67	51.35	50.90	50.93	50.82	51.35	50.85	50.93	50.63
TiO2	0.51	0.51	0.50	2.51	1.73	1.84	1.50	0.48	0.53	0.48	0.57	0.57	0.55	0.60	0.58	0.53	0.57	0.54	0.55	0.59
Al2O3	1.93	1.91	1.91	6.83	5.31	5.02	3.10	1.94	1.90	1.83	2.20	2.20	2.20	2.19	2.14	2.11	2.09	2.09	2.11	2.09
Cr2O3	0.00	0.00	0.00	0.00	0.00	0.00	0.00	0.00	0.00	0.03	0.03	0.00	0.02	0.00	0.00	0.00	0.00	0.03	0.07	0.00
FeO	8.26	8.19	8.23	7.57	7.77	7.45	6.96	8.44	8.44	8.64	8.71	8.74	8.81	8.81	8.71	8.72	8.64	8.71	8.75	8.69
MnO	0.44	0.40	0.47	0.16	0.20	0.17	0.20	0.54	0.49	0.50	0.47	0.44	0.46	0.49	0.43	0.45	0.46	0.41	0.45	0.42
MgO	13.76	13.68	13.58	13.06	13.26	14.11	14.76	13.69	13.57	13.41	13.05	13.08	13.06	13.05	13.11	13.10	13.21	13.09	13.12	13.07
CaO	22.02	22.06	22.04	21.98	21.83	21.94	22.02	21.88	21.83	22.08	21.95	22.07	22.04	22.07	21.99	22.11	22.09	22.20	22.09	22.14
Na2O	0.71	0.76	0.74	0.43	0.51	0.37	0.36	0.80	0.79	0.89	0.92	0.93	0.92	0.94	0.94	0.90	0.90	0.89	0.91	0.93
K2O	0.00	0.00	0.01	0.00	0.00	0.00	0.02	0.01	0.00	0.00	0.01	0.00	0.00	0.01	0.00	0.00	0.00	0.00	0.01	0.00
F	0.00	0.00	0.00	0.11	0.00	0.00	0.12	0.00	0.12	0.00	0.04	0.01	0.07	0.07	0.04	0.00	0.02	0.06	0.00	0.00
Tot	98.65	98.10	98.65	98.08	98.21	98.68	98.55	98.91	98.65	98.87	98.52	98.75	99.51	99.15	98.92	98.79	99.35	98.93	99.05	98.61
Structural formula (a.p.f.u.)																				
Tet																				
Si	1.93	1.93	1.94	1.74	1.81	1.81	1.87	1.93	1.94	1.93	1.93	1.93	1.94	1.93	1.93	1.93	1.94	1.93	1.93	1.93
Al	0.07	0.07	0.06	0.26	0.19	0.19	0.13	0.07	0.06	0.07	0.07	0.07	0.06	0.07	0.07	0.07	0.06	0.07	0.07	0.07
Oct																				
Al	0.02	0.02	0.02	0.05	0.05	0.03	0.01	0.02	0.02	0.02	0.03	0.02	0.03	0.03	0.03	0.03	0.03	0.02	0.02	0.02
Fe3+	0.10	0.12	0.10	0.14	0.11	0.12	0.09	0.11	0.10	0.13	0.12	0.13	0.10	0.12	0.11	0.12	0.10	0.12	0.12	0.13
Cr	0.00	0.00	0.00	0.00	0.00	0.00	0.00	0.00	0.00	0.00	0.00	0.00	0.00	0.00	0.00	0.00	0.00	0.00	0.00	0.00
Ti	0.01	0.01	0.01	0.07	0.05	0.05	0.04	0.01	0.02	0.01	0.02	0.02	0.02	0.02	0.02	0.02	0.02	0.02	0.02	0.02
Fe2+	0.16	0.14	0.17	0.10	0.14	0.12	0.13	0.16	0.17	0.15	0.16	0.15	0.18	0.16	0.16	0.16	0.17	0.16	0.16	0.15
Mn	0.01	0.01	0.02	0.01	0.01	0.01	0.01	0.02	0.02	0.02	0.02	0.01	0.01	0.02	0.01	0.01	0.01	0.01	0.01	0.01
Mg	0.78	0.78	0.77	0.75	0.75	0.80	0.83	0.77	0.77	0.76	0.74	0.74	0.73	0.74	0.74	0.74	0.74	0.74	0.74	0.74
Ca	0.89	0.90	0.90	0.90	0.89	0.89	0.89	0.89	0.89	0.90	0.90	0.90	0.89	0.90	0.89	0.90	0.89	0.90	0.90	0.90
Na	0.05	0.06	0.05	0.03	0.04	0.03	0.03	0.06	0.06	0.07	0.07	0.07	0.07	0.07	0.07	0.07	0.07	0.07	0.07	0.07
K	0.00	0.00	0.00	0.00	0.00	0.00	0.00	0.00	0.00	0.00	0.00	0.00	0.00	0.00	0.00	0.00	0.00	0.00	0.00	0.00
#Mg	74.82	74.85	74.63	75.48	75.26	77.16	79.08	74.31	74.12	73.45	72.76	72.74	72.54	72.55	72.87	72.81	73.16	72.82	72.77	72.82
Wo %	43.84	43.83	44.31	41.83	42.70	41.86	42.99	43.54	43.83	43.81	44.09	44.14	47.78	44.22	44.31	44.30	44.54	44.41	44.15	44.33
En %	45.07	45.62	44.30	48.70	46.64	48.61	47.69	45.21	44.61	45.02	44.20	44.32	40.52	43.94	43.89	44.04	43.44	43.90	44.07	44.22
Fs %	11.09	10.55	11.39	9.47	10.66	9.53	9.31	11.25	11.55	11.17	11.71	11.54	11.69	11.84	11.80	11.67	12.02	11.69	11.78	11.44

Table IV.2: Electron microprobe analysis to clinopyroxenes

Occurrence	Lomba dos Pianos sill															Malveira da Serra sill				
	rm9	rm9	rm9	rm9	rm9	rm9	rm9	rm9	rm9	rm9	rm9	rm9	rm9	rm9	rm9	rm25	rm25	rm25	rm25	rm25
sample	b6a	b6a	b6a	b6a	b6a	b6a	b6a	b6a	b7a	b7a	b7a	b7b	b7b	b7b	b7b	b1a	b1b	b1b	b1b	b1c
type	GC	GC	GC	GC	GC	PR	PR	PR	PC	PR	GC	GC	GC	PR	PR	Mx	Mx	PC	PR	PC
SiO2	50.81	51.21	47.23	44.05	47.55	44.69	48.48	47.78	47.40	49.27	51.66	44.39	51.17	51.66	46.26	42.50	43.56	47.91	43.11	45.04
TiO2	0.56	0.49	2.42	3.09	1.56	2.83	2.11	2.19	1.58	1.53	0.53	2.99	0.68	0.53	2.76	4.05	3.61	1.77	4.02	2.93
Al2O3	1.88	1.46	5.19	8.49	3.92	7.45	4.39	4.49	5.44	2.93	1.96	7.91	2.31	1.96	5.62	9.36	9.06	5.77	9.37	7.80
Cr2O3	0.02	0.02	0.04	0.03	0.00	0.00	0.00	0.00	0.00	0.02	0.01	0.00	0.00	0.01	0.04	0.02	0.05	0.04	0.00	0.02
FeO	8.29	8.28	7.34	7.96	8.02	7.66	7.33	7.37	8.36	6.93	8.49	7.63	8.24	8.49	7.59	7.61	7.36	6.34	7.30	7.06
MnO	0.47	0.55	0.15	0.11	0.30	0.14	0.22	0.15	0.25	0.17	0.57	0.10	0.54	0.57	0.14	0.10	0.15	0.08	0.10	0.11
MgO	13.62	13.99	13.61	12.38	13.26	12.63	13.92	13.88	12.45	14.96	13.34	12.55	13.57	13.34	13.50	11.34	11.71	13.60	11.42	12.47
CaO	21.96	21.51	22.22	21.95	21.65	22.17	22.10	22.13	21.77	22.11	21.93	22.21	21.78	21.93	21.98	22.94	22.82	21.54	22.81	22.23
Na2O	0.86	0.95	0.43	0.46	0.64	0.42	0.45	0.48	0.63	0.41	0.80	0.44	0.78	0.80	0.49	0.44	0.48	0.40	0.45	0.36
K2O	0.00	0.00	0.01	0.00	0.00	0.00	0.01	0.00	0.01	0.01	0.00	0.00	0.00	0.00	0.01	0.01	0.01	0.01	0.01	0.01
F	0.00	0.18	0.04	0.04	0.00	0.09	0.02	0.00	0.02	0.00	0.06	0.00	0.00	0.06	0.02	0.06	0.05	0.00	0.07	0.00
Tot	98.52	98.58	98.65	98.55	96.91	98.10	99.01	98.51	97.91	98.34	99.32	98.25	99.09	99.32	98.38	98.44	98.84	97.58	98.66	98.04
Structural formula (a.p.f.u.)																				
Tet																				
Si	1.93	1.94	1.79	1.68	1.84	1.72	1.83	1.82	1.82	1.87	1.95	1.70	1.93	1.95	1.76	1.63	1.66	1.82	1.65	1.72
Al	0.07	0.06	0.21	0.32	0.16	0.28	0.17	0.18	0.18	0.13	0.05	0.30	0.07	0.05	0.24	0.37	0.34	0.18	0.35	0.28
Oct																				
Al	0.02	0.01	0.02	0.07	0.02	0.05	0.02	0.02	0.06	0.00	0.03	0.06	0.03	0.03	0.02	0.06	0.07	0.08	0.07	0.07
Fe3+	0.12	0.13	0.11	0.16	0.14	0.15	0.09	0.12	0.11	0.12	0.08	0.15	0.08	0.08	0.14	0.16	0.14	0.04	0.12	0.10
Cr	0.00	0.00	0.00	0.00	0.00	0.00	0.00	0.00	0.00	0.00	0.00	0.00	0.00	0.00	0.00	0.00	0.00	0.00	0.00	0.00
Ti	0.02	0.01	0.07	0.09	0.05	0.08	0.06	0.06	0.05	0.04	0.02	0.09	0.02	0.02	0.08	0.12	0.10	0.05	0.12	0.08
Fe2+	0.14	0.14	0.12	0.10	0.12	0.10	0.14	0.12	0.16	0.10	0.19	0.09	0.18	0.19	0.10	0.09	0.09	0.16	0.11	0.13
Mn	0.02	0.02	0.00	0.00	0.01	0.00	0.01	0.00	0.01	0.01	0.02	0.00	0.02	0.02	0.00	0.00	0.00	0.00	0.00	0.00
Mg	0.77	0.79	0.77	0.71	0.77	0.72	0.78	0.79	0.71	0.85	0.75	0.72	0.76	0.75	0.77	0.65	0.67	0.77	0.65	0.71
Ca	0.89	0.88	0.90	0.90	0.90	0.91	0.89	0.90	0.89	0.90	0.88	0.91	0.88	0.88	0.90	0.95	0.93	0.88	0.93	0.91
Na	0.06	0.07	0.03	0.03	0.05	0.03	0.03	0.04	0.05	0.03	0.06	0.03	0.06	0.06	0.04	0.03	0.04	0.03	0.03	0.03
K	0.00	0.00	0.00	0.00	0.00	0.00	0.00	0.00	0.00	0.00	0.00	0.00	0.00	0.00	0.00	0.00	0.00	0.00	0.00	0.00
#Mg	74.55	75.08	76.79	73.50	74.67	74.61	77.19	77.05	72.65	79.38	73.69	74.56	74.59	73.69	76.03	72.65	73.93	79.28	73.59	75.90
Wo %	43.73	42.93	42.93	41.34	42.55	42.15	43.25	42.84	43.28	42.40	46.76	42.05	46.82	46.76	41.97	43.62	43.52	41.14	44.21	43.54
En %	45.59	46.63	47.38	48.44	47.27	48.15	46.60	47.73	44.64	49.39	41.29	48.39	41.98	41.29	48.65	46.42	46.72	47.98	45.34	46.07
Fs %	10.67	10.44	9.69	10.22	10.18	9.70	10.15	9.43	12.08	8.21	11.95	9.57	11.20	11.95	9.38	9.96	9.76	10.89	10.45	10.39

Table IV.2: Electron microprobe analysis to clinopyroxenes

Occurrence	Malveira da Serra sill																			
sample	rm25 b1d	rm25 b2e	rm25 b2e	rm25 b2e	rm25 b2e	rm25 b2e	rm25 b3a	rm25 b3a	rm25 b3a	rm25 b3a	rm25 b3a	rm25 b3a	rm25 b3a	rm25 b3a	rm25 b3a	rm25 b3a	rm25 b3a	rm25 b3a	rm25 b3a	rm25 b3a
type	PC	PR	PR	PR	PC	PC	PR	PR	PR	PR	PR	PR	GC	GC	GC	GC	GC	GC	GC	GC
SiO2	43.05	42.13	44.65	44.25	43.50	42.52	46.47	47.32	48.09	46.74	45.25	42.72	47.20	47.95	47.69	47.46	47.96	48.90	48.15	48.84
TiO2	3.36	3.85	2.62	2.87	2.36	3.66	2.52	2.04	1.95	2.05	2.24	3.51	1.01	0.93	0.89	0.97	0.77	0.72	0.68	0.68
Al2O3	8.74	10.01	7.75	8.24	9.14	9.26	6.29	5.67	5.50	5.62	7.16	9.49	4.90	4.51	4.75	4.74	4.46	3.98	4.13	4.04
Cr2O3	0.00	0.00	0.05	0.00	0.00	0.00	0.03	0.00	0.00	0.03	0.00	0.00	0.00	0.00	0.00	0.00	0.00	0.00	0.05	0.00
FeO	7.22	7.61	7.42	7.19	9.89	7.47	7.30	6.61	6.50	7.11	7.70	7.67	11.92	11.55	11.99	11.88	11.81	11.68	11.76	11.73
MnO	0.08	0.09	0.08	0.10	0.24	0.11	0.16	0.05	0.15	0.12	0.16	0.07	0.49	0.46	0.53	0.48	0.47	0.47	0.47	0.47
MgO	11.85	11.51	12.57	12.12	9.64	11.77	12.92	13.84	14.04	13.80	12.47	11.60	9.55	9.89	9.46	9.54	9.71	10.05	9.82	10.02
CaO	22.67	22.66	22.48	22.85	22.45	22.85	22.26	22.54	22.71	22.54	22.21	22.84	21.83	21.80	21.72	21.70	21.53	21.77	21.61	21.60
Na2O	0.42	0.50	0.53	0.45	0.88	0.43	0.47	0.37	0.37	0.33	0.64	0.47	1.35	1.33	1.40	1.37	1.41	1.33	1.43	1.45
K2O	0.04	0.00	0.00	0.00	0.00	0.02	0.01	0.01	0.01	0.00	0.00	0.01	0.00	0.00	0.00	0.00	0.01	0.00	0.00	0.00
F	0.00	0.12	0.00	0.01	0.00	0.00	0.05	0.01	0.03	0.00	0.00	0.01	0.10	0.00	0.14	0.02	0.00	0.00	0.00	0.03
Tot	97.44	98.43	98.15	98.08	98.16	98.18	98.50	98.50	99.36	98.39	97.92	98.38	98.36	98.44	98.50	98.23	98.18	98.90	98.11	98.85
Structural formula (a.p.f.u.)																				
Tet																				
Si	1.67	1.62	1.71	1.70	1.69	1.64	1.77	1.79	1.80	1.78	1.74	1.64	1.84	1.86	1.85	1.85	1.87	1.88	1.88	1.88
Al	0.33	0.38	0.29	0.30	0.31	0.36	0.23	0.21	0.20	0.22	0.26	0.36	0.16	0.14	0.15	0.15	0.13	0.12	0.12	0.12
Oct																				
Al	0.06	0.07	0.06	0.07	0.11	0.06	0.05	0.04	0.05	0.03	0.06	0.07	0.07	0.07	0.07	0.07	0.07	0.07	0.06	0.07
Fe3+	0.16	0.18	0.17	0.15	0.19	0.18	0.11	0.11	0.10	0.14	0.17	0.18	0.20	0.18	0.19	0.19	0.18	0.16	0.19	0.17
Cr	0.00	0.00	0.00	0.00	0.00	0.00	0.00	0.00	0.00	0.00	0.00	0.00	0.00	0.00	0.00	0.00	0.00	0.00	0.00	0.00
Ti	0.10	0.11	0.08	0.08	0.07	0.11	0.07	0.06	0.06	0.06	0.06	0.10	0.03	0.03	0.03	0.03	0.02	0.02	0.02	0.02
Fe2+	0.07	0.06	0.07	0.08	0.13	0.06	0.13	0.10	0.10	0.09	0.08	0.07	0.19	0.20	0.20	0.20	0.20	0.22	0.19	0.20
Mn	0.00	0.00	0.00	0.00	0.01	0.00	0.01	0.00	0.00	0.00	0.01	0.00	0.02	0.02	0.02	0.02	0.02	0.02	0.02	0.02
Mg	0.68	0.66	0.72	0.69	0.56	0.68	0.73	0.78	0.79	0.78	0.71	0.66	0.55	0.57	0.55	0.55	0.56	0.58	0.57	0.58
Ca	0.94	0.93	0.92	0.94	0.93	0.94	0.91	0.91	0.91	0.92	0.91	0.94	0.91	0.91	0.90	0.91	0.90	0.90	0.90	0.89
Na	0.03	0.04	0.04	0.03	0.07	0.03	0.03	0.03	0.03	0.02	0.05	0.03	0.10	0.10	0.11	0.10	0.11	0.10	0.11	0.11
K	0.00	0.00	0.00	0.00	0.00	0.00	0.00	0.00	0.00	0.00	0.00	0.00	0.00	0.00	0.00	0.00	0.00	0.00	0.00	0.00
#Mg	74.53	72.95	75.13	75.04	63.49	73.75	75.95	78.86	79.40	77.59	74.28	72.94	58.81	60.43	58.44	58.87	59.45	60.55	59.82	60.37
Wo %	43.23	42.40	42.25	43.51	43.51	42.64	43.48	43.38	43.56	42.36	42.36	42.74	43.83	44.28	44.15	44.08	44.03	44.53	44.02	44.19
En %	47.84	48.60	49.34	47.67	42.09	48.85	46.36	48.24	48.12	49.38	48.61	48.10	38.67	38.56	37.76	38.11	38.25	37.85	38.66	38.43
Fs %	8.93	9.00	8.41	8.82	14.39	8.52	10.15	8.37	8.31	8.26	9.03	9.15	17.50	17.15	18.10	17.80	17.71	17.62	17.32	17.38

Table IV.2: Electron microprobe analysis to clinopyroxenes

Occurrence	Malveira da Serra sill																			
	rm25	rm25	rm25	rm25	rm25	rm25	rm25	rm25	rm25	rm25	rm25	rm25	rm25	rm25	rm25	rm25	rm25	rm25	rm25	rm25
sample	b3a	b3a	b3a	b3a	b3a	b3a	b3b	b4a	b4a	b4b	b4b	b4b	b4b	b4b	b4b	b4b	b4b	b4b	b4b	b4b
type	GC	PR	PR	PR	PR	PR	Mx	PC	PR	PR	PR	PR	PR	PC	PC	PC	PC	PR	PR	PR
SiO2	38.87	46.86	46.48	47.44	47.34	46.92	44.72	43.49	41.89	44.79	43.93	44.77	44.41	45.00	45.73	45.16	45.32	44.87	42.36	41.61
TiO2	7.40	1.97	2.01	1.96	1.99	2.10	3.00	3.59	4.32	2.87	2.99	3.01	3.04	3.00	2.33	2.54	2.35	2.47	3.68	4.08
Al2O3	5.41	7.59	5.48	5.54	5.70	6.02	8.13	9.04	10.26	8.29	8.81	8.14	8.42	8.55	9.43	9.80	9.40	9.66	9.85	10.35
Cr2O3	0.06	0.01	0.00	0.00	0.00	0.00	0.07	0.03	0.00	0.09	0.00	0.00	0.02	0.08	0.23	0.13	0.25	0.34	0.03	0.00
FeO	16.18	6.89	7.02	6.59	6.57	6.69	6.91	6.98	7.51	6.79	7.03	6.67	6.60	6.67	6.15	6.47	6.25	6.38	7.48	7.39
MnO	0.05	0.08	0.12	0.15	0.14	0.17	0.08	0.13	0.11	0.10	0.11	0.12	0.14	0.12	0.08	0.09	0.07	0.07	0.08	0.09
MgO	12.16	12.65	13.92	14.11	13.90	13.56	12.55	11.81	11.11	12.15	11.97	12.36	12.43	12.45	12.93	12.65	12.74	12.61	11.49	11.25
CaO	16.85	20.70	22.34	22.62	22.82	22.92	22.42	22.72	22.79	22.97	22.90	22.90	22.96	22.98	21.44	21.07	21.56	21.24	22.28	22.63
Na2O	0.75	0.33	0.37	0.38	0.40	0.44	0.51	0.48	0.46	0.40	0.44	0.40	0.45	0.44	0.71	0.67	0.65	0.73	0.53	0.50
K2O	0.19	0.71	0.02	0.00	0.00	0.00	0.02	0.01	0.00	0.00	0.01	0.01	0.01	0.01	0.00	0.00	0.01	0.01	0.00	0.01
F	0.04	0.00	0.00	0.00	0.00	0.07	0.00	0.08	0.00	0.02	0.01	0.07	0.00	0.00	0.00	0.06	0.11	0.11	0.02	0.24
Tot	98.00	97.79	97.76	98.84	98.92	98.88	98.46	98.33	98.48	98.50	98.19	98.44	98.51	99.32	99.06	98.62	98.66	98.46	97.79	98.05
Structural formula (a.p.f.u.)																				
Tet																				
Si	1.56	1.78	1.78	1.79	1.79	1.78	1.70	1.66	1.61	1.71	1.68	1.71	1.69	1.70	1.71	1.70	1.71	1.70	1.63	1.61
Al	0.44	0.22	0.22	0.21	0.21	0.22	0.30	0.34	0.39	0.29	0.32	0.29	0.31	0.30	0.29	0.30	0.29	0.30	0.37	0.39
Oct																				
Al	-0.18	0.12	0.03	0.04	0.04	0.04	0.07	0.07	0.07	0.08	0.08	0.07	0.07	0.08	0.13	0.14	0.13	0.13	0.08	0.08
Fe3+	0.34	0.06	0.16	0.13	0.13	0.14	0.14	0.14	0.15	0.12	0.15	0.12	0.14	0.12	0.10	0.09	0.11	0.11	0.16	0.17
Cr	0.00	0.00	0.00	0.00	0.00	0.00	0.00	0.00	0.00	0.00	0.00	0.00	0.00	0.00	0.01	0.00	0.01	0.01	0.00	0.00
Ti	0.22	0.06	0.06	0.06	0.06	0.06	0.09	0.10	0.12	0.08	0.09	0.09	0.09	0.09	0.07	0.07	0.07	0.07	0.11	0.12
Fe2+	0.20	0.16	0.07	0.08	0.08	0.07	0.08	0.09	0.09	0.10	0.08	0.09	0.07	0.09	0.09	0.11	0.09	0.09	0.08	0.07
Mn	0.00	0.00	0.00	0.00	0.00	0.01	0.00	0.00	0.00	0.00	0.00	0.00	0.00	0.00	0.00	0.00	0.00	0.00	0.00	0.00
Mg	0.73	0.72	0.79	0.79	0.78	0.76	0.71	0.67	0.64	0.69	0.68	0.70	0.71	0.70	0.72	0.71	0.72	0.71	0.66	0.65
Ca	0.73	0.84	0.92	0.92	0.92	0.93	0.91	0.93	0.94	0.94	0.94	0.93	0.94	0.93	0.86	0.85	0.87	0.86	0.92	0.94
Na	0.06	0.02	0.03	0.03	0.03	0.03	0.04	0.04	0.03	0.03	0.03	0.03	0.03	0.03	0.05	0.05	0.05	0.05	0.04	0.04
K	0.01	0.03	0.00	0.00	0.00	0.00	0.00	0.00	0.00	0.00	0.00	0.00	0.00	0.00	0.00	0.00	0.00	0.00	0.00	0.00
#Mg	57.27	76.61	77.94	79.25	79.05	78.31	76.40	75.12	72.50	76.13	75.22	76.76	77.06	76.88	78.96	77.70	78.43	77.89	73.26	73.07
Wo %	27.97	36.34	41.94	42.78	43.22	43.39	42.96	43.78	43.49	44.29	43.65	44.20	43.65	43.80	41.89	41.72	42.03	41.38	42.50	42.83
En %	50.02	49.09	50.46	49.68	49.25	49.02	48.30	47.00	46.35	46.44	47.58	46.94	48.53	47.54	49.56	48.58	49.27	49.85	47.93	48.11
Fs %	22.01	14.56	7.60	7.54	7.52	7.58	8.74	9.22	10.16	9.26	8.77	8.86	7.82	8.66	8.55	9.71	8.70	8.77	9.57	9.06

Table IV.2: Electron microprobe analysis to clinopyroxenes

Occurrence	Malveira da Serra sill																			
sample	rm25 b4b	rm25 b4c	rm25 b4c	rm25 b4c	rm25 b4c	rm25 b4c	rm25 b4c	rm25 b4c	rm25 b4c	rm25 b4c	rm25 b4c	rm25 b4c	rm25 b4c	rm25 b4c	rm25 b4c	rm25 b4c	rm25 b4c	rm25 b4c	rm25 b4c	rm25 b4c
type	PR	PR	PR	PR	PR	PR	PC	PC	PC	PC	PC	PC	PC	PC	PC	PC	PC	PR	PR	PR
SiO2	41.36	44.79	43.93	44.77	44.41	45.00	46.07	46.01	45.99	46.78	48.14	46.73	47.36	45.73	45.16	45.32	44.87	42.36	41.61	41.36
TiO2	4.18	2.87	2.99	3.01	3.04	3.00	2.03	2.12	2.05	1.76	1.55	1.81	1.67	2.33	2.54	2.35	2.47	3.68	4.08	4.18
Al2O3	10.35	8.29	8.81	8.14	8.42	8.55	8.03	8.58	8.91	8.07	6.64	7.93	7.24	9.43	9.80	9.40	9.66	9.85	10.35	10.35
Cr2O3	0.00	0.09	0.00	0.00	0.02	0.08	0.15	0.34	0.24	0.30	0.16	0.17	0.18	0.23	0.13	0.25	0.34	0.03	0.00	0.00
FeO	7.29	6.79	7.03	6.67	6.60	6.67	6.09	6.26	6.26	6.22	6.05	6.20	6.11	6.15	6.47	6.25	6.38	7.48	7.39	7.29
MnO	0.09	0.10	0.11	0.12	0.14	0.12	0.11	0.09	0.10	0.10	0.07	0.08	0.08	0.08	0.09	0.07	0.07	0.08	0.09	0.09
MgO	11.21	12.15	11.97	12.36	12.43	12.45	13.09	12.78	12.86	13.43	14.26	13.76	14.06	12.93	12.65	12.74	12.61	11.49	11.25	11.21
CaO	22.42	22.97	22.90	22.90	22.96	22.98	22.02	21.90	21.55	21.40	21.14	21.21	21.21	21.44	21.07	21.56	21.24	22.28	22.63	22.42
Na2O	0.52	0.40	0.44	0.40	0.45	0.44	0.61	0.62	0.60	0.65	0.58	0.60	0.65	0.71	0.67	0.65	0.73	0.53	0.50	0.52
K2O	0.01	0.00	0.01	0.01	0.01	0.01	0.00	0.01	0.00	0.01	0.01	0.01	0.00	0.00	0.00	0.01	0.01	0.00	0.01	0.01
F	0.02	0.02	0.01	0.07	0.00	0.00	0.00	0.00	0.02	0.05	0.13	0.02	0.03	0.00	0.06	0.11	0.11	0.02	0.24	0.02
Tot	97.46	98.50	98.19	98.44	98.51	99.32	98.22	98.73	98.57	98.80	98.70	98.56	98.62	99.06	98.62	98.66	98.46	97.79	98.05	97.46
Structural formula (a.p.f.u.)																				
Tet																				
Si	1.60	1.71	1.68	1.71	1.69	1.70	1.74	1.73	1.73	1.76	1.80	1.76	1.78	1.71	1.70	1.71	1.70	1.63	1.61	1.60
Al	0.40	0.29	0.32	0.29	0.31	0.30	0.26	0.27	0.27	0.24	0.20	0.24	0.22	0.29	0.30	0.29	0.30	0.37	0.39	0.40
Oct																				
Al	0.08	0.08	0.08	0.07	0.07	0.08	0.10	0.12	0.13	0.11	0.10	0.11	0.10	0.13	0.14	0.13	0.13	0.08	0.08	0.08
Fe3+	0.17	0.12	0.15	0.12	0.14	0.12	0.11	0.10	0.09	0.10	0.07	0.10	0.10	0.10	0.09	0.11	0.11	0.16	0.17	0.17
Cr	0.00	0.00	0.00	0.00	0.00	0.00	0.00	0.01	0.01	0.01	0.00	0.01	0.01	0.01	0.00	0.01	0.01	0.00	0.00	0.00
Ti	0.12	0.08	0.09	0.09	0.09	0.09	0.06	0.06	0.06	0.05	0.04	0.05	0.05	0.07	0.07	0.07	0.07	0.11	0.12	0.12
Fe2+	0.07	0.10	0.08	0.09	0.07	0.09	0.08	0.10	0.11	0.10	0.12	0.09	0.09	0.09	0.11	0.09	0.09	0.08	0.07	0.07
Mn	0.00	0.00	0.00	0.00	0.00	0.00	0.00	0.00	0.00	0.00	0.00	0.00	0.00	0.00	0.00	0.00	0.00	0.00	0.00	0.00
Mg	0.65	0.69	0.68	0.70	0.71	0.70	0.74	0.72	0.72	0.75	0.80	0.77	0.79	0.72	0.71	0.72	0.71	0.66	0.65	0.65
Ca	0.93	0.94	0.94	0.93	0.94	0.93	0.89	0.88	0.87	0.86	0.85	0.85	0.85	0.86	0.85	0.87	0.86	0.92	0.94	0.93
Na	0.04	0.03	0.03	0.03	0.03	0.03	0.04	0.05	0.04	0.05	0.04	0.04	0.05	0.05	0.05	0.05	0.05	0.04	0.04	0.04
K	0.00	0.00	0.00	0.00	0.00	0.00	0.00	0.00	0.00	0.00	0.00	0.00	0.00	0.00	0.00	0.00	0.00	0.00	0.00	0.00
#Mg	73.28	76.13	75.22	76.76	77.06	76.88	79.30	78.45	78.56	79.37	80.79	79.82	80.39	78.96	77.70	78.43	77.89	73.26	73.07	73.28
Wo %	42.81	44.29	43.65	44.20	43.65	43.80	42.85	42.67	42.35	41.66	41.83	41.25	41.33	41.89	41.72	42.03	41.38	42.50	42.83	42.81
En %	48.13	46.44	47.58	46.94	48.53	47.54	49.37	48.48	48.42	49.83	49.47	50.48	50.73	49.56	48.58	49.27	49.85	47.93	48.11	48.13
Fs %	9.06	9.26	8.77	8.86	7.82	8.66	7.78	8.85	9.23	8.51	8.70	8.27	7.94	8.55	9.71	8.70	8.77	9.57	9.06	9.06

Table IV.2: Electron microprobe analysis to clinopyroxenes

Occurrence	Malveira da Serra sill						Ribeira d'Ilhas plug													
	rm25	rm25	rm25	rm25	rm25	rm25	rm36	rm36	rm36	rm36	rm36	rm36	rm36	rm36	rm36	rm36	rm36	rm36	rm36	rm36
sample	b5a	b5b	b5c	b5c	b5c	b5c	b1a	b1a	b1a	b1a	b1a	b1a	b1a	b1a	b1a	b1a	b1a	b1a	b1a	b1a
type	Mx	Mx	PC	PR	PC	PC	PR	PR	PR	PR	PR	PR	GC	GC	GC	GC	GC	GC	GC	GC
SiO2	44.12	42.81	45.64	47.79	45.58	45.31	43.37	44.00	45.31	45.74	45.92	46.00	48.65	47.87	48.09	48.53	48.02	48.57	46.28	48.84
TiO2	2.92	3.67	2.05	1.94	2.15	2.19	4.14	3.68	2.85	2.74	2.76	2.58	1.41	1.38	1.39	1.40	1.45	1.31	1.22	1.28
Al2O3	8.24	9.18	7.29	5.11	7.46	7.83	8.59	8.43	7.27	7.39	7.51	7.42	4.68	4.66	4.76	4.69	4.63	4.46	4.00	4.42
Cr2O3	0.03	0.00	0.01	0.03	0.02	0.01	0.00	0.00	0.12	0.24	0.17	0.30	0.06	0.00	0.00	0.01	0.04	0.00	0.05	0.00
FeO	7.10	7.29	8.04	6.37	8.33	8.36	7.18	7.67	6.93	6.74	6.80	6.83	11.00	10.83	10.86	10.97	11.08	11.00	10.48	11.07
MnO	0.10	0.10	0.13	0.11	0.12	0.11	0.09	0.09	0.08	0.09	0.08	0.09	0.33	0.32	0.32	0.35	0.30	0.32	0.34	0.32
MgO	12.20	11.61	11.90	14.24	11.45	11.48	12.36	12.89	13.59	13.76	13.70	13.87	11.19	11.19	11.20	11.23	11.22	11.20	10.93	11.09
CaO	22.51	22.73	22.32	22.57	22.18	22.11	22.69	22.50	22.43	22.12	21.72	21.97	21.26	21.26	21.10	21.17	21.22	21.14	20.35	21.02
Na2O	0.49	0.44	0.76	0.39	0.76	0.77	0.56	0.51	0.59	0.68	0.69	0.67	1.61	1.58	1.62	1.60	1.66	1.71	1.55	1.65
K2O	0.02	0.02	0.01	0.02	0.00	0.01	0.01	0.00	0.00	0.01	0.02	0.01	0.01	0.02	0.01	0.01	0.01	0.01	0.04	0.01
F	0.06	0.00	0.00	0.00	0.00	0.00	0.00	0.00	0.10	0.13	0.08	0.05	0.00	0.00	0.00	0.07	0.00	0.00	0.00	0.00
Tot	97.78	97.84	98.20	98.58	98.10	98.22	98.98	99.82	99.23	99.59	99.40	99.77	100.21	99.21	99.37	100.10	99.72	99.74	95.34	99.76
Structural formula (a.p.f.u.)																				
Tet																				
Si	1.70	1.65	1.75	1.81	1.75	1.74	1.65	1.66	1.71	1.72	1.73	1.73	1.84	1.84	1.84	1.84	1.83	1.85	1.85	1.86
Al	0.30	0.35	0.25	0.19	0.25	0.26	0.35	0.34	0.29	0.28	0.27	0.27	0.16	0.16	0.16	0.16	0.17	0.15	0.15	0.14
Oct																				
Al	0.07	0.07	0.08	0.03	0.09	0.09	0.04	0.04	0.04	0.05	0.06	0.05	0.05	0.05	0.05	0.05	0.04	0.05	0.04	0.06
Fe3+	0.15	0.15	0.16	0.12	0.14	0.15	0.17	0.19	0.18	0.18	0.15	0.17	0.21	0.23	0.22	0.21	0.24	0.22	0.24	0.19
Cr	0.00	0.00	0.00	0.00	0.00	0.00	0.00	0.00	0.00	0.01	0.01	0.01	0.00	0.00	0.00	0.00	0.00	0.00	0.00	0.00
Ti	0.08	0.11	0.06	0.06	0.06	0.06	0.12	0.10	0.08	0.08	0.08	0.07	0.04	0.04	0.04	0.04	0.04	0.04	0.04	0.04
Fe2+	0.08	0.08	0.10	0.08	0.13	0.12	0.06	0.05	0.03	0.04	0.06	0.04	0.14	0.12	0.13	0.14	0.12	0.13	0.11	0.16
Mn	0.00	0.00	0.00	0.00	0.00	0.00	0.00	0.00	0.00	0.00	0.00	0.00	0.01	0.01	0.01	0.01	0.01	0.01	0.01	0.01
Mg	0.70	0.67	0.68	0.80	0.66	0.66	0.70	0.73	0.77	0.77	0.77	0.78	0.63	0.64	0.64	0.64	0.64	0.64	0.65	0.63
Ca	0.93	0.94	0.92	0.91	0.91	0.91	0.93	0.91	0.91	0.89	0.87	0.88	0.86	0.87	0.86	0.86	0.87	0.86	0.87	0.86
Na	0.04	0.03	0.06	0.03	0.06	0.06	0.04	0.04	0.04	0.05	0.05	0.05	0.12	0.12	0.12	0.12	0.12	0.13	0.12	0.12
K	0.00	0.00	0.00	0.00	0.00	0.00	0.00	0.00	0.00	0.00	0.00	0.00	0.00	0.00	0.00	0.00	0.00	0.00	0.00	0.00
#Mg	75.40	73.95	72.50	79.94	71.03	71.01	75.41	74.98	77.76	78.44	78.22	78.36	64.46	64.83	64.77	64.61	64.36	64.48	65.05	64.10
Wo %	43.13	43.47	43.22	43.17	43.75	43.28	42.66	41.09	41.16	40.73	40.82	40.29	42.08	41.88	41.82	41.98	41.48	41.96	41.51	42.37
En %	48.08	47.13	46.57	49.25	44.44	45.15	49.26	50.82	52.41	52.90	51.75	53.05	43.48	44.62	44.33	43.67	44.94	44.13	45.24	42.65
Fs %	8.78	9.40	10.21	7.58	11.81	11.57	8.08	8.09	6.43	6.37	7.44	6.66	14.44	13.50	13.84	14.34	13.58	13.91	13.26	14.98

Table IV.2: Electron microprobe analysis to clinopyroxenes

Occurrence	Ribeira d'Ilhas plug																			
sample	rm36 b1a	rm36 b1a	rm36 b1a	rm36 b1a	rm36 b1a	rm36 b1a	rm36 b1a	rm36 b1a	rm36 b1a	rm36 b1a	rm36 b1a	rm36 b1a	rm36 b1a	rm36 b1a	rm36 b1a	rm36 b1a	rm36 b1a	rm36 b1a	rm36 b1a	rm36 b1a
type	GC	GC	GC	GC	GC	GC	GC	GC	GC	GC	GC	GC	GC	GC	PR	PR	PR	PR	PR	PR
SiO2	48.57	48.39	48.14	48.23	48.82	48.62	48.49	48.84	48.57	48.29	47.97	48.38	48.89	48.94	47.49	46.87	45.85	46.14	44.21	43.05
TiO2	1.27	1.33	1.36	1.29	1.32	1.35	1.25	1.31	1.26	1.37	1.26	1.38	1.32	1.33	2.10	2.33	2.63	2.86	3.40	4.13
Al2O3	4.46	4.48	4.49	4.58	4.41	4.41	4.46	4.44	4.43	4.40	4.45	4.56	4.46	4.20	6.37	6.94	7.67	7.13	7.64	8.78
Cr2O3	0.00	0.00	0.02	0.00	0.00	0.00	0.00	0.00	0.00	0.00	0.03	0.00	0.03	0.01	0.57	0.59	0.29	0.00	0.01	0.02
FeO	11.14	10.88	10.97	10.99	10.91	11.14	11.05	11.01	11.14	11.10	10.99	10.98	11.17	10.81	6.17	6.30	6.89	6.89	7.23	7.18
MnO	0.33	0.32	0.33	0.28	0.35	0.32	0.34	0.33	0.25	0.36	0.33	0.33	0.31	0.34	0.08	0.07	0.08	0.09	0.08	0.11
MgO	11.07	11.11	11.25	11.20	11.01	11.18	11.05	11.05	11.06	11.17	11.01	10.99	10.92	11.28	14.54	13.99	13.36	13.41	12.95	12.53
CaO	21.15	21.16	21.08	21.14	21.08	21.08	21.30	20.98	21.06	21.01	20.95	21.19	21.18	21.06	22.12	22.06	21.81	22.51	22.75	22.62
Na2O	1.65	1.66	1.61	1.73	1.64	1.67	1.66	1.69	1.71	1.73	1.62	1.70	1.75	1.61	0.62	0.62	0.70	0.56	0.51	0.60
K2O	0.01	0.01	0.01	0.01	0.02	0.02	0.01	0.02	0.01	0.01	0.00	0.00	0.01	0.01	0.02	0.01	0.02	0.00	0.00	0.01
F	0.01	0.00	0.00	0.17	0.03	0.06	0.02	0.07	0.00	0.00	0.00	0.02	0.00	0.00	0.00	0.08	0.00	0.00	0.00	0.02
Tot	99.73	99.34	99.36	99.58	99.61	99.83	99.63	99.77	99.47	99.45	98.68	99.52	100.10	99.65	100.10	99.87	99.34	99.59	98.80	99.04
Structural formula (a.p.f.u.)																				
Tet																				
Si	1.85	1.85	1.84	1.84	1.86	1.85	1.85	1.86	1.86	1.85	1.85	1.85	1.86	1.86	1.77	1.75	1.73	1.73	1.69	1.64
Al	0.15	0.15	0.16	0.16	0.14	0.15	0.15	0.14	0.14	0.15	0.15	0.15	0.14	0.14	0.23	0.25	0.27	0.27	0.31	0.36
Oct																				
Al	0.05	0.05	0.05	0.05	0.06	0.05	0.05	0.06	0.05	0.05	0.05	0.05	0.06	0.05	0.05	0.06	0.07	0.05	0.03	0.03
Fe3+	0.21	0.21	0.22	0.24	0.19	0.21	0.22	0.19	0.21	0.23	0.21	0.21	0.21	0.19	0.15	0.13	0.15	0.14	0.19	0.19
Cr	0.00	0.00	0.00	0.00	0.00	0.00	0.00	0.00	0.00	0.00	0.00	0.00	0.00	0.00	0.02	0.02	0.01	0.00	0.00	0.00
Ti	0.04	0.04	0.04	0.04	0.04	0.04	0.04	0.04	0.04	0.04	0.04	0.04	0.04	0.04	0.06	0.07	0.07	0.08	0.10	0.12
Fe2+	0.14	0.13	0.13	0.12	0.16	0.14	0.13	0.16	0.14	0.12	0.14	0.14	0.15	0.16	0.05	0.06	0.07	0.07	0.04	0.03
Mn	0.01	0.01	0.01	0.01	0.01	0.01	0.01	0.01	0.01	0.01	0.01	0.01	0.01	0.01	0.00	0.00	0.00	0.00	0.00	0.00
Mg	0.63	0.63	0.64	0.64	0.63	0.63	0.63	0.63	0.63	0.64	0.63	0.63	0.62	0.64	0.81	0.78	0.75	0.75	0.74	0.71
Ca	0.86	0.87	0.86	0.87	0.86	0.86	0.87	0.86	0.86	0.86	0.87	0.87	0.86	0.86	0.88	0.88	0.88	0.91	0.93	0.92
Na	0.12	0.12	0.12	0.13	0.12	0.12	0.12	0.12	0.13	0.13	0.12	0.13	0.13	0.12	0.04	0.04	0.05	0.04	0.04	0.04
K	0.00	0.00	0.00	0.00	0.00	0.00	0.00	0.00	0.00	0.00	0.00	0.00	0.00	0.00	0.00	0.00	0.00	0.00	0.00	0.00
#Mg	63.91	64.53	64.65	64.50	64.28	64.14	64.07	64.16	63.90	64.20	64.11	64.10	63.54	65.03	80.77	79.83	77.55	77.64	76.14	75.68
Wo %	42.17	42.29	41.66	41.69	42.76	41.95	42.29	42.46	42.19	41.64	41.98	42.37	42.55	42.52	40.61	41.01	41.06	42.55	42.00	41.79
En %	43.24	43.66	44.46	44.87	42.30	43.60	43.56	42.62	43.29	44.47	43.63	43.39	42.57	42.95	53.18	51.85	51.03	49.49	50.82	51.19
Fs %	14.60	14.05	13.89	13.44	14.94	14.45	14.15	14.92	14.53	13.89	14.39	14.24	14.88	14.54	6.21	7.14	7.91	7.96	7.18	7.02

Table IV.2: Electron microprobe analysis to clinopyroxenes

Occurrence	Ribeira d'Ilhas plug																			
sample	rm36 b1b	rm36 b1c	rm36 b1c	rm36 b1c	rm36 b1c	rm36 b1c	rm36 b1c	rm36 b1c	rm36 b1c	rm36 b1c	rm36 b1c	rm36 b1c	rm36 b1c	rm36 b1c	rm36 b1c	rm36 b1c	rm36 b1c	rm36 b1c	rm36 b1c	rm36 b1c
type	Mx	PR	PR	PR	PR	PC	PC	PC	PC	PC	PC	PC	PC	PC	PC	PC	PR	PR	PR	PR
SiO2	43.82	41.26	44.37	41.48	41.51	48.59	49.02	48.50	48.41	48.17	48.22	48.57	48.03	48.87	48.87	48.95	42.23	41.40	41.70	39.96
TiO2	3.65	5.33	3.54	5.01	4.84	1.81	1.81	1.72	1.91	1.78	1.83	1.81	1.95	1.53	1.53	1.43	5.11	4.94	4.97	5.57
Al2O3	8.59	10.25	8.70	9.94	10.06	4.68	4.48	4.55	4.96	5.03	4.98	4.94	5.00	3.99	4.00	4.04	9.46	9.57	10.81	12.03
Cr2O3	0.21	0.02	0.29	0.04	0.00	0.20	0.19	0.19	0.23	0.26	0.22	0.22	0.26	0.03	0.14	0.08	0.00	0.01	0.08	0.00
FeO	7.46	7.50	7.22	7.71	7.13	6.35	6.26	6.20	6.26	6.32	6.26	6.42	6.51	6.88	6.75	6.73	7.42	7.76	7.75	8.76
MnO	0.08	0.09	0.05	0.04	0.10	0.08	0.08	0.09	0.09	0.08	0.09	0.08	0.10	0.08	0.10	0.10	0.08	0.09	0.06	0.15
MgO	12.60	11.45	12.74	11.67	12.17	15.26	15.36	15.27	15.14	15.13	15.34	15.42	15.16	14.89	14.85	15.09	11.77	11.88	11.82	12.32
CaO	22.11	22.42	22.02	22.42	22.47	21.97	22.23	22.11	21.84	21.76	21.83	21.88	21.93	22.00	22.06	21.99	22.64	22.49	22.29	17.58
Na2O	0.59	0.61	0.67	0.59	0.68	0.54	0.54	0.51	0.55	0.54	0.56	0.56	0.57	0.68	0.70	0.69	0.59	0.56	1.02	1.96
K2O	0.02	0.03	0.01	0.02	0.04	0.00	0.02	0.00	0.01	0.01	0.00	0.01	0.00	0.02	0.01	0.01	0.03	0.02	0.08	0.68
F	0.03	0.00	0.00	0.00	0.08	0.03	0.00	0.02	0.11	0.00	0.00	0.00	0.10	0.06	0.04	0.00	0.00	0.00	0.12	0.29
Tot	99.24	98.96	99.61	98.96	99.13	99.54	100.06	99.14	99.49	99.09	99.31	99.93	99.61	99.08	99.11	99.13	99.36	98.77	100.64	99.18
Structural formula (a.p.f.u.)																				
Tet																				
Si	1.66	1.58	1.67	1.59	1.59	1.82	1.82	1.82	1.81	1.81	1.80	1.81	1.80	1.84	1.84	1.84	1.61	1.59	1.57	1.53
Al	0.34	0.42	0.33	0.41	0.41	0.18	0.18	0.18	0.19	0.19	0.20	0.19	0.20	0.16	0.16	0.16	0.39	0.41	0.43	0.47
Oct																				
Al	0.05	0.04	0.06	0.04	0.04	0.02	0.02	0.02	0.03	0.03	0.02	0.02	0.02	0.02	0.02	0.02	0.03	0.02	0.05	0.07
Fe3+	0.17	0.17	0.16	0.19	0.22	0.14	0.14	0.14	0.13	0.14	0.15	0.15	0.16	0.16	0.16	0.16	0.16	0.21	0.25	0.37
Cr	0.01	0.00	0.01	0.00	0.00	0.01	0.01	0.01	0.01	0.01	0.01	0.01	0.01	0.00	0.00	0.00	0.00	0.00	0.00	0.00
Ti	0.10	0.15	0.10	0.14	0.14	0.05	0.05	0.05	0.05	0.05	0.05	0.05	0.05	0.04	0.04	0.04	0.15	0.14	0.14	0.16
Fe2+	0.07	0.07	0.07	0.06	0.01	0.06	0.06	0.05	0.06	0.06	0.04	0.05	0.04	0.06	0.06	0.05	0.07	0.04	0.00	-0.08
Mn	0.00	0.00	0.00	0.00	0.00	0.00	0.00	0.00	0.00	0.00	0.00	0.00	0.00	0.00	0.00	0.00	0.00	0.00	0.00	0.00
Mg	0.71	0.65	0.72	0.67	0.69	0.85	0.85	0.85	0.84	0.85	0.86	0.86	0.85	0.84	0.83	0.85	0.67	0.68	0.66	0.70
Ca	0.90	0.92	0.89	0.92	0.92	0.88	0.88	0.89	0.87	0.87	0.88	0.87	0.88	0.89	0.89	0.88	0.92	0.93	0.90	0.72
Na	0.04	0.05	0.05	0.04	0.05	0.04	0.04	0.04	0.04	0.04	0.04	0.04	0.04	0.05	0.05	0.05	0.04	0.04	0.07	0.15
K	0.00	0.00	0.00	0.00	0.00	0.00	0.00	0.00	0.00	0.00	0.00	0.00	0.00	0.00	0.00	0.00	0.00	0.00	0.00	0.03
#Mg	75.05	73.13	75.87	72.97	75.26	81.07	81.39	81.45	81.17	81.01	81.39	81.07	80.58	79.43	79.69	80.00	73.89	73.18	73.11	71.50
Wo %	41.16	42.40	41.17	41.84	41.15	40.88	41.26	41.10	40.93	40.52	40.31	40.22	40.24	41.49	41.54	41.10	42.92	41.39	40.35	32.47
En %	50.18	48.41	50.34	49.24	52.70	52.72	52.50	52.89	52.43	53.01	53.85	53.62	53.68	51.70	51.80	52.64	47.97	50.48	53.31	62.00
Fs %	8.66	9.19	8.49	8.92	6.15	6.40	6.24	6.01	6.64	6.46	5.84	6.15	6.08	6.81	6.65	6.26	9.12	8.12	6.33	5.53

Table IV.2: Electron microprobe analysis to clinopyroxenes

Occurrence	Ribeira d'Ilhas plug																			
sample	rm36 b1d	rm36 b1d	rm36 b1d	rm36 b2a	rm36 b2b	rm36 b2c	rm36 b2c	rm36 b2c	rm36 b2c	rm36 b2c	rm36 b2c	rm36 b2c	rm36 b2c	rm36 b2c	rm36 b2c	rm36 b2c	rm36 b2c	rm36 b2c	rm36 b2c	rm36 b2c
type	PC	PR	PR	Mx	Mx	PR	PR	GC	GC	GC	GC	GC	GC	GC	GC	GC	GC	GC	GC	GC
SiO2	42.50	42.88	42.81	42.33	43.69	42.55	44.78	44.79	44.36	42.63	42.29	41.52	42.25	42.68	42.48	42.33	43.07	42.72	42.88	43.13
TiO2	4.30	4.69	4.56	3.96	3.59	4.68	3.48	2.81	2.52	3.34	3.72	3.93	3.93	3.44	3.66	3.41	3.41	3.45	3.33	3.37
Al2O3	8.53	9.06	9.04	8.31	6.65	9.11	8.17	8.13	8.55	9.73	10.27	10.64	10.66	10.07	10.09	10.01	9.88	9.97	9.99	9.58
Cr2O3	0.01	0.04	0.00	0.01	0.05	0.01	0.24	0.02	0.00	0.00	0.02	0.01	0.07	0.04	0.03	0.00	0.09	0.01	0.00	0.00
FeO	7.50	7.43	7.29	7.25	7.70	7.90	7.08	11.43	11.09	10.55	10.23	10.25	10.22	8.27	10.04	9.78	9.44	9.27	9.37	9.32
MnO	0.10	0.13	0.09	0.09	0.11	0.09	0.04	0.30	0.28	0.25	0.20	0.21	0.22	0.22	0.26	0.22	0.18	0.17	0.19	0.20
MgO	12.34	11.90	11.91	12.71	13.33	11.40	12.66	8.98	9.18	8.98	9.09	9.04	8.88	11.45	9.23	9.44	9.81	10.01	9.81	10.07
CaO	22.47	22.72	22.71	22.76	22.56	22.99	22.33	21.49	21.62	21.82	22.06	21.94	22.01	21.91	21.88	22.10	22.17	22.27	22.31	22.26
Na2O	0.53	0.56	0.54	0.52	0.47	0.50	0.63	1.56	1.49	1.44	1.28	1.39	1.42	1.02	1.44	1.32	1.31	1.25	1.29	1.24
K2O	0.01	0.01	0.01	0.00	0.01	0.00	0.01	0.01	0.00	0.00	0.00	0.00	0.00	0.01	0.00	0.00	0.03	0.01	0.00	0.00
F	0.13	0.00	0.06	0.00	0.00	0.00	0.01	0.03	0.00	0.00	0.00	0.00	0.00	0.23	0.03	0.00	0.00	0.04	0.00	0.00
Tot	98.36	99.42	99.00	97.94	98.14	99.27	99.44	99.55	99.08	98.77	99.15	98.98	99.64	99.23	99.13	98.62	99.45	99.15	99.20	99.20
Structural formula (a.p.f.u.)																				
Tet																				
Si	1.64	1.63	1.63	1.64	1.68	1.63	1.69	1.72	1.71	1.65	1.63	1.61	1.62	1.63	1.64	1.64	1.65	1.64	1.65	1.66
Al	0.36	0.37	0.37	0.36	0.32	0.37	0.31	0.28	0.29	0.35	0.37	0.39	0.38	0.37	0.36	0.36	0.35	0.36	0.35	0.34
Oct																				
Al	0.02	0.04	0.04	0.01	-0.01	0.04	0.05	0.09	0.10	0.10	0.10	0.09	0.10	0.08	0.10	0.10	0.10	0.09	0.10	0.09
Fe3+	0.20	0.16	0.16	0.23	0.23	0.16	0.14	0.20	0.22	0.24	0.22	0.25	0.22	0.24	0.23	0.24	0.22	0.24	0.23	0.23
Cr	0.00	0.00	0.00	0.00	0.00	0.00	0.01	0.00	0.00	0.00	0.00	0.00	0.00	0.00	0.00	0.00	0.00	0.00	0.00	0.00
Ti	0.12	0.13	0.13	0.12	0.10	0.13	0.10	0.08	0.07	0.10	0.11	0.11	0.11	0.10	0.11	0.10	0.10	0.10	0.10	0.10
Fe2+	0.05	0.08	0.08	0.00	0.02	0.09	0.08	0.16	0.13	0.10	0.11	0.08	0.11	0.03	0.09	0.08	0.08	0.06	0.07	0.07
Mn	0.00	0.00	0.00	0.00	0.00	0.00	0.00	0.01	0.01	0.01	0.01	0.01	0.01	0.01	0.01	0.01	0.01	0.01	0.01	0.01
Mg	0.71	0.67	0.68	0.73	0.77	0.65	0.71	0.52	0.53	0.52	0.52	0.52	0.51	0.65	0.53	0.55	0.56	0.57	0.56	0.58
Ca	0.93	0.93	0.93	0.94	0.93	0.94	0.90	0.89	0.89	0.91	0.91	0.91	0.91	0.90	0.90	0.92	0.91	0.92	0.92	0.92
Na	0.04	0.04	0.04	0.04	0.03	0.04	0.05	0.12	0.11	0.11	0.10	0.10	0.11	0.08	0.11	0.10	0.10	0.09	0.10	0.09
K	0.00	0.00	0.00	0.00	0.00	0.00	0.00	0.00	0.00	0.00	0.00	0.00	0.00	0.00	0.00	0.00	0.00	0.00	0.00	0.00
#Mg	74.57	74.07	74.45	75.77	75.54	72.01	76.12	58.35	59.60	60.28	61.31	61.11	60.76	71.18	62.13	63.24	64.94	65.81	65.12	65.82
Wo %	41.69	42.98	43.17	41.08	40.56	43.57	42.34	43.22	42.73	42.68	42.91	42.17	42.98	40.50	42.62	42.64	42.73	42.51	42.83	42.75
En %	50.50	47.76	47.80	53.46	52.93	46.08	48.89	39.24	41.17	42.53	42.38	44.26	42.20	51.36	43.76	44.77	45.03	46.31	45.53	45.66
Fs %	7.81	9.26	9.03	5.46	6.51	10.35	8.76	17.54	16.10	14.79	14.71	13.57	14.82	8.14	13.62	12.59	12.23	11.18	11.64	11.59

Table IV.2: Electron microprobe analysis to clinopyroxenes

Occurrence	Ribeira d'Ilhas plug																			
sample	rm36 b2c	rm36 b2c	rm36 b2c	rm36 b2c	rm36 b2c	rm36 b2d	rm36 b2d	rm36 b3a	rm36 b3b	rm36 b3c	rm36 b3d	rm36 b3e	rm36 b3a	rm36 b3b	rm36 b3c	rm36 b3c	rm36 b3d	rm36 b3f	rm36 b5a	rm36 b5a
type	GC	GC	PR	PR	PR	PCOx	PROx	Ag	Ag	Ag	Ag	Ag	Ag	Ag	Ag	Ag	Ag	Mx	PR	PR
SiO2	43.36	44.73	43.53	48.14	42.09	44.72	41.79	46.50	50.17	46.02	53.98	52.34	46.55	42.44	46.71	3.12	43.83	43.84	42.22	41.18
TiO2	3.05	1.87	2.89	1.75	5.12	3.29	4.27	3.17	2.56	3.42	0.14	0.19	3.15	4.73	0.03	0.00	4.50	4.37	4.66	4.30
Al2O3	9.08	8.06	9.12	5.37	12.56	6.86	9.09	6.26	23.41	7.37	26.33	27.49	5.50	9.57	9.66	0.24	14.44	8.28	9.24	7.23
Cr2O3	0.02	0.03	0.12	0.39	0.00	0.02	0.00	0.00	0.01	0.00	0.00	0.00	0.00	0.01	0.00	0.04	0.00	0.01	0.03	0.02
FeO	10.06	11.57	8.24	5.90	7.07	7.03	7.09	6.49	2.98	6.75	0.41	0.47	6.95	7.00	10.69	4.28	7.45	7.33	7.21	10.18
MnO	0.29	0.28	0.16	0.09	0.16	0.10	0.17	0.09	0.03	0.13	0.00	0.00	0.13	0.11	0.01	0.97	0.04	0.09	0.07	0.12
MgO	9.74	9.26	11.40	15.22	10.10	13.54	11.89	13.29	3.44	13.21	0.05	0.07	14.17	11.65	17.35	3.74	11.77	12.24	11.64	13.97
CaO	21.94	21.52	22.03	22.26	19.99	22.82	22.80	22.96	12.63	22.76	9.73	10.73	22.87	22.39	1.32	44.02	1.84	22.50	22.35	21.24
Na2O	1.40	1.58	0.78	0.57	1.02	0.46	0.60	0.49	3.96	0.58	5.08	4.52	0.41	0.60	0.12	0.04	2.16	0.56	0.52	0.46
K2O	0.00	0.00	0.00	0.01	0.21	0.01	0.03	0.02	0.47	0.01	0.50	0.41	0.00	0.07	0.25	0.04	0.73	0.05	0.01	0.00
F	0.00	0.00	0.03	0.00	0.00	0.04	0.16	0.00	0.00	0.00	0.10	0.03	0.00	0.13	0.00	0.19	0.05	0.10	0.07	0.00
Tot	98.95	98.97	98.30	99.70	98.33	98.89	97.88	99.30	99.71	100.26	96.31	96.25	99.73	98.71	86.22	56.60	86.87	99.40	98.02	98.74
Structural formula (a.p.f.u.)																				
Tet																				
Si	1.67	1.73	1.67	1.79	1.60	1.70	1.62	1.75	1.76	1.72	1.90	1.84	1.75	1.62	1.91	0.29	1.77	1.66	1.63	1.60
Al	0.33	0.27	0.33	0.21	0.40	0.30	0.38	0.25	0.24	0.28	0.10	0.16	0.25	0.38	0.09	1.71	0.23	0.34	0.37	0.40
Oct																				
Al	0.09	0.10	0.09	0.03	0.16	0.01	0.03	0.03	0.73	0.04	0.99	0.99	-0.01	0.05	0.37	-1.68	0.46	0.04	0.05	-0.07
Fe3+	0.24	0.26	0.19	0.16	0.04	0.20	0.21	0.11	-0.53	0.13	-0.84	-0.83	0.16	0.14	-0.40	3.58	-0.47	0.14	0.14	0.36
Cr	0.00	0.00	0.00	0.01	0.00	0.00	0.00	0.00	0.00	0.00	0.00	0.00	0.00	0.00	0.00	0.00	0.00	0.00	0.00	0.00
Ti	0.09	0.05	0.08	0.05	0.15	0.09	0.12	0.09	0.07	0.10	0.00	0.01	0.09	0.14	0.00	0.00	0.14	0.12	0.13	0.13
Fe2+	0.08	0.12	0.08	0.03	0.18	0.03	0.02	0.09	0.61	0.08	0.85	0.84	0.06	0.08	0.76	-3.24	0.72	0.09	0.09	-0.03
Mn	0.01	0.01	0.01	0.00	0.01	0.00	0.01	0.00	0.00	0.00	0.00	0.00	0.00	0.00	0.00	0.08	0.00	0.00	0.00	0.00
Mg	0.56	0.53	0.65	0.85	0.57	0.77	0.69	0.75	0.18	0.74	0.00	0.00	0.79	0.66	1.06	0.52	0.71	0.69	0.67	0.81
Ca	0.91	0.89	0.91	0.89	0.81	0.93	0.95	0.93	0.48	0.91	0.37	0.41	0.92	0.92	0.06	4.43	0.08	0.92	0.92	0.88
Na	0.10	0.12	0.06	0.04	0.08	0.03	0.04	0.04	0.27	0.04	0.35	0.31	0.03	0.04	0.01	0.01	0.17	0.04	0.04	0.03
K	0.00	0.00	0.00	0.00	0.01	0.00	0.00	0.00	0.02	0.00	0.02	0.02	0.00	0.00	0.01	0.00	0.04	0.00	0.00	0.00
#Mg	63.32	58.80	71.16	82.15	71.79	77.44	74.94	78.49	67.27	77.72	17.56	21.15	78.43	74.79	74.33	60.93	73.80	74.86	74.22	70.98
Wo %	42.28	41.82	41.78	40.59	33.36	41.61	42.38	44.44	-30.60	43.29	-58.24	-55.74	42.28	43.38	-29.08	51.98	-36.17	43.22	43.30	33.56
En %	44.98	42.33	48.03	54.43	48.87	52.15	51.21	47.28	37.65	48.55	0.73	1.05	50.54	47.34	80.67	-9.92	74.20	47.15	47.01	60.26
Fs %	12.73	15.86	10.19	4.98	17.77	6.23	6.42	8.28	92.95	8.17	157.52	154.69	7.18	9.27	48.41	57.95	61.97	9.62	9.69	6.17

Table IV.2: Electron microprobe analysis to clinopyroxenes

Occurrence	Ribeira d'Ilhas plug																			
sample	rm36 b5a	rm36 b5a	rm36 b5a	rm36 b5a	rm36 b5a	rm36 b5a	rm36 b5a	rm36 b5a	rm36 b5a	rm36 b5a	rm36 b5a	rm36 b5a	rm36 b5a	rm36 b5a	rm36 b5a	rm36 b5a	rm36 b5a	rm36 b5a	rm36 b5a	rm36 b5a
type	PR	PR	PR	PR	PR	PR	PR	PR	PR	PR	PR	PR	GC	GC	GC	PR	PR	PR	PR	PR
SiO2	42.96	45.79	46.01	46.88	46.84	46.17	46.12	46.25	45.41	44.17	47.89	48.83	44.17	44.22	44.33	48.79	48.77	48.49	47.71	48.24
TiO2	4.85	3.03	2.64	2.41	2.29	2.46	2.45	2.60	2.67	2.84	1.90	1.64	2.84	2.82	2.51	1.57	1.60	1.63	1.98	1.76
Al2O3	9.19	7.85	7.25	6.90	6.79	7.03	7.06	7.37	7.42	8.24	5.29	4.72	8.24	8.32	8.03	4.75	4.62	4.67	5.34	4.73
Cr2O3	0.00	0.19	0.63	0.56	0.46	0.45	0.47	0.39	0.52	0.00	0.45	0.41	0.00	0.03	0.04	0.35	0.30	0.44	0.23	0.25
FeO	7.34	6.95	6.25	6.22	6.22	6.31	6.16	6.29	6.29	8.63	6.04	5.64	8.63	9.13	10.09	5.80	5.84	5.65	6.20	6.15
MnO	0.09	0.04	0.03	0.08	0.08	0.06	0.03	0.07	0.05	0.12	0.08	0.07	0.12	0.15	0.16	0.06	0.08	0.04	0.09	0.08
MgO	12.07	13.18	13.82	14.12	14.10	14.00	14.07	13.94	13.97	11.29	15.25	15.62	11.29	10.96	10.53	15.54	15.58	15.61	15.12	15.42
CaO	22.20	21.39	21.67	21.66	21.83	21.80	21.76	21.80	21.90	22.06	21.89	21.90	22.06	21.93	22.01	21.16	21.58	21.77	21.72	21.88
Na2O	0.55	0.65	0.63	0.60	0.63	0.59	0.60	0.59	0.63	1.18	0.57	0.55	1.18	1.19	1.14	0.53	0.54	0.53	0.57	0.56
K2O	0.01	0.01	0.00	0.00	0.01	0.00	0.01	0.00	0.01	0.01	0.01	0.00	0.01	0.00	0.00	0.02	0.00	0.00	0.01	0.00
F	0.00	0.08	0.06	0.00	0.00	0.11	0.00	0.00	0.01	0.08	0.00	0.00	0.08	0.00	0.00	0.04	0.02	0.01	0.00	0.07
Tot	99.29	99.17	98.96	99.50	99.25	98.94	98.76	99.34	98.90	98.57	99.39	99.43	98.57	98.76	98.87	98.63	98.96	98.85	98.95	99.15
Structural formula (a.p.f.u.)																				
Tet																				
Si	1.63	1.72	1.73	1.75	1.76	1.74	1.74	1.74	1.72	1.70	1.79	1.82	1.70	1.70	1.71	1.83	1.83	1.82	1.79	1.81
Al	0.37	0.28	0.27	0.25	0.24	0.26	0.26	0.26	0.28	0.30	0.21	0.18	0.30	0.30	0.29	0.17	0.17	0.18	0.21	0.19
Oct																				
Al	0.04	0.07	0.06	0.06	0.06	0.05	0.05	0.06	0.05	0.07	0.02	0.03	0.07	0.08	0.07	0.04	0.03	0.02	0.03	0.02
Fe3+	0.13	0.11	0.13	0.12	0.13	0.14	0.14	0.13	0.17	0.23	0.16	0.13	0.23	0.22	0.23	0.11	0.13	0.14	0.15	0.16
Cr	0.00	0.01	0.02	0.02	0.01	0.01	0.01	0.01	0.02	0.00	0.01	0.01	0.00	0.00	0.00	0.01	0.01	0.01	0.01	0.01
Ti	0.14	0.09	0.07	0.07	0.06	0.07	0.07	0.07	0.08	0.08	0.05	0.05	0.08	0.08	0.07	0.04	0.04	0.05	0.06	0.05
Fe2+	0.10	0.11	0.07	0.08	0.06	0.06	0.05	0.07	0.03	0.05	0.03	0.04	0.05	0.07	0.10	0.08	0.06	0.04	0.04	0.04
Mn	0.00	0.00	0.00	0.00	0.00	0.00	0.00	0.00	0.00	0.00	0.00	0.00	0.00	0.00	0.01	0.00	0.00	0.00	0.00	0.00
Mg	0.68	0.74	0.78	0.79	0.79	0.79	0.79	0.78	0.79	0.65	0.85	0.87	0.65	0.63	0.60	0.87	0.87	0.87	0.85	0.86
Ca	0.90	0.86	0.87	0.87	0.88	0.88	0.88	0.88	0.89	0.91	0.88	0.87	0.91	0.90	0.91	0.85	0.87	0.87	0.87	0.88
Na	0.04	0.05	0.05	0.04	0.05	0.04	0.04	0.04	0.05	0.09	0.04	0.04	0.09	0.09	0.08	0.04	0.04	0.04	0.04	0.04
K	0.00	0.00	0.00	0.00	0.00	0.00	0.00	0.00	0.00	0.00	0.00	0.00	0.00	0.00	0.00	0.00	0.00	0.00	0.00	0.00
#Mg	74.55	77.18	79.77	80.19	80.17	79.81	80.29	79.79	79.85	69.99	81.82	83.17	69.99	68.15	65.04	82.70	82.64	83.12	81.29	81.72
Wo %	42.73	41.65	40.70	40.82	41.02	40.72	40.67	40.95	40.04	42.06	40.01	40.62	42.06	42.03	41.89	40.39	40.52	40.38	40.32	40.31
En %	47.30	48.72	52.00	51.61	51.97	52.41	52.79	51.81	54.28	48.71	54.58	54.00	48.71	47.17	45.35	52.84	53.50	54.31	53.81	54.24
Fs %	9.97	9.63	7.30	7.57	7.01	6.87	6.53	7.24	5.68	9.23	5.41	5.38	9.23	10.80	12.76	6.77	5.98	5.31	5.87	5.45

Table IV.2: Electron microprobe analysis to clinopyroxenes

Occurrence	Ribeira d'Ilhas plug									Ribeira d'Ilhas plug										
sample	rm36 b5a	rm36 b5a	rm36 b5a	rm36 b5a	rm36 b5a	rm36 b5a	rm36 b5a	rm36 b5a	rm36 b5a	rm37 b1a	rm37 b1a	rm37 b1a	rm37 b1a	rm37 b1a	rm37 b1a	rm37 b1a	rm37 b1a	rm37 b1a	rm37 b1a	rm37 b1a
type	PR	PR	PR	PR	PR	PR	PR	PR	PR	PR	PR	PR	GC	GC	GC	GC	GC	GC	PR	PR
SiO2	47.27	47.29	47.21	46.67	46.23	46.65	44.79	44.06	42.60	49.36	48.51	47.25	48.20	48.99	48.97	49.55	49.00	49.36	46.76	47.05
TiO2	2.43	2.49	2.51	2.54	2.94	2.81	3.25	3.46	3.31	1.49	2.00	2.56	1.65	1.67	1.64	1.61	1.60	1.49	2.40	2.56
Al2O3	4.96	5.13	4.94	4.91	5.45	5.06	6.09	6.47	7.05	4.63	6.18	7.15	5.26	4.92	4.84	4.80	4.91	4.63	7.19	7.47
Cr2O3	0.00	0.06	0.01	0.00	0.02	0.00	0.07	0.00	0.00	0.03	0.70	0.33	0.03	0.00	0.05	0.00	0.00	0.03	0.40	0.26
FeO	6.32	6.24	6.44	6.44	6.87	6.84	7.31	7.53	6.60	9.40	6.14	6.82	9.52	9.51	9.38	9.48	9.27	9.40	6.84	6.95
MnO	0.10	0.09	0.08	0.06	0.10	0.08	0.09	0.10	0.12	0.21	0.06	0.11	0.25	0.21	0.19	0.23	0.19	0.21	0.02	0.07
MgO	14.97	14.87	15.05	14.88	14.55	14.80	14.23	13.86	14.43	12.09	14.44	13.67	12.00	12.18	12.22	12.18	11.98	12.09	13.54	13.39
CaO	22.55	22.51	22.68	22.73	22.49	22.38	22.38	22.66	22.75	22.21	22.22	22.26	22.00	22.26	22.21	22.16	21.71	22.21	22.46	22.22
Na2O	0.40	0.42	0.40	0.40	0.40	0.42	0.40	0.43	0.54	1.30	0.60	0.69	1.41	1.29	1.26	1.24	1.26	1.30	0.61	0.67
K2O	0.00	0.00	0.00	0.01	0.00	0.00	0.01	0.00	0.00	0.00	0.00	0.01	0.01	0.00	0.00	0.00	0.00	0.00	0.00	0.00
F	0.00	0.00	0.05	0.00	0.00	0.05	0.00	0.00	0.06	0.00	0.00	0.02	0.13	0.03	0.00	0.05	0.04	0.00	0.01	0.11
Tot	99.09	99.08	99.34	98.70	99.05	99.14	98.62	98.62	97.44	100.72	100.89	100.85	100.51	101.08	100.82	101.28	99.95	100.72	100.31	100.69
Structural formula (a.p.f.u.)																				
Tet																				
Si	1.78	1.78	1.78	1.77	1.75	1.76	1.71	1.69	1.65	1.85	1.79	1.75	1.82	1.83	1.83	1.84	1.84	1.85	1.74	1.75
Al	0.22	0.22	0.22	0.23	0.25	0.24	0.29	0.31	0.35	0.15	0.21	0.25	0.18	0.17	0.17	0.16	0.16	0.15	0.26	0.25
Oct																				
Al	0.00	0.01	0.00	0.00	0.00	0.00	0.00	0.00	0.00	0.05	0.06	0.06	0.05	0.05	0.05	0.05	0.06	0.05	0.06	0.07
Fe3+	0.16	0.15	0.17	0.18	0.18	0.18	0.21	0.24	0.32	0.16	0.10	0.13	0.21	0.18	0.17	0.15	0.14	0.16	0.14	0.12
Cr	0.00	0.00	0.00	0.00	0.00	0.00	0.00	0.00	0.00	0.00	0.02	0.01	0.00	0.00	0.00	0.00	0.00	0.00	0.01	0.01
Ti	0.07	0.07	0.07	0.07	0.08	0.08	0.09	0.10	0.10	0.04	0.06	0.07	0.05	0.05	0.05	0.04	0.05	0.04	0.07	0.07
Fe2+	0.04	0.05	0.03	0.02	0.04	0.04	0.02	0.00	0.00	0.13	0.09	0.08	0.09	0.12	0.12	0.14	0.15	0.13	0.07	0.10
Mn	0.00	0.00	0.00	0.00	0.00	0.00	0.00	0.00	0.00	0.01	0.00	0.00	0.01	0.01	0.01	0.01	0.01	0.01	0.00	0.00
Mg	0.84	0.83	0.84	0.84	0.82	0.83	0.81	0.79	0.83	0.67	0.79	0.75	0.67	0.68	0.68	0.68	0.67	0.67	0.75	0.74
Ca	0.91	0.91	0.91	0.92	0.91	0.91	0.92	0.93	0.95	0.89	0.88	0.88	0.89	0.89	0.89	0.88	0.88	0.89	0.90	0.88
Na	0.03	0.03	0.03	0.03	0.03	0.03	0.03	0.03	0.04	0.09	0.04	0.05	0.10	0.09	0.09	0.09	0.09	0.09	0.04	0.05
K	0.00	0.00	0.00	0.00	0.00	0.00	0.00	0.00	0.00	0.00	0.00	0.00	0.00	0.00	0.00	0.00	0.00	0.00	0.00	0.00
#Mg	80.84	80.96	80.64	80.47	79.07	79.41	77.63	76.63	79.58	69.63	80.74	78.13	69.21	69.54	69.90	69.62	69.75	69.63	77.94	77.46
Wo %	41.58	41.76	41.32	41.41	41.06	40.93	39.92	40.06	38.29	43.70	41.49	41.80	42.41	43.14	43.16	43.59	43.73	43.70	41.77	42.14
En %	52.71	52.27	53.22	53.55	52.67	52.87	54.16	54.43	62.14	44.23	50.87	49.95	46.64	45.16	45.16	43.85	43.45	44.23	50.28	48.95
Fs %	5.71	5.97	5.45	5.04	6.27	6.20	5.92	5.51	0.00	12.07	7.65	8.25	10.95	11.70	11.68	12.56	12.83	12.07	7.95	8.91

Table IV.2: Electron microprobe analysis to clinopyroxenes

Occurrence	Ribeira d'Ilhas plug																			
sample	rm37 b1a	rm37 b1b	rm37 b1b	rm37 b1c	rm37 b1c	rm37 b2a	rm37 b2a	rm37 b2a	rm37 b2a	rm37 b1b	rm37 b1b	rm37 b1c	rm37 b1c	rm37 b1c	rm37 b1c	rm37 b2a	rm37 b2a	rm37 b2a	rm37 b2a	rm37 b2a
type	PR	MPC	MPR	MPC	MPR	PR	PR	PR	PC	PC	PR	PCox	PCox	PRox	PRox	PR	PR	PR	PR	GC
SiO2	43.62	47.02	46.22	45.82	45.75	46.82	46.22	42.61	46.30	46.97	42.12	47.13	45.88	45.73	42.06	45.02	45.08	47.20	48.60	45.78
TiO2	3.83	2.55	3.40	3.19	3.25	1.65	3.29	5.29	1.61	2.48	5.14	2.34	2.99	2.10	5.04	3.84	3.67	2.56	2.30	2.17
Al2O3	8.60	7.10	6.19	8.19	7.97	6.86	8.33	9.29	7.45	7.61	9.82	7.66	7.80	7.99	9.40	7.57	7.92	6.84	6.50	7.61
Cr2O3	0.02	0.64	0.01	0.45	0.18	0.03	0.19	0.02	0.00	0.09	0.07	0.15	0.07	0.01	0.00	0.00	0.06	0.18	0.31	0.07
FeO	7.90	6.34	7.87	7.10	7.15	13.75	7.29	7.95	14.23	7.22	8.23	7.26	7.27	9.04	8.11	7.01	7.40	6.92	6.77	11.97
MnO	0.12	0.09	0.09	0.04	0.06	0.62	0.11	0.11	0.65	0.12	0.13	0.13	0.10	0.24	0.10	0.14	0.11	0.04	0.09	0.31
MgO	12.18	13.87	13.57	12.96	13.14	8.00	12.61	11.27	7.84	12.24	11.47	13.16	13.80	12.68	11.46	12.18	12.56	13.20	13.94	8.88
CaO	22.74	22.39	22.57	22.37	22.31	20.37	21.91	22.34	20.51	22.40	22.77	22.39	21.95	21.51	22.58	22.81	22.90	21.95	21.77	20.81
Na2O	0.52	0.68	0.40	0.68	0.65	2.03	0.73	0.58	1.81	1.27	0.66	0.64	0.54	0.81	0.56	0.77	0.51	0.66	0.62	1.92
K2O	0.00	0.00	0.02	0.00	0.02	0.00	0.00	0.01	0.01	0.04	0.00	0.00	0.06	0.04	0.00	0.04	0.00	0.00	0.00	0.00
F	0.12	0.06	0.08	0.04	0.09	0.00	0.00	0.01	0.00	0.00	0.01	0.05	0.00	0.00	0.15	0.08	0.01	0.00	0.01	0.01
Tot	99.63	100.74	100.43	100.81	100.53	100.16	100.73	99.51	100.50	100.50	100.46	100.92	100.52	100.17	99.43	99.41	100.21	99.57	100.90	99.54
Structural formula (a.p.f.u.)																				
Tet																				
Si	1.66	1.74	1.73	1.70	1.71	1.80	1.72	1.62	1.78	1.75	1.59	1.75	1.71	1.72	1.61	1.70	1.69	1.77	1.79	1.76
Al	0.34	0.26	0.27	0.30	0.29	0.20	0.28	0.38	0.22	0.25	0.41	0.25	0.29	0.28	0.39	0.30	0.31	0.23	0.21	0.24
Oct																				
Al	0.04	0.05	0.01	0.06	0.06	0.11	0.08	0.04	0.12	0.09	0.03	0.08	0.05	0.08	0.03	0.04	0.04	0.07	0.07	0.11
Fe3+	0.18	0.14	0.14	0.14	0.14	0.21	0.10	0.12	0.21	0.17	0.19	0.12	0.16	0.21	0.17	0.14	0.14	0.09	0.07	0.22
Cr	0.00	0.02	0.00	0.01	0.01	0.00	0.01	0.00	0.00	0.00	0.00	0.00	0.00	0.00	0.00	0.00	0.00	0.01	0.01	0.00
Ti	0.11	0.07	0.10	0.09	0.09	0.05	0.09	0.15	0.05	0.07	0.15	0.07	0.08	0.06	0.14	0.11	0.10	0.07	0.06	0.06
Fe2+	0.07	0.06	0.10	0.09	0.08	0.23	0.13	0.13	0.24	0.06	0.07	0.10	0.07	0.08	0.09	0.08	0.10	0.13	0.14	0.16
Mn	0.00	0.00	0.00	0.00	0.00	0.02	0.00	0.00	0.02	0.00	0.00	0.00	0.00	0.01	0.00	0.00	0.00	0.00	0.00	0.01
Mg	0.69	0.77	0.76	0.72	0.73	0.46	0.70	0.64	0.45	0.68	0.65	0.73	0.77	0.71	0.65	0.69	0.70	0.74	0.77	0.51
Ca	0.93	0.89	0.91	0.89	0.89	0.84	0.87	0.91	0.84	0.89	0.92	0.89	0.88	0.87	0.92	0.92	0.92	0.88	0.86	0.86
Na	0.04	0.05	0.03	0.05	0.05	0.15	0.05	0.04	0.13	0.09	0.05	0.05	0.04	0.06	0.04	0.06	0.04	0.05	0.04	0.14
K	0.00	0.00	0.00	0.00	0.00	0.00	0.00	0.00	0.00	0.00	0.00	0.00	0.00	0.00	0.00	0.00	0.00	0.00	0.00	0.00
#Mg	73.34	79.58	75.44	76.49	76.63	50.91	75.51	71.66	49.56	75.13	71.29	76.37	77.20	71.44	71.59	75.60	75.17	77.27	78.60	56.95
Wo %	42.15	41.33	41.99	41.80	41.88	49.06	42.74	43.65	41.76	43.60	42.10	42.36	40.40	39.38	42.61	44.45	43.25	43.11	42.36	42.43
En %	48.62	51.62	48.37	49.31	49.51	30.82	46.47	44.37	34.34	48.35	48.01	48.26	51.50	50.35	46.95	46.74	47.27	47.00	47.60	39.38
Fs %	9.23	7.04	9.64	8.89	8.62	20.12	10.79	11.98	23.90	8.05	9.89	9.38	8.11	10.27	10.43	8.80	9.48	9.89	10.04	18.19

Table IV.2: Electron microprobe analysis to clinopyroxenes

Occurrence	Ribeira d'Ilhas plug																			
sample	rm37 b2a	rm37 b2a	rm37 b2a	rm37 b2a	rm37 b2a	rm37 b2a	rm37 b2a	rm37 b2a	rm37 b2a	rm37 b2b	rm37 b2c	rm37 b2d	rm37 b2d	rm37 b2d	rm37 b2d	rm37 b2d	rm37 b2d	rm37 b2d	rm37 b2d	rm37 b3a
type	GC	GC	GC	GC	PR	PR	PR	PR	PR	Mx	Mx	PR	PR	GC	GC	GC	GC	PR	PR	Mx
SiO2	49.22	49.19	48.85	49.54	49.02	47.23	49.02	44.53	42.52	46.34	48.64	42.61	45.33	45.17	45.43	44.00	46.41	45.03	42.93	47.46
TiO2	1.60	1.57	1.62	1.56	2.08	2.37	2.18	3.94	5.41	2.84	2.47	4.77	3.62	2.04	2.11	1.94	1.90	3.83	4.68	2.96
Al2O3	4.69	4.71	4.88	4.54	5.71	6.98	5.69	8.17	9.56	7.81	5.47	9.57	8.04	8.08	8.77	7.57	7.94	7.20	8.88	5.31
Cr2O3	0.06	0.02	0.01	0.04	0.15	0.17	0.16	0.04	0.00	0.19	0.09	0.00	0.00	0.03	0.06	0.00	0.00	0.00	0.00	0.04
FeO	9.22	9.12	9.15	9.28	6.64	6.92	6.54	7.49	8.02	7.21	7.34	8.32	7.76	13.23	12.20	13.80	13.19	7.68	8.13	7.38
MnO	0.24	0.18	0.23	0.22	0.09	0.05	0.08	0.07	0.14	0.10	0.12	0.09	0.09	0.36	0.27	0.30	0.34	0.11	0.07	0.12
MgO	11.87	12.21	12.32	12.13	14.47	13.37	14.18	12.31	10.96	12.74	14.16	11.85	12.37	8.16	8.53	8.98	8.12	12.63	11.65	14.15
CaO	21.78	21.85	21.77	21.77	21.54	21.90	22.17	22.51	22.55	21.73	22.01	21.69	22.44	20.89	21.63	21.29	20.99	22.19	22.41	22.26
Na2O	1.27	1.26	1.30	1.19	0.63	0.70	0.58	0.52	0.68	0.73	0.55	0.54	0.58	1.67	1.37	1.00	1.65	0.49	0.54	0.38
K2O	0.00	0.00	0.00	0.00	0.00	0.00	0.00	0.00	0.01	0.01	0.01	0.06	0.00	0.00	0.00	0.02	0.00	0.01	0.00	0.01
F	0.03	0.11	0.11	0.03	0.00	0.00	0.00	0.00	0.01	0.00	0.00	0.00	0.00	0.13	0.10	0.06	0.03	0.00	0.02	0.11
Tot	100.04	100.16	100.25	100.37	100.33	99.68	100.60	99.57	99.88	99.77	100.86	99.50	100.28	99.78	100.42	98.97	100.55	99.20	99.36	100.19
Structural formula (a.p.f.u.)																				
Tet																				
Si	1.85	1.85	1.84	1.86	1.81	1.77	1.81	1.68	1.61	1.74	1.80	1.62	1.70	1.75	1.73	1.72	1.77	1.71	1.64	1.78
Al	0.15	0.15	0.16	0.14	0.19	0.23	0.19	0.32	0.39	0.26	0.20	0.38	0.30	0.25	0.27	0.28	0.23	0.29	0.36	0.22
Oct																				
Al	0.06	0.06	0.05	0.06	0.06	0.07	0.06	0.05	0.04	0.08	0.04	0.05	0.06	0.11	0.13	0.07	0.13	0.03	0.04	0.01
Fe3+	0.13	0.14	0.17	0.12	0.08	0.11	0.07	0.12	0.13	0.10	0.09	0.15	0.12	0.22	0.17	0.25	0.17	0.12	0.15	0.11
Cr	0.00	0.00	0.00	0.00	0.00	0.01	0.00	0.00	0.00	0.01	0.00	0.00	0.00	0.00	0.00	0.00	0.00	0.00	0.00	0.00
Ti	0.05	0.04	0.05	0.04	0.06	0.07	0.06	0.11	0.15	0.08	0.07	0.14	0.10	0.06	0.06	0.06	0.05	0.11	0.13	0.08
Fe2+	0.16	0.14	0.12	0.17	0.13	0.11	0.13	0.11	0.13	0.12	0.13	0.12	0.12	0.21	0.22	0.20	0.25	0.13	0.11	0.12
Mn	0.01	0.01	0.01	0.01	0.00	0.00	0.00	0.00	0.00	0.00	0.00	0.00	0.00	0.01	0.01	0.01	0.01	0.00	0.00	0.00
Mg	0.67	0.68	0.69	0.68	0.80	0.75	0.78	0.69	0.62	0.71	0.78	0.67	0.69	0.47	0.48	0.52	0.46	0.71	0.66	0.79
Ca	0.88	0.88	0.88	0.87	0.85	0.88	0.88	0.91	0.92	0.87	0.87	0.88	0.90	0.86	0.88	0.89	0.86	0.90	0.92	0.89
Na	0.09	0.09	0.09	0.09	0.04	0.05	0.04	0.04	0.05	0.05	0.04	0.04	0.04	0.13	0.10	0.08	0.12	0.04	0.04	0.03
K	0.00	0.00	0.00	0.00	0.00	0.00	0.00	0.00	0.00	0.00	0.00	0.00	0.00	0.00	0.00	0.00	0.00	0.00	0.00	0.00
#Mg	69.65	70.47	70.59	69.98	79.52	77.50	79.45	74.54	70.91	75.91	77.47	71.75	73.98	52.37	55.48	53.71	52.32	74.56	71.85	77.36
Wo %	48.13	43.66	42.92	47.71	42.08	42.51	43.21	43.25	44.06	42.55	42.27	41.28	43.14	42.12	43.34	40.05	42.15	42.97	42.85	42.17
En %	39.71	44.12	45.54	39.92	48.59	48.20	47.53	46.47	43.98	47.08	47.73	47.02	46.09	36.24	36.30	38.88	34.73	46.28	45.95	48.28
Fs %	12.17	12.22	11.54	12.37	9.34	9.29	9.26	10.28	11.96	10.37	10.00	11.70	10.77	21.64	20.36	21.07	23.13	10.75	11.20	9.55

Table IV.2: Electron microprobe analysis to clinopyroxenes

Occurrence	Ribeira d'Ilhas plug																			
sample	rm37 b3b	rm37 b3b	rm37 b3b	rm37 b3b	rm37 b3b	rm37 b3b	rm37 b3b	rm37 b3b	rm37 b3b	rm37 b3b	rm37 b3b	rm37 b3b	rm37 b3b	rm37 b3b	rm37 b3b	rm37 b3c	rm37 b3c	rm37 b4a	rm37 b4a	rm37 b4b
type	PR	PR	PR	PR	GC	GC	GC	GC	GC	GC	GC	PR	PR	PR	PR	PC	PR	PR	PC	Mx
SiO2	41.95	44.69	47.25	45.68	45.83	46.70	46.08	46.77	47.07	46.89	46.94	46.60	47.15	44.86	41.69	49.69	45.41	40.07	45.59	43.80
TiO2	5.44	3.81	2.37	3.07	1.86	1.87	1.76	1.53	1.42	1.45	1.39	2.65	2.53	3.58	4.89	1.63	4.05	5.69	2.40	3.47
Al2O3	9.94	7.91	6.77	7.81	7.38	7.23	6.85	6.66	6.42	6.43	6.68	7.36	6.69	7.86	10.41	4.54	5.91	10.02	7.43	8.13
Cr2O3	0.04	0.00	0.16	0.08	0.04	0.01	0.00	0.04	0.06	0.10	0.01	0.12	0.20	0.03	0.00	0.37	0.00	0.04	0.35	0.19
FeO	8.22	7.29	6.96	7.86	13.22	13.04	13.33	13.34	13.52	13.27	13.45	7.44	6.83	7.34	8.40	5.99	7.63	8.25	7.19	7.22
MnO	0.12	0.08	0.04	0.14	0.28	0.28	0.27	0.28	0.25	0.23	0.29	0.10	0.06	0.06	0.08	0.09	0.13	0.12	0.07	0.08
MgO	11.01	12.63	13.61	12.75	8.36	8.58	8.66	8.64	8.55	8.66	8.60	12.91	13.61	12.77	11.28	15.01	13.24	10.87	13.67	12.93
CaO	22.68	22.98	22.24	21.87	20.97	21.06	20.94	20.89	20.56	20.50	20.95	21.94	22.55	22.74	21.64	22.32	22.60	22.50	21.71	22.18
Na2O	0.53	0.47	0.67	0.77	1.84	1.84	1.86	1.92	1.94	1.93	1.90	0.78	0.55	0.53	0.62	0.57	0.51	0.63	0.66	0.70
K2O	0.01	0.00	0.01	0.01	0.00	0.01	0.00	0.00	0.00	0.01	0.00	0.00	0.00	0.00	0.04	0.00	0.02	0.02	0.00	0.01
F	0.00	0.00	0.00	0.06	0.00	0.02	0.00	0.00	0.00	0.00	0.00	0.00	0.11	0.11	0.03	0.14	0.00	0.09	0.00	0.00
Tot	100.03	99.86	100.09	100.14	99.80	100.63	99.76	100.17	99.83	99.56	100.33	99.90	100.23	99.87	99.10	100.32	99.50	98.31	99.13	98.71
Structural formula (a.p.f.u.)																				
Tet																				
Si	1.59	1.68	1.76	1.72	1.77	1.78	1.78	1.80	1.81	1.81	1.80	1.75	1.76	1.69	1.59	1.84	1.72	1.56	1.72	1.67
Al	0.41	0.32	0.24	0.28	0.23	0.22	0.22	0.20	0.19	0.19	0.20	0.25	0.24	0.31	0.41	0.16	0.28	0.44	0.28	0.33
Oct																				
Al	0.04	0.04	0.06	0.06	0.10	0.11	0.09	0.10	0.10	0.10	0.10	0.07	0.05	0.04	0.06	0.04	-0.01	0.02	0.05	0.04
Fe3+	0.14	0.14	0.13	0.15	0.23	0.21	0.25	0.23	0.22	0.22	0.23	0.13	0.12	0.15	0.16	0.10	0.15	0.21	0.18	0.21
Cr	0.00	0.00	0.00	0.00	0.00	0.00	0.00	0.00	0.00	0.00	0.00	0.00	0.01	0.00	0.00	0.01	0.00	0.00	0.01	0.01
Ti	0.16	0.11	0.07	0.09	0.05	0.05	0.05	0.04	0.04	0.04	0.04	0.07	0.07	0.10	0.14	0.05	0.12	0.17	0.07	0.10
Fe2+	0.12	0.09	0.09	0.09	0.19	0.21	0.18	0.20	0.22	0.21	0.20	0.10	0.09	0.08	0.11	0.09	0.09	0.06	0.05	0.03
Mn	0.00	0.00	0.00	0.00	0.01	0.01	0.01	0.01	0.01	0.01	0.01	0.00	0.00	0.00	0.00	0.00	0.00	0.00	0.00	0.00
Mg	0.62	0.71	0.76	0.71	0.48	0.49	0.50	0.49	0.49	0.50	0.49	0.72	0.76	0.72	0.64	0.83	0.75	0.63	0.77	0.74
Ca	0.92	0.93	0.89	0.88	0.87	0.86	0.87	0.86	0.85	0.85	0.86	0.88	0.90	0.92	0.89	0.88	0.92	0.94	0.88	0.91
Na	0.04	0.03	0.05	0.06	0.14	0.14	0.14	0.14	0.15	0.14	0.14	0.06	0.04	0.04	0.05	0.04	0.04	0.05	0.05	0.05
K	0.00	0.00	0.00	0.00	0.00	0.00	0.00	0.00	0.00	0.00	0.00	0.00	0.00	0.00	0.00	0.00	0.00	0.00	0.00	0.00
#Mg	70.47	75.54	77.71	74.32	53.01	53.98	53.67	53.60	53.00	53.78	53.27	75.56	78.03	75.62	70.52	81.71	75.58	70.14	77.22	76.16
Wo %	43.35	43.24	42.24	41.52	42.27	42.80	41.87	42.17	42.26	42.14	42.27	42.34	42.64	42.66	41.34	42.44	42.72	42.15	39.72	40.71
En %	44.64	47.84	49.33	48.69	37.05	36.58	38.06	37.39	36.34	36.95	37.03	47.93	48.89	48.62	46.80	50.30	48.20	48.07	53.09	52.73
Fs %	12.01	8.92	8.43	9.79	20.68	20.63	20.07	20.44	21.41	20.91	20.70	9.74	8.47	8.72	11.86	7.26	9.08	9.78	7.19	6.57

Table IV.2: Electron microprobe analysis to clinopyroxenes

Occurrence	Ribeira d'Ilhas plug																			
	rm37	rm37	rm37	rm37	rm37	rm37	rm37	rm37	rm37	rm37	rm37	rm37	rm37	rm37	rm37	rm37	rm37	rm37	rm37	rm37
sample	b4c	b4a	b4a	b4a	b4a	b4a	b4a	b4a	b4a	b4a	b4a	b4a	b4a	b4a	b4a	b4a	b5a	b5a	b5a	b5a
type	Mx	GC	GC	GC	GC	GC	GC	PR	PR	PR	PR	PR	PR	PR	PR	PR	PR	PR	PR	GC
SiO2	44.83	39.80	44.76	44.18	44.77	44.09	43.78	45.17	41.36	45.23	42.23	47.06	44.77	42.78	43.69	43.77	42.48	45.40	44.64	45.26
TiO2	3.20	4.27	1.68	2.36	2.70	2.01	2.58	2.74	5.19	2.84	3.86	2.46	3.11	3.30	3.22	3.82	4.94	3.18	3.37	2.41
Al2O3	7.96	12.47	7.50	8.34	9.44	8.08	8.33	7.46	9.71	7.55	10.35	6.19	7.63	9.92	8.29	8.35	9.40	8.32	8.59	8.37
Cr2O3	0.25	0.00	0.04	0.00	0.01	0.01	0.01	0.18	0.00	0.35	0.00	0.11	0.13	0.00	0.39	0.15	0.00	0.37	0.25	0.01
FeO	7.27	9.58	13.98	12.17	9.31	13.47	11.64	7.03	8.02	6.71	9.44	6.82	6.92	9.25	7.07	7.29	8.07	7.14	7.61	11.88
MnO	0.06	0.14	0.45	0.35	0.22	0.45	0.35	0.08	0.06	0.04	0.15	0.04	0.05	0.17	0.06	0.09	0.08	0.10	0.04	0.31
MgO	12.96	9.49	8.03	8.90	9.93	8.12	9.08	13.53	11.55	13.40	10.08	14.19	13.12	10.59	12.78	12.67	11.50	12.70	12.84	8.88
CaO	21.99	21.99	20.76	21.28	21.00	21.25	21.63	21.99	22.94	22.16	22.19	22.65	22.45	22.34	22.08	22.56	22.69	22.03	21.47	21.59
Na2O	0.70	0.90	1.69	1.53	1.32	1.68	1.38	0.67	0.52	0.62	0.93	0.59	0.63	0.92	0.68	0.60	0.49	0.66	0.67	1.42
K2O	0.01	0.00	0.00	0.00	0.01	0.00	0.00	0.00	0.01	0.01	0.00	0.00	0.01	0.01	0.01	0.01	0.00	0.00	0.00	0.00
F	0.00	0.00	0.10	0.00	0.00	0.00	0.00	0.11	0.00	0.00	0.00	0.00	0.00	0.10	0.00	0.02	0.00	0.00	0.01	0.00
Tot	99.23	98.66	98.94	99.19	98.72	99.20	98.82	98.95	99.39	98.92	99.22	100.13	98.87	99.43	98.26	99.38	99.70	99.90	99.48	100.18
Structural formula (a.p.f.u.)																				
Tet																				
Si	1.70	1.54	1.75	1.71	1.71	1.72	1.70	1.71	1.58	1.71	1.62	1.76	1.70	1.64	1.67	1.66	1.62	1.70	1.68	1.73
Al	0.30	0.46	0.25	0.29	0.29	0.28	0.30	0.29	0.42	0.29	0.38	0.24	0.30	0.36	0.33	0.34	0.38	0.30	0.32	0.27
Oct																				
Al	0.05	0.11	0.10	0.10	0.14	0.09	0.08	0.05	0.02	0.05	0.09	0.03	0.04	0.09	0.05	0.04	0.04	0.07	0.07	0.11
Fe3+	0.17	0.24	0.26	0.25	0.14	0.28	0.24	0.19	0.20	0.16	0.20	0.17	0.18	0.22	0.20	0.18	0.15	0.12	0.15	0.19
Cr	0.01	0.00	0.00	0.00	0.00	0.00	0.00	0.01	0.00	0.01	0.00	0.00	0.00	0.00	0.01	0.00	0.00	0.01	0.01	0.00
Ti	0.09	0.12	0.05	0.07	0.08	0.06	0.08	0.08	0.15	0.08	0.11	0.07	0.09	0.10	0.09	0.11	0.14	0.09	0.10	0.07
Fe2+	0.06	0.07	0.20	0.15	0.16	0.16	0.14	0.03	0.06	0.05	0.10	0.05	0.04	0.07	0.03	0.05	0.11	0.10	0.09	0.19
Mn	0.00	0.00	0.01	0.01	0.01	0.01	0.01	0.00	0.00	0.00	0.00	0.00	0.00	0.01	0.00	0.00	0.00	0.00	0.00	0.01
Mg	0.73	0.55	0.47	0.51	0.57	0.47	0.53	0.76	0.66	0.76	0.58	0.79	0.74	0.61	0.73	0.72	0.65	0.71	0.72	0.51
Ca	0.89	0.91	0.87	0.88	0.86	0.89	0.90	0.89	0.94	0.90	0.91	0.91	0.91	0.92	0.91	0.92	0.92	0.89	0.87	0.88
Na	0.05	0.07	0.13	0.12	0.10	0.13	0.10	0.05	0.04	0.05	0.07	0.04	0.05	0.07	0.05	0.04	0.04	0.05	0.05	0.11
K	0.00	0.00	0.00	0.00	0.00	0.00	0.00	0.00	0.00	0.00	0.00	0.00	0.00	0.00	0.00	0.00	0.00	0.00	0.00	0.00
#Mg	76.06	63.86	50.58	56.58	65.52	51.80	58.17	77.43	71.98	78.08	65.57	78.76	77.17	67.12	76.32	75.62	71.76	76.03	75.03	57.12
Wo %	41.10	40.88	41.00	41.54	40.69	41.14	42.00	40.50	42.19	41.15	42.33	41.65	41.78	41.74	40.60	41.64	43.00	41.92	40.47	43.09
En %	50.83	46.60	36.96	40.62	43.46	38.67	41.27	52.91	48.82	51.87	44.67	51.76	51.36	46.93	52.61	50.76	46.03	48.52	49.84	37.99
Fs %	8.07	12.52	22.04	17.85	15.85	20.18	16.73	6.59	8.99	6.98	13.00	6.59	6.86	11.33	6.79	7.60	10.97	9.56	9.69	18.93

Table IV.2: Electron microprobe analysis to clinopyroxenes

Occurrence	Ribeira d'Ilhas plug										LVC flow									
sample	rm37 b5a	rm37 b5a	rm37 b5a	rm37 b5a	rm37 b5a	rm37 b5a	rm37 b5a	rm37 b5a	rm37 b5b	rm37 b5c	rm43 b1a	rm43 b1b	rm43 b1c	rm43 b1c	rm43 b1d	rm43 b1d	rm43 b1d	rm43 b1d	rm43 b2a	rm43 b2a
type	GC	GC	GC	GC	GC	PR	PR	PR	Mx	MP	Mx	Mx	PC	PR	PC	PC	PC	PC	PC	PC
SiO2	45.03	45.18	40.37	42.74	44.15	45.44	47.30	44.40	47.72	43.93	44.51	43.60	45.73	42.35	41.98	42.10	42.02	41.93	45.95	47.44
TiO2	2.56	2.04	2.94	2.32	2.90	2.74	2.50	4.14	2.64	3.79	3.67	3.55	2.20	4.07	3.00	3.01	2.97	2.99	2.47	2.03
Al2O3	8.37	8.13	9.47	10.28	8.84	7.86	6.88	8.47	4.94	8.98	9.21	6.75	6.64	8.31	9.10	9.21	9.10	9.22	7.73	6.41
Cr2O3	0.04	0.00	0.05	0.00	0.04	0.01	0.54	0.04	0.05	0.29	0.00	0.00	0.00	0.02	0.00	0.00	0.00	0.00	0.02	0.05
FeO	11.45	12.98	13.63	10.54	9.64	8.81	6.38	7.33	6.71	7.53	6.79	7.91	7.03	7.19	8.40	8.49	8.57	8.46	7.14	7.11
MnO	0.26	0.29	0.28	0.24	0.18	0.14	0.06	0.10	0.10	0.09	0.15	0.13	0.10	0.12	0.15	0.15	0.16	0.17	0.07	0.08
MgO	8.98	8.91	10.29	10.80	10.14	11.44	13.71	12.35	14.28	12.14	10.37	11.57	12.84	11.97	10.58	10.45	10.54	10.44	13.51	14.02
CaO	21.71	20.49	20.01	18.74	22.06	22.29	22.15	22.88	22.84	21.99	20.61	20.90	22.20	22.55	22.49	22.47	22.46	22.40	21.50	21.17
Na2O	1.42	1.53	0.79	1.25	1.26	0.97	0.58	0.55	0.39	0.75	1.14	0.84	0.57	0.45	0.69	0.65	0.64	0.66	0.64	0.67
K2O	0.00	0.00	0.00	0.06	0.00	0.00	0.00	0.00	0.01	0.01	0.10	0.33	0.01	0.00	0.00	0.00	0.00	0.00	0.01	0.00
F	0.00	0.11	0.00	0.09	0.00	0.02	0.00	0.00	0.00	0.09	0.00	0.00	0.08	0.03	0.00	0.05	0.00	0.00	0.01	0.02
Tot	99.81	99.64	97.84	97.06	99.28	99.76	100.23	100.34	99.72	99.62	96.53	95.63	97.40	97.09	96.38	96.59	96.53	96.32	99.03	99.00
Structural formula (a.p.f.u.)																				
Tet																				
Si	1.73	1.74	1.60	1.67	1.69	1.72	1.76	1.67	1.79	1.66	1.72	1.72	1.76	1.65	1.65	1.66	1.66	1.65	1.73	1.78
Al	0.27	0.26	0.40	0.33	0.31	0.28	0.24	0.33	0.21	0.34	0.28	0.28	0.24	0.35	0.35	0.34	0.34	0.35	0.27	0.22
Oct																				
Al	0.10	0.11	0.05	0.14	0.09	0.07	0.06	0.04	0.01	0.06	0.14	0.04	0.06	0.03	0.08	0.08	0.08	0.08	0.08	0.07
Fe3+	0.19	0.21	0.34	0.22	0.21	0.17	0.10	0.14	0.12	0.16	0.03	0.16	0.14	0.17	0.21	0.20	0.21	0.20	0.15	0.12
Cr	0.00	0.00	0.00	0.00	0.00	0.00	0.02	0.00	0.00	0.01	0.00	0.00	0.00	0.00	0.00	0.00	0.00	0.00	0.00	0.00
Ti	0.07	0.06	0.09	0.07	0.08	0.08	0.07	0.12	0.07	0.11	0.11	0.11	0.06	0.12	0.09	0.09	0.09	0.09	0.07	0.06
Fe2+	0.18	0.21	0.11	0.12	0.10	0.10	0.10	0.09	0.09	0.08	0.19	0.10	0.08	0.06	0.07	0.08	0.08	0.08	0.08	0.10
Mn	0.01	0.01	0.01	0.01	0.01	0.00	0.00	0.00	0.00	0.00	0.00	0.00	0.00	0.00	0.01	0.01	0.01	0.01	0.00	0.00
Mg	0.51	0.51	0.61	0.63	0.58	0.65	0.76	0.69	0.80	0.69	0.60	0.68	0.74	0.69	0.62	0.61	0.62	0.61	0.76	0.79
Ca	0.89	0.85	0.85	0.78	0.91	0.91	0.88	0.92	0.92	0.89	0.85	0.88	0.92	0.94	0.95	0.95	0.95	0.95	0.87	0.85
Na	0.11	0.11	0.06	0.09	0.09	0.07	0.04	0.04	0.03	0.06	0.09	0.06	0.04	0.03	0.05	0.05	0.05	0.05	0.05	0.05
K	0.00	0.00	0.00	0.00	0.00	0.00	0.00	0.00	0.00	0.00	0.00	0.02	0.00	0.00	0.00	0.00	0.00	0.00	0.00	0.00
#Mg	58.30	55.04	57.39	64.64	65.22	69.84	79.31	75.02	79.15	74.20	73.13	72.28	76.50	74.82	69.18	68.71	68.69	68.75	77.14	77.84
Wo %	43.41	40.90	33.73	36.65	42.88	42.90	42.19	43.27	43.14	41.63	36.42	42.76	43.12	42.92	42.94	43.21	42.86	43.08	40.84	40.96
En %	38.59	38.43	48.89	48.18	44.27	45.70	49.19	47.39	48.97	48.88	47.30	45.96	48.31	48.76	46.98	45.82	46.46	46.17	50.66	49.96
Fs %	18.01	20.67	17.38	15.16	12.85	11.39	8.62	9.34	7.89	9.48	16.28	11.28	8.58	8.32	10.07	10.97	10.67	10.75	8.50	9.08

Table IV.2: Electron microprobe analysis to clinopyroxenes

Occurrence	LVC flow																			
sample	rm43 b2a	rm43 b2a	rm43 b2a	rm43 b2b	rm43 b2c	rm43 b2f	rm43 b3a	rm43 b3b	rm43 b3c	rm43 b3d	rm43 b3d	rm43 b3e	rm43 b3f	rm43 b3f	rm43 b3g	rm43 b3h	rm43 b4i	rm43 b4i	rm43 b4i	rm43 b4i
type	PR	PR	PR	Mx	Mx	Mx	Mx	Mx	Ianf	Ianf	Ianf	Ianf	Ianf	Ianf	AR	AR	MC	MC	Mman	MR
SiO2	41.59	46.39	48.70	47.21	44.91	46.49	47.76	45.12	38.38	46.04	45.19	45.93	45.71	46.15	40.86	42.51	47.47	46.51	50.92	47.63
TiO2	4.45	2.45	2.13	2.67	3.32	3.12	2.79	4.12	7.27	3.11	3.22	3.09	3.24	4.21	6.77	4.86	1.76	2.31	0.82	2.29
Al2O3	9.48	7.97	4.60	4.95	6.01	5.53	5.27	7.91	12.96	8.20	8.55	8.40	8.24	7.40	11.32	10.79	7.08	7.91	4.14	4.70
Cr2O3	0.02	0.02	0.00	0.01	0.06	0.00	0.06	0.03	0.09	0.00	0.00	0.03	0.06	0.00	0.10	0.03	0.34	0.40	0.53	0.03
FeO	8.38	7.45	6.80	7.92	7.75	8.07	7.85	8.29	6.67	7.17	7.17	7.08	7.05	7.66	6.66	6.96	6.09	6.03	4.75	6.95
MnO	0.13	0.11	0.13	0.16	0.19	0.14	0.16	0.13	0.03	0.12	0.08	0.08	0.08	0.15	0.03	0.06	0.08	0.05	0.08	0.16
MgO	12.13	13.26	14.97	14.42	12.69	13.72	14.41	12.50	10.43	13.37	13.14	13.15	13.43	12.57	11.27	12.21	14.82	14.31	17.16	14.97
CaO	21.09	21.14	21.93	21.45	21.29	21.80	22.09	22.10	22.58	21.89	22.21	22.20	22.05	22.32	22.49	21.77	21.47	21.70	21.14	22.69
Na2O	0.43	0.64	0.35	0.31	0.94	0.43	0.32	0.50	0.67	0.59	0.55	0.55	0.67	0.65	0.69	0.74	0.62	0.60	0.51	0.35
K2O	0.01	0.00	0.00	0.02	0.11	0.01	0.00	0.03	0.00	0.01	0.00	0.00	0.01	0.03	0.02	0.05	0.00	0.00	0.00	0.01
F	0.08	0.05	0.08	0.00	0.02	0.11	0.01	0.00	0.10	0.08	0.01	0.12	0.12	0.00	0.00	0.00	0.00	0.00	0.00	0.02
Tot	97.83	99.47	99.66	99.15	97.36	99.40	100.72	100.72	99.13	100.62	100.14	100.57	100.62	101.15	100.21	100.05	99.73	99.91	100.14	99.85
Structural formula (a.p.f.u.)																				
Tet																				
Si	1.61	1.74	1.82	1.78	1.74	1.76	1.78	1.69	1.47	1.71	1.69	1.71	1.70	1.71	1.54	1.60	1.77	1.73	1.87	1.79
Al	0.39	0.26	0.18	0.22	0.26	0.24	0.22	0.31	0.53	0.29	0.31	0.29	0.30	0.29	0.46	0.40	0.23	0.27	0.13	0.21
Oct																				
Al	0.04	0.09	0.02	0.00	0.01	0.01	0.01	0.04	0.05	0.07	0.07	0.08	0.06	0.04	0.04	0.08	0.08	0.08	0.04	-0.01
Fe3+	0.17	0.11	0.10	0.12	0.19	0.13	0.12	0.12	0.16	0.12	0.15	0.12	0.15	0.09	0.12	0.16	0.14	0.14	0.10	0.17
Cr	0.00	0.00	0.00	0.00	0.00	0.00	0.00	0.00	0.00	0.00	0.00	0.00	0.00	0.00	0.00	0.00	0.01	0.01	0.02	0.00
Ti	0.13	0.07	0.06	0.08	0.10	0.09	0.08	0.12	0.21	0.09	0.09	0.09	0.09	0.12	0.19	0.14	0.05	0.06	0.02	0.06
Fe2+	0.10	0.12	0.11	0.13	0.06	0.12	0.13	0.14	0.06	0.10	0.08	0.10	0.07	0.15	0.09	0.06	0.05	0.05	0.05	0.05
Mn	0.00	0.00	0.00	0.00	0.01	0.00	0.01	0.00	0.00	0.00	0.00	0.00	0.00	0.00	0.00	0.00	0.00	0.00	0.00	0.01
Mg	0.70	0.74	0.83	0.81	0.73	0.77	0.80	0.70	0.60	0.74	0.73	0.73	0.75	0.70	0.63	0.68	0.82	0.79	0.94	0.84
Ca	0.88	0.85	0.88	0.87	0.88	0.88	0.88	0.89	0.93	0.87	0.89	0.88	0.88	0.89	0.91	0.88	0.86	0.87	0.83	0.91
Na	0.03	0.05	0.03	0.02	0.07	0.03	0.02	0.04	0.05	0.04	0.04	0.04	0.05	0.05	0.05	0.05	0.04	0.04	0.04	0.03
K	0.00	0.00	0.00	0.00	0.01	0.00	0.00	0.00	0.00	0.00	0.00	0.00	0.00	0.00	0.00	0.00	0.00	0.00	0.00	0.00
#Mg	72.07	76.04	79.68	76.44	74.50	75.19	76.59	72.88	73.61	76.86	76.57	76.82	77.25	74.51	75.09	75.78	81.27	80.87	86.56	79.35
Wo %	39.51	41.06	41.82	40.49	41.56	41.33	41.11	42.22	43.42	41.54	41.58	42.13	41.25	43.77	43.73	41.32	39.72	40.19	39.21	41.09
En %	49.54	48.53	49.50	49.24	49.67	48.28	48.85	45.79	47.85	49.20	49.91	48.61	50.70	44.75	46.73	50.21	54.09	53.41	56.01	52.45
Fs %	10.95	10.42	8.69	10.27	8.77	10.40	10.05	11.99	8.73	9.26	8.51	9.26	8.05	11.49	9.54	8.47	6.19	6.40	4.78	6.46

Table IV.2: Electron microprobe analysis to clinopyroxenes

Occurrence	LVC flow																			
sample	rm43 b4h	rm43 b4h	rm43 b4h	rm43 b4h	rm43 b5a	rm43 b5b	rm43 b5a	rm43 b5a	rm43 b5a	rm43 b5a	rm43 b5a	rm43 b5a	rm43 b5a	rm43 b5a	rm43 b5a	rm43 b5a	rm43 b5a	rm43 b5a	rm43 b5a	rm43 b5a
type	Mman	MC	MR	MR	Mx	Mx	PRox	PRox	PRox	PRox	PCox	PCox	PCox	PCox	PCox	PCox	PCox	PCox	PCox	PCox
SiO2	51.42	47.65	46.77	47.21	47.85	44.32	42.95	45.86	46.17	46.35	46.29	45.82	46.23	45.50	46.08	46.33	46.11	46.14	46.86	47.94
TiO2	0.75	1.84	2.47	2.26	3.12	3.92	4.91	3.08	2.73	2.80	2.77	2.87	2.90	2.81	2.81	2.86	2.72	2.88	2.85	1.98
Al2O3	3.66	7.28	5.95	4.59	5.03	6.94	9.45	8.25	7.76	8.05	7.74	7.90	8.03	7.97	8.04	8.13	7.83	7.75	6.93	6.03
Cr2O3	0.49	0.35	0.00	0.05	0.00	0.02	0.01	0.13	0.00	0.04	0.01	0.00	0.05	0.01	0.00	0.00	0.00	0.00	0.01	0.03
FeO	4.69	6.20	7.47	6.67	7.92	8.81	8.57	7.33	7.63	7.62	7.72	7.63	7.72	7.83	7.76	7.65	7.75	7.69	7.50	7.63
MnO	0.09	0.04	0.10	0.15	0.16	0.17	0.11	0.03	0.10	0.08	0.12	0.07	0.11	0.09	0.10	0.09	0.10	0.14	0.09	0.12
MgO	17.48	14.69	14.34	15.24	14.68	12.58	11.79	13.33	13.10	12.95	13.22	13.05	13.12	13.07	13.09	13.03	13.29	13.22	13.58	13.83
CaO	21.13	21.30	22.16	22.39	22.06	22.03	22.39	22.30	22.23	21.93	22.41	22.38	22.32	22.35	22.45	22.30	22.18	22.40	22.47	22.23
Na2O	0.53	0.63	0.41	0.36	0.37	0.42	0.57	0.45	0.65	0.66	0.62	0.62	0.65	0.62	0.66	0.61	0.64	0.66	0.55	0.61
K2O	0.00	0.01	0.01	0.00	0.02	0.03	0.01	0.00	0.00	0.06	0.00	0.01	0.00	0.00	0.00	0.00	0.00	0.01	0.00	0.00
F	0.00	0.00	0.14	0.05	0.00	0.00	0.00	0.00	0.00	0.00	0.11	0.00	0.00	0.02	0.07	0.00	0.01	0.05	0.00	0.00
Tot	100.27	100.01	99.77	98.97	101.24	99.23	100.74	100.78	100.37	100.58	100.95	100.35	101.16	100.30	101.06	101.06	100.69	100.94	100.84	100.43
Structural formula (a.p.f.u.)																				
Tet																				
Si	1.88	1.77	1.76	1.78	1.77	1.69	1.62	1.70	1.72	1.73	1.72	1.71	1.72	1.71	1.71	1.72	1.72	1.72	1.74	1.79
Al	0.12	0.23	0.24	0.22	0.23	0.31	0.38	0.30	0.28	0.27	0.28	0.29	0.28	0.29	0.29	0.28	0.28	0.28	0.26	0.21
Oct																				
Al	0.04	0.08	0.02	-0.01	-0.01	0.00	0.04	0.07	0.07	0.08	0.06	0.06	0.07	0.06	0.07	0.07	0.06	0.06	0.04	0.05
Fe3+	0.10	0.12	0.16	0.18	0.13	0.16	0.16	0.13	0.15	0.13	0.16	0.16	0.15	0.18	0.16	0.13	0.16	0.17	0.14	0.14
Cr	0.01	0.01	0.00	0.00	0.00	0.00	0.00	0.00	0.00	0.00	0.00	0.00	0.00	0.00	0.00	0.00	0.00	0.00	0.00	0.00
Ti	0.02	0.05	0.07	0.06	0.09	0.11	0.14	0.09	0.08	0.08	0.08	0.08	0.08	0.08	0.08	0.08	0.08	0.08	0.08	0.06
Fe2+	0.04	0.07	0.07	0.03	0.11	0.12	0.11	0.10	0.09	0.11	0.08	0.08	0.09	0.07	0.08	0.10	0.08	0.07	0.09	0.10
Mn	0.00	0.00	0.00	0.00	0.01	0.01	0.00	0.00	0.00	0.00	0.00	0.00	0.00	0.00	0.00	0.00	0.00	0.00	0.00	0.00
Mg	0.95	0.81	0.80	0.86	0.81	0.72	0.66	0.74	0.73	0.72	0.73	0.73	0.73	0.73	0.73	0.72	0.74	0.73	0.75	0.77
Ca	0.83	0.85	0.89	0.91	0.88	0.90	0.90	0.89	0.89	0.87	0.89	0.90	0.89	0.90	0.89	0.89	0.89	0.89	0.89	0.89
Na	0.04	0.05	0.03	0.03	0.03	0.03	0.04	0.03	0.05	0.05	0.04	0.04	0.05	0.04	0.05	0.04	0.05	0.05	0.04	0.04
K	0.00	0.00	0.00	0.00	0.00	0.00	0.00	0.00	0.00	0.00	0.00	0.00	0.00	0.00	0.00	0.00	0.00	0.00	0.00	0.00
#Mg	86.93	80.85	77.38	80.30	76.77	71.80	71.03	76.44	75.39	75.18	75.32	75.30	75.17	74.85	75.06	75.24	75.36	75.40	76.34	76.37
Wo %	39.16	39.89	40.59	40.39	40.75	41.21	41.72	41.49	41.73	41.85	41.54	41.71	41.52	41.09	41.52	41.97	41.05	41.44	41.99	41.74
En %	56.37	52.98	51.44	54.11	49.59	47.31	46.95	49.14	49.13	47.94	49.44	49.38	49.16	50.31	49.59	48.24	50.10	49.91	48.98	49.15
Fs %	4.47	7.13	7.98	5.49	9.66	11.49	11.33	9.37	9.14	10.21	9.02	8.91	9.32	8.60	8.89	9.79	8.84	8.65	9.02	9.11

Table IV.2: Electron microprobe analysis to clinopyroxenes

Occurrence	LVC flow																			
sample	rm43 b5a	rm43 b5a	rm43 b5a	rm43 b5a	rm43 b5a	rm43 b5a	rm43 b5b	rm43 b5b	rm43 b5b	rm43 b5b	rm43 b5b	rm43 b5b	rm43 b5b	rm43 b5b	rm43 b5b	rm43 b5b	rm43 b5b	rm43 b5b	rm43 b5b	rm43 b5b
type	PCox	PCox	PCox	PCox	PRox	PRox	PRox	PRox	PRox	PRox	PRox	PCox	PCox	PCox	PCox	PCox	PCox	PCox	PCox	PRox
SiO2	47.96	47.71	47.69	47.71	46.71	45.30	42.95	45.86	46.17	46.35	46.29	45.82	46.23	45.50	46.08	46.33	46.11	46.14	46.86	47.94
TiO2	2.09	2.07	2.11	1.94	2.75	3.16	4.91	3.08	2.73	2.80	2.77	2.87	2.90	2.81	2.81	2.86	2.72	2.88	2.85	1.98
Al2O3	6.21	6.18	6.20	6.55	7.80	6.73	9.45	8.25	7.76	8.05	7.74	7.90	8.03	7.97	8.04	8.13	7.83	7.75	6.93	6.03
Cr2O3	0.00	0.00	0.03	0.01	0.02	0.03	0.01	0.13	0.00	0.04	0.01	0.00	0.05	0.01	0.00	0.00	0.00	0.00	0.01	0.03
FeO	7.79	7.57	7.72	8.10	7.75	9.21	8.57	7.33	7.63	7.62	7.72	7.63	7.72	7.83	7.76	7.65	7.75	7.69	7.50	7.63
MnO	0.12	0.11	0.12	0.15	0.10	0.20	0.11	0.03	0.10	0.08	0.12	0.07	0.11	0.09	0.10	0.09	0.10	0.14	0.09	0.12
MgO	13.67	13.67	13.77	13.98	13.02	13.66	11.79	13.33	13.10	12.95	13.22	13.05	13.12	13.07	13.09	13.03	13.29	13.22	13.58	13.83
CaO	22.28	22.39	22.38	21.49	22.26	21.09	22.39	22.30	22.23	21.93	22.41	22.38	22.32	22.35	22.45	22.30	22.18	22.40	22.47	22.23
Na2O	0.61	0.61	0.62	0.62	0.63	0.46	0.57	0.45	0.65	0.66	0.62	0.62	0.65	0.62	0.66	0.61	0.64	0.66	0.55	0.61
K2O	0.00	0.00	0.00	0.02	0.00	0.05	0.01	0.00	0.00	0.06	0.00	0.01	0.00	0.00	0.00	0.00	0.00	0.01	0.00	0.00
F	0.00	0.03	0.08	0.00	0.02	0.04	0.00	0.00	0.00	0.00	0.11	0.00	0.00	0.02	0.07	0.00	0.01	0.05	0.00	0.00
Tot	100.78	100.33	100.73	100.57	101.05	99.97	100.74	100.78	100.37	100.58	100.95	100.35	101.16	100.30	101.06	101.06	100.69	100.94	100.84	100.43
Structural formula (a.p.f.u.)																				
Tet																				
Si	1.78	1.78	1.77	1.77	1.73	1.71	1.62	1.70	1.72	1.73	1.72	1.71	1.72	1.71	1.71	1.72	1.72	1.72	1.74	1.79
Al	0.22	0.22	0.23	0.23	0.27	0.29	0.38	0.30	0.28	0.27	0.28	0.29	0.28	0.29	0.29	0.28	0.28	0.28	0.26	0.21
Oct																				
Al	0.05	0.05	0.05	0.06	0.07	0.01	0.04	0.07	0.07	0.08	0.06	0.06	0.07	0.06	0.07	0.07	0.06	0.06	0.04	0.05
Fe3+	0.14	0.14	0.15	0.15	0.13	0.19	0.16	0.13	0.15	0.13	0.16	0.16	0.15	0.18	0.16	0.13	0.16	0.17	0.14	0.14
Cr	0.00	0.00	0.00	0.00	0.00	0.00	0.00	0.00	0.00	0.00	0.00	0.00	0.00	0.00	0.00	0.00	0.00	0.00	0.00	0.00
Ti	0.06	0.06	0.06	0.05	0.08	0.09	0.14	0.09	0.08	0.08	0.08	0.08	0.08	0.08	0.08	0.08	0.08	0.08	0.08	0.06
Fe2+	0.11	0.09	0.09	0.10	0.11	0.10	0.11	0.10	0.09	0.11	0.08	0.08	0.09	0.07	0.08	0.10	0.08	0.07	0.09	0.10
Mn	0.00	0.00	0.00	0.00	0.00	0.01	0.00	0.00	0.00	0.00	0.00	0.00	0.00	0.00	0.00	0.00	0.00	0.00	0.00	0.00
Mg	0.76	0.76	0.76	0.77	0.72	0.77	0.66	0.74	0.73	0.72	0.73	0.73	0.73	0.73	0.73	0.72	0.74	0.73	0.75	0.77
Ca	0.89	0.89	0.89	0.86	0.88	0.85	0.90	0.89	0.89	0.87	0.89	0.90	0.89	0.90	0.89	0.89	0.89	0.89	0.89	0.89
Na	0.04	0.04	0.04	0.04	0.05	0.03	0.04	0.03	0.05	0.05	0.04	0.04	0.05	0.04	0.05	0.04	0.05	0.05	0.04	0.04
K	0.00	0.00	0.00	0.00	0.00	0.00	0.00	0.00	0.00	0.00	0.00	0.00	0.00	0.00	0.00	0.00	0.00	0.00	0.00	0.00
#Mg	75.79	76.29	76.06	75.47	74.96	72.56	71.03	76.44	75.39	75.18	75.32	75.30	75.17	74.85	75.06	75.24	75.36	75.40	76.34	76.37
Wo %	41.97	42.11	41.62	40.08	42.14	38.09	41.72	41.49	41.73	41.85	41.54	41.71	41.52	41.09	41.52	41.97	41.05	41.44	41.99	41.74
En %	48.42	48.90	49.51	50.06	47.65	50.98	46.95	49.14	49.13	47.94	49.44	49.38	49.16	50.31	49.59	48.24	50.10	49.91	48.98	49.15
Fs %	9.61	8.99	8.86	9.86	10.21	10.93	11.33	9.37	9.14	10.21	9.02	8.91	9.32	8.60	8.89	9.79	8.84	8.65	9.02	9.11

Table IV.2: Electron microprobe analysis to clinopyroxenes

Occurrence	LVC flow						Eiras de Faião sill													
	rm43	rm43	rm43	rm43	rm43	rm43	rm47	rm47	rm47	rm47	rm47	rm47	rm47	rm47	rm47	rm47	rm47	rm47	rm47	rm47
sample	b5b	b5b	b5b	b5b	b5b	b5b	b1a	b1a	b1a	b1a	b1a	b1a	b1b	b1c	b1d	b1d	b1d	b1e	b1e	b1e
type	PRox	PRox	PRox	PRox	PRox	PRox	GC	GC	PR	PR	PR	PR	Mx	Mx	PC	PR	Pman	PC	PC	Pman
SiO2	47.96	47.71	47.69	47.71	46.71	45.30	45.41	49.73	49.15	49.08	50.00	49.15	48.04	48.59	46.06	47.81	48.17	45.38	48.96	46.16
TiO2	2.09	2.07	2.11	1.94	2.75	3.16	1.82	1.52	1.02	1.97	1.40	1.02	2.22	0.65	1.86	2.37	2.15	3.11	1.89	2.50
Al2O3	6.21	6.18	6.20	6.55	7.80	6.73	7.03	3.89	4.08	3.89	3.08	4.08	3.83	21.13	6.12	4.72	4.01	6.46	4.29	6.99
Cr2O3	0.00	0.00	0.03	0.01	0.02	0.03	0.03	0.05	0.04	0.00	0.02	0.04	0.03	0.01	0.00	0.00	0.00	0.00	0.00	0.00
FeO	7.79	7.57	7.72	8.10	7.75	9.21	12.42	9.35	11.33	8.15	8.07	11.33	8.64	3.79	10.85	8.44	8.42	9.15	9.08	10.74
MnO	0.12	0.11	0.12	0.15	0.10	0.20	0.45	0.27	0.51	0.30	0.31	0.51	0.28	0.09	0.35	0.28	0.29	0.25	0.24	0.26
MgO	13.67	13.67	13.77	13.98	13.02	13.66	9.76	12.95	11.24	13.47	14.06	11.24	13.43	3.81	10.82	13.14	13.43	11.91	12.96	10.88
CaO	22.28	22.39	22.38	21.49	22.26	21.09	22.14	22.45	21.75	22.71	23.22	21.75	22.95	7.16	22.24	22.92	22.97	22.42	22.64	22.10
Na2O	0.61	0.61	0.62	0.62	0.63	0.46	1.07	0.74	1.41	0.70	0.62	1.41	0.60	10.43	1.11	0.70	0.66	0.82	0.78	1.04
K2O	0.00	0.00	0.00	0.02	0.00	0.05	0.01	0.00	0.00	0.01	0.01	0.00	0.01	0.01	0.00	0.02	0.00	0.02	0.00	0.00
F	0.00	0.03	0.08	0.00	0.02	0.04	0.00	0.06	0.04	0.00	0.00	0.04	0.00	0.00	0.00	0.00	0.12	0.00	0.08	0.06
Tot	100.78	100.33	100.73	100.57	101.05	99.97	100.18	101.08	100.63	100.28	100.82	100.63	100.03	95.70	99.46	100.41	100.20	99.54	100.88	100.72
Structural formula (a.p.f.u.)																				
Tet																				
Si	1.78	1.78	1.77	1.77	1.73	1.71	1.75	1.86	1.86	1.84	1.86	1.86	1.81	1.80	1.77	1.80	1.82	1.73	1.83	1.75
Al	0.22	0.22	0.23	0.23	0.27	0.29	0.25	0.14	0.14	0.16	0.14	0.14	0.19	0.20	0.23	0.20	0.18	0.27	0.17	0.25
Oct																				
Al	0.05	0.05	0.05	0.06	0.07	0.01	0.06	0.03	0.04	0.01	0.00	0.04	-0.02	0.72	0.05	0.01	-0.01	0.02	0.02	0.06
Fe3+	0.14	0.14	0.15	0.15	0.13	0.19	0.24	0.13	0.20	0.14	0.16	0.20	0.18	0.29	0.23	0.17	0.17	0.19	0.15	0.19
Cr	0.00	0.00	0.00	0.00	0.00	0.00	0.00	0.00	0.00	0.00	0.00	0.00	0.00	0.00	0.00	0.00	0.00	0.00	0.00	0.00
Ti	0.06	0.06	0.06	0.05	0.08	0.09	0.05	0.04	0.03	0.06	0.04	0.03	0.06	0.02	0.05	0.07	0.06	0.09	0.05	0.07
Fe2+	0.11	0.09	0.09	0.10	0.11	0.10	0.16	0.17	0.15	0.12	0.10	0.15	0.10	-0.17	0.12	0.09	0.09	0.10	0.14	0.15
Mn	0.00	0.00	0.00	0.00	0.00	0.01	0.01	0.01	0.02	0.01	0.01	0.02	0.01	0.00	0.01	0.01	0.01	0.01	0.01	0.01
Mg	0.76	0.76	0.76	0.77	0.72	0.77	0.56	0.72	0.63	0.75	0.78	0.63	0.76	0.21	0.62	0.74	0.75	0.68	0.72	0.61
Ca	0.89	0.89	0.89	0.86	0.88	0.85	0.91	0.90	0.88	0.91	0.93	0.88	0.93	0.28	0.92	0.92	0.93	0.92	0.91	0.90
Na	0.04	0.04	0.04	0.04	0.05	0.03	0.08	0.05	0.10	0.05	0.05	0.10	0.04	0.75	0.08	0.05	0.05	0.06	0.06	0.08
K	0.00	0.00	0.00	0.00	0.00	0.00	0.00	0.00	0.00	0.00	0.00	0.00	0.00	0.00	0.00	0.00	0.00	0.00	0.00	0.00
#Mg	75.79	76.29	76.06	75.47	74.96	72.56	58.35	71.18	63.87	74.66	75.64	63.87	73.50	64.19	63.99	73.52	73.99	69.89	71.79	64.36
Wo %	41.97	42.11	41.62	40.08	42.14	38.09	41.31	43.23	42.30	43.55	43.33	42.30	42.67	23.97	42.01	42.96	42.89	42.35	43.18	42.21
En %	48.42	48.90	49.51	50.06	47.65	50.98	41.34	44.11	42.82	46.34	47.70	42.82	47.60	121.65	44.36	47.36	47.78	46.56	45.27	42.97
Fs %	9.61	8.99	8.86	9.86	10.21	10.93	17.35	12.66	14.88	10.11	8.97	14.88	9.73	-45.61	13.63	9.67	9.34	11.10	11.55	14.82

Table IV.2: Electron microprobe analysis to clinopyroxenes

Occurrence	Eiras de Faião sill																			
sample	rm47 b1e	rm47 b1e	rm47 b1f	rm47 b2a	rm47 b2b	rm47 b2a	rm47 b2a	rm47 b2a	rm47 b2a	rm47 b2a	rm47 b2a	rm47 b2b	rm47 b2c	rm47 b2d	rm47 b2e	rm47 b2f	rm47 b2g	rm47 b2h	rm47 b2i	rm47 b2j
type	PR	feno 3 b	PC	Mx	Mx	Xen	Xen	Xen	Xen	Xen	Xen	Xen	Xen	Xen	Xen	Xen	Xen	Xen	Xen	Xen
SiO2	45.96	45.69	45.33	44.18	48.25	46.95	46.74	49.38	48.21	46.70	48.54	46.95	46.74	49.38	48.21	46.70	48.72	46.24	46.52	47.38
TiO2	2.96	2.83	3.18	4.08	2.10	2.02	1.93	1.85	2.08	1.81	1.97	2.02	1.93	1.85	2.08	1.81	1.31	2.81	2.09	1.96
Al2O3	6.34	6.40	6.13	6.21	4.38	6.05	5.83	3.90	4.39	5.73	4.02	6.05	5.83	3.90	4.39	5.73	4.75	6.64	5.80	6.03
Cr2O3	0.00	0.00	0.00	0.00	0.00	0.03	0.00	0.01	0.00	0.03	0.00	0.03	0.00	0.01	0.00	0.03	0.02	0.00	0.07	0.00
FeO	9.32	9.27	10.79	9.03	8.24	10.13	9.87	7.54	6.92	9.11	8.40	10.13	9.87	7.54	6.92	9.11	9.81	8.50	9.28	9.43
MnO	0.24	0.23	0.28	0.16	0.32	0.24	0.30	0.24	0.15	0.21	0.21	0.24	0.30	0.24	0.15	0.21	0.30	0.19	0.19	0.24
MgO	11.92	11.86	10.93	11.71	13.22	11.38	11.39	13.66	14.09	12.26	13.58	11.38	11.39	13.66	14.09	12.26	12.16	11.79	11.78	12.04
CaO	22.46	22.59	21.50	21.92	22.75	22.46	22.42	23.00	22.89	22.68	22.28	22.46	22.42	23.00	22.89	22.68	22.05	22.36	22.52	22.22
Na2O	0.80	0.88	1.00	0.95	0.61	0.96	0.95	0.75	0.70	0.87	0.65	0.96	0.95	0.75	0.70	0.87	1.10	0.79	0.84	0.98
K2O	0.01	0.00	0.00	0.02	0.03	0.00	0.00	0.00	0.00	0.00	0.00	0.00	0.00	0.00	0.00	0.00	0.00	0.00	0.00	0.00
F	0.06	0.00	0.02	0.00	0.00	0.00	0.00	0.00	0.00	0.00	0.00	0.00	0.00	0.00	0.00	0.00	0.00	0.08	0.00	0.00
Tot	100.11	99.75	99.16	98.25	99.91	100.24	99.45	100.35	99.48	99.43	99.69	100.24	99.45	100.35	99.48	99.43	100.28	99.41	99.13	100.29
Structural formula (a.p.f.u.)																				
Tet																				
Si	1.74	1.74	1.75	1.71	1.82	1.78	1.78	1.84	1.81	1.78	1.83	1.78	1.78	1.84	1.81	1.78	1.84	1.76	1.78	1.79
Al	0.26	0.26	0.25	0.29	0.18	0.22	0.22	0.16	0.19	0.22	0.17	0.22	0.22	0.16	0.19	0.22	0.16	0.24	0.22	0.21
Oct																				
Al	0.03	0.03	0.02	-0.01	0.01	0.05	0.05	0.02	0.01	0.04	0.01	0.05	0.05	0.02	0.01	0.04	0.05	0.05	0.04	0.05
Fe3+	0.18	0.20	0.18	0.19	0.14	0.18	0.19	0.14	0.16	0.21	0.14	0.18	0.19	0.14	0.16	0.21	0.18	0.13	0.18	0.18
Cr	0.00	0.00	0.00	0.00	0.00	0.00	0.00	0.00	0.00	0.00	0.00	0.00	0.00	0.00	0.00	0.00	0.00	0.00	0.00	0.00
Ti	0.08	0.08	0.09	0.12	0.06	0.06	0.06	0.05	0.06	0.05	0.06	0.06	0.06	0.05	0.06	0.05	0.04	0.08	0.06	0.06
Fe2+	0.12	0.09	0.17	0.10	0.12	0.14	0.13	0.10	0.06	0.08	0.12	0.14	0.13	0.10	0.06	0.08	0.13	0.14	0.12	0.12
Mn	0.01	0.01	0.01	0.01	0.01	0.01	0.01	0.01	0.00	0.01	0.01	0.01	0.01	0.01	0.00	0.01	0.01	0.01	0.01	0.01
Mg	0.67	0.67	0.63	0.68	0.74	0.64	0.65	0.76	0.79	0.70	0.76	0.64	0.65	0.76	0.79	0.70	0.68	0.67	0.67	0.68
Ca	0.91	0.92	0.89	0.91	0.92	0.91	0.92	0.92	0.92	0.93	0.90	0.91	0.92	0.92	0.92	0.93	0.89	0.91	0.92	0.90
Na	0.06	0.07	0.07	0.07	0.04	0.07	0.07	0.05	0.05	0.06	0.05	0.07	0.07	0.05	0.05	0.06	0.08	0.06	0.06	0.07
K	0.00	0.00	0.00	0.00	0.00	0.00	0.00	0.00	0.00	0.00	0.00	0.00	0.00	0.00	0.00	0.00	0.00	0.00	0.00	0.00
#Mg	69.51	69.52	64.36	69.81	74.10	66.71	67.30	76.36	78.40	70.58	74.24	66.71	67.30	76.36	78.40	70.58	68.84	71.21	69.37	69.46
Wo %	42.59	42.44	41.99	42.47	43.38	42.83	43.01	44.15	43.21	42.23	42.59	42.83	43.01	44.15	43.21	42.23	42.55	43.94	43.05	42.43
En %	45.50	46.65	42.67	46.43	46.36	43.82	44.18	46.95	49.97	47.79	47.01	43.82	44.18	46.95	49.97	47.79	44.98	44.12	45.17	45.65
Fs %	11.90	10.91	15.34	11.10	10.26	13.35	12.81	8.90	6.82	9.98	10.40	13.35	12.81	8.90	6.82	9.98	12.47	11.94	11.78	11.93

Table IV.2: Electron microprobe analysis to clinopyroxenes

Occurrence	Eiras de Faião sill																			
sample	rm47 b3a	rm47 b3a	rm47 b3a	rm47 b3a	rm47 b3a	rm47 b3a	rm47 b3a	rm47 b3a	rm47 b3a	rm47 b3a	rm47 b3a	rm47 b3a	rm47 b3a	rm47 b3a	rm47 b3a	rm47 b3a	rm47 b3a	rm47 b4a	rm47 b4b	rm47 b4a
type	PR	PR	PR	PR	PR	GC	GC	GC	GC	GC	GC	GC	PR	PR	PR	PR	PR	Mx	PC	PR
SiO2	44.69	45.85	45.13	45.47	47.20	45.70	46.45	47.46	47.73	47.93	48.35	46.15	46.67	45.54	45.12	46.54	44.81	46.25	48.53	46.48
TiO2	3.20	3.31	3.83	3.54	2.71	2.13	2.18	1.82	1.18	1.08	1.00	2.18	2.70	3.61	3.42	3.13	3.19	2.55	1.48	0.93
Al2O3	7.45	6.65	6.88	6.63	5.45	6.15	5.80	5.11	4.79	5.82	4.14	7.96	6.02	6.74	6.45	6.25	7.71	4.93	3.94	4.84
Cr2O3	0.05	0.00	0.00	0.00	0.00	0.00	0.00	0.01	0.03	0.00	0.00	0.00	0.02	0.05	0.02	0.01	0.00	0.02	0.04	0.00
FeO	9.38	7.62	7.65	7.14	7.80	11.52	11.17	11.34	12.78	12.93	12.24	11.51	8.25	7.40	7.35	7.53	9.27	9.41	8.62	13.47
MnO	0.20	0.12	0.12	0.11	0.14	0.38	0.35	0.38	0.46	0.43	0.43	0.32	0.19	0.10	0.09	0.10	0.14	0.26	0.27	0.68
MgO	11.08	12.83	12.92	12.91	12.89	10.14	10.72	10.78	10.25	8.84	10.53	9.69	12.68	12.98	13.36	13.01	10.87	12.37	13.45	9.44
CaO	22.82	23.08	22.62	22.96	23.14	22.01	22.30	22.25	21.87	20.01	21.98	20.31	22.84	22.91	22.83	22.86	22.56	22.17	22.38	21.56
Na2O	0.00	0.00	0.00	0.00	0.00	0.11	0.45	0.83	1.10	1.37	1.19	1.40	0.76	0.62	0.62	0.67	0.81	0.81	0.82	1.47
K2O	0.00	0.01	0.00	0.00	0.00	0.00	0.00	0.01	0.01	0.23	0.00	0.14	0.00	0.01	0.00	0.00	0.00	0.05	0.00	0.01
F	0.03	0.11	0.02	0.00	0.12	0.00	0.00	0.00	0.00	0.09	0.00	0.05	0.00	0.00	0.00	0.00	0.00	0.08	0.00	0.00
Tot	98.96	99.55	99.22	98.78	99.47	98.16	99.44	100.00	100.23	98.71	99.88	99.79	100.20	99.95	99.26	100.16	99.39	98.91	99.54	98.89
Structural formula (a.p.f.u.)																				
Tet																				
Si	1.71	1.73	1.71	1.73	1.78	1.78	1.78	1.81	1.83	1.86	1.85	1.76	1.76	1.72	1.71	1.75	1.71	1.78	1.84	1.82
Al	0.29	0.27	0.29	0.27	0.22	0.22	0.22	0.19	0.17	0.14	0.15	0.24	0.24	0.28	0.29	0.25	0.29	0.22	0.16	0.18
Oct																				
Al	0.05	0.03	0.02	0.02	0.03	0.06	0.04	0.04	0.05	0.12	0.04	0.12	0.03	0.02	0.00	0.02	0.06	0.00	0.01	0.04
Fe3+	0.07	0.07	0.07	0.07	0.05	0.07	0.12	0.16	0.20	0.11	0.20	0.15	0.17	0.16	0.20	0.15	0.16	0.20	0.19	0.29
Cr	0.00	0.00	0.00	0.00	0.00	0.00	0.00	0.00	0.00	0.00	0.00	0.00	0.00	0.00	0.00	0.00	0.00	0.00	0.00	0.00
Ti	0.09	0.09	0.11	0.10	0.08	0.06	0.06	0.05	0.03	0.03	0.03	0.06	0.08	0.10	0.10	0.09	0.09	0.07	0.04	0.03
Fe2+	0.23	0.17	0.17	0.16	0.19	0.31	0.24	0.21	0.20	0.31	0.19	0.21	0.09	0.07	0.03	0.09	0.14	0.10	0.09	0.15
Mn	0.01	0.00	0.00	0.00	0.00	0.01	0.01	0.01	0.01	0.01	0.01	0.01	0.01	0.00	0.00	0.00	0.00	0.01	0.01	0.02
Mg	0.63	0.72	0.73	0.73	0.73	0.59	0.61	0.61	0.59	0.51	0.60	0.55	0.71	0.73	0.76	0.73	0.62	0.71	0.76	0.55
Ca	0.94	0.93	0.92	0.93	0.94	0.92	0.92	0.91	0.90	0.83	0.90	0.83	0.92	0.92	0.93	0.92	0.92	0.91	0.91	0.90
Na	0.00	0.00	0.00	0.00	0.00	0.01	0.03	0.06	0.08	0.10	0.09	0.10	0.06	0.05	0.05	0.05	0.06	0.06	0.06	0.11
K	0.00	0.00	0.00	0.00	0.00	0.00	0.00	0.00	0.00	0.01	0.00	0.01	0.00	0.00	0.00	0.00	0.00	0.00	0.00	0.00
#Mg	67.80	75.02	75.06	76.31	74.66	61.08	63.12	62.88	58.85	54.93	60.54	60.01	73.25	75.77	76.43	75.48	67.62	70.10	73.55	55.55
Wo %	44.40	44.23	43.45	44.48	45.07	43.97	43.45	43.31	41.99	38.67	42.72	40.42	42.99	43.00	41.95	43.45	43.85	41.83	41.99	40.95
En %	39.75	44.13	44.76	44.45	42.56	35.95	38.94	39.93	39.66	36.20	40.21	39.99	47.46	48.66	51.36	47.58	42.94	47.12	48.63	40.90
Fs %	15.85	11.64	11.79	11.06	12.37	20.08	17.61	16.76	18.35	25.13	17.08	19.58	9.55	8.33	6.69	8.97	13.21	11.05	9.38	18.15

Table IV.2: Electron microprobe analysis to clinopyroxenes

Occurrence	Eiras de Faião sill					LVC necks										Fontanelas seamount				
	rm47	rm47	rm47	rm47	rm47	rm66	rm66	rm66	rm66	rm66	rm66	rm66	rm66	rm66	rm66	AT690	AT690	AT690	AT690	AT690
sample	b4a	b4c	b4b	b4b	b4d	b1a	b1b	b1c	b1d	b3a	b3b	b3c	b3d	b3e	b3f	B1a	B1a	B1a	B1a	b1b
type	PR	PC	PR	PR	PC	Mx	Mx	MPC	MPR	Mx	Mx	Mx	Amg	Amg	Amg	PR	PR	PC	PC	PR
SiO2	46.43	47.17	46.67	46.86	46.13	51.24	46.71	46.39	45.33	47.84	45.04	48.96	47.61	44.44	47.29	43.71	39.28	41.18	41.75	38.91
TiO2	0.96	0.92	2.36	1.51	2.95	1.46	3.09	3.07	3.11	2.38	3.42	1.93	2.68	3.96	2.56	3.96	6.20	4.24	4.00	5.98
Al2O3	4.92	4.92	4.34	5.34	5.48	3.51	6.77	6.78	7.33	5.76	11.86	4.94	6.23	8.07	6.12	7.86	11.47	10.91	10.14	11.83
Cr2O3	0.02	0.01	0.01	0.01	0.00	0.52	0.38	0.09	0.02	0.18	0.02	0.60	0.20	0.05	0.00	0.00	0.01	0.02	0.00	0.01
FeO	13.59	13.44	9.18	11.07	8.57	5.80	6.87	7.71	7.95	6.80	6.94	6.17	7.35	8.11	7.79	7.60	8.13	9.66	9.43	8.34
MnO	0.70	0.74	0.24	0.42	0.32	0.07	0.10	0.09	0.14	0.08	0.06	0.08	0.11	0.13	0.14	0.11	0.08	0.22	0.17	0.03
MgO	9.31	9.17	12.67	10.83	12.46	16.29	14.37	13.70	13.86	15.11	10.59	15.93	14.53	12.53	14.23	12.73	10.79	9.71	10.17	10.73
CaO	21.93	21.63	22.69	21.95	22.43	22.43	22.51	22.90	21.54	22.54	21.43	22.53	22.39	22.65	20.98	23.25	22.78	22.53	22.33	22.74
Na2O	1.45	1.49	0.69	1.18	0.99	0.39	0.34	0.45	0.45	0.23	0.96	0.24	0.39	0.49	0.51	0.34	0.43	0.90	0.93	0.46
K2O	0.00	0.01	0.00	0.00	0.02	0.01	0.00	0.00	0.02	0.00	0.03	0.00	0.00	0.00	0.11	0.00	0.01	0.00	0.00	0.03
F	0.00	0.00	0.00	0.00	0.06	0.01	0.02	0.09	0.15	0.05	0.13	0.00	0.00	0.06	0.00	0.00	0.01	0.02	0.00	0.01
Tot	99.35	99.52	98.84	99.26	99.42	101.74	101.15	101.30	99.88	100.99	100.42	101.46	101.50	100.47	99.78	99.63	99.17	99.43	98.90	99.22
Structural formula (a.p.f.u.)																				
Tet																				
Si	1.81	1.83	1.79	1.80	1.76	1.86	1.73	1.72	1.71	1.77	1.67	1.80	1.75	1.67	1.77	1.66	1.51	1.59	1.61	1.50
Al	0.19	0.17	0.21	0.20	0.24	0.14	0.27	0.28	0.29	0.23	0.33	0.20	0.25	0.33	0.23	0.34	0.49	0.41	0.39	0.50
Oct																				
Al	0.04	0.06	-0.01	0.05	0.00	0.01	0.02	0.02	0.03	0.02	0.19	0.01	0.03	0.03	0.04	0.01	0.03	0.08	0.07	0.04
Fe3+	0.30	0.25	0.20	0.22	0.21	0.09	0.13	0.17	0.17	0.14	0.03	0.13	0.14	0.16	0.12	0.19	0.19	0.23	0.23	0.22
Cr	0.00	0.00	0.00	0.00	0.00	0.01	0.01	0.00	0.00	0.01	0.00	0.02	0.01	0.00	0.00	0.00	0.00	0.00	0.00	0.00
Ti	0.03	0.03	0.07	0.04	0.08	0.04	0.09	0.09	0.09	0.07	0.10	0.05	0.07	0.11	0.07	0.11	0.18	0.12	0.12	0.17
Fe2+	0.15	0.18	0.09	0.13	0.06	0.09	0.08	0.07	0.08	0.08	0.19	0.06	0.09	0.09	0.12	0.06	0.07	0.08	0.08	0.05
Mn	0.02	0.02	0.01	0.01	0.01	0.00	0.00	0.00	0.00	0.00	0.00	0.00	0.00	0.00	0.00	0.00	0.00	0.01	0.01	0.00
Mg	0.54	0.53	0.73	0.62	0.71	0.88	0.79	0.76	0.78	0.83	0.59	0.87	0.80	0.70	0.80	0.72	0.62	0.56	0.58	0.62
Ca	0.92	0.90	0.93	0.91	0.92	0.87	0.89	0.91	0.87	0.89	0.85	0.89	0.88	0.91	0.84	0.95	0.94	0.93	0.92	0.94
Na	0.11	0.11	0.05	0.09	0.07	0.03	0.02	0.03	0.03	0.02	0.07	0.02	0.03	0.04	0.04	0.03	0.03	0.07	0.07	0.03
K	0.00	0.00	0.00	0.00	0.00	0.00	0.00	0.00	0.00	0.00	0.00	0.00	0.00	0.00	0.01	0.00	0.00	0.00	0.00	0.00
#Mg	54.98	54.89	71.10	63.56	72.18	83.35	78.85	76.00	75.66	79.84	73.13	82.15	77.90	73.37	76.51	74.93	70.28	64.20	65.79	69.63
Wo %	41.17	41.98	42.41	42.13	42.41	41.36	40.77	41.49	39.31	40.64	34.02	39.81	40.66	41.95	40.01	42.28	42.04	42.12	42.00	41.30
En %	40.71	38.70	47.25	43.46	48.53	51.74	51.31	50.10	51.74	51.93	49.38	53.95	50.82	48.02	49.67	49.75	47.79	45.14	46.10	49.09
Fs %	18.12	19.32	10.34	14.40	9.07	6.90	7.92	8.41	8.95	7.43	16.60	6.25	8.52	10.04	10.33	7.97	10.17	12.74	11.90	9.61

Table IV.2: Electron microprobe analysis to clinopyroxenes

Occurrence	Fontanelas seamount																			
sample	AT690 b1b	AT690 b1b	AT690 b1b	AT690 b1b	AT690 b1b	AT690 b1b	AT690 b1b	AT690 b1b	AT690 b1b	AT690 b1b	AT690 b1b	AT690 b1b	AT690 b1b	AT690 b1b	AT690 b1c	AT690 b1d	AT690 b1e	AT690 b1f	AT690 b2a	AT690 b2a
type	PR	PR	PR	PR	GC	GC	GC	GC	PR	PR	PR	PR	PR	PR	Mx	Mx	Ag	Ag	GC	GC
SiO2	43.28	45.46	45.03	46.16	47.23	46.81	47.15	46.93	45.28	46.54	44.39	44.22	41.96	38.96	43.18	43.37	47.21	45.08	42.18	42.04
TiO2	2.51	1.51	2.54	1.57	1.47	1.32	1.41	1.33	2.55	1.48	2.95	3.16	4.75	6.39	4.15	4.17	2.10	2.84	2.39	2.37
Al2O3	8.97	7.15	7.86	7.06	6.54	6.50	6.45	6.42	7.81	6.47	8.15	8.02	9.90	11.76	8.23	8.11	5.79	8.39	9.56	9.42
Cr2O3	0.10	0.01	0.00	0.02	0.02	0.00	0.00	0.00	0.00	0.00	0.03	0.02	0.14	0.02	0.05	0.00	0.47	0.63	0.00	0.00
FeO	9.58	10.80	8.76	9.42	10.63	10.18	10.24	10.76	8.67	11.00	8.98	8.05	7.32	8.46	7.74	7.94	5.61	6.15	12.09	12.06
MnO	0.20	0.24	0.14	0.12	0.17	0.16	0.19	0.21	0.14	0.19	0.16	0.07	0.04	0.08	0.09	0.06	0.04	0.02	0.36	0.37
MgO	11.15	10.39	11.45	11.03	10.60	10.66	10.62	10.39	11.40	10.34	11.22	11.73	11.75	10.30	12.62	12.44	15.06	13.40	9.11	8.88
CaO	22.88	22.35	23.34	22.74	22.33	22.22	22.54	22.26	22.91	22.24	23.09	23.19	23.10	23.05	23.08	22.94	22.74	22.57	22.56	22.53
Na2O	0.90	1.11	0.82	1.17	1.13	1.28	1.25	1.23	0.75	1.15	0.64	0.66	0.39	0.39	0.36	0.33	0.38	0.46	0.89	0.84
K2O	0.01	0.00	0.00	0.00	0.00	0.00	0.00	0.00	0.00	0.00	0.00	0.00	0.01	0.00	0.00	0.00	0.00	0.00	0.00	0.01
F	0.10	0.01	0.00	0.02	0.02	0.00	0.00	0.00	0.00	0.00	0.03	0.02	0.14	0.02	0.05	0.00	0.47	0.63	0.00	0.00
Tot	99.58	99.04	99.94	99.30	100.16	99.18	99.89	99.54	99.60	99.47	99.66	99.13	99.40	99.47	99.51	99.39	99.40	99.55	99.18	98.61
Structural formula (a.p.f.u.)																				
Tet																				
Si	1.66	1.75	1.71	1.76	1.79	1.79	1.79	1.79	1.72	1.78	1.69	1.69	1.60	1.50	1.64	1.65	1.77	1.69	1.64	1.65
Al	0.34	0.25	0.29	0.24	0.21	0.21	0.21	0.21	0.28	0.22	0.31	0.31	0.40	0.50	0.36	0.35	0.23	0.31	0.36	0.35
Oct																				
Al	0.06	0.08	0.06	0.08	0.08	0.09	0.08	0.08	0.07	0.08	0.06	0.05	0.04	0.03	0.01	0.02	0.02	0.06	0.08	0.09
Fe3+	0.29	0.24	0.21	0.23	0.18	0.21	0.20	0.20	0.17	0.20	0.19	0.19	0.17	0.19	0.20	0.17	0.16	0.14	0.29	0.28
Cr	0.00	0.00	0.00	0.00	0.00	0.00	0.00	0.00	0.00	0.00	0.00	0.00	0.00	0.00	0.00	0.00	0.01	0.02	0.00	0.00
Ti	0.07	0.04	0.07	0.05	0.04	0.04	0.04	0.04	0.07	0.04	0.08	0.09	0.14	0.18	0.12	0.12	0.06	0.08	0.07	0.07
Fe2+	0.02	0.11	0.06	0.08	0.16	0.12	0.13	0.14	0.10	0.15	0.10	0.07	0.07	0.08	0.05	0.08	0.02	0.05	0.10	0.12
Mn	0.01	0.01	0.00	0.00	0.01	0.01	0.01	0.01	0.00	0.01	0.01	0.00	0.00	0.00	0.00	0.00	0.00	0.00	0.01	0.01
Mg	0.64	0.60	0.65	0.63	0.60	0.61	0.60	0.59	0.65	0.59	0.64	0.67	0.67	0.59	0.72	0.71	0.84	0.75	0.53	0.52
Ca	0.94	0.92	0.95	0.93	0.91	0.91	0.92	0.91	0.93	0.91	0.94	0.95	0.94	0.95	0.94	0.94	0.91	0.91	0.94	0.95
Na	0.07	0.08	0.06	0.09	0.08	0.10	0.09	0.09	0.06	0.09	0.05	0.05	0.03	0.03	0.03	0.02	0.03	0.03	0.07	0.06
K	0.00	0.00	0.00	0.00	0.00	0.00	0.00	0.00	0.00	0.00	0.00	0.00	0.00	0.00	0.00	0.00	0.00	0.00	0.00	0.00
#Mg	67.48	63.16	69.97	67.63	63.99	65.11	64.89	63.27	70.08	62.62	69.01	72.22	74.11	68.44	74.41	73.63	82.71	79.52	57.32	56.76
Wo %	40.41	42.11	43.19	43.20	43.47	43.31	43.77	43.33	43.57	43.04	43.13	43.35	42.77	42.61	41.71	42.20	41.02	41.28	40.57	41.11
En %	50.70	44.22	47.16	45.98	41.54	43.46	42.72	41.97	45.31	41.81	45.50	47.59	48.41	46.06	50.28	48.47	54.43	52.07	43.36	42.14
Fs %	8.89	13.67	9.65	10.82	14.99	13.23	13.51	14.70	11.12	15.15	11.37	9.06	8.82	11.33	8.01	9.34	4.55	6.65	16.07	16.75

Table IV.2: Electron microprobe analysis to clinopyroxenes

Occurrence	Fontanelas seamount																			
sample	AT690 b2a	AT690 b2a	AT690 b2a	AT690 b2a	AT690 b2b	AT690 b2c	AT690 b3a	AT690 b3a	AT690 b3a	AT690 b3a	AT690 b3a	AT690 b3a	AT690 b3a	AT690 b3a	AT690 b3a	AT690 b3a	AT690 b3a	AT690 b3a	AT690 b3a	AT690 b3b
type	GC	GC	PR	PR	MP	MP	PR	PR	PR	GC	GC	GC	GC	GC	GC	GC	GC	PR	PR	Mx
SiO2	41.48	39.89	43.54	44.43	43.82	44.01	37.96	42.28	39.37	44.33	44.59	44.62	44.95	44.25	43.97	43.04	43.19	44.03	42.71	38.81
TiO2	2.31	3.11	3.37	3.81	3.25	3.73	6.52	4.05	4.79	2.15	2.00	2.18	1.85	2.17	2.12	2.17	2.79	3.06	3.74	5.72
Al2O3	9.96	11.37	7.46	7.38	8.95	7.18	11.94	8.43	10.96	7.56	8.11	7.57	7.17	7.99	7.89	9.22	8.49	6.40	7.26	10.93
Cr2O3	0.03	0.06	0.08	0.06	0.39	0.02	0.03	0.00	0.03	0.00	0.00	0.04	0.00	0.01	0.00	0.00	0.02	0.05	0.03	0.00
FeO	13.98	12.80	7.03	7.65	6.41	7.49	8.51	7.62	8.19	10.29	9.96	10.18	9.67	9.77	9.57	10.45	10.41	6.60	7.59	8.15
MnO	0.52	0.34	0.05	0.07	0.07	0.06	0.01	0.08	0.07	0.17	0.11	0.17	0.13	0.12	0.09	0.10	0.23	0.09	0.11	0.08
MgO	7.60	7.96	13.43	12.65	13.05	13.09	10.28	12.73	11.39	10.47	9.46	10.66	11.15	10.82	10.87	9.77	10.31	13.64	12.96	10.99
CaO	21.80	22.40	23.11	22.99	22.38	23.02	22.64	22.93	22.72	22.19	19.98	22.30	22.46	22.53	22.61	22.80	22.46	22.63	23.06	22.64
Na2O	1.16	0.86	0.34	0.35	0.48	0.30	0.43	0.36	0.43	1.02	0.94	1.04	0.92	0.94	0.94	0.73	0.80	0.29	0.31	0.43
K2O	0.00	0.00	0.01	0.00	0.00	0.00	0.01	0.00	0.00	0.00	0.13	0.00	0.01	0.00	0.00	0.02	0.00	0.00	0.00	0.00
F	0.03	0.06	0.08	0.06	0.39	0.02	0.03	0.00	0.03	0.00	0.00	0.04	0.00	0.01	0.00	0.00	0.02	0.05	0.03	0.00
Tot	98.95	98.78	98.47	99.43	98.80	98.94	98.32	98.57	97.97	98.26	95.35	98.89	98.35	98.68	98.12	98.37	98.70	96.82	97.79	97.76
Structural formula (a.p.f.u.)																				
Tet																				
Si	1.64	1.57	1.67	1.69	1.66	1.68	1.48	1.63	1.53	1.72	1.77	1.72	1.74	1.71	1.71	1.68	1.68	1.71	1.66	1.52
Al	0.36	0.43	0.33	0.31	0.34	0.32	0.52	0.37	0.47	0.28	0.23	0.28	0.26	0.29	0.29	0.32	0.32	0.29	0.34	0.48
Oct																				
Al	0.10	0.10	0.01	0.02	0.06	0.00	0.03	0.01	0.04	0.07	0.15	0.07	0.07	0.07	0.07	0.10	0.06	0.00	-0.01	0.02
Fe3+	0.31	0.31	0.22	0.15	0.17	0.18	0.21	0.23	0.26	0.23	0.07	0.23	0.23	0.24	0.25	0.23	0.23	0.19	0.23	0.23
Cr	0.00	0.00	0.00	0.00	0.01	0.00	0.00	0.00	0.00	0.00	0.00	0.00	0.00	0.00	0.00	0.00	0.00	0.00	0.00	0.00
Ti	0.07	0.09	0.10	0.11	0.09	0.11	0.19	0.12	0.14	0.06	0.06	0.06	0.05	0.06	0.06	0.06	0.08	0.09	0.11	0.17
Fe2+	0.15	0.12	0.00	0.09	0.04	0.06	0.07	0.02	0.00	0.10	0.26	0.09	0.08	0.08	0.06	0.11	0.10	0.02	0.01	0.03
Mn	0.02	0.01	0.00	0.00	0.00	0.00	0.00	0.00	0.00	0.01	0.00	0.01	0.00	0.00	0.00	0.00	0.01	0.00	0.00	0.00
Mg	0.45	0.47	0.77	0.72	0.74	0.75	0.60	0.73	0.66	0.61	0.56	0.61	0.64	0.62	0.63	0.57	0.60	0.79	0.75	0.64
Ca	0.92	0.95	0.95	0.94	0.91	0.94	0.94	0.95	0.95	0.92	0.85	0.92	0.93	0.93	0.94	0.95	0.93	0.94	0.96	0.95
Na	0.09	0.07	0.03	0.03	0.04	0.02	0.03	0.03	0.03	0.08	0.07	0.08	0.07	0.07	0.07	0.05	0.06	0.02	0.02	0.03
K	0.00	0.00	0.00	0.00	0.00	0.00	0.00	0.00	0.00	0.00	0.01	0.00	0.00	0.00	0.00	0.00	0.00	0.00	0.00	0.00
#Mg	49.21	52.59	77.30	74.67	78.41	75.70	68.29	74.86	71.27	64.47	62.88	65.12	67.28	66.38	66.95	62.49	63.85	78.66	75.28	70.61
Wo %	39.83	40.01	41.01	42.89	41.06	42.01	41.68	40.84	40.00	42.08	37.21	41.96	42.10	41.98	42.04	42.54	41.69	41.65	41.11	41.12
En %	38.70	41.25	53.84	47.70	52.49	50.16	47.60	52.68	53.04	44.94	41.40	45.50	46.65	46.59	47.41	43.29	44.86	52.66	52.70	50.34
Fs %	21.47	18.74	5.15	9.41	6.45	7.82	10.72	6.47	6.96	12.98	21.39	12.55	11.25	11.43	10.55	14.17	13.44	5.69	6.19	8.53

Table IV.2: Electron microprobe analysis to clinopyroxenes

Occurrence	Fontanelas seamount																			
sample	AT690 b3c	AT690 b3d	AT690 b3e	AT690 b4a	AT690 b4a	AT690 b4a	AT690 b4a	AT690 b4b	AT690 b4b	AT690 b4b	AT690 b4b	AT690 b4c	AT690 b4d	AT690 b4e	AT690 b4f	AT690 b4f	AT690 b4f	AT690 b4g	AT690 b4g	AT690 b4h
type	Mx	PC	PC	PC	PC	PR	PR	GC	GC	PR	PR	Mx	Mx	Xen	Xen	Xen	Xen	Xen	Xen	Xen
SiO2	41.93	42.86	43.43	43.50	43.40	37.43	37.00	44.47	41.76	38.80	39.22	44.16	46.65	41.92	42.61	45.42	44.86	43.71	44.91	45.38
TiO2	4.53	3.13	3.14	2.89	2.87	6.06	3.75	0.90	1.23	6.10	5.65	3.35	1.66	3.29	3.43	2.74	2.65	1.97	1.46	0.94
Al2O3	8.24	8.38	8.13	7.78	7.91	12.56	17.35	6.66	8.30	11.75	10.99	6.68	5.53	9.65	9.01	6.45	6.65	8.03	7.43	6.46
Cr2O3	0.00	0.05	0.00	0.00	0.01	0.00	0.02	0.00	0.00	0.03	0.03	0.00	0.05	0.00	0.00	0.00	0.00	0.00	0.00	0.00
FeO	8.28	8.07	7.94	8.87	9.12	8.41	7.18	17.32	17.89	8.37	8.11	7.34	10.10	9.60	9.51	8.87	9.03	12.97	13.79	13.98
MnO	0.05	0.12	0.05	0.17	0.10	0.06	0.05	0.97	1.03	0.07	0.09	0.10	0.28	0.15	0.17	0.16	0.20	0.28	0.30	0.32
MgO	12.61	12.23	12.19	11.58	11.20	10.65	7.94	6.08	5.28	10.49	10.83	13.70	11.82	10.32	10.50	12.09	11.52	8.97	8.63	8.72
CaO	22.67	22.83	22.84	23.12	23.07	22.91	14.82	20.76	20.84	22.69	23.02	22.99	22.10	22.80	22.65	22.82	22.81	21.86	21.80	21.47
Na2O	0.36	0.62	0.62	0.68	0.70	0.42	0.33	1.67	1.52	0.42	0.44	0.27	1.09	0.72	0.74	0.57	0.76	1.04	1.17	1.31
K2O	0.00	0.00	0.00	0.00	0.00	0.00	0.48	0.01	0.00	0.00	0.00	0.01	0.00	0.00	0.00	0.00	0.00	0.00	0.00	0.00
F	0.00	0.05	0.00	0.00	0.01	0.00	0.02	0.00	0.00	0.03	0.03	0.00	0.05	0.00	0.00	0.00	0.00	0.00	0.00	0.00
Tot	98.83	98.37	98.42	98.68	98.40	98.53	89.12	98.87	97.91	98.78	98.38	98.62	99.35	98.50	98.63	99.14	98.54	98.90	99.62	98.66
Structural formula (a.p.f.u.)																				
Tet																				
Si	1.62	1.65	1.67	1.68	1.68	1.46	1.53	1.78	1.70	1.50	1.52	1.69	1.79	1.63	1.65	1.74	1.73	1.71	1.75	1.78
Al	0.38	0.35	0.33	0.32	0.32	0.54	0.47	0.22	0.30	0.50	0.48	0.31	0.21	0.37	0.35	0.26	0.27	0.29	0.25	0.22
Oct																				
Al	-0.01	0.04	0.04	0.03	0.04	0.03	0.38	0.09	0.10	0.04	0.03	-0.01	0.04	0.07	0.06	0.03	0.03	0.08	0.09	0.08
Fe3+	0.23	0.25	0.22	0.25	0.24	0.27	-0.15	0.31	0.36	0.20	0.22	0.21	0.24	0.24	0.22	0.18	0.21	0.26	0.25	0.27
Cr	0.00	0.00	0.00	0.00	0.00	0.00	0.00	0.00	0.00	0.00	0.00	0.00	0.00	0.00	0.00	0.00	0.00	0.00	0.00	0.00
Ti	0.13	0.09	0.09	0.08	0.08	0.18	0.12	0.03	0.04	0.18	0.17	0.10	0.05	0.10	0.10	0.08	0.08	0.06	0.04	0.03
Fe2+	0.04	0.01	0.03	0.04	0.06	0.00	0.40	0.27	0.24	0.07	0.04	0.02	0.09	0.07	0.09	0.10	0.09	0.17	0.20	0.19
Mn	0.00	0.00	0.00	0.01	0.00	0.00	0.00	0.03	0.04	0.00	0.00	0.00	0.01	0.00	0.01	0.01	0.01	0.01	0.01	0.01
Mg	0.72	0.70	0.70	0.67	0.65	0.62	0.49	0.36	0.32	0.61	0.63	0.78	0.67	0.60	0.61	0.69	0.66	0.52	0.50	0.51
Ca	0.94	0.94	0.94	0.96	0.96	0.96	0.66	0.89	0.91	0.94	0.96	0.94	0.91	0.95	0.94	0.93	0.94	0.92	0.91	0.90
Na	0.03	0.05	0.05	0.05	0.05	0.03	0.03	0.13	0.12	0.03	0.03	0.02	0.08	0.05	0.06	0.04	0.06	0.08	0.09	0.10
K	0.00	0.00	0.00	0.00	0.00	0.00	0.03	0.00	0.00	0.00	0.00	0.00	0.00	0.00	0.00	0.00	0.00	0.00	0.00	0.00
#Mg	73.08	72.98	73.24	69.93	68.66	69.31	66.34	38.49	34.47	69.09	70.43	76.90	67.60	65.70	66.32	70.86	69.46	55.21	52.75	52.65
Wo %	40.30	40.79	41.79	41.94	42.36	40.10	7.62	40.29	38.87	41.79	41.86	40.95	41.27	41.90	42.39	42.78	43.02	40.97	41.34	41.04
En %	51.86	52.65	50.74	49.32	47.80	52.42	52.51	29.65	28.84	47.58	49.42	52.93	47.35	46.61	45.51	46.33	46.37	39.99	37.68	38.24
Fs %	7.85	6.55	7.46	8.74	9.84	7.48	39.86	30.06	32.28	10.62	8.72	6.12	11.38	11.49	12.09	10.89	10.61	19.04	20.98	20.72

Table IV.2: Electron microprobe analysis to clinopyroxenes

Occurrence	Fontanelas seamount							Loulé lamprophyre											
sample	AT690 b4i	AT690 b4j	AT690 b4j	AT690 b4j	AT690 b4j	AT690 b4j	AT690 b4j	C20 b1a	C20 b1a	C20 b1a	C20 b1a	C20 b1a	C20 b1a	C20 b1a	C20 b1a	C20 b1a	C20 b1a	C20 b1a	C20 b1a
type	Xen	Xen	Xen	Xen	Xen	Xen	Xen	PR	PR	PC	PC	PC	PC	PC	PC	PC	PC	PC	PC
SiO2	44.25	43.62	42.89	42.40	44.40	42.69	45.57	40.81	41.69	41.28	44.62	40.38	50.28	45.54	51.95	51.67	51.29	49.27	49.95	48.78
TiO2	3.52	2.22	2.47	2.86	1.51	2.28	2.88	5.47	4.63	2.44	2.54	0.75	0.97	2.46	0.41	0.46	0.64	0.70	0.65	0.45
Al2O3	7.00	7.88	9.06	9.08	7.50	8.66	6.92	10.38	10.49	9.04	6.71	6.48	3.59	7.23	1.80	1.88	2.78	3.95	3.78	4.75
Cr2O3	0.04	0.09	0.07	0.00	0.07	0.02	0.07	0.00	0.12	0.00	0.00	0.02	0.00	0.03	0.00	0.02	0.00	0.01	0.00	0.01
FeO	7.27	12.27	12.24	11.66	13.70	12.63	8.39	6.99	7.49	12.78	11.15	15.44	10.23	11.00	9.82	10.08	10.78	12.36	11.82	12.66
MnO	0.08	0.29	0.22	0.24	0.29	0.25	0.10	0.06	0.09	0.20	0.19	0.32	0.26	0.21	0.70	0.71	0.66	0.56	0.58	0.62
MgO	13.32	9.05	8.87	9.46	8.76	8.99	12.75	11.30	11.28	10.61	9.94	9.93	11.07	9.72	13.00	13.05	12.13	9.98	10.35	9.25
CaO	23.12	22.04	21.97	22.17	21.56	21.95	22.90	23.25	22.80	19.76	22.07	16.92	21.09	21.90	19.70	19.64	18.61	19.71	20.14	21.15
Na2O	0.33	1.03	0.97	0.90	1.14	1.10	0.36	0.50	0.57	0.64	1.27	1.40	1.84	1.27	1.66	1.69	2.29	2.15	1.97	1.69
K2O	0.00	0.00	0.00	0.00	0.00	0.04	0.01	0.01	0.00	0.00	0.01	0.20	0.01	0.02	0.04	0.03	0.01	0.00	0.00	0.01
F	0.04	0.09	0.07	0.00	0.07	0.02	0.07	0.04	0.05	0.05	0.00	0.23	0.00	0.00	0.00	0.01	0.02	0.00	0.00	0.00
Tot	98.94	98.50	98.84	98.81	98.98	98.73	99.96	98.88	99.22	96.89	98.50	92.11	99.40	99.36	99.14	99.31	99.24	98.71	99.31	99.39
Structural formula (a.p.f.u.)																				
Tet																				
Si	1.69	1.71	1.67	1.65	1.74	1.67	1.72	1.57	1.59	1.64	1.74	1.72	1.91	1.75	1.96	1.96	1.94	1.90	1.91	1.88
Al	0.31	0.29	0.33	0.35	0.26	0.33	0.28	0.43	0.41	0.36	0.26	0.28	0.09	0.25	0.04	0.04	0.06	0.10	0.09	0.12
Oct																				
Al	0.00	0.07	0.09	0.07	0.08	0.08	0.03	0.04	0.06	0.07	0.05	0.04	0.07	0.08	0.05	0.04	0.07	0.08	0.08	0.09
Fe3+	0.19	0.24	0.24	0.26	0.26	0.29	0.16	0.18	0.17	0.28	0.24	0.46	0.15	0.19	0.13	0.16	0.18	0.20	0.17	0.19
Cr	0.00	0.00	0.00	0.00	0.00	0.00	0.00	0.00	0.00	0.00	0.00	0.00	0.00	0.00	0.00	0.00	0.00	0.00	0.00	0.00
Ti	0.10	0.07	0.07	0.08	0.04	0.07	0.08	0.16	0.13	0.07	0.07	0.02	0.03	0.07	0.01	0.01	0.02	0.02	0.02	0.01
Fe2+	0.04	0.16	0.16	0.12	0.19	0.12	0.10	0.05	0.06	0.15	0.12	0.09	0.17	0.17	0.18	0.16	0.17	0.20	0.21	0.22
Mn	0.00	0.01	0.01	0.01	0.01	0.01	0.00	0.00	0.00	0.01	0.01	0.01	0.01	0.01	0.02	0.02	0.02	0.02	0.02	0.02
Mg	0.76	0.53	0.52	0.55	0.51	0.53	0.72	0.65	0.64	0.63	0.58	0.63	0.63	0.56	0.73	0.74	0.69	0.57	0.59	0.53
Ca	0.94	0.92	0.92	0.93	0.90	0.92	0.93	0.96	0.93	0.84	0.92	0.77	0.86	0.90	0.80	0.80	0.76	0.81	0.83	0.87
Na	0.02	0.08	0.07	0.07	0.09	0.08	0.03	0.04	0.04	0.05	0.10	0.12	0.14	0.09	0.12	0.12	0.17	0.16	0.15	0.13
K	0.00	0.00	0.00	0.00	0.00	0.00	0.00	0.00	0.00	0.00	0.00	0.01	0.00	0.00	0.00	0.00	0.00	0.00	0.00	0.00
#Mg	76.57	56.79	56.36	59.13	53.26	55.94	73.03	74.24	72.86	59.67	61.38	53.42	65.87	61.16	70.23	69.77	66.73	58.99	60.95	56.56
Wo %	41.85	41.76	41.44	40.96	40.61	40.37	42.15	43.68	42.67	35.05	42.56	29.08	47.95	43.52	44.32	44.93	43.75	47.59	47.11	43.50
En %	51.33	40.20	40.04	43.00	38.73	42.24	47.48	48.46	48.21	47.31	42.79	51.10	38.36	40.02	42.72	42.59	42.46	35.99	36.66	37.02
Fs %	6.81	18.04	18.52	16.03	20.66	17.38	10.37	7.86	9.11	17.64	14.65	19.82	13.68	16.46	12.96	12.48	13.79	16.43	16.22	19.48

Table IV.2: Electron microprobe analysis to clinopyroxenes

Occurrence	Loulé lamprophyre																			
sample	C20 b1a	C20 b1a	C20 b1a	C20 b1a	C20 b1a	C20 b1a	C20 b1a	C20 b1b	C20 b1b	C20 b1b	C20 b1b	C20 b2a	C20 b2a	C20 b2a	C20 b2a	C20 b2a	C20 b2a	C20 b3a	C20 b3a	C20 b3a
type	PR	PR	PR	PR	PR	PR	PR	PC	PC	PR	PR	PC	PC	PC	PR	PR	PR	PR	PR	PR
SiO2	47.10	44.10	41.45	42.74	41.87	42.61	40.72	40.58	45.15	44.79	40.99	42.00	42.12	47.11	46.19	46.29	42.23	42.61	42.41	41.84
TiO2	1.78	3.51	5.25	4.45	4.84	4.77	5.74	4.17	3.43	3.38	5.52	4.50	3.95	2.09	3.11	2.98	4.83	3.83	4.23	4.47
Al2O3	6.69	8.69	10.06	9.31	9.59	9.36	11.06	11.12	6.97	8.07	10.38	9.08	9.38	4.92	6.41	6.17	9.39	8.33	8.79	8.92
Cr2O3	0.43	0.26	0.02	0.02	0.03	0.00	0.00	0.00	0.00	0.10	0.00	0.01	0.01	0.06	0.00	0.00	0.00	0.01	0.04	0.01
FeO	7.78	6.58	7.34	6.86	6.77	6.59	7.49	9.56	6.11	6.61	6.87	6.70	7.25	6.63	5.85	5.86	6.74	7.36	6.70	6.73
MnO	0.20	0.06	0.05	0.06	0.08	0.11	0.10	0.15	0.04	0.13	0.06	0.05	0.04	0.06	0.11	0.12	0.07	0.12	0.12	0.07
MgO	12.09	12.47	11.41	11.96	12.00	12.00	10.82	9.27	13.44	12.80	11.53	12.15	11.91	14.05	13.65	13.56	11.85	11.73	12.17	12.14
CaO	22.82	23.09	23.30	23.32	23.34	23.08	23.11	22.68	23.60	23.30	23.13	23.29	23.39	23.55	23.56	23.55	23.17	23.06	23.18	23.39
Na2O	0.75	0.47	0.43	0.44	0.46	0.55	0.49	0.83	0.36	0.49	0.53	0.49	0.44	0.41	0.48	0.52	0.56	0.70	0.52	0.45
K2O	0.00	0.00	0.00	0.00	0.00	0.00	0.04	0.01	0.00	0.00	0.00	0.00	0.00	0.00	0.01	0.01	0.00	0.04	0.01	0.00
F	0.00	0.02	0.08	0.00	0.00	0.00	0.08	0.00	0.08	0.13	0.00	0.02	0.04	0.00	0.00	0.00	0.00	0.05	0.00	0.05
Tot	99.66	99.26	99.39	99.17	99.00	99.09	99.68	98.37	99.18	99.81	99.06	98.29	98.56	98.97	99.44	99.14	98.86	97.85	98.16	98.11
Structural formula (a.p.f.u.)																				
Tet																				
Si	1.78	1.67	1.58	1.63	1.60	1.62	1.55	1.58	1.71	1.69	1.57	1.62	1.62	1.79	1.74	1.75	1.61	1.65	1.63	1.61
Al	0.22	0.33	0.42	0.37	0.40	0.38	0.45	0.42	0.29	0.31	0.43	0.38	0.38	0.21	0.26	0.25	0.39	0.35	0.37	0.39
Oct																				
Al	0.07	0.06	0.03	0.04	0.03	0.04	0.05	0.09	0.02	0.05	0.04	0.03	0.04	0.01	0.02	0.02	0.04	0.03	0.03	0.02
Fe3+	0.14	0.15	0.17	0.16	0.18	0.16	0.16	0.22	0.15	0.16	0.18	0.20	0.21	0.17	0.15	0.15	0.17	0.22	0.19	0.20
Cr	0.01	0.01	0.00	0.00	0.00	0.00	0.00	0.00	0.00	0.00	0.00	0.00	0.00	0.00	0.00	0.00	0.00	0.00	0.00	0.00
Ti	0.05	0.10	0.15	0.13	0.14	0.14	0.16	0.12	0.10	0.10	0.16	0.13	0.11	0.06	0.09	0.08	0.14	0.11	0.12	0.13
Fe2+	0.11	0.06	0.07	0.06	0.03	0.05	0.08	0.09	0.04	0.05	0.04	0.02	0.02	0.04	0.04	0.04	0.05	0.02	0.02	0.01
Mn	0.01	0.00	0.00	0.00	0.00	0.00	0.00	0.00	0.00	0.00	0.00	0.00	0.00	0.00	0.00	0.00	0.00	0.00	0.00	0.00
Mg	0.68	0.70	0.65	0.68	0.68	0.68	0.62	0.54	0.76	0.72	0.66	0.70	0.68	0.79	0.77	0.76	0.67	0.68	0.70	0.70
Ca	0.92	0.94	0.95	0.95	0.96	0.94	0.94	0.95	0.96	0.94	0.95	0.96	0.96	0.96	0.95	0.95	0.95	0.96	0.96	0.97
Na	0.06	0.03	0.03	0.03	0.03	0.04	0.04	0.06	0.03	0.04	0.04	0.04	0.03	0.03	0.04	0.04	0.04	0.05	0.04	0.03
K	0.00	0.00	0.00	0.00	0.00	0.00	0.00	0.00	0.00	0.00	0.00	0.00	0.00	0.00	0.00	0.00	0.00	0.00	0.00	0.00
#Mg	73.47	77.17	73.48	75.67	75.96	76.44	72.04	63.38	79.70	77.55	74.95	76.39	74.55	79.08	80.62	80.50	75.80	73.98	76.42	76.29
Wo %	43.66	43.17	43.58	43.77	43.18	43.81	43.77	42.97	43.95	43.35	43.39	43.09	42.72	43.33	44.34	44.59	43.76	43.14	43.11	43.10
En %	45.92	49.23	47.47	48.33	50.11	48.70	46.19	43.86	50.13	49.67	49.10	50.95	50.52	50.76	50.04	49.78	48.92	50.07	50.74	51.15
Fs %	10.42	7.60	8.95	7.91	6.71	7.49	10.05	13.18	5.92	6.99	7.51	5.96	6.76	5.91	5.62	5.63	7.32	6.80	6.15	5.75

Table IV.2: Electron microprobe analysis to clinopyroxenes

Occurrence	Loulé lamprophyre																		Mafra
sample	C20 b3a	C20 b3a	C20 b3a	C20 b3a	C20 b3a	C20 b3a	C20 b3a	C20 b3a	C20 b3a	C20 b3a	C20 b3a	C20 b3a	C20 b3a	C20 b3a	C20 b3a	C20 b3a	C20 b3a	C20 b3b	C20 b3b	rm83 b1a
type	PR	PR	PR	GC	GC	GC	GC	GC	GC	GC	GC	PR	PR	PR	PR	PR	PR	PC	PR	C
SiO2	41.50	42.36	40.54	47.67	47.95	48.22	47.01	48.00	48.30	47.40	47.46	42.13	40.02	39.73	40.94	41.47	42.51	45.18	45.67	50.23
TiO2	4.29	3.75	4.97	1.25	0.80	0.68	1.70	1.14	0.65	1.72	0.94	4.07	5.26	5.23	4.82	4.88	3.82	3.18	2.55	1.24
Al2O3	9.19	8.76	10.40	3.50	2.73	2.34	3.96	3.81	2.59	6.64	4.93	9.27	10.70	10.32	9.57	9.26	8.68	6.38	5.07	3.91
Cr2O3	0.00	0.22	0.00	0.00	0.03	0.00	0.00	0.01	0.01	0.19	0.14	0.23	0.00	0.00	0.01	0.02	0.01	0.00	0.00	0.96
FeO	7.31	6.98	7.68	15.01	18.07	18.41	11.06	15.59	18.14	10.09	15.28	6.84	8.05	7.55	6.92	6.59	7.55	5.70	7.89	5.00
MnO	0.05	0.10	0.07	0.54	0.65	0.55	0.29	0.36	0.60	0.20	0.46	0.06	0.10	0.07	0.07	0.11	0.17	0.14	0.21	0.08
MgO	11.86	12.35	11.15	8.21	6.84	6.87	11.54	8.67	6.68	11.90	8.68	12.27	10.72	11.33	11.87	11.80	11.44	13.65	12.55	16.29
CaO	23.32	23.26	22.59	19.15	18.41	18.45	22.55	19.55	18.47	21.65	19.43	22.87	22.70	22.94	23.05	23.27	23.14	23.43	23.06	23.30
Na2O	0.43	0.50	0.60	2.47	2.78	2.62	0.76	2.00	2.85	1.13	2.32	0.52	0.61	0.46	0.43	0.49	0.64	0.47	0.73	0.35
K2O	0.00	0.00	0.01	0.01	0.03	0.02	0.00	0.02	0.01	0.00	0.00	0.00	0.01	0.00	0.00	0.00	0.00	0.00	0.00	0.00
F	0.02	0.14	0.00	0.00	0.00	0.04	0.00	0.01	0.05	0.00	0.00	0.03	0.00	0.00	0.00	0.00	0.00	0.04	0.21	0.00
Tot	97.98	98.52	98.02	97.89	98.30	98.20	98.86	99.21	98.42	100.95	99.71	98.31	98.26	97.62	97.67	97.92	98.03	98.18	97.96	101.37
Structural formula (a.p.f.u.)																				
Tet																				
Si	1.61	1.63	1.57	1.89	1.91	1.93	1.82	1.87	1.93	1.78	1.84	1.62	1.55	1.55	1.59	1.60	1.65	1.72	1.77	1.84
Al	0.39	0.37	0.43	0.11	0.09	0.07	0.18	0.13	0.07	0.22	0.16	0.38	0.45	0.45	0.41	0.40	0.35	0.28	0.23	0.16
Oct																				
Al	0.03	0.03	0.05	0.05	0.04	0.04	0.00	0.05	0.05	0.07	0.07	0.04	0.04	0.02	0.03	0.02	0.04	0.01	0.00	0.00
Fe3+	0.22	0.23	0.21	0.26	0.31	0.29	0.21	0.24	0.30	0.19	0.29	0.20	0.21	0.23	0.20	0.19	0.21	0.17	0.21	0.13
Cr	0.00	0.01	0.00	0.00	0.00	0.00	0.00	0.00	0.00	0.01	0.00	0.01	0.00	0.00	0.00	0.00	0.00	0.00	0.00	0.03
Ti	0.12	0.11	0.14	0.04	0.02	0.02	0.05	0.03	0.02	0.05	0.03	0.12	0.15	0.15	0.14	0.14	0.11	0.09	0.07	0.03
Fe2+	0.02	0.00	0.04	0.24	0.30	0.33	0.15	0.27	0.31	0.12	0.20	0.02	0.05	0.02	0.02	0.03	0.04	0.01	0.05	0.02
Mn	0.00	0.00	0.00	0.02	0.02	0.02	0.01	0.01	0.02	0.01	0.02	0.00	0.00	0.00	0.00	0.00	0.01	0.00	0.01	0.00
Mg	0.68	0.71	0.64	0.48	0.41	0.41	0.67	0.51	0.40	0.67	0.50	0.70	0.62	0.66	0.69	0.68	0.66	0.78	0.72	0.89
Ca	0.97	0.96	0.94	0.81	0.79	0.79	0.93	0.82	0.79	0.87	0.81	0.94	0.94	0.96	0.96	0.96	0.96	0.96	0.96	0.91
Na	0.03	0.04	0.05	0.19	0.22	0.20	0.06	0.15	0.22	0.08	0.18	0.04	0.05	0.03	0.03	0.04	0.05	0.03	0.05	0.02
K	0.00	0.00	0.00	0.00	0.00	0.00	0.00	0.00	0.00	0.00	0.00	0.00	0.00	0.00	0.00	0.00	0.00	0.00	0.00	0.00
#Mg	74.31	75.94	72.13	49.38	40.30	39.94	65.03	49.80	39.64	67.77	50.31	76.17	70.38	72.78	75.37	76.15	72.99	81.01	73.91	85.30
Wo %	42.54	41.80	42.21	49.51	49.75	49.23	42.45	40.48	49.68	40.78	38.94	41.77	42.35	41.91	42.58	43.69	43.39	43.81	43.54	40.96
En %	50.93	52.91	49.34	30.45	25.50	25.01	43.46	35.16	25.05	46.32	38.46	52.13	48.44	50.99	51.02	49.90	48.84	51.84	48.69	55.12
Fs %	6.53	5.29	8.44	20.03	24.75	25.76	14.08	24.35	25.27	12.89	22.60	6.10	9.21	7.10	6.40	6.41	7.76	4.35	7.77	3.92

Table IV.2: Electron microprobe analysis to clinopyroxenes

Occurrence	Mafra gabbro																			
sample	rm83 b1a	rm83 b1a	rm83 b1a	rm83 b1a	rm83 b1b	rm83 b1b	rm83 b1b	rm83 b1c	rm83 b1c	rm83 b1c	rm83 b1c	rm83 b2a	rm83 b2a	rm83 b2a	rm83 b2a	rm83 b2a	rm83 b2c	rm83 b2c	rm83 b2c	rm83 b2c
type	C	R	R	R	C	C	R	R	C	C	R	C	C	R	R	R	C	C	C	C
SiO2	50.86	46.57	48.83	48.82	49.72	49.96	47.84	49.40	49.78	50.03	49.14	49.64	48.16	45.93	48.90	47.71	48.23	45.95	48.81	47.61
TiO2	1.22	2.36	2.16	1.60	1.44	1.23	2.36	1.79	1.41	1.42	1.84	2.08	2.56	3.16	2.07	2.87	2.54	3.33	2.29	2.84
Al2O3	3.38	7.10	5.00	4.15	3.88	3.49	5.62	4.64	3.79	3.80	5.06	5.39	6.50	8.31	5.19	6.40	6.15	7.84	5.98	6.87
Cr2O3	0.02	0.00	0.04	0.00	0.00	0.00	0.07	0.08	0.05	0.04	0.07	0.13	0.00	0.01	0.09	0.00	0.00	0.00	0.16	0.12
FeO	8.05	7.35	7.34	9.41	7.96	8.40	7.15	7.37	9.44	7.71	6.09	5.83	6.66	8.04	6.35	7.57	7.83	7.88	6.71	7.30
MnO	0.19	0.08	0.16	0.24	0.19	0.24	0.09	0.15	0.18	0.20	0.10	0.10	0.10	0.11	0.07	0.04	0.10	0.13	0.08	0.15
MgO	14.24	13.88	14.26	12.56	14.33	14.08	14.55	14.91	12.46	14.26	15.14	15.14	14.35	12.83	14.98	13.72	13.93	12.96	14.08	13.58
CaO	23.00	23.17	23.04	23.11	22.96	23.16	22.68	22.62	23.48	23.15	23.31	23.20	23.10	22.65	23.19	22.94	22.80	22.59	23.05	22.84
Na2O	0.64	0.33	0.52	0.86	0.60	0.64	0.58	0.58	0.84	0.58	0.43	0.30	0.39	0.39	0.31	0.39	0.45	0.46	0.45	0.46
K2O	0.00	0.00	0.00	0.00	0.01	0.00	0.01	0.00	0.00	0.01	0.00	0.00	0.00	0.00	0.00	0.00	0.00	0.00	0.01	0.00
F	0.00	0.00	0.00	0.00	0.07	0.00	0.00	0.07	0.00	0.03	0.07	0.00	0.02	0.00	0.00	0.01	0.00	0.01	0.00	0.18
Tot	101.58	100.84	101.38	100.77	101.13	101.20	100.98	101.61	101.46	101.24	101.27	101.81	101.84	101.46	101.15	101.69	102.04	101.17	101.62	101.92
Structural formula (a.p.f.u.)																				
Tet																				
Si	1.87	1.73	1.80	1.83	1.84	1.86	1.77	1.82	1.85	1.85	1.81	1.81	1.76	1.70	1.80	1.76	1.77	1.71	1.79	1.75
Al	0.13	0.27	0.20	0.17	0.16	0.14	0.23	0.18	0.15	0.15	0.19	0.19	0.24	0.30	0.20	0.24	0.23	0.29	0.21	0.25
Oct																				
Al	0.02	0.04	0.02	0.02	0.01	0.01	0.02	0.02	0.02	0.02	0.03	0.04	0.04	0.07	0.02	0.04	0.04	0.05	0.05	0.05
Fe3+	0.13	0.17	0.14	0.18	0.16	0.17	0.17	0.15	0.15	0.14	0.14	0.08	0.12	0.13	0.12	0.11	0.12	0.13	0.09	0.11
Cr	0.00	0.00	0.00	0.00	0.00	0.00	0.00	0.00	0.00	0.00	0.00	0.00	0.00	0.00	0.00	0.00	0.00	0.00	0.00	0.00
Ti	0.03	0.07	0.06	0.05	0.04	0.03	0.07	0.05	0.04	0.04	0.05	0.06	0.07	0.09	0.06	0.08	0.07	0.09	0.06	0.08
Fe2+	0.12	0.06	0.09	0.12	0.09	0.09	0.05	0.07	0.14	0.10	0.05	0.09	0.09	0.12	0.07	0.12	0.12	0.11	0.11	0.11
Mn	0.01	0.00	0.00	0.01	0.01	0.01	0.00	0.00	0.01	0.01	0.00	0.00	0.00	0.00	0.00	0.00	0.00	0.00	0.00	0.00
Mg	0.78	0.77	0.78	0.70	0.79	0.78	0.80	0.82	0.69	0.79	0.83	0.82	0.78	0.71	0.82	0.75	0.76	0.72	0.77	0.74
Ca	0.91	0.92	0.91	0.93	0.91	0.92	0.90	0.89	0.94	0.92	0.92	0.91	0.91	0.90	0.91	0.91	0.90	0.90	0.91	0.90
Na	0.05	0.02	0.04	0.06	0.04	0.05	0.04	0.04	0.06	0.04	0.03	0.02	0.03	0.03	0.02	0.03	0.03	0.03	0.03	0.03
K	0.00	0.00	0.00	0.00	0.00	0.00	0.00	0.00	0.00	0.00	0.00	0.00	0.00	0.00	0.00	0.00	0.00	0.00	0.00	0.00
#Mg	75.92	77.10	77.61	70.42	76.24	74.94	78.40	78.29	70.17	76.74	81.60	82.24	79.35	73.98	80.80	76.37	76.03	74.58	78.91	76.82
Wo %	43.38	41.57	42.72	43.54	42.44	42.63	41.24	41.31	44.61	43.18	42.62	43.29	42.78	42.14	42.63	42.93	42.26	42.22	43.49	42.79
En %	46.86	50.96	48.96	45.27	48.90	48.31	51.92	51.04	43.47	48.02	51.60	49.45	49.31	46.94	50.37	47.17	47.88	47.45	47.67	47.56
Fs %	9.76	7.47	8.32	11.20	8.65	9.05	6.84	7.65	11.92	8.80	5.77	7.26	7.92	10.92	6.99	9.90	9.86	10.33	8.84	9.65

Table IV.2: Electron microprobe analysis to clinopyroxenes

Occurrence	Mafra gabbro																			
sample	rm83 b2c	rm83 b2c	rm83 b2c	rm83 b2c	rm83 b2c	rm83 b2c	rm83 b2c	rm83 b2c	rm83 b2c	rm83 b2c	rm83 b2c	rm83 b2c	rm83 b3a	rm83 b3a	rm83 b3a	rm83 b3a	rm83 b3a	rm83 b3a	rm83 b3a	rm83 b3a
type	C	C	C	R	R	R	R	R	R	R	R	R	C	C	Man	Man	Man	Man	Man	R
SiO2	45.01	46.95	48.79	49.85	50.90	51.26	49.78	49.13	49.14	48.85	50.62	50.72	47.80	48.30	49.61	50.71	51.01	51.21	50.46	47.71
TiO2	3.85	2.94	2.21	1.87	1.59	1.39	1.91	2.12	2.24	2.53	1.64	1.19	3.03	2.80	1.94	1.62	1.55	1.56	1.70	2.75
Al2O3	9.67	6.92	5.91	4.83	3.47	3.67	4.44	5.37	5.32	5.03	3.63	3.17	6.33	5.82	5.18	4.23	4.02	3.53	3.91	5.78
Cr2O3	0.06	0.06	0.19	0.15	0.19	0.23	0.01	0.09	0.03	0.05	0.00	0.00	0.10	0.04	0.40	0.17	0.28	0.28	0.10	0.00
FeO	8.99	7.43	6.28	6.17	5.71	5.42	6.25	6.48	7.16	7.49	7.70	8.73	7.07	6.95	5.91	5.81	5.38	5.46	5.88	7.37
MnO	0.09	0.14	0.04	0.08	0.08	0.05	0.06	0.08	0.10	0.16	0.18	0.24	0.06	0.09	0.08	0.08	0.04	0.05	0.12	0.13
MgO	13.01	13.64	14.78	15.27	16.13	16.20	15.53	14.87	14.85	14.11	14.29	13.41	13.94	14.32	15.07	15.87	15.85	15.97	15.70	13.80
CaO	18.79	22.75	23.18	23.26	23.21	23.36	23.02	23.06	22.68	22.77	22.93	23.02	22.65	22.53	23.13	23.03	23.19	23.16	23.30	22.98
Na2O	1.52	0.47	0.32	0.38	0.26	0.28	0.27	0.32	0.31	0.55	0.54	0.69	0.48	0.48	0.29	0.30	0.25	0.26	0.30	0.47
K2O	0.36	0.01	0.01	0.01	0.00	0.00	0.01	0.01	0.00	0.00	0.01	0.04	0.00	0.00	0.00	0.01	0.00	0.00	0.00	0.01
F	0.04	0.00	0.00	0.04	0.02	0.07	0.00	0.00	0.00	0.12	0.00	0.01	0.00	0.00	0.00	0.11	0.00	0.00	0.00	0.00
Tot	101.42	101.34	101.72	101.94	101.61	101.98	101.29	101.53	101.91	101.61	101.63	101.31	101.50	101.33	101.62	101.88	101.61	101.51	101.51	101.07
Structural formula (a.p.f.u.)																				
Tet																				
Si	1.67	1.74	1.78	1.82	1.86	1.86	1.83	1.80	1.80	1.80	1.86	1.88	1.76	1.78	1.81	1.84	1.85	1.86	1.84	1.77
Al	0.33	0.26	0.22	0.18	0.14	0.14	0.17	0.20	0.20	0.20	0.14	0.12	0.24	0.22	0.19	0.16	0.15	0.14	0.16	0.23
Oct																				
Al	0.09	0.04	0.04	0.03	0.00	0.02	0.02	0.03	0.03	0.02	0.02	0.02	0.03	0.03	0.03	0.02	0.03	0.02	0.01	0.02
Fe3+	0.22	0.14	0.11	0.11	0.10	0.09	0.11	0.11	0.11	0.12	0.10	0.12	0.10	0.10	0.08	0.09	0.06	0.07	0.10	0.13
Cr	0.00	0.00	0.01	0.00	0.01	0.01	0.00	0.00	0.00	0.00	0.00	0.00	0.00	0.00	0.01	0.00	0.01	0.01	0.00	0.00
Ti	0.11	0.08	0.06	0.05	0.04	0.04	0.05	0.06	0.06	0.07	0.05	0.03	0.08	0.08	0.05	0.04	0.04	0.04	0.05	0.08
Fe2+	0.06	0.09	0.08	0.08	0.08	0.07	0.08	0.09	0.11	0.11	0.14	0.15	0.12	0.11	0.10	0.09	0.10	0.10	0.08	0.10
Mn	0.00	0.00	0.00	0.00	0.00	0.00	0.00	0.00	0.00	0.00	0.01	0.01	0.00	0.00	0.00	0.00	0.00	0.00	0.00	0.00
Mg	0.72	0.75	0.81	0.83	0.88	0.88	0.85	0.81	0.81	0.78	0.78	0.74	0.77	0.79	0.82	0.86	0.86	0.87	0.86	0.76
Ca	0.75	0.90	0.91	0.91	0.91	0.91	0.90	0.91	0.89	0.90	0.90	0.92	0.89	0.89	0.90	0.90	0.90	0.90	0.91	0.91
Na	0.11	0.03	0.02	0.03	0.02	0.02	0.02	0.02	0.02	0.04	0.04	0.05	0.03	0.03	0.02	0.02	0.02	0.02	0.02	0.03
K	0.02	0.00	0.00	0.00	0.00	0.00	0.00	0.00	0.00	0.00	0.00	0.00	0.00	0.00	0.00	0.00	0.00	0.00	0.00	0.00
#Mg	72.06	76.60	80.75	81.52	83.44	84.19	81.59	80.37	78.71	77.06	76.79	73.26	77.85	78.61	81.98	82.97	84.00	83.91	82.64	76.96
Wo %	36.10	42.13	42.66	42.77	42.73	42.96	42.57	42.75	41.99	42.90	43.79	44.24	42.81	42.62	42.88	42.64	43.46	43.43	43.10	43.01
En %	53.05	48.88	49.92	50.39	50.93	51.04	50.32	49.47	49.04	47.75	46.17	44.36	47.86	48.49	49.61	50.52	49.60	49.63	50.33	48.09
Fs %	10.86	8.99	7.42	6.83	6.34	6.00	7.11	7.78	8.97	9.34	10.04	11.40	9.34	8.89	7.51	6.84	6.94	6.95	6.56	8.90

Table IV.2: Electron microprobe analysis to clinopyroxenes

Occurrence	Mafra gabbro		Sines gabbro													Monchique gabbro				
sample	rm83 b3b	rm83 b3b	rm100 b2a	rm100 b2a	rm100 b2a	rm100 b2b	rm100 b2b	rm100 b2b	rm100 b1a	rm100 b1a	rm100 b1a	rm100 b1a	rm100 b1a	rm100 b1b	rm100 b1b	mon84 b3a	mon84 b3a	mon84 b3b	mon84 b3b	mon84 b1a
type	C	R	C	R	R	C	R	R	C	C	Man	R	R	C	R	C	R	C	R	C
SiO2	49.81	49.63	52.22	50.76	41.46	49.45	49.63	45.09	50.22	47.69	50.51	50.84	48.10	52.89	41.55	47.24	43.94	47.72	45.58	46.44
TiO2	1.51	2.28	0.93	1.34	5.30	2.64	1.86	3.19	1.78	1.77	1.77	0.92	2.32	0.58	5.21	2.86	4.30	2.73	3.57	2.72
Al2O3	4.20	4.98	2.82	3.18	11.45	7.77	4.26	9.29	3.88	5.44	3.50	2.82	5.23	1.87	11.44	5.77	8.82	5.34	7.63	5.87
Cr2O3	0.11	0.00	0.08	0.10	0.03	0.03	0.11	0.01	0.04	0.10	0.02	0.07	0.10	0.03	0.04	0.04	0.06	0.03	0.03	0.00
FeO	6.08	7.33	7.24	7.62	12.26	8.79	7.57	11.19	7.59	8.19	7.60	7.91	8.07	7.51	12.34	6.70	7.62	6.40	6.77	6.48
MnO	0.09	0.15	0.16	0.15	0.10	0.14	0.14	0.11	0.18	0.16	0.13	0.16	0.12	0.10	0.12	0.13	0.14	0.12	0.10	0.09
MgO	15.81	13.68	14.84	15.23	13.38	14.99	15.01	15.39	15.20	15.17	15.58	15.57	14.29	15.58	13.06	14.23	11.97	14.75	13.72	14.14
CaO	22.65	22.50	23.24	21.88	11.50	19.20	22.22	11.71	21.87	19.99	21.85	21.43	21.99	22.77	11.79	23.52	23.32	23.25	22.81	23.37
Na2O	0.25	0.57	0.35	0.42	2.43	1.18	0.44	2.08	0.45	0.56	0.36	0.47	0.47	0.37	2.55	0.41	0.68	0.36	0.42	0.51
K2O	0.06	0.00	0.00	0.03	1.14	0.64	0.02	1.02	0.00	0.04	0.00	0.17	0.00	0.01	1.10	0.00	0.01	0.01	0.08	0.01
F	0.10	0.05	0.02	0.00	0.10	0.00	0.00	0.11	0.00	0.23	0.02	0.00	0.06	0.03	0.00	0.00	0.00	0.00	0.03	0.05
Tot	100.70	101.21	101.89	100.69	99.12	104.87	101.36	99.13	101.22	99.27	101.32	100.42	100.75	101.76	99.25	100.95	100.92	100.77	100.72	99.65
Structural formula (a.p.f.u.)																				
Tet																				
Si	1.84	1.83	1.91	1.88	1.59	1.76	1.83	1.70	1.85	1.80	1.86	1.89	1.79	1.93	1.59	1.75	1.65	1.77	1.70	1.75
Al	0.16	0.17	0.09	0.12	0.41	0.24	0.17	0.30	0.15	0.20	0.14	0.11	0.21	0.07	0.41	0.25	0.35	0.23	0.30	0.25
Oct																				
Al	0.02	0.05	0.03	0.01	0.10	0.09	0.01	0.11	0.02	0.04	0.01	0.01	0.02	0.01	0.10	0.01	0.04	0.00	0.03	0.01
Fe3+	0.12	0.06	0.06	0.09	0.35	0.18	0.12	0.30	0.10	0.16	0.10	0.13	0.14	0.08	0.36	0.16	0.18	0.15	0.15	0.19
Cr	0.00	0.00	0.00	0.00	0.00	0.00	0.00	0.00	0.00	0.00	0.00	0.00	0.00	0.00	0.00	0.00	0.00	0.00	0.00	0.00
Ti	0.04	0.06	0.03	0.04	0.15	0.07	0.05	0.09	0.05	0.05	0.05	0.03	0.07	0.02	0.15	0.08	0.12	0.08	0.10	0.08
Fe2+	0.07	0.17	0.16	0.14	0.04	0.08	0.11	0.05	0.13	0.10	0.14	0.11	0.12	0.15	0.03	0.05	0.06	0.05	0.06	0.01
Mn	0.00	0.00	0.01	0.00	0.00	0.00	0.00	0.00	0.01	0.01	0.00	0.01	0.00	0.00	0.00	0.00	0.00	0.00	0.00	0.00
Mg	0.87	0.75	0.81	0.84	0.76	0.80	0.82	0.87	0.83	0.85	0.85	0.86	0.79	0.85	0.74	0.79	0.67	0.82	0.76	0.79
Ca	0.89	0.89	0.91	0.87	0.47	0.73	0.88	0.47	0.86	0.81	0.86	0.85	0.88	0.89	0.48	0.94	0.94	0.92	0.91	0.94
Na	0.02	0.04	0.03	0.03	0.18	0.08	0.03	0.15	0.03	0.04	0.03	0.03	0.03	0.03	0.19	0.03	0.05	0.03	0.03	0.04
K	0.00	0.00	0.00	0.00	0.06	0.03	0.00	0.05	0.00	0.00	0.00	0.01	0.00	0.00	0.05	0.00	0.00	0.00	0.00	0.00
#Mg	82.24	76.91	78.52	78.09	66.05	75.26	77.94	71.04	78.11	76.75	78.51	77.82	75.94	78.70	65.36	79.10	73.69	80.42	78.31	79.56
Wo %	41.71	44.18	44.54	41.58	23.23	35.97	41.20	23.52	41.26	36.96	41.00	40.11	40.80	43.26	23.82	42.87	43.26	42.55	41.95	42.55
En %	51.62	44.77	45.32	48.39	60.45	52.83	49.66	62.25	49.00	53.43	49.26	50.33	49.27	46.87	60.05	50.63	48.13	51.15	50.70	52.44
Fs %	6.67	11.05	10.14	10.03	16.32	11.20	9.13	14.23	9.74	9.61	9.74	9.56	9.92	9.87	16.14	6.50	8.61	6.30	7.35	5.01

Table IV.2: Electron microprobe analysis to clinopyroxenes

Occurrence	Monchique gabbro			Sintra gabbro				Montelevar sill											
sample	mon84 b1a	mon84 b1	mon84 b1	RM11- b2a	RM11- b2a	RM11- b2b	RM11- b2b	rm50 b1a	rm50 b1a	rm50 b1a	rm50 b1a	rm50 b1a	rm50 b1a	rm50 b1a	rm50 b3a	rm50 b3a	rm50 b3b	rm50 b3b	rm50 b3b
type	R	C	R	C	R	C	R	C	C	C	C	R	R	R	C	R	C	Man	Man	R
SiO2	45.16	44.40	46.83	50.60	52.44	51.47	53.52	51.12	51.58	52.42	51.89	51.10	52.39	51.32	50.61	51.84	52.59	51.27	51.60	51.02
TiO2	2.90	2.14	2.63	0.11	0.31	0.15	0.18	0.84	0.83	0.65	0.83	0.01	0.54	0.62	1.15	0.69	0.79	1.11	0.78	1.11
Al2O3	6.66	5.72	5.10	5.64	0.98	4.43	1.19	1.86	1.66	1.13	1.67	0.21	1.04	1.35	3.53	1.32	1.47	2.31	1.66	2.61
Cr2O3	0.04	0.00	0.00	0.00	0.02	0.07	0.03	0.04	0.01	0.00	0.00	0.03	0.03	0.00	0.00	0.00	0.04	0.00	0.03	0.00
FeO	9.30	9.27	6.38	10.49	7.89	10.03	5.51	10.86	11.08	10.92	11.35	16.16	11.23	11.24	9.10	11.23	10.32	10.18	10.40	9.84
MnO	0.20	0.27	0.12	0.18	0.35	0.19	0.21	0.31	0.39	0.38	0.36	0.41	0.46	0.39	0.22	0.38	0.30	0.29	0.30	0.29
MgO	11.55	12.83	14.74	16.48	14.06	16.46	14.91	14.37	14.49	15.06	14.42	11.36	14.72	14.59	15.83	14.94	15.87	15.03	15.15	15.09
CaO	22.76	22.70	23.18	12.75	22.70	13.00	23.99	20.71	20.44	20.52	20.45	21.11	20.39	20.31	20.20	20.27	20.15	20.64	20.60	20.97
Na2O	0.97	1.11	0.40	0.90	0.53	0.67	0.46	0.43	0.36	0.32	0.40	0.23	0.42	0.35	0.39	0.41	0.31	0.42	0.41	0.38
K2O	0.01	0.01	0.01	0.09	0.00	0.05	0.00	0.00	0.00	0.00	0.01	0.03	0.02	0.01	0.01	0.00	0.01	0.01	0.00	0.00
F	0.13	0.01	0.00	0.27	0.23	0.21	0.05	0.00	0.08	0.00	0.00	0.00	0.00	0.00	0.12	0.09	0.00	0.00	0.05	0.00
Tot	99.68	98.48	99.41	97.50	99.52	96.74	100.05	100.57	100.89	101.40	101.44	100.74	101.24	100.22	101.13	101.18	101.93	101.25	100.97	101.40
Structural formula (a.p.f.u.)																				
Tet																				
Si	1.73	1.72	1.76	1.90	1.97	1.94	1.97	1.91	1.92	1.94	1.93	1.96	1.95	1.93	1.87	1.93	1.93	1.90	1.92	1.89
Al	0.27	0.28	0.24	0.10	0.03	0.06	0.03	0.09	0.08	0.06	0.07	0.04	0.05	0.07	0.13	0.07	0.07	0.10	0.08	0.11
Oct																				
Al	0.03	-0.02	-0.01	0.15	0.01	0.14	0.03	0.00	0.00	-0.01	0.00	-0.03	-0.01	-0.01	0.02	-0.01	-0.01	0.00	-0.01	0.00
Fe3+	0.22	0.37	0.19	0.01	0.06	-0.07	0.03	0.11	0.08	0.08	0.08	0.13	0.09	0.11	0.11	0.11	0.08	0.10	0.11	0.11
Cr	0.00	0.00	0.00	0.00	0.00	0.00	0.00	0.00	0.00	0.00	0.00	0.00	0.00	0.00	0.00	0.00	0.00	0.00	0.00	0.00
Ti	0.08	0.06	0.07	0.00	0.01	0.00	0.00	0.02	0.02	0.02	0.02	0.00	0.01	0.02	0.03	0.02	0.02	0.03	0.02	0.03
Fe2+	0.07	-0.06	0.01	0.32	0.19	0.39	0.14	0.23	0.26	0.26	0.27	0.39	0.26	0.25	0.17	0.24	0.24	0.21	0.21	0.19
Mn	0.01	0.01	0.00	0.01	0.01	0.01	0.01	0.01	0.01	0.01	0.01	0.01	0.01	0.01	0.01	0.01	0.01	0.01	0.01	0.01
Mg	0.66	0.74	0.83	0.92	0.79	0.93	0.82	0.80	0.81	0.83	0.80	0.65	0.82	0.82	0.87	0.83	0.87	0.83	0.84	0.83
Ca	0.93	0.94	0.94	0.51	0.91	0.53	0.95	0.83	0.82	0.81	0.81	0.87	0.81	0.82	0.80	0.81	0.79	0.82	0.82	0.83
Na	0.07	0.08	0.03	0.07	0.04	0.05	0.03	0.03	0.03	0.02	0.03	0.02	0.03	0.03	0.03	0.03	0.02	0.03	0.03	0.03
K	0.00	0.00	0.00	0.00	0.00	0.00	0.00	0.00	0.00	0.00	0.00	0.00	0.00	0.00	0.00	0.00	0.00	0.00	0.00	0.00
#Mg	68.88	71.16	80.47	73.70	76.06	74.52	82.82	70.24	70.00	71.10	69.36	55.64	70.03	69.82	75.62	70.35	73.29	72.47	72.20	73.23
Wo %	42.53	38.79	41.98	17.99	45.61	16.66	48.41	39.48	39.30	39.11	39.35	40.11	39.06	38.67	37.54	38.26	38.05	39.00	38.75	39.18
En %	47.03	57.36	53.16	60.46	43.00	59.76	43.64	45.36	44.70	45.43	44.20	35.86	45.01	45.56	50.56	46.31	47.50	47.04	47.22	47.66
Fs %	10.43	3.85	4.86	21.55	11.39	23.58	7.95	15.16	16.01	15.46	16.46	24.03	15.93	15.77	11.90	15.44	14.45	13.96	14.03	13.16

Table IV.2: Electron microprobe analysis to clinopyroxenes

Occurrence	Montelevar sill						Monchique ne-syenite													
sample	rm50 b3c	rm50 b3c	rm50 b3d	rm50 b3e	rm50 b3f	rm50 b3f	749 b1a	749 b1a	749 b1b	749 b1b	749 b1b	749 b1b	749 b1c	749 b1c	749 b1d	749 b1d	749 b1e	749 b1e	749 b1f	749 b1f
type	C	R	C	C	C	R	C	R	C	C	R	R	C	R	C	R	C	R	C	R
SiO2	51.96	51.18	50.41	48.90	52.21	51.27	49.78	50.20	49.86	49.45	49.89	50.18	49.56	49.94	49.82	50.27	50.49	49.31	50.17	50.16
TiO2	0.88	0.06	1.29	1.01	0.71	0.24	0.88	0.56	0.93	1.13	0.96	0.46	1.21	0.51	1.00	0.39	0.84	1.12	0.99	0.68
Al2O3	1.84	0.34	2.82	3.82	1.44	0.39	2.25	1.47	2.57	2.53	2.36	1.54	3.29	1.52	2.53	1.30	2.46	2.79	2.82	1.97
Cr2O3	0.00	0.06	0.00	0.00	0.00	0.00	0.04	0.04	0.00	0.20	0.00	0.03	0.00	0.00	0.03	0.01	0.02	0.00	0.02	0.02
FeO	10.73	16.79	11.24	15.31	10.32	16.57	12.29	14.08	9.83	10.84	10.30	15.03	10.58	15.62	10.12	15.99	9.67	10.51	9.66	11.34
MnO	0.31	0.48	0.33	0.27	0.32	0.57	0.76	0.88	0.53	0.66	0.56	0.94	0.59	0.95	0.53	1.00	0.48	0.54	0.48	0.66
MgO	14.88	11.12	14.53	16.09	15.47	11.88	10.34	9.39	11.99	11.08	11.64	8.75	11.15	8.50	11.67	8.04	12.13	11.37	12.20	11.34
CaO	20.78	20.51	20.04	9.96	20.53	19.37	20.87	19.11	22.26	21.44	21.88	18.91	21.66	18.07	22.23	18.63	22.37	21.91	22.34	21.55
Na2O	0.35	0.24	0.38	2.51	0.32	0.34	2.07	3.80	1.39	1.76	1.50	3.13	1.66	3.17	1.42	3.17	1.08	1.45	1.22	1.63
K2O	0.00	0.01	0.01	0.78	0.01	0.00	0.00	0.06	0.01	0.00	0.01	0.00	0.00	0.00	0.01	0.00	0.00	0.01	0.00	0.02
F	0.05	0.00	0.00	2.85	0.00	0.07	0.04	0.04	0.00	0.20	0.00	0.03	0.00	0.00	0.03	0.01	0.02	0.00	0.02	0.02
Tot	101.81	100.80	101.10	100.28	101.31	100.77	99.39	99.60	99.46	99.14	99.13	99.04	99.80	98.33	99.39	98.87	99.58	99.10	99.99	99.41
Structural formula (a.p.f.u.)																				
Tet																				
Si	1.92	1.96	1.88	1.87	1.93	1.96	1.92	1.95	1.90	1.90	1.91	1.96	1.89	1.97	1.90	1.98	1.92	1.89	1.90	1.92
Al	0.08	0.04	0.12	0.13	0.07	0.04	0.08	0.05	0.10	0.10	0.09	0.04	0.11	0.03	0.10	0.02	0.08	0.11	0.10	0.08
Oct																				
Al	0.00	-0.02	0.00	0.05	-0.01	-0.02	0.02	0.02	0.02	0.01	0.02	0.03	0.03	0.04	0.02	0.04	0.03	0.02	0.02	0.01
Fe3+	0.09	0.10	0.11	0.36	0.09	0.10	0.24	0.42	0.20	0.21	0.19	0.32	0.19	0.30	0.19	0.30	0.14	0.19	0.17	0.22
Cr	0.00	0.00	0.00	0.00	0.00	0.00	0.00	0.00	0.00	0.01	0.00	0.00	0.00	0.00	0.00	0.00	0.00	0.00	0.00	0.00
Ti	0.02	0.00	0.04	0.03	0.02	0.01	0.03	0.02	0.03	0.03	0.03	0.01	0.03	0.02	0.03	0.01	0.02	0.03	0.03	0.02
Fe2+	0.24	0.44	0.24	0.13	0.23	0.43	0.16	0.04	0.12	0.14	0.14	0.18	0.14	0.21	0.13	0.22	0.17	0.14	0.14	0.15
Mn	0.01	0.02	0.01	0.01	0.01	0.02	0.02	0.03	0.02	0.02	0.02	0.03	0.02	0.03	0.02	0.03	0.02	0.02	0.02	0.02
Mg	0.82	0.64	0.81	0.92	0.85	0.68	0.59	0.54	0.68	0.63	0.66	0.51	0.63	0.50	0.66	0.47	0.69	0.65	0.69	0.65
Ca	0.82	0.84	0.80	0.41	0.81	0.79	0.86	0.79	0.91	0.88	0.90	0.79	0.88	0.76	0.91	0.78	0.91	0.90	0.91	0.89
Na	0.03	0.02	0.03	0.19	0.02	0.03	0.15	0.29	0.10	0.13	0.11	0.24	0.12	0.24	0.11	0.24	0.08	0.11	0.09	0.12
K	0.00	0.00	0.00	0.04	0.00	0.00	0.00	0.00	0.00	0.00	0.00	0.00	0.00	0.00	0.00	0.00	0.00	0.00	0.00	0.00
#Mg	71.20	54.14	69.75	65.20	72.76	56.10	60.01	54.33	68.51	64.58	66.85	50.94	65.26	49.25	67.28	47.27	69.09	65.85	69.25	64.07
Wo %	39.37	39.51	37.79	19.22	38.78	37.58	42.72	39.56	43.94	43.16	43.96	50.33	43.80	48.44	44.23	49.57	44.84	43.86	44.15	43.02
En %	45.53	34.79	46.29	61.92	46.97	37.11	41.06	46.10	44.32	43.04	43.06	32.25	42.38	31.87	43.16	30.09	41.97	42.66	43.57	42.63
Fs %	15.10	25.70	15.92	18.86	14.25	25.30	16.22	14.34	11.73	13.80	12.98	17.42	13.82	19.69	12.62	20.34	13.19	13.48	12.28	14.35

Table IV.2: Electron microprobe analysis to clinopyroxenes

Occurrence	Monchique ne-syenite											Paço d'Ilhas		Cascais dyke						
sample	749 b2a	749 b2a	749 b2b	749 b2b	749 b2c	749 b2c	749 b2d	749 b2d	749 b2e	749 b2e	749 b2e	PI-b2a	PI-b2b	RM90- b1a	RM90- b1a	RM90- b1b	RM90- b1c	RM90- b2a	RM90- b2a	RM90- b2a
type	C	R	C	R	C	R	C	R	C	C	R	C	C	PC	PR	Mx	Mx	PC	PC	PR
SiO2	49.58	49.27	51.25	51.86	50.25	49.94	49.75	50.22	48.09	47.40	49.04	51.83	52.42	50.29	47.88	47.03	46.05	48.52	49.02	49.05
TiO2	0.86	0.97	0.45	0.30	0.51	0.59	1.01	0.72	1.69	0.67	1.33	0.72	0.66	1.26	2.25	2.46	2.99	1.84	1.92	1.99
Al2O3	2.41	3.00	1.37	0.78	1.49	1.69	2.62	2.02	4.08	1.46	3.27	1.86	1.71	3.13	5.21	5.24	6.62	5.10	4.99	4.52
Cr2O3	0.00	0.00	0.01	0.00	0.01	0.00	0.02	0.00	0.06	0.03	0.00	0.04	0.00	0.00	0.00	0.00	0.00	0.02	0.02	0.03
FeO	10.91	10.18	15.35	9.30	16.36	15.62	11.49	11.16	10.56	16.73	10.29	8.79	8.58	7.77	8.43	8.87	9.22	8.50	8.39	8.39
MnO	0.65	0.59	1.02	0.63	1.01	0.99	0.67	0.65	0.56	1.02	0.47	0.46	0.39	0.24	0.17	0.19	0.18	0.19	0.18	0.14
MgO	11.19	11.59	8.48	13.17	7.91	8.33	10.70	10.99	10.86	8.76	11.51	14.04	14.47	15.43	13.73	13.01	13.04	14.08	13.91	14.12
CaO	21.54	22.33	18.49	22.46	18.22	18.44	21.10	21.27	21.53	15.25	21.86	20.57	20.60	20.72	21.32	21.18	20.85	20.70	20.83	21.18
Na2O	1.85	1.29	3.35	1.35	3.40	3.37	2.05	1.78	1.75	3.60	1.46	0.37	0.35	0.27	0.37	0.35	0.43	0.37	0.41	0.35
K2O	0.01	0.00	0.00	0.00	0.00	0.00	0.02	0.00	0.00	0.94	0.00	0.00	0.00	0.00	0.00	0.00	0.00	0.01	0.00	0.00
F	0.00	0.00	0.01	0.00	0.01	0.00	0.02	0.00	0.06	0.03	0.00	0.09	0.06	0.00	0.00	0.00	0.00	0.00	0.02	0.00
Tot	99.08	99.27	99.77	99.90	99.27	99.04	99.54	98.83	99.29	96.19	99.26	98.78	99.26	99.12	99.36	98.32	99.38	99.32	99.69	99.77
Structural formula (a.p.f.u.)																				
Tet																				
Si	1.91	1.89	1.98	1.96	1.97	1.96	1.91	1.93	1.85	1.94	1.88	1.95	1.96	1.88	1.80	1.80	1.74	1.82	1.83	1.84
Al	0.09	0.11	0.02	0.04	0.03	0.04	0.09	0.07	0.15	0.06	0.12	0.05	0.04	0.12	0.20	0.20	0.26	0.18	0.17	0.16
Oct																				
Al	0.02	0.02	0.05	-0.01	0.04	0.04	0.03	0.02	0.03	0.01	0.02	0.04	0.04	0.02	0.04	0.03	0.04	0.05	0.05	0.03
Fe3+	0.24	0.20	0.29	0.19	0.32	0.33	0.23	0.20	0.23	0.50	0.20	-0.01	-0.02	0.06	0.09	0.08	0.11	0.07	0.05	0.06
Cr	0.00	0.00	0.00	0.00	0.00	0.00	0.00	0.00	0.00	0.00	0.00	0.00	0.00	0.00	0.00	0.00	0.00	0.00	0.00	0.00
Ti	0.02	0.03	0.01	0.01	0.02	0.02	0.03	0.02	0.05	0.02	0.04	0.02	0.02	0.04	0.06	0.07	0.09	0.05	0.05	0.06
Fe2+	0.11	0.13	0.21	0.10	0.22	0.18	0.13	0.16	0.11	0.07	0.13	0.29	0.28	0.18	0.18	0.20	0.18	0.19	0.21	0.20
Mn	0.02	0.02	0.03	0.02	0.03	0.03	0.02	0.02	0.02	0.04	0.02	0.01	0.01	0.01	0.01	0.01	0.01	0.01	0.01	0.00
Mg	0.64	0.66	0.49	0.74	0.46	0.49	0.61	0.63	0.62	0.53	0.66	0.79	0.81	0.86	0.77	0.74	0.74	0.79	0.78	0.79
Ca	0.89	0.92	0.77	0.91	0.77	0.77	0.87	0.88	0.89	0.67	0.90	0.83	0.83	0.83	0.86	0.87	0.85	0.83	0.83	0.85
Na	0.14	0.10	0.25	0.10	0.26	0.26	0.15	0.13	0.13	0.29	0.11	0.03	0.03	0.02	0.03	0.03	0.03	0.03	0.03	0.03
K	0.00	0.00	0.00	0.00	0.00	0.00	0.00	0.00	0.00	0.05	0.00	0.00	0.00	0.00	0.00	0.00	0.00	0.00	0.00	0.00
#Mg	64.66	67.00	49.63	71.63	46.29	48.74	62.43	63.71	64.71	48.30	66.62	74.00	75.04	77.97	74.37	72.34	71.61	74.71	74.73	75.00
Wo %	43.09	43.92	48.08	43.91	49.21	50.15	43.05	43.85	43.05	32.74	43.56	39.36	38.92	40.42	41.42	41.94	40.11	40.52	41.51	41.57
En %	44.08	43.41	32.11	45.92	30.12	31.52	42.38	41.32	43.85	44.44	43.46	44.63	45.39	48.33	46.24	44.35	46.31	46.63	45.17	45.67
Fs %	12.83	12.67	19.81	10.17	20.67	18.33	14.56	14.83	13.10	22.82	12.98	16.01	15.69	11.26	12.35	13.71	13.58	12.85	13.32	12.76

Table IV.2: Electron microprobe analysis to clinopyroxenes

Occurrence	Cascais dyke																	
sample	RM90-b2a	RM90-b2b	RM90-b2b	RM90-b2c	RM90-b2d	RM90-b2e	RM90-b3a	RM90-b3a	RM90-b3a	RM90-b3a	RM90-b3b	RM90-b3c	RM90-b3d	RM90-b4a	RM90-b4a	RM90-b4a	RM90-b4a	RM90-b4a
type	PR	PC	PR	Mx	Mx	Mx	PC	PC	PR	PR	Mx	MP	MP	PC	Pman	Pman	PR	PR
SiO2	47.95	48.95	48.38	48.19	51.81	47.54	49.82	52.35	48.44	48.30	47.69	47.47	47.95	47.40	46.38	45.78	47.28	44.92
TiO2	2.80	2.01	2.51	2.24	1.23	2.64	0.97	0.53	1.62	1.91	2.05	2.28	2.00	0.76	0.96	1.14	0.65	1.85
Al2O3	5.14	4.69	5.25	5.13	2.30	5.72	5.28	3.48	5.00	5.12	5.80	5.85	5.79	4.78	5.50	6.21	4.62	5.73
Cr2O3	0.04	0.00	0.06	0.04	0.00	0.00	0.27	0.47	0.00	0.06	0.00	0.03	0.00	0.31	0.12	0.03	0.30	0.13
FeO	8.96	8.42	9.23	8.80	8.49	8.86	5.52	5.72	8.45	8.71	9.32	9.47	9.72	5.86	6.29	6.63	6.42	8.07
MnO	0.17	0.20	0.20	0.15	0.19	0.19	0.04	0.02	0.15	0.15	0.25	0.21	0.25	0.12	0.05	0.09	0.07	0.14
MgO	13.23	13.86	13.55	13.50	15.59	12.95	15.35	16.91	13.68	13.65	13.11	12.92	12.80	15.62	14.97	14.45	16.59	14.21
CaO	20.50	21.30	20.71	21.01	20.10	21.37	21.67	20.33	21.34	21.37	21.06	20.78	20.87	20.68	21.01	21.03	19.21	20.49
Na2O	0.36	0.32	0.36	0.35	0.26	0.35	0.33	0.35	0.35	0.31	0.40	0.40	0.42	0.32	0.35	0.33	0.35	0.38
K2O	0.01	0.00	0.00	0.00	0.00	0.00	0.01	0.00	0.00	0.01	0.01	0.00	0.00	0.00	0.00	0.01	0.01	0.00
F	0.11	0.00	0.12	0.02	0.03	0.00	0.00	0.00	0.00	0.00	0.02	0.00	0.00	0.00	0.04	0.00	0.00	0.02
Tot	99.25	99.74	100.37	99.41	99.99	99.61	99.25	100.17	99.03	99.59	99.70	99.41	99.80	95.84	95.68	95.69	95.50	95.95
Structural formula (a.p.f.u.)																		
Tet																		
Si	1.81	1.83	1.81	1.82	1.92	1.79	1.85	1.91	1.83	1.82	1.80	1.79	1.81	1.83	1.80	1.78	1.83	1.76
Al	0.19	0.17	0.19	0.18	0.08	0.21	0.15	0.09	0.17	0.18	0.20	0.21	0.19	0.17	0.20	0.22	0.17	0.24
Oct																		
Al	0.04	0.04	0.04	0.04	0.02	0.04	0.08	0.06	0.05	0.04	0.05	0.05	0.06	0.05	0.05	0.06	0.04	0.02
Fe3+	0.03	0.05	0.05	0.06	0.01	0.06	0.06	0.01	0.08	0.08	0.09	0.07	0.07	0.14	0.17	0.17	0.17	0.20
Cr	0.00	0.00	0.00	0.00	0.00	0.00	0.01	0.01	0.00	0.00	0.00	0.00	0.00	0.01	0.00	0.00	0.01	0.00
Ti	0.08	0.06	0.07	0.06	0.03	0.07	0.03	0.01	0.05	0.05	0.06	0.06	0.06	0.02	0.03	0.03	0.02	0.05
Fe2+	0.26	0.21	0.24	0.22	0.25	0.22	0.12	0.16	0.19	0.19	0.20	0.22	0.23	0.05	0.04	0.05	0.04	0.06
Mn	0.01	0.01	0.01	0.00	0.01	0.01	0.00	0.00	0.00	0.00	0.01	0.01	0.01	0.00	0.00	0.00	0.00	0.00
Mg	0.74	0.77	0.76	0.76	0.86	0.73	0.85	0.92	0.77	0.77	0.74	0.73	0.72	0.90	0.87	0.84	0.96	0.83
Ca	0.83	0.85	0.83	0.85	0.80	0.86	0.86	0.80	0.86	0.86	0.85	0.84	0.84	0.85	0.87	0.88	0.80	0.86
Na	0.03	0.02	0.03	0.03	0.02	0.03	0.02	0.02	0.03	0.02	0.03	0.03	0.03	0.02	0.03	0.02	0.03	0.03
K	0.00	0.00	0.00	0.00	0.00	0.00	0.00	0.00	0.00	0.00	0.00	0.00	0.00	0.00	0.00	0.00	0.00	0.00
#Mg	72.46	74.59	72.35	73.22	76.60	72.28	83.22	84.06	74.26	73.65	71.51	70.86	70.11	82.63	80.92	79.54	82.17	75.84
Wo %	40.29	42.06	40.93	41.60	39.25	42.39	42.02	36.52	41.72	41.42	40.92	41.00	41.18	38.68	39.14	39.38	35.05	37.45
En %	43.99	44.81	44.20	44.47	46.87	43.39	50.05	53.84	45.67	45.48	44.91	43.95	43.31	55.57	55.12	53.98	59.03	54.15
Fs %	15.73	13.13	14.87	13.93	13.88	14.22	7.94	9.65	12.61	13.10	14.17	15.06	15.51	5.75	5.74	6.64	5.92	8.40

Table IV.3: Electron microprobe analysis to plagioclases and feldspars

Occurrence	Lomba dos Pianos sill																		
	rm9	rm9	rm9	rm9	rm9	rm9	rm9	rm9		rm9	rm9	rm9	rm9	rm9	rm9	rm9	rm9	rm9	rm9
sample	b1a	b1a	b1a	b1a	b1b	b1b	b1c	b1d	rm9 b2	b2a	b2a	b2a	b2a	b3a	b3a	b3b	b3b	b3c	b3c
type	PC	PM	PM	PR	PM	PR	Mx	Mx	PC	PC	PM	PM	PR	PC	PR	PC	PR	PC	PR
SiO2	50.27	50.32	50.30	50.53	52.01	48.60	52.44	52.71	55.72	56.07	54.42	54.29	60.61	50.19	57.02	52.14	57.62	51.58	56.82
TiO2	0.06	0.06	0.04	0.05	0.03	0.06	0.11	0.09	0.06	0.05	0.04	0.07	0.09	0.05	0.06	0.08	0.00	0.12	0.04
Al2O3	30.03	29.89	30.07	29.70	28.95	30.98	28.89	28.45	26.53	26.42	27.27	27.67	23.41	30.13	25.70	28.84	25.65	28.04	26.01
FeO	0.46	0.44	0.47	0.47	0.44	0.49	0.55	0.51	0.43	0.43	0.44	0.43	0.48	0.34	0.32	0.56	0.35	1.91	0.35
MgO	0.04	0.05	0.05	0.05	0.05	0.05	0.03	0.09	0.05	0.07	0.06	0.06	0.12	0.01	0.02	0.09	0.05	0.48	0.04
CaO	14.82	14.52	14.23	14.07	13.43	15.68	13.38	12.62	10.15	10.32	11.10	11.80	6.05	14.48	9.08	13.28	9.35	12.30	9.52
Na2O	2.67	2.85	2.94	3.09	3.36	2.15	3.30	3.91	5.28	5.22	4.77	4.43	7.50	2.78	5.74	3.40	5.55	3.38	5.54
K2O	0.11	0.13	0.14	0.14	0.18	0.07	0.10	0.22	0.29	0.29	0.26	0.21	0.56	0.12	0.38	0.17	0.35	0.17	0.32
SrO	0.15	0.20	0.10	0.14	0.17	0.13	0.14	0.15	0.22	0.15	0.24	0.25	0.14	0.12	0.18	0.17	0.29	0.16	0.21
BaO	0.00	0.05	0.00	0.02	0.06	0.05	0.00	0.04	0.04	0.03	0.01	0.01	0.21	0.06	0.08	0.02	0.07	0.04	0.05
TOTAL	98.6	98.5	98.3	98.3	98.7	98.3	98.9	98.8	98.8	99.0	98.6	99.2	99.2	98.3	98.6	98.7	99.3	98.2	98.9
Structural formula (a.p.f.u.)																			
Si	9.30	9.32	9.32	9.37	9.58	9.05	9.61	9.68	10.16	10.19	9.97	9.90	10.91	9.30	10.38	9.59	10.42	9.55	10.32
Ti	0.01	0.01	0.01	0.01	0.00	0.01	0.01	0.01	0.01	0.01	0.01	0.01	0.01	0.01	0.01	0.01	0.00	0.02	0.01
Al	6.54	6.52	6.56	6.49	6.28	6.80	6.24	6.16	5.70	5.66	5.89	5.95	4.96	6.58	5.51	6.25	5.47	6.12	5.57
MgO	0.13	0.12	0.13	0.13	0.12	0.14	0.15	0.14	0.12	0.12	0.12	0.12	0.13	0.10	0.09	0.15	0.10	0.53	0.10
Fe(ii)	0.01	0.01	0.01	0.01	0.01	0.01	0.00	0.01	0.01	0.01	0.01	0.01	0.02	0.00	0.00	0.01	0.01	0.07	0.01
Ca	2.94	2.88	2.82	2.79	2.65	3.13	2.63	2.48	1.98	2.01	2.18	2.31	1.17	2.88	1.77	2.62	1.81	2.44	1.85
Na	0.96	1.02	1.05	1.11	1.20	0.77	1.17	1.39	1.87	1.84	1.69	1.56	2.62	1.00	2.03	1.21	1.94	1.21	1.95
K	0.03	0.03	0.03	0.03	0.04	0.02	0.02	0.05	0.07	0.07	0.06	0.05	0.13	0.03	0.09	0.04	0.08	0.04	0.07
SrO	0.02	0.02	0.01	0.01	0.02	0.01	0.01	0.02	0.02	0.02	0.03	0.03	0.01	0.01	0.02	0.02	0.03	0.02	0.02
BaO	0.00	0.00	0.00	0.00	0.00	0.00	0.00	0.00	0.00	0.00	0.00	0.00	0.02	0.00	0.01	0.00	0.00	0.00	0.00
An	74.94	73.25	72.21	70.95	68.13	79.81	68.71	63.20	50.63	51.30	55.40	58.83	29.84	73.65	45.57	67.62	47.21	66.04	47.77
Ab	24.38	25.99	26.95	28.19	30.80	19.76	30.66	35.47	47.63	46.98	43.06	39.92	66.91	25.60	52.17	31.36	50.69	32.88	50.30
Or	0.68	0.76	0.83	0.86	1.07	0.42	0.62	1.34	1.73	1.72	1.54	1.25	3.26	0.74	2.26	1.02	2.10	1.09	1.92

P- Phenocryst, R- Rim, C- Core, M - Middle, Mx - Matrix, Am - amygdule, AR - amphibole reaction rim

Table IV.3: Electron microprobe analysis to plagioclases and feldspars

Occurrence	Lomba dos Pianos sill																			
	rm9	rm9	rm9	rm9	rm9	rm9	rm9	rm9	rm9	rm9	rm9	rm9	rm9	rm9	rm9	rm9	rm9	rm9	rm9	rm9
sample	b3d	b4a	b4a	b4b	b4b	b5a	b5a	b5a	b5a	b5a	b5b	b5b	b5b	b7a	b7a	b7a	b7a	b7a	b7a	b7a
type	PC	PR	PC	PC	PR	PC	PM	PM	PR	PR	PC	PM	PR	PR	PR	PC	PC	PC	PC	PR
SiO2	50.12	52.92	50.63	52.48	56.75	56.90	56.93	56.88	53.88	55.21	55.49	55.89	67.10	51.21	49.73	50.94	51.25	51.86	51.48	51.80
TiO2	0.05	0.15	0.08	0.12	0.12	0.05	0.05	0.06	0.10	0.05	0.04	0.08	0.13	0.05	0.06	0.06	0.07	0.05	0.03	0.05
Al2O3	30.02	28.15	29.56	27.82	25.34	25.86	25.91	26.05	27.65	27.11	26.94	26.81	18.48	29.47	29.99	29.70	29.48	29.14	29.32	28.93
FeO	0.49	0.56	0.57	0.51	0.36	0.35	0.36	0.32	0.58	0.61	0.23	0.30	0.20	0.45	0.68	0.45	0.46	0.47	0.46	0.42
MgO	0.02	0.03	0.06	0.05	0.02	0.01	0.02	0.01	0.04	0.04	0.01	0.01	0.00	0.08	0.28	0.04	0.05	0.06	0.06	0.07
CaO	14.54	12.14	14.02	12.28	7.91	9.35	9.59	9.34	11.89	11.12	10.80	10.71	0.99	14.26	14.67	14.13	13.95	13.65	13.74	13.21
Na2O	2.81	4.07	3.17	3.88	6.52	5.60	5.49	5.68	4.40	4.74	4.93	4.92	6.34	2.66	2.39	2.68	2.86	3.01	2.83	3.24
K2O	0.15	0.17	0.12	0.18	0.23	0.42	0.42	0.43	0.22	0.28	0.40	0.40	6.57	0.14	0.10	0.14	0.14	0.17	0.15	0.19
SrO	0.13	0.14	0.12	0.17	0.14	0.19	0.19	0.17	0.15	0.15	0.14	0.11	0.00	0.15	0.19	0.22	0.13	0.17	0.16	0.19
BaO	0.00	0.00	0.02	0.00	0.04	0.09	0.10	0.07	0.00	0.02	0.02	0.07	0.00	0.00	0.04	0.05	0.00	0.00	0.01	0.00
TOTAL	98.3	98.3	98.3	97.5	97.4	98.8	99.1	99.0	98.9	99.3	99.0	99.3	99.8	98.5	98.1	98.4	98.4	98.6	98.2	98.1
Structural formula (a.p.f.u.)																				
Si	9.29	9.74	9.38	9.75	10.43	10.35	10.33	10.32	9.86	10.03	10.11	10.14	12.01	9.45	9.25	9.42	9.46	9.55	9.51	9.58
Ti	0.01	0.02	0.01	0.02	0.02	0.01	0.01	0.01	0.01	0.01	0.01	0.01	0.02	0.01	0.01	0.01	0.01	0.01	0.00	0.01
Al	6.56	6.11	6.45	6.09	5.49	5.54	5.54	5.57	5.96	5.80	5.78	5.73	3.90	6.41	6.57	6.47	6.41	6.32	6.38	6.31
MgO	0.14	0.15	0.16	0.14	0.10	0.09	0.10	0.09	0.16	0.17	0.06	0.08	0.05	0.12	0.19	0.12	0.13	0.13	0.13	0.12
Fe(ii)	0.00	0.01	0.01	0.01	0.00	0.00	0.00	0.00	0.01	0.01	0.00	0.00	0.00	0.01	0.04	0.01	0.01	0.01	0.01	0.01
Ca	2.89	2.39	2.78	2.44	1.56	1.82	1.86	1.82	2.33	2.16	2.11	2.08	0.19	2.82	2.92	2.80	2.76	2.69	2.72	2.62
Na	1.01	1.45	1.14	1.40	2.32	1.97	1.93	2.00	1.56	1.67	1.74	1.73	2.20	0.95	0.86	0.96	1.02	1.07	1.01	1.16
K	0.03	0.04	0.03	0.04	0.05	0.10	0.10	0.10	0.05	0.06	0.09	0.09	1.50	0.03	0.02	0.03	0.03	0.04	0.03	0.04
SrO	0.01	0.01	0.01	0.02	0.02	0.02	0.02	0.02	0.02	0.02	0.01	0.01	0.00	0.02	0.02	0.02	0.01	0.02	0.02	0.02
BaO	0.00	0.00	0.00	0.00	0.00	0.01	0.01	0.00	0.00	0.00	0.00	0.00	0.00	0.00	0.00	0.00	0.00	0.00	0.00	0.00
An	73.41	61.62	70.48	62.92	39.58	46.77	47.88	46.39	59.09	55.54	53.48	53.31	4.86	74.16	76.75	73.85	72.32	70.79	72.17	68.48
Ab	25.70	37.38	28.79	35.96	59.05	50.71	49.65	51.07	39.62	42.80	44.19	44.32	56.59	24.99	22.61	25.31	26.84	28.19	26.93	30.36
Or	0.88	1.00	0.72	1.12	1.38	2.51	2.47	2.54	1.30	1.66	2.33	2.37	38.55	0.85	0.64	0.84	0.84	1.02	0.91	1.16

Table IV.3: Electron microprobe analysis to plagioclases and feldspars

Occurrence	Lomba	Malvei	Ribeira d'Illhas plug											LVC flow						
	rm9	rm25	rm36	rm36	rm36	rm36	rm36	rm36	rm36	rm37	rm37	rm37	rm37	rm43	rm43	rm43	rm43	rm43	rm43	rm43
sample	b7a	b2a	b2a	b2b	b2c	b2d	b4a	b4b	b4c	b5a	b5b	b5c	b5d	b3a	b3b	b3c	b3d	b3e	b3f	b3g
type	PR	Mx	Mx	Mx	Mx	Mx	Am	Am	Am	Mx	Mx	Mx	Mx	AR	AR	AR	Mx	Mx	Mx	Mx
SiO2	51.28	64.83	54.24	54.44	55.37	53.65	56.95	57.56	54.52	54.90	54.54	55.55	53.56	55.46	50.76	56.56	56.07	55.78	54.97	55.30
TiO2	0.02	0.00	0.20	0.18	0.17	0.19	0.17	0.12	0.19	0.24	0.41	0.26	0.31	0.18	0.17	0.26	0.21	0.27	0.41	0.19
Al2O3	29.59	20.41	27.06	26.57	26.32	27.07	23.77	24.40	26.50	26.96	24.67	26.31	27.18	28.05	30.54	26.00	26.16	26.31	25.24	23.92
FeO	0.47	0.22	0.44	0.35	0.43	0.41	1.23	0.93	0.44	0.82	1.74	0.86	0.92	2.03	0.78	0.52	0.51	0.65	2.81	1.26
MgO	0.04	0.11	0.05	0.05	0.03	0.04	0.97	0.82	0.10	0.11	0.61	0.13	0.08	2.72	0.08	0.21	0.07	0.02	2.02	0.84
CaO	14.02	1.05	10.01	9.42	9.33	10.07	5.81	7.05	8.67	10.17	7.78	7.72	10.75	0.71	0.76	8.39	7.22	8.68	6.19	7.47
Na2O	2.80	10.97	5.00	5.20	5.30	4.85	4.97	5.38	4.76	4.64	4.79	6.20	4.56	8.37	14.07	5.70	6.53	5.32	7.45	6.34
K2O	0.14	0.12	0.46	0.55	0.63	0.47	2.96	1.64	1.22	0.40	2.31	1.28	0.46	2.10	2.72	0.43	1.53	1.04	1.22	1.68
SrO	0.17	0.11	1.10	1.42	0.92	1.41	0.82	0.54	1.37	0.58	0.43	0.44	0.50	0.00	0.00	0.75	0.29	0.30	0.21	0.29
BaO	0.00	0.00	0.26	0.34	0.32	0.35	0.44	0.23	0.44	0.14	0.21	0.14	0.18	0.04	0.01	0.48	0.18	0.24	0.08	0.15
TOTAL	98.5	97.8	98.8	98.5	98.8	98.5	98.1	98.7	98.2	99.0	97.5	98.9	98.5	99.6	99.9	99.3	98.8	98.6	100.6	97.4
Structural formula (a.p.f.u.)																				
Si	9.46	11.65	9.98	10.06	10.16	9.93	10.57	10.54	10.11	10.03	10.20	10.17	9.87	10.07	9.38	10.29	10.27	10.21	10.00	10.34
Ti	0.00	0.00	0.03	0.02	0.02	0.03	0.02	0.02	0.03	0.03	0.06	0.04	0.04	0.02	0.02	0.04	0.03	0.04	0.06	0.03
Al	6.43	4.32	5.87	5.79	5.69	5.91	5.20	5.27	5.79	5.80	5.43	5.68	5.90	6.00	6.65	5.58	5.64	5.68	5.41	5.27
MgO	0.13	0.06	0.12	0.10	0.12	0.11	0.34	0.25	0.12	0.22	0.48	0.23	0.25	0.55	0.22	0.14	0.14	0.18	0.76	0.35
Fe(ii)	0.01	0.02	0.01	0.01	0.01	0.01	0.15	0.13	0.02	0.02	0.09	0.02	0.01	0.41	0.01	0.03	0.01	0.00	0.31	0.13
Ca	2.77	0.20	1.97	1.87	1.83	2.00	1.16	1.38	1.72	1.99	1.56	1.51	2.12	0.14	0.15	1.64	1.42	1.70	1.21	1.50
Na	1.00	3.82	1.78	1.86	1.88	1.74	1.79	1.91	1.71	1.64	1.73	2.20	1.63	2.95	5.04	2.01	2.32	1.89	2.63	2.30
K	0.03	0.03	0.11	0.13	0.15	0.11	0.70	0.38	0.29	0.09	0.55	0.30	0.11	0.49	0.64	0.10	0.36	0.24	0.28	0.40
SrO	0.02	0.01	0.12	0.15	0.10	0.15	0.09	0.06	0.15	0.06	0.05	0.05	0.05	0.00	0.00	0.08	0.03	0.03	0.02	0.03
BaO	0.00	0.00	0.02	0.02	0.02	0.03	0.03	0.02	0.03	0.01	0.02	0.01	0.01	0.00	0.00	0.03	0.01	0.02	0.01	0.01
An	72.81	5.00	51.03	48.36	47.42	51.90	31.71	37.61	46.28	53.40	40.55	37.71	54.99	3.85	2.57	43.66	34.62	44.41	29.30	35.68
Ab	26.32	94.35	46.16	48.28	48.75	45.20	49.07	51.95	45.95	44.08	45.11	54.84	42.21	82.55	86.45	53.65	56.65	49.28	63.80	54.79
Or	0.87	0.65	2.81	3.36	3.84	2.90	19.22	10.44	7.77	2.52	14.34	7.45	2.80	13.61	10.98	2.68	8.74	6.31	6.90	9.53

Table IV.3: Electron microprobe analysis to plagioclases and feldspars

Occurrence	LVC flow			LVC neck								Loulé lamprophyre			Eiras de Faião sill			Montelevar sill		
	rm43	rm43	rm43	rm66	rm66	rm66	rm66	rm66	rm66	rm66	rm66	c20	c20	c20	rm47	rm47	rm47	rm50	rm50	rm50
sample	b5a	b5b	b5c	b3a	b3a	b3a	b3a	b3a	b3b	b3c	b3d	b1a	b1b	b3a	b4a	b4b	b4c	b3a	b3a	b3a
type	Mx	Mx	Mx	PC	PC	PR	PR	PM	Mx	Mx	Mx	Mx	Mx	Mx	Mx	Mx	Mx			R
SiO2	51.96	53.35	51.87	49.02	54.81	61.08	49.01	48.60	50.59	62.19	50.30	55.52	66.60	65.37	66.29	59.62	63.26	55.20	54.44	56.90
TiO2	0.16	0.32	0.19	0.10	0.14	0.19	0.09	0.12	0.76	0.12	0.14	0.00	0.01	0.03	0.09	0.08	0.13	0.04	0.08	0.06
Al2O3	28.77	27.11	28.75	30.97	27.17	22.47	30.95	30.98	29.97	22.47	30.36	25.59	17.34	17.90	18.17	22.20	19.92	26.42	27.05	25.49
FeO	0.93	0.87	0.71	0.54	0.35	0.20	0.56	0.54	0.84	0.23	0.53	0.15	0.32	0.35	0.35	0.46	0.27	0.43	0.40	0.46
MgO	0.16	0.19	0.03	0.07	0.06	0.00	0.01	0.09	0.04	0.02	0.06	0.00	0.01	0.02	0.01	0.08	0.00	0.07	0.07	0.05
CaO	12.66	11.82	12.91	14.89	10.07	3.99	14.91	15.08	12.23	4.60	13.24	0.03	0.03	0.14	0.58	0.48	0.65	10.32	11.37	9.67
Na2O	3.86	4.34	3.94	2.67	5.24	7.00	2.67	2.55	3.68	7.73	3.47	14.20	0.84	1.91	4.58	8.43	6.56	5.09	4.41	5.19
K2O	0.25	0.36	0.16	0.18	0.43	2.55	0.18	0.14	0.85	1.49	0.20	0.01	15.26	13.25	9.01	5.68	7.33	0.47	0.34	0.43
SrO	0.27	0.19	0.26	0.05	0.22	0.29	0.08	0.10	0.05	0.05	0.13	0.00	0.00	0.00	0.11	0.17	0.08	0.10	0.02	0.09
BaO	0.16	0.05	0.09	0.00	0.16	1.24	0.04	0.00	0.11	0.29	0.10	0.03	0.00	0.14	0.36	0.16	0.28	0.02	0.03	0.06
TOTAL	99.2	98.6	98.9	98.5	98.6	99.0	98.5	98.2	99.1	99.2	98.5	95.5	100.4	99.1	99.6	97.4	98.5	98.1	98.2	98.4
Structural formula (a.p.f.u.)																				
Si	9.54	9.82	9.55	9.09	10.04	11.12	9.09	9.05	9.31	11.17	9.30	10.43	12.18	12.06	12.03	11.10	11.62	10.14	10.00	10.38
Ti	0.02	0.04	0.03	0.01	0.02	0.03	0.01	0.02	0.10	0.02	0.02	0.00	0.00	0.00	0.01	0.01	0.02	0.00	0.01	0.01
Al	6.23	5.88	6.24	6.77	5.86	4.82	6.77	6.80	6.50	4.76	6.61	5.67	3.74	3.89	3.88	4.87	4.31	5.72	5.86	5.48
MgO	0.25	0.24	0.19	0.15	0.09	0.06	0.15	0.15	0.23	0.06	0.15	0.04	0.09	0.10	0.09	0.13	0.07	0.12	0.11	0.12
Fe(ii)	0.02	0.03	0.01	0.01	0.01	0.00	0.00	0.01	0.01	0.00	0.01	0.00	0.00	0.00	0.00	0.01	0.00	0.01	0.01	0.01
Ca	2.49	2.33	2.55	2.96	1.98	0.78	2.96	3.01	2.41	0.88	2.62	0.01	0.01	0.03	0.11	0.10	0.13	2.03	2.24	1.89
Na	1.37	1.55	1.40	0.96	1.86	2.47	0.96	0.92	1.31	2.69	1.24	5.17	0.30	0.68	1.61	3.05	2.34	1.81	1.57	1.83
K	0.06	0.09	0.04	0.04	0.10	0.59	0.04	0.03	0.20	0.34	0.05	0.00	3.56	3.12	2.09	1.35	1.72	0.11	0.08	0.10
SrO	0.03	0.02	0.03	0.01	0.02	0.03	0.01	0.01	0.00	0.00	0.01	0.00	0.00	0.00	0.01	0.02	0.01	0.01	0.00	0.01
BaO	0.01	0.00	0.01	0.00	0.01	0.09	0.00	0.00	0.01	0.02	0.01	0.00	0.00	0.01	0.03	0.01	0.02	0.00	0.00	0.00
An	63.50	58.77	63.83	74.72	50.21	20.25	74.71	75.90	61.45	22.59	67.01	0.12	0.16	0.72	2.96	2.12	3.07	51.36	57.53	49.41
Ab	35.04	39.08	35.22	24.23	47.27	64.33	24.24	23.24	33.49	68.72	31.79	99.82	7.71	17.82	42.26	67.83	55.85	45.87	40.42	47.95
Or	1.46	2.15	0.95	1.05	2.52	15.42	1.05	0.86	5.06	8.69	1.20	0.05	92.13	81.46	54.78	30.05	41.08	2.77	2.05	2.64

Table IV.3: Electron microprobe analysis to plagioclases and feldspars

Occurrence	Montelevar sill																			
	rm50	rm50	rm50	rm50	rm50	rm50	rm50	rm50	rm50	rm50	rm50	rm50	rm50	rm50	rm50	rm50	rm50	rm50	rm50	rm50
sample	b3a	b3b	b3b	b3c	b3c	b1a	b1a	b1a	b1a	b1a	b1b	b1b	b1c	b1c	b2a	b2a	b2a	b2a	b2a	b2a
type	R	C	R	C	R	C	C	R	R	R	C	R	C	R	R	R	C	C	C	C
SiO2	66.26	57.38	66.21	57.97	66.24	59.21	59.16	70.67	70.30	69.35	59.70	67.21	59.39	68.67	54.18	55.76	55.49	53.03	52.05	51.36
TiO2	0.00	0.10	0.02	0.09	0.07	0.10	0.05	0.03	0.05	0.03	0.07	0.09	0.03	0.07	0.08	0.09	0.08	0.11	0.09	0.09
Al2O3	17.68	25.26	17.38	24.87	18.17	25.25	25.02	16.45	17.56	17.88	25.12	19.07	25.18	18.25	27.20	26.14	25.85	27.80	28.42	28.82
FeO	0.30	0.39	1.13	0.44	0.27	0.42	0.41	0.39	0.42	0.40	0.38	0.22	0.43	0.50	0.57	0.46	0.60	0.52	0.62	0.58
MgO	0.01	0.05	0.26	0.04	0.00	0.05	0.05	0.00	0.00	0.00	0.06	0.01	0.06	0.10	0.08	0.05	0.13	0.09	0.08	0.08
CaO	0.31	8.86	0.38	8.46	0.57	8.32	8.11	0.24	0.42	0.30	8.25	1.73	8.40	0.93	10.28	9.42	9.40	11.76	12.66	13.03
Na2O	4.82	5.97	5.36	6.09	5.76	6.22	6.32	3.83	5.55	5.50	6.24	6.52	6.17	5.68	5.25	5.82	5.47	4.43	3.89	3.79
K2O	9.44	0.42	7.76	0.51	7.92	0.64	0.66	10.13	7.84	7.97	0.68	5.73	0.62	7.65	0.31	0.47	0.52	0.33	0.26	0.24
SrO	0.00	0.05	0.00	0.12	0.00	0.10	0.05	0.00	0.00	0.00	0.09	0.00	0.06	0.00	0.08	0.05	0.06	0.08	0.05	0.11
BaO	0.06	0.07	0.05	0.02	0.00	0.08	0.10	0.00	0.01	0.01	0.04	0.42	0.10	0.12	0.06	0.00	0.09	0.00	0.02	0.00
TOTAL	98.9	98.5	98.6	98.6	99.0	100.4	99.9	101.7	102.1	101.4	100.6	101.0	100.4	102.0	98.1	98.3	97.7	98.1	98.1	98.1
Structural formula (a.p.f.u.)																				
Si	12.10	10.44	12.06	10.54	12.02	10.57	10.60	12.46	12.28	12.21	10.62	11.91	10.59	12.08	9.97	10.22	10.23	9.79	9.63	9.52
Ti	0.00	0.01	0.00	0.01	0.01	0.01	0.01	0.00	0.01	0.00	0.01	0.01	0.00	0.01	0.01	0.01	0.01	0.01	0.01	0.01
Al	3.80	5.42	3.73	5.33	3.89	5.31	5.28	3.42	3.62	3.71	5.27	3.98	5.29	3.78	5.90	5.64	5.62	6.05	6.19	6.30
MgO	0.08	0.11	0.31	0.12	0.07	0.11	0.11	0.10	0.11	0.11	0.10	0.06	0.11	0.13	0.16	0.13	0.17	0.14	0.17	0.16
Fe(ii)	0.00	0.01	0.04	0.01	0.00	0.01	0.01	0.00	0.00	0.00	0.01	0.00	0.01	0.01	0.01	0.01	0.02	0.01	0.01	0.01
Ca	0.06	1.73	0.07	1.65	0.11	1.59	1.56	0.05	0.08	0.06	1.57	0.33	1.61	0.17	2.03	1.85	1.86	2.33	2.51	2.59
Na	1.70	2.11	1.89	2.15	2.03	2.15	2.20	1.31	1.88	1.88	2.15	2.24	2.13	1.94	1.88	2.07	1.96	1.58	1.39	1.36
K	2.20	0.10	1.80	0.12	1.83	0.15	0.15	2.28	1.75	1.79	0.15	1.30	0.14	1.72	0.07	0.11	0.12	0.08	0.06	0.06
SrO	0.00	0.00	0.00	0.01	0.00	0.01	0.00	0.00	0.00	0.00	0.01	0.00	0.01	0.00	0.01	0.01	0.01	0.01	0.01	0.01
BaO	0.00	0.01	0.00	0.00	0.00	0.01	0.01	0.00	0.00	0.00	0.00	0.03	0.01	0.01	0.00	0.00	0.01	0.00	0.00	0.00
An	1.54	43.94	1.98	42.09	2.78	40.92	39.90	1.24	2.12	1.51	40.54	8.48	41.40	4.57	51.01	45.91	47.19	58.32	63.27	64.59
Ab	42.99	53.59	50.17	54.90	51.05	55.33	56.26	36.06	50.72	50.42	55.49	57.99	54.96	50.62	47.19	51.36	49.69	39.73	35.17	34.00
Or	55.47	2.47	47.85	3.01	46.17	3.75	3.84	62.70	47.16	48.07	3.97	33.54	3.64	44.82	1.80	2.73	3.12	1.94	1.57	1.41

Table IV.3: Electron microprobe analysis to plagioclases and feldspars

Occurrence	Montelevar sill																			
	rm50	rm50	rm50	rm50	rm50	rm50	rm50	rm50	rm50	rm50	rm50	rm50	rm50	rm50	rm50	rm50	rm50	rm50	rm50	rm50
sample	b2a	b2a	b2a	b2a	b2a	b2a	b2a	b2a	b2a	b2a	b2a	b2a	b2a	b2a	b2a	b2a	b2a	b2b	b2b	b3a
type	C	C	C	C	C	C	C	C	C	C	C	C	C	C	R	R	R	C	R	C
SiO2	53.69	52.87	52.81	54.61	54.43	52.47	53.64	52.62	52.48	53.41	52.79	53.20	53.62	53.05	53.16	54.09	55.28	52.55	55.18	55.20
TiO2	0.05	0.04	0.07	0.07	0.07	0.06	0.05	0.02	0.02	0.07	0.05	0.06	0.05	0.07	0.08	0.07	0.07	0.05	0.12	0.04
Al2O3	27.47	28.03	28.10	26.66	27.03	28.57	27.65	28.25	28.25	27.73	28.24	27.02	27.94	28.01	27.61	27.30	24.73	28.06	26.07	26.42
FeO	0.48	0.46	0.47	0.49	0.42	0.46	0.44	0.43	0.44	0.47	0.48	0.88	0.43	0.46	0.47	0.48	0.53	0.68	0.62	0.43
MgO	0.08	0.11	0.09	0.09	0.08	0.08	0.07	0.08	0.07	0.06	0.06	0.24	0.08	0.08	0.07	0.08	0.08	0.13	0.11	0.07
CaO	11.31	11.77	11.97	10.25	10.78	12.61	11.25	11.95	12.17	11.33	11.98	11.03	11.59	11.47	11.39	11.06	9.58	12.21	9.42	10.32
Na2O	4.70	4.39	4.29	5.24	4.88	4.09	4.67	4.41	4.34	4.61	4.33	4.68	4.56	4.56	4.68	4.89	4.84	4.17	5.78	5.09
K2O	0.36	0.36	0.35	0.49	0.43	0.30	0.39	0.35	0.33	0.37	0.33	0.39	0.35	0.36	0.35	0.36	2.38	0.31	0.41	0.47
SrO	0.04	0.04	0.06	0.02	0.04	0.06	0.04	0.06	0.05	0.08	0.05	0.07	0.07	0.03	0.11	0.02	0.08	0.05	0.03	0.10
BaO	0.07	0.00	0.00	0.03	0.02	0.04	0.03	0.03	0.00	0.05	0.00	0.00	0.01	0.00	0.03	0.05	0.08	0.03	0.07	0.02
TOTAL	98.3	98.1	98.2	98.0	98.2	98.7	98.2	98.2	98.1	98.2	98.3	97.6	98.7	98.1	97.9	98.4	97.6	98.3	97.8	98.1
Structural formula (a.p.f.u.)																				
Si	9.89	9.77	9.75	10.06	10.01	9.65	9.88	9.72	9.70	9.84	9.73	9.87	9.83	9.79	9.83	9.94	10.30	9.70	10.17	10.14
Ti	0.01	0.01	0.01	0.01	0.01	0.01	0.01	0.00	0.00	0.01	0.01	0.01	0.01	0.01	0.01	0.01	0.01	0.01	0.02	0.00
Al	5.96	6.10	6.11	5.79	5.86	6.19	6.00	6.15	6.15	6.02	6.13	5.91	6.04	6.09	6.02	5.91	5.43	6.11	5.66	5.72
MgO	0.13	0.13	0.13	0.14	0.12	0.13	0.12	0.12	0.12	0.13	0.13	0.24	0.12	0.13	0.13	0.13	0.15	0.19	0.17	0.12
Fe(ii)	0.01	0.02	0.01	0.01	0.01	0.01	0.01	0.01	0.01	0.01	0.01	0.04	0.01	0.01	0.01	0.01	0.01	0.02	0.02	0.01
Ca	2.23	2.33	2.37	2.02	2.12	2.48	2.22	2.36	2.41	2.24	2.37	2.19	2.28	2.27	2.26	2.18	1.91	2.42	1.86	2.03
Na	1.68	1.57	1.53	1.87	1.74	1.46	1.67	1.58	1.55	1.65	1.55	1.68	1.62	1.63	1.68	1.74	1.75	1.49	2.06	1.81
K	0.08	0.08	0.08	0.11	0.10	0.07	0.09	0.08	0.08	0.09	0.08	0.09	0.08	0.08	0.08	0.08	0.56	0.07	0.10	0.11
SrO	0.00	0.00	0.01	0.00	0.00	0.01	0.00	0.01	0.01	0.01	0.01	0.01	0.01	0.00	0.01	0.00	0.01	0.01	0.00	0.01
BaO	0.00	0.00	0.00	0.00	0.00	0.00	0.00	0.00	0.00	0.00	0.00	0.00	0.00	0.00	0.00	0.00	0.01	0.00	0.00	0.00
An	55.84	58.45	59.42	50.50	53.54	61.90	55.78	58.72	59.62	56.36	59.31	55.25	57.19	56.92	56.22	54.38	45.29	60.67	46.28	51.36
Ab	42.04	39.44	38.54	46.66	43.89	36.35	41.95	39.25	38.45	41.44	38.73	42.44	40.73	40.94	41.75	43.54	41.35	37.53	51.35	45.87
Or	2.12	2.11	2.04	2.84	2.56	1.75	2.27	2.04	1.93	2.20	1.96	2.30	2.08	2.13	2.03	2.08	13.36	1.80	2.37	2.77

Table IV.3: Electron microprobe analysis to plagioclases and feldspars

Occurrence	Montelevar sill							Mafra gabbro												
	rm50	rm50	rm50	rm50	rm50	rm50	rm50	rm83	rm83	rm83	rm83	rm83	rm83	rm83	rm83	rm83	rm83	rm83	rm83	rm83
sample	b3a	b3a	b3a	b3b	b3b	b3c	b3c	b2a	b2a	b2a	b2a	b2a	b2a	b2a	b2a	b2a	b2a	b2a	b2a	b2a
type	C	R	R	C	R	C	R	R	R	C	C	C	C	C	C	C	C	C	C	C
SiO2	54.44	56.90	66.26	57.38	66.21	57.97	66.24	54.20	53.34	49.94	48.48	48.80	48.21	48.11	47.78	47.95	51.69	48.23	48.64	49.19
TiO2	0.08	0.06	0.00	0.10	0.02	0.09	0.07	0.06	0.11	0.10	0.09	0.12	0.09	0.06	0.08	0.09	0.05	0.06	0.10	0.15
Al2O3	27.05	25.49	17.68	25.26	17.38	24.87	18.17	26.72	28.18	29.97	30.81	30.81	31.11	31.27	31.47	31.42	28.51	31.53	31.05	30.24
FeO	0.40	0.46	0.30	0.39	1.13	0.44	0.27	0.27	0.24	0.34	0.36	0.34	0.37	0.32	0.30	0.34	0.30	0.34	0.33	0.47
MgO	0.07	0.05	0.01	0.05	0.26	0.04	0.00	0.00	0.00	0.01	0.00	0.02	0.01	0.02	0.00	0.01	0.48	0.01	0.00	0.01
CaO	11.37	9.67	0.31	8.86	0.38	8.46	0.57	8.63	11.01	13.86	14.88	14.55	14.98	15.22	15.39	15.32	7.15	15.36	15.03	14.42
Na2O	4.41	5.19	4.82	5.97	5.36	6.09	5.76	5.63	4.79	3.39	2.83	2.94	2.73	2.35	2.32	2.40	6.82	2.34	2.63	2.94
K2O	0.34	0.43	9.44	0.42	7.76	0.51	7.92	0.33	0.29	0.14	0.11	0.11	0.11	0.09	0.09	0.09	0.24	0.08	0.10	0.18
SrO	0.02	0.09	0.00	0.05	0.00	0.12	0.00	0.18	0.21	0.08	0.09	0.09	0.08	0.06	0.08	0.10	0.00	0.12	0.07	0.16
BaO	0.03	0.06	0.06	0.07	0.05	0.02	0.00	0.08	0.10	0.00	0.06	0.09	0.00	0.01	0.00	0.00	0.00	0.03	0.01	0.03
TOTAL	98.2	98.4	98.9	98.5	98.6	98.6	99.0	96.1	98.3	97.8	97.7	97.9	97.7	97.5	97.5	97.7	95.2	98.1	98.0	97.8
Structural formula (a.p.f.u.)																				
Si	10.00	10.38	12.10	10.44	12.06	10.54	12.02	10.13	9.82	9.30	9.08	9.11	9.03	9.02	8.96	8.98	9.78	8.99	9.07	9.19
Ti	0.01	0.01	0.00	0.01	0.00	0.01	0.01	0.01	0.02	0.01	0.01	0.02	0.01	0.01	0.01	0.01	0.01	0.01	0.01	0.02
Al	5.86	5.48	3.80	5.42	3.73	5.33	3.89	5.89	6.12	6.58	6.80	6.78	6.86	6.91	6.96	6.93	6.36	6.93	6.82	6.66
MgO	0.11	0.12	0.08	0.11	0.31	0.12	0.07	0.08	0.07	0.09	0.10	0.09	0.10	0.09	0.08	0.09	0.08	0.09	0.09	0.13
Fe(ii)	0.01	0.01	0.00	0.01	0.04	0.01	0.00	0.00	0.00	0.00	0.00	0.00	0.00	0.00	0.00	0.00	0.08	0.00	0.00	0.00
Ca	2.24	1.89	0.06	1.73	0.07	1.65	0.11	1.73	2.17	2.77	2.98	2.91	3.00	3.06	3.09	3.07	1.45	3.07	3.00	2.89
Na	1.57	1.83	1.70	2.11	1.89	2.15	2.03	2.04	1.71	1.22	1.03	1.06	0.99	0.85	0.84	0.87	2.50	0.85	0.95	1.07
K	0.08	0.10	2.20	0.10	1.80	0.12	1.83	0.08	0.07	0.03	0.03	0.03	0.03	0.02	0.02	0.02	0.06	0.02	0.02	0.04
SrO	0.00	0.01	0.00	0.00	0.00	0.01	0.00	0.02	0.02	0.01	0.01	0.01	0.01	0.01	0.01	0.01	0.00	0.01	0.01	0.02
BaO	0.00	0.00	0.00	0.01	0.00	0.00	0.00	0.01	0.01	0.00	0.00	0.01	0.00	0.00	0.00	0.00	0.00	0.00	0.00	0.00
An	57.53	49.41	1.54	43.94	1.98	42.09	2.78	44.91	54.99	68.76	73.94	72.74	74.68	77.76	78.13	77.52	36.16	77.99	75.47	72.27
Ab	40.42	47.95	42.99	53.59	50.17	54.90	51.05	53.02	43.32	30.40	25.44	26.60	24.67	21.71	21.34	21.97	62.39	21.51	23.92	26.67
Or	2.05	2.64	55.47	2.47	47.85	3.01	46.17	2.07	1.69	0.84	0.62	0.67	0.65	0.52	0.53	0.52	1.45	0.51	0.61	1.05

Table IV.3: Electron microprobe analysis to plagioclases and feldspars

Occurrence	Mafra gabbro												Sines gabbro							
	rm83	rm83	rm83	rm83	rm83	rm83	rm83	rm83	rm83	rm83	rm83	rm83	rm101	rm101	rm101	rm101	rm101	rm101	rm101	rm101
sample	b2a	b2a	b2a	b2a	b2b	b2c	b2d	b3a	b3b	b3c	b3d	b3e	b2a	b2a	b2a	b2a	b2b	b2c	b1a	b1a
type	C	C	R	R	Mx	Mx	Mx	Mx	Mx	Mx	Mx	Mx	C	C	R	R	C	IA	C	R
SiO2	49.87	49.89	51.58	53.39	54.39	56.94	56.83	50.90	56.43	64.37	56.96	58.80	50.90	50.79	55.24	56.59	58.27	57.18	51.17	56.50
TiO2	0.11	0.14	0.12	0.10	0.09	0.07	0.08	0.17	0.06	0.03	0.08	0.05	0.05	0.05	0.09	0.07	0.03	0.07	0.07	0.02
Al2O3	30.47	30.04	29.04	27.92	27.16	25.54	25.74	29.66	26.40	17.95	25.91	24.40	31.39	29.80	28.94	28.13	26.68	26.94	30.62	27.58
FeO	0.31	0.31	0.25	0.24	0.37	0.25	0.28	0.40	0.28	0.01	0.32	0.25	0.40	0.35	0.39	0.36	0.40	0.39	0.38	0.38
MgO	0.00	0.00	0.00	0.00	0.02	0.05	0.01	0.02	0.01	0.00	0.01	0.01	0.02	0.22	0.02	0.03	0.02	0.02	0.04	0.05
CaO	14.16	13.61	13.07	10.97	10.18	7.96	8.41	13.16	9.25	0.00	8.80	7.06	16.09	15.79	12.72	11.52	10.04	10.61	15.01	11.62
Na2O	3.09	3.32	3.32	4.86	5.31	6.33	6.19	3.82	6.12	0.61	6.23	7.24	1.94	2.03	3.91	4.68	5.51	5.18	2.66	4.79
K2O	0.14	0.17	0.14	0.23	0.33	0.31	0.53	0.13	0.25	15.34	0.44	0.63	0.06	0.05	0.07	0.07	0.04	0.03	0.05	0.06
SrO	0.05	0.09	0.16	0.14	0.15	0.14	0.15	0.16	0.16	0.03	0.24	0.17	0.06	0.10	0.12	0.07	0.06	0.12	0.06	0.09
BaO	0.04	0.03	0.05	0.04	0.07	0.08	0.09	0.05	0.11	0.27	0.09	0.08	0.03	0.08	0.04	0.00	0.00	0.06	0.02	0.10
TOTAL	98.2	97.6	97.7	97.9	98.1	97.7	98.3	98.5	99.1	98.6	99.1	98.7	100.9	99.3	101.5	101.5	101.0	100.6	100.1	101.2
Structural formula (a.p.f.u.)																				
Si	9.25	9.31	9.57	9.86	10.01	10.44	10.38	9.41	10.25	12.04	10.34	10.67	9.19	9.34	9.82	10.03	10.33	10.21	9.31	10.07
Ti	0.02	0.02	0.02	0.01	0.01	0.01	0.01	0.02	0.01	0.00	0.01	0.01	0.01	0.01	0.01	0.01	0.00	0.01	0.01	0.00
Al	6.66	6.60	6.35	6.07	5.89	5.52	5.54	6.46	5.65	3.96	5.54	5.22	6.68	6.46	6.07	5.88	5.57	5.67	6.56	5.79
MgO	0.08	0.08	0.07	0.07	0.10	0.07	0.08	0.11	0.08	0.00	0.09	0.07	0.11	0.10	0.10	0.10	0.11	0.10	0.10	0.10
Fe(ii)	0.00	0.00	0.00	0.00	0.00	0.01	0.00	0.00	0.00	0.00	0.00	0.00	0.00	0.03	0.00	0.00	0.00	0.00	0.01	0.01
Ca	2.81	2.72	2.60	2.17	2.01	1.56	1.65	2.61	1.80	0.00	1.71	1.37	3.11	3.11	2.42	2.19	1.91	2.03	2.93	2.22
Na	1.11	1.20	1.19	1.74	1.89	2.25	2.19	1.37	2.16	0.22	2.19	2.55	0.68	0.72	1.35	1.61	1.89	1.79	0.94	1.65
K	0.03	0.04	0.03	0.05	0.08	0.07	0.12	0.03	0.06	3.66	0.10	0.14	0.01	0.01	0.02	0.02	0.01	0.01	0.01	0.01
SrO	0.01	0.01	0.02	0.01	0.02	0.01	0.02	0.02	0.02	0.00	0.03	0.02	0.01	0.01	0.01	0.01	0.01	0.01	0.01	0.01
BaO	0.00	0.00	0.00	0.00	0.01	0.01	0.01	0.00	0.01	0.02	0.01	0.01	0.00	0.01	0.00	0.00	0.00	0.00	0.00	0.01
An	71.14	68.65	67.94	54.75	50.47	40.26	41.52	65.05	44.84	0.00	42.73	33.76	81.80	80.91	63.98	57.37	50.02	52.99	75.47	57.09
Ab	28.06	30.34	31.19	43.86	47.61	57.89	55.36	34.21	53.71	5.73	54.75	62.68	17.83	18.78	35.58	42.20	49.72	46.84	24.22	42.57
Or	0.81	1.01	0.87	1.38	1.92	1.84	3.12	0.74	1.45	94.27	2.52	3.56	0.38	0.31	0.44	0.43	0.26	0.17	0.31	0.34

Table IV.3: Electron microprobe analysis to plagioclases and feldspars

Occurrence	Sines gabbro								Monchique gabbro									Monchique ne-syenite		
	rm101	rm101	rm101	rm101	rm101	rm101	rm101	rm101	mon84	mon84	mon84	mon84	mon84	mon84	mon84	mon84	mon84	749	749	749
sample	b1b	b1b	b1c	b1c	b1d	b1d	b1	b1	b1a	b1a	b1a	b3a	b3a	b3b	b3b	b3c	b3c	b1a	b1a	b1b
type	C	R	C	R	C	R	IC	IC	C	C	C	C	R	C	R	C	R	C	R	C
SiO2	56.05	58.94	51.01	58.79	55.96	54.16	51.91	53.65	53.97	46.64	55.21	55.92	56.21	54.72	55.70	48.84	60.14	67.82	69.34	67.56
TiO2	0.05	0.05	0.11	0.04	0.06	0.08	0.01	0.06	0.00	0.00	0.02	0.07	0.09	0.10	0.11	0.01	0.00	0.00	0.01	0.02
Al2O3	27.56	27.00	30.89	26.16	27.86	27.48	30.18	28.72	30.05	31.97	28.16	26.63	26.26	27.08	26.64	29.03	22.64	17.74	17.91	17.96
FeO	0.34	0.24	0.36	0.30	0.29	1.53	0.29	0.30	1.04	0.05	0.06	0.19	0.17	0.23	0.27	0.09	0.10	0.16	0.19	0.22
MgO	0.05	0.02	0.02	0.14	0.00	1.72	0.42	0.04	0.73	0.00	0.00	0.00	0.00	0.01	0.00	0.00	0.01	0.02	0.00	0.01
CaO	11.61	9.67	15.07	9.73	11.93	10.12	14.76	12.47	3.42	5.42	1.60	9.81	9.47	10.21	9.78	1.98	0.31	0.06	0.05	0.04
Na2O	4.52	5.79	2.60	5.58	4.45	4.41	2.65	3.94	5.16	10.28	11.65	5.35	5.68	5.21	5.32	13.52	12.11	5.12	6.63	5.03
K2O	0.11	0.05	0.05	0.05	0.04	0.74	0.04	0.08	0.07	0.08	0.82	0.28	0.26	0.21	0.29	0.12	0.41	9.18	6.95	9.43
SrO	0.05	0.18	0.04	0.14	0.01	0.10	0.06	0.07	0.19	0.00	0.00	0.64	0.61	0.74	0.75	0.00	0.00	0.00	0.00	0.00
BaO	0.02	0.03	0.00	0.03	0.00	0.02	0.04	0.04	0.00	0.00	0.04	0.17	0.15	0.12	0.21	0.02	0.00	0.11	0.10	0.06
TOTAL	100.4	102.0	100.1	101.0	100.6	100.3	100.4	99.4	94.6	94.4	97.6	99.1	98.9	98.6	99.1	93.6	95.7	100.2	101.2	100.3
Structural formula (a.p.f.u.)																				
Si	10.05	10.35	9.27	10.43	10.02	9.83	9.42	9.76	10.04	9.01	10.16	10.19	10.25	10.04	10.16	9.50	11.14	12.18	12.22	12.13
Ti	0.01	0.01	0.01	0.01	0.01	0.01	0.00	0.01	0.00	0.00	0.00	0.01	0.01	0.01	0.02	0.00	0.00	0.00	0.00	0.00
Al	5.83	5.59	6.62	5.47	5.88	5.88	6.45	6.16	6.59	7.28	6.11	5.72	5.64	5.86	5.73	6.66	4.94	3.76	3.72	3.80
MgO	0.09	0.06	0.10	0.08	0.08	0.41	0.08	0.08	0.29	0.01	0.02	0.05	0.05	0.06	0.07	0.03	0.03	0.04	0.05	0.06
Fe(ii)	0.01	0.00	0.00	0.02	0.00	0.26	0.06	0.01	0.11	0.00	0.00	0.00	0.00	0.00	0.00	0.00	0.00	0.00	0.00	0.00
Ca	2.23	1.82	2.93	1.85	2.29	1.97	2.87	2.43	0.68	1.12	0.32	1.91	1.85	2.01	1.91	0.41	0.06	0.01	0.01	0.01
Na	1.57	1.97	0.92	1.92	1.54	1.55	0.93	1.39	1.86	3.85	4.16	1.89	2.01	1.85	1.88	5.10	4.35	1.78	2.27	1.75
K	0.02	0.01	0.01	0.01	0.01	0.17	0.01	0.02	0.02	0.02	0.19	0.06	0.06	0.05	0.07	0.03	0.10	2.10	1.56	2.16
SrO	0.01	0.02	0.00	0.01	0.00	0.01	0.01	0.01	0.02	0.00	0.00	0.07	0.06	0.08	0.08	0.00	0.00	0.00	0.00	0.00
BaO	0.00	0.00	0.00	0.00	0.00	0.00	0.00	0.00	0.00	0.00	0.00	0.01	0.01	0.01	0.01	0.00	0.00	0.01	0.01	0.00
An	58.29	47.88	75.98	48.91	59.58	53.31	75.32	63.33	26.66	22.48	6.76	49.48	47.23	51.36	49.49	7.46	1.36	0.29	0.22	0.22
Ab	41.07	51.86	23.73	50.77	40.19	42.07	24.44	36.18	72.70	77.13	89.13	48.87	51.25	47.39	48.74	92.02	96.51	45.73	59.08	44.68
Or	0.65	0.27	0.29	0.31	0.23	4.62	0.24	0.48	0.64	0.39	4.11	1.65	1.52	1.25	1.77	0.53	2.13	53.99	40.70	55.10

Table IV.3: Electron microprobe analysis to plagioclases and feldspars

Occurrence	Monchique ne-syenite								Lomba dos Pianos sill	Malveira da serra sill
	749	749	749	749	749	749	749	749		
sample	b1b	b1c	b2a	b2a	b2b	b2b	b2c	b2c	rm9 b7	rm25 b2
type	R	C	R	C	R	C	R	C	PR	Mx
SiO2	68.61	67.62	67.38	68.51	67.76	54.75	67.30	66.67	51.28	64.83
TiO2	0.02	0.06	0.01	0.02	0.02	0.01	0.05	0.00	0.02	0.00
Al2O3	17.75	18.32	18.23	17.70	17.84	22.34	17.79	17.47	29.59	20.41
FeO	0.18	0.17	0.16	0.19	0.20	0.15	0.21	0.20	0.47	0.22
MgO	0.00	0.00	0.00	0.00	0.00	0.00	0.00	0.00	0.04	0.11
CaO	0.03	0.34	0.20	0.09	0.06	0.08	0.05	0.00	14.02	1.05
Na2O	4.59	5.86	5.79	4.86	5.18	12.62	4.83	2.47	2.80	10.97
K2O	9.94	7.78	7.73	9.39	9.15	1.58	9.53	13.00	0.14	0.12
SrO	0.00	0.00	0.00	0.00	0.00	0.00	0.00	0.00	0.17	0.11
BaO	0.14	0.25	0.58	0.09	0.07	0.08	0.13	0.05	0.00	0.00
TOTAL	101.3	100.4	100.1	100.8	100.3	91.6	99.9	99.9	98.5	97.8
Structural formula (a.p.f.u.)										
Si	12.21	12.08	12.10	12.22	12.16	10.77	12.15	12.18	9.46	11.65
Ti	0.00	0.01	0.00	0.00	0.00	0.00	0.01	0.00	0.00	0.00
Al	3.72	3.86	3.86	3.72	3.77	5.18	3.78	3.76	6.43	4.32
MgO	0.05	0.04	0.04	0.05	0.05	0.04	0.06	0.05	0.13	0.06
Fe(ii)	0.00	0.00	0.00	0.00	0.00	0.00	0.00	0.00	0.01	0.02
Ca	0.01	0.06	0.04	0.02	0.01	0.02	0.01	0.00	2.77	0.20
Na	1.58	2.03	2.01	1.68	1.80	4.81	1.69	0.87	1.00	3.82
K	2.26	1.77	1.77	2.14	2.09	0.40	2.19	3.03	0.03	0.03
SrO	0.00	0.00	0.00	0.00	0.00	0.00	0.00	0.00	0.02	0.01
BaO	0.01	0.02	0.04	0.01	0.01	0.01	0.01	0.00	0.00	0.00
An	0.16	1.66	1.02	0.46	0.28	0.33	0.23	0.00	72.81	5.00
Ab	41.14	52.47	52.69	43.81	46.13	92.08	43.39	22.37	26.32	94.35
Or	58.70	45.87	46.29	55.73	53.60	7.60	56.38	77.63	0.87	0.65

Table IV.4: Electron microprobe analysis to Amphiboles

Occurrence	Lomba dos Pianos sill					Malveira da Serra sill														
	rm9	rm9	rm9	rm9	rm9	rm25	rm25	rm25	rm25	rm25	rm25	rm25	rm25	rm25	rm25	rm25	rm25	rm25	rm25	rm25
sample	b3a	b3a	b3a	b3b	b3b	b1a	b1a	b1a	b1a	b1a	b1a	b1a	b1a	b1a	b1a	b1a	b1a	b1a	b1a	b1a
type	X	X	X	X	X	PR	PR	PM	PM	PM	PM	PM	PM	PM	PC	PC	PC	PC	PC	PC
SiO2	38.75	38.34	38.12	38.39	38.57	39.07	38.89	39.75	36.66	39.22	39.36	39.88	39.56	38.98	38.06	38.70	38.77	38.17	39.35	37.88
TiO2	5.21	5.30	5.40	5.31	5.23	4.99	5.47	5.50	5.46	5.83	4.62	4.63	4.57	4.68	4.48	4.65	4.56	4.55	4.18	4.54
Al2O3	12.99	13.04	13.06	12.91	13.00	12.75	12.73	12.53	12.45	12.77	13.45	13.47	13.49	13.56	13.97	14.01	13.94	14.04	14.24	14.28
Cr2O3	0.06	0.00	0.01	0.00	0.07	0.00	0.00	0.00	0.00	0.00	0.11	0.09	0.08	0.13	0.03	0.01	0.01	0.00	0.00	0.02
FeO	10.99	10.74	11.22	11.21	10.85	13.02	10.33	9.89	9.21	9.53	9.18	9.10	9.13	10.33	12.70	12.69	12.51	12.78	11.87	12.55
MnO	0.12	0.17	0.11	0.08	0.09	0.25	0.13	0.13	0.09	0.10	0.09	0.08	0.05	0.08	0.15	0.17	0.14	0.19	0.13	0.14
MgO	12.79	12.80	12.61	12.78	12.56	11.44	13.28	13.64	12.46	13.68	14.37	14.35	14.41	13.17	11.46	11.32	11.56	11.46	10.76	11.31
CaO	12.28	12.57	12.56	12.71	12.55	12.30	12.65	12.85	16.37	13.13	12.71	12.69	12.72	12.70	12.47	12.47	12.52	12.33	11.77	12.64
Na2O	2.48	2.59	2.50	2.79	2.53	2.73	2.59	2.53	2.56	2.47	2.37	2.40	2.32	2.51	2.73	2.73	2.63	2.63	2.48	2.68
K2O	0.91	0.87	0.87	0.85	0.90	1.32	0.98	1.00	0.97	0.99	1.26	1.33	1.36	1.25	1.11	1.10	1.09	1.11	1.04	1.09
F	0.15	0.22	0.25	0.15	0.15	0.06	0.29	0.15	0.21	0.14	0.23	0.10	0.03	0.00	0.03	0.00	0.11	0.05	0.24	0.20
ZnO	0.04	0.01	0.00	0.00	0.00	0.01	0.08	0.02	0.00	0.00	0.08	0.06	0.04	0.02	0.06	0.03	0.05	0.00	0.04	0.06
Total	96.75	96.64	96.70	97.17	96.50	97.92	97.42	97.98	96.43	97.84	97.82	98.18	97.76	97.42	97.24	97.90	97.88	97.32	96.10	97.40
Structural formula (a.p.f.u.)																				
Si	5.83	5.78	5.76	5.77	5.82	5.87	5.82	5.88	5.60	5.81	5.82	5.86	5.84	5.81	5.75	5.80	5.81	5.76	5.96	5.72
Al (iv)	2.17	2.22	2.24	2.23	2.18	2.13	2.18	2.12	2.24	2.19	2.18	2.14	2.16	2.19	2.25	2.20	2.19	2.24	2.04	2.28
site T total	8.00	8.00	8.00	8.00	8.00	8.00	8.00	8.00	7.84	8.00	8.00	8.00	8.00	8.00	8.00	8.00	8.00	8.00	8.00	8.00
Al (vi)	0.13	0.10	0.09	0.06	0.13	0.13	0.06	0.06	0.00	0.04	0.16	0.19	0.18	0.19	0.24	0.27	0.27	0.26	0.50	0.27
Ti	0.59	0.60	0.61	0.60	0.59	0.56	0.62	0.61	0.63	0.65	0.51	0.51	0.51	0.52	0.51	0.52	0.51	0.52	0.48	0.52
Cr	0.01	0.00	0.00	0.00	0.01	0.00	0.00	0.00	0.00	0.00	0.01	0.01	0.01	0.02	0.00	0.00	0.00	0.00	0.00	0.00
Fe(iii)	0.00	0.00	0.00	0.00	0.00	0.00	0.00	0.00	0.00	0.00	0.04	0.00	0.02	0.00	0.00	0.00	0.00	0.00	0.00	0.00
Fe(ii)	1.38	1.36	1.42	1.41	1.37	1.64	1.29	1.22	1.18	1.18	1.10	1.12	1.11	1.29	1.61	1.59	1.57	1.61	1.50	1.59
Mn	0.02	0.02	0.01	0.01	0.01	0.03	0.02	0.02	0.01	0.01	0.01	0.01	0.01	0.01	0.02	0.02	0.02	0.02	0.02	0.02
Mg	2.87	2.88	2.84	2.87	2.83	2.56	2.96	3.01	2.84	3.02	3.17	3.14	3.17	2.93	2.58	2.53	2.58	2.58	2.43	2.55
site C total	5.00	4.96	4.98	4.95	4.94	4.93	4.95	4.92	4.65	4.90	5.00	4.99	5.00	4.96	4.96	4.94	4.95	4.99	4.92	4.94
Ca	1.98	2.03	2.03	2.05	2.03	1.98	2.03	2.04	2.68	2.08	2.01	2.00	2.01	2.03	2.02	2.00	2.01	1.99	1.91	2.05
Na	0.02	0.00	0.00	0.00	0.00	0.02	0.00	0.00	0.00	0.00	0.00	0.00	0.00	0.00	0.00	0.00	0.00	0.01	0.09	0.00
site B total	2.00	2.00	2.00	2.00	2.00	2.00	2.00	2.00	2.00	2.00	2.00	2.00	2.00	2.00	2.00	2.00	2.00	2.00	2.00	2.00
Na	0.70	0.79	0.77	0.86	0.77	0.78	0.78	0.76	1.44	0.79	0.69	0.68	0.68	0.75	0.82	0.80	0.77	0.76	0.64	0.83
K	0.17	0.17	0.17	0.16	0.17	0.25	0.19	0.19	0.19	0.19	0.24	0.25	0.26	0.24	0.21	0.21	0.21	0.21	0.20	0.21
site A total	0.88	0.96	0.93	1.02	0.94	1.03	0.97	0.95	1.63	0.98	0.93	0.93	0.93	0.99	1.03	1.01	0.98	0.98	0.84	1.04

P- Phenocryst, R- Rim, C- Core, M - Middle, Mx - Matrix, Am amygdule, X - xenocryst, Xen - crystal in xenolith, Poi - Poikilitic crystal; I inclusion; Cpx - clinopyronexe

Table IV.4: Electron microprobe analysis to Amphiboles

Occurrence	Malveira da Serra sill																			
	rm25	rm25	rm25	rm25	rm25	rm25	rm25	rm25	rm25	rm25	rm25	rm25	rm25	rm25	rm25	rm25	rm25	rm25	rm25	rm25
sample	b1a	b1a	b1a	b1a	b1a	b1b	b1b	b1b	b1b	b1b	b1b	b1b	b1b	b1b	b1b	b1b	b1b	b1b	b1b	b1b
type	PM	PM	PM	PM	PR	PR	PM	PC	PC	PC	PC	PC	PC	PC	PC	PC	PC	PC	PC	PC
SiO2	39.44	39.30	38.98	38.57	39.13	38.34	39.57	38.44	38.55	38.38	38.29	38.46	39.00	38.66	38.49	38.85	38.33	38.76	38.40	38.36
TiO2	4.62	4.58	4.74	5.83	5.24	6.23	4.65	4.79	4.66	4.25	4.40	4.44	4.53	4.66	4.50	4.70	4.75	4.62	4.76	4.73
Al2O3	13.50	13.51	13.92	13.39	13.23	13.41	13.47	14.23	14.15	14.02	14.35	14.23	14.19	14.12	13.97	14.03	14.16	14.02	14.17	14.14
Cr2O3	0.10	0.13	0.08	0.01	0.03	0.04	0.09	0.01	0.00	0.01	0.00	0.05	0.04	0.00	0.00	0.00	0.01	0.04	0.06	0.03
FeO	9.48	8.93	9.30	9.68	10.26	9.91	9.27	11.95	12.01	12.18	12.16	12.14	11.90	12.09	12.69	12.37	11.98	12.04	11.95	12.01
MnO	0.07	0.02	0.06	0.06	0.12	0.13	0.05	0.22	0.20	0.11	0.20	0.16	0.17	0.20	0.17	0.15	0.15	0.20	0.18	0.16
MgO	14.02	14.40	14.04	13.43	13.14	13.05	14.12	11.67	11.79	11.71	11.79	11.68	11.83	11.72	11.47	11.43	11.68	11.72	11.52	11.61
CaO	12.86	12.65	12.64	13.33	12.73	13.25	12.78	12.57	12.68	12.70	12.67	12.62	12.49	12.51	12.48	12.63	12.51	12.56	12.63	12.37
Na2O	2.44	2.34	2.35	2.30	2.54	2.29	2.40	2.70	2.70	2.61	2.63	2.65	2.70	2.69	2.62	2.75	2.65	2.60	2.64	2.72
K2O	1.32	1.34	1.34	1.06	1.11	1.09	1.26	0.99	0.97	1.05	0.97	0.98	0.99	0.94	0.99	0.93	0.95	0.94	0.97	0.97
F	0.02	0.09	0.16	0.12	0.46	0.22	0.00	0.01	0.12	0.16	0.00	0.16	0.05	0.06	0.12	0.03	0.00	0.16	0.00	0.00
ZnO	0.06	0.10	0.04	0.03	0.00	0.11	0.04	0.04	0.05	0.02	0.08	0.05	0.00	0.00	0.06	0.02	0.00	0.02	0.01	0.00
Total	97.92	97.40	97.63	97.80	97.99	98.05	97.69	97.61	97.87	97.19	97.54	97.60	97.89	97.63	97.55	97.89	97.16	97.67	97.30	97.09
Structural formula (a.p.f.u.)																				
Si	5.83	5.82	5.77	5.73	5.82	5.70	5.84	5.76	5.77	5.79	5.75	5.77	5.81	5.79	5.79	5.81	5.76	5.81	5.77	5.77
Al (iv)	2.17	2.18	2.23	2.27	2.18	2.30	2.16	2.24	2.23	2.21	2.25	2.23	2.19	2.21	2.21	2.19	2.24	2.19	2.23	2.23
site T total	8.00	8.00	8.00	8.00	8.00	8.00	8.00	8.00	8.00	8.00	8.00	8.00	8.00	8.00	8.00	8.00	8.00	8.00	8.00	8.00
Al (vi)	0.18	0.18	0.20	0.07	0.14	0.05	0.19	0.27	0.26	0.28	0.29	0.29	0.31	0.28	0.27	0.28	0.27	0.28	0.28	0.28
Ti	0.51	0.51	0.53	0.65	0.59	0.70	0.52	0.54	0.52	0.48	0.50	0.50	0.51	0.52	0.51	0.53	0.54	0.52	0.54	0.53
Cr	0.01	0.02	0.01	0.00	0.00	0.00	0.01	0.00	0.00	0.00	0.00	0.01	0.00	0.00	0.00	0.00	0.00	0.00	0.01	0.00
Fe(iii)	0.00	0.01	0.02	0.00	0.00	0.00	0.00	0.00	0.00	0.00	0.00	0.00	0.00	0.00	0.00	0.00	0.00	0.00	0.00	0.00
Fe(ii)	1.17	1.09	1.13	1.20	1.28	1.23	1.14	1.50	1.50	1.54	1.53	1.52	1.48	1.51	1.60	1.55	1.51	1.51	1.50	1.51
Mn	0.01	0.00	0.01	0.01	0.01	0.02	0.01	0.03	0.03	0.01	0.03	0.02	0.02	0.02	0.02	0.02	0.02	0.03	0.02	0.02
Mg	3.09	3.18	3.10	2.97	2.91	2.89	3.11	2.61	2.63	2.63	2.64	2.61	2.63	2.61	2.57	2.55	2.62	2.62	2.58	2.60
site C total	4.97	5.00	5.00	4.90	4.93	4.89	4.98	4.94	4.94	4.95	4.97	4.96	4.95	4.96	4.97	4.92	4.95	4.95	4.93	4.95
Ca	2.04	2.01	2.01	2.12	2.03	2.11	2.02	2.02	2.03	2.05	2.04	2.03	1.99	2.01	2.01	2.02	2.01	2.01	2.03	1.99
Na	0.00	0.00	0.00	0.00	0.00	0.00	0.00	0.00	0.00	0.00	0.00	0.00	0.01	0.00	0.00	0.00	0.00	0.00	0.00	0.01
site B total	2.00	2.00	2.00	2.00	2.00	2.00	2.00	2.00	2.00	2.00	2.00	2.00	2.00	2.00	2.00	2.00	2.00	2.00	2.00	2.00
Na	0.73	0.68	0.68	0.78	0.76	0.77	0.71	0.80	0.82	0.82	0.80	0.80	0.77	0.79	0.78	0.82	0.79	0.77	0.80	0.79
K	0.25	0.25	0.25	0.20	0.21	0.21	0.24	0.19	0.19	0.20	0.19	0.19	0.19	0.18	0.19	0.18	0.18	0.18	0.19	0.19
site A total	0.98	0.94	0.93	0.98	0.97	0.98	0.95	0.99	1.00	1.02	0.99	0.99	0.96	0.97	0.97	1.00	0.97	0.95	0.99	0.97

Table IV.4: Electron microprobe analysis to Amphiboles

Occurrence	Malveira da Serra sill																		Ribeira d'Ilhas plu	
	rm25	rm25	rm25	rm25	rm25	rm25	rm25	rm25	rm25	rm25	rm25	rm25	rm25	rm25	rm25	rm25	rm25	rm25	rm36	rm36
sample	b1b	b1b	b1b	b1b	b1b	b1	b2a	b2a	b2a	b2a	b2a	b2a	b2b	b2b	b5	b5	b5	b5	b2a	b2a
type	PC	PM	PM	PM	PR	Mx	PR	PR	PC	PC	PM	PR	PR	PC	PC	PC	PM	PR	X	X
SiO2	38.62	39.24	39.16	38.69	39.19	39.11	38.91	38.38	39.19	39.41	39.24	39.58	37.94	38.35	39.36	39.63	39.07	39.27	38.79	39.70
TiO2	4.61	4.76	4.65	6.12	5.07	5.37	5.23	6.03	4.70	4.77	4.34	4.27	4.65	5.83	4.29	4.18	4.41	4.48	5.14	4.19
Al2O3	14.14	13.67	13.69	13.42	12.83	13.06	12.91	13.20	13.61	13.46	13.32	13.29	12.22	13.50	13.43	13.22	13.60	13.92	14.22	13.60
Cr2O3	0.00	0.05	0.08	0.10	0.00	0.03	0.00	0.01	0.09	0.05	0.01	0.01	0.00	0.00	0.01	0.04	0.05	0.18	0.01	0.10
FeO	12.17	9.36	9.26	9.42	10.89	10.48	10.38	9.59	9.14	9.19	11.23	11.43	12.15	10.30	11.46	11.34	10.58	8.69	9.17	9.49
MnO	0.22	0.09	0.05	0.09	0.12	0.16	0.17	0.05	0.06	0.04	0.08	0.14	0.22	0.15	0.09	0.07	0.10	0.06	0.06	0.02
MgO	11.65	14.04	14.18	13.32	12.68	12.97	13.22	13.37	14.10	14.11	12.79	12.62	11.42	12.97	12.82	12.76	13.14	14.31	13.56	13.76
CaO	12.60	12.88	12.85	13.23	12.64	12.28	12.63	13.07	12.76	12.68	12.53	12.50	13.65	12.36	12.63	12.61	12.64	12.60	12.53	12.63
Na2O	2.63	2.28	2.28	2.36	2.65	2.59	2.56	2.37	2.26	2.28	2.54	2.48	2.68	2.58	2.41	2.34	2.29	2.28	2.78	2.78
K2O	0.96	1.38	1.32	1.08	1.16	1.28	1.05	1.07	1.30	1.32	1.27	1.27	1.17	1.13	1.33	1.34	1.49	1.53	1.39	1.36
F	0.01	0.10	0.01	0.14	0.34	0.21	0.19	0.35	0.12	0.29	0.00	0.09	0.37	0.19	0.09	0.00	0.25	0.20	0.00	0.01
ZnO	0.00	0.03	0.08	0.07	0.06	0.04	0.06	0.01	0.00	0.03	0.02	0.01	0.05	0.04	0.01	0.08	0.00	0.03	0.00	0.06
Total	97.60	97.87	97.58	98.03	97.63	97.58	97.30	97.48	97.33	97.64	97.37	97.69	96.51	97.38	97.93	97.60	97.62	97.55	97.65	97.68
Structural formula (a.p.f.u.)																				
Si	5.79	5.80	5.80	5.73	5.87	5.84	5.82	5.73	5.81	5.84	5.87	5.90	5.82	5.73	5.86	5.91	5.83	5.81	5.74	5.88
Al (iv)	2.21	2.20	2.20	2.27	2.13	2.16	2.18	2.27	2.19	2.16	2.13	2.10	2.18	2.27	2.14	2.09	2.17	2.19	2.26	2.12
site T total	8.00	8.00	8.00	8.00	8.00	8.00	8.00	8.00	8.00	8.00	8.00	8.00	8.00	8.00	8.00	8.00	8.00	8.00	8.00	8.00
Al (vi)	0.28	0.18	0.19	0.07	0.13	0.13	0.10	0.05	0.19	0.19	0.22	0.24	0.04	0.11	0.22	0.24	0.22	0.24	0.22	0.25
Ti	0.52	0.53	0.52	0.68	0.57	0.60	0.59	0.68	0.52	0.53	0.49	0.48	0.54	0.66	0.48	0.47	0.49	0.50	0.57	0.47
Cr	0.00	0.01	0.01	0.01	0.00	0.00	0.00	0.00	0.01	0.01	0.00	0.00	0.00	0.00	0.00	0.00	0.01	0.02	0.00	0.01
Fe(iii)	0.00	0.00	0.00	0.00	0.00	0.00	0.00	0.00	0.00	0.00	0.00	0.00	0.00	0.00	0.00	0.00	0.00	0.00	0.00	0.00
Fe(ii)	1.52	1.16	1.15	1.17	1.36	1.31	1.30	1.20	1.13	1.14	1.40	1.43	1.56	1.29	1.43	1.41	1.32	1.08	1.13	1.17
Mn	0.03	0.01	0.01	0.01	0.01	0.02	0.02	0.01	0.01	0.01	0.01	0.02	0.03	0.02	0.01	0.01	0.01	0.01	0.01	0.00
Mg	2.60	3.09	3.13	2.94	2.83	2.88	2.95	2.97	3.12	3.12	2.85	2.81	2.61	2.89	2.85	2.84	2.92	3.16	2.99	3.04
site C total	4.95	4.98	5.00	4.88	4.91	4.95	4.96	4.90	4.99	4.99	4.97	4.97	4.77	4.96	4.99	4.97	4.98	5.00	4.93	4.94
Ca	2.02	2.04	2.04	2.10	2.03	1.96	2.02	2.09	2.03	2.01	2.01	2.00	2.25	1.98	2.02	2.02	2.02	2.00	1.99	2.00
Na	0.00	0.00	0.00	0.00	0.00	0.04	0.00	0.00	0.00	0.00	0.00	0.00	0.00	0.02	0.00	0.00	0.00	0.00	0.01	0.00
site B total	2.00	2.00	2.00	2.00	2.00	2.00	2.00	2.00	2.00	2.00	2.00	2.00	2.00	2.00	2.00	2.00	2.00	2.00	2.00	2.00
Na	0.79	0.69	0.69	0.77	0.80	0.71	0.76	0.77	0.68	0.67	0.74	0.71	1.04	0.73	0.71	0.69	0.68	0.65	0.78	0.80
K	0.18	0.26	0.25	0.20	0.22	0.24	0.20	0.20	0.25	0.25	0.24	0.24	0.23	0.21	0.25	0.25	0.28	0.29	0.26	0.26
site A total	0.97	0.95	0.94	0.98	1.02	0.95	0.96	0.98	0.92	0.92	0.99	0.95	1.27	0.94	0.97	0.95	0.97	0.94	1.05	1.06

Table IV.4: Electron microprobe analysis to Amphiboles

Occurrence	Ribeira d'Ilhas plug							LVC flow					Eiras de Faião sill							
	rm36	rm36	rm36	rm36	rm36	rm36	rm36	rm43	rm43	rm43	rm43	rm43	rm47	rm47	rm47	rm47	rm47	rm47	rm47	rm47
sample	b2a	b2a	b2b	b2b	b2b	b4a	b4b	b3a	b3a	b3a	b3b	b3b	b2a	b2b	b2c	b2d	b2e	b2f	b2g	b2g
type	X	X	X	X	X	Am	Am	X	X	X	X	X	Xen	Xen	Xen	Xen	Xen	Xen	PC	PR
SiO2	39.33	38.66	39.07	37.99	39.18	37.40	37.42	38.13	38.15	38.31	38.23	38.46	37.94	37.25	37.39	37.33	37.44	38.02	37.21	38.35
TiO2	4.20	4.33	4.23	6.55	4.04	6.15	6.23	5.91	5.71	5.44	5.89	5.77	4.73	4.67	4.65	5.55	5.13	5.09	5.33	5.55
Al2O3	13.66	13.98	13.83	13.68	14.24	13.43	13.82	13.62	13.69	13.75	13.73	13.66	12.32	12.39	12.27	12.47	12.27	12.12	12.81	11.94
Cr2O3	0.00	0.03	0.01	0.00	0.07	0.02	0.00	0.04	0.00	0.05	0.02	0.00	0.00	0.05	0.02	0.03	0.00	0.02	0.00	0.00
FeO	10.42	9.97	9.40	9.10	9.46	10.51	9.64	8.85	9.02	9.07	8.93	8.91	13.75	13.95	13.57	13.28	12.86	13.23	12.04	10.73
MnO	0.07	0.07	0.05	0.10	0.05	0.17	0.18	0.04	0.01	0.02	0.05	0.06	0.21	0.28	0.26	0.19	0.16	0.19	0.17	0.13
MgO	13.07	13.30	13.31	13.31	13.91	12.71	13.10	14.14	14.04	14.23	14.11	13.85	11.27	11.54	11.37	11.42	11.75	11.43	12.13	12.51
CaO	12.31	12.32	12.75	13.15	12.57	12.06	12.58	12.97	12.93	12.60	12.91	12.96	12.54	12.56	12.77	12.64	12.79	12.56	12.84	12.93
Na2O	2.79	2.81	2.45	2.44	2.66	2.46	2.44	2.23	2.06	2.34	2.23	2.20	2.80	2.80	2.60	2.58	2.62	2.66	2.69	2.50
K2O	1.40	1.41	1.53	1.08	1.46	1.27	1.16	1.44	1.52	1.56	1.45	1.46	1.19	1.23	1.21	1.46	1.37	1.28	1.24	1.27
F	0.10	0.13	0.17	0.33	0.18	0.43	0.38	0.07	0.20	0.16	0.16	0.07	0.00	0.13	0.13	0.00	0.14	0.24	0.12	0.13
ZnO	0.00	0.05	0.07	0.06	0.07	0.07	0.07	0.02	0.05	0.01	0.04	0.03	0.10	0.03	0.00	0.00	0.00	0.00	0.00	0.08
Total	97.35	97.06	96.87	97.80	97.89	96.68	97.00	97.47	97.36	97.54	97.73	97.43	96.85	96.88	96.23	96.94	96.53	96.85	96.58	96.12
Structural formula (a.p.f.u.)																				
Si	5.87	5.79	5.85	5.65	5.80	5.67	5.63	5.67	5.68	5.69	5.67	5.71	5.81	5.73	5.77	5.71	5.75	5.82	5.68	5.84
Al (iv)	2.13	2.21	2.15	2.35	2.20	2.33	2.37	2.33	2.32	2.31	2.33	2.29	2.19	2.25	2.23	2.25	2.22	2.18	2.31	2.14
site T total	8.00	8.00	8.00	8.00	8.00	8.00	8.00	8.00	8.00	8.00	8.00	8.00	8.00	7.98	8.00	7.96	7.97	8.00	7.99	7.99
Al (vi)	0.27	0.25	0.28	0.05	0.28	0.06	0.08	0.05	0.09	0.10	0.07	0.10	0.03	0.00	0.00	0.00	0.00	0.01	0.00	0.00
Ti	0.47	0.49	0.48	0.73	0.45	0.70	0.70	0.66	0.64	0.61	0.66	0.64	0.54	0.54	0.54	0.64	0.59	0.59	0.61	0.64
Cr	0.00	0.00	0.00	0.00	0.01	0.00	0.00	0.00	0.00	0.01	0.00	0.00	0.00	0.01	0.00	0.00	0.00	0.00	0.00	0.00
Fe(iii)	0.00	0.00	0.00	0.00	0.00	0.00	0.00	0.00	0.00	0.00	0.00	0.00	0.00	0.00	0.00	0.00	0.00	0.00	0.00	0.00
Fe(ii)	1.30	1.25	1.18	1.13	1.17	1.33	1.21	1.10	1.12	1.13	1.11	1.11	1.76	1.79	1.75	1.70	1.65	1.69	1.54	1.37
Mn	0.01	0.01	0.01	0.01	0.01	0.02	0.02	0.01	0.00	0.00	0.01	0.01	0.03	0.04	0.03	0.02	0.02	0.03	0.02	0.02
Mg	2.91	2.97	2.97	2.95	3.07	2.87	2.94	3.13	3.12	3.15	3.12	3.07	2.57	2.65	2.62	2.60	2.69	2.61	2.76	2.84
site C total	4.96	4.97	4.91	4.87	4.99	4.99	4.95	4.95	4.97	5.00	4.96	4.93	4.94	5.02	4.95	4.97	4.95	4.92	4.94	4.86
Ca	1.97	1.98	2.04	2.09	1.99	1.96	2.03	2.07	2.06	2.01	2.05	2.06	2.06	2.07	2.11	2.07	2.10	2.06	2.10	2.11
Na	0.03	0.02	0.00	0.00	0.01	0.04	0.00	0.00	0.00	0.00	0.00	0.00	0.00	0.00	0.00	0.00	0.00	0.00	0.00	0.00
site B total	2.00	2.00	2.00	2.00	2.00	2.00	2.00	2.00	2.00	2.00	2.00	2.00	2.00	2.00	2.00	2.00	2.00	2.00	2.00	2.00
Na	0.77	0.79	0.76	0.80	0.76	0.68	0.74	0.71	0.66	0.68	0.69	0.69	0.89	0.90	0.89	0.84	0.88	0.85	0.90	0.85
K	0.27	0.27	0.29	0.20	0.28	0.25	0.22	0.27	0.29	0.30	0.27	0.28	0.23	0.24	0.24	0.29	0.27	0.25	0.24	0.25
site A total	1.04	1.06	1.05	1.00	1.03	0.93	0.96	0.98	0.95	0.98	0.97	0.97	1.12	1.15	1.13	1.12	1.15	1.10	1.14	1.10

Table IV.4: Electron microprobe analysis to Amphiboles

Occurrence	Eiras de Faião sill								Mafra gabbro											
	rm47	rm47	rm47	rm47	rm47	rm47	rm47	rm47	RM83	RM83	RM83	RM83	RM83	RM83	RM83	RM83	RM83	RM83	RM83	rm101
sample	b2g	b3a	b3a	b3b	b3b	b3c	b3c	b4	b1a	b1a	b1a	b1b	b1b	b1b	b1c	b1c	b2	b2	b2	b2a
type	PR	Xen	Xen	Xen	Xen	Xen	Xen	Mx	Poi	Poi	Poi	Poi	Poi	Poi	Poi	Poi	C	C	R	Poi
SiO2	37.99	39.72	39.47	39.86	39.15	39.63	39.13	35.35	40.13	38.99	39.39	39.68	39.10	39.60	39.26	37.17	40.55	40.12	39.63	39.95
TiO2	4.97	5.34	5.50	5.47	5.54	5.44	5.61	6.85	5.27	5.36	5.31	5.50	5.77	5.32	5.47	5.15	5.42	5.68	5.81	5.33
Al2O3	12.12	12.21	12.16	11.80	12.14	12.12	12.28	13.15	11.47	11.50	11.78	11.75	11.91	11.65	11.73	11.83	11.43	11.69	11.62	11.21
Cr2O3	0.00	0.00	0.00	0.00	0.02	0.00	0.01	0.00	0.10	0.16	0.02	0.00	0.03	0.00	0.00	0.08	0.12	0.05	0.01	0.02
FeO	13.42	9.62	10.98	9.46	11.12	10.74	9.80	15.27	13.14	15.46	12.63	11.35	11.28	12.50	12.33	18.14	14.36	13.88	14.34	11.52
MnO	0.18	0.11	0.21	0.14	0.16	0.13	0.08	0.39	0.19	0.19	0.16	0.13	0.14	0.18	0.16	0.23	0.16	0.18	0.21	0.08
MgO	11.32	13.87	12.22	14.06	12.86	12.99	13.46	13.98	11.20	9.57	11.72	12.29	12.52	11.56	11.69	8.12	10.37	10.36	10.17	13.14
CaO	12.60	12.81	12.95	13.00	12.73	12.77	13.07	0.02	12.39	12.34	12.38	12.43	12.43	12.48	12.35	11.97	12.29	12.38	12.53	12.39
Na2O	2.62	2.61	2.42	2.52	2.50	2.58	2.52	0.71	2.73	2.42	2.68	2.78	2.68	2.67	2.60	2.22	2.53	2.68	2.31	2.54
K2O	1.25	1.39	1.31	1.34	1.28	1.31	1.36	9.01	1.35	1.72	1.28	1.18	1.15	1.23	1.24	1.91	1.49	1.50	1.65	1.09
F	0.05	0.02	0.03	0.36	0.23	0.15	0.21	2.46	0.01	0.22	0.23	0.23	0.13	0.10	0.42	0.11	0.16	0.00	0.19	0.09
ZnO	0.00	0.01	0.04	0.05	0.04	0.02	0.03	0.06	0.03	0.03	0.06	0.05	0.01	0.02	0.03	0.00	0.02	0.04	0.03	0.00
Total	96.52	97.71	97.29	98.05	97.77	97.87	97.56	97.24	97.99	97.95	97.64	97.39	97.15	97.31	97.28	96.93	98.89	98.57	98.50	97.36
Structural formula (a.p.f.u.)																				
Si	5.83	5.89	5.92	5.91	5.86	5.91	5.84	5.11	6.02	5.96	5.94	5.96	5.88	5.98	5.94	5.83	6.07	6.01	5.97	5.99
Al (iv)	2.17	2.11	2.08	2.06	2.14	2.09	2.16	2.24	1.98	2.04	2.06	2.04	2.11	2.02	2.06	2.17	1.93	1.99	2.03	1.98
site T total	8.00	8.00	8.00	7.98	8.00	8.00	8.00	7.35	8.00	8.00	8.00	8.00	8.00	8.00	8.00	8.00	8.00	8.00	8.00	7.97
Al (vi)	0.02	0.03	0.07	0.00	0.00	0.03	0.00	0.00	0.05	0.03	0.04	0.04	0.00	0.05	0.04	0.01	0.08	0.07	0.04	0.00
Ti	0.57	0.60	0.62	0.61	0.62	0.61	0.63	0.74	0.60	0.62	0.60	0.62	0.65	0.60	0.62	0.61	0.61	0.64	0.66	0.60
Cr	0.00	0.00	0.00	0.00	0.00	0.00	0.00	0.00	0.01	0.02	0.00	0.00	0.00	0.00	0.00	0.01	0.01	0.01	0.00	0.00
Fe(iii)	0.00	0.00	0.00	0.00	0.00	0.00	0.00	1.85	0.00	0.00	0.00	0.00	0.00	0.00	0.00	0.00	0.00	0.00	0.00	0.00
Fe(ii)	1.72	1.19	1.38	1.17	1.39	1.34	1.22	0.00	1.65	1.97	1.59	1.43	1.42	1.58	1.56	2.38	1.80	1.74	1.81	1.44
Mn	0.02	0.01	0.03	0.02	0.02	0.02	0.01	0.05	0.02	0.02	0.02	0.02	0.02	0.02	0.02	0.03	0.02	0.02	0.03	0.01
Mg	2.59	3.07	2.73	3.11	2.87	2.89	2.99	3.01	2.51	2.18	2.64	2.75	2.81	2.60	2.64	1.90	2.31	2.31	2.29	2.94
site C total	4.92	4.90	4.83	4.91	4.91	4.89	4.86	5.65	4.84	4.84	4.89	4.86	4.90	4.86	4.88	4.93	4.83	4.80	4.82	4.99
Ca	2.07	2.04	2.08	2.07	2.04	2.04	2.09	0.00	1.99	2.02	2.00	2.00	2.00	2.02	2.00	2.01	1.97	1.99	2.02	1.99
Na	0.00	0.00	0.00	0.00	0.00	0.00	0.00	0.20	0.01	0.00	0.00	0.00	0.00	0.00	0.00	0.00	0.03	0.01	0.00	0.01
site B total	2.00	2.00	2.00	2.00	2.00	2.00	2.00	0.20	2.00	2.00	2.00	2.00	2.00	2.00	2.00	2.00	2.00	2.00	2.00	2.00
Na	0.85	0.79	0.79	0.79	0.77	0.78	0.82	0.00	0.79	0.73	0.79	0.81	0.79	0.80	0.76	0.68	0.70	0.76	0.70	0.73
K	0.24	0.26	0.25	0.25	0.24	0.25	0.26	1.66	0.26	0.34	0.25	0.23	0.22	0.24	0.24	0.38	0.28	0.29	0.32	0.21
site A total	1.09	1.05	1.04	1.05	1.01	1.03	1.08	1.66	1.04	1.07	1.03	1.04	1.01	1.03	1.00	1.07	0.99	1.05	1.02	0.93

Table IV.4: Electron microprobe analysis to Amphiboles

Occurrence	Sines gabbro							Monchique gabbro								Fontanelas smt.			Sintra gabbro	
sample	rm101	rm101	rm101	rm101	rm101	rm101	rm101	mon84	mon84	mon84	mon84	mon84	mon84	mon84	mon84	at690	at690	at690	RM11-	RM11-
type	b2a Poi	b2b Poi	b2b Poi	b1a Poi	b1a Poi	b1b ICpx	b1b ICpx	b3a C	b3a C	b3a R	b3a R	b3b C	b3b C	b3b R	b3b R	b1a PC	b1a PC	b1a PR	b1a C	b1a C
SiO2	39.99	39.90	39.92	39.17	40.02	40.20	40.86	36.32	36.01	37.73	37.35	36.66	36.70	37.88	37.60	37.98	38.06	38.58	42.83	42.53
TiO2	5.51	5.73	5.57	4.45	5.41	4.74	4.90	6.51	6.61	5.53	5.68	5.42	5.94	5.56	5.83	5.05	5.11	4.95	5.43	5.27
Al2O3	11.47	11.62	11.34	11.60	11.47	11.87	10.69	13.91	13.99	12.91	12.74	12.54	13.06	12.63	12.42	13.35	13.32	13.30	10.76	10.96
Cr2O3	0.05	0.04	0.03	0.07	0.07	0.07	0.15	0.00	0.00	0.00	0.02	0.00	0.05	0.03	0.00	0.00	0.03	0.04	0.00	0.00
FeO	10.44	10.39	10.88	10.83	10.66	10.40	11.48	12.25	12.02	12.87	13.12	12.32	12.83	12.99	13.16	10.82	11.37	10.83	10.50	10.40
MnO	0.11	0.12	0.05	0.09	0.06	0.10	0.09	0.21	0.14	0.23	0.21	0.23	0.23	0.17	0.23	0.14	0.11	0.05	0.21	0.20
MgO	13.64	13.45	13.64	13.49	13.33	13.48	13.12	11.45	11.44	11.03	11.23	10.85	11.41	11.33	11.30	12.81	12.66	12.88	13.45	13.19
CaO	12.43	12.65	12.42	13.10	12.61	12.88	12.42	12.76	12.83	12.53	12.64	12.33	12.71	12.61	12.55	13.00	13.06	13.11	11.99	12.12
Na2O	2.54	2.55	2.53	2.45	2.54	2.39	2.27	2.58	2.31	2.52	2.53	2.39	2.52	2.56	2.44	1.99	2.17	2.11	2.44	2.51
K2O	1.01	0.97	1.06	0.88	0.99	1.08	1.26	1.55	1.56	1.61	1.58	1.55	1.56	1.59	1.80	1.89	1.84	1.92	0.74	0.81
F	0.27	0.28	0.06	0.13	0.14	0.23	0.12	0.28	0.30	0.00	0.15	0.11	0.25	0.02	0.11	0.14	0.10	0.20	0.42	0.50
ZnO	0.01	0.04	0.00	0.07	0.00	0.00	0.02	0.09	0.08	0.00	0.04	0.09	0.00	0.02	0.04	0.05	0.04	0.02	0.03	0.03
Total	97.46	97.73	97.50	96.30	97.29	97.42	97.37	97.90	97.28	96.96	97.28	94.49	97.26	97.40	97.47	97.22	97.86	97.97	98.79	98.51
Structural formula (a.p.f.u.)																				
Si	5.97	5.94	5.95	5.93	5.98	5.99	6.11	5.51	5.49	5.75	5.70	5.74	5.61	5.75	5.73	5.73	5.72	5.77	6.25	6.24
Al (iv)	2.02	2.04	1.99	2.07	2.02	2.01	1.89	2.49	2.51	2.25	2.29	2.26	2.35	2.25	2.23	2.27	2.28	2.23	1.75	1.76
site T total	7.98	7.98	7.95	8.00	8.00	8.00	8.00	7.99	8.00	8.00	7.99	8.00	7.96	8.00	7.96	8.00	8.00	8.00	8.00	8.00
Al (vi)	0.00	0.00	0.00	0.01	0.00	0.08	0.00	0.00	0.00	0.07	0.00	0.06	0.00	0.02	0.00	0.10	0.07	0.12	0.10	0.13
Ti	0.62	0.64	0.62	0.51	0.61	0.53	0.55	0.74	0.76	0.63	0.65	0.64	0.68	0.64	0.67	0.57	0.58	0.56	0.60	0.58
Cr	0.01	0.00	0.00	0.01	0.01	0.01	0.02	0.00	0.00	0.00	0.00	0.00	0.01	0.00	0.00	0.00	0.00	0.00	0.00	0.00
Fe(iii)	0.00	0.00	0.00	0.00	0.00	0.00	0.00	0.00	0.00	0.00	0.00	0.00	0.00	0.00	0.00	0.00	0.00	0.00	0.00	0.00
Fe(ii)	1.30	1.29	1.36	1.37	1.33	1.30	1.44	1.55	1.53	1.64	1.67	1.61	1.64	1.65	1.68	1.36	1.43	1.35	1.28	1.28
Mn	0.01	0.01	0.01	0.01	0.01	0.01	0.01	0.03	0.02	0.03	0.03	0.03	0.03	0.02	0.03	0.02	0.01	0.01	0.03	0.02
Mg	3.03	2.99	3.03	3.05	2.97	3.00	2.93	2.59	2.60	2.51	2.56	2.53	2.60	2.57	2.57	2.88	2.83	2.87	2.93	2.88
site C total	4.97	4.94	5.02	4.95	4.92	4.92	4.94	4.91	4.91	4.88	4.91	4.87	4.96	4.89	4.94	4.94	4.93	4.91	4.94	4.90
Ca	1.99	2.02	1.98	2.13	2.02	2.06	1.99	2.07	2.10	2.05	2.07	2.07	2.08	2.05	2.05	2.10	2.10	2.10	1.88	1.90
Na	0.01	0.00	0.02	0.00	0.00	0.00	0.01	0.00	0.00	0.00	0.00	0.00	0.00	0.00	0.00	0.00	0.00	0.00	0.00	0.10
site B total	2.00	2.00	2.00	2.00	2.00	2.00	2.00	2.00	2.00	2.00	2.00	2.00	2.00	2.00	2.00	2.00	2.00	2.00	2.00	2.00
Na	0.72	0.75	0.72	0.84	0.75	0.75	0.65	0.83	0.78	0.79	0.82	0.79	0.83	0.81	0.77	0.68	0.73	0.71	0.57	0.62
K	0.19	0.18	0.20	0.17	0.19	0.20	0.24	0.30	0.30	0.31	0.31	0.31	0.30	0.31	0.35	0.36	0.35	0.37	0.14	0.15
site A total	0.91	0.94	0.92	1.01	0.94	0.95	0.89	1.13	1.08	1.10	1.12	1.10	1.13	1.12	1.12	1.05	1.09	1.08	0.70	0.77

Table IV.4: Electron microprobe analysis to Amphiboles

Occurrence	Sintra gabbro																			
sample type	RM11-b1aR	RM11-b1aR	RM11-b1bC	RM11-b1bC	RM11-b1bR	RM11-b1bR	RM11-b1cC	RM11-b1cR	RM11-b1dGC	RM11-b1dGR	RM11-b2aC	RM11-b2aC	RM11-b2aR	RM11-b2aR	RM11-b2bC	RM11-b2bC	RM11-b2bR	RM11-b2bR	RM11-b2cC	RM11-b2cR
SiO2	43.45	42.60	42.62	42.93	43.06	42.67	42.86	42.69	50.39	49.95	42.52	42.64	42.71	39.76	41.87	41.92	42.35	42.36	42.04	41.92
TiO2	4.42	5.78	5.48	5.37	5.48	5.21	5.35	5.42	0.32	0.34	5.35	5.40	5.04	5.23	5.28	5.38	5.35	5.54	5.60	5.16
Al2O3	10.29	11.26	11.21	11.07	11.00	11.04	10.85	11.18	7.14	7.07	10.92	10.87	10.68	12.37	10.92	11.02	10.94	10.82	10.72	10.68
Cr2O3	0.00	0.06	0.03	0.00	0.00	0.00	0.00	0.02	0.00	0.00	0.00	0.00	0.01	0.00	0.01	0.00	0.00	0.04	0.06	0.00
FeO	11.57	9.49	9.71	9.73	10.33	10.96	10.20	9.84	11.12	11.39	9.73	10.15	10.75	12.59	10.42	10.33	10.15	10.21	10.17	11.16
MnO	0.23	0.18	0.15	0.15	0.21	0.26	0.21	0.11	0.24	0.17	0.14	0.16	0.17	0.18	0.22	0.24	0.20	0.19	0.19	0.23
MgO	12.80	13.31	13.26	13.38	12.94	12.89	13.57	13.23	14.93	14.91	13.47	12.97	12.81	16.41	13.14	12.98	12.97	13.06	13.07	12.58
CaO	12.13	12.51	12.30	12.24	12.41	12.19	12.12	12.32	12.84	12.95	12.20	12.21	12.16	0.13	12.09	12.09	12.35	12.25	12.27	12.16
Na2O	2.47	2.73	2.63	2.73	2.75	2.66	2.52	2.69	1.32	1.35	2.72	2.79	2.88	0.43	2.79	2.75	2.78	2.84	2.77	2.71
K2O	1.05	0.77	0.77	0.77	0.74	0.76	0.79	0.73	0.24	0.23	0.81	0.76	0.81	8.83	0.77	0.78	0.73	0.82	0.75	0.81
F	0.12	0.13	0.15	0.28	0.21	0.20	0.33	0.25	0.27	0.09	0.27	0.18	0.21	0.41	0.44	0.39	0.22	0.20	0.28	0.25
ZnO	0.03	0.00	0.02	0.02	0.03	0.05	0.00	0.07	0.06	0.03	0.00	0.09	0.06	0.06	0.03	0.02	0.02	0.00	0.04	0.06
Total	98.57	98.82	98.32	98.65	99.16	98.90	98.78	98.54	98.86	98.47	98.10	98.22	98.28	96.39	97.98	97.90	98.06	98.33	97.96	97.71
Structural formula (a.p.f.u.)																				
Si	6.37	6.19	6.22	6.25	6.25	6.23	6.25	6.23	7.21	7.17	6.23	6.25	6.28	5.53	6.19	6.19	6.22	6.21	6.20	6.22
Al (iv)	1.63	1.81	1.78	1.75	1.75	1.77	1.75	1.77	0.79	0.83	1.77	1.75	1.72	2.03	1.81	1.81	1.78	1.79	1.80	1.78
site T total	8.00	8.00	8.00	8.00	8.00	8.00	8.00	8.00	8.00	8.00	8.00	8.00	8.00	7.56	8.00	8.00	8.00	8.00	8.00	8.00
Al (vi)	0.15	0.12	0.15	0.15	0.14	0.14	0.11	0.15	0.41	0.37	0.12	0.13	0.13	0.00	0.09	0.11	0.12	0.08	0.06	0.09
Ti	0.49	0.63	0.60	0.59	0.60	0.57	0.59	0.59	0.03	0.04	0.59	0.60	0.56	0.55	0.59	0.60	0.59	0.61	0.62	0.58
Cr	0.00	0.01	0.00	0.00	0.00	0.00	0.00	0.00	0.00	0.00	0.00	0.00	0.00	0.00	0.00	0.00	0.00	0.00	0.01	0.00
Fe(iii)	0.00	0.00	0.00	0.00	0.00	0.00	0.00	0.00	0.00	0.00	0.00	0.00	0.00	1.46	0.00	0.00	0.00	0.00	0.00	0.00
Fe(ii)	1.42	1.15	1.19	1.19	1.26	1.34	1.24	1.20	1.33	1.37	1.19	1.24	1.32	0.00	1.29	1.28	1.25	1.25	1.25	1.38
Mn	0.03	0.02	0.02	0.02	0.03	0.03	0.03	0.01	0.03	0.02	0.02	0.02	0.02	0.02	0.03	0.03	0.02	0.02	0.02	0.03
Mg	2.80	2.88	2.88	2.90	2.80	2.81	2.95	2.88	3.18	3.19	2.94	2.84	2.81	3.40	2.90	2.86	2.84	2.86	2.87	2.79
site C total	4.89	4.81	4.84	4.85	4.82	4.89	4.91	4.84	4.99	4.99	4.86	4.83	4.84	5.44	4.89	4.87	4.83	4.83	4.84	4.87
Ca	1.91	1.95	1.92	1.91	1.93	1.91	1.89	1.93	1.97	1.99	1.92	1.92	1.92	0.02	1.91	1.91	1.94	1.92	1.94	1.93
Na	0.09	0.05	0.08	0.09	0.07	0.09	0.11	0.07	0.03	0.01	0.08	0.08	0.08	0.12	0.09	0.09	0.06	0.08	0.06	0.07
site B total	2.00	2.00	2.00	2.00	2.00	2.00	2.00	2.00	2.00	2.00	2.00	2.00	2.00	0.13	2.00	2.00	2.00	2.00	2.00	2.00
Na	0.61	0.72	0.67	0.68	0.70	0.66	0.60	0.69	0.33	0.37	0.69	0.71	0.74	0.00	0.71	0.70	0.74	0.73	0.73	0.72
K	0.20	0.14	0.14	0.14	0.14	0.14	0.15	0.14	0.04	0.04	0.15	0.14	0.15	1.57	0.14	0.15	0.14	0.15	0.14	0.15
site A total	0.81	0.86	0.81	0.82	0.84	0.80	0.75	0.82	0.38	0.41	0.84	0.85	0.89	1.57	0.86	0.85	0.87	0.89	0.87	0.87

Table IV.4: Electron microprobe analysis to Amphiboles

Occurrence	Sintra gabbro			
sample	RM11-b2d	RM11-b2d	RM11-b2d	RM11-b2d
type	C	C	R	R
SiO2	42.44	42.10	42.09	43.65
TiO2	5.43	5.53	5.81	3.76
Al2O3	11.05	11.20	11.26	9.74
Cr2O3	0.00	0.00	0.01	0.02
FeO	9.74	9.60	9.47	11.83
MnO	0.14	0.11	0.13	0.21
MgO	13.17	13.26	13.23	13.26
CaO	12.28	12.32	12.32	12.21
Na2O	2.89	2.86	2.82	2.44
K2O	0.82	0.76	0.77	1.15
F	0.28	0.11	0.16	0.30
ZnO	0.01	0.02	0.00	0.08
Total	98.24	97.87	98.06	98.63
Structural formula (a.p.f.u.)				
Si	6.22	6.18	6.17	6.43
Al (iv)	1.78	1.82	1.83	1.57
site T total	8.00	8.00	8.00	8.00
Al (vi)	0.13	0.12	0.11	0.12
Ti	0.60	0.61	0.64	0.42
Cr	0.00	0.00	0.00	0.00
Fe(iii)	0.00	0.00	0.00	0.00
Fe(ii)	1.19	1.18	1.16	1.46
Mn	0.02	0.01	0.02	0.03
Mg	2.88	2.90	2.89	2.91
site C total	4.81	4.82	4.82	4.93
Ca	1.93	1.94	1.93	1.93
Na	0.07	0.06	0.07	0.07
site B total	2.00	2.00	2.00	2.00
Na	0.75	0.75	0.73	0.62
K	0.15	0.14	0.14	0.22
site A total	0.90	0.89	0.88	0.84

Table IV.5a: Electron microprobe analysis to oxides - spinels (s.l.)

Occurrence	Lomba dos Pianos sill																			
	rm9	rm9	rm9	rm9	rm9	rm9	rm9	rm9	rm9	rm9	rm9	rm9	rm9	rm9	rm9	rm9	rm9	rm9	rm9	rm9
sample	b1a	b1b	b1c	b1d	b1e	b1f	b1g	b3a	b3b	b3c	b3d	b3e	b3f	b5a	b5b	b5c	b6a	b6b	b6c	b7a
type	Iplag	Iplag	Iplag	MP	IRCpx	Mx	MP	Mx	Mx	Iplag	Iplag	Iplag	Mx	IGCpx	IGCpx	Mx	MP	MP	MP	IGCpx
SiO2	1.02	0.21	0.79	0.64	1.24	0.34	1.31	0.76	0.42	4.12	0.63	0.95	1.31	0.42	0.28	0.76	0.42	0.28	1.01	1.91
TiO2	17.01	15.46	19.10	23.05	24.98	21.72	23.72	23.70	22.34	21.06	24.49	24.33	21.80	23.87	24.34	19.87	22.43	22.61	25.21	11.21
Cr2O3	0.13	0.13	0.12	0.25	0.13	0.15	0.23	0.39	0.27	0.13	0.15	0.07	0.13	0.10	0.11	0.10	0.30	0.28	0.25	0.10
Al2O3	5.82	6.02	5.18	1.97	3.22	1.50	1.97	1.91	1.83	3.74	3.00	2.87	1.48	1.04	1.07	0.88	2.11	2.01	2.08	1.12
V2O3	0.22	0.22	0.27	0.25	0.24	0.21	0.28	0.30	0.30	0.23	0.24	0.23	0.26	0.25	0.24	0.25	0.32	0.30	0.30	0.25
CaO	0.16	0.21	0.28	0.07	0.35	0.22	0.17	0.07	0.06	0.18	0.09	0.14	0.33	0.41	0.44	0.18	0.04	0.05	0.11	0.57
MnO	0.48	0.50	0.58	1.29	0.96	1.61	1.60	1.22	1.41	1.01	1.11	1.02	1.52	1.49	1.47	1.19	1.26	1.30	1.32	0.23
MgO	4.72	4.50	4.32	1.92	3.27	1.58	1.79	1.90	1.80	4.12	2.81	2.92	1.34	1.77	1.68	1.37	2.02	1.68	2.27	0.26
Fe2O3	27.65	32.84	22.92	18.20	11.89	22.34	15.41	16.54	20.62	11.59	14.46	13.70	19.75	17.87	17.43	25.07	20.13	20.03	12.95	37.94
FeO	40.65	38.72	41.76	47.98	48.45	46.44	49.34	48.85	47.34	47.16	48.13	47.96	48.11	47.69	48.16	45.75	47.25	47.66	49.79	41.32
total	97.86	98.81	95.32	95.60	94.72	96.09	95.80	95.63	96.39	93.33	95.12	94.20	96.01	94.89	95.21	95.42	96.27	96.19	95.30	94.91
Structural formula (a.p.f.u.)																				
Si	0.29	0.06	0.24	0.19	0.37	0.11	0.40	0.23	0.13	1.24	0.19	0.29	0.40	0.13	0.09	0.24	0.13	0.08	0.31	0.60
Ti	3.68	3.34	4.26	5.30	5.66	5.01	5.42	5.44	5.11	4.75	5.58	5.58	5.01	5.56	5.65	4.64	5.12	5.19	5.77	2.65
Cr	0.03	0.03	0.03	0.06	0.03	0.04	0.06	0.09	0.06	0.03	0.04	0.02	0.03	0.02	0.03	0.02	0.07	0.07	0.06	0.02
Al	1.97	2.04	1.81	0.71	1.14	0.54	0.71	0.69	0.66	1.32	1.07	1.03	0.53	0.38	0.39	0.32	0.75	0.72	0.75	0.41
V	0.05	0.05	0.06	0.06	0.06	0.05	0.07	0.07	0.07	0.05	0.06	0.06	0.06	0.06	0.06	0.06	0.08	0.07	0.07	0.06
Fe(iii)	5.99	7.09	5.11	4.19	2.70	5.15	3.53	3.80	4.72	2.62	3.30	3.15	4.54	4.16	4.05	5.85	4.60	4.60	2.97	8.99
Fe(ii)	9.78	9.29	10.35	12.26	12.21	11.90	12.55	12.47	12.04	11.83	12.19	12.24	12.30	12.35	12.44	11.87	12.00	12.16	12.67	10.88
Mn	0.12	0.12	0.14	0.33	0.24	0.42	0.41	0.31	0.36	0.26	0.29	0.26	0.39	0.39	0.38	0.31	0.32	0.34	0.34	0.06
Mg	2.03	1.92	1.91	0.88	1.47	0.72	0.81	0.87	0.82	1.84	1.27	1.33	0.61	0.82	0.77	0.63	0.91	0.76	1.03	0.12
Ca	0.05	0.07	0.09	0.02	0.11	0.07	0.06	0.02	0.02	0.06	0.03	0.04	0.11	0.13	0.15	0.06	0.01	0.02	0.04	0.19
TOTAL	24	24	24	24	24	24	24	24	24	24	24	24	24	24	24	24	24	24	24	24

M - Micro, P - Phenocrist, C - Core, R - Rim, Exs - exsolved crystal; EP exsolved phenocryst, I - inclusion, GCpx - green cored clinopyroxene, cpx - clinopyroxene, biot - biotite, anf- amphibole, plag - plagioclase, Xen - crystal in xenolith, AR - amphibole reaction rim

Table IV.5a: Electron microprobe analysis to oxides - spinels (s.l.)

Occurrence	Lomba dos Pianos sill				Malveira da Serra sill														
	rm9	rm9	rm9	rm9	rm25	rm25	rm25	rm25	rm25	rm25	rm25	rm25	rm25	rm25	rm25	rm25	rm25	rm25	rm25
sample	b7b	b7c	b7d	b7e	b1a	b1b	b1c	b1d	b1e	b1f	b2a	b2a	b2a	b2a	b2b	b2b	b2c	b2d	b2e	b3a
type	IGCpx	IGCpx	Mx	Mx	Icpx	Icpx	MP	Mx	MP	Mx	PC	PR	PR	PR	PR	PC	MP	Icpx	Icpx	Mx
SiO2	0.08	2.23	0.05	1.35	5.20	2.15	1.96	3.75	3.57	2.80	0.08	0.12	0.13	0.12	5.21	0.11	1.50	3.79	1.02	0.21
TiO2	9.02	17.86	24.04	20.94	4.40	12.26	14.48	4.89	14.31	15.23	13.29	13.81	13.85	14.63	16.81	13.15	13.44	9.55	18.00	17.36
Cr2O3	0.11	0.16	0.11	0.14	0.14	0.11	0.88	0.14	0.30	0.14	0.18	0.16	0.16	0.18	0.19	0.14	0.12	0.16	0.11	0.14
Al2O3	0.37	1.49	1.68	1.69	1.50	2.21	1.53	0.84	2.12	1.11	6.51	7.42	7.02	7.63	1.73	6.47	4.04	3.97	5.56	7.48
V2O3	0.32	0.22	0.25	0.27	0.11	0.23	0.29	0.11	0.26	0.26	0.26	0.29	0.29	0.31	0.29	0.32	0.19	0.19	0.28	0.30
CaO	0.38	0.74	0.07	0.15	3.17	1.72	1.15	3.35	2.55	1.95	0.00	0.03	0.04	0.04	3.17	0.00	1.41	3.60	0.48	0.63
MnO	0.70	0.92	1.03	1.25	0.46	1.00	0.97	0.43	0.78	0.93	0.28	1.20	1.21	2.18	0.11	0.34	0.93	1.22	0.52	0.83
MgO	0.05	0.32	1.40	1.24	0.29	0.06	0.08	0.21	0.30	0.06	4.92	3.83	3.85	2.78	0.34	5.31	0.03	0.12	0.77	0.07
Fe2O3	49.51	22.67	17.85	20.48	42.64	34.20	30.02	45.46	26.66	27.57	36.08	33.20	33.12	30.56	18.15	36.41	31.58	34.15	21.06	22.25
FeO	37.87	46.43	49.13	47.84	35.67	41.02	43.27	33.85	43.43	43.95	36.06	37.40	37.16	38.77	47.54	35.25	42.17	38.53	45.89	45.45
total	98.41	93.03	95.60	95.35	93.59	94.96	94.63	93.04	94.28	94.01	97.64	97.45	96.83	97.18	93.53	97.51	95.41	95.29	93.68	94.73
Structural formula (a.p.f.u.)																				
Si	0.02	0.71	0.02	0.42	1.63	0.67	0.61	1.19	1.11	0.88	0.02	0.03	0.04	0.04	1.61	0.03	0.46	1.15	0.31	0.06
Ti	2.10	4.26	5.57	4.85	1.04	2.87	3.42	1.17	3.33	3.60	2.89	3.02	3.05	3.22	3.91	2.86	3.11	2.18	4.18	3.98
Cr	0.03	0.04	0.03	0.03	0.03	0.03	0.22	0.03	0.07	0.04	0.04	0.04	0.04	0.04	0.05	0.03	0.03	0.04	0.03	0.03
Al	0.14	0.56	0.61	0.61	0.55	0.81	0.57	0.32	0.77	0.41	2.22	2.54	2.42	2.63	0.63	2.20	1.47	1.42	2.02	2.69
V	0.08	0.06	0.06	0.07	0.03	0.06	0.07	0.03	0.06	0.07	0.06	0.07	0.07	0.07	0.07	0.07	0.05	0.05	0.07	0.07
Fe(iii)	11.51	5.41	4.14	4.75	10.05	8.02	7.08	10.89	6.21	6.52	7.85	7.26	7.30	6.73	4.22	7.92	7.31	7.81	4.89	5.11
Fe(ii)	9.79	12.32	12.65	12.32	9.34	10.68	11.35	9.01	11.25	11.55	8.72	9.09	9.10	9.49	12.28	8.52	10.85	9.80	11.85	11.59
Mn	0.18	0.25	0.27	0.33	0.12	0.26	0.26	0.12	0.20	0.25	0.07	0.30	0.30	0.54	0.03	0.08	0.24	0.32	0.14	0.21
Mg	0.02	0.15	0.64	0.57	0.14	0.03	0.04	0.10	0.14	0.03	2.12	1.66	1.68	1.21	0.16	2.29	0.02	0.05	0.35	0.03
Ca	0.13	0.25	0.02	0.05	1.07	0.57	0.38	1.14	0.85	0.66	0.00	0.01	0.01	0.01	1.05	0.00	0.46	1.17	0.16	0.21
TOTAL	24	24	24	24	24	24	24	24	24	24	24	24	24	24	24	24	24	24	24	24

Table IV.5a: Electron microprobe analysis to oxides - spinels (s.l.)

Occurrence	Malveira da Serra sill																	Ribeira dIlhas plug		
	rm25	rm25	rm25	rm25	rm25	rm25	rm25	rm25	rm25	rm25	rm25	rm25	rm25	rm25	rm25	rm25	rm25	rm36	rm36	rm36
sample	b3b	b3c	b3d	b3e	b3f	b3g	b4a	b4b	b4c	b4d	b4e	b4f	b4g	b4g	b4g	b4h	b4i	b2a	b2b	b2c
type	Mx	Mx	Icpx	Icpx	MP	MP	Icpx	Icpx	Icpx	Icpx	Icpx	Icpx	PR	PM	PC	Mx	Mx	Mx	Mx	Mx
SiO2	3.52	7.21	0.14	11.35	1.37	0.16	1.82	4.33	0.14	0.10	9.60	10.96	0.08	0.14	0.05	9.82	5.14	0.71	0.25	0.29
TiO2	17.20	8.71	14.62	11.94	12.92	16.50	3.63	6.92	15.67	15.13	7.74	13.42	12.04	8.52	6.90	17.33	8.39	22.61	22.16	16.08
Cr2O3	0.24	0.06	0.13	0.06	1.93	0.17	0.19	0.15	0.16	0.13	0.20	0.17	0.13	0.07	0.12	0.14	0.13	0.13	0.30	7.14
Al2O3	2.34	2.00	7.43	8.03	7.52	8.06	0.34	0.70	5.05	4.39	1.57	1.46	2.54	1.75	1.56	2.14	1.02	3.09	3.43	5.19
V2O3	0.26	0.12	0.29	0.16	0.30	0.31	0.13	0.11	0.35	0.27	0.10	0.18	0.20	0.19	0.20	0.22	0.16	0.29	0.26	0.29
CaO	1.05	6.57	0.33	10.25	0.94	0.13	1.24	1.35	0.22	0.34	6.31	9.54	0.04	0.02	0.02	7.67	4.73	0.23	0.12	0.12
MnO	0.33	0.27	0.43	0.25	3.11	0.70	0.61	0.72	0.77	0.39	0.36	0.06	2.76	0.60	0.99	0.91	0.17	0.93	0.92	0.85
MgO	0.54	0.16	5.14	7.86	0.20	0.12	0.02	0.08	0.27	5.22	0.26	0.12	0.31	1.83	1.70	0.17	0.00	2.47	3.47	5.60
Fe2O3	19.77	30.73	31.93	17.06	27.12	22.76	51.99	38.40	25.13	32.53	23.66	11.78	38.88	48.00	51.63	4.86	36.01	14.78	17.89	22.63
FeO	47.50	39.26	36.42	34.67	40.39	45.11	32.43	38.09	42.09	35.25	39.85	44.36	37.90	34.72	32.95	47.47	38.21	45.78	43.94	35.97
total	92.74	95.09	96.85	101.63	95.80	94.01	92.40	90.85	89.85	93.75	89.64	92.04	94.88	95.83	96.12	90.73	93.97	91.02	92.73	94.17
Structural formula (a.p.f.u.)																				
Si	1.11	2.17	0.04	2.88	0.41	0.05	0.60	1.41	0.04	0.03	3.03	3.31	0.03	0.04	0.02	3.01	1.60	0.23	0.08	0.09
Ti	4.06	1.97	3.18	2.28	2.92	3.81	0.89	1.70	3.84	3.44	1.84	3.05	2.85	1.99	1.61	4.00	1.96	5.38	5.15	3.60
Cr	0.06	0.02	0.03	0.01	0.46	0.04	0.05	0.04	0.04	0.03	0.05	0.04	0.03	0.02	0.03	0.03	0.03	0.03	0.07	1.68
Al	0.87	0.71	2.53	2.40	2.67	2.92	0.13	0.27	1.94	1.56	0.58	0.52	0.94	0.64	0.57	0.77	0.37	1.15	1.25	1.82
V	0.06	0.03	0.07	0.03	0.07	0.08	0.03	0.03	0.09	0.07	0.02	0.04	0.05	0.05	0.05	0.05	0.04	0.07	0.07	0.07
Fe(iii)	4.67	6.96	6.94	3.25	6.14	5.26	12.81	9.44	6.16	7.40	5.62	2.68	9.22	11.23	12.09	1.12	8.43	3.52	4.16	5.07
Fe(ii)	12.48	9.88	8.80	7.35	10.15	11.58	8.88	10.40	11.46	8.91	10.51	11.20	9.98	9.02	8.57	12.18	9.94	12.12	11.35	8.95
Mn	0.09	0.07	0.10	0.05	0.79	0.18	0.17	0.20	0.21	0.10	0.10	0.02	0.74	0.16	0.26	0.24	0.05	0.25	0.24	0.21
Mg	0.25	0.07	2.21	2.97	0.09	0.05	0.01	0.04	0.13	2.35	0.12	0.05	0.14	0.85	0.79	0.08	0.00	1.16	1.60	2.48
Ca	0.35	2.12	0.10	2.78	0.30	0.04	0.44	0.47	0.08	0.11	2.13	3.09	0.01	0.00	0.01	2.52	1.58	0.08	0.04	0.04
TOTAL	24	24	24	24	24	24	24	24	24	24	24	24	24	24	24	24	24	24	24	24

Table IV.5a: Electron microprobe analysis to oxides - spinels (s.l.)

Occurrence	Ribeira d'Ilhas plug																			
sample	rm36 b2d	rm36 b2e	rm36 b2f	rm37 b1a	rm37 b1b	rm37 b1c	rm37 b1d	rm37 b1e	rm37 b1f	rm37 b1g	rm37 b1h	rm37 b1i	rm37 b1j	rm37 b1k	rm37 b2a	rm37 b2b	rm37 b2c	rm37 b2d	rm37 b2e	rm37 b2f
type	Icpx	Icpx	Ianf	Iol	Iol	Iol	Iol	Iol	Iol	Iol	Mx	Mx	Mx	Mx	Mx	Mx	Mx	Icpx	Ianf	Icpx
SiO2	6.07	18.63	7.23	0.18	0.19	0.08	0.12	0.14	0.35	0.23	0.11	0.11	0.16	0.15	0.16	0.10	0.04	0.06	1.21	0.12
TiO2	16.00	13.51	16.48	8.34	10.11	11.32	6.66	6.23	11.16	16.08	22.38	21.79	22.22	21.87	20.05	12.95	17.71	21.23	0.03	20.20
Cr2O3	0.31	0.15	0.22	13.00	12.65	12.78	15.66	15.91	7.79	7.89	0.18	1.24	0.18	0.76	2.61	11.25	0.30	1.42	0.08	0.59
Al2O3	3.78	4.39	4.43	19.36	15.31	11.45	18.90	18.85	12.51	7.14	2.79	3.32	3.37	3.57	5.59	9.97	6.12	4.12	0.28	4.02
V2O3	0.31	0.23	0.26	0.25	0.23	0.22	0.22	0.19	0.29	0.23	0.24	0.22	0.25	0.28	0.29	0.28	0.36	0.29	0.00	0.28
CaO	2.36	8.35	6.59	0.03	0.05	0.02	0.01	0.06	0.07	0.10	0.27	0.20	0.15	0.17	0.03	0.00	0.01	0.10	0.12	0.54
MnO	0.42	0.39	0.41	0.60	0.69	0.56	0.27	0.24	0.28	0.64	0.94	0.84	0.88	0.81	0.74	0.63	0.68	0.85	0.01	0.88
MgO	6.99	6.39	8.91	8.25	7.31	6.52	10.41	9.57	8.68	5.53	4.33	4.69	4.28	4.72	5.31	6.45	5.13	5.06	3.85	2.86
Fe2O3	17.80	-8.02	19.86	21.22	22.39	23.06	22.23	21.35	27.70	23.62	24.20	23.89	23.80	23.99	23.58	23.72	30.06	23.85	56.94	25.27
FeO	38.36	46.05	34.47	29.53	31.80	32.92	24.26	24.65	30.17	38.35	44.57	43.78	44.95	44.05	42.11	34.56	40.25	42.77	21.77	44.54
total	92.40	90.07	98.85	100.77	100.75	98.93	98.74	97.17	99.00	99.82	100.00	100.08	100.24	100.36	100.47	99.91	100.66	99.76	84.30	99.29
Structural formula (a.p.f.u.)																				
Si	1.78	5.23	1.93	0.05	0.05	0.02	0.03	0.04	0.10	0.07	0.03	0.03	0.05	0.04	0.04	0.03	0.01	0.02	0.42	0.03
Ti	3.53	2.85	3.32	1.61	2.01	2.34	1.30	1.24	2.26	3.38	4.83	4.68	4.78	4.68	4.23	2.67	3.73	4.55	0.01	4.42
Cr	0.07	0.03	0.05	2.65	2.64	2.77	3.20	3.32	1.66	1.74	0.04	0.28	0.04	0.17	0.58	2.44	0.07	0.32	0.02	0.14
Al	1.31	1.45	1.40	5.87	4.76	3.70	5.77	5.86	3.97	2.35	0.94	1.12	1.14	1.20	1.85	3.22	2.02	1.38	0.12	1.38
V	0.07	0.05	0.05	0.05	0.05	0.05	0.05	0.04	0.06	0.05	0.05	0.05	0.06	0.06	0.07	0.06	0.08	0.07	0.00	0.07
Fe(iii)	3.93	0.00	4.00	4.11	4.44	4.76	4.33	4.24	5.61	4.97	5.23	5.13	5.12	5.13	4.97	4.89	6.34	5.11	15.00	5.53
Fe(ii)	9.41	9.11	7.71	6.35	7.01	7.55	5.25	5.44	6.79	8.96	10.70	10.45	10.74	10.47	9.87	7.92	9.44	10.18	6.37	10.82
Mn	0.10	0.09	0.09	0.13	0.15	0.13	0.06	0.05	0.06	0.15	0.23	0.20	0.21	0.20	0.17	0.15	0.16	0.21	0.00	0.22
Mg	3.06	2.67	3.55	3.17	2.88	2.67	4.02	3.76	3.48	2.30	1.85	2.00	1.82	2.00	2.22	2.63	2.14	2.15	2.01	1.24
Ca	0.74	2.51	1.89	0.01	0.01	0.01	0.00	0.02	0.02	0.03	0.08	0.06	0.05	0.05	0.01	0.00	0.00	0.03	0.04	0.17
TOTAL	24	24	24	24	24	24	24	24	24	24	24	24	24	24	24	24	24	24	24	24

Table IV.5a: Electron microprobe analysis to oxides - spinels (s.l.)

Occurrence	Ribeira d'Ilhas plug																	LVC flow		
	rm37	rm37	rm37	rm37	rm37	rm37	rm37	rm37	rm37	rm37	rm37	rm37	rm37	rm37	rm37	rm37	rm37	rm43	rm43	rm43
sample	b4a	b4b	b4c	b4d	b4e	b4f	b4f	b4g	b4h	b5a	b5a	b5a	b5a	b5b	b5c	b5d	b5e	b1a	b1a	b1b
type	IGCpx	IGCpx	Icpx	Mx	Mx	PC	PR	Icpx	Icpx	PC	PC	PR	PR	MP	Mx	MP	MP	EP	EP	EP
SiO2	0.19	4.67	0.14	0.17	0.06	0.06	0.07	0.20	0.10	0.07	1.13	0.15	0.13	0.09	1.47	0.09	0.11	0.01	0.05	0.58
TiO2	10.12	9.59	16.53	20.43	22.19	10.85	13.74	21.01	14.92	5.48	10.73	17.80	15.33	18.70	20.55	19.00	22.41	18.60	18.74	17.77
Cr2O3	0.47	0.43	0.25	0.24	0.22	0.17	0.14	2.05	9.61	0.10	0.11	0.57	0.12	1.82	0.19	4.42	0.22	0.18	0.15	0.08
Al2O3	6.76	7.60	6.42	2.74	3.12	3.48	5.80	4.74	8.77	2.12	4.32	4.64	6.02	5.10	2.85	5.23	3.16	2.62	2.60	2.83
V2O3	0.23	0.23	0.23	0.23	0.24	0.38	0.36	0.27	0.23	0.26	0.29	0.32	0.31	0.27	0.24	0.19	0.22	0.44	0.42	0.36
CaO	0.61	0.73	0.42	3.80	0.16	0.03	0.03	0.08	0.04	0.00	0.03	0.12	0.04	0.06	0.92	0.07	0.14	0.03	0.03	0.04
MnO	0.56	0.59	0.53	0.81	0.91	0.54	0.56	0.87	0.79	0.39	0.53	0.90	0.65	0.79	0.90	0.83	0.91	0.53	0.54	0.47
MgO	4.67	5.88	7.17	3.98	4.31	3.75	4.18	4.77	6.07	2.52	4.20	4.02	3.83	4.26	3.57	4.75	4.18	3.53	3.54	3.55
Fe2O3	43.05	31.51	32.04	24.20	23.66	45.36	37.13	21.88	22.01	56.91	41.74	29.90	33.91	26.70	22.95	23.82	23.71	30.16	30.11	29.64
FeO	33.45	36.24	35.38	37.42	44.31	35.54	37.85	43.08	36.16	32.40	35.96	41.28	40.08	41.97	44.55	41.59	45.11	42.34	42.59	42.02
total	100.10	97.46	99.09	94.00	99.20	100.16	99.85	98.94	98.69	100.26	99.04	99.69	100.41	99.75	98.19	99.99	100.15	98.43	98.75	97.34
Structural formula (a.p.f.u.)																				
Si	0.05	1.31	0.04	0.05	0.02	0.02	0.02	0.06	0.03	0.02	0.33	0.04	0.04	0.02	0.43	0.03	0.03	0.00	0.01	0.17
Ti	2.15	2.03	3.48	4.65	4.82	2.37	2.95	4.52	3.13	1.22	2.34	3.84	3.28	4.01	4.51	4.05	4.83	4.13	4.14	3.97
Cr	0.10	0.09	0.06	0.06	0.05	0.04	0.03	0.46	2.12	0.02	0.02	0.13	0.03	0.41	0.04	0.99	0.05	0.04	0.03	0.02
Al	2.26	2.52	2.12	0.98	1.06	1.19	1.95	1.60	2.88	0.74	1.47	1.57	2.02	1.72	0.98	1.75	1.07	0.91	0.90	0.99
V	0.05	0.05	0.05	0.05	0.05	0.09	0.08	0.06	0.05	0.06	0.07	0.07	0.07	0.06	0.06	0.04	0.05	0.10	0.10	0.09
Fe(iii)	9.17	6.66	6.74	5.51	5.15	9.90	7.99	4.71	4.62	12.69	9.10	6.46	7.25	5.73	5.04	5.08	5.11	6.69	6.66	6.63
Fe(ii)	7.92	8.51	8.28	9.47	10.71	8.62	9.05	10.31	8.44	8.03	8.71	9.91	9.53	10.02	10.88	9.85	10.81	10.44	10.46	10.44
Mn	0.13	0.14	0.12	0.21	0.22	0.13	0.14	0.21	0.19	0.10	0.13	0.22	0.16	0.19	0.22	0.20	0.22	0.13	0.13	0.12
Mg	1.97	2.46	2.99	1.80	1.86	1.62	1.78	2.03	2.52	1.12	1.82	1.72	1.62	1.81	1.55	2.00	1.79	1.55	1.55	1.57
Ca	0.18	0.22	0.13	1.23	0.05	0.01	0.01	0.02	0.01	0.00	0.01	0.04	0.01	0.02	0.29	0.02	0.04	0.01	0.01	0.01
TOTAL	24	24	24	24	24	24	24	24	24	24	24	24	24	24	24	24	24	24	24	24

Table IV.5a: Electron microprobe analysis to oxides - spinels (s.l.)

Occurrence	LVC flow																			
	rm43	rm43	rm43	rm43	rm43	rm43	rm43	rm43	rm43	rm43	rm43	rm43	rm43	rm43	rm43	rm43	rm43	rm43	rm43	rm43
sample	b1c	b1d	b1e	b1f	b2a	b2a	b2b	b2b	b2c	b2d	b2e	b2f	b2g	b2h	b2i	b2j	b3a	b3b	b3c	b3d
type	MP	MP	Mx	Mx	PC	PR	MP	MP	MP	Mx	MP	MP	Mx	Icpx	Icpx	Iol	AR	Ianf	AR	Mx
SiO2	0.02	0.12	0.38	0.29	0.03	0.03	0.00	0.03	0.28	0.27	0.03	0.16	0.07	0.86	0.12	0.18	0.00	0.03	0.02	0.02
TiO2	18.77	24.06	22.86	23.71	20.35	20.23	20.74	20.56	23.70	24.34	18.63	19.75	23.25	13.38	17.82	17.70	18.34	15.36	18.60	17.88
Cr2O3	0.19	0.16	0.13	0.18	0.11	0.13	0.13	0.17	0.16	0.18	0.13	0.18	0.11	0.23	0.19	0.49	0.52	0.45	0.12	0.25
Al2O3	1.93	1.27	1.32	1.24	5.04	5.10	4.63	4.58	2.03	2.05	2.78	2.35	1.90	2.54	2.65	4.55	6.09	6.24	5.10	2.71
V2O3	0.36	0.27	0.25	0.27	0.33	0.34	0.34	0.32	0.24	0.30	0.38	0.31	0.23	0.41	0.39	0.52	0.47	0.43	0.41	0.38
CaO	0.01	0.12	0.26	0.29	0.00	0.05	0.05	0.02	0.47	0.04	0.03	0.12	0.25	0.25	0.15	0.03	0.06	0.09	0.04	0.03
MnO	0.91	1.07	0.93	1.16	0.92	0.96	1.00	1.00	1.22	1.19	0.98	1.03	1.22	0.37	1.04	0.76	0.38	0.34	0.82	0.83
MgO	2.72	2.84	3.03	2.87	3.44	3.37	3.44	3.38	2.40	2.87	2.32	2.27	2.60	2.47	2.25	2.91	5.28	6.99	3.63	2.16
Fe2O3	30.80	19.80	20.93	19.45	24.78	24.96	24.25	24.65	18.25	18.36	30.19	27.08	20.59	36.09	31.22	27.72	29.33	35.62	29.40	32.74
FeO	43.52	47.28	45.89	46.52	44.55	44.46	44.51	44.54	47.03	47.97	44.19	44.75	46.56	39.36	43.27	42.44	41.08	35.63	43.24	44.44
total	99.21	96.99	95.98	95.98	99.57	99.62	99.09	99.23	95.76	97.58	99.66	98.00	96.77	95.95	99.09	97.29	101.54	101.17	101.38	101.43
Structural formula (a.p.f.u.)																				
Si	0.01	0.04	0.12	0.09	0.01	0.01	0.00	0.01	0.09	0.08	0.01	0.05	0.02	0.26	0.04	0.05	0.00	0.01	0.01	0.01
Ti	4.17	5.45	5.21	5.41	4.40	4.37	4.51	4.47	5.42	5.45	4.11	4.44	5.27	3.07	3.96	3.94	3.83	3.19	3.96	3.89
Cr	0.04	0.04	0.03	0.04	0.03	0.03	0.03	0.04	0.04	0.04	0.03	0.04	0.03	0.05	0.04	0.11	0.11	0.10	0.03	0.06
Al	0.67	0.45	0.47	0.45	1.71	1.73	1.58	1.56	0.73	0.72	0.96	0.83	0.67	0.91	0.92	1.59	1.99	2.03	1.70	0.92
V	0.09	0.07	0.06	0.07	0.08	0.08	0.08	0.07	0.06	0.07	0.09	0.07	0.05	0.10	0.09	0.12	0.10	0.10	0.09	0.09
Fe(iii)	6.85	4.48	4.78	4.44	5.36	5.40	5.28	5.36	4.17	4.11	6.67	6.09	4.67	8.28	6.95	6.18	6.13	7.39	6.26	7.13
Fe(ii)	10.75	11.90	11.64	11.81	10.71	10.69	10.77	10.77	11.95	11.94	10.85	11.17	11.73	10.03	10.70	10.51	9.54	8.22	10.22	10.76
Mn	0.23	0.27	0.24	0.30	0.22	0.23	0.24	0.24	0.31	0.30	0.24	0.26	0.31	0.10	0.26	0.19	0.09	0.08	0.20	0.20
Mg	1.20	1.28	1.37	1.30	1.48	1.44	1.48	1.46	1.09	1.28	1.02	1.01	1.17	1.12	0.99	1.29	2.18	2.87	1.53	0.93
Ca	0.00	0.04	0.08	0.09	0.00	0.02	0.02	0.01	0.15	0.01	0.01	0.04	0.08	0.08	0.05	0.01	0.02	0.03	0.01	0.01
TOTAL	24	24	24	24	24	24	24	24	24	24	24	24	24	24	24	24	24	24	24	24

Table IV.5a: Electron microprobe analysis to oxides - spinels (s.l.)

Occurrence	LVC flow																			
	rm43	rm43	rm43	rm43	rm43	rm43	rm43	rm43	rm43	rm43	rm43	rm43	rm43	rm43	rm43	rm43	rm43	rm43	rm43	rm43
sample	b3e	b3f	b4a	b4b	b4c	b4d	b4e	b5a	b5a	b5a	b5a	b5b	b5c	b5d	b5e	b5f	b5g	b5h	b5i	b6a
type	Mx	Mx	Icpx	Icpx	Icpx	Icpx	Mx	PC	PC	PR	PR	MP	MP	Mx	Mx	Icpx	Icpx	Icpx	Icpx	PC
SiO2	0.01	0.03	0.79	0.37	0.03	1.03	0.11	0.06	0.08	0.06	0.06	0.05	0.02	12.19	0.31	0.11	0.21	0.05	0.07	0.08
TiO2	24.34	18.14	17.46	18.61	18.74	19.76	18.67	17.59	17.80	17.67	17.61	19.15	19.08	17.60	24.35	17.53	24.53	18.21	19.14	18.21
Cr2O3	0.15	0.17	1.03	0.18	0.18	0.74	0.19	0.61	0.65	0.43	0.58	0.19	0.17	0.00	0.17	0.17	0.22	0.17	0.17	0.12
Al2O3	2.42	2.94	6.75	6.08	4.20	4.09	2.57	6.83	6.47	6.51	6.24	2.76	2.61	3.96	2.00	6.60	2.09	2.66	3.03	6.23
V2O3	0.31	0.38	0.41	0.28	0.37	0.32	0.37	0.38	0.35	0.36	0.33	0.34	0.37	0.04	0.23	0.34	0.29	0.38	0.38	0.37
CaO	0.10	0.05	0.09	0.38	0.17	0.84	0.10	0.00	0.00	0.06	0.05	0.06	0.06	3.31	0.23	0.14	0.17	0.17	0.17	0.00
MnO	0.92	0.80	0.52	0.83	0.86	0.86	0.87	0.66	0.66	0.71	0.68	0.88	0.98	0.92	1.17	0.63	1.18	0.84	0.88	0.54
MgO	3.16	2.64	4.01	4.29	3.17	3.02	2.23	4.25	4.19	4.10	4.12	2.58	2.46	9.34	2.68	4.20	2.82	2.23	2.78	4.07
Fe2O3	20.76	32.50	26.07	27.21	29.45	24.01	30.22	29.24	29.02	29.57	29.28	30.15	31.02	6.02	18.68	29.71	19.13	31.40	30.11	28.65
FeO	48.38	44.09	42.69	42.14	43.54	44.86	44.54	41.97	42.18	42.11	41.73	44.75	44.97	44.50	48.28	41.76	48.51	44.10	44.46	42.66
total	100.53	101.74	99.81	100.34	100.72	99.51	99.86	101.59	101.39	101.59	100.67	100.91	101.74	97.88	98.11	101.19	99.17	100.21	101.18	100.92
Structural formula (a.p.f.u.)																				
Si	0.00	0.01	0.22	0.10	0.01	0.30	0.03	0.02	0.02	0.02	0.02	0.01	0.01	3.25	0.09	0.03	0.06	0.02	0.02	0.02
Ti	5.28	3.92	3.72	3.95	4.04	4.28	4.12	3.69	3.74	3.71	3.74	4.17	4.13	3.52	5.43	3.69	5.41	4.01	4.14	3.86
Cr	0.03	0.04	0.23	0.04	0.04	0.17	0.04	0.13	0.14	0.10	0.13	0.04	0.04	0.00	0.04	0.04	0.05	0.04	0.04	0.03
Al	0.82	0.99	2.25	2.02	1.42	1.39	0.89	2.24	2.13	2.14	2.07	0.94	0.88	1.24	0.70	2.18	0.72	0.92	1.03	2.07
V	0.07	0.09	0.09	0.06	0.09	0.07	0.09	0.08	0.08	0.08	0.07	0.08	0.09	0.01	0.05	0.08	0.07	0.09	0.09	0.08
Fe(iii)	4.51	7.02	5.55	5.78	6.35	5.21	6.67	6.13	6.11	6.22	6.22	6.57	6.72	1.21	4.17	6.26	4.22	6.91	6.52	6.07
Fe(ii)	11.67	10.59	10.10	9.94	10.44	10.81	10.93	9.78	9.87	9.84	9.84	10.84	10.82	9.91	11.97	9.78	11.89	10.79	10.70	10.04
Mn	0.22	0.19	0.12	0.20	0.21	0.21	0.22	0.16	0.16	0.17	0.16	0.22	0.24	0.21	0.29	0.15	0.29	0.21	0.22	0.13
Mg	1.36	1.13	1.69	1.80	1.35	1.30	0.98	1.77	1.75	1.71	1.73	1.11	1.06	3.71	1.19	1.75	1.23	0.97	1.19	1.71
Ca	0.03	0.02	0.03	0.11	0.05	0.26	0.03	0.00	0.00	0.02	0.02	0.02	0.02	0.94	0.07	0.04	0.05	0.05	0.05	0.00
TOTAL	24	24	24	24	24	24	24	24	24	24	24	24	24	24	24	24	24	24	24	24

Table IV.5a: Electron microprobe analysis to oxides - spinels (s.l.)

Occurrence	LVC flow						Eiras do Faião sill													
	rm43	rm43	rm43	rm43	rm43	rm43	rm47	rm47	rm47	rm47	rm47	rm47	rm47	rm47	rm47	rm47	rm47	rm47	rm47	rm47
sample	b6a	b6a	b6a	b6a	b6a	b6a	b1a	b1a	b1b	b1c	b1d	b1e	b1f	b2a	b2a	b2b	b2b	b2c	b2d	b2e
type	PC	PC	PR	PR	PR	PR	PC	PR	Mx	Mx	Mx	IGCpx	IGCpx	Xen	Xen	Xen	Xen	Xen	Xen	Xen
SiO2	0.07	0.00	0.06	0.06	0.04	0.02	0.49	1.33	0.50	0.39	0.63	0.36	0.10	1.62	2.07	1.66	0.90	2.07	2.16	1.94
TiO2	18.82	17.87	18.09	18.78	18.21	18.39	16.67	19.09	13.25	15.50	13.66	15.29	17.21	10.72	9.96	16.39	11.31	4.07	2.66	13.47
Cr2O3	0.14	0.14	0.22	0.22	0.27	0.29	0.10	0.13	0.09	0.09	0.12	0.14	0.14	0.14	0.17	0.13	0.14	0.14	0.10	0.10
Al2O3	6.13	7.26	6.84	6.14	6.24	6.98	0.33	0.32	0.32	0.38	0.26	0.38	0.29	0.55	0.54	0.55	0.39	0.52	0.58	0.51
V2O3	0.38	0.41	0.41	0.34	0.38	0.34	0.27	0.18	0.28	0.23	0.26	0.32	0.29	0.28	0.25	0.28	0.27	0.32	0.30	0.25
CaO	0.00	0.00	0.02	0.02	0.03	0.07	0.20	0.45	0.19	0.13	0.41	0.12	0.49	0.30	0.32	0.34	0.16	0.44	0.48	0.42
MnO	0.59	0.64	0.74	0.61	0.61	0.68	3.47	2.58	1.86	3.47	2.52	3.53	4.00	0.49	0.47	0.47	1.29	0.47	0.34	0.37
MgO	4.82	4.13	4.09	4.00	3.98	4.69	0.00	0.07	0.00	0.03	0.01	0.03	0.00	0.04	0.05	0.04	0.09	0.10	0.04	0.05
Fe2O3	29.03	28.97	28.40	27.61	28.55	27.99	32.83	24.56	38.05	35.30	36.50	36.05	32.35	38.37	37.28	27.36	41.10	48.36	51.48	32.14
FeO	42.45	42.55	42.50	43.16	42.65	41.82	42.58	45.65	40.41	41.38	39.78	41.30	41.49	40.06	39.24	45.36	39.79	33.42	32.70	42.86
total	102.42	101.97	101.36	100.93	100.98	101.28	96.93	94.37	94.94	96.90	94.17	97.50	96.35	92.56	90.35	92.56	95.46	89.91	90.84	92.11
Structural formula (a.p.f.u.)																				
Si	0.02	0.00	0.02	0.02	0.01	0.01	0.15	0.42	0.16	0.12	0.20	0.11	0.03	0.53	0.69	0.54	0.29	0.70	0.72	0.63
Ti	3.91	3.73	3.80	3.98	3.86	3.85	3.90	4.55	3.17	3.63	3.30	3.56	4.05	2.62	2.49	3.98	2.69	1.03	0.67	3.29
Cr	0.03	0.03	0.05	0.05	0.06	0.06	0.03	0.03	0.02	0.02	0.03	0.03	0.03	0.04	0.04	0.03	0.04	0.04	0.03	0.03
Al	2.00	2.37	2.25	2.04	2.07	2.29	0.12	0.12	0.12	0.14	0.10	0.14	0.11	0.21	0.21	0.21	0.15	0.21	0.23	0.20
V	0.09	0.09	0.09	0.08	0.09	0.08	0.07	0.05	0.07	0.06	0.07	0.08	0.07	0.07	0.07	0.07	0.07	0.09	0.08	0.07
Fe(iii)	6.03	6.05	5.97	5.85	6.05	5.86	7.68	5.85	9.12	8.28	8.81	8.40	7.62	9.39	9.32	6.65	9.79	12.22	12.89	7.86
Fe(ii)	9.81	9.87	9.93	10.16	10.04	9.73	11.07	12.09	10.77	10.78	10.67	10.70	10.86	10.89	10.91	12.25	10.53	9.39	9.10	11.65
Mn	0.14	0.15	0.17	0.15	0.14	0.16	0.91	0.69	0.50	0.92	0.68	0.92	1.06	0.13	0.13	0.13	0.35	0.13	0.10	0.10
Mg	1.98	1.71	1.71	1.68	1.67	1.94	0.00	0.03	0.00	0.01	0.01	0.01	0.00	0.02	0.03	0.02	0.04	0.05	0.02	0.03
Ca	0.00	0.00	0.01	0.01	0.01	0.02	0.06	0.15	0.07	0.04	0.14	0.04	0.16	0.10	0.11	0.12	0.06	0.16	0.17	0.14
TOTAL	24	24	24	24	24	24	24	24	24	24	24	24	24	24	24	24	24	24	24	24

Table IV.5a: Electron microprobe analysis to oxides - spinels (s.l.)

Occurrence	Eiras do Faião sill																LVC vent			
	rm47	rm47	rm47	rm47	rm47	rm47	rm47	rm47	rm47	rm47	rm47	rm47	rm47	rm47	rm47	rm47	RM66	RM66	RM66	RM66
sample	b2f	b2g	b2h	b2i	b3a	b3a	b3a	b3a	b3a	b3b	b3c	b3d	b3d	b3e	b3f	b3g	b1a	b1a	b1b	b1b
type	Mx	Mx	Mx	Icpx	PC	PM	PR	PR	PR	Xen	Xen	Xen	Xen	Xen	Icpx	Icpx	PC	PR	PC	PR
SiO2	0.70	0.43	0.15	0.38	1.42	1.74	1.84	2.43	1.80	1.71	1.87	1.76	1.93	2.23	1.48	1.47	0.05	0.25	0.80	3.42
TiO2	15.07	14.01	15.03	14.70	20.05	9.34	6.99	6.18	6.36	12.57	7.47	13.56	12.34	5.50	7.20	3.34	24.75	25.86	23.56	22.65
Cr2O3	0.11	0.11	0.09	0.12	0.14	0.12	0.16	0.14	0.11	0.14	0.09	0.15	0.11	0.10	0.12	0.12	1.34	0.47	1.54	1.11
Al2O3	0.35	0.32	0.33	0.38	0.50	0.52	0.43	0.47	0.50	0.64	0.52	0.56	0.51	0.62	0.40	0.52	2.88	2.39	3.61	4.66
V2O3	0.28	0.20	0.27	0.21	0.34	0.36	0.33	0.33	0.32	0.32	0.33	0.28	0.30	0.30	0.34	0.33	0.38	0.41	0.40	0.41
CaO	0.20	0.24	0.08	0.15	0.36	0.38	0.49	0.50	0.41	0.32	0.42	0.46	0.47	0.55	0.50	0.72	0.01	0.22	0.12	2.54
MnO	1.96	2.80	3.24	3.02	0.24	0.38	0.31	0.25	0.43	0.46	0.35	0.37	0.36	0.36	0.29	0.33	0.75	0.98	0.64	0.52
MgO	0.01	0.01	0.00	0.01	0.06	0.05	0.05	0.04	0.04	0.08	0.05	0.04	0.04	0.03	0.03	0.13	3.96	3.47	4.54	3.84
Fe2O3	34.08	38.14	37.03	36.39	21.76	40.72	45.00	44.79	45.56	34.48	42.54	32.56	35.03	46.11	45.93	53.26	19.05	16.13	18.21	12.35
FeO	42.28	40.61	41.07	40.87	49.03	38.90	36.73	36.69	35.77	41.87	36.62	42.84	42.08	35.47	36.69	32.58	48.23	49.03	47.06	47.86
total	95.03	96.88	97.28	96.22	93.91	92.50	92.35	91.82	91.29	92.59	90.26	92.58	93.16	91.25	92.97	92.79	101.41	99.20	100.48	99.35
Structural formula (a.p.f.u.)																				
Si	0.22	0.14	0.05	0.12	0.45	0.56	0.60	0.80	0.59	0.55	0.62	0.57	0.62	0.74	0.48	0.48	0.02	0.07	0.23	0.96
Ti	3.60	3.29	3.52	3.47	4.79	2.29	1.72	1.52	1.58	3.06	1.87	3.30	2.99	1.36	1.76	0.82	5.28	5.65	5.02	4.79
Cr	0.03	0.03	0.02	0.03	0.04	0.03	0.04	0.04	0.03	0.04	0.02	0.04	0.03	0.02	0.03	0.03	0.30	0.11	0.34	0.25
Al	0.13	0.12	0.12	0.14	0.19	0.20	0.17	0.18	0.19	0.25	0.20	0.21	0.19	0.24	0.15	0.20	0.96	0.82	1.20	1.54
V	0.07	0.05	0.07	0.05	0.09	0.09	0.09	0.09	0.09	0.08	0.09	0.07	0.08	0.08	0.09	0.09	0.09	0.10	0.09	0.09
Fe(iii)	8.14	8.96	8.67	8.60	5.20	9.98	11.06	11.05	11.34	8.41	10.69	7.93	8.48	11.45	11.24	13.09	4.07	3.53	3.88	2.61
Fe(ii)	11.22	10.60	10.68	10.73	13.03	10.59	10.04	10.06	9.89	11.34	10.22	11.59	11.33	9.79	9.98	8.89	11.44	11.91	11.14	11.25
Mn	0.53	0.74	0.85	0.80	0.07	0.11	0.09	0.07	0.12	0.13	0.10	0.10	0.10	0.10	0.08	0.09	0.18	0.24	0.15	0.12
Mg	0.00	0.01	0.00	0.00	0.03	0.02	0.03	0.02	0.02	0.04	0.03	0.02	0.02	0.01	0.01	0.06	1.67	1.50	1.92	1.61
Ca	0.07	0.08	0.03	0.05	0.12	0.13	0.17	0.17	0.14	0.11	0.15	0.16	0.16	0.19	0.17	0.25	0.00	0.07	0.04	0.77
TOTAL	24	24	24	24	24	24	24	24	24	24	24	24	24	24	24	24	24	24	24	24

Table IV.5a: Electron microprobe analysis to oxides - spinels (s.l.)

Occurrence	LVC neck																		Mafra gabbro	
sample	RM66 b1c	RM66 b1d	RM66 b2a	RM66 b2b	RM66 b2c	RM66 b2d	RM66 b2e	RM66 b2f	RM66 b3a	RM66 b3b	RM66 b3c	RM66 b3d	RM66 b3e	RM66 b3f	RM66 b3g	RM66 b3h	RM66 b3i	RM66 b3j	RM83 b1a	RM83 b1b
type	Mx	Mx	MP	MP	MP	Mx	MP	Mx	Iol	Iol	Mx	MP	MP	Mx	Amg	Amg	Amg	Amg	Iol	Iol
SiO2	0.06	0.49	0.17	0.03	0.81	0.14	0.07	0.20	0.09	0.02	0.25	0.03	0.06	0.17	0.06	0.03	0.08	0.02	0.08	0.24
TiO2	24.45	26.18	26.00	23.95	23.90	26.14	26.32	26.38	20.55	8.34	26.89	25.44	24.18	25.22	20.47	22.91	34.06	26.70	2.81	2.62
Cr2O3	0.47	0.24	0.66	1.65	1.84	0.29	0.67	0.52	7.01	18.85	0.48	0.90	1.11	0.21	0.33	0.65	0.60	0.49	35.01	32.04
Al2O3	2.28	2.09	2.58	3.52	3.22	1.78	2.20	1.79	5.42	10.43	1.94	2.71	2.76	1.59	2.23	2.48	1.72	2.17	18.05	16.28
V2O3	0.38	0.28	0.35	0.48	0.42	0.29	0.38	0.31	0.46	0.26	0.31	0.36	0.44	0.26	0.37	0.31	0.26	0.31	0.18	0.15
CaO	0.03	0.44	0.08	0.10	0.29	0.09	0.08	0.08	0.06	0.02	0.05	0.03	0.04	0.09	0.04	0.00	0.04	0.05	0.03	0.08
MnO	0.81	0.95	0.98	0.83	0.76	0.92	0.79	1.09	0.60	0.35	1.08	0.82	0.80	0.97	0.95	0.90	0.86	0.81	0.46	0.76
MgO	3.12	2.79	3.71	4.47	4.23	3.08	3.43	3.06	4.67	6.05	2.73	4.04	3.58	2.72	3.04	3.05	4.23	3.63	9.15	3.58
Fe2O3	20.31	14.88	16.29	19.60	17.87	17.14	16.82	15.64	17.87	24.66	14.24	18.39	20.27	18.25	28.28	23.16	2.31	16.10	11.71	13.91
FeO	48.86	50.18	49.10	46.51	47.64	50.08	50.11	49.95	43.56	31.36	51.09	48.56	48.21	49.40	45.15	47.55	55.65	49.88	23.06	30.96
total	100.77	98.51	99.90	101.13	100.98	99.95	100.87	99.01	100.27	100.33	99.07	101.28	101.45	98.87	100.91	101.02	99.80	100.16	100.54	100.61
Structural formula (a.p.f.u.)																				
Si	0.02	0.14	0.05	0.01	0.23	0.04	0.02	0.06	0.02	0.00	0.07	0.01	0.02	0.05	0.02	0.01	0.02	0.00	0.02	0.06
Ti	5.30	5.79	5.63	5.09	5.08	5.71	5.68	5.81	4.35	1.71	5.93	5.43	5.17	5.59	4.45	4.96	7.34	5.79	0.54	0.53
Cr	0.11	0.06	0.15	0.37	0.41	0.07	0.15	0.12	1.56	4.07	0.11	0.20	0.25	0.05	0.08	0.15	0.14	0.11	7.11	6.81
Al	0.78	0.72	0.88	1.17	1.07	0.61	0.74	0.62	1.80	3.36	0.67	0.91	0.93	0.55	0.76	0.84	0.58	0.74	5.46	5.16
V	0.09	0.07	0.08	0.11	0.09	0.07	0.09	0.07	0.10	0.06	0.07	0.08	0.10	0.06	0.09	0.07	0.06	0.07	0.04	0.03
Fe(iii)	4.40	3.29	3.53	4.16	3.80	3.75	3.63	3.45	3.79	5.07	3.14	3.93	4.34	4.05	6.15	5.01	0.50	3.49	2.26	2.81
Fe(ii)	11.77	12.34	11.83	10.98	11.26	12.17	12.01	12.24	10.26	7.17	12.52	11.53	11.47	12.18	10.91	11.44	13.34	12.02	4.95	6.96
Mn	0.20	0.24	0.24	0.20	0.18	0.23	0.19	0.27	0.14	0.08	0.27	0.20	0.19	0.24	0.23	0.22	0.21	0.20	0.10	0.17
Mg	1.34	1.22	1.59	1.88	1.78	1.33	1.47	1.34	1.96	2.46	1.19	1.71	1.52	1.19	1.31	1.31	1.81	1.56	3.50	1.44
Ca	0.01	0.14	0.02	0.03	0.09	0.03	0.02	0.03	0.02	0.01	0.02	0.01	0.01	0.03	0.01	0.00	0.01	0.02	0.01	0.02
TOTAL	24	24	24	24	24	24	24	24	24	24	24	24	24	24	24	24	24	24	24	24

Table IV.5a: Electron microprobe analysis to oxides - spinels (s.l.)

Occurrence	Mafra gabbro											Sines gabbro								
	RM83	RM83	RM83	RM83	RM83	RM83	RM83	RM83	RM83	RM83	RM83	rm 101	rm 101	rm 101	rm 101	rm 101	rm 101	rm 101	rm 101	rm 101
sample	b1c	b1d	b1d	b1e	b1f	b3a	b3b	b3c	b3d	b3e	b3f	b1a	b1a	b1b	b1c	b1d	b1e	b1f	b1g	b2a
type	Iol	Mx	Mx	Icpx	Icpx	Icpx	Mx	Mx	Mx	Mx	Mx	EC	EC	Iol	Iol	Icpx	Iol	Icpx	Icpx	C
SiO2	0.97	0.01	0.09	1.26	1.69	0.08	0.09	1.49	0.16	0.29	0.05	0.04	0.00	0.04	0.18	0.03	0.31	0.27	0.06	0.68
TiO2	15.16	7.32	27.40	21.02	3.95	17.15	5.33	12.13	20.73	5.79	14.06	6.93	5.21	5.04	0.23	3.63	25.76	5.04	5.69	4.76
Cr2O3	0.80	0.20	0.19	0.15	0.35	0.76	0.15	0.22	0.19	0.17	0.19	1.46	1.30	1.81	0.12	1.77	0.97	0.94	1.12	1.45
Al2O3	3.87	2.09	1.44	1.85	2.54	2.95	2.08	1.31	1.24	1.92	1.99	3.48	3.52	3.76	0.59	1.46	1.66	2.54	2.47	2.31
V2O3	0.37	0.40	0.28	0.41	0.64	0.49	0.25	0.48	0.31	0.48	0.40	0.92	0.96	1.04	0.04	1.03	0.48	0.88	0.87	0.87
CaO	0.02	0.02	0.05	0.04	0.05	0.43	0.10	0.06	0.07	0.02	0.02	0.00	0.01	0.01	0.00	0.01	0.03	0.02	0.02	0.00
MnO	0.81	0.30	1.31	1.30	0.33	0.46	0.70	1.14	1.10	0.46	0.86	0.18	0.23	0.22	0.05	0.19	0.44	0.29	0.25	0.25
MgO	2.37	0.67	1.14	2.90	1.91	1.98	0.55	1.06	0.75	0.69	0.62	0.78	0.46	0.58	0.22	0.39	1.06	0.42	0.16	1.33
Fe2O3	32.61	52.51	13.88	23.48	53.95	32.02	32.82	39.85	26.72	55.07	39.31	49.29	52.34	51.76	66.26	55.30	14.54	53.84	53.07	52.19
FeO	42.49	37.03	53.57	46.41	33.89	43.57	24.41	41.43	48.27	35.83	42.78	36.74	35.43	35.19	30.69	32.93	53.11	35.52	36.38	33.77
total	99.47	100.54	99.34	98.82	99.29	99.89	66.47	99.17	99.53	100.72	100.27	99.83	99.45	99.44	98.37	96.73	98.36	99.75	100.09	97.61
Structural formula (a.p.f.u.)																				
Si	0.28	0.00	0.03	0.37	0.50	0.02	0.04	0.45	0.05	0.09	0.01	0.01	0.00	0.01	0.06	0.01	0.09	0.08	0.02	0.21
Ti	3.33	1.65	6.12	4.65	0.88	3.78	1.80	2.74	4.67	1.30	3.16	1.56	1.18	1.14	0.05	0.86	5.80	1.14	1.29	1.09
Cr	0.18	0.05	0.05	0.04	0.08	0.18	0.05	0.05	0.04	0.04	0.04	0.35	0.31	0.43	0.03	0.44	0.23	0.22	0.27	0.35
Al	1.33	0.74	0.50	0.64	0.89	1.02	1.10	0.46	0.44	0.68	0.70	1.22	1.25	1.33	0.22	0.54	0.59	0.90	0.88	0.83
V	0.09	0.10	0.07	0.10	0.15	0.12	0.09	0.12	0.07	0.12	0.10	0.22	0.23	0.25	0.01	0.26	0.11	0.21	0.21	0.21
Fe(iii)	7.17	11.82	3.10	5.19	12.10	7.07	11.08	9.00	6.02	12.39	8.82	11.07	11.85	11.69	15.53	13.04	3.28	12.21	12.03	12.00
Fe(ii)	10.38	9.27	13.30	11.41	8.44	10.69	9.16	10.40	12.08	8.96	10.67	9.17	8.92	8.83	7.99	8.63	13.30	8.95	9.16	8.63
Mn	0.20	0.08	0.33	0.32	0.08	0.12	0.27	0.29	0.28	0.12	0.22	0.05	0.06	0.05	0.01	0.05	0.11	0.07	0.06	0.07
Mg	1.03	0.30	0.50	1.27	0.85	0.86	0.37	0.48	0.33	0.31	0.27	0.35	0.20	0.26	0.10	0.18	0.47	0.19	0.07	0.60
Ca	0.01	0.01	0.02	0.01	0.02	0.14	0.05	0.02	0.02	0.01	0.01	0.00	0.00	0.00	0.00	0.00	0.01	0.01	0.01	0.00
TOTAL	24	24	24	24	24	24	24	24	24	24	24	24	24	24	24	24	24	24	24	24

Table IV.5a: Electron microprobe analysis to oxides - spinels (s.l.)

Occurrence	Montelevar sill								Monchique gabbro					Monchique ne-syenite						
	rm50	rm50	rm50	rm50	rm50	rm50	rm50	rm50	mon84	mon84	mon84	mon84	mon84	749	749b1	749	749	749	749	749
sample	b1a	b1a	b1b	b1c	b1d	b1d	b3a	b3b	b1a	b1b	b3a	b3a	b3a	b1a	a	b1a	b1b	b1b	b1c	b1c
type	C	R	C	C	C	R	C	C	Icpx	Icpx	R	C	R	C	R	C	Ibio	Ibio	C	R
SiO2	2.48	0.35	3.00	0.66	0.41	2.39	0.21	0.78	0.10	0.04	0.00	0.11	0.02	0.00	0.05	0.05	1.54	0.05	0.02	0.04
TiO2	15.23	13.58	18.10	14.94	16.26	14.40	13.89	15.03	6.48	0.69	0.52	4.82	1.17	7.43	2.93	7.42	0.57	0.41	8.09	0.26
Cr2O3	0.17	0.18	0.15	0.14	0.15	0.13	0.24	0.16	0.11	0.11	0.14	0.12	0.11	0.22	0.19	0.15	0.19	0.17	0.25	0.13
Al2O3	0.35	0.58	0.30	0.44	0.41	0.31	0.68	0.74	0.96	0.34	0.36	1.44	0.54	0.17	0.57	0.17	0.27	0.04	0.04	0.09
V2O3	0.33	0.32	0.30	0.38	0.34	0.34	0.57	0.43	0.33	0.37	0.47	0.36	0.39	0.25	0.26	0.25	0.26	0.27	0.22	0.28
CaO	0.24	0.06	0.47	0.19	0.03	0.36	0.01	0.10	0.03	0.02	0.00	0.11	0.02	0.00	0.01	0.00	0.04	0.05	0.03	0.04
MnO	0.27	0.33	0.10	0.21	0.53	0.14	1.04	1.01	1.33	0.19	0.27	0.62	0.32	4.26	1.44	3.57	0.54	0.26	1.04	0.27
MgO	0.12	0.11	0.09	0.09	0.31	0.08	0.19	0.10	0.32	0.09	0.17	1.04	0.63	0.05	0.05	0.07	0.14	0.08	0.00	0.03
Fe2O3	29.86	39.49	22.08	35.47	34.26	31.45	38.73	35.28	54.23	66.81	67.72	55.50	66.61	54.68	61.41	53.99	62.06	67.96	50.73	68.06
FeO	46.43	43.08	49.25	44.37	45.05	45.47	42.37	44.27	35.22	31.50	31.37	32.51	31.28	33.92	32.09	34.32	32.20	31.21	36.58	31.06
total	95.47	98.09	93.83	96.87	97.75	95.06	97.92	97.89	99.10	100.18	101.00	96.62	101.08	100.99	99.00	99.99	97.80	100.49	97.00	100.26
Structural formula (a.p.f.u.)																				
Si	0.78	0.11	0.95	0.20	0.13	0.75	0.06	0.24	0.03	0.01	0.00	0.03	0.00	0.00	0.02	0.01	0.48	0.01	0.01	0.01
Ti	3.58	3.15	4.31	3.50	3.77	3.41	3.22	3.47	1.49	0.16	0.12	1.13	0.27	1.69	0.68	1.70	0.13	0.09	1.92	0.06
Cr	0.04	0.04	0.04	0.04	0.04	0.03	0.06	0.04	0.03	0.03	0.03	0.03	0.03	0.05	0.05	0.04	0.05	0.04	0.06	0.03
Al	0.13	0.21	0.11	0.16	0.15	0.12	0.25	0.27	0.35	0.12	0.13	0.53	0.19	0.06	0.21	0.06	0.10	0.02	0.01	0.03
V	0.08	0.08	0.07	0.09	0.08	0.08	0.14	0.11	0.08	0.09	0.11	0.09	0.09	0.06	0.07	0.06	0.06	0.07	0.06	0.07
Fe(iii)	7.03	9.15	5.26	8.31	7.94	7.45	8.99	8.16	12.50	15.41	15.49	13.03	15.14	12.44	14.29	12.40	14.56	15.66	12.02	15.72
Fe(ii)	12.15	11.10	13.03	11.55	11.61	11.96	10.92	11.38	9.02	8.07	7.97	8.48	7.90	8.58	8.30	8.76	8.40	7.99	9.64	7.97
Mn	0.07	0.09	0.03	0.05	0.14	0.04	0.27	0.26	0.34	0.05	0.07	0.16	0.08	1.09	0.38	0.92	0.14	0.07	0.28	0.07
Mg	0.06	0.05	0.04	0.04	0.14	0.04	0.09	0.04	0.15	0.04	0.08	0.48	0.28	0.02	0.02	0.03	0.06	0.04	0.00	0.02
Ca	0.08	0.02	0.16	0.06	0.01	0.12	0.00	0.03	0.01	0.00	0.00	0.04	0.01	0.00	0.00	0.00	0.01	0.01	0.01	0.01
TOTAL	24	24	24	24	24	24	24	24	24	24	24	24	24	24	24	24	24	24	24	24

Table IV.5a: Electron microprobe analysis to oxides - spinels (s.l.)

Occurrence	Monchique ne-syenite							Fontanelas seamount												
	749	749	749	749b2	749b2	749	749	at690	at690	at690	at690	at690	at690	at690	at690	at690	at690	at690	at690	at690
sample	b2a	b2b	b2c	c	c	b2d	b2e	b1a	b1b	b1c	b1d	b1e	b2f	b2f	b2g	b2g	b3a	b3b	b4a	b4b
type	Ibio	Ibio	R	C	R	Icpx	Icpx	Mx	Mx	Mx	Mx	Icpx	PC	PR	PC	PC	Mx	Mx	Mx	Mx
SiO2	0.11	0.02	0.00	0.04	0.01	0.02	0.03	0.85	1.84	0.14	1.36	9.93	0.08	0.07	0.08	0.09	1.63	0.09	0.09	1.97
TiO2	0.35	0.30	0.45	19.78	0.85	0.53	1.22	12.47	15.20	15.50	15.27	13.79	16.69	16.19	15.83	15.82	15.49	14.07	15.94	15.17
Cr2O3	0.16	0.16	0.22	0.20	0.20	0.21	0.20	5.43	0.48	0.16	0.26	0.85	0.32	0.36	0.16	0.17	0.18	3.42	0.16	0.52
Al2O3	0.05	0.06	0.08	0.17	0.06	0.10	0.19	9.94	8.08	7.61	7.51	8.93	6.89	7.48	5.58	6.51	7.92	8.10	7.34	7.67
V2O3	0.15	0.18	0.29	0.22	0.28	0.27	0.32	0.31	0.33	0.31	0.29	0.28	0.36	0.37	0.36	0.38	0.35	0.30	0.31	0.24
CaO	0.00	0.03	0.00	0.00	0.02	0.08	0.06	0.16	5.68	0.24	0.80	4.43	0.05	0.03	0.02	0.06	0.48	0.20	0.35	2.78
MnO	0.33	0.18	0.29	9.17	0.21	0.54	1.14	0.32	0.31	0.39	0.41	0.37	0.38	0.28	0.35	0.31	0.50	0.38	0.49	0.46
MgO	0.03	0.00	0.02	0.17	0.06	0.03	0.03	8.34	8.60	8.76	8.83	8.55	9.38	9.36	7.81	8.43	8.25	8.64	8.03	9.01
Fe2O3	68.01	67.73	67.73	29.66	67.21	67.87	65.86	29.77	34.55	34.31	31.85	10.68	33.74	34.05	35.94	35.40	29.85	33.02	33.14	31.83
FeO	31.28	31.05	31.25	39.76	31.71	31.12	30.98	32.17	30.45	32.93	33.43	38.90	33.39	33.23	34.71	34.02	35.21	31.80	33.97	31.99
total	100.45	99.71	100.33	99.16	100.61	100.77	100.03	99.77	105.53	100.36	100.02	96.70	101.26	101.41	100.86	101.18	99.86	100.01	99.81	101.63
Structural formula (a.p.f.u.)																				
Si	0.03	0.01	0.00	0.01	0.00	0.01	0.01	0.23	0.47	0.04	0.37	2.64	0.02	0.02	0.02	0.02	0.44	0.02	0.03	0.52
Ti	0.08	0.07	0.10	4.52	0.20	0.12	0.28	2.54	2.92	3.17	3.12	2.76	3.39	3.27	3.28	3.24	3.17	2.89	3.30	3.02
Cr	0.04	0.04	0.05	0.05	0.05	0.05	0.05	1.16	0.10	0.04	0.06	0.18	0.07	0.08	0.04	0.04	0.04	0.74	0.04	0.11
Al	0.02	0.02	0.03	0.06	0.02	0.03	0.07	3.17	2.43	2.44	2.40	2.80	2.19	2.37	1.81	2.09	2.54	2.60	2.38	2.40
V	0.04	0.05	0.07	0.05	0.07	0.07	0.08	0.07	0.07	0.07	0.06	0.06	0.08	0.08	0.08	0.08	0.08	0.07	0.07	0.05
Fe(iii)	15.68	15.74	15.64	6.78	15.47	15.59	15.22	6.06	6.63	7.03	6.50	2.14	6.85	6.89	7.46	7.26	6.11	6.78	6.86	6.35
Fe(ii)	8.02	8.02	8.02	10.10	8.11	7.95	7.96	7.28	6.50	7.50	7.59	8.67	7.53	7.47	8.01	7.75	8.01	7.25	7.82	7.09
Mn	0.09	0.05	0.08	2.36	0.06	0.14	0.30	0.07	0.07	0.09	0.09	0.08	0.09	0.06	0.08	0.07	0.11	0.09	0.11	0.10
Mg	0.01	0.00	0.01	0.08	0.03	0.01	0.01	3.37	3.27	3.55	3.57	3.40	3.77	3.75	3.21	3.43	3.35	3.51	3.29	3.56
Ca	0.00	0.01	0.00	0.00	0.01	0.03	0.02	0.05	1.55	0.07	0.23	1.26	0.02	0.01	0.01	0.02	0.14	0.06	0.10	0.79
TOTAL	24	24	24	24	24	24	24	24	24	24	24	24	24	24	24	24	24	24	24	24

Table IV.5a: Electron microprobe analysis to oxides - spinels (s.l.)

Occurrence	Fontanelas seamount												Loulé lamprophyre							
	at690	at690	at690	at690	at690	at690	at690	at690	at690	at690	at690	at690	C20	C20	C20	C20	C20	C20	C20	C20
sample	b4c	b4d	b4e	b4f	b4g	b4h	b4i	b4j	b4k	b4l	b4m	b4n	b1a	b1b	b1c	b1d	b3a	b3b	b3c	b3d
type	Mx	Mx	Xen	Xen	Xen	Xen	Xen	Xen	Xen	Xen	Xen	Xen	Mx	Mx	Mx	Icpx	Mx	Mx	Mx	IGCpx
SiO2	1.46	0.91	0.06	0.04	0.06	0.04	0.07	0.03	0.08	0.08	0.05	0.07	6.95	1.06	7.74	11.82	8.71	8.57	2.56	6.95
TiO2	15.42	15.31	6.53	5.86	5.80	7.10	6.22	7.17	6.98	6.96	6.80	6.63	15.43	8.12	17.48	15.39	13.40	20.28	17.24	14.09
Cr2O3	0.10	0.11	0.18	0.12	0.13	0.13	0.10	0.12	0.16	0.18	0.15	0.10	0.15	0.12	0.22	0.10	0.14	0.10	0.17	0.42
Al2O3	7.55	7.34	3.17	3.13	3.09	3.02	3.09	2.99	3.01	2.98	3.09	3.06	1.69	0.76	2.10	2.17	1.88	1.74	1.64	1.68
V2O3	0.34	0.31	0.46	0.49	0.49	0.45	0.41	0.51	0.48	0.45	0.49	0.49	0.25	0.20	0.25	0.19	0.29	0.20	0.22	0.30
CaO	3.19	0.30	0.06	0.01	0.07	0.02	0.11	0.03	0.07	0.31	0.03	0.05	8.87	0.55	7.49	11.04	8.58	7.25	2.24	5.55
MnO	0.49	0.73	0.87	0.73	0.74	0.80	0.78	0.88	0.69	0.68	0.87	0.91	0.89	1.18	1.72	0.79	1.39	0.97	5.20	2.18
MgO	7.63	6.03	1.32	1.03	1.20	1.21	1.58	1.22	1.95	1.74	1.20	1.25	0.01	0.02	0.12	0.04	0.01	0.00	0.15	0.14
Fe2O3	32.77	30.59	52.96	53.69	53.96	51.74	53.83	51.84	52.47	51.55	52.21	52.69	20.55	39.67	12.93	7.51	19.02	4.71	26.17	20.10
FeO	33.31	37.00	34.95	34.72	34.36	35.56	34.25	35.61	34.54	34.12	35.29	35.02	42.71	33.75	45.91	45.97	42.59	50.19	41.84	42.95
total	102.24	98.63	100.55	99.82	99.91	100.07	100.43	100.41	100.44	99.04	100.18	100.25	97.49	85.43	95.96	95.00	96.01	94.00	97.42	94.36
Structural formula (a.p.f.u.)																				
Si	0.39	0.26	0.02	0.01	0.02	0.01	0.02	0.01	0.02	0.02	0.02	0.02	2.03	0.37	2.28	3.42	2.56	2.56	0.77	2.11
Ti	3.09	3.24	1.45	1.32	1.30	1.59	1.39	1.60	1.55	1.57	1.52	1.48	3.38	2.16	3.87	3.35	2.96	4.56	3.92	3.21
Cr	0.02	0.02	0.04	0.03	0.03	0.03	0.02	0.03	0.04	0.04	0.03	0.02	0.03	0.03	0.05	0.02	0.03	0.02	0.04	0.10
Al	2.37	2.43	1.11	1.10	1.09	1.06	1.08	1.05	1.05	1.05	1.08	1.07	0.58	0.32	0.73	0.74	0.65	0.61	0.58	0.60
V	0.07	0.07	0.11	0.12	0.12	0.11	0.10	0.12	0.11	0.11	0.12	0.12	0.06	0.06	0.06	0.04	0.07	0.05	0.05	0.07
Fe(iii)	6.57	6.48	11.80	12.09	12.12	11.60	11.99	11.58	11.65	11.62	11.69	11.78	4.51	10.54	2.86	1.64	4.21	1.06	5.95	4.59
Fe(ii)	7.43	8.70	8.65	8.68	8.58	8.86	8.48	8.84	8.53	8.54	8.78	8.70	10.41	9.96	11.30	11.14	10.47	12.56	10.57	10.89
Mn	0.11	0.17	0.22	0.18	0.19	0.20	0.20	0.22	0.17	0.17	0.22	0.23	0.22	0.35	0.43	0.19	0.35	0.25	1.33	0.56
Mg	3.03	2.53	0.58	0.46	0.54	0.54	0.70	0.54	0.86	0.78	0.53	0.55	0.00	0.01	0.05	0.02	0.01	0.00	0.07	0.06
Ca	0.91	0.09	0.02	0.00	0.02	0.01	0.03	0.01	0.02	0.10	0.01	0.02	2.77	0.21	2.36	3.43	2.70	2.32	0.72	1.80
TOTAL	24	24	24	24	24	24	24	24	24	24	24	24	24	24	24	24	24	24	24	24

Table IV.5a: Electron microprobe analysis to oxides - spinels (s.l.)

Occurrence	Loulé lamprophyre	Paço d'ilhas sill					Cascais dyke					Sintra gabbro						
sample	C20 b3e	PI-b2-ox	PI-b2-ox	PI-b2-ox	PI-b2-ox	PI-b3-ox	RM90-b1-ox	RM90-b1-ox	RM90-b3-ox	RM90-b3-ox	RM90-b2-ox	RM11-b1-ox	RM11-b1-ox	RM11-b1-ox	RM11-b1-ox	RM11-b1-ox	RM11-b1-ox	RM11-b1-ox
type	IGCpx	Exs	Exs	Exs	Exs	C	C	Mx	Mx	Mx	Mx	C	R	Exs	Exs	Exs	C	R
SiO2	12.74	1.61	1.86	1.30	1.51	1.43	0.51	2.78	1.13	2.50	0.59	0.04	0.04	0.02	0.02	0.05	0.02	1.16
TiO2	16.30	8.80	21.53	5.03	4.85	17.68	17.27	18.59	19.57	21.61	58.59	3.83	3.94	4.11	4.64	3.70	4.45	3.26
Cr2O3	0.11	0.10	0.15	0.09	0.12	0.13	0.19	0.21	0.14	0.18	0.10	0.14	0.12	0.12	0.11	0.12	0.13	0.13
Al2O3	2.38	0.34	0.33	0.25	0.18	1.41	4.57	0.96	4.51	3.30	0.10	0.75	0.62	0.58	0.61	0.62	0.67	0.58
V2O3	0.23	0.21	0.32	0.21	0.14	0.32	0.37	0.33	0.42	0.43	0.43	0.32	0.32	0.29	0.28	0.30	0.28	0.23
CaO	12.30	0.23	0.24	0.15	0.17	0.29	0.03	0.55	0.07	0.11	0.27	0.02	0.01	0.01	0.01	0.00	0.00	0.35
MnO	0.65	0.25	0.30	0.30	0.30	1.30	0.39	0.26	0.60	0.55	0.23	0.39	0.36	0.30	0.42	0.27	0.33	0.26
MgO	0.06	0.06	0.02	0.05	0.00	0.09	2.30	0.85	1.87	1.14	0.95	0.10	0.09	0.06	0.05	0.07	0.06	0.45
Fe2O3	3.55	41.04	16.46	50.38	49.54	24.66	26.07	19.67	20.64	13.78	-55.40	60.61	60.62	60.16	58.85	60.75	58.84	59.14
FeO	46.73	37.88	50.39	34.55	34.35	45.66	42.98	47.40	46.61	50.93	79.92	34.41	34.56	34.70	34.95	34.34	34.73	34.30
total	95.04	90.51	91.58	92.30	91.16	92.96	94.68	91.58	95.57	94.54	85.78	100.63	100.66	100.35	99.94	100.23	99.50	99.85
Structural formula (a.p.f.u.)																		
Si	3.66	0.54	0.60	0.43	0.50	0.46	0.16	0.89	0.34	0.76	0.19	0.01	0.01	0.01	0.01	0.02	0.01	0.35
Ti	3.52	2.21	5.26	1.24	1.22	4.25	3.96	4.48	4.44	4.98	14.64	0.88	0.90	0.94	1.07	0.85	1.03	0.74
Cr	0.02	0.03	0.04	0.02	0.03	0.03	0.05	0.05	0.03	0.04	0.03	0.03	0.03	0.03	0.03	0.03	0.03	0.03
Al	0.80	0.13	0.12	0.10	0.07	0.53	1.64	0.36	1.61	1.19	0.04	0.27	0.22	0.21	0.22	0.22	0.24	0.21
V	0.05	0.06	0.08	0.05	0.04	0.08	0.09	0.08	0.10	0.11	0.12	0.08	0.08	0.07	0.07	0.07	0.07	0.06
Fe(iii)	0.77	10.30	4.02	12.48	12.42	5.94	5.98	4.75	4.69	3.18	0.00	13.84	13.85	13.79	13.54	13.95	13.60	13.52
Fe(ii)	11.21	10.56	13.69	9.51	9.57	12.21	10.96	12.71	11.77	13.04	8.35	8.73	8.78	8.84	8.94	8.76	8.92	8.71
Mn	0.16	0.07	0.08	0.08	0.09	0.35	0.10	0.07	0.15	0.14	0.07	0.10	0.09	0.08	0.11	0.07	0.09	0.07
Mg	0.02	0.03	0.01	0.02	0.00	0.04	1.05	0.41	0.84	0.52	0.47	0.05	0.04	0.03	0.02	0.03	0.03	0.20
Ca	3.78	0.08	0.08	0.05	0.06	0.10	0.01	0.19	0.02	0.04	0.10	0.01	0.00	0.00	0.00	0.00	0.00	0.12
TOTAL	24	24	24	24	24	24	24	24	24	24	24	24	24	24	24	24	24	24

Table IV.5a: Electron microprobe analysis to oxides - spinels (s.l.)

Occurrence	Sintra gabbro								
sample	RM11-b1-ox	RM11-b1-ox	RM11-b2-ox	RM11-b2-ox	RM11-b2-ox	RM11-b2-ox	RM11-b2-ox	RM11-b2-ox	RM11 b2-ox
type	Exs	Exs	C	C	R	R	C	Ianf	C
SiO2	0.04	0.01	0.03	0.06	0.08	0.04	0.06	0.06	0.03
TiO2	2.83	3.10	3.45	3.38	3.83	3.20	3.49	3.65	3.46
Cr2O3	0.15	0.13	0.13	0.15	0.17	0.12	0.12	0.12	0.15
Al2O3	0.56	0.58	0.59	0.55	0.47	0.48	0.38	0.41	0.60
V2O3	0.27	0.27	0.32	0.29	0.30	0.31	0.25	0.25	0.27
CaO	0.01	0.05	0.00	0.00	0.02	0.02	0.02	0.04	0.02
MnO	0.36	0.29	0.37	0.22	0.30	0.25	0.32	0.26	0.31
MgO	0.05	0.09	0.08	0.07	0.09	0.09	0.03	0.07	0.08
Fe2O3	62.64	62.23	61.53	61.63	60.65	61.70	61.64	61.37	61.41
FeO	33.50	33.69	34.07	34.20	34.42	33.74	34.18	34.36	34.07
total	100.40	100.44	100.57	100.54	100.33	99.94	100.50	100.59	100.4
Structural formula (a.p.f.u.)									
Si	0.01	0.00	0.01	0.02	0.02	0.01	0.02	0.02	0.01
Ti	0.65	0.71	0.79	0.77	0.88	0.74	0.80	0.83	0.79
Cr	0.04	0.03	0.03	0.04	0.04	0.03	0.03	0.03	0.04
Al	0.20	0.21	0.21	0.20	0.17	0.17	0.14	0.15	0.21
V	0.06	0.07	0.08	0.07	0.07	0.08	0.06	0.06	0.07
Fe(iii)	14.37	14.26	14.08	14.11	13.91	14.22	14.14	14.05	14.08
Fe(ii)	8.54	8.58	8.67	8.70	8.78	8.64	8.71	8.74	8.68
Mn	0.09	0.08	0.09	0.06	0.08	0.06	0.08	0.07	0.08
Mg	0.02	0.04	0.04	0.03	0.04	0.04	0.02	0.03	0.04
Ca	0.00	0.02	0.00	0.00	0.01	0.01	0.01	0.01	0.01
TOTAL	24	24	24	24	24	24	24	24	24

Table IV.5b: Electron microprobe analysis to oxides - ilmenites

Occurrence	Lomba dos Pianos sill						Ribeira d'Ilhas plug				LVC flow								Sines gabbro	
sample	rm9 b6a	rm9 b1a	rm9 b1b	rm9 b6b	rm9 b3a	rm9 b5a	rm36 b2a	rm36 b2a	rm36 b2a	rm36 b2b	rm43 b5a	rm43 b1a	rm43 b1a	rm43 b1a	rm43 b1b	rm43 b1c	rm43 b3a	rm43 b3b	rm 101 b1a	rm 101 b1b
type	MP	ExsP	ExsP	ExsP	AR	IGCpx	ExsP	ExsP	ExsP	AR	ExsMP	ExsP	ExsP	ExsP	ExsP	ExsP	AR	AR	Icpx	Icpx
SiO2	0.03	0.03	0.02	0.03	0.04	0.06	0.02	0.06	0.01	5.48	0.01	0.04	0.01	0.00	0.03	0.07	3.66	0.02	0.07	0.06
TiO2	51.48	51.79	52.23	51.48	52.03	40.93	51.36	51.95	51.56	48.04	53.58	54.30	54.77	54.36	54.32	53.82	49.08	54.78	51.89	51.21
Cr2O3	0.14	0.10	0.10	0.14	0.15	0.12	0.17	0.15	0.15	0.16	0.10	0.11	0.11	0.11	0.07	0.07	0.13	0.12	0.13	0.23
Al2O3	0.04	0.03	0.04	0.04	0.12	0.05	0.35	0.30	0.31	0.82	0.06	0.05	0.06	0.03	0.05	0.05	2.91	0.08	0.03	0.03
V2O3	0.03	0.09	0.10	0.03	0.09	0.19	0.21	0.17	0.20	0.03	0.01	0.08	0.03	0.06	0.03	0.00	0.09	0.07	0.11	0.09
CaO	0.01	0.06	0.06	0.01	0.17	0.10	0.04	0.07	0.07	5.16	0.04	0.01	0.01	0.01	0.01	0.14	0.21	0.10	0.03	0.08
MnO	1.18	1.16	1.20	1.18	0.63	0.84	0.62	0.83	0.66	0.45	1.14	0.65	0.61	0.68	0.58	1.01	0.78	0.88	1.14	1.14
MgO	2.72	2.65	2.65	2.72	5.34	2.11	7.45	7.06	7.18	11.37	4.53	5.87	5.84	5.89	5.86	5.21	4.25	6.24	1.30	1.46
Fe2O3	3.75	4.05	3.09	3.75	4.30	23.37	7.98	6.85	7.09	7.48	3.14	2.08	1.49	2.34	2.22	2.05	0.00	2.48	3.34	4.27
FeO	40.29	40.64	40.98	40.29	36.47	32.16	32.26	33.28	32.82	22.43	38.93	37.76	38.25	37.69	37.86	38.02	39.90	37.15	43.23	42.27
total	99.67	100.62	100.48	99.67	99.34	99.92	100.46	100.72	100.05	101.42	101.53	100.95	101.17	101.17	101.02	100.43	98.57	101.93	101.27	100.85
Structural formula (a.p.f.u.)																				
Si	0.00	0.00	0.00	0.00	0.00	0.00	0.00	0.00	0.00	0.24	0.00	0.00	0.00	0.00	0.00	0.00	0.18	0.00	0.00	0.00
Ti	1.92	1.92	1.94	1.92	1.91	1.55	1.84	1.86	1.86	1.61	1.94	1.96	1.97	1.95	1.96	1.96	1.78	1.95	1.93	1.91
Cr	0.01	0.00	0.00	0.01	0.01	0.00	0.01	0.01	0.01	0.01	0.00	0.00	0.00	0.00	0.00	0.00	0.00	0.00	0.00	0.01
Al	0.00	0.00	0.00	0.00	0.01	0.00	0.02	0.02	0.02	0.04	0.00	0.00	0.00	0.00	0.00	0.00	0.17	0.00	0.00	0.00
V	0.00	0.00	0.00	0.00	0.00	0.01	0.01	0.01	0.01	0.00	0.00	0.00	0.00	0.00	0.00	0.00	0.00	0.00	0.00	0.00
Fe(iii)	0.14	0.15	0.11	0.14	0.16	0.88	0.29	0.25	0.26	0.25	0.11	0.08	0.05	0.08	0.08	0.07	0.00	0.09	0.12	0.16
Fe(ii)	1.67	1.67	1.69	1.67	1.49	1.35	1.28	1.32	1.31	0.83	1.57	1.51	1.53	1.51	1.51	1.54	1.52	1.47	1.79	1.75
Mn	0.05	0.05	0.05	0.05	0.03	0.04	0.02	0.03	0.03	0.02	0.05	0.03	0.02	0.03	0.02	0.04	0.03	0.04	0.05	0.05
Mg	0.20	0.19	0.19	0.20	0.39	0.16	0.53	0.50	0.51	0.75	0.32	0.42	0.42	0.42	0.42	0.38	0.31	0.44	0.10	0.11
Ca	0.00	0.00	0.00	0.00	0.01	0.01	0.00	0.00	0.00	0.25	0.00	0.00	0.00	0.00	0.00	0.01	0.01	0.01	0.00	0.00
TOTAL	4.00	4.00	4.00	4.00	4.00	4.00	4.00	4.00	4.00	4.00	4.00	4.00	4.00	4.00	4.00	4.00	4.00	4.00	4.00	4.00

Exs - exsolved crystal; EP exsolved phenocryst, I - inclusion, GCpx - green cored clinopyroxene, cpx - clinopyroxene, biot - biotite, anf- amphibole, plag - plagioclase, Xen - crystal in xenolith, AR - amphibole reaction rim

Table IV.5b: Electron microprobe analysis to oxides - ilmenites

Occurrence	Sines gabbro														Monchique gabbro					
sample	rm 101 b2c	rm 101 b2a	rm 101 b2b	rm 101 b1a	rm 101 b1a	rm 101 b1b	rm 101 b1b	rm 101 b1a	rm 101 b1a	rm 101 b1b	rm 101 b2b	rm 101 b2b	rm 101 b2b	rm 101 b2c	mon84 b1a	mon84 b3a	mon84 b3a	mon84 b3b	mon84 b3b	rm50 b3a
type	Icpx	Icpx	Icpx	Exs	Exs	Exs	Exs	Exs	Exs	Exs	Exs	Exs	Exs	Exs	Icpx	Exs	Exs	Exs	Exs	Exs
SiO2	0.04	0.03	0.00	0.03	0.00	0.01	0.06	1.17	0.64	0.05	0.01	0.01	0.01	0.04	0.05	0.01	0.05	0.05	0.00	0.03
TiO2	51.59	49.87	52.11	52.60	52.23	52.30	51.48	51.18	51.42	51.93	52.93	52.49	52.47	52.78	51.27	53.07	51.70	52.41	52.61	49.75
Cr2O3	0.20	0.30	0.17	0.14	0.15	0.19	0.22	0.15	0.11	0.16	0.19	0.15	0.20	0.15	0.09	0.09	0.12	0.09	0.10	0.14
Al2O3	0.00	0.06	0.02	0.12	0.04	0.06	0.00	0.61	0.16	0.05	0.04	0.05	0.03	0.04	0.04	0.02	0.04	0.03	0.02	0.05
V2O3	0.10	0.17	0.06	0.05	0.09	0.04	0.12	0.03	0.08	0.02	0.06	0.04	0.08	0.05	0.00	0.06	0.06	0.06	0.00	0.11
CaO	0.00	0.05	0.03	0.01	0.01	0.02	0.03	0.02	0.01	0.02	0.02	0.01	0.01	0.00	0.07	0.05	0.07	0.01	0.00	0.00
MnO	1.21	0.72	1.04	0.70	0.98	0.81	0.95	0.83	0.75	1.16	0.72	0.80	0.68	0.90	5.00	5.95	4.96	3.92	4.38	0.62
MgO	0.25	0.84	0.90	1.86	0.54	0.99	0.35	2.85	2.43	0.71	2.54	2.20	1.86	1.76	1.35	1.81	1.69	3.47	2.60	0.75
Fe2O3	3.14	6.41	2.78	1.99	2.13	2.18	3.26	2.03	2.63	2.67	1.94	2.66	2.44	2.45	3.44	3.01	4.95	5.00	4.62	6.60
FeO	44.79	42.59	44.18	43.30	45.01	44.44	44.74	41.49	41.90	44.29	42.34	42.47	43.18	43.48	38.63	38.43	38.43	37.03	38.25	42.83
total	101.32	101.04	101.28	100.80	101.18	101.03	101.21	100.36	100.12	101.07	100.79	100.88	100.97	101.64	99.92	102.49	102.08	102.07	102.58	100.87
Structural formula (a.p.f.u.)																				
Si	0.00	0.00	0.00	0.00	0.00	0.00	0.00	0.06	0.03	0.00	0.00	0.00	0.00	0.00	0.00	0.00	0.00	0.00	0.00	0.00
Ti	1.93	1.87	1.94	1.95	1.95	1.95	1.93	1.88	1.91	1.94	1.96	1.95	1.95	1.95	1.93	1.94	1.90	1.90	1.91	1.87
Cr	0.01	0.01	0.01	0.01	0.01	0.01	0.01	0.01	0.00	0.01	0.01	0.01	0.01	0.01	0.00	0.00	0.00	0.00	0.00	0.01
Al	0.00	0.00	0.00	0.01	0.00	0.00	0.00	0.04	0.01	0.00	0.00	0.00	0.00	0.00	0.00	0.00	0.00	0.00	0.00	0.00
V	0.00	0.01	0.00	0.00	0.00	0.00	0.00	0.00	0.00	0.00	0.00	0.00	0.00	0.00	0.00	0.00	0.00	0.00	0.00	0.00
Fe(iii)	0.12	0.24	0.10	0.07	0.08	0.08	0.12	0.07	0.10	0.10	0.07	0.10	0.09	0.09	0.13	0.11	0.18	0.18	0.17	0.25
Fe(ii)	1.87	1.77	1.83	1.79	1.87	1.84	1.86	1.70	1.73	1.84	1.74	1.75	1.78	1.78	1.62	1.56	1.57	1.50	1.55	1.79
Mn	0.05	0.03	0.04	0.03	0.04	0.03	0.04	0.03	0.03	0.05	0.03	0.03	0.03	0.04	0.21	0.24	0.21	0.16	0.18	0.03
Mg	0.02	0.06	0.07	0.14	0.04	0.07	0.03	0.21	0.18	0.05	0.19	0.16	0.14	0.13	0.10	0.13	0.12	0.25	0.19	0.06
Ca	0.00	0.00	0.00	0.00	0.00	0.00	0.00	0.00	0.00	0.00	0.00	0.00	0.00	0.00	0.00	0.00	0.00	0.00	0.00	0.00
TOTAL	4.00	4.00	4.00	4.00	4.00	4.00	4.00	4.00	4.00	4.00	4.00	4.00	4.00	4.00	4.00	4.00	4.00	4.00	4.00	4.00

Table IV.5b: Electron microprobe analysis to oxides - ilmenites

Occurrence	Montelevar sill										Paço d'Ilhas sill									
sample	rm50 b3b	rm50 b1a	rm50 b3c	rm50 b3d	rm50 b1b	rm50 b1c	rm50 b1d	rm50 b3e	rm50 b3e	rm50 b1e	RM11-b1a	RM11-b1a	RM11-b1a	RM11-b1b	RM11-b1b	PI-b1a	PI-b1b	PI-b1c	PI-b1c	PI-b1d
type	Exs	Iplag	Icpx	Icpx	C	C	Exs	Exs	Exs	Exs	Exs	Exs	Exs	Exs	Exs	C	C	C	C	C
SiO2	0.04	0.03	0.00	0.01	0.20	0.03	0.06	0.01	0.02	0.02	0.01	0.07	0.03	0.00	0.02	0.01	0.00	0.03	0.02	0.03
TiO2	50.38	49.91	50.57	49.68	50.82	50.57	50.10	49.72	50.08	49.55	44.37	44.35	44.14	44.63	44.56	50.49	50.55	49.54	49.74	48.53
Cr2O3	0.15	0.09	0.11	0.08	0.16	0.14	0.12	0.11	0.14	0.08	0.14	0.13	0.14	0.16	0.12	0.13	0.12	0.13	0.12	0.10
Al2O3	0.05	0.05	0.06	0.06	0.01	0.02	0.00	0.06	0.05	0.02	0.00	0.00	0.00	0.00	0.00	0.03	0.03	0.00	0.01	0.00
V2O3	0.13	0.11	0.09	0.13	0.12	0.06	0.06	0.05	0.07	0.05	0.37	0.35	0.33	0.30	0.34	0.23	0.26	0.26	0.32	0.27
CaO	0.00	0.15	0.08	0.04	0.02	0.04	0.03	0.02	0.02	0.01	0.00	0.02	0.04	0.07	0.08	0.03	0.00	0.03	0.03	0.06
MnO	0.64	0.67	0.71	0.71	0.78	0.72	0.68	0.57	0.67	0.64	2.65	2.63	2.62	2.69	2.78	1.14	1.20	0.98	1.29	1.11
MgO	1.27	1.39	2.16	1.41	1.04	0.94	0.29	1.07	1.34	0.35	0.27	0.28	0.27	0.34	0.31	1.61	1.61	0.79	1.17	0.29
Fe2O3	6.03	6.09	6.14	7.45	4.56	4.91	6.45	7.12	6.38	7.03	16.64	16.29	16.98	16.54	16.37	6.26	6.13	7.04	7.08	8.00
FeO	42.45	41.58	40.82	41.41	43.28	43.08	43.89	42.22	41.98	43.30	36.76	36.77	36.56	36.74	36.65	41.36	41.39	42.16	41.31	41.97
total	101.14	100.07	100.74	100.98	100.98	100.50	101.67	100.96	100.73	101.04	101.21	100.90	101.10	101.47	101.22	101.30	101.29	100.96	101.09	100.34
Structural formula (a.p.f.u.)																				
Si	0.00	0.00	0.00	0.00	0.01	0.00	0.00	0.00	0.00	0.00	0.00	0.00	0.00	0.00	0.00	0.00	0.00	0.00	0.00	0.00
Ti	1.88	1.88	1.88	1.85	1.90	1.90	1.87	1.86	1.87	1.86	1.67	1.68	1.67	1.68	1.68	1.88	1.88	1.86	1.86	1.84
Cr	0.01	0.00	0.00	0.00	0.01	0.01	0.00	0.00	0.01	0.00	0.01	0.01	0.01	0.01	0.00	0.01	0.00	0.01	0.00	0.00
Al	0.00	0.00	0.00	0.00	0.00	0.00	0.00	0.00	0.00	0.00	0.00	0.00	0.00	0.00	0.00	0.00	0.00	0.00	0.00	0.00
V	0.01	0.00	0.00	0.01	0.00	0.00	0.00	0.00	0.00	0.00	0.01	0.01	0.01	0.01	0.01	0.01	0.01	0.01	0.01	0.01
Fe(iii)	0.22	0.23	0.23	0.28	0.17	0.18	0.24	0.27	0.24	0.26	0.63	0.62	0.64	0.62	0.62	0.23	0.23	0.26	0.26	0.30
Fe(ii)	1.76	1.74	1.69	1.72	1.80	1.80	1.82	1.76	1.75	1.81	1.54	1.55	1.54	1.54	1.54	1.71	1.71	1.76	1.72	1.77
Mn	0.03	0.03	0.03	0.03	0.03	0.03	0.03	0.02	0.03	0.03	0.11	0.11	0.11	0.11	0.12	0.05	0.05	0.04	0.05	0.05
Mg	0.09	0.10	0.16	0.10	0.08	0.07	0.02	0.08	0.10	0.03	0.02	0.02	0.02	0.02	0.02	0.12	0.12	0.06	0.09	0.02
Ca	0.00	0.01	0.00	0.00	0.00	0.00	0.00	0.00	0.00	0.00	0.00	0.00	0.00	0.00	0.00	0.00	0.00	0.00	0.00	0.00
TOTAL	4.00	4.00	4.00	4.00	4.00	4.00	4.00	4.00	4.00	4.00	4.00	4.00	4.00	4.00	4.00	4.00	4.00	4.00	4.00	4.00

Table IV.5b: Electron microprobe analysis to oxides - ilmenites

Occurrence	Paço d'ilhas sill															Cascais dyke				
sample	PI-b1-e	PI-b2a	PI-b2a	PI-b2a	PI-b2a	PI-b2b	PI-b2c	PI-b2d	PI-b3a	PI-b3b	PI-b3c	PI-b3d	PI-b3e	PI-b1f	PI-b1f	RM90-b1a	RM90-b1b	RM90-b2c	RM90-b3d	RM90-b3e
type	C	Exs	Exs	C	C	Exs	Exs	C	C	C	C	C	C	C	C	Mx	Mx	Mx	Mx	Exs
SiO2	0.01	0.03	0.04	0.00	0.03	0.39	0.04	0.02	0.00	0.00	0.03	0.04	0.03	0.04	0.00	0.07	0.01	0.06	0.03	0.00
TiO2	49.47	49.73	49.52	48.62	49.14	48.70	50.02	49.28	48.23	49.18	50.04	49.97	49.88	49.90	50.11	48.08	48.87	50.54	46.54	46.90
Cr2O3	0.12	0.13	0.12	0.17	0.07	0.13	0.13	0.08	0.13	0.15	0.11	0.14	0.17	0.10	0.07	0.13	0.10	0.10	0.14	0.10
Al2O3	0.00	0.00	0.03	0.00	0.00	0.03	0.00	0.00	0.02	0.00	0.02	0.00	0.02	0.00	0.00	0.01	0.03	0.04	0.57	0.48
V2O3	0.27	0.24	0.22	0.26	0.21	0.24	0.24	0.27	0.27	0.30	0.24	0.24	0.26	0.22	0.28	0.32	0.35	0.30	0.39	0.33
CaO	0.02	0.01	0.03	0.02	0.01	0.05	0.03	0.00	0.02	0.01	0.10	0.03	0.04	0.02	0.02	0.18	0.12	0.52	0.01	0.00
MnO	0.97	1.33	1.17	1.02	1.01	1.21	1.13	0.94	0.95	1.02	1.40	1.06	1.24	1.07	1.05	0.99	0.89	0.91	0.43	0.50
MgO	0.63	1.15	1.20	0.54	0.57	0.89	0.83	0.83	1.03	0.53	1.49	0.62	1.22	0.76	0.81	0.80	1.74	1.76	3.81	3.60
Fe2O3	7.47	6.36	6.22	8.06	7.19	7.81	5.49	6.81	6.68	7.21	6.42	6.06	6.47	6.66	6.06	8.60	8.29	3.53	14.56	14.18
FeO	42.36	41.36	41.23	41.73	42.19	41.40	42.38	41.91	40.55	42.25	40.85	42.78	41.44	42.47	42.53	40.67	39.81	40.82	34.65	35.27
total	101.32	100.34	99.77	100.41	100.42	100.85	100.27	100.14	97.87	100.65	100.69	100.94	100.75	101.24	100.93	99.85	100.20	98.56	101.12	101.36
Structural formula (a.p.f.u.)																				
Si	0.00	0.00	0.00	0.00	0.00	0.02	0.00	0.00	0.00	0.00	0.00	0.00	0.00	0.00	0.00	0.00	0.00	0.00	0.00	0.00
Ti	1.85	1.87	1.87	1.84	1.86	1.83	1.89	1.86	1.86	1.85	1.87	1.88	1.87	1.87	1.88	1.82	1.83	1.92	1.71	1.72
Cr	0.00	0.00	0.00	0.01	0.00	0.01	0.01	0.00	0.01	0.01	0.00	0.01	0.01	0.00	0.00	0.01	0.00	0.00	0.01	0.00
Al	0.00	0.00	0.00	0.00	0.00	0.00	0.00	0.00	0.00	0.00	0.00	0.00	0.00	0.00	0.00	0.00	0.00	0.00	0.03	0.03
V	0.01	0.01	0.01	0.01	0.01	0.01	0.01	0.01	0.01	0.01	0.01	0.01	0.01	0.01	0.01	0.01	0.01	0.01	0.02	0.01
Fe(iii)	0.28	0.24	0.24	0.30	0.27	0.29	0.21	0.26	0.26	0.27	0.24	0.23	0.24	0.25	0.23	0.33	0.31	0.13	0.53	0.52
Fe(ii)	1.76	1.73	1.73	1.75	1.77	1.73	1.78	1.76	1.74	1.77	1.70	1.79	1.73	1.77	1.77	1.72	1.66	1.72	1.41	1.44
Mn	0.04	0.06	0.05	0.04	0.04	0.05	0.05	0.04	0.04	0.04	0.06	0.04	0.05	0.05	0.04	0.04	0.04	0.04	0.02	0.02
Mg	0.05	0.09	0.09	0.04	0.04	0.07	0.06	0.06	0.08	0.04	0.11	0.05	0.09	0.06	0.06	0.06	0.13	0.13	0.28	0.26
Ca	0.00	0.00	0.00	0.00	0.00	0.00	0.00	0.00	0.00	0.00	0.01	0.00	0.00	0.00	0.00	0.01	0.01	0.03	0.00	0.00
TOTAL	4.00	4.00	4.00	4.00	4.00	4.00	4.00	4.00	4.00	4.00	4.00	4.00	4.00	4.00	4.00	4.00	4.00	4.00	4.00	4.00

Table IV.6: Electron microprobe analysis to Biotites

Occurrence	Monchique ne-syenite										Loulé lamprophyre									
	749	749	749	749	749	749	749	749	749	749	C20	C20	C20	C20	C20	C20	C20	C20	C20	C20
sample	b1a	b1a	b1a	b1a	b2a	b2a	b2a	b2a	b2b	b2b	b1a	b1a	b1a	b1a	b1b	b1b	b1b	b1c	b1c	b1c
type	C	C	R	R	C	C	R	R	C	R	C	C	R	R	C	C	R	C	R	R
SiO2	37.16	38.59	38.30	38.13	38.37	36.40	38.42	36.51	36.67	35.01	35.49	35.72	35.94	35.88	35.37	35.22	34.93	36.05	35.72	35.55
TiO2	2.34	2.31	2.33	2.38	2.29	3.34	2.20	3.18	3.15	2.82	6.72	6.50	6.74	6.23	6.90	6.93	7.05	6.69	6.40	6.88
Al2O3	11.61	11.15	11.16	11.34	11.24	12.44	11.78	12.48	12.19	12.64	15.71	15.62	15.67	15.69	15.21	15.13	15.28	15.03	15.14	15.15
FeO	16.66	17.34	16.15	16.66	16.88	18.73	16.69	18.95	17.96	21.05	8.84	9.40	8.89	11.14	8.57	8.71	8.99	8.75	9.61	8.50
MnO	0.97	0.92	0.89	0.92	0.90	1.02	0.91	1.04	1.03	1.01	0.09	0.12	0.09	0.09	0.09	0.02	0.09	0.08	0.08	0.09
MgO	15.39	14.80	15.64	14.73	15.20	13.24	14.93	13.12	14.10	13.07	18.17	18.00	18.27	16.70	17.84	17.47	17.57	17.98	17.33	18.02
CaO	0.00	0.00	0.00	0.00	0.00	0.00	0.00	0.00	0.00	0.01	0.02	0.04	0.01	0.00	0.02	0.03	0.00	0.01	0.04	0.00
Na2O	0.35	0.32	0.36	0.37	0.40	0.36	0.44	0.37	0.35	0.40	0.87	0.80	0.96	0.83	0.82	0.87	0.85	0.86	0.77	0.77
K2O	9.54	8.68	9.64	9.61	9.55	9.47	9.51	9.52	9.60	8.76	8.18	8.47	8.43	8.77	8.32	8.38	8.27	8.52	8.69	8.41
BaO	0.01	0.04	0.10	0.07	0.11	0.16	0.14	0.14	0.08	0.09	2.29	1.48	1.34	0.95	0.00	0.00	0.00	0.00	0.00	0.00
Cl	0.01	0.02	0.01	0.02	0.02	0.00	0.00	0.00	0.02	0.00	0.05	0.04	0.06	0.02	0.00	0.00	0.00	0.00	0.00	0.00
F	2.56	2.24	2.36	2.07	2.12	1.57	2.28	1.70	1.66	1.62	0.39	0.65	0.35	0.46	0.58	0.41	0.57	0.31	0.82	0.60
total	96.59	96.41	96.94	96.28	97.07	96.71	97.29	96.98	96.80	96.47	96.83	96.83	96.76	96.74	93.73	93.17	93.59	94.28	94.60	93.96
Structural formula (a.p.f.u.)																				
Si	5.74	5.96	5.91	5.89	5.92	5.62	5.93	5.64	5.66	5.41	5.48	5.52	5.55	5.54	5.46	5.44	5.39	5.57	5.52	5.49
Al iv	2.11	2.03	2.03	2.06	2.04	2.26	2.07	2.27	2.22	2.30	2.52	2.48	2.45	2.46	2.54	2.56	2.61	2.43	2.48	2.51
Al vi	0.00	0.00	0.00	0.00	0.00	0.00	0.08	0.00	0.00	0.00	0.34	0.36	0.40	0.39	0.23	0.19	0.17	0.30	0.27	0.25
Ti	0.27	0.27	0.27	0.28	0.27	0.39	0.26	0.37	0.37	0.33	0.78	0.75	0.78	0.72	0.80	0.81	0.82	0.78	0.74	0.80
Fe(ii)	2.15	2.24	2.09	2.15	2.18	2.42	2.15	2.45	2.32	2.72	1.14	1.21	1.15	1.44	1.11	1.12	1.16	1.13	1.24	1.10
Mn	0.13	0.12	0.12	0.12	0.12	0.13	0.12	0.14	0.13	0.13	0.01	0.02	0.01	0.01	0.01	0.00	0.01	0.01	0.01	0.01
Mg	3.54	3.41	3.60	3.39	3.50	3.05	3.44	3.02	3.24	3.01	4.18	4.14	4.20	3.84	4.11	4.02	4.04	4.14	3.99	4.15
Ca	0.00	0.00	0.00	0.00	0.00	0.00	0.00	0.00	0.00	0.00	0.00	0.01	0.00	0.00	0.00	0.00	0.00	0.00	0.01	0.00
Na	0.10	0.10	0.11	0.11	0.12	0.11	0.13	0.11	0.11	0.12	0.26	0.24	0.29	0.25	0.25	0.26	0.25	0.26	0.23	0.23
K	1.88	1.71	1.90	1.89	1.88	1.87	1.87	1.87	1.89	1.72	1.61	1.67	1.66	1.73	1.64	1.65	1.63	1.68	1.71	1.66
Ba	0.00	0.00	0.01	0.00	0.01	0.01	0.01	0.01	0.00	0.01	0.14	0.09	0.08	0.06	0.00	0.00	0.00	0.00	0.00	0.00
Cl	0.00	0.00	0.00	0.01	0.00	0.00	0.00	0.00	0.01	0.00	0.01	0.01	0.02	0.01	0.00	0.00	0.00	0.00	0.00	0.00
Total	8.08	7.85	8.09	7.95	8.07	7.97	8.05	7.97	8.07	8.04	8.48	8.50	8.60	8.45	8.14	8.06	8.09	8.30	8.20	8.19

P- Phenocryst, R- Rim, C- Core, M - Middle, Mx - Matrix, NO - Near Oxides

Table IV.6: Electron microprobe analysis to Biotites

Occurrence	Loulé lamprophyre										Eiras de Faião sill									
	C20	C20	C20	C20	C20	C20	C20	C20	C20	C20	rm47									
sample	b2a	b2a	b2b	b2b	b2c	b2c	b3a	b3a	b3b	b3b	b4a	PI-b1a	Pia	PI-b1b	PI-b2a	PI-b2b	PI-b3a	PI-b3a	PI-b3b	PI-b3b
type	C	R	C	R	C	R	C	R	C	R	Mx	NO	NO	NO	NO	NO	NO	NO	NO	NO
SiO2	35.41	34.61	34.75	35.19	35.38	35.10	35.95	35.91	35.17	34.62	35.35	38.77	39.39	39.90	41.79	42.13	38.69	38.71	40.02	39.69
TiO2	5.53	6.46	6.81	6.40	6.78	6.65	6.62	6.42	7.12	6.67	6.85	6.70	6.70	6.60	4.06	4.04	6.64	6.58	6.33	6.59
Al2O3	15.77	14.64	15.74	15.70	15.11	14.15	15.63	15.46	15.88	15.71	13.15	12.83	12.56	11.77	11.25	11.15	12.61	12.50	11.58	12.18
FeO	10.49	15.45	8.64	9.34	8.74	17.88	9.03	10.97	8.51	10.69	15.27	13.85	13.39	13.65	11.54	11.47	14.04	13.74	16.02	14.26
MnO	0.16	0.20	0.07	0.11	0.08	0.31	0.13	0.10	0.07	0.12	0.39	0.20	0.18	0.19	0.19	0.20	0.21	0.14	0.14	0.13
MgO	16.64	13.36	18.32	18.03	17.92	10.88	17.93	16.70	17.75	16.39	13.98	15.63	15.54	15.83	19.19	19.51	15.38	15.46	14.61	15.01
CaO	1.07	0.03	0.02	0.03	0.01	0.01	0.01	0.00	0.00	0.03	0.02	0.08	0.08	0.11	0.06	0.04	0.03	0.05	0.09	0.03
Na2O	0.59	0.71	0.89	0.93	0.82	0.57	0.83	0.86	0.83	0.77	0.71	0.78	0.71	0.72	0.72	0.73	0.68	0.67	0.64	0.74
K2O	7.38	8.67	8.35	8.63	8.44	8.66	8.49	8.58	8.12	8.49	9.01	7.73	7.88	7.95	8.14	8.37	8.01	8.09	8.10	8.09
BaO	1.52	1.04	1.85	1.03	0.00	0.00	1.33	1.00	2.50	1.71	0.00	0.67	0.68	0.57	0.03	0.02	0.66	0.62	0.07	0.32
Cl	0.05	0.05	0.07	0.04	0.00	0.00	0.04	0.03	0.03	0.03	0.00	0.05	0.05	0.13	0.14	0.12	0.04	0.05	0.12	0.03
F	0.30	0.75	0.39	0.67	0.51	0.70	0.50	0.57	0.46	0.90	0.00	2.89	2.85	3.24	3.48	3.76	2.89	2.73	2.47	2.54
total	94.92	95.96	95.91	96.10	93.78	94.92	96.46	96.60	96.43	96.11	97.24	100.17	100.00	100.66	100.58	101.54	99.87	99.33	100.17	99.61
Structural formula (a.p.f.u.)																				
Si	5.47	5.34	5.37	5.43	5.46	5.42	5.55	5.55	5.43	5.35	5.46	5.99	6.08	6.16	6.45	6.51	5.97	5.98	6.18	6.13
Al iv	2.53	2.66	2.63	2.57	2.54	2.57	2.45	2.45	2.57	2.65	2.39	2.01	1.92	1.84	1.55	1.49	2.03	2.02	1.82	1.87
Al vi	0.34	0.01	0.23	0.29	0.21	0.00	0.39	0.36	0.32	0.20	0.00	0.32	0.37	0.30	0.50	0.54	0.27	0.25	0.29	0.34
Ti	0.64	0.75	0.79	0.74	0.79	0.77	0.77	0.75	0.83	0.77	0.80	0.78	0.78	0.77	0.47	0.47	0.77	0.76	0.73	0.77
Fe(ii)	1.35	1.99	1.12	1.21	1.13	2.31	1.17	1.42	1.10	1.38	1.97	1.79	1.73	1.76	1.49	1.48	1.81	1.77	2.07	1.84
Mn	0.02	0.03	0.01	0.01	0.01	0.04	0.02	0.01	0.01	0.02	0.05	0.03	0.02	0.02	0.02	0.03	0.03	0.02	0.02	0.02
Mg	3.83	3.07	4.22	4.15	4.12	2.50	4.13	3.84	4.09	3.77	3.22	3.60	3.58	3.64	4.42	4.49	3.54	3.56	3.36	3.46
Ca	0.18	0.00	0.00	0.00	0.00	0.00	0.00	0.00	0.00	0.00	0.00	0.01	0.01	0.02	0.01	0.01	0.00	0.01	0.01	0.01
Na	0.18	0.21	0.27	0.28	0.25	0.17	0.25	0.26	0.25	0.23	0.21	0.23	0.21	0.22	0.22	0.22	0.20	0.20	0.19	0.22
K	1.45	1.71	1.65	1.70	1.66	1.71	1.67	1.69	1.60	1.67	1.77	1.52	1.55	1.57	1.60	1.65	1.58	1.59	1.60	1.59
Ba	0.09	0.06	0.11	0.06	0.00	0.00	0.08	0.06	0.15	0.10	0.00	0.04	0.04	0.03	0.00	0.00	0.04	0.04	0.00	0.02
Cl	0.01	0.01	0.02	0.01	0.00	0.00	0.01	0.01	0.01	0.01	0.00	0.01	0.01	0.03	0.04	0.03	0.01	0.01	0.03	0.01
Total	8.10	7.86	8.41	8.46	8.17	7.51	8.48	8.39	8.35	8.16	8.03	8.33	8.31	8.37	8.77	8.91	8.26	8.22	8.31	8.27

Table IV.6: Electron microprobe analysis to Biotites

Occurrence	Paço d'Ilhas sill		Sintra gabbro
sample	PI-b3c	PI-b3d	RM11-b2a
type	NO	NO	NO
SiO2	40.63	38.38	39.76
TiO2	4.75	6.68	5.23
Al2O3	10.97	12.99	12.37
FeO	12.58	13.16	12.59
MnO	0.10	0.17	0.18
MgO	18.18	15.95	16.41
CaO	0.05	0.08	0.13
Na2O	0.69	0.74	0.43
K2O	7.62	7.95	8.83
BaO	0.25	0.68	0.06
Cl	0.11	0.04	0.00
F	3.40	2.96	0.41
total	99.32	99.78	96.39
Structural formula (a.p.f.u.)			
Si	6.27	5.93	6.14
Al iv	1.73	2.07	1.86
Al vi	0.27	0.29	0.39
Ti	0.55	0.78	0.61
Fe(ii)	1.62	1.70	1.63
Mn	0.01	0.02	0.02
Mg	4.18	3.67	3.78
Ca	0.01	0.01	0.02
Na	0.21	0.22	0.13
K	1.50	1.56	1.74
Ba	0.02	0.04	0.00
Cl	0.03	0.01	0.00
Total	8.40	8.31	8.32

Table IV.7: Electron microprobe analysis to feldspathoids

Occurrence	Lomba dos Pianos sill			Malveira da Serra sill		Mafra gabbro	Eiras de Faião sill	Monchique ne-syenite						Loulé lamprophyre		
	rm9	rm9	rm9	rm25	rm25	rm83		749	749	749	749	749	749	c20	c20	c20
sample	b2a	b4a	b7a	b2a	b2b	b2a	rm47 b4a	b2a	b1a	b1a	b2a	b2a	b2b	b3a	b3b	b1a
type	Mx	Mx	Mx	Mx	Mx	Mx	Mx	R	C	R	R	C	C	Mx	Mx	Mx
mineral	analcite							nepheline								
SiO2	57.78	54.73	56.55	57.34	56.61	54.728	55.626	54.75	46.2	46.15	46.01	46.41	46.34	39.44	39.93	41.73
TiO2	0.003	0.014	0	0.012	0.02	0.027	0.003	0.012	0	0	0.019	0.037	0.001	0.03	0.003	0.025
Al2O3	22.98	23.95	24.22	25.04	23	27.063	21.674	22.34	31.38	31.37	31.52	30.65	31.19	33.21	33.17	31.32
FeO	0.038	0.06	0.078	0.085	0.131	0.007	0.147	0.152	0.601	0.656	0.661	0.591	0.636	0.433	0.204	0.637
MgO	0	0.019	0	0	0	0	0.042	0	0.019	0.02	0	0.001	0	0	0	0
CaO	0.312	1.088	0.616	1.303	0.626	0.454	0.283	0.081	0.26	0.223	0.277	0.246	0.251	0.114	0.182	0.124
Na2O	12.97	11.67	11.19	8.276	12.9	12.77	11.085	12.62	16.54	16.55	16.35	15.93	16.2	24.95	24.72	24.5
K2O	0.034	0.086	0.108	0.027	0.025	0.071	0.905	1.582	4.713	4.565	4.947	5.138	5.005	0.007	0.001	0.006
SrO	0	0.101	0.011	0	0	0	0.015	0	0	0	0	0	0	0	0	0
BaO	0.014	0	0.022	0	0	0	0.054	0.082	0.013	0.026	0	0	0.029	0	0	0.027
TOTAL	94.13	91.71	92.79	92.08	93.3	95.12	89.834	91.62	99.73	99.56	99.78	99	99.65	98.19	98.2	98.37

C - core; R - Rim, Mx - matrix

Annex V: CIPW normative compositions

Table V.1: CIPW normative compositions of the studied samples

occurrence	Foz da Fonte sill	Foz da Fonte sill	Foz da Fonte sill	Paço d'Ilhas sill	Paço d'Ilhas sill	Paço d'Ilhas sill	Paço d'Ilhas sill	Paço d'Ilhas sill	Paço d'Ilhas sill	Paço d'Ilhas sill	Paço d'Ilhas sill	Paço d'Ilhas sill	Paço d'Ilhas sill
sample ref.	FF 2	FF 3	FF 4	PI01	Pl02	PI03	PI04	PI05	PI06	PI07	PI08	PI09	PI10
Fe2O3/FeO	0.20	0.20	0.20	0.35	0.35	0.20	0.40	0.35	0.35	0.40	0.20	0.35	0.40
quartz	-	-	-	-	-	3.42	0.52	0.44	-	-	6.13	-	-
corundum	-	-	-	-	-	-	-	-	-	-	-	-	-
Orthoclase	13.49	14.20	15.99	20.94	18.71	7.90	21.79	16.01	18.54	23.52	11.38	20.59	24.71
Albite	3.02	12.71	9.95	42.79	37.00	24.74	41.94	36.48	36.04	42.13	21.12	37.49	42.39
Anorthite	25.35	25.96	25.34	14.29	19.95	20.02	12.46	20.77	19.69	14.54	17.61	18.14	11.87
Leucite	-	-	-	-	-	-	-	-	-	-	-	-	-
Nepheline	6.37	0.62	2.29	-	-	-	-	-	-	0.59	-	-	-
Diopside	29.24	12.99	14.15	8.14	4.41	12.34	9.95	9.18	3.57	8.35	15.87	6.57	7.41
Wollastonite	-	-	-	-	-	-	-	-	-	-	-	-	-
Hypersthene	-	-	-	1.29	1.61	16.92	4.84	7.81	8.97	-	14.11	0.70	6.16
Olivine	7.81	18.45	17.40	4.08	8.23	-	-	-	3.06	3.28	-	7.32	0.02
Magnetite	2.81	2.92	2.91	2.70	3.29	3.33	2.91	2.97	3.25	2.68	3.06	3.00	2.66
Ilmenite	9.14	9.30	9.13	3.69	4.38	8.10	3.68	4.16	4.41	3.22	8.08	4.01	3.01
Haematite	-	-	-	-	-	-	-	-	-	-	-	-	-
Apatite	1.59	1.60	1.61	1.39	1.62	1.87	1.28	1.44	1.66	1.09	1.39	1.43	1.17
TOTAL	98.83	98.77	98.78	99.32	99.19	98.65	99.36	99.27	99.20	99.40	98.75	99.26	99.40

occurrence	Paço d'Ilhas sill	Loulé lamprophyres	Loulé lamprophyres	Monchique basic rocks	Monchique basic rocks	Monchique basic rocks	Monchique basic rocks	Monchique basic rocks	Monchique basic rocks	Monchique ne-syenite	LVC neck
sample ref.	PI11	C-20	C-12-1	b 468 B	b 468 A	b 84 A	b 84 B	b 132	b 629	s 598	RM 1
Fe2O3/FeO	0.40	0.20	0.20	0.20	0.30	0.20	0.20	3.00	0.35	0.50	0.20
quartz	0.14	-	-	-	-	-	-	-	-	-	-
corundum	-	-	-	-	-	-	-	-	-	-	-
Orthoclase	22.24	-	-	-	18.90	14.75	15.80	15.85	23.78	40.72	9.71
Albite	40.80	-	-	-	-	-	3.98	5.29	17.72	23.60	15.25
Anorthite	14.41	5.62	13.67	16.70	8.92	16.40	16.79	13.41	11.35	2.29	23.21
Leucite	-	12.31	7.64	6.71	5.44	2.97	-	-	-	-	-
Nepheline	-	21.22	10.21	9.55	19.64	15.31	14.29	17.41	13.20	23.11	5.87
Diopside	9.19	47.22	46.07	34.70	31.35	29.21	26.65	28.88	17.93	5.90	21.68
Wollastonite	-	-	-	-	-	-	-	-	-	-	-
Hypersthene	5.11	-	-	-	-	-	-	-	-	-	-
Olivine	-	5.07	16.15	9.15	4.19	9.34	7.63	0.55	4.17	0.54	13.76
Magnetite	2.76	2.79	2.86	3.76	4.06	3.33	2.71	-	3.07	1.50	2.64
Ilmenite	3.46	7.82	7.18	14.54	8.90	9.17	8.26	8.01	5.80	1.70	5.87
Haematite	-	-	-	-	-	-	-	10.15	-	-	-
Apatite	1.27	3.43	3.31	5.71	4.42	1.95	2.77	2.37	2.21	0.33	0.91
TOTAL	99.39	105.47	107.10	100.81	105.81	102.43	98.87	101.93	99.24	99.69	98.89

occurrence	LVC neck	LVC neck	LVC neck	LVC neck	LVC neck	LVC neck	LVC neck	LVC flow	LVC flow	LVC flow	LVC flow	LVC flow	LVC flow
sample ref.	RM 4	RM 28	RM 29	RM 30	RM 66	RM 92	RM 57	RM 7	RM 42	RM 43	RM 69	RM 71	RM 80
Fe2O3/FeO	0.20	0.20	0.30	0.20	0.20	0.20	0.30	0.20	0.20	0.20	0.20	0.20	0.20
quartz	-	-	-	-	-	-	-	-	-	-	-	-	-
corundum	-	-	-	-	-	-	-	-	-	-	-	-	-
Orthoclase	10.61	9.69	15.11	12.06	6.11	11.98	13.64	8.28	11.29	10.38	11.66	13.34	5.00
Albite	12.44	17.36	14.24	4.46	11.34	2.66	19.71	0.89	10.49	11.88	3.93	16.20	7.80
Anorthite	22.54	23.26	20.38	20.79	21.17	17.43	19.38	20.70	22.92	22.44	20.62	22.02	19.66
Leucite	-	-	-	-	-	-	-	-	-	-	-	-	-
Nepheline	7.24	6.38	9.48	10.57	5.91	14.16	7.69	11.24	7.93	8.09	7.48	5.65	11.02
Diopside	20.57	16.76	17.26	24.07	27.89	31.22	15.03	28.58	21.15	21.31	27.59	15.31	26.13
Wollastonite	-	-	-	-	-	-	-	-	-	-	-	-	-
Hypersthene	-	-	-	-	-	-	-	-	-	-	-	-	-
Olivine	11.74	13.40	8.98	14.26	16.72	14.76	10.05	15.87	11.75	11.72	17.46	13.20	17.11
Magnetite	2.98	2.93	3.93	3.11	2.74	2.96	3.84	3.23	3.05	3.01	2.71	2.86	2.94
Ilmenite	8.28	7.57	6.62	7.55	5.90	7.60	7.27	8.69	8.00	7.85	6.14	8.56	7.82
Haematite	-	-	-	-	-	-	-	-	-	-	-	-	-
Apatite	2.37	1.44	2.92	1.85	1.05	1.63	2.31	1.14	2.14	2.08	1.25	1.67	1.29
TOTAL	98.78	98.79	98.92	98.71	98.83	104.40	98.93	98.64	98.73	98.76	98.83	98.82	98.78

occurrence	LVC neck	Lomba dos Pianos sill	Malveira da Serra sill	Eiras do Faião sill	Eiras do Faião sill	Montelevar Sill	Anços sill	Anços sill	Anços sill	Ribeira d'Ilhas plug	Ribeira d'Ilhas plug	Cascais dyke
sample ref.	RM 3	RM 9	RM 25	RM 46	RM 47	RM 50	RM 55	RM 67	RM 68	RM 36	RM 37	RM 52
Fe2O3/FeO	0.20	0.30	0.20	0.35	0.35	0.35	0.40	0.35	0.35	0.20	0.20	0.20
quartz	-	-	-	-	-	1.98	2.24	2.92	2.58	-	-	-
corundum	-	-	-	-	-	-	-	-	-	-	-	-
Orthoclase	9.00	11.04	14.19	19.43	21.13	15.97	18.11	15.86	16.16	11.12	9.01	16.19
Albite	16.81	25.08	6.20	25.25	23.61	34.45	40.23	35.60	37.20	1.06	4.68	19.92
Anorthite	24.24	25.61	21.33	7.46	9.32	21.77	21.03	23.80	23.86	20.93	17.73	24.80
Leucite	-	-	-	-	-	-	-	-	-	-	-	-
Nepheline	4.68	2.44	10.49	16.81	14.36	-	-	-	-	10.05	12.01	3.14
Diopside	20.58	10.03	18.53	15.60	14.26	9.67	1.14	3.23	3.50	29.60	25.42	0.78
Wollastonite	-	-	-	-	-	-	-	-	-	-	-	-
Hypersthene	-	-	-	-	-	7.96	9.99	10.69	9.27	-	-	-
Olivine	14.11	13.15	16.39	4.38	6.02	-	-	-	-	14.12	17.61	18.53
Magnetite	2.63	3.86	3.10	3.19	3.29	2.76	2.55	2.63	2.40	2.88	3.01	3.32
Ilmenite	5.90	6.02	6.54	4.95	5.07	3.49	2.85	3.23	3.07	7.24	7.32	7.66
Haematite	-	-	-	-	-	-	-	-	-	-	-	-
Apatite	0.93	1.69	1.94	2.18	2.14	1.21	1.27	1.40	1.34	1.80	1.94	4.33
TOTAL	98.88	98.92	98.70	99.25	99.19	99.27	99.42	99.36	99.37	98.80	98.73	98.66

occurrence	Cascais dyke	Sintra gabbro	Sintra gabbro	Sintra gabbro	Sintra gabbro	Sintra gabbro	Sintra gabbro	Sintra diorite	Sines diorite	Sines gabbro	Sines gabbro	Sines gabbro	Sines gabbro
sample ref.	RM 64	RM 11	RM 16	RM 17	RM 20	RM 22	RM 23	RM 24	RM 95	RM 96	RM 98	RM 99	RM 100
Fe2O3/FeO	0.20	0.20	0.20	0.20	0.20	0.20	0.20	0.30	0.30	0.20	0.20	0.20	0.20
quartz	-	-	-	-	-	-	-	-	-	-	-	-	-
corundum	-	-	-	-	-	-	-	-	-	-	-	-	-
Orthoclase	7.96	7.93	9.76	6.77	5.75	6.66	6.79	8.76	13.93	6.17	8.75	2.84	3.18
Albite	14.29	14.60	19.93	15.95	19.66	19.73	14.36	30.50	28.27	20.89	33.26	11.52	9.39
Anorthite	17.94	25.17	23.72	23.68	37.93	36.16	34.96	25.13	22.77	37.23	25.70	26.41	20.23
Leucite	-	-	-	-	-	-	-	-	-	-	-	-	-
Nepheline	2.16	7.53	7.27	8.04	5.44	4.82	6.73	0.13	-	4.85	4.27	-	0.64
Diopside	28.19	14.54	11.52	11.44	12.59	13.65	12.28	11.54	8.30	6.35	8.45	15.95	31.15
Wollastonite	-	-	-	-	-	-	-	-	-	-	-	-	-
Hypersthene	-	-	-	-	-	-	-	-	12.81	-	-	3.72	-
Olivine	19.60	13.84	13.26	15.92	8.39	8.07	11.59	11.67	2.39	11.67	8.98	30.31	23.90
Magnetite	2.60	2.96	2.81	3.24	2.22	2.34	2.56	3.50	3.51	2.45	2.00	3.34	3.36
Ilmenite	5.18	7.68	7.05	8.76	5.94	6.45	7.08	5.40	5.51	6.12	5.06	4.02	5.99
Haematite	-	-	-	-	-	-	-	-	-	-	-	-	-
Apatite	0.89	4.52	3.54	4.88	1.20	1.15	2.56	2.39	1.51	3.28	2.64	0.44	0.75
TOTAL	98.82	98.77	98.84	98.67	99.12	99.04	98.91	99.02	98.99	99.02	99.10	98.55	98.58

occurrence	Sines gabbro	Cascais dyke	Mafra gabbro	Fontanelas seamount	Fontanelas seamount	Fontanelas seamount	Fontanelas seamount	Fontanelas seamount	Fontanelas seamount
sample ref.	RM 101	RM 90	RM 83	AT 690A	AT 690B	AT 691A	AT 693P1	AT 693P2	AT 693E
Fe2O3/FeO	0.20	0.30	0.20	0.20	0.20	0.20	0.20	0.20	0.20
quartz	-	-	-	-	-	-	-	-	-
corundum	-	-	-	-	-	-	-	-	-
Orthoclase	3.29	10.95	7.50	-	-	-	-	-	0.91
Albite	9.60	30.56	6.91	-	-	-	-	-	18.50
Anorthite	24.22	25.81	20.49	32.54	31.75	29.48	27.36	27.87	31.13
Leucite	-	-	-	3.78	3.94	5.84	5.37	4.89	-
Nepheline	1.71	-	8.83	2.99	3.55	2.79	3.24	3.01	-
Diopside	27.59	15.48	35.02	45.99	46.78	52.72	45.07	46.81	22.88
Wollastonite	-	-	-	-	-	-	-	-	-
Hypersthene	-	1.92	-	-	-	-	-	-	9.98
Olivine	22.49	4.93	9.77	5.16	4.95	2.75	9.78	8.72	10.04
Magnetite	3.23	3.22	2.79	3.20	3.11	3.01	2.96	2.87	2.60
Ilmenite	6.02	5.01	6.39	9.21	8.80	7.21	6.93	7.14	2.56
Haematite	-	-	-	-	-	-	-	-	-
Apatite	0.49	1.23	1.14	1.61	1.54	2.20	1.71	1.54	0.24
TOTAL	98.63	99.11	98.85	104.49	104.42	106.00	102.43	102.86	98.85